Proceedings of the

12th International Probabilistic Workshop

Editors: Tom Lahmer, Maximilian Huber,
Thomas Most, Dirk Proske, Frank Werner

Weimar, November 5th and 6th 2014

Mitteilung 11
des Graduiertenkollegs 1462
"Bewertung gekoppelter numerischer und experimenteller Partialmodelle im Konstruktiven Ingenieurbau"'
Bauhaus-Universität Weimar, Germany, 2014

Editoren:
Jun.-Prof. Dr.rer.nat. T. Lahmer (tom.lahmer@uni-weimar.de)
Dr.-Ing. M. Huber (hubermaximilian@gmx.at)
Dr.-Ing. habil. T. Most (thomas.most@dynardo.de)
Dr.-Ing. habil. D. Proske (dirk.proske@boku.at)
Univ.-Prof. Dr.-Ing. habil. F. Werner (frank.werner@uni-weimar.de)

Berkaerstr. 9
99 423 Weimar
Germany

Keywords: probabilistic method, reliability, statistics, design of experiments

Printed by Bauhaus-Universitätsverlag Weimar, Schriftenreihe des DFG Graduiertenkollegs 1462 Modellqualitäten, Germany, 2014

Online Version
DOI: 10.1466/20141125.01

Preface

The proceedings at hand are the result from the 12th International Probabilistic Workshop held at the Bauhaus-University Weimar, 2014. It comprises a collection of more that 40 articles devoted to future oriented fields of stochastic theory, statistics and optimization both in applied sciences and theory. The total content is therefore a very valuable screen of the current state of art in the field and provides by the sketched outlooks a hint on the necessary activities in the next decade.

Among the covered topics and techniques applied are: Risk analysis, robust topology optimization, the quantification of uncertainties, sensitivity analysis, reliability methods, model quality assessment, design of experiments and surrogate modeling. The applications comprise fields of structural analysis, material science, geosciences, natural hazard and electrical engineering. Even though the list of covered topics is large, the common interest is in the term randomness.

The authors are both, well experienced specialists and young researchers, from more than 12 countries worldwide who share their deep interest in modern probability theory and stochastic simulation techniques. By the conducted scientific analysis, numerical simulations and discussion of results, the outcome of the conference might be regarded as a, however, small piece in our common attitude as Faustus said, to "see what holds the earth together in its innermost elements" (Goethe, Faust).

The workshop took place on the 04th and 05th November 2014 at Bauhaus-University Weimar, Germany and was organized jointly by Bauhaus-University Weimar (Germany), Deltares (The Netherlands), University of Natural Resources and Applied Life Sciences (Austria) and Dynardo GmbH (Germany). The proceedings are published in a series issued by the Research Training Group “Evaluation of Coupled Numerical and Experimental Partial Models in Civil Engineering” which is funded since 2008 by the German Research Foundation.

The organizers of the workshop want to use the chance to thank for their support: Anne-Marie Nöthlich, Dr. Lars Abrahamczyk and in particular Frank Zigan and Klaus Kraemer for all their efforts in establishing a unified layout of the proceeding contributions.

The organizers of the workshop want additionally like to thank to all contributors to the conference and are looking forward to the next meeting in this series 2015.

The local scientific committee 2014

Prof. Dr.-Ing. habil. F. Werner, Germany
Dr.-Ing. M. Huber, The Netherlands
Prof. Dr.rer.nat. T. Lahmer, Germany
Dr.-Ing. habil. T. Most, Germany
Dr.-Ing. habil. D. Proske, Austria

Contents

Extended Abstracts of the Keynote Speakers of the 12$^{\text{th}}$ International Probabilistic Workshop, Weimar 2014

A probabilistic framework for robust topology optimization of structures sensitive to geometric imperfections

Geert Lombaert[1], Miche Jansen[1], and Mattias Schevenels[2]

[1]Department of Civil Engineering, KU Leuven
Leuven, Belgium
e-mail: geert.lombaert@bwk.kuleuven.be
[2]Department of Architecture, KU Leuven
Leuven, Belgium
e-mail: mattias.schevenels@asro.kuleuven.be

Extended abstract

Topology optimization [2] is a powerful tool which has been used in various fields of application including civil engineering. The design obtained by classical topology optimization usually forms a very efficient solution for the specific problem at hand. In practice, however, its performance might be strongly reduced by uncertainties inevitably present in the system. This paper focuses on robust topology optimization while taking into account geometric imperfections. The methodology is illustrated in the design of a shallow arch. The design domain and boundary conditions for the problem are shown in figure 1. The design domain, which spans an angle $\alpha = 30°$ with an inner radius $R_{\text{in}} = 100$ m, outer radius $R_{\text{out}} = 104$ m and out-of-plane thickness $t = 1$ cm, is discretized by 800×60 finite elements. The structure is parameterized by assigning a physical material density $\bar{\rho}_e$ to

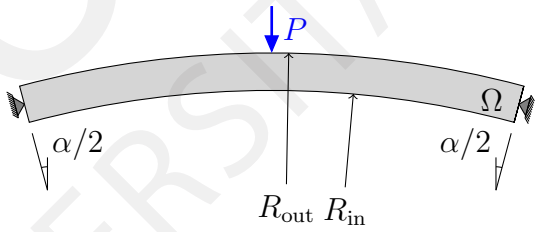

Figure 1: Topology optimization of shallow arch: design domain and boundary conditions.

every element in the design domain [2]. The volume densities indicate whether material is present ($\bar{\rho}_e = 1$) or absent ($\bar{\rho}_e = 0$). The aim of this problem is to find the material distribution that minimizes the end-compliance of the structure, limiting the volume fraction of the design to $V_{\max} = 30$ %. Note that in a nonlinear setting, this is not equivalent to minimizing the external work done by the force as in the linear case [3].

By considering the volume densities as continuous optimization variables, efficient gradient-based optimization algorithms can be used to solve the topology optimization problem. Intermediate densities ($0 < \bar{\rho}_e < 1$) lack a physical interpretation and are penalized using the Solid Isotropic Material with Penalization (SIMP) method [2] in this

study. Projection filters [4] are used to avoid mesh dependence of the solution and restrict the complexity of the optimized design. The vector of physical densities $\bar{\boldsymbol{\rho}}$ is therefore defined as a function of a new set of design variables $\boldsymbol{\rho} \in \mathbb{R}^{n_e}$ in two steps: (1) a density filter and (2) Heavyside projection.

Geometric imperfections in the design are modeled as a zero-mean Gaussian random field $\mathbf{p}(\mathbf{x}, \theta) : \Omega \times \Theta \to \mathbb{R}^n$ which is added to the coordinates $\mathbf{x}$ of the nominal design:

$$\tilde{\mathbf{x}}(\mathbf{x}, \theta) = \mathbf{x} + \mathbf{p}(\mathbf{x}, \theta) \tag{1}$$

where $\tilde{\mathbf{x}}(\mathbf{x}, \theta)$ are the uncertain material coordinates of the imperfect design. In the shallow arch problem, the horizontal and vertical components of imperfections are initially described by stationary random fields $p_i(\mathbf{x}, \theta)$ with squared exponential covariance function with $\sigma_{\mathrm{p}_i} = 0.33$ m and $l_{cx} = l_{cy} = 17.45$ m. Furthermore, it is assumed that the structure is placed correctly on the supports, i.e., the geometric imperfections are zero at the location of the supports. Conditional random fields are applied to incorporate these constraints [1]. The variance of the conditioned random field is shown in figure 2 which illustrates that the imperfections are small close to the supports and increase towards the center of the design domain.

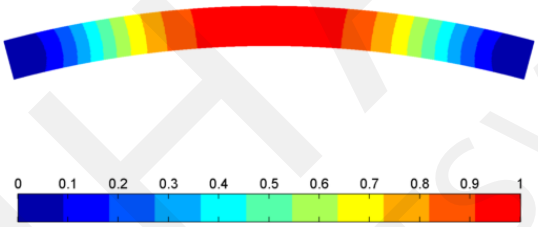

Figure 2: Normalized variation $C_{\mathrm{p}_i}/\sigma^2_{\mathrm{p}_i}$ of conditional random field of imperfections

The uncertainties in the minimum end-compliance of the structure due to the geometric imperfections are taken into account by defining the objective function as a weighted sum of the mean m_f and the standard deviation σ_f of the performance $f(\boldsymbol{\rho}) = \mathbf{P}^{\mathsf{T}}\mathbf{u}(\boldsymbol{\rho})$:

$$\begin{aligned} \min_{\boldsymbol{\rho}} \; & f_{\mathrm{R}}(\boldsymbol{\rho}) = m_f(\boldsymbol{\rho}) + \omega\sigma_f(\boldsymbol{\rho}) \\ \text{s.t. } & V(\boldsymbol{\rho}) - V_{\max} \leq 0 \\ & \mathbf{0} \leq \boldsymbol{\rho} \leq \mathbf{1} \end{aligned} \tag{2}$$

where the weighting parameter ω is chosen equal to 1. The displacements $\mathbf{u}(\boldsymbol{\rho})$ are computed by finite element analysis accounting for geometric nonlinear effects by means of a Total Lagrangian formulation for large displacements. The optimization is performed numerically by means of the method of moving asymptotes [6]. In each iteration of the optimization algorithm, the stochastic moments m_f and σ_f (and their sensitivities) have to be estimated. In order to avoid multiple calls to the nonlinear finite element solver per design iteration, a second-order perturbation method [5] is adopted. The design obtained by solving the robust optimization using the perturbation method is shown in figure 3. The performance of the imperfect designs is assessed by an elaborate Monte Carlo simulation with 10 000 samples. The results of the robust design and the nominal design,

Figure 3: Robust design for the shallow arch.

Design	f_{nl}	$\hat{m}_f$	$\hat{\sigma}_f$	$m_{f_{\text{nl}}}$	$\sigma_{f_{\text{nl}}}$	f_{Rnl}
Nominal	97.1	/	/	337.3	1033.3	1370.6
Robust	121.1	126.3	12.1	126.6	13.1	139.7

Table 1: Results for the optimized shallow arch designs including the nominal nonlinear performance f_{nl}, the estimated statistics at the end of the robust optimization $\hat{m}_f$ and $\hat{\sigma}_f$ and the mean $m_{f_{\text{nl}}}$ and standard deviation $\sigma_{f_{\text{nl}}}$ of the nonlinear end-compliance. All results are in kJ.

which has been obtained disregarding imperfections and adopting a linear finite element analysis, are compared in table 1. It can be seen that the nominal design is very sensitive to imperfections as indicated by the large mean $m_{f_{\text{nl}}}$ and standard deviation $\sigma_{f_{\text{nl}}}$ of the nonlinear end-compliance. Although the nominal performance f_{nl} of the robust design is slightly worse than for the nominal design, the robust design is less sensitive to geometric imperfections as the statistics $m_{f_{\text{nl}}}$ and $\sigma_{f_{\text{nl}}}$ are much better. It should furthermore be noted that the second-order perturbation method proves to be very accurate in the present robust optimization as indicated by the small difference between the estimates $\hat{m}_f$ and $\hat{\sigma}_f$ and the statistics $m_{f_{\text{nl}}}$ and $\sigma_{f_{\text{nl}}}$ in table 1.

References

[1] M. Baitsch and D. Hartmann. Optimization of slender structures considering geometrical imperfections. *Inverse Problems in Science and Engineering*, 14(6):623–637, 2006.

[2] M.P. Bendsøe and O. Sigmund. *Topology optimization: Theory, Methods and Applications*. Springer, Berlin, second edition, 2004.

[3] T. Buhl, C.B.W. Pedersen, and O. Sigmund. Stiffness design of geometrically nonlinear structures using topology optimization. *Structural and Multidisciplinary Optimization*, 19:93–104, 2000.

[4] O. Sigmund. Morphology-based black and white filters for topology optimization. *Structural and Multidisciplinary Optimization*, 33(4–5):401–424, 2007.

[5] B. Sudret and A. Der Kiureghian. Stochastic finite element methods and reliability – A state-of-the-art report. Report UCB/SEMM-2000/08, Department of Civil & Environmental Engineering, University of California, Berkeley, November 2000.

[6] K. Svanberg. The method of moving asymptotes – A new method for structural optimization. *International Journal for Numerical Methods in Engineering*, 24:359–373, 1987.

Advanced computational methods for structural reliability analysis – Applications in civil engineering

Bruno Sudret, Stefano Marelli

Chair of Risk, Safety and Uncertainty Quantification,
Institute of Structural Engineering
ETH Zürich,
Stefano-Franscini-Platz 5, 8093, Zürich, Switzerland
sudret@ibk.baug.ethz.ch

Abstract. Metamodelling is an important tool for modern applications in structural reliability, especially in the presence of high fidelity computational models. A review of several state-of-the-art metamodel-based applications in structural reliability is given.

1 Introduction

Structural reliability analysis aims at assessing the safety of a system in the presence of uncertainty in its components. Given a random vector that represents the input uncertainty $\boldsymbol{X}$ (*e.g.* a joint probability density function PDF $f_{\boldsymbol{X}}$), the safety level is defined through a probability of failure P_f. By defining a performance function $g(\boldsymbol{X})$ that is negative in case of system failure, P_f can be defined as follows (*e.g.* [3]):

$$P_f = \mathbb{P}\left(\{g(\boldsymbol{X}) \leq 0\}\right) = \int_{\mathcal{D}_f = \{\boldsymbol{x} \in \mathbb{R}^M : g(\boldsymbol{X}) \leq 0\}} f_{\boldsymbol{X}}(\boldsymbol{x}) d\boldsymbol{x} \tag{1}$$

where $\mathcal{D}_f$ is the failure domain defined by $g(\boldsymbol{x}) \leq 0$. Introducing the failure indicator function $\mathbf{1}_{\mathcal{D}_f}$ as the characteristic function of $g(\boldsymbol{x}) \leq 0$, P_f can be recast as:

$$P_f = \int_{\mathbb{R}^M} \mathbf{1}_{\mathcal{D}_f}(\boldsymbol{x})\, f_{\boldsymbol{X}}(\boldsymbol{x})\, d\boldsymbol{x} \equiv \mathbb{E}\left[\mathbf{1}_{\mathcal{D}_f}(\boldsymbol{X})\right] \tag{2}$$

with associated Monte-Carlo (MC) estimator:

$$\hat{P}_f = \frac{1}{N} \sum_{k=1}^{N} 1_{\mathcal{D}_f}\left(\boldsymbol{X}^{(k)}\right) = \frac{N_f}{N}. \tag{3}$$

Due to the slow convergence rate of MC methods, the accurate computation of the expectation value estimator in Eq. (3) can rapidly become prohibitive with high fidelity computational models commonly used today in industrial applications. More efficient strategies for the computation of probability of failures are then needed.

A number of improvements on Monte-Carlo based simulation have been proposed in the literature to effectively precondition the estimation in Eq. (3) and reduce the associated computational costs (*e.g.* Importance Sampling, Subset Simulation, etc.), but their overall cost (typically $N = 10^{3-4}$) may remain prohibitive.

Recent developments in surrogate modelling, however, have proven that metamodels can be ideal candidates for the accurate estimation of P_f while keeping computational costs manageable.

2 Surrogate models

Surrogate models are functional approximations to the full complex computational models that can be built from a comparatively small set of full model evaluations (the experimental design), typically comprising tens to hundreds of samples. Such approximations are much cheaper to evaluate than their full counterpart and in some cases they can even provide additional useful information. Several metamodelling techniques have been successfully applied for the solution of structural reliability problems (*e.g.* Polynomial Chaos Expansions (PCE) and Kriging, see [6]). This contribution will focus on Kriging.

2.1 Kriging

Kriging, or Gaussian process metamodelling, is based on the representation of the random output $Y = \mathcal{M}(\boldsymbol{X})$ as the superimposition of a deterministic trend and a realization of a zero-mean stationary Gaussian process (see, *e.g.* [4]):

$$Y(\boldsymbol{x}, \omega) = \boldsymbol{f}(\boldsymbol{x})^{\mathsf{T}} \boldsymbol{a} + Z(\boldsymbol{x}, \omega) \tag{4}$$

where $\boldsymbol{f}(\boldsymbol{x})^{\mathsf{T}} \boldsymbol{a}$ represents the deterministic trend and $Z(\boldsymbol{x}, \omega)$ represents the Gaussian process with variance σ^2 and covariance function:

$$C_{YY}(\boldsymbol{x}, \boldsymbol{x}') = \sigma^2 R(\boldsymbol{x} - \boldsymbol{x}', \boldsymbol{\theta}) \tag{5}$$

The autocorrelation function family R is a parameter of the metamodel. The hyperparameters $\boldsymbol{\theta}$ of the Gaussian process can be calculated from a learning set of full model evaluations by maximum likelihood estimation.

Two properties of Kriging are especially useful in the context of structural reliability: it is an interpolant and it provides a built-in estimation of the local epistemic error of the surrogate model, known as the Kriging variance $\sigma^2_{\widehat{Y}}(\boldsymbol{x})$.

3 Surrogate models in structural reliability

3.1 As surrogates of $g(\boldsymbol{x})$

The most straightforward application of surrogate models in structural reliability is that of providing an inexpensive surrogate of the performance function, hence offsetting the costs of a direct application of the MC estimator in Eq. (3). However, the accuracy of the metamodel, especially in low probability regions of the model space, can be difficult to assess.

3.2 Adaptive experimental design

Leveraging on the local error estimate $\sigma^2_{\widehat{Y}}(\boldsymbol{x})$ provided by the Kriging metamodel, it is possible to devise experimental design enrichment strategies aimed at minimizing the

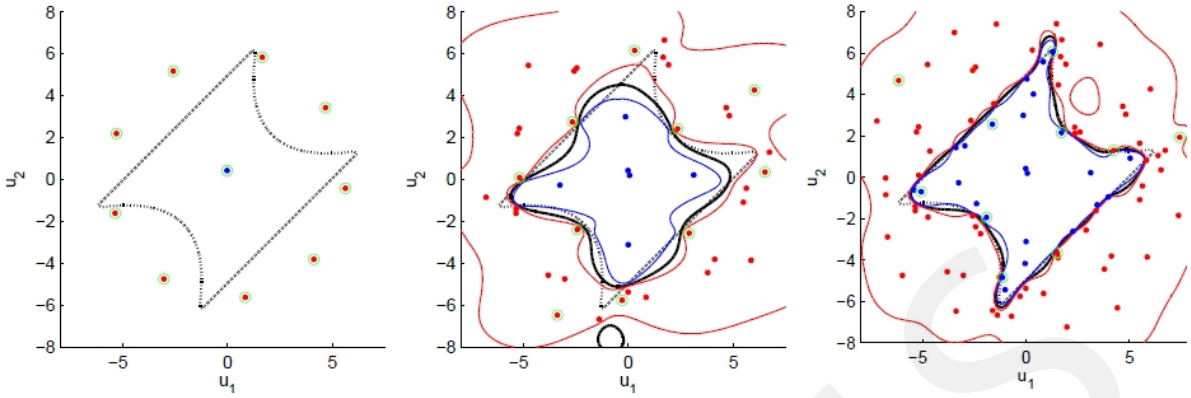

Figure 1: Example of experimental design enrichment based on the learning function in Eq. (6) at three different iterations for the Four Branch Function from [5]. The black line represents the true limit state surface, while the blue and red lines represents the 95% quantiles of the currently estimated failure regions.

metamodelling error near the limit state surface. This allows one to initialize the metamodel with a small experimental design, followed by its iterative refinement in the regions of interest. This can be achieved by defining enrichment criteria that identify the regions where the maximum improvement in the classification power of the metamodel are expected. One example is the learning function from [2]:

$$U(\boldsymbol{x}) = \frac{|\mu_{\widehat{Y}}(\boldsymbol{x})|}{\sigma_{\widehat{Y}}(\boldsymbol{x})} \tag{6}$$

This indicator can be interpreted as *the reliability index of the classification* of each metamodelled sample as being in the safe or failure domain. Lower values of $U(\boldsymbol{x})$ indicate high misclassification probability and closeness of $\boldsymbol{x}$ to the limit state surface. Thus they are ideal candidates for the addition of experimental design points. An example application of adaptive refinement of the failure domain can be found in Figure 1 for a test-case (Four Branch benchmark, see *e.g.* [5]).

3.3 Metamodel-based importance sampling

Further improvements can be attained with a metamodel-based extension of the Importance Sampling (IS) Monte-Carlo simulation method. Importance Sampling consists in defining an instrumental probability density function $h(\boldsymbol{X})$ which allows one to recast Eq. (1) as:

$$P_f = \int_{\mathbb{R}^M} \mathbf{1}_{\mathcal{D}_f}(\boldsymbol{x}) \frac{f_{\boldsymbol{X}}(\boldsymbol{x})}{h(\boldsymbol{x})} h(\boldsymbol{x})\, d\boldsymbol{x} = \mathbb{E}_h\left[\mathbf{1}_{\mathcal{D}_f}(\boldsymbol{X}) \frac{f_{\boldsymbol{X}}(\boldsymbol{X})}{h(\boldsymbol{X})}\right] \tag{7}$$

The choice of $h(\boldsymbol{X})$ significantly affects the accuracy of the Monte-Carlo estimation of P_f. An approximation to the optimal instrumental PDF can be built from the Kriging metamodel (see, *e.g.* , [1]), with which Eq. (7) can be rewritten as:

$$P_f = P_{f\varepsilon} \cdot \mathbb{E}_{\tilde{h}}\left[\frac{\mathbf{1}_{\mathcal{D}_f}(\boldsymbol{x})}{\pi(\boldsymbol{x})}\right] = P_{f\varepsilon} \cdot \alpha_{\text{corr}} \tag{8}$$

where $P_{f\varepsilon}$ is the probability of failure calculated with the inexpensive Kriging surrogate, while α_{corr} is a correction factor calculated from an additional validation set of full model evaluations sampled from the approximated optimal instrumental PDF $\tilde{h}(\boldsymbol{x})$. Based on the Kriging predictor $\mu_{\widehat{Y}}$ and variance $\sigma^2_{\widehat{Y}}$, the terms in Eq. (8) read:

$$\pi(\boldsymbol{x}) = \Phi\left(-\mu_{\widehat{Y}}(\boldsymbol{x})/\sigma_{\widehat{Y}}(\boldsymbol{x})\right), \quad \tilde{h}(\boldsymbol{x}) = \frac{\pi(\boldsymbol{x}) f_X(\boldsymbol{x})}{P_{f\epsilon}}, \quad P_{f\epsilon} = \mathbb{E}\left[\pi(\boldsymbol{x})\right]. \tag{9}$$

Several application examples of this method show that it can significantly help improving the stability and efficiency existing approaches based on metamodelling or adaptive design alone ([1, 6]).

4 Conclusions

Metamodelling has become an established tool in structural reliability applications in the presence of expensive computational models. The research community is actively developing new and more sophisticated approaches than the straightforward surrogation of the limit state function, *e.g.* by exploiting the stochastic properties of Kriging surrogates to create quasi-optimal instrumental densities in Importance Sampling algorithms.

References

[1] V. Dubourg, B. Sudret, and F. Deheeger. Metamodel-based importance sampling for structural reliability analysis. *Prob. Eng. Mech.*, 33(0):47–57, July 2013.

[2] B. Echard, N. Gayton, and M. Lemaire. AK-MCS: An active learning reliability method combining Kriging and Monte Carlo Simulation. *Struct. Saf.*, 33(2):145–154, March 2011.

[3] M. Lemaire. *Structural reliability*, volume 84. John Wiley & Sons, 2010.

[4] T. Santner, B. Williams, and W. Notz. *The design and analysis of computer experiments*. Springer series in Statistics. Springer, 2003.

[5] R. Schöbi and B. Sudret. PC-Kriging: A new meta-modelling method and its application to quantile estimation. In Y.G. Li, J and Zhao, editor, *Proc. 17th IFIP WG7.5 Conf. Reliab. Optim. Struct. Syst. Huangshan, China*, number 1. Taylor & Francis, 2014.

[6] B. Sudret. Meta-models for structural reliability and uncertainty quantification. *Proc. 5th Asian-Pacific Symp. Struct. Reliab. (APSSRA'2012), Singapore*, pages 53–76, 2012.

Robustness of optimal sensor location for parameter estimation of spatiotemporal systems

Dariusz Uciński

Institute of Control and Computation Engineering
University of Zielona Góra
ul. Podgórna 50, 65–246 Zielona Góra, Poland
e-mail: d.ucinski@issi.uz.zgora.pl

Distributed-parameter systems (DPSs) are dynamical systems whose state depends not only on time but also on spatial coordinates. They are frequently encountered in practical engineering problems. Their appropriate mathematical modelling most often yields partial differential equations (PDEs), but descriptions by integral equations or integro-differential equations can sometimes be considered. Clearly, such models involve using very sophisticated mathematical methods, but in recompense for this effort we are in a position to describe the process more accurately and to implement more effective control strategies. Early lumping, which means approximation of a PDE by ordinary differential equations of possibly high order, may completely mask the distributed nature of the system and therefore is not always satisfactory.

One of the basic and most important questions in DPSs is parameter estimation, which refers to the determination from observed data of unknown parameters in the system model such that the predicted response of the model is close, in some well-defined sense, to the process observations. The parameter-estimation problem is also referred to as parameter identification or simply the inverse problem. In order to identify the unknown parameters (in other words, to calibrate the considered model), the system's behaviour or response is observed with the aid of some suitable collection of sensors termed the measurement or observation system. In many industrial processes the nature of state variables does not allow much flexibility as to which they can be measured. For variables which can be measured online, it is usually possible to make the measurements continuously in time. However, it is generally impossible to measure process states over the entire spatial domain.

The inability to take distributed measurements of process states leads to the question of where to locate sensors so that the information content of the resulting signals with respect to the distributed state and PDE model be as high as possible. This is an appealing problem since in most applications these locations are not prespecified and therefore provide design parameters. The location of sensors is not necessarily dictated by physical considerations or by intuition and, therefore, some systematic approaches should still be developed in order to reduce the cost of instrumentation and to increase the efficiency of identifiers.

Motivations to study the sensor-location problem stem from practical engineering issues. Optimization of air quality-monitoring networks is among the most interesting. One of the tasks of environmental protection systems is to provide expected levels of pollutant concentrations. But to produce such a forecast, a smog-prediction model is necessary, which is usually chosen in the form of an advection-diffusion PDE. Its calibration requires parameter estimation (e.g., the unknown spatially varying turbulent diffusivity

tensor should be identified based on the measurements from monitoring stations). Since measurement transducers are usually rather costly and their number is limited, we are inevitably faced with the problem of how to optimize their locations in order to obtain the most precise model.

In general, the following main strategies of taking measurements can be distunguished:

- Locating a given number of stationary sensors
- Using moving sensors
- Scanning, i.e., only a part of a given total number of stationary sensors take measurements at a given moment in time

Trying to implement the above-mentioned techniques, we are faced with the corresponding problems:

- How to determine an optimal sensor placement in a given admissible spatial domain?
- How to design optimal sensor trajectories?
- How to select the best subset of all available sensors to take measurements at a given time?

Additionally, in all cases we should also address the question of a minimal number of sensors which will guarantee sufficient accuracy of the estimates.

Instead of the wasteful and tedious exhaustive search of the solution space, which constitutes quite a naive approach, approaches originating in statistical optimum experimental design and its extensions to models for dynamic systems, especially in the context of the optimal choice of sampling instants and input signals turn out extremely useful. In this vein, various computational schemes have been developed to attack directly the original problem or its convenient approximation. The adopted optimization criteria are essentially the same, i.e., various scalar measures of performance based on the Fisher information matrix (FIM) associated with the parameters to be identified are maximized. The underlying idea is to express the goodness of parameter estimates in terms of the covariance matrix of the estimates. For sensor-location purposes, one assumes that an unbiased and efficient (or minimum-variance) estimator is employed. This leads to a great simplification since the Cramér-Rao lower bound for the aforementioned covariance matrix is merely the inverse of the FIM, which can be computed with relative ease, even though the exact covariance matrix of a particular estimator is very difficult to obtain.

Over the past two decades, this methodology has been substantially refined to extend its applicability. A comprehensive treatment of both theoretical and algorithmic aspects of the resulting sensor location strategies is contained in the monograph [1].

One of the main difficulties associated with optimization of sensor locations is the dependence of optimal solutions on the values of the parameters to be estimated. Since these values are unknown, an obvious and common approach is to use the so-called locally optimal designs in which some prior estimate is assumed in lieu of the unknown true value (this estimate can be, e.g., a nominal value or a result of a preliminary experiment). But this guess may be far from the true value and, simultaneously, properties of locally optimal designs can be very sensitive to changes in the prior guess.

Since a good choice of design depends on true parameter values, a very natural idea is

to alternate experimentation and estimation steps. Accordingly, the total time horizon is divided into several contiguous parts and each of them is related to the corresponding stage of the experiment. At each stage, in turn, a locally optimal sensor location is determined based on the available parameter estimates (nominal parameter values can be assumed as initial guesses for the first stage), measurements are taken at the newly calculated sensor positions, and the data obtained are then analysed and used to update the parameter estimates. Owing to its simplicity, sequential design is commonly considered as a universal panacea for the shortcomings of local designs. Let us note, however, that the following important questions are to be faced and the answers to them are by no means straightforward:

1. How many subintervals should be chosen?
2. How do the initial estimates of parameters influence the design?
3. What are the asymptotic properties of sequential procedures, i.e., does the generated design 'tend' in any sense to a design which would be optimal in terms of the true value?

What is more, this technique it is often impractical because the required experimental time may be too long and the experimental cost may be too high. Therefore, the talk is focused on alternative robust approaches.

If it is known that the range of possible values of the unknown parameter θ reduces to a given compact set Θ_{ad}, then a more cautious approach to the control of the properties of the sensor location over Θ_{ad} consists in a probabilistic description of the prior uncertainty in θ, characterized by a prior distribution ς which may have been inferred, e.g., from previous observations collected on similar processes. The criterion to be minimized is then the expectation of the corresponding local optimality criterion over Θ_{ad}. Unfortunately, its direct use necessitates evaluation of multidimensional integrals, which is extremely time consuming. Luckily, the situation is by no means hopeless, as this framework is typical for the application of stochastic-approximation techniques. Based on the validity of the law of large numbers, a stochastic optimization problem is approximated in such a way that the uncertain random quantities in the original problem are replaced by artificially generated random variables. If these random variables are produced in advance to construct an approximate empirical problem, then we deal with the so-called nonrecursive methods being part of the broad family of Monte Carlo methods. From a practical point of view, recursive methods are sometimes more interesting. In these methods random samples are drawn only at the moment when they are requested. The total number of such random draws does not have to be determined at the beginning, but it can be adaptively chosen during the progress of estimation.

The above experiment, which is good on the average, may prove very poor for some particular values of the parameters associated with very low probability densities. If we do not accept such a situation, then a way out is to optimize the worst possible performance of the experiment over the prior admissible domain for the parameters Θ_{ad}, which leads to a minimax problem. In other words, we provide maximum information to a parameter vector θ which is the most difficult to identify in Θ_{ad}. The initial minimax optimization problem can then be solved with the use of some algorithms for inequality-constrained, semi-infinite optimization.

Each choice between the above two robust approaches has some advantages and some disadvantages. A final selection has to be made on the basis of secondary considerations. For example, if we are anxious to optimize the worst possible performances of the experiment designed, then optimal designs in the minimax sense are preferred. On the other hand, if the prior uncertainty on the parameters to be identified is characterized by some prior distribution, then the average experimental design is particularly suited for making the designs independent of the parameters.

References

[1] Uciński D (2005) *Optimal Measurement Methods for Distributed-Parameter System Identification*. CRC Press, Boca Raton

Contributions of the Participants of the 12th International Probabilistic Workshop, Weimar 2014

Assessment of the Flutter Stability of Bridges using a Probabilistic Approach

Tajammal Abbas, Guido Morgenthal

Research Training Group 1462
Faculty of Civil Engineering,
Bauhaus University Weimar,
Berkaer Strasse 9, 99425 Weimar, Germany
tajammal.abbas@uni-weimar.de

Abstract. The phenomenon of aerodynamic instability caused by wind is usually a major design criterion for the long-span cable supported bridges. If the wind speed exceeds the critical flutter speed of the bridge, this constitutes an Ultimate Limit State. The prediction of the flutter boundary therefore requires accurate and robust models. The state-of-the-art theory concerning determination of flutter stability limit is presented. A probabilistic flutter analysis is used to evaluate the effect of parameter uncertainty. A bridge section is numerically modelled in the CFD simulations. A methodology for carrying out sensitivity analysis of the flutter phenomenon is developed. The sensitivity with respect to uncertainty of flutter derivatives and structural parameters is assessed by considering the probability distribution of the flutter limit. A significant influence on the flutter limit is found by including uncertainties of the flutter derivatives due to different interpretation of scatter in the CFD simulations. The results indicate that the proposed probabilistic flutter analysis provides extended information concerning the accuracy in the prediction of flutter limits. The final aim is to setup a method to estimate the flutter limit without performing wind-tunnel tests. Such a tool could be useful for bridge engineers at pre-design stages. The study also shows the difficulties in this regard which have to be overcome but also highlights some interesting and promising results.

1 Introduction

The interaction of the aerodynamic forces and the structural motion can lead to instability when the energy input from the wind flow exceeds that dissipated by the structural damping. The coupling of torsional and bending mode occurs and amplitude of the motion progressively increases at this stage which is known as classical flutter. The negative aerodynamic damping is produced such that the deformations reach to a level that failure happens. The main objective of studying flutter phenomena is to find the instability limit which is also known as flutter limit and making sure that this wind speed is not exceeded, with a certain probability, during the design life of the bridge.

Theodorsen [1], developed a theory to build the self-excited forces for airfoils based on potential flow past a flat plate by using circulation functions. Scanlan and Tomko [2] gave a popular linearised form to represent the self-excited forces by using aerodynamic derivatives. Free vibration [3] or forced vibration [4] approaches are used to extract the aerodynamic derivatives. Walther and Larsen used *Computational Fluid Dynamics* (CFD)

to compute flutter derivatives numerically [4]. The analytical solutions for the two degree of freedom aeroelastic instability include eigenvalue analysis [5].

Mannini and Bartoli [6] presents a flutter instability in a probabilistic way and and the effect of correlation between flutter derivatives in the definition of the probability distribution of the flutter wind speed. Cheng and Xiao [7] used response surface method for the probabilistic free vibration and flutter analyses of suspension bridges. Jurado and Hernández [8] presented an analytical sensitivity analysis of flutter phenomenon in long-span bridges.

In this paper, the study is made on the aeroelastic phenomena of flutter and flutter analysis is performed for bridges by using the deterministic and probabilistic approaches. Finally application of these approaches is presented on the bridges to calculate ultimately their critical flutter limit. The main objective of this study is to create a framework for probabilistic flutter analysis. To achieve this, the approach demonstrates to take parameter uncertainty into account according to the importance of each parameter by performing sensitivity analysis.

2 Flutter Phenomenon

Flutter is a coupling of aerodynamic forcing with a structural dynamics problem. The flutter analysis is performed by complex eigenvalue solution. Models for aerodynamic forces employed are the analytical Theodorsen expressions for the motion-induced aerodynamic forces of a flat plate and Scanlan derivatives of a bridge section as a Meta model. CFD simulations using the *Vortex Particle Method* (VPM) are used to compute aerodynamic derivatives. The structural representation is dimensionally reduced to a two degree of freedom section model calibrated from global model.

A simplified two degree of freedom representation of the bridge deck may be considered as shown in Figure 1 where U_∞ is the wind speed and B is the width of the section. The equations of motion can be written as

$$m\ddot{h} + 2m\xi_h\omega_h\dot{h} + m\omega_h^2 h = F_L \tag{1}$$

$$I\ddot{\alpha} + 2I\xi_\alpha\omega_\alpha\dot{\alpha} + I\omega_\alpha^2\alpha = F_M \tag{2}$$

where m and I are the mass and mass moment of inertia, ξ_h and ξ_α are the damping ratios, ω_h and ω_α are the natural circular frequencies for the heave and pitch mode, h and α are the vertical displacement and rotation, F_L and F_M are the lift force and moment respectively.

Scanlan [2] expressed the motion-induced aerodynamic forces on a cross section as a meta model which assumes that the self-excited lift F_L and moment F_M for a bluff body may be treated as linear in displacement h and rotation α and their first derivatives in a linearised form:

$$F_L = \frac{1}{2}\rho U_\infty^2 B\left[KH_1^*\frac{\dot{h}}{U_\infty} + KH_2^*\frac{B\dot{\alpha}}{U_\infty} + K^2H_3^*\alpha + K^2H_4^*\frac{h}{B}\right] \tag{3}$$

$$F_M = \frac{1}{2}\rho U_\infty^2 B^2\left[KA_1^*\frac{\dot{h}}{U_\infty} + KA_2^*\frac{B\dot{\alpha}}{U_\infty} + K^2A_3^*\alpha + K^2A_4^*\frac{h}{B}\right] \tag{4}$$

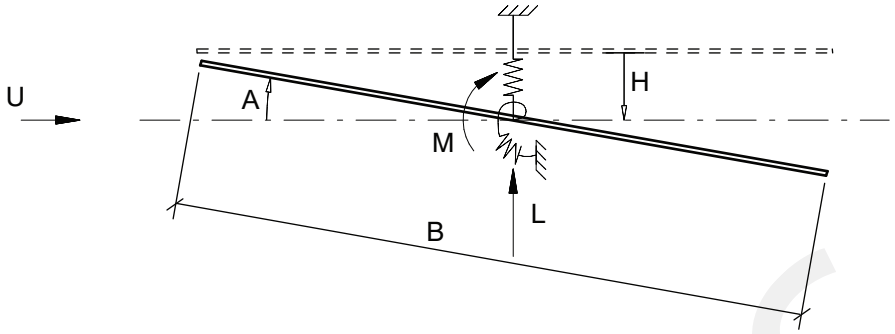

Figure 1: Definition of degrees of freedom (heave h and pitch α) for flutter analysis: (- -) undeformed, (−) deformed.

where ρ is the air density, H_i^* and A_i^* (i=1,..,4) are non-dimensional function of $K(=\frac{B\omega}{U_\infty})$ known as aerodynamic or flutter derivatives which are associated with self-excited lift and moment, respectively, K is the reduced frequency and ω is the frequency of the bridge oscillation under aerodynamic forcing. These aerodynamic derivatives are usually measured in special wind tunnel tests but can also be computed from CFD simulations.

Fully Analytical (Model #1) Fully analytical models are simple, easy to implement and allow a better insight into the force coupling. Theodorsen investigated the flutter phenomenon for aircraft wings and gave a very popular analytical approach for the flutter analysis [1]. It considers a flat plate subjected to the action of a smooth oncoming flow with two degrees of freedom only (see Figure 1). The main idea is to represent instability as an eigenvalue problem. The formulation of the system of differential equations to the eigenvalue problem is given in [9].

Derivative-based Eigenvalue Analysis (Model #2) Motion-induced forces can also be determined from numerical forced vibration simulations. The resulting lift force and moment time histories are then used to compute the aerodynamic derivatives. A flow solver based on the VPM has been used here to perform forced vibration simulations on the sections. Aerodynamic derivatives then can be computed in a least square sense from the resulting force and moment time histories.

The results of simulations performed on the bridge sections are shown in Figure 3. Analytical values are also plotted for comparison. The quality of the results varies along the v_r range depending on different factors. Eigenvalue solution is then performed to compute the flutter limit.

3 Reference Objects

The *Lillebælt* (LB) suspension bridge, Denmark and *Tacoma Narrows* (TN) suspension bridge, USA have been used as reference objects in this study. These two cross sections (see Figure 2) have been considered to cover a wide range of structural parameters as shown in Table 1.

Figure 2: Simplified LB and TN suspension bridge deck sections (dimensions: [m]).

Table 1: Basic data and structural properties of the bridge sections.

Section	Span [m]	B [m]	m [kg/m]	I [kgm^2/m]	f_h [Hz]	f_α [Hz]	ξ_h, ξ_α [-]
LB	600	33	11667	1017778	0.156	0.500	0.01
TN	854	12	4250	177730	0.130	0.200	0.01

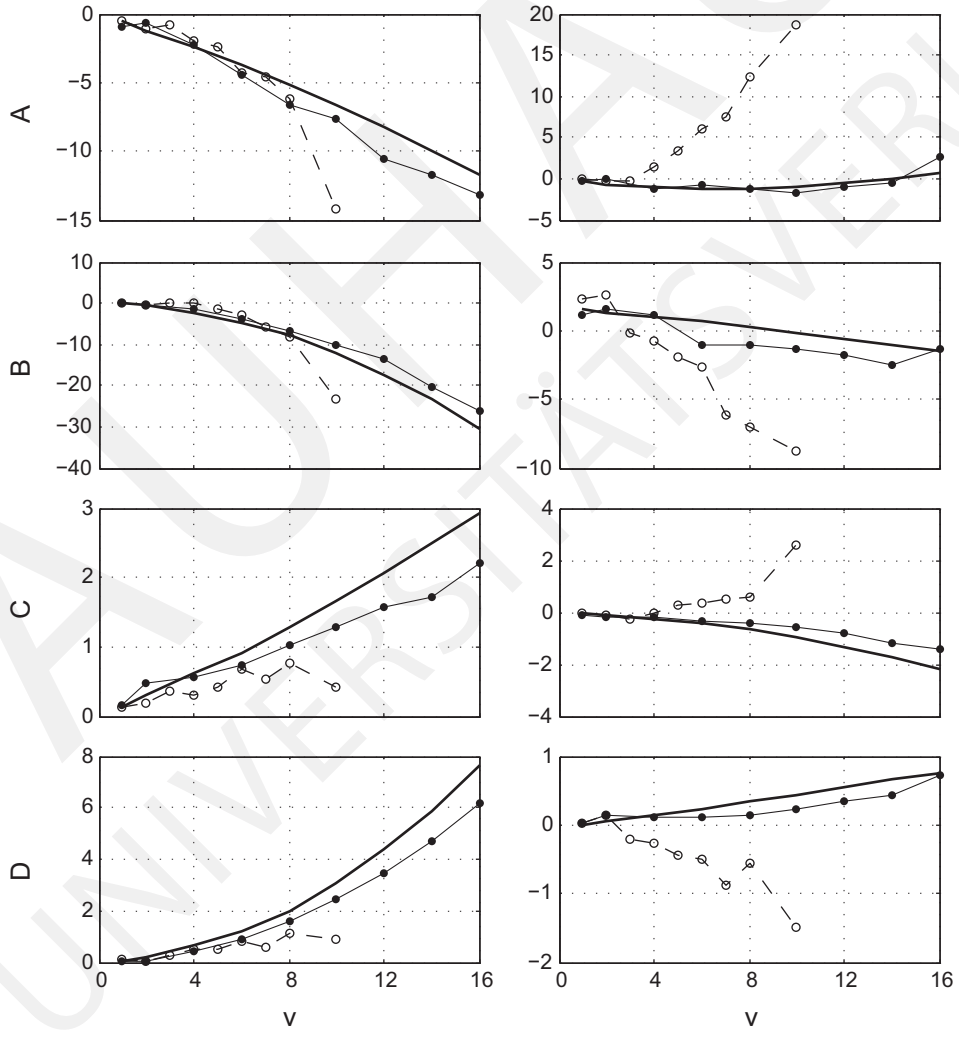

Figure 3: Aerodynamic derivatives (H_i^* and A_i^* where i =1, 2, 3, 4) w.r.t. v_r; (—) flat plate by Theodorsen theory, forced vibration analysis on (−•−) LB section and (--○--) TN section.

4 Probabilistic Flutter Analysis

Flutter analysis is commonly performed through deterministic approach by using the mean values of the input parameters and the aerodynamic derivatives. However, the final flutter limit is significantly influenced by a small change in one or few input parameters. Therefore, it is important to consider such variation in the input parameters and perform the flutter analysis using a probabilistic approach.

It is not desirable to perform variance based sensitivity or uncertainty analysis in case of complex simulation as it will become expensive. The response surface may be used in this case to make the process more efficient. Polynomial regression can be used to approximate the modal response by polynomial basis function. These parametric models relate the input parameters to the global model response. Figure 4 shows the process of using response surface method for flutter prediction and utilizing it for further analyses.

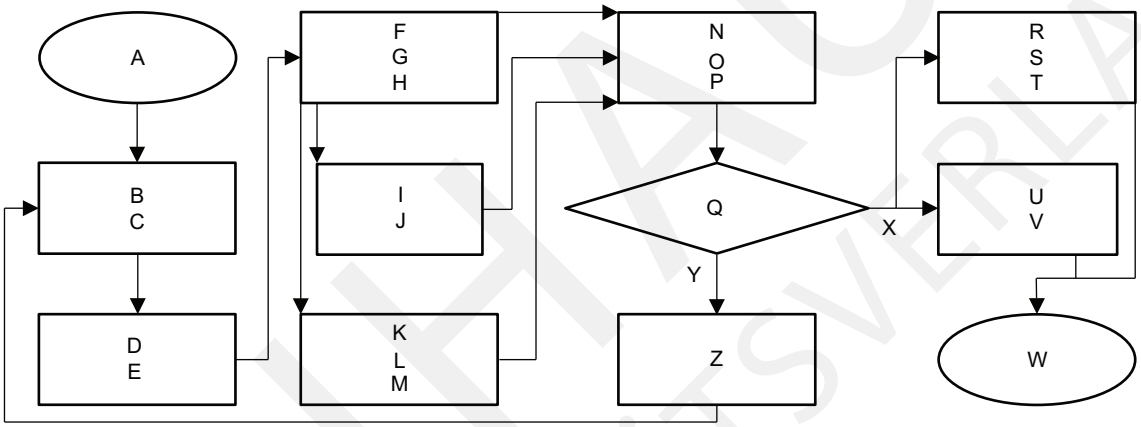

Figure 4: Response surface method for sensitivity and uncertainty analyses.

Table 2: Flutter stability analysis using actual model and the response surface method.

		Actual model			Response surface		
Model	Section	U_{cr} [m/s]	ω_{cr} [rad/s]	$v_{r_{cr}}$ [-]	U_{cr} [m/s]	ω_{cr} [rad/s]	$v_{r_{cr}}$ [-]
Model#1	LB	93.8	2.08	8.62	93.8	2.07	8.63
Model#1	TN	13.5	1.08	6.56	13.3	1.11	6.48
Model#2	LB	94.2	2.21	8.15	98.5	2.16	8.68
Model#2	TN	11.1	1.23	4.88	11.8	1.23	5.10

Linear regression model was used with quartic terms as response surface for the models. *Latin Hypercube Sampling* (LHS) has been used here which requires less number of samples to obtain reasonable convergence. The actual model took 10,200 seconds whereas response surface approach took only 1 second to solve 10,000 samples. There is significant improvement in the computational time. The *Coefficient of Determination* (CoD) shows the quality of approximation of a polynomial regression model. The computed CoD was 0.998 which is close to 1 that means the simplified mathematical model describes very well the behaviour of the complex model. Table 2 shows a good agreement between the flutter limits computed from response surface method and those from the actual model.

5 Sensitivity Analysis

A sensitivity analysis determines the change in model output values that results from the changes in model input values. Variance based methods are very suitable to quantify this contribution. The total effect sensitivity indices is defined as

$$S_{T_i} = \frac{E(V(Y|\mathbf{X}_{\sim X_i}))}{V(Y)} \tag{5}$$

where $V(Y)$ is the unconditional variance of the model output and $V(Y|\mathbf{X}_{\sim X_i})$ is the variance of Y caused by all model inputs without X_i.

The structural parameters used for the sensitivity analysis are shown in Table 1. The variations in the parameters were assumed independent of each other. Sensitivity analysis of the structural input parameters (Figure 5, left) shows that the torsional frequency is the most important input parameter which affects the flutter limit. Then the width of the section and the mass moment of inertia also have significant effect. Mass of the section and the bending frequency have less influence whereas the damping ratio has the least effect as compared to the other input parameters.

Similarly, the variation in the aerodynamic derivatives was considered and sampling was done for eight aerodynamic derivatives. Figure 5 (right) shows that H_3^*, A_1^*, A_2^*, A_3^* and upto some extent H_1^* are the most significant. H_4^* seems to have almost no effect which verifies the outcome of other studies [10]. However, A_4^* has still some visible effect. H_4^* and A_4^* represents the aerodynamic stiffness induced by the vertical displacement of the deck, and are considered to have small influence on the flutter limit. However, the results of this study shows that H_4^* and A_4^* can have high coefficient of variation, and thus significantly contributions to the overall uncertainty in the prediction of flutter limit.It is important to mention here that the sensitivity analysis depends on a number of factors such as the cross section shape and the structural input parameters. Changing these parameters will result in a different outcome.

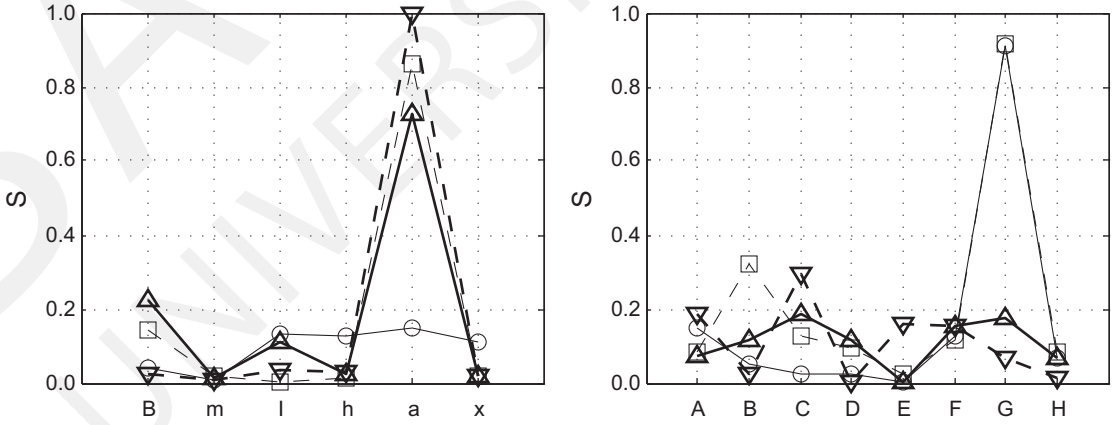

Figure 5: Global sensitivity analysis for flutter limit considering probabilistic (left) input parameters, (right) aerodynamic derivatives; (△) Model#1 LB section, (▽) Model#1 TN section, (○) Model#2 LB section, (□) Model#2 TN section.

6 Uncertainty Analysis

The main objective of uncertainty analysis is to quantify the uncertainty in the output as a result of uncertainty in the input parameters. It also includes the identification of characteristics of various probability distributions of model input and output. The uncertainty in parameters is assumed to be represented by a normal distribution and it is further assumed that the uncertainty of structural input parameters and aerodynamic derivatives are independent. All other input parameters are assumed deterministic. A probabilistic approach of modelling the aerodynamic derivatives is suggested. The condition of linearly increasing standard deviation of derivatives along v_r is also to be satisfied. The correlation considered between the aerodynamic derivatives generally reduces the scatter of the model output in turn reduces the model uncertainty. Therefore, ignoring correlation will lead to conservative solution. This is also desirable because the actual correlation between the parameters is not well established.

(a) Synthetic or artificial correlation introduced between all aerodynamic derivatives as
   (i) no correlation $(\rho(x_i, x_j)=0.0)$
   (ii) full correlation $(\rho(x_i, x_j)=1.0)$
   (iii) partial correlation $(\rho(x_i, x_j)=0.5)$

(b) Correlation for lift force aerodynamic derivatives $H_1^* - H_4^*$ and $H_2^* - H_3^*$
Correlation for moment aerodynamic derivatives $A_1^* - A_4^*$ and $A_2^* - A_3^*$

(c) Dependence of derivatives on each other
   (i) from flat plate approximation as $H_1^* = -K.H_3^*$ and $A_1^* = -K.A_3^*$ [11, 12]
   (ii) also interesting is correlation between $H_1^* - H_2^*$, $H_3^* - H_4^*$, $A_1^* - A_2^*$ and $A_3^* - A_4^*$

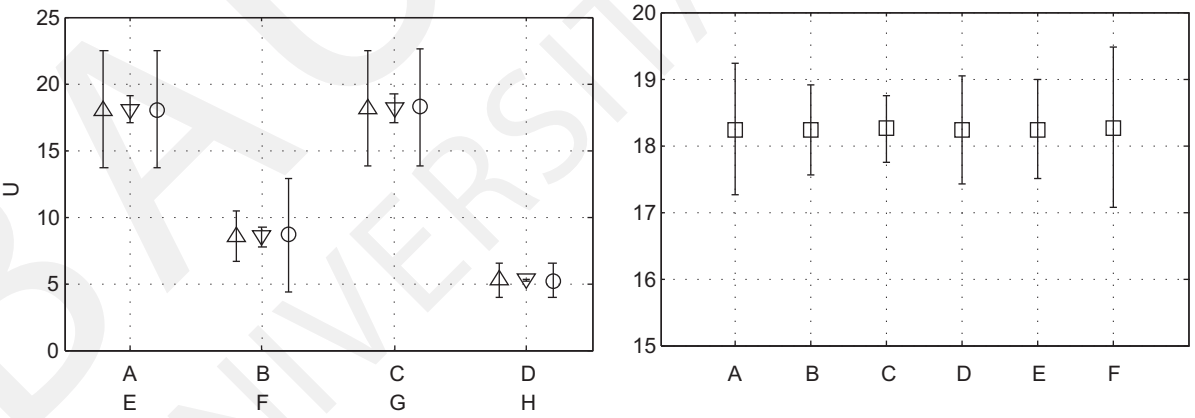

Figure 6: Uncertainty analysis (left) uncorrelated input parameters and aerodynamic derivatives (right) correlated aerodynamic derivatives (LB section, Model#1);
(△) input parameters, (▽) aerodynamic derivatives,
(○) input parameters and aerodynamic derivatives.

Figure 6 summarises the results for uncertainty analysis. It can be seen that the uncertainty in the model output is more by considering the uncertainty in the input parameters and is less if the uncertainty only in aerodynamic derivatives is considered.

7 Conclusions

A framework of probabilistic flutter analysis is presented. Response surface method was suggested to be used here for complex models in order to make the probabilistic approach more efficient. An approach is used to quantify sensitivity of the input parameters and the aerodynamic derivatives for flutter analysis. The aerodynamic derivatives were identified as important which have major influence on the flutter limit.

The effect of parameter uncertainty on the flutter limit was also quantified. Linearly increasing variation of scatter with the reduced speed was assumed in the aerodynamic derivatives to account for uncertainty. The importance of correlation between the aerodynamic derivatives was also highlighted by using fully correlated, uncorrelated and partially correlated aerodynamic derivatives. The approach of using several conditions of correlation was used in the absence of information about the actual correlation. Higher correlations lead to the smaller uncertainty in the model output.

The results show that the flutter limit is sensitive to the modelled parameter uncertainty and to some extent aerodynamic derivatives uncertainty. The mean value is not sensitive to uncertainties due to normally distributed scatter of CFD simulation results. The probabilistic flutter analysis is superior over deterministic method of calculating flutter limit as it also shows the distribution of the flutter limit and the interval of likelihood of occurrence of flutter limit. It provides more information about the nature of the flutter limit, than a corresponding deterministic analysis. Moreover, this method can also be used for probabilistic design or performance based design.

References

[1] Theodorsen, T. General theory of aerodynamic instability and the mechanism of flutter. Report 496, NACA, 1935.

[2] Scanlan, R. H. and Tomko, J. J. Airfoil and bridge deck flutter derivatives. *ASCE Journal of Engineering Mechanics*, 97:1717–1737, 1971.

[3] Iwamoto, M. and Fujino, Y. Identification of flutter derivatives of bridge deckfrom free vibration data. *Journal of Wind Engineering and Industrial Aerodynamics*, 54–55:55–63, 1995.

[4] Larsen, A. and Walther, J. H. Aeroelastic analysis of bridge girder section based on discrete vortex simulations. *Journal of Wind Engineering and Industrial Aerodynamics*, 67-68:253–265, 1997.

[5] Simiu, E. and Scanlan, R. H. *Wind Effects on Structures: Fundamentals and Applications to Design*. J. Wiley and Sons, New York, Chichester, Brisbane, 3rd edition, 1996.

[6] Mannini, C. and Bartoli, G. Uncertainty propagation in bridge flutter analysis. In *11th International Conference on Structural Safety and Reliability (ICOSSAR2013)*, 2013.

[7] Cheng, J. and Xiao, R. Probabilistic free vibration and flutter analyses of suspension

bridges. *Engineering Structures*, 27:1509–1518, 2005.

[8] Jurado, J. and Hernández, S. Sensitivity analysis of bridge flutter with respect to mechanical parameters of the deck. *Structural and Multidisciplinary Optimization*, 27(4):272–283, 2004.

[9] Abbas, T. and Morgenthal, G. Model combinations for assessing the flutter stability of bridges. 2014.

[10] Bartoli, G. and Mannini, C. A simplified approach to bridge deck flutter. *Journal of Wind Engineering and Industrial Aerodynamics*, 96:229–256, 2008.

[11] Matsumoto, M. Aerodynamic damping of prisms. *Journal of WindEngineering and Industrial Aerodynamics*, 59:159–175, 1996.

[12] Scanlan, R., Jones, N., and Singh, L. Inter-relations among flutter derivatives. *Journal of Wind Engineering and Industrial Aerodynamics*, 69-71:829–837, 1997.

Full Probabilistic Analysis of Reinforced Concrete Columns Subjected to Standard Fire

[1]Marcus Achenbach, [2]Guido Morgenthal

1 LGA KdöR
Tillystraße 2, 90431 Nürnberg, Germany
marcus.achenbach@lga.de

2 Modelling and Simulation of Structures
Prof. Dr.
Bauhaus Universität Weimar
Marienstraße 13, 90431 Weimar, Germany
guido.morgenthal@uni-weimar.de

Abstract. The advanced method using the material laws given in DIN EN 1992-1-2 is state of the art for the determination of fire resistance of concrete structures. The "quality" of the resistance model is proofed by the recalculation of fire tests. But most results published in Germany only consider older material laws, which do not exactly match those of DIN EN 1992-1-2. German examinations of the reliability and senstivity analysis of concrete members subjected to fire use FORM and do not consider newer results of the model uncertainties. The calculated sensitivity indices α_i are only valid at the "performance" point.

A Monte Carlo simulation of reinforced concrete columns subjected to a standard fire is set up. The uncertainties of the thermal calculation and the resistance model are taken from newer examinations, where current physical properties and material laws are used. The evaluation of the results of the limit state function with a global sensitivity analysis reveal, that the advanced method according to DIN EN 1992-1-2 is highly sensitive to calculated temperatures.

1 Introduction

The advanced method according to DIN EN 1992-1-2 [5] is state of the art for the check of fire resistance and widely accepted by engineers and building authorities in Europe [6, 15]. The accuracy of this calculation scheme is proofed by recalculation of laboratory tests, which have been carried out by Haß [7]. The sensitivity against the input parameters has been examined by Henke [8].

But the material laws used by Haß [7] for the calibration differ from those given in DIN EN 1992-1-2 [5]. The model uncertainties of the resistance model have not been considered by Henke [8], because the test series have not been finished. Newer recalculations by Hosser, Richter and Wöckener [9] use the material laws given in DIN EN 1992-1-2 - but only four columns are examined. The results of a probabilistic study using current material laws have been published by Hosser et al. [10], where the reliability of concrete, timber and steel members subjected to natural and standard fires is determined. Therefore only a reduced set of stochastic parameters is taken into account, because the analysis has to be carried out for every time step.

Achenbach and Morgenthal [1] recalculate measured temperatures of columns and experimental times to failure of concrete columns subjected to a standard fire using the material laws from DIN EN 1992-1-2 [5]. A Monte Carlo simulation of reinforced concrete walls subjected to a standard fire is carried out using the uncertainties of the thermal calculation and the resistance model given by the calibration.

In this conference paper the Monte Carlo simulation is extended to square columns heated on all sides by a standard fire.

2 Examinations from Achenbach and Morgenthal

Achenbach and Morgenthal [1] recalculate the measured temperatures of reinforced concrete columns subjected to a standard fire. The columns have been tested at TU Braunschweig. At the tests, no thermal properties of the concrete mixture have been determined. The recalculation is carried out using the lower limit of the thermal conductivity λ_c and a moisture content $u = 3\%$ of weight, as given in DIN EN 1992-1-2. The statistical key data of the ratio of calculated to the measured temperatures $\eta_t = T_{cal}/T_{exp}$ is a mean of $\mu_t = 1.05$ and a standard deviation of $\sigma_t = 0.19$, containing all uncertainties of the temperature distribution in the testing furnace and thermal properties.

56 laboratory tests from TU Braunschweig, Université de Liège and Universiteit Gent are used as database for the recalculation [1] with the advanced method using the material parameters of DIN EN 1992-1-2 [5]. The ratio of the calculated to experimental time to failure is $\eta = t_{cal}/t_{exp}$, with the statistical key data $\mu(\eta) = 0.92$ and $\sigma(\eta) = 0.47$ assuming a normal distribution. The Anderson-Darling test [16] is used to check the assumption of a normal distribution in combination with Grubbs' test [16] for the detection of outliers. The level of significance for both tests is chosen to $\alpha = 0.1$ and eight outliers are removed. The statistical key data changes to $\mu = 0.76$ with $\sigma = 0.17$.

The results from the calibration of the thermal calculation and the mechanical model are used by Achenbach and Morgenthal [1] to consider the model uncertainties in the Monte Carlo simulation of reinforced concrete walls. For walls, the temperature distribution must only be solved in one dimension, which simplifies the calculation procedure and allows the consideration of all possible stochastic variables.

Walls with an ratio of wall length to cross section height $l_{col}/h = 40$ and 25 are simulated. The evaluation of the results by Spearman's rank correlation coefficient [16] and the main effect of the global sensitivity analysis according to Saltelli [17] reveal, that the uncertainty of the temperature calculation governs all other basic variables. Especially the wall length l_{col}, the area of reinforcement a_s, the height h of the cross section and the eccentricity e_0 only have an negligible influence on the variance of the limit state function.

3 Applied Methods

3.1 Calculated examples

Square columns, heated on four sides by a standard fire [3], are used in the full probabilistic analysis. The structural system with loads is displayed in Figure 1, the range of parameters is given in Table 1. The ultimate load $P_d = 1.35G_k + 1.5Q_k$ with given area of reinforcement $A_{s,tot}$ is determined with the simplified method for the design of columns based on nominal curvature. The ratio of live load to dead load Q_k/G_k is assumed to 0.7. The fire resistance t_{fire} according to DIN EN 1992-1-2 [5] of the examples is determined by the tabulated data given in Table 5.2a [5], assuming that the buckling length in the cold and hot condition are the same.

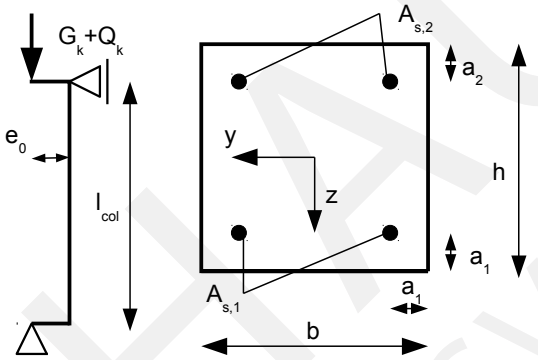

Figure 1: Structural System and cross section of examined columns

no.	l_{col} [cm]	$b = h$ [cm]	$a_1 = a_2$ [cm]	$A_{s,tot}$ [cm^2]	f_{ck} [MPa]	f_{yk} [MPa]	G_k [kN]	Q_k [kN]	e_0/h [-]	t_{fire} [min]
1	300	20	4	12.57	20	500	340	240	0.0	60
2	300	20	4	12.57	20	500	250	170	0.1	60
3	300	20	4	12.57	20	500	120	80	0.5	60
4	300	30	5	19.64	20	500	710	500	0.0	90
5	300	30	5	19.64	20	500	540	380	0.1	90
6	300	30	5	19.64	20	500	260	180	0.5	90

Table 1: Parameters of simulated columns

3.2 Thermal calculation, resistance model and limit state function

A finite difference scheme with local variable thermal properties [2] is implemented for the temperature calculation of the cross section. The heat transfer coefficient $\alpha_c = 25$ [W/m^{2}K] and the emissivity $\varepsilon = 0.7$ [-] are taken as the recommended values [3, 4]. The thermal conductivity λ_c is considered with its lower limit, a density of the concrete of $\rho = 2400$ [kg/m^3] and a moisture content $u = 3$ % of weight is taken for the thermal properties of the concrete [5].

The calculated temperatures at t_{fire} are used as input for the cross section analysis according to the advanced method given in DIN EN 1992-1-2 [5]. The moment-curvature diagram $M_R(\kappa)$ is evaluated to describe the nonlinear behavior of the heated cross section. The curvatures are assumed to have a parabolic distribution over the length of the column. With the notation of Figures 1 and 2 the displacement in the middle of the span, taking second order effects into account, can be calculated as

$$e^{II}(\kappa) = \left(\frac{l_{col}}{2}\right)^2 \cdot \left(\frac{4}{10}\kappa - \frac{1}{10}\kappa_0\right) \tag{1}$$

according to Kordina and Quast[12]. The limit state function is defined as

$$G = \max\left(M_R(\kappa) - M_E(\kappa)\right). \tag{2}$$

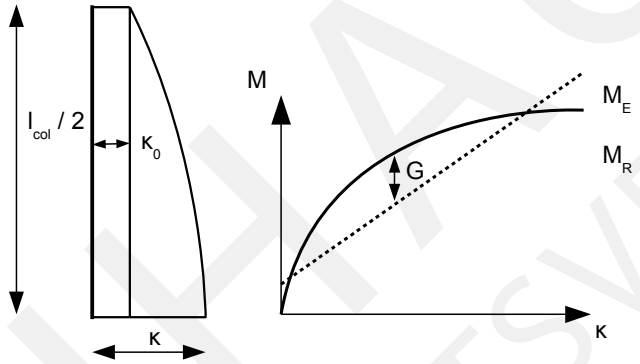

Figure 2: Left side: shape of curvature, right side: qualitative limit state function in the M-κ-diagram

3.3 Basic variables

The probabilistic modeling of the basic variables is given in Table 2. Due to the results from Achenbach and Morgenthal [1], the length of the column l_{col}, the dimensions of the cross section b and h and the area of reinforcement $A_{s,1}$ and $A_{s,2}$ are fixed to their nominal values.

The uncertainty of the thermal calculation is considered by the basic variable X_t, using the results of the calibration carried out by Achenbach and Morgenthal [1]. The calibration has been carried out with the nominal values of the thermal properties. The deviations contain the uncertainties of the thermal properties, the uncertainty of the calculation method and the uncertainty of the temperature distribution in the test furnace. Therefore the thermal properties of the concrete are also considered to be deterministic in the full probabilistic analysis. The calculated temperatures are multiplied by X_t to simulate the uncertainty of the thermal calculation method and the physical properties.

The calculated resistance of the cross section for given curvature $M_R(\kappa)$ is multiplied by X_m regarding the uncertainty of the mechanical model. The parameters of the normal distribution can be derived from the results of the calibration. With $X_m = 1/\eta$ the

parameters of the normal distribution can be transformed [16] from the results of the calibration by $\mu_{X_m} = \frac{1}{\mu} \cdot (1 + \nu^2)$ and $v_{X_m} \approx v = \frac{\sigma}{\mu}$.

		stochastic distribution		
variable	comment	type	parameters	source
l_{col} [cm]	length of column	DET	Table 1	-
$b = h$ [cm]	height and width	DET	Table 1	-
a_1 [cm]	distance of reinforcement	N	$\mu = a_1$, $\sigma = 0.5$ cm	[11, 18]
a_2 [cm]	distance of reinforcement	N	$\mu = a_2$, $\sigma = 0.5$ cm	[11, 18]
$A_{s,1}$ [cm^2]	area of reinforcement	DET	Table 1	-
$A_{s,2}$ [cm^2]	area of reinforcement	DET	Table 1	-
f_c [MPa]	compressive strength	LN	$\mu = f_{ck} + 8$ MPa, $\sigma = 5$ MPa	[10, 18]
f_y [MPa]	yield strength	N	$\mu = f_{yk} + 2\sigma$ MPa, $\sigma = 30$ MPa	[10, 11]
G [kN]	dead load	N	$\mu = G_k$, $v = 0.1$	[10, 18]
Q [kN]	live load	G	Q_k : 98% fractile, $v = 0.4$	[18]
e_0 [cm]	constant eccentricity	DET	Table 1	-
e_f [cm]	initial curvature	N	$\mu = 0$, $\sigma = l_{col}/1000$	[11]
X_t [-]	uncertainty of calculated temperatures	N	$\mu_t = 1.0$, $v_t = 0.2$	[1]
X_m [-]	uncertainty of mechanical model	N	$\mu = 1.4$, $v = 0.2$	[1]

Table 2: Basic variables of examined columns (DET = deterministic, N = normal, LN = two-parametric log-normal, G = Gumbel)

3.4 Probabilistic method

A Monte Carlo simulation with the parameters given in Table 1 and the stochastic models for each basic variable shown in Table 2 is set up. Latin hypercube sampling [13] is applied to generate the random numbers. Two sample sets are generated: the first set assumes that the model uncertainties of the thermal calculation X_t and the resistance model X_m are randomly distributed. In the second set both are fixed to 1.0. This allows to study the influence of the model uncertainties on the failure rate.

3.5 Evaluation of the results of the limit state function

The results of the limit state function are evaluated with two methods. First, the data is analyzed with Spearman's rank correlation coefficient [16], which evidences the positive or negative correlation of the examined basic variable and the results of the limit

state function. Second, a global sensitivity analysis according to Saltelli et al. [17] is performed. For the calculation of the first-order Sobol indices, the limit state function G is approximated by a linear response surface [14]:

$$\hat{G}(X) = c_0 + \sum_{i=1}^{n} c_i \cdot X_i. \tag{3}$$

The coefficients c are calculated by multiple linear regression [16]. The first-order Sobol indices [17]

$$S_i = \frac{V(E(G|X_i))}{V(G)} \tag{4}$$

are determined with the response surface $\hat{G}(X)$. They are only calculated for a coefficient of determination $R^2 > 0.8$ for the response surface.

4 Results

The coefficient of determination R^2, the failure rate p_{f1} with random model uncertainties and the failure rate p_{f2} with fixed model uncertainties are shown in Table 3. The probability of failure is dependent on the slenderness and relative eccentricity of the applied loads. Slender columns fail more often compared to short columns. This is in accordance with the results from Henke [8]. Columns with a higher eccentricity are more "safe" than centrically loaded ones, which is also in accordance with earlier published results [1, 8].

Regarding columns no. 1 and 2, fixing the uncertainties of the thermal calculation and the resistance model leads to higher probabilities of failure, compared to stochastic modeling of those uncertainties. This is reverted for columns no. 3 to 5: neglecting the model uncertainties leads to "unsafe" results.

In Figure 3 the results for Spearman's rank correlation coefficient and the main effect S_i are shown. The results for the first order Sobol index indicate, that the variance of the limit state function is controlled by X_t, which is the uncertainty of the thermal calculation. With increasing eccentricity of applied loads, the uncertainty of the resistance model X_m becomes more important. Further parameter uncertainties only have inferior influence on the variance of the limit state function.

Spaerman's rank correlation coefficient indicates clearly, that X_t and the results of the limit state function G correlate negatively, which is in accordance with the resistance model. An increase in temperature leads to higher deterioration of the material properties.

no.		X_t and X_m stochastic R^2	p_{f1}	$X_t = X_m = 1$ p_{f2}
1:	$l_{col}/h = 15,\ e_0/h = 0.0$	0.680	0.262	0.417
2:	$l_{col}/h = 15,\ e_0/h = 0.1$	0.873	0.250	0.323
3:	$l_{col}/h = 15,\ e_0/h = 0.5$	0.927	0.061	0.001
4:	$l_{col}/h = 10,\ e_0/h = 0.0$	0.890	0.100	0.060
5:	$l_{col}/h = 10,\ e_0/h = 0.1$	0.934	0.066	0.007
6 :	$l_{col}/h = 10,\ e_0/h = 0.5$	0.923	0.024	<0.001

Table 3: Coefficient of determination R^2 and probabilities of failure p_{f1} and p_{f2}

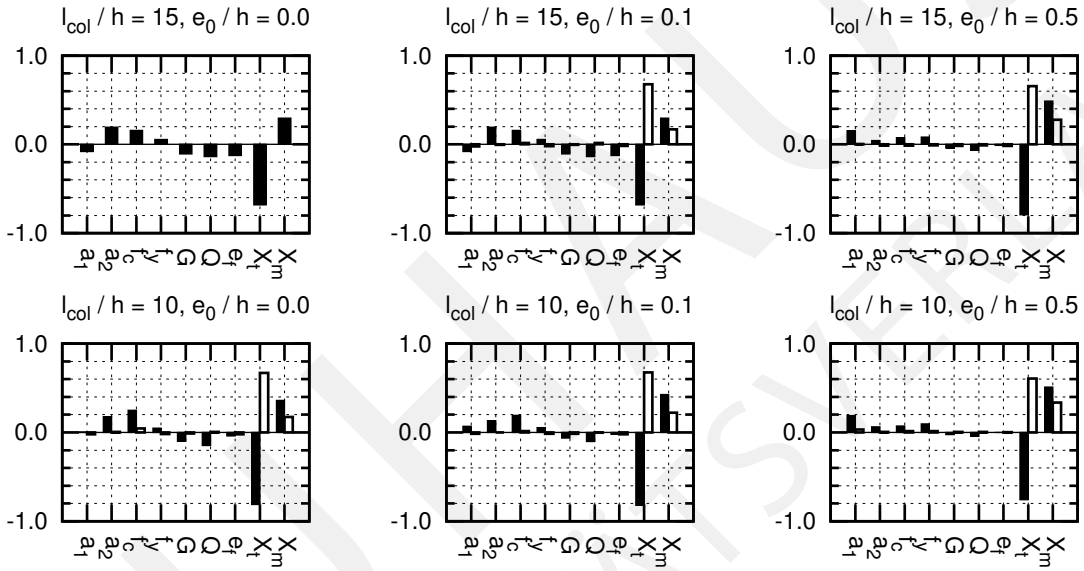

Figure 3: Spearman's rank correlation coefficient (black) and first order Sobol indices (white) for examined columns

5 Conclusions

The results of the examined columns confirm, that the advanced method according to DIN EN 1992-1-2 [5] is highly sensitive to calculated temperatures. The uncertainties of the resistance model only have a secondary effect. Neglecting the uncertainties of the thermal calculation can lead to unsafe results.

References

[1] Marcus Achenbach and Guido Morgenthal. Vollprobabilistische Analyse von Stahlbetonwänden unter Brandeinwirkung. *Bauingenieur*. Accepted for publication.

[2] Hans Dieter Baehr and Karl Stephan. *Wärme- und Stoffübertragung*. Springer, Berlin, 3rd edition, 1998.

[3] DIN EN 1991-1-2. Eurocode 1: Einwirkungen auf Tragwerke - Teil 1-2: Allgemeine Einwirkungen - Brandeinwirkungen auf Tragwerke, Dezember 2010.

[4] DIN EN 1992-1-1. Eurocode 2: Bemessung und Konstruktion von Stahlbeton- und Spannbetontragwerken - Teil 1-1: Allgemeine Bemessungsregeln für den Hochbau, Oktober 2005.

[5] DIN EN 1992-1-2. Eurocode 2: Bemessung und Konstruktion von Stahlbeton- und Spannbetontragwerken - Teil 1-2: Allgemeine Regeln - Tragwerksbemessung für den Brandfall, Oktober 2006.

[6] Thomas Gernay and Jean-Marc Franssen. A formulation of the Eurocode 2 concrete model at elevated temperature that includes an explicit term for transient creep. *Fire Safety Journal*, 51:1–9, 2012.

[7] Rüdiger Haß. *Zur praxisgerechten brandschutztechnischen Beurteilung von Stützen aus Stahl und Beton.* PhD thesis, Technische Universität Braunschweig, 1986.

[8] Volker Henke. *Ein Beitrag zur Zuverlässigkeit frei gelagerter Stahlbetonstützen unter genormter Brandeinwirkungen.* PhD thesis, Technische Universität Braunschweig, 1980.

[9] Dietmar Hosser, Ekkehard Richter, and A. Wöckener. Ermittlung der Wärmeleitfähigkeit von Beton aus dem Schlussentwurf prEN 1992-1-2 Fassung 10/02 durch Vergleich von berechneten und gemessenen Temperaturen. Schlussbericht, Institut für Baustoffe, Massivbau und Brandschutz, Braunschweig, 2004.

[10] Dietmar Hosser, Astrid Weilert, Christoph Klinzmann, Ralf Schnetgöke, and Cornelius Albrecht. Sicherheitskonzept zur Brandschutzbemessung. Abschlussbericht, Institut für Baustoffe, Massivbau und Brandschutz, Braunschweig, 2008.

[11] JCSS. Probabilistic model code, 2001.

[12] Karl Kordina and Ulrich Quast. Bemessung von schlanken Bauteilen - Knicksicherheitsnachweis. In *Betonkalender 1997, Teil I*, pages 479–575. Ernst & Sohn, Berlin, 1997.

[13] M. D. McKay, R. J. Beckman, and W. J. Conover. A comparison of three methods for selecting values of input variables in the analysis of output from a computer code. *Technometrics*, 21:239–245, 1979.

[14] Robert E. Melchers. *Structural Reliability Analysis and Prediction.* John Wiley & Sons, Chichester, 2nd edition, 1999.

[15] John A. Purkiss. *Fire Safety Engineering - Design of Structures.* Butterworth-Heinemann, Oxford, 1st edition, 1996.

[16] Horst Rinne. *Taschenbuch der Statistik.* Harri Deutsch, Frankfurt, 4th edition, 2008.

[17] Andrea Saltelli, Marco Ratto, Terry Andres, Francesca Campolongo, Jessica Cariboni, Debora Gatelli, Michaela Saisana, and Stefano Tarantola. *Global sensitivity analysis. The primer.* John Wiley & Sons, Chichester, 1st edition, 2008.

[18] Michael Six. *Sicherherheitskonzept für nichtlineare Traglastverfahren im Betonbau.* PhD thesis, Technische Universität Darmstadt, 2001.

Considering the non-simultaneous occurrence of extremes in the bivariate design using Copula functions

Jens Bender[1,2], Thomas Wahl[4], Christoph Mudersbach[2,3], Jürgen Jensen[1]

[1]University of Siegen, Research Institute for Water and Environment,
jens.bender@uni-siegen.de
[2]wbu consulting Ingenieurgesellschaft mbH, Siegen
[3]Bochum University of Applied Sciences, Institute for Water and Environment
[4]College of Marine Science, University of South Florida, USA

Abstract. Over the last years Copula functions were often used to derive multivariate design events in hydrology and other fields. In most of the studies, however, the simultaneous or even non-simultaneous occurrence of the variables to be modeled was not considered. In the bivariate case usually two approaches are commonly applied: (i) the maximum values of both variables were modeled despite their time of occurrence or (ii) the maximum values of either of the variables was modeled comprising the simultaneously occurred value of the other variable. In this study we introduce a novel approach to estimate bivariate design quantiles where the maxima values of the variables of interest do not necessarily have to occur simultaneously. The methodology is based on the common Copula theory using Archimedean Copula functions to model two variables X and Y. First, the maximum values of X are modeled considering the simultaneously occurred values of Y. Next, the maximum values of Y are modeled considering the simultaneous values of X. The envelop of both quantile-isolines of a given exceedance probability P represents the design relevant design value combinations of X and Y. The methodology is exemplarily applied to estimate design relevant water levels in the confluence reach of the rivers Rhine and Sieg in Germany. The results show, that the new approach leads to distinctively different results in contrast to the very conservative approach of analyzing the annual maximum values of both variables (despite their time of occurrence relative to each other). The introduced methodology can be applied to any data set (also for higher dimensions than the bivariate case) where the maximum values of the variable of interest do not always occur simultaneously. Furthermore, we show that the most relevant design data pair should be identified taking the consequences (here the resulting water levels) into account.

1 Introduction

Over the last years copula functions have been used to solve many different multivariate problems, among others in a hydrological context. They were applied for example for rainfall frequency analysis (e.g. [3]; [7]), flood frequency analysis considering peak flow and flood volume (e.g. [15], [9] , [1]), drought frequency analysis (e.g. [8]), storm surge modelling (e.g. [14]), and for several other multivariate problems. All above mentioned approaches have in common that they either consider the block maxima of one (primary) parameter together with concurrent values of the second parameter or the block maxima of both parameters. The latter concept assumes that both values occurred simultaneously. However, depending on the type of variables one is interested in and their possibly

independent physical genesis, this issue requires a more careful interpretation as already stated by [2].

Here we introduce a methodology to estimate multivariate design values where the maxima values of the two variables of interest do not necessarily have to occur simultaneously. To illustrate the practical use of this approach, we estimate the design water levels in the direct reach of a confluence of two rivers with very different catchment sizes where flood events usually do not occur simultaneously. Due to the bivariate nature of the case study and for simplicity, the focus is on the bivariate case, but it is noted that the methodology can be extended to higher dimensions to include further variables.

2 Methods

2.1 General copula theory

Since copula functions have recently been extensively used (especially in hydrology) and a corresponding number of papers have been published, we only provide a short introduction of the theoretical background of copula functions. Much more detailed information can be found for example in [10] and references therein.

Copulas are flexible joint distributions for modeling the dependence structure of two or more random variables. First mentioned by [12], the joint behavior of two (or more) random variables X and Y with continuous marginal distributions $u = FX(x) = P(X \leq x)$ and $v = FY(y) = P(Y \leq y)$ can be described uniquely by an associated dependence function or copula-function C. In the bivariate case, the relationship between all $(u, v) \in [0, 1]^2$ can be written as

$$F_{X,Y}(x, y) = C[F_X(x), F_Y(y)] = C(u, v) \tag{1}$$

where $F_{X,Y}(x, y)$ is the joint cumulative distribution function (cdf) of the random variables X and Y. A copula function with a strictly monotonically decreasing generator function $\phi : [0, 1] \rightarrow [0, \infty]$ with $\phi(1) = 0$ belongs to the Archimedean copula family. The general form of one-parametric Archimedean copulas is

$$C_\Phi(u, v) = \phi^{-1}[\phi(u) + \phi(v)] \tag{2}$$

where Φ denotes the copula parameter. Here we consider three Archimedean copulas, namely the Clayton, Frank, and Gumbel copulas, since they are relatively easy to construct, flexible, and capable to cover the full range of tail dependence. The Clayton copula has lower tail dependence, while the Frank copula has no tail dependence and the Gumbel copula has upper tail dependence ([10]). To identify the best copula to model the prevailing dependence we exploit the parametric bootstrapping goodness of fit test (GoF-test) for copulas as proposed in [5]. This test is based on Cramér-von-Mises statistics. The acceptance or rejection of a copula depends on the p-value which is calculated via bootstrapping procedures. Large p-values support its suitability whereas small values indicate its infeasibility to model the dependence structure in the given dataset. In hydrology and hydraulic engineering one is mostly interested in the recurrence intervals (or

return periods, RP) of certain extreme events. In the univariate case the RP is commonly defined as

$$T_{uni} = \frac{\mu_T}{1 - F_X(x)}. \tag{3}$$

Where F_X is the cumulative distribution of the variable X to be modelled and x represents the corresponding design quantile. μ_T denotes the mean interarrival time (typically given in years; when using annual maxima values, μ_T equals 1 year). The definition of the return period (Equation 3), however, is not directly applicable to the multivariate case. In the scientific community there is still an ongoing discussion about the definition of joint return periods (JRP) (see e.g. [6] and references herein). Here, we follow the approach introduced by [11]. This concept of the JRP is based on the bivariate cumulative distribution function $F_{XY}(x, y)$, formulated by the bivariate copula function $C_{UV}(u, v)$ (Equation 1) and the cdf's of the marginal distributions. This JRP is often denoted as AND-joint return period ($\mathrm{T}^{\wedge}$) as it expresses the probability that X and Y exceed the values x and y at the same time: $P[X > x \wedge Y > y]$. Hence, the bivariate AND-JRP $\mathrm{T}^{\wedge}$ can be written as

$$T^{\wedge}_{X,Y} = \frac{\mu_T}{P(X \geq x \wedge Y \geq y)} = \frac{\mu_T}{1 - F_X(x) - F_Y(y) + C[F_X(x), F_Y(y)]} \tag{4}$$

Since the method to derive the JRP is of minor interest in this study, we focus on bivariate design events derived by the AND-joint exceedance probability based on Equation 4.

2.2 Considering non-simultaneous occurrence of the variables

When modeling two random variables X and Y, it is (especially in hydrology) essential to cover the dependence (or independence) of the physical genesis of the extreme events. Block maxima series can be gathered for the two variables of interest independently and then used in the multivariate statistics. Although there might be an analytical dependence between both variables, the two maxima values (for example in a year) may have not occurred simultaneously. It might even be that the simultaneous occurrence is physically impossible or at least very unlikely. When modeling the common parameters flood peak discharge (Q) and flood volume (V) of a small catchment for instance, where snow melt influences the discharge regime, it is very unlikely that the highest values of Q and V coincide. This is because in such cases high runoffs are mostly caused by short but intensive precipitation events whereas floods with high volumes often emerge from moderate but continuous rainfalls or even snow melt.

Therefore, an obvious approach consists in modelling the block maxima series of X (from here on referred to as X_{BM}) and the simultaneously measured value of Y (Y_{SIM}) and vice versa (i.e. Y_{BM} and X_{SIM}). This requires fitting four marginal distributions $F_{X_{BM}}(x_{BM})$, $F_{Y_{BM}}(y_{BM})$, $F_{X_{SIM}}(x_{SIM})$, and $F_{Y_{SIM}}(y_{SIM})$ to the data sets as well as two copula functions (C_I and C_{II}) to model the mutual dependency between the variable pairs (see the following Equation 5):

$$F_I(x_{BM}, y_{SIM}) = C_I[F_{X_{BM}}(x_{BM}), F_{Y_{SIM}}(y_{SIM})] = C_I(u_{BM}, v_{SIM})$$

and

$$F_{II}(x_{SIM}, y_{BM}) = C_{II}[F_{X_{SIM}}(x_{SIM}), F_{Y_{BM}}(y_{BM})] = C_{II}(u_{SIM}, v_{BM}) \tag{5}$$

In cases where both variables always occurred simultaneously (i.e. $X_{BM} = X_{SIM}$ and $Y_{BM} = Y_{SIM}$ the two corresponding marginal distributions would be identical, $F_{X_{BM}} = F_X \wedge F_{Y_{BM}} = F_Y$. This would furthermore result in identical dependence structures of the variables and hence in identical copula functions $C_I = C_{II}$.

When analyzing flood peaks of two streams at a confluence it is unlikely that all block maxima values occur simultaneously. Therefore, it can be assumed that in the majority of cases four marginal distributions and two distinct copula functions are required to fully describe the stochastic behavior of the system.

The question that instantly arises from applying this procedure is how the relevant design events can be derived from the two copulas. This can be realized by overlapping the quantile-isolines of the distribution functions F_I and F_{II}. The outer envelope of both quantile-isolines then contains all possible variations of the design relevant data combinations.

For a given $\alpha \in (0, 1)$ we define the quantile-isoline functions $q_I(x)$ and $q_{II}(x)$ implicitly by the equation $F_I(x, q_I(x)) = \alpha$, and similarly $F_{II}(x, q_{II}(x)) = \alpha$. The envelope is then given by the maximum of both functions:

$$x \rightarrow \max \{q_I(x), q_{II}(x)\} \tag{6}$$

3 Case study

The methods outlined above are exemplarily applied to the confluence of the rivers Rhine and Sieg in Germany. The Rhine River has a total catchment size of 185,300 km^2 with a total flow length of 1,239 km. At the confluence of both rivers the Rhine River drains a catchment of 141,008 km^2 with a water course length of 659.5 km. The run-off regime is dominated by winter floods occurring mostly between November and March. At river station 654.8 (4.7 km upstream of the confluence) gauge station Bonn has measured the discharge since 1820. For this study the daily mean discharge time series from 1954 to 2012 was available. The average discharge over this period was MQ = 2,082 m^3/s with a standard deviation of s = 1,056 m^3/s. The two highest discharges were observed on 23 December 1993 and 30 January 1995 with both HHQ = 10,500 m^3/s. The flood indicator to be modeled in this study is the annual maximum discharge series (AMAX). The mean annual maximum discharge (MHQ) at gauge Bonn amounts to 6,383 m^3/s. At river station km 659.5 the Sieg River enters the Rhine. The Sieg has a total catchment size of 2,856.9 km^2 with a water course length of 155.2 km. 8.4 km upstream of the confluence gauge Menden is located. We use the time series of 15-minute mean discharges covering the 48 year period from 1964 to 2012. The overall mean discharge is MQ = 52.6 m^3/s with a standard deviation of s = 68.5 m^3/s and there are no major channels entering the Sieg River between the gauge and the confluence with the Rhine. The highest discharge at gauge Menden was measured on 23 February 1970 with HHQ = 931 m^3/s and the mean annual maximum discharge amounts to MHQ = 477 m^3/s. Although the run-off regime at River Sieg is also dominated by winter floods (see Figure 3), only 24 of the 48 annual maximum discharges of both rivers occurred within a time window of 14 days. In order to take this into account we use two bivariate data sets for the statistical analyses: (i) the

annual maximum discharges of the main stream (from here on referred to as peak on main stream, PM) and the concurrent flows of the tributary (CT) and (ii) the annual maximum discharges of the tributary (PT) and the concurrent flows of the main stream (CM). In order capture discharges that occurred almost concurrently, CT and CM can be chosen as the maximum values within a certain time period around the PM and PT values. A meaningful choice of the size of this time window can be, for example, based on common criteria which are usually considered to assure that two flood peaks are independent. Following [13], the time window can be selected depending on the catchment size of the river to ± 5, 7 or 10 days. Due to the small catchment size of the Sieg River (of only 2,856.9 km^2) and a corresponding average run time of flood waves of 20 hours, we selected a time window of ± 1 day. Following this definition, only three annual maximum discharge events of both rivers can be considered as 'simultaneous events'.

4 Results

First we fit the marginal distributions to the four samples comprising the peak on the main stream, concurrent flow on the tributary, peak on the tributary, and concurrent flow on the main stream. For identifying the best fitting distribution functions we calculated the root mean square error of the theoretical non-exceedance probabilities compared to the empirical non-exceedance probabilities. For the two AMAX series the Generalized Extreme Value distribution (GEV) fits best, whereas the Log-Normal (LogN) distribution fits the two concurrent flow series best. The 100-yr event of the AMAX series at the main stream, for example, amounts to 10,820 m^3/s. In case of an PM-PT model, i.e. a simultaneous occurrence of both annual maximum discharges, the second parameter (AMAX at tributary) would amount to 894 m^3/s, whereas the actual 100-yr discharge of the concurrent flow series at the tributary only amounts to 568 m^3/s. Ignoring these differences in the bivariate statistical analyses would strongly affect the results and potentially lead to a costly overdesign. Next, the two bivariate copula functions can be selected and fitted to the parameter pairs PM-CT and CM-PT. For the PM-CT dataset only the Gumbel copula ($\Phi_{Gumbel} = 1.631$) passes the goodness of fit test on the 95% confidence level. For the CM-PT dataset p-values are high for all three copulas and all pass the GoF test. Therefore, as a second test, we compare the observed data pairs with those simulated with the copulas and transformed to their original units with the marginal distributions (see Figure 1). Although the Clayton copula leads to the lowest p-value we select it since it provides the best optical fit.

In Figure 1 the difference of the statistic results is evidently illustrated. Considering for instance an event combination of 8,000 m^3/s (Rhine River) and 400 m^3/s (Sieg River) for the PM-CT case, the annual exceedance probability would result to P = 0.05 (20-yr). The same event would lead in the CM-PT case to an annual exceedance probability of some P = 0.02 (50-yr).

Considering the two statistic results (PM-CT and CM-PT) the exceedance probabilities of discharge pairs still vary significantly. Therefore it is required to derive an overall quantile-isoline representing the results of both statistics. This is achieved by overlapping the quantile-isolines of both copulas to determine the design relevant envelope with

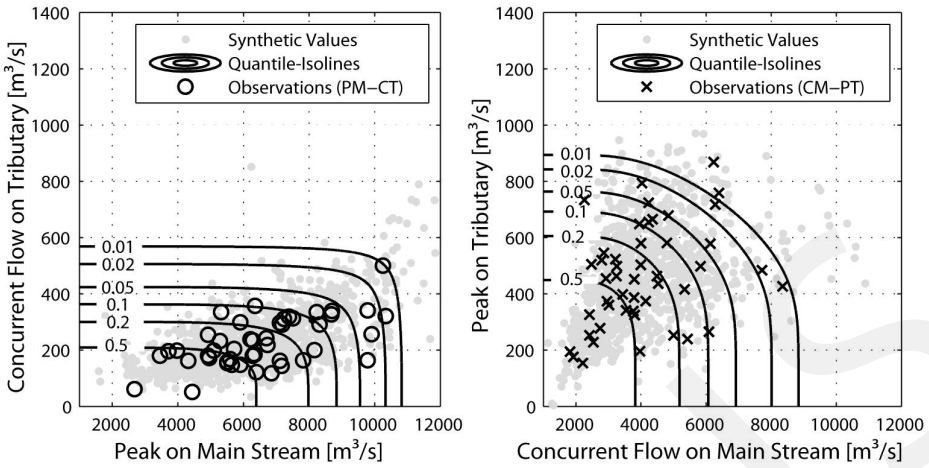

Figure 1: Results of the bivariate statistic for the data pairs PM-CT (left) and CM-PT (right)

Equation 2. In Germany flood protection structures are usually designed to withstand a 100-yr event; thus we focus on discharge combinations at the joint exceedance level of P = 0.01. The red line in Figure 2 represents the outer envelope of the overlapped quantile-isolines. The envelope is bounded by the 99.5% values of the univariate design values of the given annual exceedance probability (here P = 0.01). This boundary was chosen since discharge combinations on the envelope below or left of these points would lead to lower design water levels in the confluence reach and do not need to be further considered.

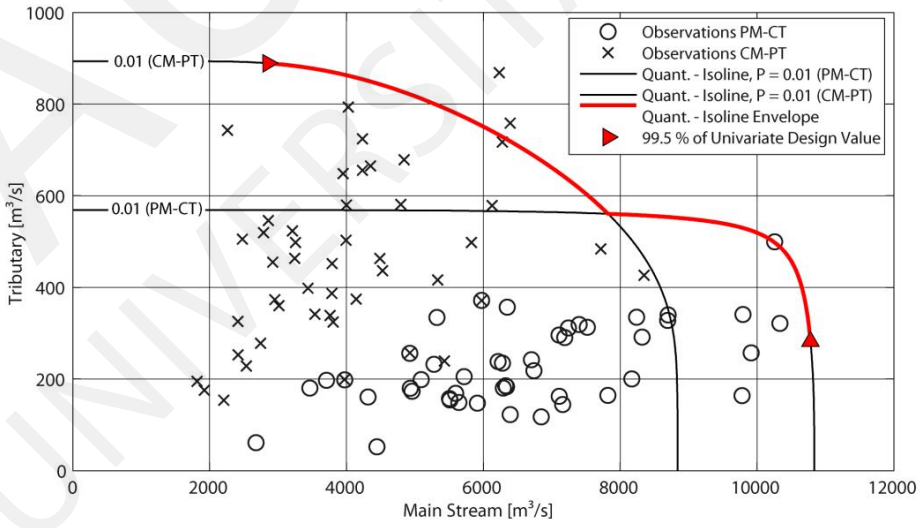

Figure 2: Overlapped quantile-isolines with annual exceedance probability of P = 0.01 derived from the two bivariate copulas fitted to the PM-CT and CM-PT data sets

As in common bivariate statistics, the question arises which combination along the quantile-isolines is most relevant for design purposes, i.e. which combination leads to the highest design parameter (here water level). We recommend employing numerical models to compute a variety of combinations on the desired quantile-isoline. The combination leading to the highest design parameter should than be chosen for the design.

5 Conclusions

We introduced a novel approach to model multivariate data when the maxima of both variables in a year are unlikely to occur always simultaneously. The approach is based on performing common bivariate statistical analyses with suitable copula models considering the block maxima of each variable together with the simultaneously observed values of the other variable and then overlapping the quantile-isolines. This allows defining the design relevant data pairs lying on the outer envelope of both isolines of a given quantile. The introduced methodology can be applied to any data set (also for higher dimensions than the bivariate case) where the maximum values of the variables of interest do not always occur simultaneously. Furthermore, the basic approach of this method also provides several advantages for other multivariate models, such as linear correlation models, where the non-simultaneous occurrence of extremes is automatically descripted in the joint probability density function.

References

[1] J Bender, T Wahl, and J Jensen. Multivariate design in the presence of non-stationarity. *Journal of Hydrology*, 514:123–130, 2014.

[2] S Coles, J Heffernan, and J Tawn. Dependence measures for extreme value analyses. *Extremes*, 2(4):339–365, 1999.

[3] C De Michele and G Salvadori. A generalized pareto intensity-duration model of storm rainfall exploiting 2-copulas. *Journal of Geophysical Research: Atmospheres (1984–2012)*, 108(D2), 2003.

[4] C De Michele, G Salvadori, M Canossi, A Petaccia, and R Rosso. Bivariate statistical approach to check adequacy of dam spillway. *Journal of Hydrologic Engineering*, 10(1):50–57, 2005.

[5] C Genest, B Rémillard, and D Beaudoin. Goodness-of-fit tests for copulas: A review and a power study. *Insurance: Mathematics and economics*, 44(2):199–213, 2009.

[6] B Gräler, MJ van den Berg, S Vandenberghe, A Petroselli, S Grimaldi, B De Baets, and NEC Verhoest. Multivariate return periods in hydrology: a critical and practical review focusing on synthetic design hydrograph estimation. *Hydrology and Earth System Sciences*, 17(4):1281–1296, 2013.

[7] S Grimaldi and F Serinaldi. Design hyetograph analysis with 3-copula function. *Hydrological sciences journal*, 51(2):223–238, 2006.

[8] S-C Kao and R S Govindaraju. A copula-based joint deficit index for droughts. *Journal of Hydrology*, 380(1):121–134, 2010.

[9] S Karmakar and SP Simonovic. Bivariate flood frequency analysis. part 2: a copula-based approach with mixed marginal distributions. *Journal of Flood Risk Management*, 2(1):32–44, 2009.

[10] R B Nelsen. *An Introduction to Copulas*. Springer, 2006.

[11] G Salvadori. *Extremes in nature: an approach using copulas*, volume 56. Springer, 2007.

[12] M Sklar. *Fonctions de répartition à n dimensions et leurs marges*. Université Paris 8, 1959.

[13] C Svensson, W Z Kundzewicz, and T Maurer. Trend detection in river flow series: 2. flood and low-flow index series/détection de tendance dans des séries de débit fluvial: 2. séries d'indices de crue et d'étiage. *Hydrological Sciences Journal*, 50(5), 2005.

[14] T Wahl, C Mudersbach, and J Jensen. Assessing the hydrodynamic boundary conditions for risk analyses in coastal areas: a multivariate statistical approach based on copula functions. *Natural Hazards and Earth System Science*, 12(2):495–510, 2012.

[15] L Zhang and VP Singh. Bivariate flood frequency analysis using the copula method. *Journal of Hydrologic Engineering*, 11(2):150–164, 2006.

Monte Carlo cross-validation for response surface benchmark

A. Beschorner, M. Voigt, K. Vogeler

Institute for Fluid Mechanics,
Faculty of Mechanical Engineering
Technische Universität Dresden
Germany
andre.beschorner@mailbox.tu-dresden.de

Abstract. When meta-models are fitted to the underlying data it is essential to validate the model by a trustworthy criterion. Many industry relevant applications are characterized by a high input parameter dimension and time consuming, cost intensive deterministic computations. In these typical cases the data size is not much higher than the amount of coefficients in the polynomial equation of the meta-model, which will lead to an overestimation of the model quality determined by the Coefficient of Determination (CoD).
An alternative benchmark criterion for response surfaces can be delivered by cross-validation (CV), where an overestimation of the meta-model quality is unusual.
This paper will use a published industry relevant example [4] to compare the simple CoD with a Monte Carlo cross-validation CoD (CoD_{MCCV}). Detailed investigations of the MCCV-method are made using a fast calculating test-model with similar characteristics as the original deterministic model. The results will show the influence of the splitting ratio, the number of cross-validation runs and the number of the deterministic samples in the database on the CoD_{MCCV} result values and their variance. To predict the variance we will give correlations, for a code internal adjustment of MCCV calculation parameters. The discussion will point out the importance of the sample to coefficients ratio (SCR) and conclude the advantages and disadvantages of the tested method.

a, b, c, d, e, f, g, h	adjustment parameter	O	order of response surface
C	number of coefficients	SCR	sample to coefficient ratio
CoD	Coefficient of Determination	SR	splitting ratio
CoD_{MCCV}	cross-validation CoD	$SRCV$	simple random CV
CV	cross-validation	x	input variable
E	number of input variables	y	result variable
i, j	count variables	$\tilde{y}$	meta-model result variable
K	number of folds	$\overline{y}$	mean of variable
$KFCV$	K-fold CV	σ	standard deviation
$MCCV$	Monte Carlo CV	$_t$	training (samples)
n	number of samples	$_v$	validation (samples)

1 Introduction

"When a validity coefficient is computed from the same data used in making an item analysis, this coefficient cannot be interpreted uncritically. And, contrary to many statements

in the literature, it cannot be interpreted 'with caution' either. There is one clear interpretation for all such validity coefficients. This interpretation is – 'Baloney!'" [1]
This conclusion by Cureton should remind the investigator of any data fitting problem, that the commonly used Coefficient of Determination (CoD) is not a stable criterion for model fitness estimation in any way. In the second part of this paper we will discuss the dependency of the CoD on the number of coefficients n in the meta-model and the number of simulations in the dataset. Afterwards we will show how this misleading model fitness interpretation by the CoD can be avoided by using a cross-validation procedure.
Cross-validation as a method for model fitness evaluation was proposed by Mosier [6]. The concept of cross-validation is to use separate data sets for model training and evaluation respectively. Since in most real applications the amount of data is limited, it is necessary to split the number of data-points n into a training data set n_t and a validation data set n_v. Over the last decades different kinds of cross-validation had been proposed, which uses different splitting procedures. A selection of them should be described here.

1.1 Cross-validation procedures

Leave-one-out cross-validation (LOOCV), which is also called delete-one CV or ordinary CV is the simplest exhaustive CV procedure. Every single data point is successively left out from the training dataset and used for validation as described by Stone [11]. The number of CV-runs is equal to the number of samples n in the dataset. As a test criteria for the LOOCV Myers and Montgomery [7] suggest the $R^2_{prediction}$ that uses the predictive error sum of squares ($PRESS$)

$$R^2_{prediction} = 1 - \frac{PRESS}{SST} = 1 - \frac{\sum_{i=1}^{n}[y_{vi} - \tilde{y}_{vi}]^2}{SST} \tag{1}$$

and the total sum of squares (SST)

$$SST = \mathbf{y}^T\mathbf{y} - \frac{\left[\sum_{i=1}^{n} y_i\right]^2}{n}. \tag{2}$$

Alternatively they show the possibility to compute the $R^2_{prediction}$ without cross validation by using the diagonal elements h_{ii} of the hat matrix $\mathbf{H} = \mathbf{X}(\mathbf{X}^T\mathbf{X})^{-1}\mathbf{X}^T$

$$R^2_{prediction} = 1 - \frac{\sum_{i=1}^{n}\left(\frac{y_i - \tilde{y}_i}{1-h_{ii}}\right)^2}{SST}. \tag{3}$$

Leave-p-out cross-validation (LPOCV) or delete-d multifold CV (Zhang [13]) is very close to the LOOCV, but here a defined number p of data points are left out from the training set and used to validate each response surface. This procedure is also exhaustive since every possible subset p is left out once.

K-fold cross-validation (KFCV) also called V-fold cross-validation is computationally less expensive compared to LOOCV and LPOCV. It was introduced by Geisser [3]. The complete dataset is split into K subsets of approximately equal size n/K. Each subset is successively used as validation set, whilst the other subsets are used to train the response surface. The number of CV-runs is equal to K – the number of folds which is defined

between $2, \ldots, n$ but should not be higher than $n/3$ in a practical sense. If K would be equal to n the procedure would be identical to LOOCV. The described method is a partially data splitting procedure since not every possible combination of validation subsets is used.

Another method with partial data splitting is **simple random cross-validation (SRCV)** or **Monte Carlo cross-validation (MCCV)** respectively. The method has been presented by Picard and Cook [8] and has been compared to the above listed procedures by Shao [10] and Xu [12], while they demonstrate outperforming results for the MCCV applied in model selection. Compared to the KFCV the subsets are selected randomly. Moreover the number of CV-runs and the validation subset size expressed by the splitting ratio $SR = n_t/n$ are independently selectable. This additional freedom of method configuration makes it necessary to identify practical ranges for the configuration parameters.

The MCCV method will be evaluated in paragraph three of this paper by using a test-model, which is emulating an industry relevant probabilistic investigation. Next to the variation of the splitting ratio $SR = n_t/n$ and the number of CV-runs we will also show the influence of n – the number of data points in the complete data set. We will also compare the CoD [2], [9]

$$CoD = \left(\frac{\sum_{i=1}^{n}[(\tilde{y}_i - \bar{\tilde{y}}) \cdot (y_i - \bar{y})]}{\sqrt{\sum_{i=1}^{n}(\tilde{y}_i - \bar{\tilde{y}})^2 \cdot \sum_{i=1}^{n}(y_i - \bar{y})^2}} \right)^2 = \left(\frac{Cov(\tilde{\mathbf{y}}, \mathbf{y})}{\sqrt{Var(\tilde{\mathbf{y}})} \cdot \sqrt{Var(\mathbf{y})}} \right)^2 \tag{4}$$

to the CoD_{CV} results that are computed in the same way but using only the selected validation samples

$$CoD_{CV} = \left(\frac{\sum_{i=1}^{n_v}[(\tilde{y}_{iv} - \bar{\tilde{y}}_v) \cdot (y_{iv} - \bar{y}_v)]}{\sqrt{\sum_{i=1}^{n_v}(\tilde{y}_{iv} - \bar{\tilde{y}}_v)^2 \cdot \sum_{i=1}^{n_v}(y_{iv} - \bar{y}_v)^2}} \right)^2 = \left(\frac{Cov(\tilde{\mathbf{y}}_\mathbf{v}, \mathbf{y}_\mathbf{v})}{\sqrt{Var(\tilde{\mathbf{y}}_\mathbf{v})} \cdot \sqrt{Var(\mathbf{y}_\mathbf{v})}} \right)^2 \tag{5}$$

to discuss the usefulness of cross-validation. Note that none of the response surfaces computed with a training subset and validated with the corresponding validation subset is used as the final meta-model. The polynomial equation of the final meta-model is computed with all data points.

In general it is very important to know about the predictability of a meta-model since it might be used to rapidly produce new data with a Monte Carlo simulation using the polynomial equation. Another application is to estimate the importance of the input parameters using the meta-model, which is expressed by the Coefficient of Importance (CoI). If the model fitness to the underlying data is lower than expected by the investigator it might lead to misinterpretation of parameter importance or erroneous interpretations with the new data calculated on the meta-model.

1.2 Deterministic test-model used for evaluation

The probabilistic investigation of the impact of manufacturing variability on the performance of a ten stage high pressure compressor, by Lange et al. [4] is in the core of interest in this paper. In his investigation Lange described the rotor blade geometry of each rotor

stage by 14 classical profile parameters. Due to the ten compressor stages there are 140 probabilistic input variables in the complete simulation.
The parameter scatter has been determined by real blade measurement with a 3D scanner. For the probabilistic post processing by meta-models, linear regression models have been used, which need 141 data points in minimum.
Since the CFD simulation of a ten stage compressor at seven operation points took about 3 days on an Intel® Core™ i7 machine, it was decided to use 200 virtual realizations created by optimized Latin Hypercube sampling. The results of this huge probabilistic simulation showed that there are mainly two important parameters in each stage, with a variation of their influence depending on the stage and the operation point. The fitness of the meta-models evaluated with the CoD is between 0.95 and 0.98.

For a detailed investigation of the CoD behavior and possible improvements on meta-model benchmark by cross-validation it was necessary to replace the above described deterministic model by a fast calculating test-model. The created test-model follows the idea of broadly emulating the main characteristics of the original model, but neglecting the operation point variation.

The here used HiPar-test-model (for **hi**gh input **par**ameter space) is using 140 input variables x_i with $i \in \{0, \ldots, 139\}$ computing six different solution variables $y_1, \ldots, y_6$. The input space of 140 dimensions is internally split into 10 groups - similar to the 10 compressor stages, controlled by $k \in \{1, \ldots, 10\}$. Hence there are 14 input parameters in each group.
The HiPar-test-model uses a combination of two public test-models mentioned in the collection of Molga et. al [5]. For $i = i_G \in \{0, 14, 28, 42, \ldots, 126\}$ a modified version of Griewangk's test function is used. Two variables x_i and x_{i+1} are computed within this function with a strong influence on the solution. Hence two variables of each group have a higher importance. If $i \neq i_G$ Rosenbrock's test function is used. It has a lower influence and is hard to approximate by a polynomial regression model. The standard formulations of the test functions can be found in [5]. The modified Griewangk function as implemented in the deterministic test-model is as follows:

$$y_{Griew.k} = a\left(bx_i{}^{(e_1\cdot(c_1-j)/c_1)} + dbx_{i+1}{}^{(e_2\cdot(c_2-j)/c_2)}\right) + f\left(\frac{\cos(bx_i)}{\sqrt{i+1}} \cdot \frac{\cos(bx_{i+1})}{\sqrt{i+2}}\right). \quad (6)$$

The step-wise exponent reduction using variable j as a counter is deactivated by setting j to a fixed value of 1. All other model adjustment parameters are given in Tab. 1.

$$y_{Rose.k} = y_{Griew.k} + \sum_{i=p+q(k)=0}^{p+q(k)=139} \left[h_1(x_{i+1} - x_i^2)^2 + h_2(1 - x_i)^2\right] \quad (7)$$

$$y_1, \ldots, y_6 = \sum_{k=1}^{10} \left[\frac{g}{g+k} \cdot \frac{y_{Rose.k}}{14}\right] \quad (8)$$

Rosenbrock's function as implemented in the test-model is defined by equation (7), where $p \in \{1, \ldots, 13\}$ and $q(k) = 14 \cdot (k-1)$. So that, $i \in \{1, \ldots, 13\}; \{15, \ldots, 27\}; \ldots$. The results of each input variable group are added up to the result value $y_1, \ldots, y_6$, as shown in equation (8). There is a parameter influence reduction with increasing k.

The parameter settings for the six output variables has been chosen to determine first order response surfaces with Coefficients of Determination of 0.98, 0.97, 0.96, 0.95, 0.94, 0.93 using a number of samples of $n = 200$. For a higher sample size the CoD will decrease as described in the next paragraph. All 140 input parameter distributions are generated by latin hypercube sampling with an uniform distribution in the interval [0,1].

variable	y_1	y_2	y_3	y_4	y_5	y_6
a	1/175	1/150	1/185	1/240	1/250	1/150
b	600	600	600	600	600	600
c_1	140	110	85	60	66	75
c_2	300	180	200	500	500	300
d	1.3	1.3	1.3	1.4	1.3	1.3
e_1	1.44	1.40	1.45	1.49	1.51	1.455
e_2	1.28	1.26	1.3	1.23	1.2	1.3
f	1000	200	400	300	2500	300
g	30	30	30	25	20	30
h_1	5	7.5	9.5	10.45	11.3	17.9
h_2	3	2	2.2	12	13	2

Table 1: Model adjustment parameter setting in the HiPar-test-model for the six different meta-models $y_1, \ldots, y_6$

The test-model is coded in C++ and is designed very flexible. It can be easily changed in its amount of input parameters and other model characteristics, to perform further investigations e.g. on the computation time in chapter 3.3. Next to the described test-model with six solution variables, we used two other test-model types to enlarge the insight of this investigation for some aspects. So there are up to 22 meta-models included in the result analysis.

2 Characteristics of the CoD

The used test-model with 140 input variables is designed to produce data which can be approximated by first order response surfaces with CoD values between 0.93 and 0.98 for the six result variables, which is the same range as in the ten stage compressor model investigated by Lange [4]. This is of course only true for the same sample to coefficients ratio of $SCR = 1.4$ when the number of samples is $n = 200$. It is important to see the models CoD values always with respect to the existing SCR, since the CoD strongly depends on the SCR.

The left graph of Figure 1 shows the CoD for the six solution response surfaces as function of the SCR. For a SCR of 1.4 the values are equal to the original deterministic model. By increasing n, the estimated quality of the meta-models is strongly decreasing. The slope of the decrease is stronger for models with lower CoD values.
When the SCR reaches 12 the decrease stops and the CoD becomes nearly constant with values between 0.71 and 0.91. Here the meta-model quality reaches its real maximum.

Below the saturation threshold of $SCR = 12$ the quality of the meta-models is clearly overestimated by the CoD.

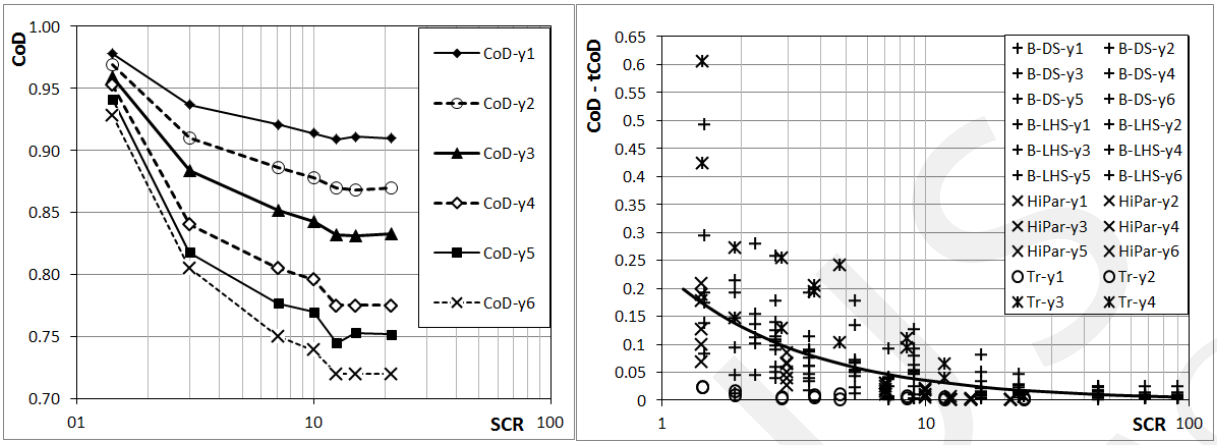

Figure 1: left: CoD of the six HiPar-response surfaces as function of the sample to coefficient ratio (SCR), right: Difference between CoD and target-CoD ($tCoD$) as function of the SCR for all tested meta-models

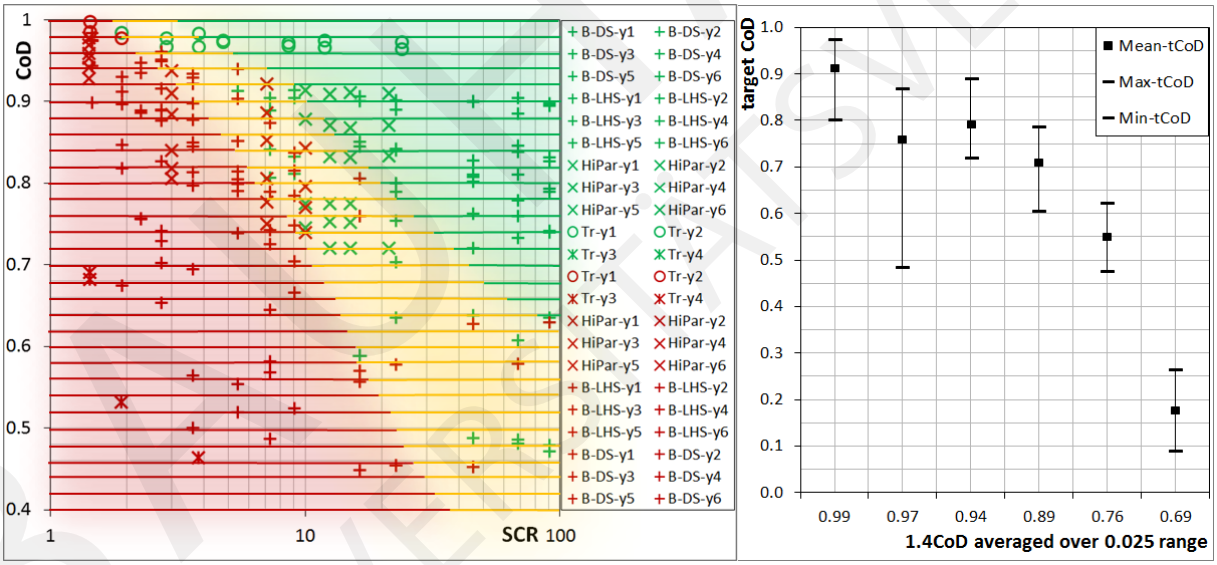

Figure 2: left: CoD as function of SCR, green symbols are above and red symbols are below the saturation threshold, right: $tCoD$ ranges as function of the $1.4CoD$ revealed by the used 22 test-models

To verify this connection between the CoD saturation and the SCR, some more test-models should be used. The right graph in Figure 1 shows the absolute difference of the CoD to the target-CoD ($tCoD$), which is the average of the CoD at the two highest SCR-values. The shown data include all 22 tested meta-models.
For models with a very high $tCoD$ close to unity the deviation is small for the complete SCR-range. In this case the saturation starts at low SCR values of about 3.

The highest observed deviation values $(0.4 - 0.6)$ for a SCR of 1.4 occur for meta-models with a low $tCoD < 0.5$.
All models with a $tCoD$ between 0.5 and 0.975 show a similar saturation behavior. The SCR-range of their saturation is between 7 and 22. The included trend line approximates the averages of all shown values.

Figure 2 gives the computed CoD depending on the SCR, while the color of the data points shows if the CoD is already saturated (green) or has still a difference to the $tCoD$ higher than 0.015. Most of the points (74%) achieve the saturation threshold in a SCR range between 7 and 22. Moreover there is the clear tendency, that models with a low $tCoD$ achieve the saturation at high SCR values. An explicit connection between the two variables can not be given due to the high observed scatter in the data and a quite small database. But the chart is divided into three areas, that can help the investigator to decide whether the computed CoD is reliable or not. In the red area we observed no saturated result. In the green area all computations are close or equal to the $tCoD$. In the yellow marked area we observed both, results above and below the saturation threshold.

The right graph of Figure 2 shows the connection between the CoD computed at an SCR of 1.4 ($1.4CoD$) and the $tCoD$. The data points include the $1.4CoD$ values averaged over a 0.025 wide range. For the first point this is for example the range between 0.975 and 1. The vertical axis represents the mean, min and max values of the corresponding $tCoD$ values. An interpretation of the shown data derived by 22 meta-models can be for example: If the $1.4CoD$ is 0.97, the saturated $tCoD$ can be between 0.48 and 0.87.

Generally spoken, it is important for the interpretation of any CoD value to know about the SCR as well. If the CoD should be useful as test criterion the SCR should be in or above the saturation range $(7 - 22)$.

3 Results of the Monte Carlo cross-validation

In this part we want to analyze the characteristics of the CoD_{MCCV} by varying the computation settings splitting ratio (SR), the number of samples (n) and the number of CV-runs for different meta-models. The splitting ratio has been varied between 0.5 and 0.995. The number of samples n has been varied between 200 and 1763 which corresponds to a SCR between 1.4 and 12.5. The number of CV-runs is varied between 20 and 2000, while each run includes the sample splitting, computation of a response surface using the training samples n_t and the computation of the single-run-CoD using n_v. The result CoD_{MCCV} is the average of all this CV-runs.

If the complete calculation with all its internal CV-runs is repeated, the resulting CoD_{MCCV} will not be exactly the same since each selection of n_v is randomly. But if the number of CV-runs is high enough the variance of the CoD_{MCCV} will be small. To estimate the variation of the results in chapter 3.2, each computation has been repeated 20 times with constant computation settings.
The data points shown in Figure 3 are averaged over the 20 repetitions. The splitting ratio is $SR = 0.975$. This leads to a number of validation samples $n_v = 5$ for $n = 200$.
The left graph compares the CoD with the CoD_{MCCV} for all calculated SCR values. The CoD_{MCCV} predicts a much lower response surface quality in particular if the SCR is low.

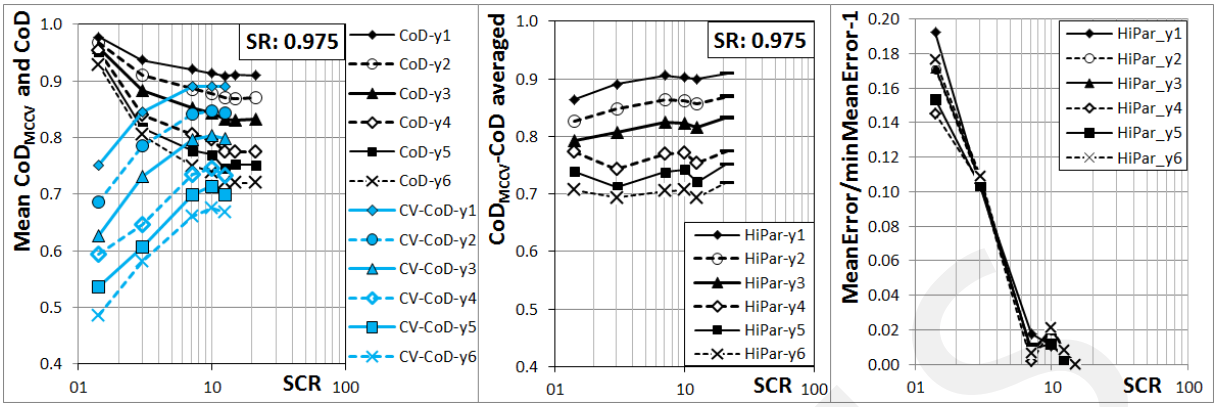

Figure 3: left: Comparison of CoD_{MCCV} that is averaged over 20 repetitions to the CoD results for the HiPar-test-model; middle: average of CoD_{MCCV} and CoD; right: mean error of response surface approximation normalized with minimum mean error tested with a complete independent sample set of $n = 3000$

For the six response surfaces of the HiPar-test-model there is no overestimation of the quality by the CoD_{MCCV}. For SCR values in the saturation range, CoD_{MCCV} and CoD converge into each other.
The improving response surface quality while increasing the SCR is shown by the right graph in Figure 3. Here we present the mean error computed with 3000 independent data points normalized with the minimum mean error that occurred. The graph shows, that the response surfaces at a $SCR = 1.4$ have about 14% to 20% higher errors than the best computed meta-models. The meta-models with minimum errors are reached at SCR values of 7 or higher.

The center graph in Figure 3 shows the average of the CoD_{MCCV} and the CoD up to an SCR of 12.5 - the last given values present the CoD. These average values are nearly constant over the complete SCR range, hence this criterion can be used as a rough estimator of the $tCoD$ that would be reached with a big database. The predictability of the $tCoD$ worked well for 91% of our test cases (20 out of 22 meta-models).

3.1 Influence of the splitting ratio

Figure 4 shows the variation of the splitting ratio for the complete test range. There is a positive correlation between the SR and the CoD_{MCCV} if the SCR is low, e.g. $SCR = 1.4$ as shown in the left graph. Here the low SR values 0.71 and 0.75 with many validation samples and the lowest possible n_t do not give useful results. The practical relevant SR-range for a low SCR is here between 0.9 and 0.975.

For a SCR of 3 the influence of the splitting ratio has decreased. Here the suggested range is between 0.9 and 0.975 as well.

Response surfaces with a large database are only marginal affected by a SR variation (Figure 4 right). The influence is only visible for an extremely high splitting ratio of 0.995, with 5 samples in the validation group. The useful SR-range is between 0.8 and

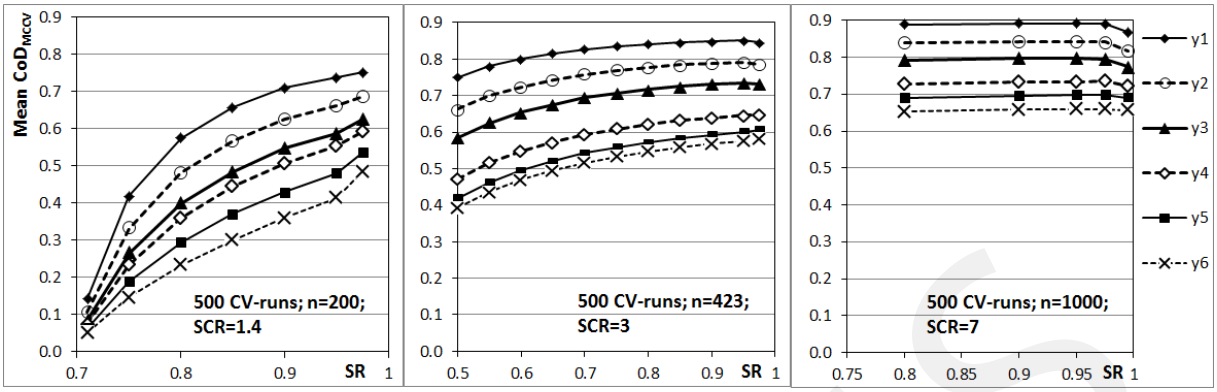

Figure 4: Influence of the splitting ratio (SR) on the CoD_{MCCV} that is averaged over 20 repetitions and shown for different data sizes

0.975.

3.2 Result variation due to randomness

Due to the random selection of the test samples, the results of the CoD_{MCCV} will vary although the used data set is fixed for constant SCR. The amount of this variation depends on the number of CV-runs and on the splitting ratio.

For the used test-model the σ is strongly increasing for very high splitting ratios above 0.975. For lower SR values there is a low positive correlation between SR and σ. For the

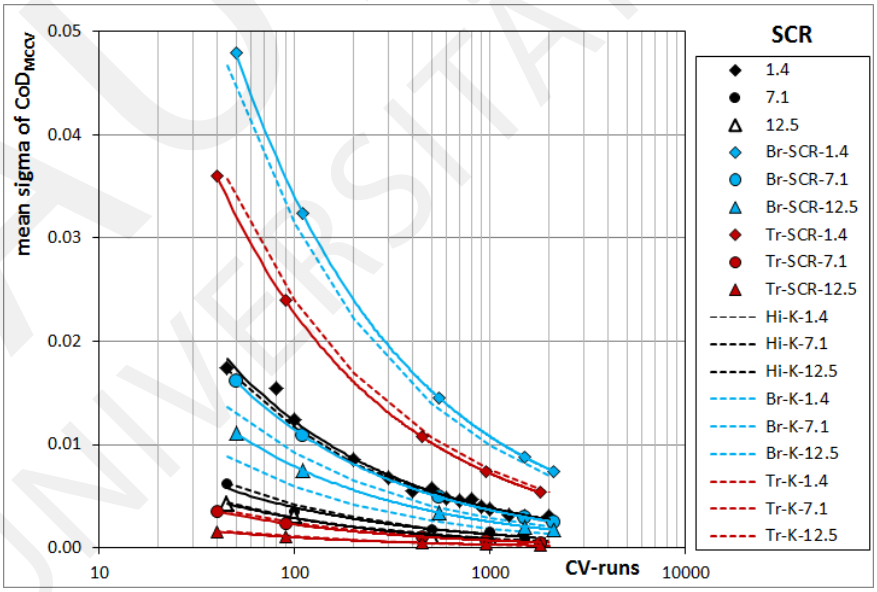

Figure 5: Variance of the MCCV results depending on model type, CV-runs and SCR

implementation of the MCCV-procedure in a probabilistic code it is important to predict the variation of the CoD_{MCCV} result value for a specific model type, to compute only

as many CV-runs as necessary to reach a specific min-max-range or σ of the CoD_{MCCV}. Therefore the three different model types have been analyzed regarding their dependency of the variation expressed by sigma or the min-max-range respectively. Graph 5 shows this data with SCR as parameter. Symbols represent the results of the simulations (averaged over three relevant splitting rations and all the models of the given type) and solid lines are the trend-lines for the data-points. To estimate the necessary number of CV-runs we developed correlations

$$\text{range} = \frac{[-0.0081 \cdot C + 1.6114] \cdot SCR^{[1.5986 \cdot \frac{E \cdot O}{C} - 2.1763]}}{\sqrt{\text{CV-runs}}} \tag{9}$$

$$\sigma = \frac{[-0.002 \cdot C + 0.4265] \cdot SCR^{[1.5063 \cdot \frac{E \cdot O}{C} - 2.1283]}}{\sqrt{\text{CV-runs}}}. \tag{10}$$

The dashed lines in Figure 5 represents the approximation of σ (10).

3.3 Computation time

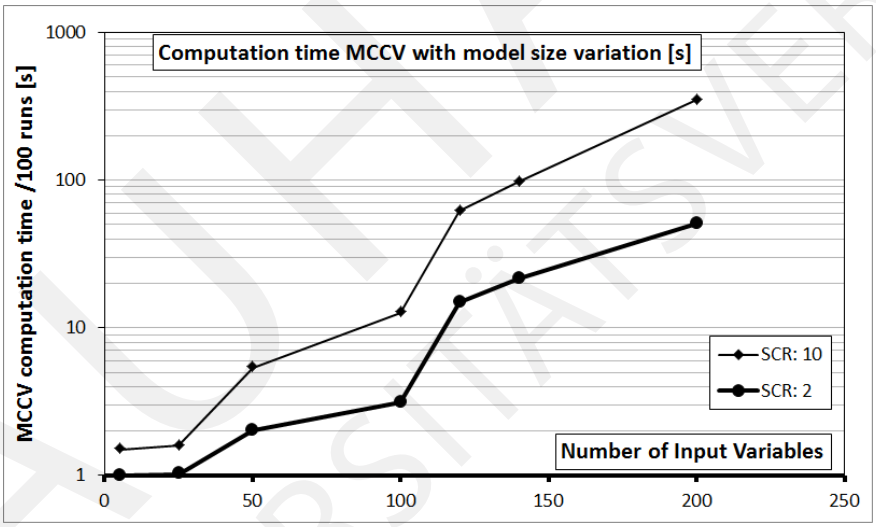

Figure 6: Computation time of the MCCV

The computation time of the CoD_{MCCV} is influenced by the number of CV-runs and the model size. Figure 6 shows the measured time for the MCCV of a linear meta-model. The number of coefficients is equal to the number of input variables plus one. The shown data points are scaled to 100 CV-runs. The used machine is a ThinkPad® T61 with a 64bit OS, 4GB RAM and a Intel® Core™ 2 Duo T8100 at 2.1Ghz. There is plenty of room for improvements on hardware side and on the code optimization as well.
Figure 6 reveals, that there is a strong increase in computation time, when the model size exceeds 100 input parameters. Fortunately it was shown in chapter 3.2, that huge models need less CV-runs to achieve the same variance. Nevertheless the computation time will increase for models with a high input parameter dimension, since a minimum number of CV-runs will be necessary. This limit can be between 50 and 100.

Moreover the graph shows that there is a strong dependency on n, the number of samples in the database, which is here expressed by the SCR. For a model with 200 dimensions the computation needs 50s when 400 samples are used ($SCR = 2$) and 350s when 2000 samples are used ($SCR = 10$).

4 Conclusions and summary

The presented paper showed that the CoD_{MCCV} calculated by MCCV can give a more realistic quality estimation of the response surface than the CoD. This is in particular true for small sample to coefficient ratios $(3 - 8)$. Here we started with very small SCR-values of 1.4, where a strong overestimation of the meta-model quality by the CoD was visible. In the saturated range, where the CoD becomes constant while enlarging the database, the CoD_{MCCV} and the CoD converge into each other. Using the results 22 different meta models we developed a graph (Figure 2 left) that can be used to estimate the reliability of any computed CoD value.

The cross-validation results are influenced by the splitting ratio (SR) only for very low sample to coefficient ratios (SCR). In our test-model with 141 coefficients in the response surface equation, a high SR of 0.975 showed good results for all sample to coefficient ratios.

For the small test-models with only five input dimensions, smaller splitting ratios $(0.6 - 0.9)$ work well.
For high SCR-values the influence of the SR is negligible.
The disadvantage of a high splitting ratio is the increasing scatter of the result values. The investigation showed that the σ, estimated by a twenty times repeated computation, is strongly increasing if the number of validation samples is below 10 in our HighParameter-test-model.

To reduce the standard deviation for a fixed SCR, the number of CV-runs can be increased. The necessary number of runs to achieve a target σ or min-max-range can be estimated with the developed correlations given in (9) and (10). But be aware that the equations are developed with the data of only three different test-model-types with all together 16 meta-models.
The reason to prefer low numbers of CV-runs, is the computation time, which is strongly increasing for high dimensional models. Fortunately these models showed lower variances.

A good estimation of the target-CoD that would be reached if the SCR is high ($>$7 to 22) can be found by averaging the CoD and the CoD_{MCCV}. The evaluation of 22 meta-models showed that for 91% of the tested models the difference to the target-value is small in the complete SCR-range. Hence this additional criterion can be used to predict the possible meta model improvement that can be achieved by enlarging the database.

An overestimation of the response surface quality by the CoD_{MCCV} can occur at very low SCR values ($<$3), combined with a low target-CoD ($<$0.5). This untypical CV-result occurred for three out of 22 meta-models. The observed effect must be investigated in more detail by using more test meta-models with a low quality. This was not the core of interest in the presented investigation.

Future work on this topic should reinforce the findings in this paper by using a greater

variety of test-models. Moreover we will include an alternative validation sample selection algorithm. The K-fold cross-validation will deliver new data, that will be compared with the current results. Advantages and disadvantages of both procedures will be compared.

References

[1] Edward E Cureton. Validity, reliability and baloney. *Educational and Psychological Measurement*, 1950.

[2] Ludwig Fahrmeir, Thomas Kneib, and Stefan Lang. Regression, 2009.

[3] Seymour Geisser. The predictive sample reuse method with applications. *Journal of the American Statistical Association*, 70(350):320–328, 1975.

[4] Alexander Lange, Matthias Voigt, Konrad Vogeler, Henner Schrapp, Erik Johann, and Volker Gümmer. Impact of manufacturing variability and nonaxisymmetry on high-pressure compressor stage performance. *Journal of Engineering for Gas Turbines and Power*, 134(3):032504, 2012.

[5] Marcin Molga and Czesław Smutnicki. Test functions for optimization needs. *Test functions for optimization needs*, 2005.

[6] Charles I Mosier. The need and means of cross-validation. i. problems and designs of cross-validation. *Educational and Psychological Measurement*, 1951.

[7] Raymond H. Myers and Douglas C. Montgomery. Response surface methodology / process and product optimization using designed experiments, 1995.

[8] Richard R Picard and R Dennis Cook. Cross-validation of regression models. *Journal of the American Statistical Association*, 79(387):575–583, 1984.

[9] Lothar Sachs. Angewandte statistik: Anwendung statistischer methoden, 2004.

[10] Jun Shao. Linear model selection by cross-validation. *Journal of the American Statistical Association*, 88(422):pp. 486–494, 1993.

[11] Mervyn Stone. Cross-validatory choice and assessment of statistical predictions. *Journal of the Royal Statistical Society. Series B (Methodological)*, pages 111–147, 1974.

[12] Qing-Song Xu and Yi-Zeng Liang. Monte carlo cross validation. *Chemometrics and Intelligent Laboratory Systems*, 56(1):1–11, 2001.

[13] Ping Zhang. Model selection via multifold cross validation. *The Annals of Statistics*, 21(1):pp. 299–313, 1993.

On the uncertainty modelling of membrane action in concrete plates in the framework of robustness assessment

W. Botte, R. Caspeele, L. Taerwe

Department of Structural Engineering,
Ghent University,
Ghent, Belgium

When a continuous reinforced concrete slab is excessively loaded or a certain support is lost due to an accidental event, membrane action can be activated in order to generate an additional load transfer to neighbouring supports, which can considerably enhance the load-carrying capacity. This can delay or even prevent a progressive collapse and increase the robustness of concrete structures. In this contribution, the sensitivity of the collapse load of a one-way RC slab to variations of the different design variables is assessed, both for an undamaged situation and a damaged situation considering the removal of an intermediate support. Consequently, a probabilistic model for the load-bearing capacity is established and finally the quantification of the structural robustness is discussed using deterministic and reliability-based robustness indices.

1 Introduction

Interest in the robustness of concrete structures increased strongly after the partial collapse of the apartment building at Ronan Point (UK) in 1968. This event resulted in extensive research associated with the progressive collapse of structures. In addition, the terrorist attacks on the World Trade Centre in New York and the Pentagon in Washington in 2001 triggered a renewed interest in this research topic.

Numerous recent publications have been focusing on the concept of robustness, the definition of robustness indicators, etc. Different design strategies that increase the robustness have been identified, one of which is to provide alternative load paths. However, only limited research is available with respect to the accurate quantification and modelling of the residual bearing capacity of structural systems after the establishment of an alternative load path. In case of reinforced concrete slabs, such an alternative load path can be obtained by the transition from bending behaviour to compressive or tensile membrane action. The appropriate modelling of the residual bearing capacity after the establishment of an alternative load path is of crucial importance in order to adequately quantify structural robustness using robustness indicators and to facilitate robustness-based design.

In this contribution some first steps are undertaken to quantify and incorporate the uncertainties which are associated to the development of tensile membrane action in concrete slabs after the accidental removal of a support. The outcomes of the experimental and numerical analysis of a set of large-scale tests are considered. A sensitivity study is performed in order to provide insight in the influence of most important variables on the load-bearing capacity. Consequently, the effect of the membrane action on the structural reliability quantification is investigated and discussed. Finally, some observations

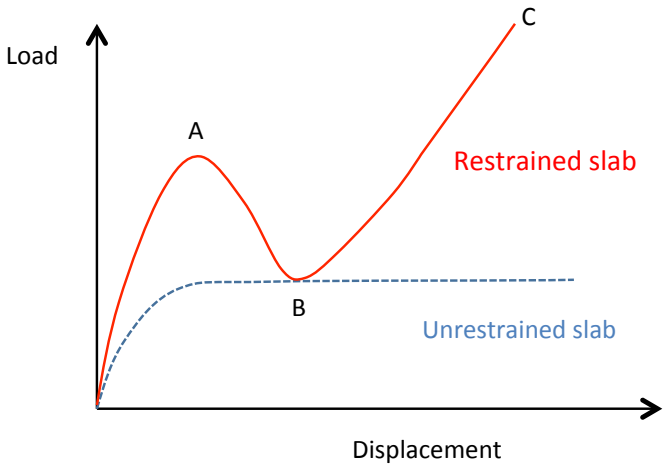

Figure 1: Schematic representation of the response curve of an unrestrained slab and a fully restrained slab under membrane action

are made with respect to the quantification of robustness indicators and some critical observations are made.

2 Membrane action

2.1 General behaviour of RC slabs subjected to membrane action

Figure 1 shows a typical load – deflection diagram for an unrestrained slab as well as for a fully restrained slab. In case no horizontal restraint is present, the slab will deflect under the applied load until a yielding plateau establishes and the slab fails either due to concrete crushing or rupture of the reinforcement. No increase in the load-carrying capacity is observed.

Considering a slab with perfect edge restraints against lateral displacement, compressive membrane action is induced at small deflections due to restraining the outward movement along the slab edges. This may offer a much higher flexural load than the maximum load predicted by [7] Johansen's Yield Line Theory (1962), especially in case of elements with small slenderness. After the outermost flexural load has been reached in point A, the load-displacement graph shows a rapid decrease of the supported load with further increasing deflection as a result of the reduction of compressive membrane forces. Further, near point B, membrane forces reach the stage where they change from compression to tension. The slab's boundary restraints start to resist inward movement of the edges. Accordingly, cracks extend over the full thickness of the slab and the yielding of steel reinforcement is established due to the elongation of the slab surface. It is observed that beyond point B the reinforcement acts as a tensile net that enables additional load-carrying capacity under increasing deflections. The load increases for a second time until the rupture of the reinforcement at point C.

(a) (b)

Figure 2: Global overview of the real-scale test set-up: original system 2a; after collapse 2b

In case of robustness quantification or robustness-based design, the quantification of the residual capacity of the alternative load path established by the development of tensile membrane action becomes of crucial importance.

2.2 Experimental and numerical investigations into tensile membrane action

In order to investigate the tensile membrane action under accidental events in more detail, an experimental test set-up was developed as depicted in Figure 2.

The configuration basically consisted of a 160 mm thick and 1800 mm wide reinforced concrete slab strip. The total length of the specimen was 14,30 m with the distance between the inner supports and the central support being 4 m, changing to one span of 8 m at the removal of the latter, simulating an accidental situation. As it was the goal to investigate only tensile membrane action (not compressive membrane action), outward horizontal movement of the slab was not prevented, while inward movement was restricted by concrete anchor blocks.

A detailed description of the test set-up and the results for a first experimental large-scale test is described in [4](Gouverneur et al., 2013). In total, three different slabs were tested. Each slab specimen was exposed to an artificial failure of the central support and subsequent vertical loading until collapse. The first slab strip was reinforced with continuous longitudinal reinforcement bars. A second reinforced concrete slab strip differing only in the reinforcement arrangement, considering a more realistic situation of reinforcement curtailment according to the [2] Eurocode EN 1992-1-1 (2004) was tested as well as a third concrete slab specimen with a reduced thickness of 140 mm.

2.3 Numerical modeling

In the present study, an advanced finite element software (TNO Diana) was used to perform the analysis of a reinforced concrete slab subjected to large deformations.

As a result of the symmetry of the specimen regarding its geometry and loading, only half of the specimen was modelled. The geometrical nonlinearity was taken into account by a total Lagrange approach. Eight-node quadrilateral isoparametric plane stress elements (CQ16M) based on quadratic interpolation and Gauss integration were used to model

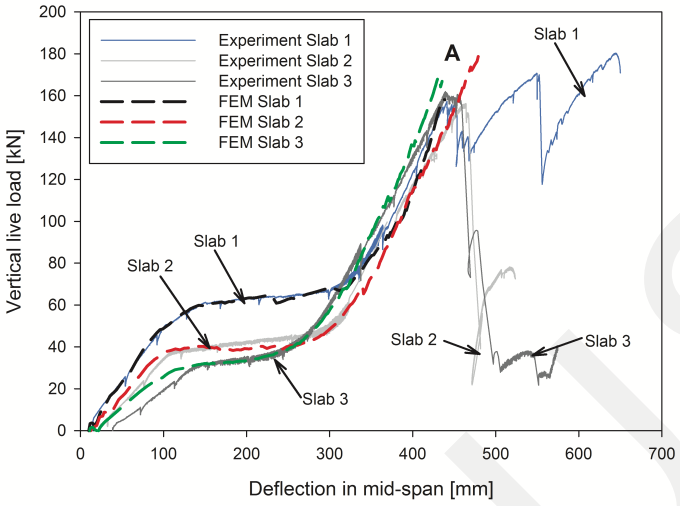

Figure 3: Load-displacement curves slab 1 (continuous reinforcement), slab 2 (curtailed reinforcement) and slab 3 (reduced thickness) in comparison with numerical analyses

the concrete elements. For reinforcement, one dimensional fully embedded bar reinforcement (truss elements) were applied with perfect bond between the reinforcement and the neighboring concrete elements. Strains for the reinforcement are calculated based on the surrounding concrete elements.

The concrete compressive behaviour was implemented as a bi-linear stress-strain relationship considering the obtained test results on control specimens. A Hordijk tension softening model and a total strain fixed crack model was adopted for concrete in tension. For reinforcing steel, a multi-linear stress-strain relationship in accordance with laboratory testing on reference specimens was applied. Further, the strain hardening hypothesis together with the Von Mises plastic criterion was used.

The loading procedure implemented in the numerical analysis was applied in accordance with the laboratory tests by making use of a phased analysis. The obtained stresses and strains were transmitted from one phase to the next. Interface as well as spring elements provided the vertical boundary conditions at the slab's ends, allowing for unrestrained outward movement, while inward movement was restricted. Values of all the model parameters were taken in accordance to the measured values obtained from material testing.

Figure 3 illustrates the load-displacement curves of slab 1 (continuous reinforcement), slab 2 (curtailed reinforcement) and slab 3 (reduced thickness) measured during the laboratory testing in comparison with the numerical simulations. Both, the laboratory tests and numerical simulations showed that the development of tensile membrane action can indeed significantly increase the load-carrying capacity of a slab strip in accidental situations when very large displacements occur. Further, the established FE model is able to predict this increase in the load-carrying capacity due to tensile membrane forces rather accurately. The load-displacement curves until the rupture of the top reinforcement bars over the inner supports (Point A, Figure 3) was calculated within a reasonable tolerance

Property	Distribution	μ	COV
Concrete compressive stress f_c	LN	36 MPa	0,10
Reinforcement yield stress f_y	LN	555 MPa	0,03
Reinforcement tensile strength f_t	LN	605 MPa	0,03
Reinforcement strain at maximum load ϵ_u	LN	8,3 %	0,15
Young's modulus of reinforcement E_s	LN	210 GPa	0,08
Spring constant of horizontal restraints k	LN	303 kN/mm	0,25
Reinforcement area A_s	N	1257 mm^2	0,02

Table 1: Probabilistic models for the basic variables involved in the uncertainty quantification of the investigated concrete slabs

and showed good agreement with the laboratory tests. Further in this contribution, the established model of the first concrete slab (with continuous reinforcement) will be used in order to investigate the influence of uncertainties of the most influencing variables with respect to tensile membrane action on the variability of the load bearing capacity. Consequently, the influence of the tensile membrane action on the value of the reliability index will be discussed as well as its influence on robustness quantification.

3 Probabilistic models for design parameters

The probabilistic models that are considered for the design parameters in this contribution, are shown in Table 1. The mean values and coefficients of variation (COV) for the different parameters are based on experimental investigations together with the suggestions provided in the [6] Probabilistic Model Code from the Joint Committee for Structural Safety (JCSS, 2001). The variation of the stiffness of the boundary conditions (represented by a linear spring with spring stiffness k) is based on the non-linear behaviour observed in the experiments.

4 Sensitivity analysis

Based on the suggested probabilistic models in Table 1 a set of 12 Latin Hypercube samples (LHS) of the input variables were generated according to the method described in ([8] Olssen et al., 2003). The Latin Hypercube Sampling procedure significantly reduces the number of required simulations 'n' compared to regular Monte Carlo simulations, by ensuring that even for a very small number of samples the entire domain of the cumulative distribution function of the input variables θ_j is represented, i.e. the Latin Hypercube Sampling procedure subdivides the entire domain of possible values for each stochastic variable in 'n' (the number of simulations) subsequent areas with equal probability. Within each area a random value of θ_j is generated and combined with similarly generated values of the other input variables. Combining the random samples of each variable θ_j requires the composition of a Latin Hypercube and a Cholesky decomposition in order to avoid spurious correlation ([8] Olssen et al., 2003). A set of 12 samples was found to provide

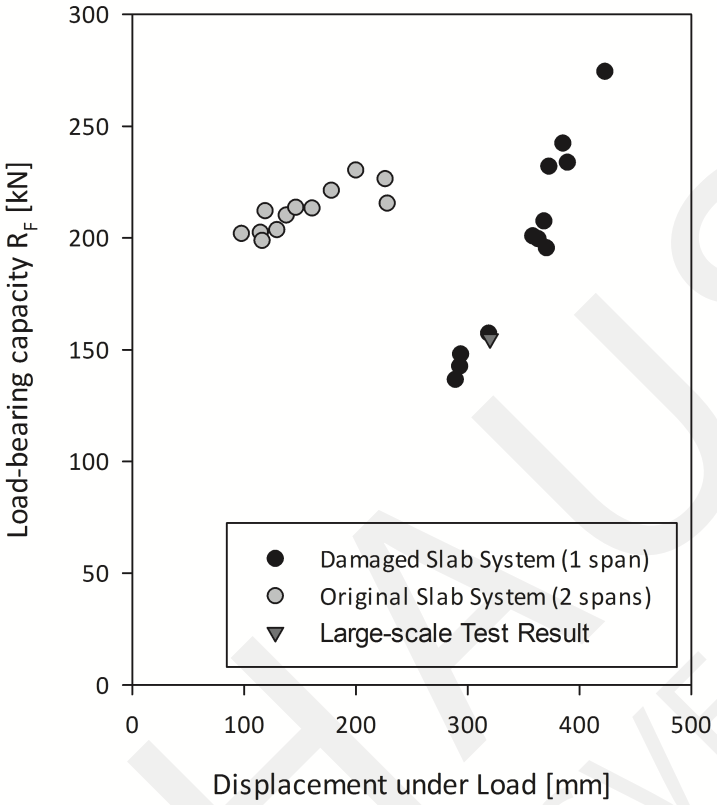

Figure 4: Collapse load–ultimate displacement of the different LHS sets for the original slab system and the damaged slab system

sufficiently accurate results.

A set of 12 FEM analyses were executed using these sets of realizations of the variables. These FEM analyses were executed using the established FEM model from paragraph 2.3, both for the situation with and without the central support, i.e. considering the original and the damaged system. The ultimate load and ultimate displacements obtained through the FEM analysis for the different LHS sets are shown in Figure 4, together with the result of the large-scale test set-up of slab 1.

One can already notice the large variability for the load-bearing capacity of the damaged slab system. This variability can be attributed to the uncertainties related to the basic variables. The results of the Latin Hypercube simulations can consequently be used to determine the sensitivity of the output (i.e. the failure load) to variations of each input variables as proposed by ([9] Yang, 2007). The output of each Latin Hypercube simulation Y_i can be approximated by a linear combination of the k input variables $\theta_{ij} (j = 1, \ldots, k)$:

$$\widehat{Y}_i = b_0 + \sum_{j=1}^{k} b_j \cdot \theta_{ij} \tag{1}$$

The constant b_0 and the regression coefficient b_j can be obtained by the methods of least

Parameter	B_u^*	B_d^*
E_s	0,04	-0,14
ϵ_u	0,17	0,38
f_c	0,30	-0,01
f_t	0,59	0,51
f_y	0,40	0,24
k	0,00	0,07
A_s	0,46	0,16

Table 2: Standardized regression coefficients for the undamaged (B_u^*) and the damaged system (B_d^*).

squares. However, these coefficients are dependent on the units in which the variables are expressed. In order to overcome this problem, the output and the different variables should be standardized as follows:

$$\theta^* = \frac{\theta - \mu_\theta}{\sigma_\theta} \tag{2}$$

$$Y^* = \frac{Y - \mu_Y}{\sigma_Y} \tag{3}$$

Where μ_θ and μ_Y are the sample means and σ_θ and σ_Y are the sample standard deviations. Consequently, the regression model (1) can be rewritten as follows:

$$Y_i^* = \sum_{j=1}^{k} b_j^* \cdot \theta_{ij}^* \tag{4}$$

The coefficients b_j^* are called the standardized regression coefficients. Such coefficients provide a direct measure of relative importance of the input variables. The larger the absolute value of b_j^*, the more influence the variable θ_{ij} has, while values of b_j^* close to zero indicate that the associated variable θ_{ij} has only little influence on the output Y_i. The standardized regression coefficients can be determined from equation (5):

$$B^* = (X^T X)^{-1} X^T Y^* \tag{5}$$

With:

$$B^* = \begin{bmatrix} b_1^* \\ b_2^* \\ \vdots \\ b_k^* \end{bmatrix} \qquad X = \begin{bmatrix} \theta_{11}^* & \cdots & \theta_{1k}^* \\ \vdots & \ddots & \vdots \\ \theta_{n1}^* & \cdots & \theta_{nk}^* \end{bmatrix} \qquad \textit{and} \qquad Y^* = \begin{bmatrix} Y_1^* \\ Y_2^* \\ \vdots \\ Y_k^* \end{bmatrix} \tag{6}$$

Using equations (2)-(6), the standardized regression coefficients for the undamaged and the damaged system are calculated and represented in Table 2. This table shows how the importance of the different input parameters changes when the system is altered from the undamaged configuration consisting of two spans (B_u^*) to a damaged configuration with only one span (B_d^*).

It is noted that the standardized regression coefficient of the ultimate reinforcement strain increases, indicating that the contribution of this parameter to the resistance of the damaged system is more important than it was the case for the undamaged system.

The opposite is valid for the cross-section, yield stress and the tensile strength of the reinforcement and for the compressive strength of the concrete. Their contribution to the resistance of the system is less important in case of a damaged system than it was for the undamaged system. This is especially the case for the concrete compressive strength: it contributes significantly to the resistance in case of the undamaged system, while it does not contribute significantly to the resistance of the undamaged system. This is reflected by the very low (slightly negative) standardized regression coefficient B_d^*. Indeed, failure of the damaged system occurs in the tensile membrane stage where the entire cross-section of the slab is subjected to tension. In this state, the concrete is cracked, hence the concrete compressive strength does not contribute significantly to the load-bearing capacity of this system.

The stiffness of the horizontal boundary condition (k) and the Young's modulus of the reinforcement steel have (almost) no influence on the resistance of the undamaged system. However, when the accidental situation occurs, the contribution of these parameters to the load-bearing capacity becomes significant: the stiffness of the horizontal boundary condition has a positive effect on the resistance of the damaged slab, while the Young's modulus of the reinforcement has a negative effect. This means that increasing the stiffness of the horizontal boundary condition will lead to a higher load-carrying capacity, while increasing the Young's modulus of the reinforcement will result in a decrease of the collapse load.

It should be noted that the formulation of the regression model influences the values of the standardized regression coefficients. In this contribution a linear combination of the input variables was adopted (Equation 4). Figure 5 compares the model response according to Equation 4 with the FEM response (i.e. ultimate load) in standardized space (i.e. according to Equation 3). The solid line represents the response of an unbiased model. In case of the undamaged system, the model has a good performance and is nearly unbiased. However, in case of the damaged system, a larger scatter is observed. Better performance might be obtained in case a model is adopted where also higher order terms in the input variables are incorporated.

5 Probabilistic model for the load-bearing capacity of the investigated slab system

Considering the LHS in combination with the FEM analysis (Figure 4), the stochastic distribution of the output variable Y can be fitted to a chosen distribution (e.g. normal or lognormal) and an estimation of the mean μ_Y and coefficient of variation δ_Y or standard deviation σ_Y can be made according to well-known estimation methods such as the Method of Moments or the Maximum Likelihood Method ([1]Benjamin & Cornell, 1970). In this study, a lognormal distribution is assumed for the load-bearing capacity of the reinforced concrete slab, both in case of the undamaged and the damaged situation (Figure 6). The mean μ_Y and standard deviation $\sigma_Y 0,23$ can be estimated by (7) and (8) in accordance

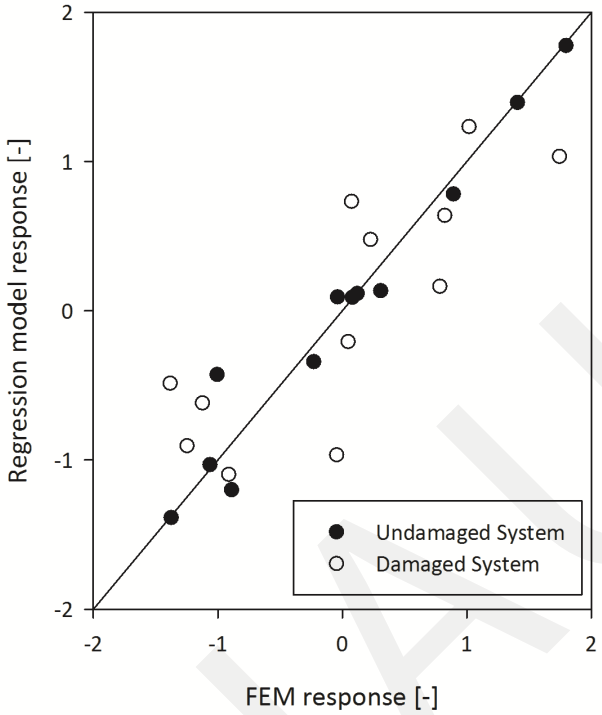

Figure 5: Standardized ultimate load obtained by FEM calculations compared to the model response for the undamaged and the damaged system

Slab system	Distribution	μ [kN]	COV [-]
Original slab system	LN	213	0,05
Damaged slab system	LN	198	0,23

Table 3: Probabilistic models for the load-bearing capacity of the original and the damaged slab system

with the Method of Moments.

$$\mu_Y = \frac{1}{n}\sum_i Y_i \tag{7}$$

$$\sigma_Y = \frac{1}{n}\sum_i Y_i^2 - \mu_Y^2 \tag{8}$$

The mean and coefficient of variation (COV) for the resistance of the original slab system with two spans and of the damaged slab system with one span, are summarized in Table 3. Table 3 and Figure 6 show again the quite high scatter for the load-bearing capacity of the damaged slab system, indicated by the large coefficient of variation, while the uncertainty associated with the load-bearing capacity of the undamaged slab system seems to be rather low (COV = 0,05).

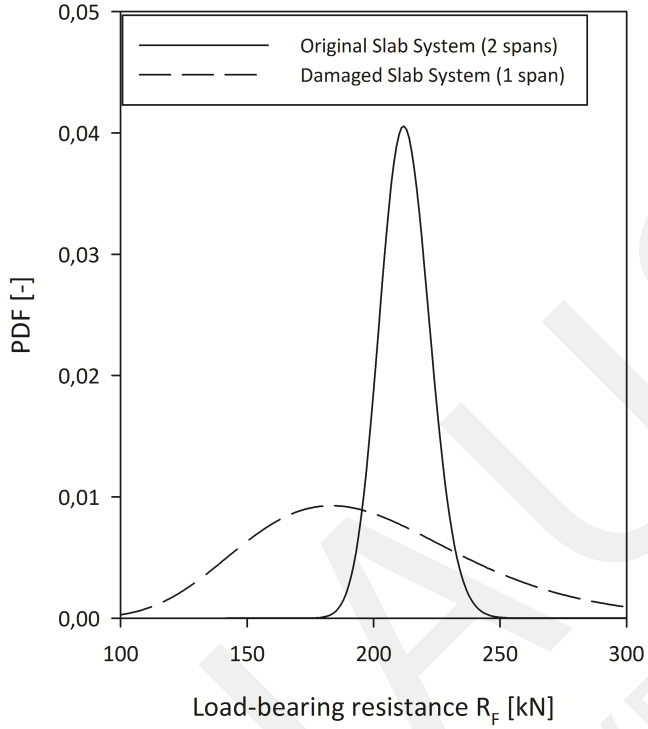

Figure 6: PDF of the load-bearing capacity R_F

6 Robustness assessment

In this paragraph, the robustness of the slab system under consideration is investigated through two types of robustness indicators: a deterministic one and a reliability-based one. In order to do so, one has to assume a distribution for the load that is applied on the slab. The original slab configuration was designed for a load Q_d with a design value of 90 kN. Considering a reference period of 50 years and assuming a COV of 0,25, this variable load Q is modeled as a Gumbel distribution with mean value $\mu_Q = 45\ kN$.

6.1 Deterministic robustness quantification

In the offshore industry, a simple measure of structural redundancy is used, based on the so-called Residual Influence Factor (RIF) ([3] Faber et al., 2006 and [5] ISO19902:2007). First, the Reserve Strength Ratio (RSR) is defined as follows:

$$RSR = \frac{R_{F,c}}{Q_c} \tag{9}$$

with $R_{F,c}$ the characteristic value of the resistance and Q_c the characteristic value of the design load. Consequently, the RIF is defined by:

$$RIF = \frac{RSR_{damaged}}{RSR_{original}} \tag{10}$$

Slab system	$R_{F,c}$ $[kN]$	Q_c $[kN]$	RSR $[-]$	RIF $[-]$
Original slab system	196,70	39,60	4,97	0,67
Damaged slab system	132,43		3,34	

Table 4: Characteristic value for the load-bearing capacity and the load, RSR values and the RIF value for both slab systems

where $RSR_{original}$ is the RSR value of the intact structure and $RSR_{damaged}$ is the RSR value of the damaged structure. The RIF takes values between zero and one, with larger values indicating larger redundancy.

Considering the characteristics of the probabilistic variables R_F and Q as mentioned in the previous paragraphs, their characteristic value can be calculated. The 98% fractile is used for the characteristic value of the load variable Q_c, while the 5% fractile is used for the characteristic value of the resistance $R_{F,c}$. The characteristic values of the resistance and load are shown in Table 4. These values are consequently used to calculate the Reserve Strength Ratios ($RSR_{damaged}$ and RSR_{intact}) and finally the Residual Influence Factor RIF. All values are summarized in Table 4. Table 4 shows that the RSR values for both the undamaged and the damaged slab system are quite high, indicating that the slab system has a high strength reserve with respect to the characteristic load Q_c. These RSR values result in a RIF value of 0,67 for this particular accidental situation. This value is closer to one than to zero, indicating that the slab is quite redundant with respect to the removal of the central support. Note that this RIF is independent on the applied load Q_c.

6.2 Reliability-based robustness quantification

A probabilistic measure of robustness is the redundancy index RI, defined by (Fu & Frangopol 1990):

$$RI = \frac{P_{f,damaged} - P_{f,intact}}{P_{f,intact}} \tag{11}$$

where $P_{f,damaged}$ is the probability of failure of the damaged system and $P_{f,intact}$ is the probability of failure of the undamaged system. This redundancy index takes values between infinity, for structures that are not robust, and zero, for structures that are very robust.

Alternatively, also the redundancy factor β_R defined by (Frangopol & Curley 1987) can be considered:

$$\beta_R = \frac{\beta_i}{\beta_i - \beta_d} \tag{12}$$

where β_i is the reliability index of the intact system and β_d is the reliability index of the damaged system. The redundancy factor takes values between 0 (i.e. $\beta_d = -\infty$), for structures that are not robust, and infinity (i.e. $\beta_d = \beta_i$), for very robust structures.

In order to calculate these robustness indices, the reliability index for the intact and the damaged configuration are calculated according to the simplified limit state equation (13),

Slab system	Reliability Index β [−]	Failure Probability P_f [−]	Redundancy Index RI [−]	Redundancy factor β_R [−]
Original slab system	5,72	$5,3 \cdot 10^{-9}$	58,69	7,72
Damaged slab system	4,98	$3,2 \cdot 10^{-7}$		

Table 5: Reliability index, redundancy index and redundancy factor for the original and the damaged slab system

in combination with the probabilistic models for the load-bearing capacity RF and the load Q as mentioned in the previous paragraphs.

$$g(\underline{X}) = R_F - Q \tag{13}$$

The reliability index for the intact and the damaged system are summarized in Table 5. Consequently, the redundancy factor β_R can be calculated, as well as the redundancy index RI. These factors are also presented in Table 5. The reliability index of the slab system decreases from 5,72 to 4,98 when the central support is removed. Note that it is difficult to assess the robustness of this structural system, as both the redundancy index and the redundancy factor have an infinite range, i.e. respectively between infinity and zero and between zero and infinity. Nevertheless, it can be concluded that the system possesses some robustness with respect to the removal of the central support, since the redundancy index is not extremely high and the redundancy factor differs definitely from zero.

7 Conclusions

The numerical model in combination with LHS for the design parameters allowed for the investigation of the structural robustness of a reinforced concrete slab subjected to membrane action. It was shown that parameter uncertainties have a significant influence on the ultimate load-bearing capacity of a reinforced concrete slab subjected to large deformations.

A sensitivity analysis was performed in order to detect the most important variables that should be addressed during the design of reinforced concrete slabs, especially in case one want to account for membrane action. This sensitivity analysis revealed that the influence of the variables is different for the undamaged and the damaged situation: the influence of some variables becomes significant or more important in the damaged situation (e.g. the stiffness of the boundary condition, the Young's modulus of the reinforcement steel and the ultimate reinforcement strain), while the influence of others decreases or disappears for the load-carrying capacity of the damaged system (e.g. the concrete compressive stress, the yield stress and cross-section of the reinforcement,...).

In order to assess the structural robustness of the slab system, a lognormal distribution was fitted to the data obtained by Latin Hypercube Sampling. Consequently, the structural robustness was quantified by means of two types of robustness indices: a deterministic one, based on the characteristic values of the resistance and the load, and a reliability-based

robustness index, based on the reliability index or probability of failure of the damaged and intact system. Both robustness indices indicated that the slab system under consideration possesses some robustness/redundancy with respect to the removal of the central support.

8 Acknowledgements

Wouter Botte is a Research Assistant of the FWO Research Foundation Flanders. The authors wish to thank the FWO for the financial support on the research project "Structural reliability and robustness assessment of existing structures considering membrane action effects and Bayesian updating of test information".

References

[1] C Allin Cornell and Jack R Benjamin. *Probability, Statistics and Decisions for Civil Engineering*. McGraw Hill Book Company, 1970.

[2] EN. *EN 1992-1-1 Eurocode 2: Design of concrete structures - Part 1-1: General ruels and rules for buildings*, Brussels, 2004. CEN.

[3] Michael H Faber, Marc A Maes, Daniel Straub, and Jack Baker. On the quantification of robustness of structures. In *25th International Conference on Offshore Mechanics and Arctic Engineering*, pages 79–87. American Society of Mechanical Engineers, 2006.

[4] Dirk Gouverneur, Robby Caspeele, and Luc Taerwe. Experimental investigation of the load–displacement behaviour under catenary action in a restrained reinforced concrete slab strip. *Engineering Structures*, 49:1007–1016, 2013.

[5] ISO. 19902:2007. *Petroleum and natural gas industries. Fixed steel offshore structures.*, 2007.

[6] JCSS. Probabilistic model code, 2001.

[7] Knud Winstrup Johansen et al. *Yield-line theory*. Cement and concrete association London, 1962.

[8] Anders Olsson, Göran Sandberg, and Ola Dahlblom. On latin hypercube sampling for structural reliability analysis. *Structural safety*, 25(1):47–68, 2003.

[9] In Hwan Yang. Uncertainty and sensitivity analysis of time-dependent effects in concrete structures. *Engineering structures*, 29(7):1366–1374, 2007.

40 Years FORM: Some New Aspects?

Karl Breitung

Engineering Risk Analysis Group
Faculty of Civil, Geo and Environmental Engineering
Technical University of Munich,
Theresienstr. 90, 80333 Munich, Germany
breitu@aol.com

Abstract. 40 years ago Hasofer and Lind wrote their seminal paper [7] about FORM where they described an algorithm for finding the beta point. This algorithm, later in 1978 generalized by Rackwitz and Fiessler in [14] to include non-normal random variables, is known as Hasofer-Lind- Rackwitz-Fiessler (HL-RF) algorithm and till now it is an important tool for reliability calculations. Here its relation with standard numerical optimization is explained. Further a simple method for computing the SORM factor is given and the connection of FORM/SORM with dimension reduction concepts is explained.

1 The HL-RF algorithm

The original Hasofer-Lind algorithm finds for a limit state function (LSF) $g(\boldsymbol{u})$ in the standard normal space a point $\boldsymbol{u}^*$ such that

$$|\boldsymbol{u}^*| = \min_{g(\boldsymbol{u})=0} |\boldsymbol{u}| = \min_{g(\boldsymbol{u})\leq 0} |\boldsymbol{u}|. \tag{1}$$

The basic idea was to linearize the LSF at a given point, find the beta/design point for this linearized LSF and then to proceed iteratively always again linearizing to obtain a further point.

Writing this as an algorithm, one has:

1. Starting point $\boldsymbol{u}_1$. Define a convergence criterion for stopping.
2. Calculate $\boldsymbol{u}_{k+1}$ by

$$\boldsymbol{u}_{k+1} = |\nabla g(\boldsymbol{u}_k)|^{-2}(\nabla g(\boldsymbol{u}_k)^T \boldsymbol{u}_k - g(\boldsymbol{u}_k))\nabla g(\boldsymbol{u}_k). \tag{2}$$

3. If the convergence criterion is fulfilled, stop, elsewhere repeat step 2.

In general, if the curvatures of the LSF are not too large, experience has shown that this procedure converges to the beta point. But in a number of cases, convergence problems appeared. So various improvements and modifications of this method were proposed (see for example [1], [16], [10]). In the next section basics of numerical optimization are outlined and in the third section the relation of the HL-RF algorithm with these is explained.

2 Numerical optimization methods

Deterministic unconstrained minimization methods are usually line search methods ([11], chap. 3). This means that a sequence $\boldsymbol{x}_k$ of points which should converge towards a minimum of f is calculated iteratively by

$$\boldsymbol{x}_{k+1} = \boldsymbol{x}_k - \alpha_k \boldsymbol{H}_k^{-1} \nabla f(\boldsymbol{x}_k). \tag{3}$$

Here $\boldsymbol{x}_k$ is the present iteration point, $\nabla f(\boldsymbol{x}_k)$ the gradient, $\boldsymbol{H}_k$ a symmetric and positive definite matrix and α_k the step length. The search direction $\boldsymbol{H}_k \nabla f(\boldsymbol{x}_k)$ is chosen as a direction in which the target function decreases and α_k such that the decrease is sufficient according to some criterion. Usually no exact line search is made for α_k, but only a step length is taken for a somehow sufficient decrease (inexact line search, see [11], chap. 3.1). The choice of $\boldsymbol{H}_k$ depends on the available information and storage space; if no second derivative information is available, steepest descent (which use $\boldsymbol{H}_k = \boldsymbol{I}_n$, i.e. the n-dimensional unity matrix) or conjugate gradient methods are used. If information about the second derivatives information can be gathered, quasi-Newton methods where $\boldsymbol{H}_k$ is an approximation of the Hessian or Newton methods where $\boldsymbol{H}_k = \nabla^2 f(\boldsymbol{x}_k)$, are utilized.

At the first glance it looks as the optimal choice for the search direction would be $-\nabla f(\boldsymbol{x})$, i.e. the steepest descent method. Unfortunately this method has not optimal convergence properties ([11], chap. 3.3, p. 49). Its convergence speed is linear and its use is discouraged in textbooks, since it tends to a zigzag behavior. A method using only gradient information but superior to this approach is the method of conjugate gradients ([11], chap. 5.2). Also more efficient are quasi-Newton methods where the Hessian is reconstructed from the change in the gradients. Here one avoids the computation of the second derivatives, but one needs to store the approximate Hessian, an $n \times n$-matrix.

Modified, these procedures are used also for finding constrained extrema. Under some regularity conditions the extrema of $f(\boldsymbol{x})$ under $g(\boldsymbol{x})$ are found under the stationary points of the Lagrangian function $L(\boldsymbol{x}, \lambda) = f(\boldsymbol{x}) + \lambda g(\boldsymbol{x})$, i.e. the points with $\nabla_{\boldsymbol{x}} L(\boldsymbol{x}, \lambda) = \boldsymbol{0}$, $g(\boldsymbol{x}) = 0$. So the minimization algorithms are altered to find these points.

One approach, the SQP (sequential quadratic programming) method replaces in each iteration step the original problem by a quadratic function whose minimum under the linearized constraint has to be computed, i.e.:

$$\boldsymbol{x}^T \boldsymbol{A}_k \boldsymbol{x} + \boldsymbol{b}_k^T \boldsymbol{x} + c \quad \text{under} \quad g(\boldsymbol{x}_k) + \nabla g(\boldsymbol{x}_k)^T (\boldsymbol{x} - \boldsymbol{x}_k) = 0 \tag{4}$$

This approach gives a direction where the target function $f(\boldsymbol{x})$ is decreasing, but one has to ensure that also the original constraint condition $g(\boldsymbol{x}) = 0$ is not violated too much. This is achieved by minimizing a so-called merit function $M(\boldsymbol{x}, C)$ in the direction given by $\boldsymbol{p}$ by adjusting the step length. A merit function depending on a parameter C is a function whose unconstrained minimum coincides with the constrained minimum of the target function for sufficiently large values of the parameter μ.

In the augmented Lagrangian approach the constrained optimization problem is replaced by a series of unconstrained optimization problems. For a given Lagrangian $L(\boldsymbol{x}, \lambda)$ this function is replaced by the augmented Lagrangian $L(\boldsymbol{x}, \lambda, \mu) = f(\boldsymbol{x}) + \lambda g(\boldsymbol{x}) + \mu^2 g(\boldsymbol{x})$ which is minimized and then the parameters λ and μ are adjusted. For large enough μ

the unconstrained minima of $L(\boldsymbol{x}, \lambda, \mu)$ are also the minima of the constrained problem ([11], chap. 18.5, p. 542 ff.). For finding the minimum of the augmented Lagrangian any method for unconstrained optimization can be used.

3 Modified HL-RF algorithm

In 1970 Pshenichnyj [12] (see also [13]) proposed a method for constrained minimization. He considered the linearizations of the target function f and the constraint function g:

$$f(\boldsymbol{x}) \approx f(\boldsymbol{x}_0) + \nabla f(\boldsymbol{x}_0)^T(\boldsymbol{x} - \boldsymbol{x}_0),\ g(\boldsymbol{x}) \approx g(\boldsymbol{x}_0) + \nabla g(\boldsymbol{x}_0)^T(\boldsymbol{x} - \boldsymbol{x}_0) \tag{5}$$

To find a solution he added a *damping term* $|\boldsymbol{x} - \boldsymbol{x}_0|^2/2$ to the function f restricting so the step length and ensuring that a solution exists. This gives as function $f^*(\boldsymbol{x})$ to be minimized under $g(\boldsymbol{x}_0) + \nabla g(\boldsymbol{x}_0)^T(\boldsymbol{x} - \boldsymbol{x}_0) = 0$ now

$$f^*(\boldsymbol{x}) = f(\boldsymbol{x}_0) + \nabla f(\boldsymbol{x}_0)^T(\boldsymbol{x} - \boldsymbol{x}_0) + |\boldsymbol{x} - \boldsymbol{x}_0|^2/2. \tag{6}$$

If one considers the design point search problem and sets $f(\boldsymbol{u}) = |\boldsymbol{u}|^2/2$, then one has for the damped function $f^*(\boldsymbol{u}) = |\boldsymbol{u}_0|^2/2 + \boldsymbol{u}_0^T(\boldsymbol{u} - \boldsymbol{u}_0) + |\boldsymbol{u} - \boldsymbol{u}_0|^2/2$. But then:

$$\begin{aligned} f^*(\boldsymbol{u}) &= |\boldsymbol{u}_0|^2/2 + \boldsymbol{u}_0^T(\boldsymbol{u} - \boldsymbol{u}_0) + (\boldsymbol{u} - \boldsymbol{u}_0)^T(\boldsymbol{u} - \boldsymbol{u}_0)/2 \\ &= |\boldsymbol{u}_0|^2/2 + \boldsymbol{u}_0^T\boldsymbol{u} - |\boldsymbol{u}_0|^2 + |\boldsymbol{u}|^2/2 - \boldsymbol{u}^T\boldsymbol{u}_0 + |\boldsymbol{u}_0^2|/2 = |\boldsymbol{u}|^2/2 = f(\boldsymbol{u}). \end{aligned} \tag{7}$$

So in the case of the beta point search the linearized function plus the damping term is equal to the function itself. The search direction here is found by determining the minimum of f^* under $g(\boldsymbol{u}_k) + \nabla g(\boldsymbol{u}_k)^T(\boldsymbol{u} - \boldsymbol{u}_k) = 0$. The result is the same as found in eq.(2). Then as merit function is used $M(\boldsymbol{u}, C) = |\boldsymbol{u}|^2/2 + C|g(\boldsymbol{u})|$ with $C > 0$ and the step length adjusted to give a sufficient decrease for it. This method was proposed in [3] for searching the beta point.

Variants of this method were developed then in [1] and [16]. In these papers the approach is different, no damping term is added, but the target function is directly $|\boldsymbol{u}|^2/2$ with the constraint $g(\boldsymbol{u}) = 0$. In the first paper the merit function is an augmented Lagrangian $M(\boldsymbol{u}, C) = f(\boldsymbol{u}) + \lambda g(\boldsymbol{u}) + C^2 g(\boldsymbol{u})$ and in the second the same used by Pshenichnyj.

All three algorithms have the following form:

1. Starting point $\boldsymbol{u}_1$, a positive value for C and a convergence criterion.
2. For $\boldsymbol{u}_k$ calculate the search direction $\boldsymbol{p}_k$ as
   $\boldsymbol{p}_k = -\boldsymbol{u}_k - \lambda_{k+1}\nabla g(\boldsymbol{u}_k)$ with $\lambda_{k+1} = |\nabla g(\boldsymbol{u}_k)|^{-2}(g(\boldsymbol{u}_k) - \nabla g(\boldsymbol{u}_k)^T\boldsymbol{u}_k)$.
3. Choose a step length $|\alpha_k| \leq 1$ which gives a sufficient decrease of the merit function $M(\boldsymbol{u}, C)$.
4. Take as the next point in the iteration $\boldsymbol{u}_{k+1} = \boldsymbol{u}_k + \alpha_k\boldsymbol{p}_k$. If necessary, increase C.
5. Set $k = k + 1$ and return to step 2 if the convergence criterion is not satisfied, elsewhere stop.

All these three methods can be classified as SQP methods, where in each step $\boldsymbol{A}_k$ is set equal to the unity matrix $\boldsymbol{I}_n$ and for all convergence can be shown under some regularity conditions.

What is the search direction $\boldsymbol{p}_k = \boldsymbol{u}_{k+1} - \boldsymbol{u}_k$? This can be seen expressing $\boldsymbol{u}_{k+1}$ with $L(\boldsymbol{u}, \lambda)$. The gradient of $L(\boldsymbol{u}, \lambda)$ is $\nabla_{\boldsymbol{u}} L(\boldsymbol{u}, \lambda) = \boldsymbol{u} + \lambda \nabla g(\boldsymbol{u})$. This gives:

$$\begin{aligned}
\boldsymbol{u}_{k+1} &= \underbrace{|\nabla g(\boldsymbol{u}_k)|^{-2} (\nabla g(\boldsymbol{u}_k)^T \cdot \boldsymbol{u}_k - g(\boldsymbol{u}_k))}_{=-\lambda_{k+1}} \nabla g(\boldsymbol{u}_k) = -\lambda_{k+1} \nabla g(\boldsymbol{u}_k) \\
\boldsymbol{u}_{k+1} &= \boldsymbol{u}_k + (-\lambda_{k+1} \nabla g(\boldsymbol{u}_k) - \boldsymbol{u}_k) = \boldsymbol{u}_k - (\boldsymbol{u}_k + \lambda_{k+1} \nabla g(\boldsymbol{u}_k)) \\
\boldsymbol{u}_{k+1} &= \boldsymbol{u}_k - \nabla_{\boldsymbol{u}} L(\boldsymbol{u}_k, \lambda_{k+1}). \qquad (8)
\end{aligned}$$

The value of λ_{k+1} is derived from the linearization of the Lagrangian at $\boldsymbol{u}_k$ so that at $\boldsymbol{u}_{k+1}$ its gradient vanishes. So these methods are *also* steepest descent methods for the Lagrangian. There are therefore – as already said – some disadvantages in using them. For starting points far away from the beta point steepest descent procedures may run a long time through valleys since they use only the local information about the descent direction and do not try to build more efficient search directions as conjugate gradient or quasi-Newton methods by varying the search direction. Then the problem of the steepest descent near the beta point is that the Lagrangian in the tangential space there is approximately equal to its second order Taylor expansion $L(\boldsymbol{u}^*, \lambda^*) + (\boldsymbol{u} - \boldsymbol{u}^*)^T \nabla^2_{\boldsymbol{u}} L(\boldsymbol{u}^*, \lambda^*)(\boldsymbol{u} - \boldsymbol{u}^*)$ at the beta point, where the gradient is vanishing, so these methods have in general a slower convergence and might begin to zigzag. On the other hand these methods seem to be quite robust and need only one evaluation of the gradient of the LSF in each step.

So in the neighborhood of the beta point methods which try to reconstruct the Hessian might be a better choice. In [1] it is warned that the approximating matrix for the Hessian found in SQP methods is not reliable and tends to be become indefinite. This is due to the fact that the Hessian at the beta point is not necessarily positive definite, it can be indefinite there. The Hessian is surely positive semi-definite only in tangential space at the beta point. So reduced Hessian methods, which try to reconstruct only the Hessian projected into the tangential space, seem to be more appropriate ([11], chap. 18.7, p. 547 ff.). This projected matrix is positive definite if the constrained minimum is regular. From the reduced Hessian one can compute easily the SORM factor as shown in the next section. A rudimentary reduced Hessian method was proposed in [5]. It appears to be difficult to give a general advice which method to use, much depends here on the specific problem. Approaches as conjugate gradients, quasi-Newton or reduced Hessian might have better convergence properties near the beta point, but less robustness than the HL-RF algorithm if the LSF is not smooth enough. All the methods considered here are variants of the SQP method, since augmented Lagrangian methods seem not to be efficient for the beta point search ([9]).

4 The SORM Factor

The SORM factor is usually given in the form $\prod_{i=1}^{n-1}(1 - \beta\kappa_i)^{-1/2}$. Some authors replace the minus sign before the term $\beta\kappa_i$ by a plus sign which leads to confusions. To clear the problem, there are two different definitions for curvature, one for functions and one for surfaces. Civil engineering textbooks mainly use the first definition that a function has positive curvature if $f''(x) > 0$ and negative if $f''(x) < 0$. Using this definition for example for a circle would give curvatures with different signs for the upper and lower part of it.

For surfaces S defined by a function $g(\boldsymbol{u})$ as $S = \{\boldsymbol{u}; g(\boldsymbol{u}) = 0\}$ it depends on the orientation of the surface. For a unit vector $\boldsymbol{v}$ in the tangential space of S oriented by $|\nabla g(\boldsymbol{u})|^{-1}\nabla g(\boldsymbol{u})$ at the beta point $\boldsymbol{u}^*$ the curvature $\kappa(\boldsymbol{v})$ in the direction of the vector $\boldsymbol{v}$ is given by (see [15], chap. 12, exercise 12.1):

$$\kappa(\boldsymbol{v}) = -|\nabla g(\boldsymbol{u}^*)|^{-1}\boldsymbol{v}^T\nabla^2 g(\boldsymbol{u}^*)\boldsymbol{v}. \tag{9}$$

The surface can be oriented by the normal vector field $|\nabla g(\boldsymbol{u})|^{-1}\nabla g(\boldsymbol{u})$ or by the field $-|\nabla g(\boldsymbol{u})|^{-1}\nabla g(\boldsymbol{u})$. The surface curvature in a direction is said to be positive if it bends towards the normal vector defining the orientation. It seems to be natural in reliability contexts to orient the surface by $|\nabla g(\boldsymbol{u})|^{-1}\nabla g(\boldsymbol{u})$. Then a sphere around the origin with radius r has constant positive curvature $1/r$ which is also the usual definition. This gives then a minus sign in the SORM factor. *So one has to be careful with the definition of curvature.*

The form of the SORM factor above is not suitable for computational purposes requiring an eigenvalue analysis of a symmetric $(n-1)\times(n-1)$ matrix. A form better suited for computation was derived in [4]. Consider the case that the beta point has been rotated into $(0,\ldots,0,\beta)$, the tangent space at the beta point is spanned by the first $n-1$ axis vectors and by a suitable rotation of the coordinates the main curvature directions are given by these axis vectors. Then the square of the inverse of the SORM term is:

$$\prod_{i=1}^{n-1}(1-\beta\kappa_i) = \det(\underbrace{\mathbf{I}_{n-1}+\beta\boldsymbol{B}}_{=\mathbf{A}}) \quad \text{where} \quad \boldsymbol{B} = |\nabla g(\boldsymbol{u}^*)|^{-1}\left(\frac{\partial^2 g(\boldsymbol{u}^*)}{\partial u_i \partial u_j}\right)_{i,j=1,\ldots,n-1} \tag{10}$$

is the Hessian of g at $\boldsymbol{u}^*$ with respect to the first $(n-1)$ variables *only*. Adding now to the $(n-1)\times(n-1)$ matrix $\mathbf{A}$ an n-th row and an n-th column with zeros and only in the diagonal unity gives a matrix $\tilde{\boldsymbol{A}}$

$$\tilde{\boldsymbol{A}} = \begin{pmatrix} & & 0 \\ & \mathbf{A} & \vdots \\ & & 0 \\ 0 & \cdots & 0 \quad 1 \end{pmatrix} \tag{11}$$

whose determinant is equal to the determinant of $\boldsymbol{A}$. We define $\boldsymbol{P}$ as the projection matrix onto the vector $\nabla g(\boldsymbol{u}^*)$ given by $\boldsymbol{P} = |\nabla g(\boldsymbol{u}^*)|^{-2}\nabla g(\boldsymbol{u}^*)\nabla g(\boldsymbol{u}^*)^T$ (For properties of projections used in the following see for example [2], p.124 ff.) In the special coordinate system here $|\nabla g(\boldsymbol{u}^*)|^{-1}\nabla g(\boldsymbol{u}^*) = (0,\ldots,0,1)$. The matrix $\boldsymbol{I}_n - \boldsymbol{P}$ is then the projection matrix on the orthogonal complement of the gradient, the tangential space. One has for a vector $\boldsymbol{x}$ then that $\boldsymbol{x} = \boldsymbol{P}\boldsymbol{x} + (\boldsymbol{I}_n - \boldsymbol{P})\boldsymbol{x}$ and $(\boldsymbol{P}\boldsymbol{x})^T(\boldsymbol{I}_n - \boldsymbol{P})\boldsymbol{x} = 0$. The matrix $\tilde{\boldsymbol{A}}$ can be then written as

$$\tilde{\boldsymbol{A}} = (\boldsymbol{I}_n - \boldsymbol{P})^T\tilde{\boldsymbol{H}}(\boldsymbol{I}_n - \boldsymbol{P}) + \boldsymbol{P}^T\boldsymbol{P} = (\boldsymbol{I}_n - \boldsymbol{P})\tilde{\boldsymbol{H}}(\boldsymbol{I}_n - \boldsymbol{P}) + \boldsymbol{P} \tag{12}$$

with $\tilde{\boldsymbol{H}} = \boldsymbol{I}_n + \beta|\nabla g(\boldsymbol{u}^*)|^{-1}\nabla^2 g(\boldsymbol{u})$. The second equality follows from the property of a projection matrix $\boldsymbol{Q}$ that $\boldsymbol{Q}^T = \boldsymbol{Q}$ and $\boldsymbol{Q}^T\boldsymbol{Q} = \boldsymbol{Q}$. This gives finally:

$$\prod_{i=1}^{n-1}(1-\beta\kappa_i) = \det((\mathbf{I}_n - \mathbf{P})\tilde{\mathbf{H}}(\mathbf{I}_n - \mathbf{P}) + \mathbf{P}) \tag{13}$$

This result is invariant under rotations of the coordinates. Therefore no rotation or/and eigenvalue analysis is needed to calculate the SORM factor.

5 Dimension Reduction and FORM/SORM

Given many variables $\boldsymbol{X} = (X_1, \ldots, X_n)$ describing a system by $Y = f(\boldsymbol{X})$, can a simpler structure having *much less* variables be found without *much* loss of information about the system? More formally, for a function $Y = (X_1, \ldots, X_n)$ of the rv's $X_1, \ldots, X_n$ find a function $h : \boldsymbol{R}^n \to \boldsymbol{R}^p$ with $p \ll n$ such that

$$Y = f^*(h(\boldsymbol{X})) + \boldsymbol{\epsilon} = f^*(h_1(\boldsymbol{X}), \ldots, h_p(\boldsymbol{X})) + \boldsymbol{\epsilon} \tag{14}$$

where the term $\boldsymbol{\epsilon}$ is small in some sense. Methods to find such functions h are called dimension reduction methods. An overview can be found in [6]. (In [8] dimension reduction methods were studied the first time in connection with structural reliability but with another perspective, i.e. to approximate an LSF given only by data points by function families.)

If h is a linear function, such a structure is found by a projection on a suitable plane $h(\boldsymbol{X}) = \boldsymbol{P}_M \boldsymbol{X}$ where $\boldsymbol{P}_M$ is a projection matrix onto a p-dimensional plane M.

If the plane is spanned by p orthonormal vectors $\boldsymbol{v}_1, \ldots, \boldsymbol{v}_p$:

$$f(\boldsymbol{x}) \approx f^*(\boldsymbol{v}_1^T \boldsymbol{x}, \ldots, \boldsymbol{v}_p^T \boldsymbol{x}) + \boldsymbol{\epsilon} \tag{15}$$

FORM is a linear dimension reduction method. The original LSF $g(\boldsymbol{u})$ is replaced by the linearized form

$$g^*(\boldsymbol{u}) = a_0 + \sum_{i=1}^{n} a_i U_i = a_0 + \boldsymbol{a}^T \boldsymbol{U} \tag{16}$$

which is the projection on the vector $Y = \boldsymbol{a}^T \boldsymbol{U}$, $g^*(Y) = a_0 + Y$, $g(\boldsymbol{u}) \approx g^*(y)$. This is a reduction from n to one dimension. In the same way in SORM the limit state function is replaced by a quadratic form of normal random variables.

Now, the reduction to one dimension is not always possible, so for more complex problems it seem to be useful to make reductions where p is still small compared with n, but greater than unity. Such methods are for example SIR (Sliced Inverse Regression) and SAVE (Sliced Average Variance Estimates) described in [6].

The idea of these methods is that if Y is a function of the $\boldsymbol{v}_i^T \boldsymbol{X}$ vectors only as in eq. (15), then the inverse regression, i.e. estimating the $\boldsymbol{X}$'s from the y's will afflict only these variables. Therefore the curve of the inverse regression mean $I\!E(\boldsymbol{X}|y)$ lies in the subspace M spanned by the vectors $\boldsymbol{v}_1, \ldots, \boldsymbol{v}_p$ if Y is a function of $\boldsymbol{v}_1^T \boldsymbol{X}, \ldots, \boldsymbol{v}_p^T \boldsymbol{X}$ only. Since the curve $I\!E(\boldsymbol{X}|y)$ lies in M, the vectors connecting the points $I\!E(\boldsymbol{X}|y_i)$ for various values of y_i must lie in the plane M. So if we can construct enough such points $I\!E(\boldsymbol{X}|y_i)$ from their differences $I\!E(\boldsymbol{X}|y_i) - I\!E(\boldsymbol{X}|y_j)$ we can find the vectors which span M.

In SAVE we use estimates about the variation of the conditional mean to find the vectors spanning M. Since $\mathrm{cov}(\boldsymbol{U}) = I\!E(\mathrm{cov}(\boldsymbol{U}|y)) + \mathrm{cov}(I\!E(\boldsymbol{U}|y))$ (law of total variance) the matrix $I\!E(\mathrm{cov}(\boldsymbol{U}|y))$ can be estimated from $\boldsymbol{I}_n - \mathrm{cov}(I\!E(\boldsymbol{U}|y))$. We cannot find the values of $\mathrm{cov}(I\!E(\boldsymbol{U}|y))$, but we can approximate them by taking slices. This means, we can find the values $I\!E(\boldsymbol{U}|y \in S_i)$ with $S_i = [a, b]$ an interval. These $I\!E(\boldsymbol{U}|y \in S_h)$ points lie in the subspace M too.

Let $\boldsymbol{P}$ the projection matrix onto M, then

$$\begin{aligned} \operatorname{cov}(\boldsymbol{U}|y) &= \boldsymbol{I}_n - \boldsymbol{P} + \boldsymbol{P}\operatorname{cov}(\boldsymbol{U}|y)\,\boldsymbol{P} \quad , \quad \boldsymbol{I}_n - \operatorname{cov}(\boldsymbol{U}|y) = \boldsymbol{P} - \boldsymbol{P}\operatorname{cov}(\boldsymbol{U}|y)\,\boldsymbol{P} \\ \boldsymbol{I}_n - \operatorname{cov}(\boldsymbol{U}|y) &= \boldsymbol{P}\boldsymbol{I}_n\boldsymbol{P} - \boldsymbol{P}\operatorname{cov}(\boldsymbol{U}|y)\,\boldsymbol{P} \quad , \quad \boldsymbol{I}_n - \operatorname{cov}(\boldsymbol{U}|y) = \boldsymbol{P}(\boldsymbol{I}_n - \operatorname{cov}(\boldsymbol{U}|y))\boldsymbol{P} \end{aligned} \tag{17}$$

So the matrix $\boldsymbol{I}_n - \operatorname{cov}(\boldsymbol{U}|y)$ is equal to its projection onto the subspace M. If M is spanned by the first p unit vectors $\boldsymbol{e}_1, \ldots, \boldsymbol{e}_p$ then this means

$$\boldsymbol{I}_n - \operatorname{cov}(\boldsymbol{U}|y) = \begin{pmatrix} \boldsymbol{I}_p - \operatorname{cov}(U_1, \ldots, U_p|y) & \boldsymbol{0}_{p,n-p} \\ \boldsymbol{0}_{n-p,p} & \boldsymbol{0}_{n-p,n-p} \end{pmatrix} \tag{18}$$

with $\boldsymbol{0}_{k,l}$ the zero matrix with k rows and l columns. So the p non-zero eigenvectors of $\boldsymbol{I}_n - \operatorname{cov}(\boldsymbol{U}|y)$ span M.

We make an estimate $\boldsymbol{S}$ of $\boldsymbol{I}_n - \operatorname{cov}(\boldsymbol{U}|y)$. Then the eigenvalues and eigenvectors of $\boldsymbol{S}$ will approximate those of $\boldsymbol{I}_n - \operatorname{cov}(\boldsymbol{U}|y)$. Here m is the number of the data, the real line is partitioned into h slices S_i, and m_i is the number of data in slice S_i. Then an estimate of $\boldsymbol{S}$ is given by:

$$\hat{\boldsymbol{S}} = m^{-1} \sum_{i=1}^{h} m_i (\boldsymbol{I}_n - \operatorname{cov}(\boldsymbol{U}|y \in S_i))^2 \tag{19}$$

Here we take the square of $\boldsymbol{I}_n - \operatorname{cov}(\boldsymbol{U}|y)$ to get non-negative eigenvalues. This matrix has $N - p$ eigenvalues approximately equal to zero and the eigenvectors for the remaining p positive eigenvalues span the subspace M.

An example for SAVE:
Given is the three-dimensional random vector (U_1, U_2, U_3) with standard normal distribution and LSF $g(\boldsymbol{u}) = 2 - u_1^2 - u_2^2$. Here FORM/SORM breaks down, since there is no unique beta point. A sample of 1000 realizations of the random vector is taken.

From this the eigenvectors for SAVE are using eq.(19):

$$\hat{\boldsymbol{S}} = \begin{pmatrix} 0.030 & -0.725 & -0.688 \\ 0.061 & 0.688 & -0.723 \\ 0.998 & -0.021 & 0.065 \end{pmatrix} \tag{20}$$

and the corresponding eigenvalues

$$(0.033, 0.749, 0.986). \tag{21}$$

Since the first eigenvalue is approximately zero, the remaining eigenvectors $\boldsymbol{v}_2 = (-0.725, 0.688, -0.021)$ and $\boldsymbol{v}_3 = (-0.688, -0.723, 0.065)$ span the subspace M. This is nearly the correct subspace spanned by the first two unit vectors.

6 Conclusions

There are still some aspects of FORM/SORM as beta point search methods and dimension reduction problems which have not been researched thoroughly. The computing of the SORM factor should be done with the result in eq. (13) to avoid problems with the definition of curvature.

References

[1] T. Abdo and R. Rackwitz. A new beta-point algorithm for large time-invariant and time-variant reliability problems. In A. Der Kiureghian and P. Thoft-Christensen, ed., *Reliability and Optimization of Structural Systems '90*, p. 1–12, Berlin, 1991. Springer. Lecture Notes in Engineering 61.

[2] S. Biswas. *Textbook of Matrix Algebra*. PHI Learning, New Delhi, 3rd edition, 2012.

[3] K. Breitung. Asymptotic approximations for multinormal integrals. *Journal of the Engineering Mechanics Division ASCE*, 110(3):357–366, 1984.

[4] K. Breitung. Laplace integrals and structural reliability. In A.G. Razaqpur and M.S. Cheung, ed., *Second Canadian Conference on Computing in Civil Engineering*, p. 437–447, Montreal, P.Q., Canada, 1992. Canadian Society for Civil Engineering.

[5] K. Breitung, F. Casciati, and L. Faravelli. Minimization and Approximate SORM Factors. In C. Guedes Soares *et al.*, ed., *Proc. of OMAE 1996, Florence, Italy*, p. 193–198, New York, 1996. ASME. Vol. II Safety and Reliability.

[6] C.J.C. Burges. Dimension reduction: a guided tour. *Machine Learning*, 2(4):275–365, 2009.

[7] A.M. Hasofer and N.C. Lind. An exact and invariant first-order reliability format. *Journal of the Engineering Mechanics Division ASCE*, 100(1):111–121, 1974.

[8] J. Hurtado. *Structural Reliability: Statistical Learning Perspectives*. Springer, 2004.

[9] P.-L. Liu and A. Der Kiureghian. Optimization algorithms for structural reliability. *Structural Safety*, 9(3):161–177, 1991.

[10] L. C. Matioli, S. R. Santos, and A. T. Beck. New Optimization Algorithms for Structural Reliability Analysis. *Computer Modeling in Eng. & Sci.*, 83:23–55, 2012.

[11] J. Nocedal and S. J. Wright. *Numerical Optimization*. Springer Series in Operations Research. Springer, New York, 1999.

[12] B.N. Pshenichnyj. Algorithms for general mathematical programming problems. *Cybernetics*, 6(5):120–125, 1970. Translation of the journal "Kibernetika".

[13] B.N. Pshenichnyj. *The Linearization Method for Constrained Optimization*. Springer, Berlin, 1994.

[14] R. Rackwitz and B. Fiessler. Structural reliability under combined random load sequences. *Computers and Structures*, 9:489–494, 1978.

[15] J.A. Thorpe. *Elementary Topics in Differential Geometry*. Springer, New York, 1979.

[16] Y. Zhang and A. Der Kiureghian. Two improved algorithms for reliability analysis. In R. Rackwitz *et al.*, ed., *Reliability and Optimization of Structural Systems*, Proc. 6th IFIP WG 7.5 working conference, p. 297–304. Chapman & Hall, 1994.

Reliability based quality assessment of fatigue crack growth models

Sharmistha Chowdhury, Maher Deeb, Volkmar Zabel

Research Training Group 1462,
Civil Engineering
Bauhaus University,
Berkaerstrasse 9, 99425, Weimar, Germnay
sharmistha.chowdhury@uni-weimar.de

Abstract.

The estimation of the remaining fatigue life (RFL) is essential to evaluate the remaining serviceability of a structure subjected to cyclic and/or random loading over its operational period. Therefore, several fatigue crack growth models (CGM) developed based on laboratory fatigue tests that can be chosen to predict certain fatigue driven crack propagation. However, due to different sources of uncertainty, the reliability of the chosen model to predict a certain fatigue crack size in a real engineering structure is questionable. The aim of this work is to present a reliability-based strategy to assess and compare the performance of specific fatigue crack growth models applied to engineering structures. The test data has been obtained from the NASGRO data manual where the test example is a low-carbon 1005-1012 hot rolled compact tension specimen subjected to a sinusoidal load with constant amplitude. Two well known fatigue crack growth models with different complexity were selected to fit the test data set. Uncertainty related to the stress intensity factor and the number of loading cycles was assigned in the laboratory test conditions to represent the test condition of a real engineering structure. The obtained results provide a suitable indicator to evaluate the model quality based on the reliability of the fatigue crack growth models.

1 Introduction

Fatigue is a localized progressive process in which structural damage accumulates continuously due to the repetitive application of external loading leading to complete fracture of the structure [8]. Structures under cyclic and/or random operational loading are susceptible to fatigue failure while the loading may be well below the structural resistance capacity. Estimating the remaining fatigue life of the structure is a challenging task for the responsible engineers. Therefore, the performance of these kinds of structures has to be assessed during the entire service life which in turn requires long-term monitoring and non-destructive evaluation (NDE). However, constant and long-term monitoring, especially for large structures, is very expensive and can be troublesome with respect to data storage and data assessment [7]. Since the actual loading conditions are usually not monitored through the life of a structure, an approach for reliable prediction about remaining fatigue life (RFL) is proposed. The proposed approach integrates several fatigue crack growth models (CGM) with reliability approach.

The greatest challenge to predict the remaining fatigue life (RFL) is not only to select the right fatigue CGM from the existing numerous mathematical models [11, 15, 5, 10, 3] but also to assess the reliability of a specific model for a certain damage scenario. Generally, the reliability refers to the probability that a system performs successfully without failure for a certain period of time. Probabilistic modelling is prerequisite for any prediction in fatigue, because a number of factors, such as, initial crack length, loading history of environmental and mechanical stress, material properties, geometry of the structural member, unexpected loading change can influence the monitored data and has been considered in several mathematical models [10, 17, 16, 13]. Extensive research has been conducted on probabilistic modeling of fatigue crack growth and reliability based inspection of structure [9, 7, 18, 6]. However, these studies introduced different fatigue reliability models (FRM) but largely based on linear elastic fracture mechanics approach i.e., only considering the Paris-Erdogan [11] model for the inspection of fatigue crack growth. Since reliability based inspection of a structure depends to a great extent on the ability of a fatigue model to predict some certain damage scenario, it is therefore necessary to consider more fatigue CGMs apart from Paris-Erdogan.

Two fatigue crack growth models, the Paris-Erdogan [11] and the Walker models [15] are considered in the present study. The parameters associated with both fatigue CGMs have been estimated considering several parameter estimation techniques. Reliability of each CGM has been assessed based on their ability to predict the RFL of specific elements of a structure by considering uncertainty in the estimated parameters. A set of experimental data, available in literature [10, 19], is used to demonstrate the proposed approach. The obtained results emphasize not only in the selection of crack growth model but also on the parameter estimation techniques.

2 Methodology

A fatigue crack growth curve (i.e., CGM) is a graphical representation of the stress intensity factor range, ΔK, and crack growth rate, $\frac{da}{dN}$, where a = crack length and N = number of loading cycle. The curve is subdivided into three regions namely: Region I- describing initiation or early development of the crack, Region II- describing linear and stable propagation of the crack and Region III- describing the unstable fatigue crack growth which leads to ultimate failure of the structure [4], see figure 1. The chosen Paris and Walker models, briefly discussed in section 2.1, are appropriate for region II but the Walker model is more advanced than the Paris model by means of taking the loading or stress ratio, R, into account. Though the Paris model is the most conservative model among all fatigue CGMs, it is still the most applicable model due to its simplicity.

Section 2.2 and 2.3 shortly discuss the parameter estimation and reliability approach considered in this paper. Parameters of both models have been estimated considering two methodologies: least square estimation (LSE) and maximum likelihood estimation (MLE). Reliability of each model has been assessed by estimating their ability to predict a damage scenario under a particular random loading condition applying an estimated parameters set in the respective model.

In this study, parameters and other related notations concerning the Paris-Erdogan model are denoted with subscript 'p' and concerning the Walker model with subscript 'w'.

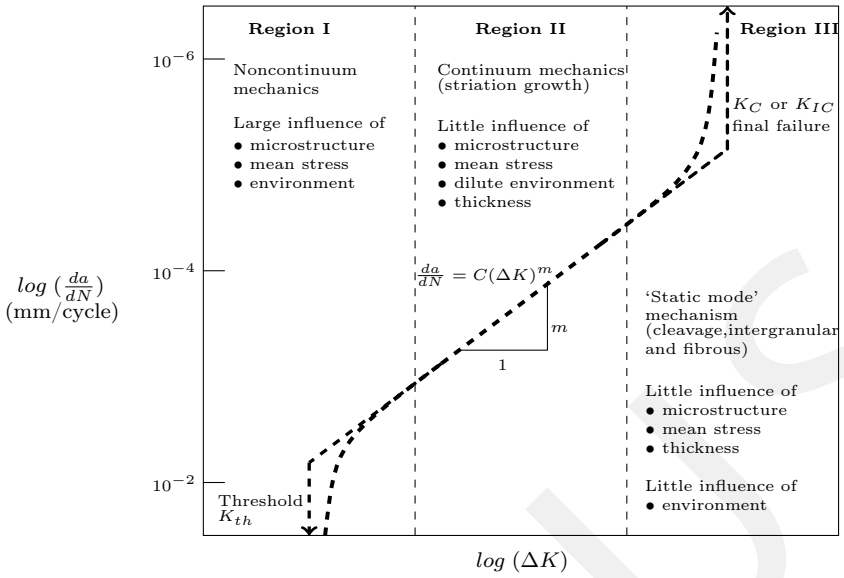

Figure 1: Regions in a typical fatigue crack growth curve

2.1 Fatigue crack growth models (CGM)

Paris-Erdogan: The well known Paris' law, described by Paris and Erdogan(1963), is the simplest method for predicting fatigue crack propagation and can be represented by the following relationship [11]:

$$\frac{da}{dN_p} = C_p\,\Delta K^{m_p} \tag{1}$$

where a = crack length, N_p = number of loading cycles, ΔK = stress intensity factor, C_p = fatigue coefficient and m_p is the slope on the log-log plot of $\frac{da}{dN}$ versus ΔK. This model requires the determination of the parameters C_p and m_p.

Walker: The drawback of the Paris law, which does not include the stress ratio R, has been overcome by Walker(1970) and can be written as follows [15]:

$$\frac{da}{dN_w} = C_w \left[\frac{\Delta K}{(1-R)^{1-\gamma_w}}\right]^{m_w} \tag{2}$$

The significance of this model is that it introduces a third parameter γ_w beside C_w and m_w. For $\gamma_w = 1$, the Walker model converts to the Paris model. In this case, the stress ratio has no effect on the crack growth model.

Since both models are only capable to describe data in region II, they can overestimate the crack propagation rate in region I or underestimate in region III.

2.2 Parameter estimation

Parameter estimation is the most compelling task for assessing model quality. Based on studies from researchers in the early 60's, mainly focused on Paris' law, it can be demonstrated that the parameters C and m are material constants but largely influenced by the initial crack length [14], the stress or loading ratio, R [12], the geometry and the size of the structural component [2, 1].

The applied methodologies for estimating the parameters influence the outcome. In order to observe the effect of these estimating methods, two methodologies have been considered: Least square estimation (LSE) and Maximum Likelihood Estimation (MLE).

Once the parameters are estimated, the number of cycles N to propagate the crack from any initial crack stage a_0 to a certain final crack stage a_f can be obtained by rearranging and integrating Eq. (1) and (2), which provides the relation respectively as follows:

$$N_p = \frac{1}{C_p\,\sigma^{m_p}} \int_{a_o}^{a_f} \frac{1}{(\sqrt{a}F_1)^{m_p}}\,\mathrm{d}a. \tag{3}$$

$$N_w = \frac{1}{C_w} \left(\frac{1-R}{\sigma}\right)^{m_w} \int_{a_o}^{a_f} \frac{1}{(\sqrt{a}F_1)^{m_w}}\,\mathrm{d}a. \tag{4}$$

where, σ = stress, $F_1 = f(a)$ = compliance function for a certain geometry and boundary condition.

2.3 Reliability analysis

In order to compare the results related to several numerical fatigue CGMs, an approach to quantify the quality of a fatigue CGM was developed based on its ability to predict the fatigue crack size measured in the physical model after considering the same number of cycles in both numerical and physical models.

Because of different sources of uncertainty, a direct comparison between the outputs of the physical and numerical models was not possible. Therefore, a probabilistic quality measure based on reliability principles was developed. In general, a fatigue model is written as follows

$$\frac{da}{dN} = f(\theta \sim \Theta) \tag{5}$$

$$dN = \frac{da}{f(\{\theta\} \sim \{\Theta\})} \tag{6}$$

where $\{\theta\}$ refers to the set of input parameters based on a chosen fatigue model. A set of probability density functions $\{\Theta\}$ was assigned to the uncertainty of the inputs. Based on the Eq. (5) and (6), a number of cycle $dN = N_{i+1} - N_i$ is required to increase a crack size with a certain size $da = a_{i+1} - a_i$, where $i = 1, 2....$
As a result, it is possible to write

$$N_{i+1} = N_i + \int_{a_i}^{a_{i+1}} \frac{da}{f(\{\theta\} \sim \{\Theta\})} \tag{7}$$

Because of the influence of the uncertainty of the inputs $\{\theta\}$, the number of cycles N_i at a crack size a_i has a probability distribution function which is based on the chosen fatigue model. Accordingly, the mean value $\bar{N}_i$ and the standard error of the mean $\sigma_{\bar{N}_i}$ can be obtained at any crack size a_i.

Let's assume a crack length a_f has been measured at time t_e in a studied physical model where the expected loading cycle is $N_f \pm \Delta N_f$. Now, the quality Q_M of the chosen fatigue model M can be assessed by the probability of how close the calculated number of cycles $\bar{N}_i$ for model M is to the expected loading cycle N_f, for the same crack length a_f. This can be expressed as follows

$$Q_M = P(\bar{N}_i = N_f | M, \Delta N_f, a_f) \tag{8}$$

In ideal case, if $\bar{N}_i = N_f$, the quality of the model M is $Q_M = 1$. If $\bar{N}_i >> N_f$ or $\bar{N}_i << N_f$, the quality of the model M is $Q_M \approx 0$. In the latter case, the chosen model M is not suitable to represent the measured data. This means the model M is not reliable.

For the comparison among several numerical fatigue models at a specific loading cycle $N_f \pm \Delta N_f$, the relationships between crack length a_i and model quality Q_M, for all considered models were plotted and compared in section 4. In the current study, the best fatigue model is considered as the one, which gives the highest value for Q_M for a crack size a_f where $1 \geq Q_M \geq 0$. For example, if $1 \geq Q_{M_1}(a_f) > Q_{M_2}(a_f) \geq 0$, then model M_1 is better than the model M_2. If $Q_{M_1}(a_f) = Q_{M_2}(a_f) \geq 0$, then the less complex model associated with less uncertainty should be chosen.

3 Application example

To illustrate the approach, experimental data has been obtained from the NASGRO data manual [10, 19] where the test example is a low-carbon 1005-1012 hot rolled compact tension test specimen subjected to a sinusoidal load with constant amplitude, see figure 2.

The general formula that describes the stress intensity factor is as follows [4]:

$$\Delta K = \sigma\sqrt{a}\, F_1\left(\frac{a}{W}\right) \tag{9}$$

where, σ = stress caused by the applied load P ahead of the crack tip, a = crack length, W = width of the plate.

The compliance function to compute the crack length in the CT specimen has the form [19]:

$$F_1\left(\frac{a}{W}\right) = 29.6 - 185.5\left(\frac{a}{W}\right) + 655.7\left(\frac{a}{W}\right)^2 - 1017\left(\frac{a}{W}\right)^3 + 638.9\left(\frac{a}{W}\right)^4 \tag{10}$$

Incorporating Eq. (9) into Eqs. (3) and (4), one can get the number of loading cycle for a given crack length according to the respective model.

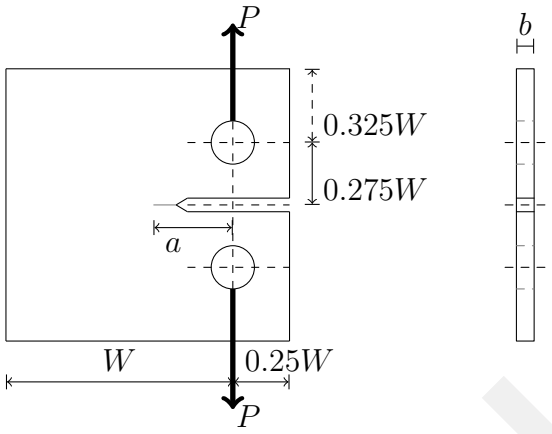

Figure 2: Typical compact tension test specimen for fracture test

4 Results

Table 1 summarizes the parameters estimated from both Paris and Walker models according to least square estimation(LSE) and maximum likelihood estimation(MLE). Parameters m and C were considered as respectively normally and log-normally distributed. In the LSE method, the coefficients of variation (COV) for $log(C)$, m were chosen as 0.01. The MLE method automatically detects the covariance between the parameters. For both methods, coefficients of variation (CoV) for ΔK and R were considered as 0.1. In the current study, the parameter γ_w is was chosen equal to 0.

	Paris		Walker	
Parameters	LSE	MLE	LSE	MLE
C	2.16E-16	2.25E-16	1.40E-16	1.49E-16
m	3.968	3.96	3.968	3.96

Table 1: Estimated parameters with LSE and MLE

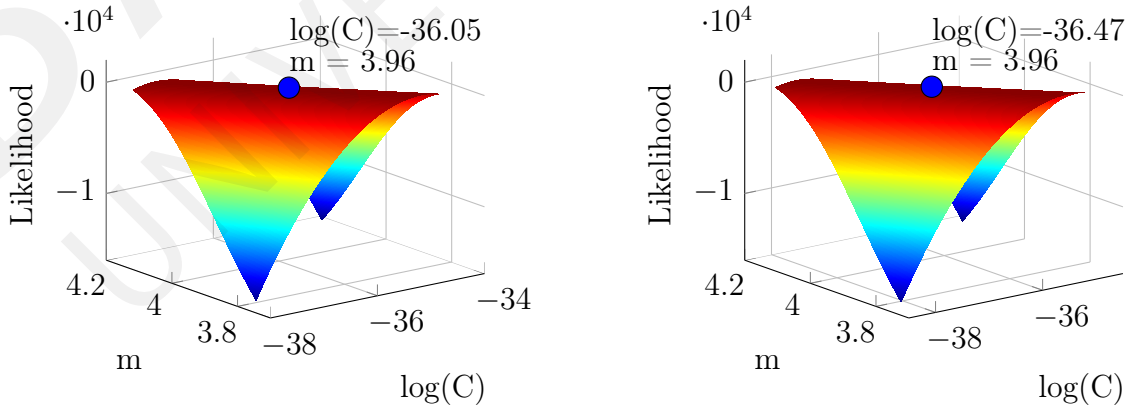

Figure 3: Likelihood values estimated by MLE: Paris(left) and Walker(right)

The parameters obtained from the methodologies for a single model are very close to each other. In general, m is similar for all models but the value of C is smaller in the Walker model than for the Paris model due to the effect of the stress ratio R. Fig. 3 shows the likelihood of the parameters for both models and the best $log(C)$ and m combination giving the highest likelihood is marked. Fatigue crack growth rate curves have been plotted by using the estimated parameters and also by using the parameters obtained from the NASGRO data manual [10, 19], in Fig. 4 and Fig. 5.

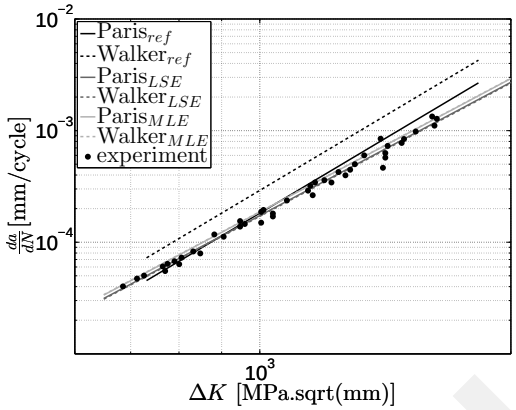

Figure 4: Fatigue crack growth rate curve with estimated C and m values

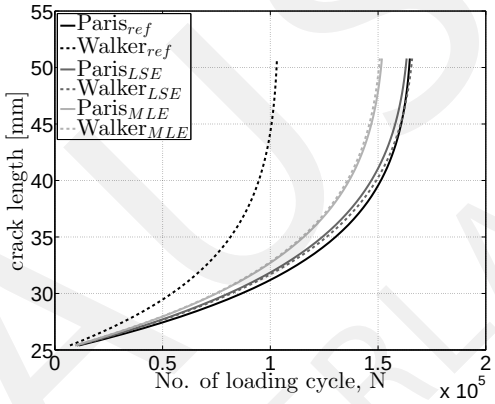

Figure 5: Number of loading cycles with increasing crack length

Fig. 6 shows an overview about the reliability of each model under a certain crack size or loading condition. The uncertainties in loading cycles, N, was considered as normally distributed with COV= 0.3. At a crack length of 32 mm which occurs after 1.2×10^5 load cycles, the reliability of the Paris model is higher if the parameters, C and m, were estimated by LSE and the reliability of the Walker model is higher if the parameters were estimated by MLE, in Fig 6c and Fig 6i respectively. Similar outcome is also observed at a higher crack length of 50 mm which occurs after 2×10^5 load cycle, Fig 6f and Fig 6l. Reliability of a model is thus depends not only in the observed crack length after a loading cycle but also on the parameter estimation technique.

5 Conclusion and outlook

A reliability based model quality assessment of several fatigue CGM to predict a certain damage scenario was presented in this paper. The methodology considers uncertainty associated with the parameters and takes into account the influences of parameter estimation techniques. The proposed framework was verified for the quality assessment of a fatigue CGM. However, the validation based real structural measurements is still necessary. As both the Paris and the Walker models represent the crack growth in region II, models capable of describing the region I and region III will be considered in further studies.

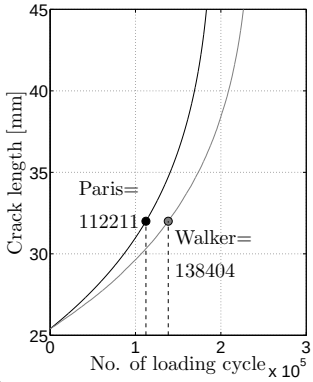

(a) loading cycle for 32 mm crack length(LSE)

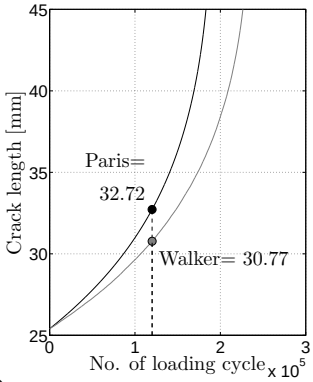

(b) crack length after 120000 loading cycle(LSE)

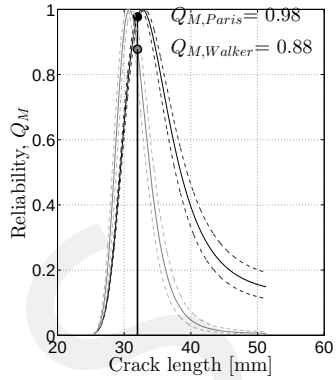

(c) after 120000 loading cycle with 30% uncertainty(LSE)

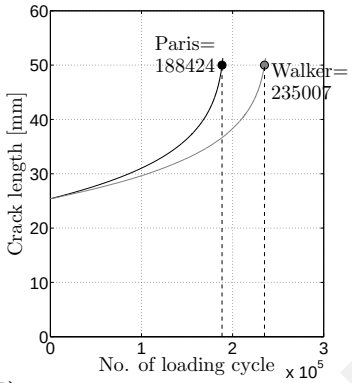

(d) loading cycle for 50 mm crack length(LSE)

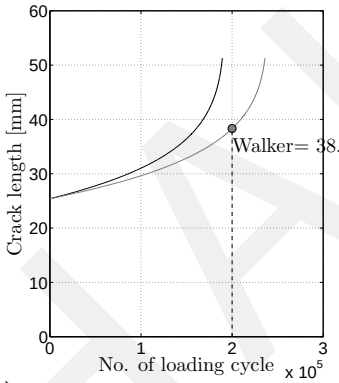

(e) crack length after 200000 loading cycle(LSE)

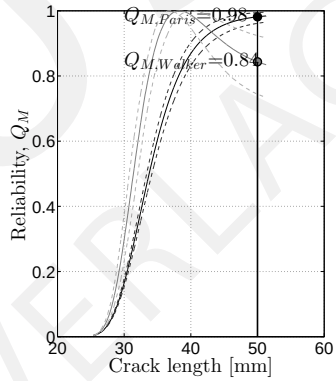

(f) after 200000 loading cycle with 30% uncertainty(LSE)

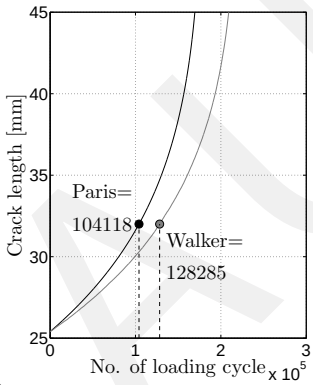

(g) loading cycle for 32 mm crack length(MLE)

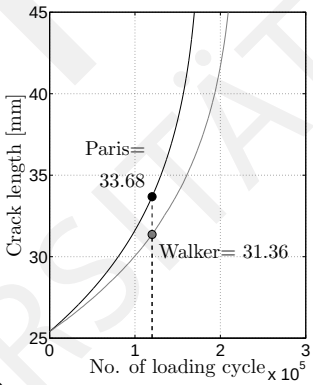

(h) crack length after 120000 loading cycle(MLE)

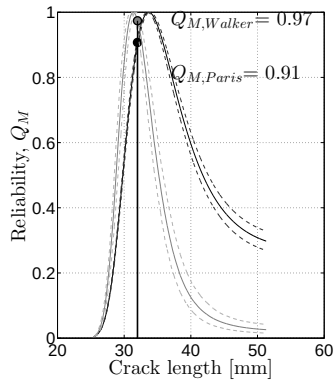

(i) after 120000 loading cycle with 30% uncertainty(MLE)

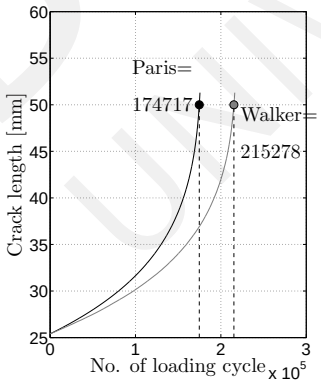

(j) loading cycle for 50 mm crack length(MLE)

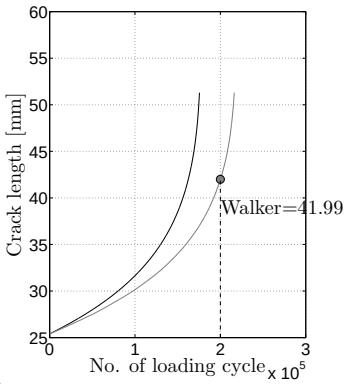

(k) crack length after 200000 loading cycle(MLE)

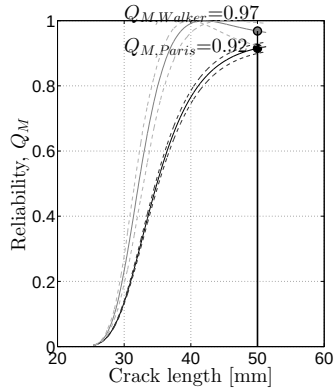

(l) after 200000 loading cycle with 30% uncertainty(MLE)

Figure 6: Reliability of the models, based on the estimated parameters using LSE and MLE, under a certain loading of damaged condition of the structure

References

[1] GI Barenblatt and LR Botvina. Incomplete self-similarity of fatigue in the linear range of crack growth. *Fatigue & Fracture of Engineering Materials & Structures*, 3(3):193–202.

[2] Grigory I Barenblatt. *Scaling, self-similarity, and intermediate asymptotics: dimensional analysis and intermediate asymptotics*, volume 14. Cambridge University Press, 1996.

[3] JE Collipriest Jr. An experimentalist's view of the surface flaw problem. *The Surface Crack- Physical Problems and Computational Solutions*, pages 43–61, 1972.

[4] John W Fisher. *Fatigue and fracture in steel bridges. Case studies*. John Wiley and Sons, 1984.

[5] RG Forman. Study of fatigue crack initiation from flaws using fracture mechanics theory. *Engineering fracture mechanics*, 4(2):333–345, 1972.

[6] Dae-Hung Kang, Changhwan Jang, Yeon-Soo Park, Suk-Yeol Han, and Jin Ho Kim. Fatigue reliability assessment of steel member using probabilistic stress-life method. *Advances in Mechanical Engineering*, 2012(Mlm):1–10, 2012.

[7] Kihyon Kwon and Dan M Frangopol. Bridge fatigue assessment and management using reliability-based crack growth and probability of detection models. *Probabilistic Engineering Mechanics*, 26(3):471–480, 2011.

[8] Steven R Lampman. *ASM Handbook: Volume 19, Fatigue and Fracture*. ASM International, 1996.

[9] Henrik O Madsen. Stochastic modeling of fatigue crack growth and inspection. *Probabilistic methods for structural design*, pages 59–83, 1997.

[10] NASGRO Fracture Mechanics and Fatigue Crack Growth Analysis Software(2006). http://www.swri.org/4org/d18/mateng/matint/nasgro/. v5.0, NASA-JSC and Southwest Research Centre.

[11] PC Paris and F Erdogan. A critical analysis of crack propagation laws. *Journal of Fluids Engineering*, 85(4):528–533, 1963.

[12] VM Radhakrishnan. Parameter representation of fatigue crack growth. *Engineering Fracture Mechanics*, 11(2):359–372, 1979.

[13] Małgorzata Skorupa. *Empirical trends and prediction models for fatigue crack growth under variable amplitude loading*. ECN, 1996.

[14] Andrea Spagnoli. Self-similarity and fractals in the paris range of fatigue crack growth. *Mechanics of materials*, 37(5):519–529, 2005.

[15] K Walker. The effect of stress ratio during crack propagation and fatigue for 2024-t3 and 7075-t6 aluminum. *Effects of environment and complex load history on fatigue life, ASTM STP*, 462:1–14, 1970.

[16] Orville Eugene Wheeler. Spectrum loading and crack growth. *Journal of Fluids Engineering*, 94(1):181–186, 1972.

[17] James Willenborg, RM Engle, and HA Wood. A crack growth retardation model

using an effective stress concept. 1971.

[18] J.J. Xiong and R.A. Shenoi. *Fatigue and Fracture Reliability Engineering*. Springer Series in Reliability Engineering. Springer, 2011.

[19] K. Youseffi and I. Finnie. Fatigue crack initiation and propagation in steels exposed to inert and corrosive environments. final report, may 1, 1977–december 31, 1977. *DOI: 10.2172/5005512*, Feb 1978.

Uncertainty quantification of damping based on free vibration decay testing and Bayesian model updating

Maher Deeb[1], Ingmar Stade[1], Volkmar Zabel[2], Carsten Könke[2]

[1]Research Training Group 1462,
[2]Institute of Structural Mechanics
Bauhaus-Universität Weimar, Germany
maher.deeb@uni-weimar.de ingmar.stade@uni-weimar.de volkmar.zabel@uni-weimar.de
carsten.könke@uni-weimar.de

Abstract. Several methods, applicable in frequency or time domain, are available for the determination of damping ratios from measurements using vibration-based methods. Due to unavoidable measurement uncertainties, a significant variation of the estimated damping ratios can be observed. This paper discusses a methodology to quantify the uncertainty in experimentally determined damping parameters due to a specific measurement uncertainty.
In a first step, data from simulated experiments under impulse excitations was used. The measurement uncertainty due to ambient vibration was considered as a Gaussian white noise signal added to the computed acceleration time history. Damping ratios were estimated from the noisy time history of several simulated tests by the amplitude decay of a free-vibration in order to estimate their initial values. The determined damping ratios were subsequently applied as prior knowledge for a Bayesian model updating approach. An objective function based on the acceleration signal energy was used to compute the posterior distribution density function of the damping ratio. The described procedure was applied to a simple multi degrees of freedom system. This work concludes that the damping results taking into account the uncertainty of measured values leads to better estimates of damping values.

1 Introduction

Designing a civil engineering structure under dynamic excitation requires sufficient information about the dynamic properties of the structure, such as stiffness, mass and especially in resonance damping properties. Damping is caused by the irreversible conversion of mechanical potential or kinetic energy into other forms of energy, usually heat. Damping sources can be divided into internal and external damping depending on the definition of the system boundaries [4]. Furthermore, a classification in material, joints and radiating damping is common according to the mechanisms of energy dissipation. Damping or the dissipation of mechanical energy into heat is usually caused by internal or external friction mechanisms. These mechanisms can occur in the case of external damping, for example by moving of a structure through a surrounding medium and in the case of internal damping friction due to minimal relative movements in joints or reversible time-dependent atomic rearrangements which are caused for instance by dislocation move in the crystal lattice in the case of material damping. Since initial calculations can provide an idea about stiffness and mass of the structure, natural frequencies and mode shapes

are predictable. In comparison to a structure's stiffness and mass the damping properties are not predictable in the same way. Up to now damping is taken into account by using properties from known similar structures or by determination of modal damping values from experimental tests [6], [3]. The inclusion of damping in numerical simulations mostly relies on the assumption of a proportional viscous damping model [1], introduced by assembling the damping matrix proportional to the mass and stiffness matrices. Many studies indicated that the uncertainty of damping ratios is significant in comparison to the uncertainty of natural frequencies and mode shapes e.g. [13], [11], [10], [5], etc.

The aim of this paper is to provide information about the damping ratio of each mode that should be selected out of the variation range and used in further calculations. For this purpose, uncertainty quantification by means of a Bayesian framework is used. The basic concepts of Bayesian methods and their application in structural dynamics and civil engineering can be found in [14]. [2] studied the relationship between the data quantity and the uncertainty of modal parameters including small damping ratios of well-separated modes. A Bayesian approach was applied to develop a close-form analytical formula for the accuracy of the modal parameters if sufficient ambient vibration data was used. [12] applied a Bayesian modeling framework to jointly detect and estimate low-amplitude and strongly overlapping resonances in noisy signals. [7] applied a Bayesian framework to a structural health monitoring benchmark in order to obtain the modal parameters and their uncertainty for output-only modal identification. The aim of this work is to present an approach based on Bayesian framework in order to study the influence of the considered uncertainty on selecting reliable modal damping ratios for further investigations.

2 Method

The proposed method is based on obtaining the initial values of the damping ratio of each mode separately using the amplitude decay functions. The obtained damping ratios were considered as prior knowledge that had to be updated by a Bayesian updating approach using a numerical model G_M. A specific objective function for the model updating approach was used. The objective function is based on the cumulative signal energy d of the response time history $\ddot{x}$, eq. (1). The time signal started at time t_0 and ended at time t_e. In this study, a constant time step dt has been used, therefore, it was omitted.

$$d = dt \sum_{i=t_0}^{t_e} \ddot{x}^2(i) \tag{1}$$

2.1 Model

A numerical model should be developed using a sufficient number of degrees of freedom (DOF) to obtain all desired modes. The model was used to simulate the modal test and to obtain the dynamic response of the studied structure. Since estimating the damping ratios requires a free vibration dynamic test, the response of the structure due to an impulse force was computed. There are several numerical methods to compute the structural

response under dynamic forces. In this work, the Newmark Beta method (constant average acceleration) was applied as a numerical method to solve the equations of motion eq.(2).

$$[M][\ddot{x}] + [C][\dot{x}] + [K][x] = [F(t)] \tag{2}$$

where $[M], [C]$ and $[K]$ are the mass, the damping and the stiffness matrix of the studied structure respectively. $[\ddot{x}], [\dot{x}]$ and $[\dot{x}]$ are the acceleration, the velocity and the displacement response of the studied structure respectively. $[F(t)]$ refers to the applied excitation.

2.2 Uncertainty

In order to consider uncertainty, a white noise $\delta \sim \mathcal{N}(0, \sigma_\delta^2)$ was generated and added to the computed virtual experiments output $\ddot{x}(t)$, eq.(3). After that, the noisy measurements $\ddot{x}_N(t)$ were used to update the numerical model G_M. The value of the standard deviation σ_δ of the considered noise depends on the intensity of the ambient vibration coming from surrounding environment.

$$\ddot{x}_N(t) = \ddot{x}(t) + \delta \tag{3}$$

2.3 Vibration decay testing

In a prior step damping ratios were roughly determined with the help of the amplitude decay of free vibration tests. The procedure was directly applied to the measured time signal and assumes that the measured responses only contain the contribution of one mode [9]. To fullfil this assumption the structure has to be lightly damped and the modes have to be well seperated.
Both, a continous excitation which is suddenly switched off or impulse forces can be used to generate free vibrations. The measured data, especialy in the case of impulse loads, were further processed by applying a bandpass filter to isolate the contribution of a single mode. Then the part of the signal which contained the decaying of the amplitudes was extracted. The instances and the amplitudes of the maximum and minimum values of the processed signal were detected and an exponential fit through the peaks using least squares approximation was calculated.

$$\ddot{x}(t) = Ae^{\lambda t} \tag{4}$$

After detecting the frequency f of the filtered signal, the logarithmic decrement Λ was obtained. For the low damping properties the damping ratio was computed by equation

$$\zeta = \frac{(-1) \cdot \lambda}{2\pi f} = \frac{\Lambda}{2\pi} \tag{5}$$

The strategy has been implemented by using the software package LabView, a graphical programming platform for acquisition and analyzing of measured data [8]. In figure 1 the exponentional fit of the filtered time history data is shown.

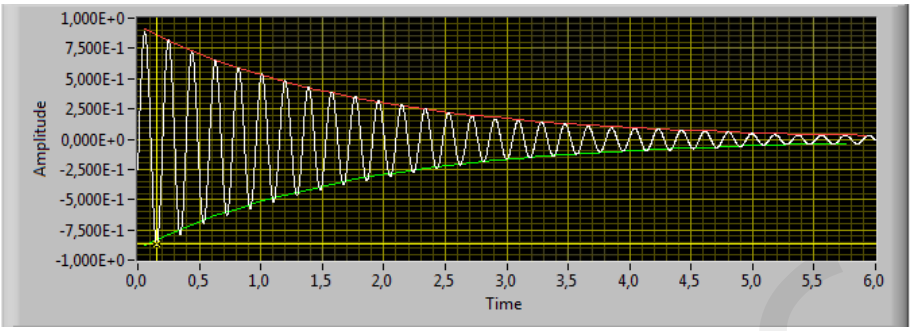

Figure 1: Computed exponentional fit on filtered data

2.4 Model updating

In order to quantify the uncertainty of the modal damping ratios, a Bayesian probabilistic model updating was applied. The approach is based on the principles of conditional probability. The application of this approach required defining a prior information about the inputs $p(\{\theta\})$ and the likelihood function $p(\{\bar{d}\}|\{\theta\})$ which was estimated based on the normal distribution function, eq.(6). Computing the posterior probability density functions of the inputs $p(\{\theta\}|\{\bar{d}\})$ is accomplished using eq.(7)

$$L(\{\bar{d}\}|\{\theta\}) \equiv \prod_{l=1}^{N_d} p(\bar{d}_l|\{\theta\}) = \prod_{l=1}^{N_d} exp[-\sigma_{\alpha,l}^{-2}(\bar{d}_l - d_l)^2] \tag{6}$$

$$p(\{\theta\}|\{\bar{d}\}) \propto p(\{\bar{d}\}|\{\theta\})p(\{\theta\}) \tag{7}$$

where N_d refers to the number of outputs. $l = 1, 2...N_d$. The standard deviation σ_α combines all types of uncertainty that were considered. A latin hypercube sampling method was applied to generate n samples from the prior probability density functions. The resulting posteriors were normalized by the constant $c = \sum_{i=1}^{n}(p(\{\bar{d}\}|\{\theta\})p(\{\theta\}))$ in order to have the area under the probability density function equal to 1. The updating procedure was repeated several times m in order to illustrate the influence of the considered uncertainty on the updated damping values. Finally, the mean of the estimated values and the standard deviation of the updated damping ratios were computed as follows:

$$\mu_{\zeta_k} = \frac{\sum_{j=1}^{m}\sum_{i=1}^{n}\zeta_{j,i} \times p(\{\theta\}_i|\{\bar{d}\})}{m} \tag{8}$$

$$\sigma_{\zeta_k} = \frac{\sum_{j=1}^{m}\sum_{i=1}^{n}[(\zeta_{j,i} - \mu_{\zeta_k})^2 \times p(\{\theta\}_i|\{\bar{d}\})]^{0.5}}{m} \tag{9}$$

3 Application

3.1 Frame structure

A three degree of freedom (DOF) frame , figure 2, is used to illustrate the influence of the considered uncertainty types on the damping ratio. In this example a stiffness-damping-lumped mass model G_M was developed considering the stiffness $\{\theta_1, \theta_2, \theta_3\} = \{k_1, k_2, k_3\}$, the masses $\{\theta_4, \theta_5, \theta_6\} = \{m_1, m_2, m_3\}$ and the damping ratios $\{\theta_7, \theta_8\, \theta_9\} = \{\zeta_1, \zeta_2, \zeta_3\}$. Three modal dynamic tests were simulated. For the first simulated test, the impulse was applied at the top x_1. In second test the impulse was applied at the middle x_2 and for the third at the bottom x_3. As a result, 9 outputs were computed and used to update 9 inputs.

Different durations of impulses $F(t)$ were chosen in order to obtain different excited ranges of frequencies. An example is shown in figure 3 (a) and (b). The true values of the input parameters $\{\theta^*\}$ were chosen as in table 1. As a result, the true natural frequencies of the studied frame are $[f_{n1}, f_{n2}, f_{n3}] = [5.27, 11.36, 16.82]$ Hz.Therefore, the time step was chosen as $dt = 0.002s$ in order to obtain all 3 modes of the structure and to ensure a robust numerical solution. The acquisition time was chosen as $10s$ to gain sufficient information related to the influence of the damping on the structural response.An example of the resulting acceleration time histories $\ddot{x}(t)$ without noise at each DOF are shown in figure 3 (c) and (d). In order to obtain the initial values of the damping ratios $\{\zeta_1, \zeta_2, \zeta_3\}$, the vibration decay testing method explained before was applied on the acceleration time histories $\ddot{x}(t)$ which obtained by performing the transient analysis.

A Latin hypercube sampling method was used to generate 500 samples from the prior probability density functions defined in 2.2. The structural response $\ddot{x}(t)$ at each degree of freedom and for each excitation was computed for each sample. The cumulative signal energy values d of the acceleration time histories $\ddot{x}(t)$ were calculated and used as an objective function to obtain the posterior probability density function $P(\{\theta\}|\bar{d})$ of the damping ratios. $\bar{d}$ refers to the signal energy obtained from measured acceleration time history. In this work, virtual experiments were generated by solving the problem using the assumed real values $\{\theta^*\}$.

Table 1: True values of the studied input parameters

	$\theta_1^* =$ k_1 [N/m]	$\theta_2^* =$ k_2 [N/m]	$\theta_3^* =$ k_3 [N/m]	$\theta_4^* =$ m_1 [kg]	$\theta_5^* =$ m_2 [kg]	$\theta_6^* =$ m_3 [kg]	$\theta_7^* =$ $\zeta_1\%$	$\theta_8^* =$ $\zeta_2\%$	$\theta_9^* =$ $\zeta_3\%$
$\{\theta^*\}$	1616000	3168000	4704000	507.5	757.5	1000	1.7	3.1	1.1

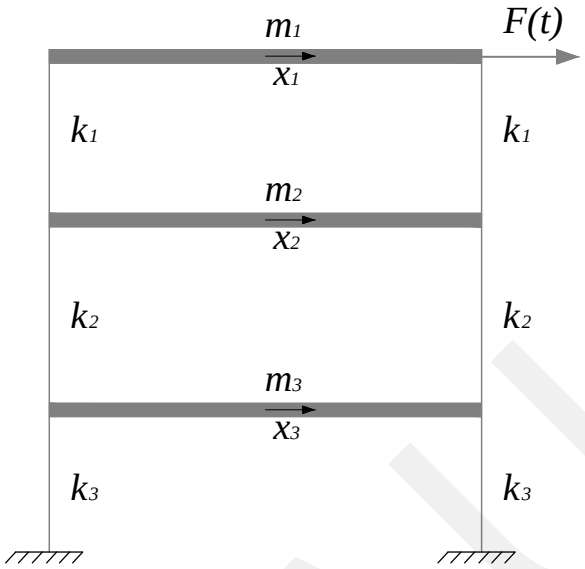

Figure 2: Three degree of freedom frame structure excited by an impulse force $F(t)$ at x_1

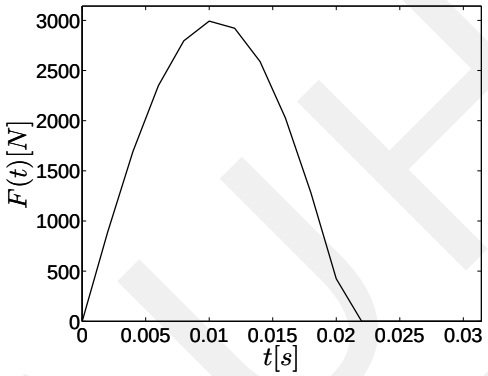

(a) Impulse 1 applied at at x_1

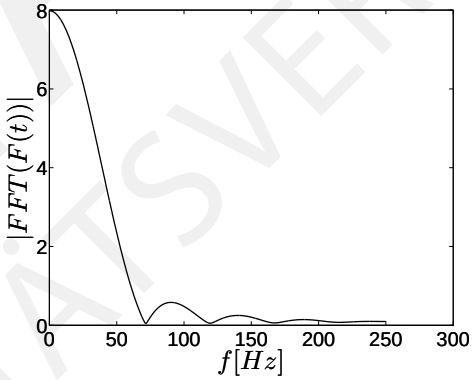

(b) FFT of Impulse 1

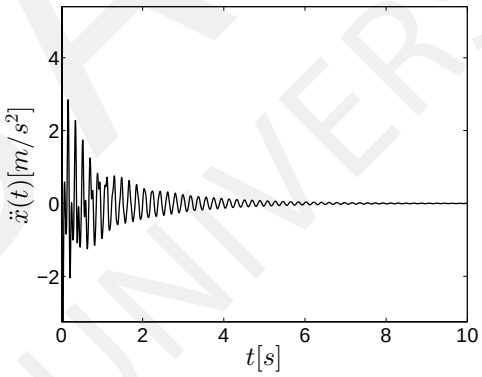

(c) Acceleration time history $\ddot{x}_1(t)$

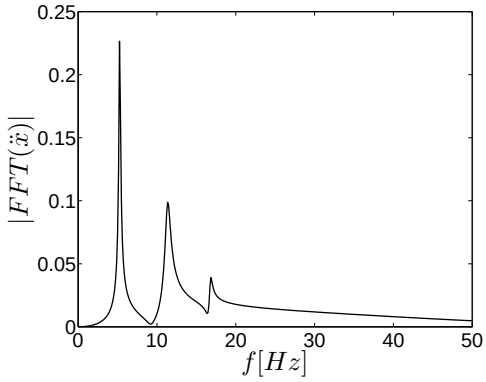

(d) FFT of the acceleration time history $\ddot{x}_1(t)$

Figure 3: Time series and Fourier transforms of impulse forces used to simulate the modal tests

3.1.1 Free vibration decay results

The damping ratios determined using the decay of free vibration amplitudes explained in section 2.3 are shown in table 2. The obtained results vary for the applied different duration, location and strength of excitation, noise and sensor positions. This variation can be caused by coupling of the modes due to close spacing and elevated damping ratios.

Table 2: Damping ratios obtained from vibrant decrement decay

Mode	min damping ratio [%]	max damping ratio [%]
1	1.63	1.83
2	2.38	3.11
3	0.97	1.18

3.1.2 White noise

Two white noise levels were studied: $\delta \sim \mathcal{N}(0, 0.01^2)$ and $\delta \sim \mathcal{N}(0, 0.1^2)$ $[m/s^2]$. In this case, the total uncertainty is given as $\sigma_\alpha^2 = \sigma_{d|\delta}^2 + \sigma_{d|\zeta}^2$. $\sigma_{d|\zeta}$ refers to the variation of the output d due to the uncertainty of the damping ratios $\{\zeta\}$. $\sigma_{d|\delta}^2$ refers to the variation of the output d due to considered white noise. It is important to mention that while the updating procedure was applied, a random white noise was generated and added to the model output each time the model was solved. Table 3 shows the statistical properties of the updated damping ratios using the given experiments $\bar{d}$. Figure 4 shows the variation of the posterior density functions and their means of the updated damping ratios if the updating procedure was repeated 10 times.

Table 3: The updated damping ratios including white noise, the uncertainty of the other inputs were not considered

	$\delta \sim \mathcal{N}(0, 0.01^2)$			$\delta \sim \mathcal{N}(0, 0.1^2)$		
	$\theta_7 = \zeta_1\%$	$\theta_8 = \zeta_2\%$	$\theta_9 = \zeta_3\%$	$\theta_7 = \zeta_1\%$	$\theta_8 = \zeta_2\%$	$\theta_9 = \zeta_3\%$
$\{\theta^*\}$	1.8	3.1	1.1	1.8	3.1	1.1
$\{\mu_\theta\}$	1.78	3.13	1.1	1.78	3.13	1.1
$\{\sigma_\theta\}$	0.009	0.017	0.003	0.04	0.07	0.012
COV	0.005	0.006	0.002	0.019	0.024	0.011

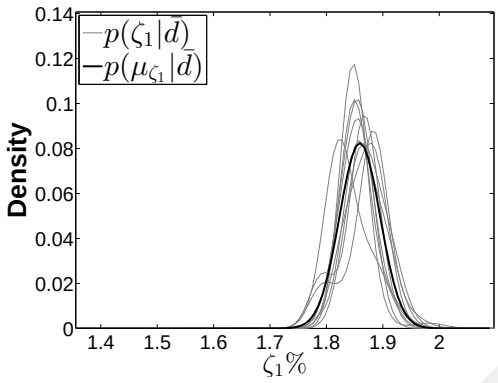

(a) Ten posterior density functions $P(\zeta_1|\bar{d})$ (in gray) obtained from applying 10 times model updating before estimating $P(\mu_{\zeta_1}|\bar{d})$ (in black) from eq.(8) and (9)

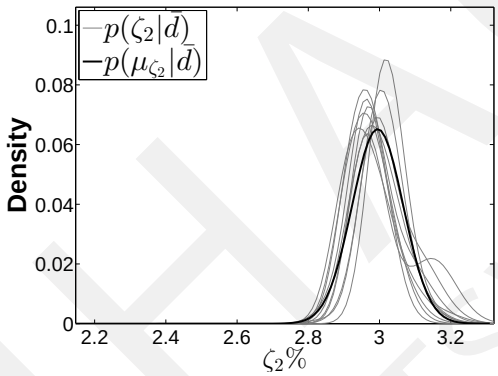

(b) Ten posterior density functions $P(\zeta_2|\bar{d})$ (in gray) obtained from applying 10 times model updating before estimating $P(\mu_{\zeta_2}|\bar{d})$ (in black) from eq.(8) and (9)

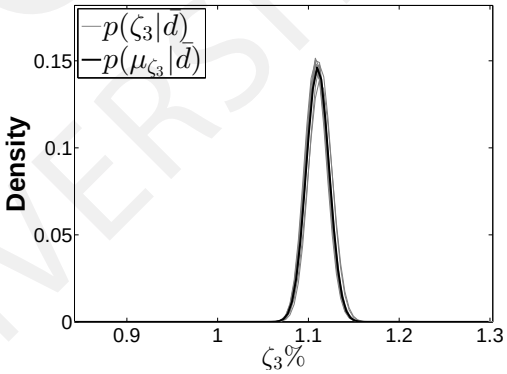

(c) Ten posterior density functions $P(\zeta_3|\bar{d})$ (in gray) obtained from applying 10 times model updating before estimating $P(\mu_{\zeta_3}|\bar{d})$ (in black) from eq.(8) and (9)

Figure 4: The influence of the white noise $\delta \sim \mathcal{N}(0, 0.1^2)$ on the updated damping ratios

4 Conclusion

An initial objective of the study was to identify a specific value of a modal damping ratio that should be used later in further calculations. As expected, the applied Bayesian framework helped to quantify the uncertainty of the damping ratios. The results of this study indicate that using the signal energy as an objective function provides valuable information to update the uncertainty of the damping ratios. Moreover, the results show that choosing the estimated mean values obtained from the posterior density function for further calculation is reasonable. This is because the chosen value is associated with the maximum value of the estimated posterior density function.

It is visible that the considered uncertainty influences the modal damping ratios with different quantity. The posterior density function of ζ_3 is more robust than the one of the other damping ratios in all studied cases. An explanation of this observation requires further investigation. Moreover, it is important to study the relationship between the chosen excitation and the uncertainty of damping ratios if different excitation properties (amplitude, location, frequency range, type) will be used to estimate the damping ratios.

The future step is to consider other types of uncertainty and to apply the approach to physical models including real structures where the modes are not well-separated.

Acknowledgements

The authors would like to express their gratitude towards the German Research Foundation (DFG) that supports their research through the Graduiertenkolleg GRK 1462 "Bewertung gekoppelter numerischer und experimenteller Partialmodelle im konstruktiven Ingenieurbau".

References

[1] S. Adhikari. Damping modelling using generalized proportional damping. *Journal of Sound and Vibration*, 293(1–2):156 – 170, 2006.

[2] SK Au. Uncertainty law in operational modal analysis. *Safety, Reliability, Risk and Life-Cycle Performance of Structures and Infrastructures*, pages 1855–1862, 2014.

[3] A.K. Chopra. *Dynamics of Structures: Theory and Applications to Earthquake Engineering*. Tsinghua University Press, 2001.

[4] AP Jeary. Damping in structures. *Journal of wind engineering and industrial ...*, 72:345–355, 1997.

[5] A Kareem and K Gurley. Damping in structures: its evaluation and treatment of uncertainty. *Journal of Wind Engineering and Industrial ...*, 59:131–157, 1996.

[6] Tracy Kijewski and Ahsan Kareem. Estimation and modeling of damping and engineering auxiliary damping systems in civil engineering structures: an overview. *NatHaz Modeling Laboratory Report*, pages 1–43, 2000.

[7] Sin-Chi Kuok and Ka-Veng Yuen. Structural health monitoring of Canton Tower using Bayesian framework. *Smart Structures and Systems*, 10(4_5):375–391, October 2012.

[8] LabVIEW. http://www.ni.com/labview/d/.

[9] Filipe Magalhães, Álvaro Cunha, Elsa Caetano, and Rune Brincker. Damping estimation using free decays and ambient vibration tests. *Mechanical Systems and Signal Processing*, 24(5):1274 – 1290, 2010. Special Issue: Operational Modal Analysis.

[10] R. Pintelon, P. Guillaume, and J. Schoukens. Uncertainty calculation in (operational) modal analysis. *Mechanical Systems and Signal Processing*, 21(6):2359–2373, August 2007.

[11] Edwin Reynders, Rik Pintelon, and Guido De Roeck. Uncertainty bounds on modal parameters obtained from stochastic subspace identification. *Mechanical Systems and Signal Processing*, 22(4):948–969, May 2008.

[12] Denis V Rubtsov and Julian L Griffin. Time-domain Bayesian detection and estimation of noisy damped sinusoidal signals applied to NMR spectroscopy. *Journal of magnetic resonance (San Diego, Calif. : 1997)*, 188(2):367–79, October 2007.

[13] Gilles Tondreau and Arnaud Deraemaeker. Numerical and experimental analysis of uncertainty on modal parameters estimated with the stochastic subspace method. *Journal of Sound and Vibration*, 333(18):4376–4401, September 2014.

[14] KV Yuen. *Bayesian methods for structural dynamics and civil engineering*. John Wiley & Sons, 2010.

Analysis for foundations of electricity pylons

Glowienka S., Fischer A.

HOCHTIEF Engineering GmbH

Abstract. The supply of energy is an important concern of modern societies. The electricity which is produced by power plants is transported mainly by cables on electricity pylons. These structures therefore play a critical role for the electrical supply. Due to the failure of pylons caused by extreme wind loads or ice rain, these loads have been raised in the last years to avoid damage of the structure and subsequently many pylons need to be redesigned and fastened. Beside the carrying capacity of the pylon itself, the foundation has to be analysed. To check the stability of the tower and the foundation, semi probabilistic or probabilistic design methods are allowed. The paper shows the result of the probabilistic design of a typical foundation type build in former times as a concrete structure without any reinforcement.

1 Introduction

For the design of electrical pylons and its foundation semi probabilistic and probabilistic methods are allowed in Germany [2, 7]. While semi probabilistic methods are mostly used for the design of new structures, the probabilistic approach allows using capacities in the design considering the specific location conditions of the pylon for existing structures. This is important, as the fastening of existing pylons is difficult to execute and the pylon cannot be used during the construction time, which leads to high economical effort. In some cases the application of probabilistic methods in the redesign of existing pylons can avoid these costs. Many of the existing pylons are based on 4 single foundations (stepped foundations) made of unreinforced concrete (see picture 1).

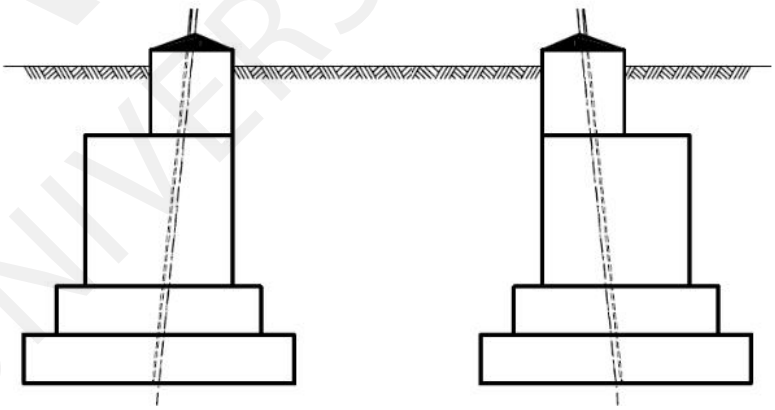

Picture 1: Section of pylon with step foundation

Due to the increase of the wind velocity higher tensile loads need to be considered in the design for the foundations (also for existing pylons). Even though the pylon itself has to be fastened in many cases to fulfill the reliability required by the code [7], this is not the topic of this paper. In addition, the foundation of the pylon has to be checked.

In the following the result of the probabilistic design of a typical foundation type made of concrete without any reinforcement will be analyzed. The main focus will be set on the outer bearing capacity of existing foundations and the design for tensile loads which governs the design in most cases, especially for existing foundations. For the assessment of the inner bearing capacity and the connection between concrete foundation and the steel pylon further investigations are necessary.

2 System

Picture 2 shows the geometry of the foundation which is analysed in the following. Note that it is designed and build without any reinforcement. The steel profile is embedded directly in the concrete.

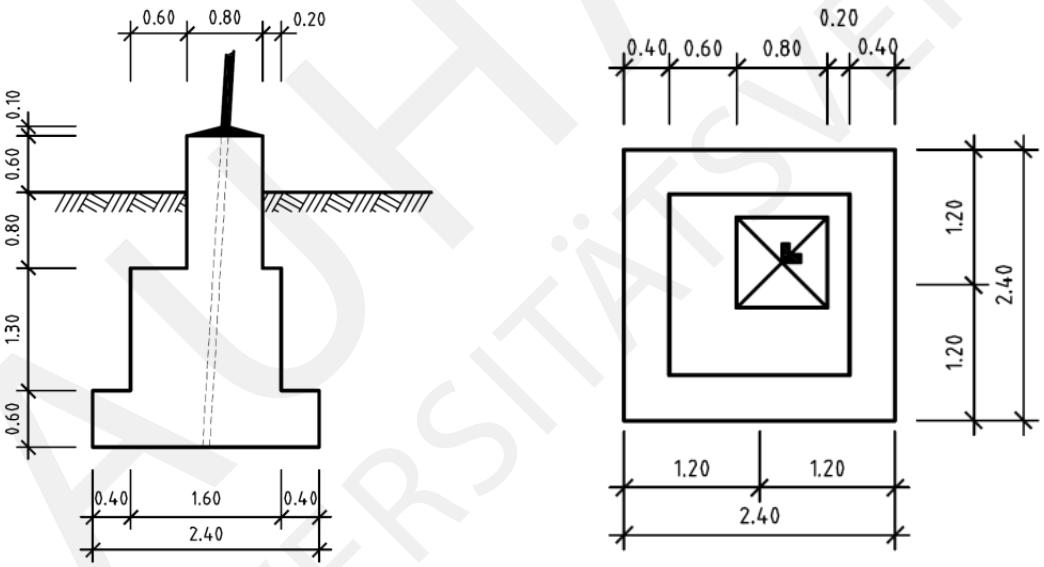

Picture 2: Geometry of the step foundation

In some cases the anchorage in the concrete is provided by additional steel profile pieces which are revited to the steel profile of the pylon (picture 3). To determine the carrying capacity of the anchorage (pull out resistance of the steel profile from the concrete) additional test are necessary and are conducted at present. This inner carrying capacity of the foundation will therefore, not be analysed in the following.

In case of wind loads, the pylon is subjected to bending moments leading the tensile forces in at least one foundation. For the stability of the pylon the self weight of the pylon, the concrete foundation embedded in the soil has to be higher than the uplifting loads due

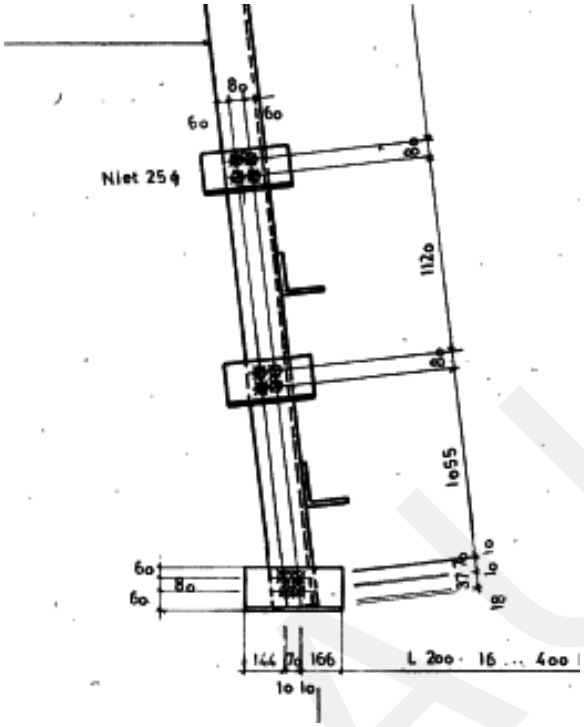

Picture 3: Anchorage

to wind. Compression forces are transferred to the soils by the foundation. However the design of this load case does not lead to problems in most cases even for existing foundations. The same holds for the design against horizontal forces due to the wind.

3 Design assumptions

The design for compression load normally does not govern the design and will not be analysed. Beside the self weight of the steel structure and the self weight of the concrete foundation (volume V_F) an earth body activated in case of tension load (P) is considered for the pullout resistance (see picture 4). The earth body (volume V_S) is supported on the foundation.

The geometry and the weight of the earth body depend on the soil properties, the compaction of the backfill as well as on the geometry and the construction of the foundation itself. It is assumed that the earth body is a truncated pyramid or cone. The design approach has been estimated based on actual size test conducted in the past [1].

It was found that for the pull out resistance of the foundation, parameters as density of the soil (γs), friction angle for tension load (β) and the self weight of the foundation are the most important ones. Picture 4 gives information about the design model.

The tension load of the foundation is mainly provided by wind on the steel tower and the cables suspended on it. The dominating parameter for the wind load is the gust wind speed, which is controlled by the location of the pylon. The wind direction is also important for the internal forces inside the construction. For the example, which will

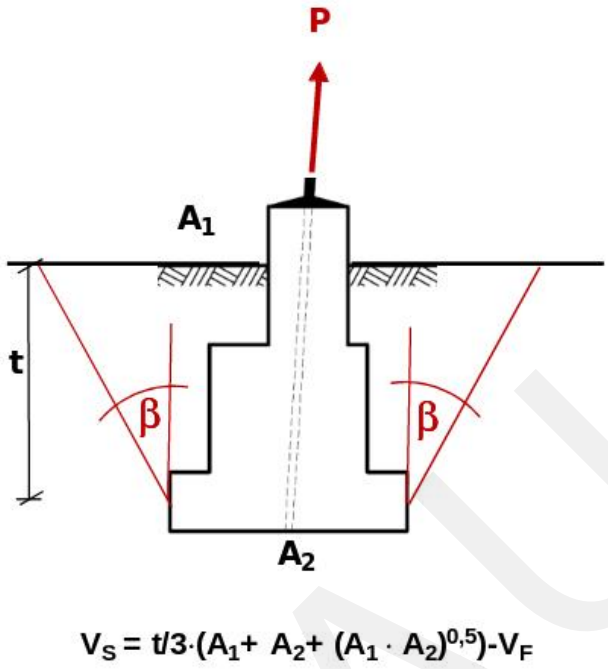

Picture 4: Design assumptions

be analysed in the following a sandy soil (loose compacted) according to [2] is assumed ($\beta = 17.5$, $\gamma S = 18KN/m^3$). The pylon is located at "wind area 1" according to [7] with a characteristic gust wind speed of 21.4m/s.

4 Deterministic design

For the deterministic design of electrical pylons and its foundation code DIN 50341 [2] is used in Germany. For the design of the foundation the code provides a priory values for the soil parameters in accordance of foundation type and the soil conditions. Beside the allowable compression of the soil, the load eccentricity (in case compression), the slide resistance and the pull out resistance have to be checked.

For the design check of existing foundations the latter is decisive in most cases. The minimum safety margin for the design is 1.5, which is a global safety factor according to the code [2]. This factor can be reduced, according to the location of the pylon respectively the risk in case of failure. For our example the pylon is located afield. The acceptable reliability level is Z3 and thus a reduction of the allowable safety margin by a factor of 0.9 is permitted according to [7]. The characteristic value of the pullout resistance is calculated according to [2]:

$$R_k = G_S(\gamma s, \beta, t) + G_F(\gamma c, Vc) = 504kN$$

The effect on the pylon needs to be calculated for different wind directions. The resulting wind load on the foundation is reduced by the self weight of the tower. The characteristic

value of the effect is:

$$E_k = W_k - G_k = 488 - 54 = 394kN$$

The provided safety margin of the pylon foundation is:

$$\mu = R_k/E_k = 504/394 = 1.28 < 0.9 \cdot 1.5 = 1.35$$

The deterministic design does not fulfill the code requirements.

5 Probabilistic design

The probabilistic design is conducted for a reference period of one year [7], that means the wind parameter have to be defined according to this. The limit values for the reliability $\beta_{1,sys}$ can be extracted from [7] and are shown in table 1.

Reliability level Z	required $\beta_{1,sys}$
1	4.3
2	3.8
3	3.3
4	3.0
5	2.6

Table 1: limit values for the reliability $\beta_{1,sys}$ according to [2]

The design model must consider the variability of the soil parameter, the geometry of the foundation and its density, but also the scatter of the wind load respectively the wind speed and the geometry of the tower resulting in different wind pressures on the construction. Additionally uncertainties Θ_E for the modelling of the effect and the resistance Θ_R have to be considered. The latter is estimated based on full-scale tests [1, 5]. The friction angle of the soil in case of tensile load can be described by the friction angle of the soil ϕ.

$$Z = \Theta_R \cdot R(\gamma s, \gamma c, \phi, t, b) - \Theta_E \cdot W(v, a) + \Theta_E \cdot G$$

For a realistic estimation of the extreme wind load a Weibull distribution is used, as in general the wind load converges to a maximum value. The parameters for the wind model can be extracted from [7]. According to this code, the ratio between mean and characteristic values (98% fractile) can be assumed to 1.4. The value “a” is a constant factor for the transmission of the wind pressure to the internal force.

The probabilistic modelling is summarized in table 2. Values for the scatter are defined according to [5, 3, 4]. Variations of the aerodynamic factor c_p are included in the scatter of the gust wind speed v.

Parameter	Distribution	X_k/m_x	V_x
Self weight of the tower G	N	1	0.05
Wind speed v (gust) [1]	W	1.4	0.16
Model uncertainty Θ_F	N	1.0	0.025
Density of the soil γS	N	1.0	0.05
Density of the concrete γC	N	1.0	0.05
Friction angle of the soil ϕ [2]	N	1.0	0.09
Model uncertainty Θ_R	LN	0.95	0.10
Foundation width b	N	1.0	0.03
Foundation depth t [3]	N	1.0	0.03

1 Parameter to describe the Weibull distribution $\tau = 0,06$

2 including the uncertainty of the parameter estimation

3 Definition according to Picture 4

Table 2: Probabilistic model

The probability of failure is calculated based on SORM using COMREL. The resulting $\beta_{1,sys}$-value is estimated as:

$$\beta_{1,sys} = 3.40 > 3.30$$

The probabilistic design fulfils the code requirements. The sensitivity factors inform about a high correlation of the wind speed and the probability of failure ($\alpha = 0.9$). On the resistance site the model uncertainty is dominating ($\alpha = -0.3$).

6 Conclusion

The probabilistic design approach allows using capacities in the design, especially for existing structures. Whereas the deterministic design approach does not fulfil the requirements according to the code, the probabilistic design provides a sufficient margin of safety for the analysed structure. Thus the probabilistic design approach can be used to avoid expensive rehabilitation measures of existing foundations in some cases.

References

[1] Deutsche Verbundgesellschaft e.V. Heidelberg: Mastumbruch und Fundamentversuche 1951/52, Forschungsbericht.

[2] DIN EN 50341-1-1 (VDE 0210):2011-01: Freileitungen über AC 45kV – Teil3 Nationale Normative Festlegungen (NNA); Deutsche Fassung EN 50341-3-4:2001 + Cor. 1:2006 + Cor. 2:2010.

[3] Glowienka, S.: Zuverlässigkeit von Mauerwerkswänden aus großformatigen Steinen, Dissertation TU Darmstadt 2007.

[4] Joint Committee on Structural Safety (JCSS): Probabilistic Model Code, www.jcss.ethz.ch, 2003.

[5] Max Süberkrüb: Mastgründungen für Freileitungen, Fahrleitungsanlagen und Bahnspeiseleitungen, Ernst und Sohn Verlag 1958.

[6] Niemann H.-J., Prognose extremer Sturmstärken mithilfe von PROGumbel, enthalten in Tagungsband „Workshop PROGumbel“, 2009.

[7] VDE: 2013-07: Anforderungen an die Zuverlässigkeit bestehender Stützpunkte von Freileitungen, Entwurf Stand Juli 2013.

General Approach to Model Uncertainties

M. Holicky[1], M. Sykora[1], J.V. Retief[2]

[1]Czech Technical University in Prague, Klokner Institute, Prague, Czech Republic

[2]University of Stellenbosch, Stellenbosch, South Africa

1 Introduction

Appropriate safety formats for the analysis of civil engineering structures have been investigated in numerous previous studies. Amongst others Schlune et al. (2011), Allaix et al. (2013), Cervenka (2013) and Sykora et al. (2013a) proposed approaches to reliability analysis of concrete structures; Byfield & Nethercot (1998) and Helmerich et al. (2007) were focused on steel structures and Dithinde et al. (2011) discussed reliability of pile foundations. It was indicated that structural resistances can be predicted by appropriate modelling of material properties, geometric parameters and uncertainties associated with a model under consideration. The effect of variability of materials and geometry is relatively well understood and was extensively addressed by the aforementioned studies. However, better description of model uncertainties is desired.

It is widely recognised that uncertainties in resistance models and also in load effects play a significant role in the reliability analysis of structures. Consequently they affect material and action models applied in engineering practice such as those based on the partial factor method, EN 1990:2002. Existing knowledge concerning model uncertainties and their characteristics seems to be mostly based on intuitive judgements and to suffer from imprecise definitions and lack of experimental data. Test campaigns are mostly focused on verifications of a particular model for a specified material and failure mode under assumptions that may be incompatible with other studies. This often leads to discrepancies in description of the uncertainties related to a particular theoretical model. Moreover, as a full overview of test parameters and conditions is often missing, a subsequent identification of causes of the differences may be impossible. That is why a general methodology for assessment and reporting on model uncertainties seems to be urgently needed.
The present paper attempts to improve definitions of model uncertainties, propose a general methodology for their quantification by comparing experimental and model results, and suggest their treatment in practical applications. More specifically, the study is focused on:

- Uncertainties in resistance (physical, structural or statistical) models – hereafter "theoretical models",
- Ultimate limit states; recognising serviceability limit states equally important and possibly associated with significant

economic consequences, but being more complex and requiring a separate study.
Implications of model uncertainty for new and existing structures are explored. The present study is a sub-stantial extension of the recent contribution by Holicky et al. (2013).

2 Model uncertainty

2.1 General concept

Model uncertainties can be related to:

- Resistance models (based on simplified relationships or complex numerical models),
- Models for action effects (assessment of load effects and their combinations).

In this study uncertainties in resistance models are addressed only. However, principles provided here form a basis for treatment of uncertainties in load effects as well.
ISO/DIS 2394:2014 – Committee approved revision of ISO 2394:1998 – defines the model uncertainty as a basic variable related to the accuracy of physical or statistical models. Consistently, JCSS (2001a) indicates the model uncertainty be generally a random variable accounting for effects neglected in the models and simplifications in the mathematical relations.
Obviously the model uncertainty should be associated with a computational model under consideration. As a rule the theoretical model is incomplete and inexact due to lack of knowledge or deliberate simplifications of the model accepted for the convenience of users. According to ISO/DIS 2394:2014 the difference between the model and real value can be then expressed by one or several random variables – model uncertainties. As far as possible their statistical properties shall be derived from experiments, observations and from calculations using more accurate models. The model uncertainties are treated as random variables. In principle the approach is the same as for other basic variables such as material properties or action effects. Mean values of model uncertainties should be determined in such a way that, on average, the theoretical model correctly predicts test results.
In principle the distinction between the following cases can be made:

- Modelling of a physical process is possible; in such cases model uncertainty has commonly a low to medium effect on structural reliability and is treated as situation 1 or 2 defined in Section 3.1,
- Modelling of a physical process is impossible or difficult; in such cases model uncertainty often dominates structural reliability and is treated as situation 3 (Section 3.1), recognizing a strong need to quantify and include model uncertainty explicitly in the reliability analysis.

Examples of the former case include bending of ordinary-seized reinforced concrete beams or verifications of steel members without local instabilities. The latter cases can be represented by shear of concrete members analyzed by simplified design formulas, verifications of steel members with local instabilities including cold formed steel profiles, or resistance of geotechnical structures. Typically, the latter cases can be identified by the lack of consensus amongst experts, alternative models used in research studies and practical applications, and different levels of approximation introduced in codes of practice.

2.2 Contributing factors

Typically the model uncertainty is obtained from comparisons of physical tests and model results. Real structural conditions not covered by tests should be taken into account if needed. A general concept of model uncertainty is indicated in Figure 1. The significance of factors affecting test and model results, and real structural conditions depends substantially on an analyzed structural member and failure mode.

Treatment of the test uncertainty was proposed by Sykora et al. (2014). It appears that unbiased test results with coefficient of variation around 0.05 can be assumed for reinforced concrete members. Moreover, the test uncertainty was proved to be of low significance and possible negligible for the cases with higher coefficients of variation of model uncertainty (say, greater than 0.1).
It is emphasized that in many cases, it is more important to quantify the differences between structure and specimens rather than to investigate the test uncertainty. Characteristics of the test uncertainty may be indicative for the difference between structure and specimens under ideal conditions.

2.3 Quantification

In this study the model uncertainty θ is considered to be a random variable. The multiplicative relationship is assumed in accordance with JCSS (2001a):

$$\mathrm{R}(X,Y) = \theta(X,Y)\,\mathrm{R}_{model}(X) \tag{1}$$

where R = response of a structure real resistance estimated from test results and structural conditions; $\mathrm{R}_{\mathrm{model}}$= model resistance estimate of the resistance based on a model; X = vector of basic (random) variables Xi included in the model; and Y = vector of variables neglected in the model, but possibly affecting the resistance. Variables X should be clearly defined. For instance, when resistance of a steel member is affected by ultimate tensile strength, this strength should be directly included in the model rather than yield strength multiplied by some factor.
In addition to X and Y variables, it is purposeful to define test parameters, i.e. variables observed during testing. Obviously the test parameters should include all X and Y variables, but may also cover other variables that for instance affect outcomes of a test procedure. As an example ambient air humidity hardly affects real tensile strength of steel, but may affect accuracy of sensors.

Note that an additive relationship may be considered as an alternative to the multiplicative format given in Equation (1), JCSS (2001a). As models are typically of a multiplicative nature and non-normal (lognormal) distributions are often used for basic variables, the multiplicative format seems to be preferable. Moreover, it is more appropriate when the difference between test and model results is proportional to an observed variable. For instance this difference mostly increases proportionally with increasing structural resistance. Model uncertainty based on the additive format is then dominated by values for greatest resistances and information obtained by testing of specimens with lower resistances is lost.

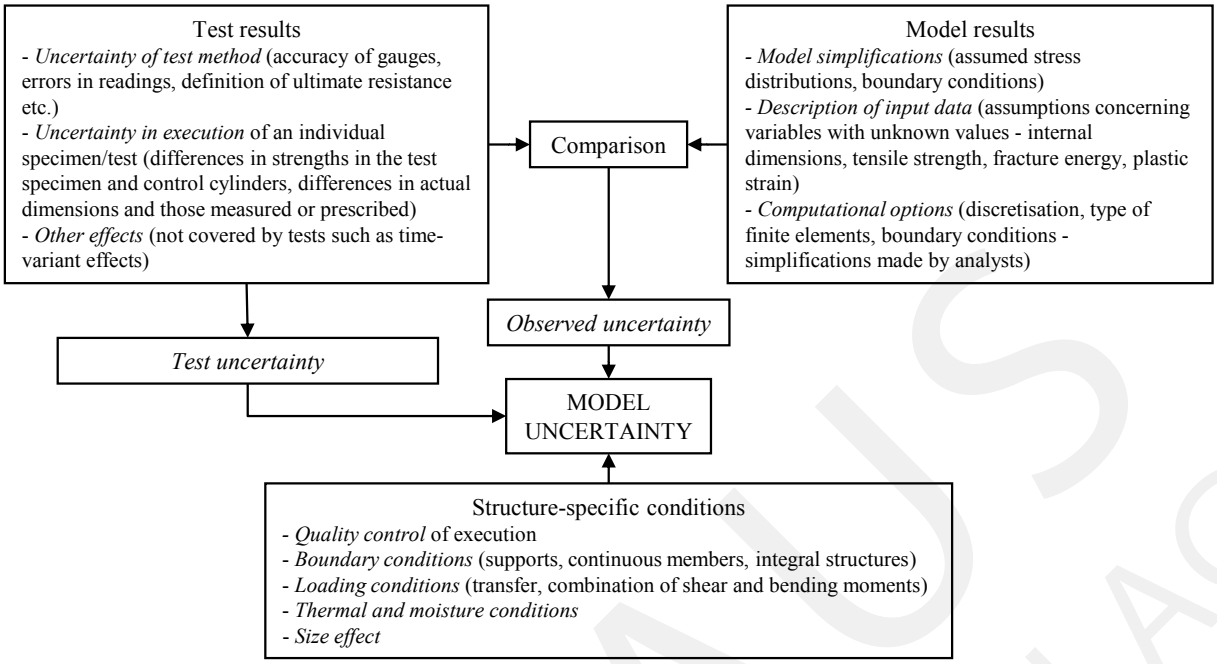

Figure 1: General concept of the model uncertainty.

The additive format applies particularly for geometric parameters where the difference between test and model results is not proportional to the magnitude of basic variables, but it is rather affected by tolerances of measurement technique.
Model uncertainty could be improved by a multi-parameter regression as considered e.g. by Song et al. (2010). However, purely physical models then become hybrid of rational and empirical modelling. That is why it is recommended to improve the physical model.
Realistically assuming a lognormal distribution with the origin at zero (hereafter simply "lognormal distribution") for R and $R_{model}(\cdot)$, the model uncertainty is also lognormal. Its characteristics can be assessed using standard statistical techniques such as the Method of moments, Maximum likelihood method or Bayesian up-dating; see JCSS (2001b) and Holicky (2013). An alternative procedure of the assessment of the model uncertainty is provided in Annex D of EN 1990:2002. However, this method, based on the regression analysis and the Least Square Method, is focused on estimation of a regression coefficient rather than on the assessment of statistical characteristics of a random variable according to the JCSS definition.
In general the model uncertainty depends on basic variables X. Influence of individual variables can be assessed by a regression analysis as described e.g. by Ditlevsen & Madsen (1996).

It is also indicated that the model describes well the essential dependency of R on X only if the model uncertainty:

- Has either a suitably small coefficient of variation (how small is the question of the practical importance of the accuracy of the model) or
- Is statistically independent of the basic variables.

3 Methodology of assessment

The assessment of model uncertainty should be done in terms of a systematic methodology that consists of the following steps:

- Characterization of the assessment;
- Compilation of a database of model uncertainty observations;
- Statistical assessment of the dataset;
- Derivation of a suitable probabilistic model of model uncertainty and
- Application of the model considering both operational use and further investigations including acquisition of new test data or use of a more advanced model.

Examples of various elements of the methodology can be found in by Dithinde et al. (2011), Dithinde & Retief (2013), Huber (2005), Mensah (2012), Mensah et al. (2013a,b) and Sykora et al. (2013b).

3.1 Characterization of assessment

The degree to which the systematic treatment of model uncertainty is followed depends on the relative importance of the model uncertainty with respect to the uncertainties contributed by the basic variables. The following classification of effects and treatment of model uncertainty provides a convenient framework (with reference to classes defined in Section 2.1):

1. *Nominal effect:* Partial factors for basic variables are adjusted to provide a nominal contribution of model uncertainty; for guidance, this approach could be followed when the FORM sensitivity factor (see ISO/DIS 2394:2014 and EN 1990:2002) for model uncertainty is less than $0.4 \times 0.8 = 0.32$. This approach is typically taken across a general class of conditions, for example differentiating only between models for permanent and variable actions; or for the resistance of structural materials.
2. *Significant effect:* The contribution of model uncertainty is sufficiently significant to justify a separate partial factor, typically with a sensitivity factor between 0.32 and 0.8; considering importance of model uncertainty to be equivalent to the basic variables. Explicit provision for model uncertainty allows for differentiation between various failure modes, execution process, levels of approximation for the resistance of a specific material class or proneness to local instabilities. Examples include, respectively, bending or shear, rolled or welded steel sections, ordinary- or high-strength concrete and different classes of steel cross-sections.
3. *Dominating effect:* Limitations of functions to comprehensively predict structural resistance in operational terms result in model uncertainty to be the dominating factor for some cases even for routine situations in-cluded in standardized design procedures. Special attention to the assessment of model uncertainty is then required to ensure the economic attainment of sufficient reliability. Examples include the shear resistance of reinforced concrete sections and pile foundation resistance.

The methodology for the treatment of model uncertainty outlined here is primarily formulated in terms of the most severe situation (3) where it is dominating structural reliability. The methodology can be relaxed and simplified accordingly for situation (2). Treatment of situation (1) is typically based on generic models for model uncertainty or experience.

3.2 Database of model uncertainty observations

The database of model uncertainty observations (θ_i) is derived from a set of experimental observations R_i for which all basic variables X and other deterministic parameters are available to calculate corresponding values of model prediction ($R_{model,i}$). Note that any design bias should be excluded from the calculation of R_{model}. Although certain design parameters are not explicitly applied in the model (variables Y in Equation (1)), they affect model uncertainty and should be included in the assessment process. The strength reduction factor for concrete cracked in shear, longitudinal reinforcement and aggregate size are examples of such extended interpretation of the relevant basic variables not included in several models for shear of reinforced concrete members. Another important attribute of the experimental dataset is the range of parameter values that represents the sample space of experimental observations (Λ_O) for which model uncertainty is investigated. The correspondence of Λ_O to the population space representing the range of design conditions (Λ_d) is indicative of the representativeness of the assessment. Constraints on basic variables such as minimum and maximum reinforcement ratios or dimensional limits should be included in defining Λ_d.

Note that it may be sufficient to:

- Consider values of some variables on the basis of previous experience (modulus of elasticity of steel) or
- Derive them from known relationships with measured basic variables (tensile strength derived from compressive strength of concrete)

and measurements on specimens may not be necessary. However, additional uncertainty is then introduced.
In practical terms the most important constraint in model uncertainty assessment is often the compilation of R_i, including difficulties in obtaining a sufficient number of observations for proper analysis and assessment. The quality of the data is a function of the quality of the experimental measurements, in addition to the control of basic variables and the availability of this information in order to obtain ($R_{model,i}$), particularly when use is made of published experimental results. It should always be assured that a specimen fails in an investigated failure mode; e.g. when the model uncertainty in shear is investigated beams failed in bending should be eliminated from a database.
As a general observation the probabilistic treatment of model uncertainty is equivalent to that of basic variables. However, when model uncertainty is dominant, the relationship between experiment and model rather approaches that of the initial development or verification of the model.

3.3 Statistical assessment

In addition to the quality assessment of the physical observations indicated above (meta-data in statistical terms), the set of model uncertainty observations θ_i shall be tested to represent unbiased sampling; outlier observations considered and goodness of fit of the probability distribution should be verified. Strictly speak-ing experimental campaigns to measure structural resistance are typically devised for the investigation of the effect of certain ranges of basic variables for a defined sample space (Λ_O), rather than for the unbiased sampling of the design population space (Λ_d). An indication of the representativeness of Λ_O to Λ_d can be obtained by considering the ranges and distributions of basic variables from the experimental dataset in the form of histograms. A scatterplot of model uncertainty observations against any basic variable provides an indication of the degree to which the basic variable is accounted for in the model, both in terms of the trend of observations and scatter around the trend.
Since the higher statistical moments are sensitive to outlying observations, they should be carefully identified. Various uni- and multivariate techniques can be followed. Box plots are used to identify any observation falling outside 1.5-times the range of the inner two quartiles of observations. The z-score method identifies an observation more than three standard deviations from the sample mean as an outlier. Scatterplots are used to identify an outlier falling outside a random range around the trend line. Outliers should not be rejected outright since they may represent truly extreme observations. However, the relevant meta-data on the specific outliers are scrutinized typically for errors or indications of not qualifying for inclusion into the sample space.
The final dataset can then be used for conventional statistical assessment by the calculation of sample moments on which distribution parameters are based.
Deviations from such statistical treatment introduce uncertainties which should be accounted for. When generalizing the model uncertainty beyond the scope of the database, trends in its mean and dispersion should be carefully considered. Extrapolation with respect to basic variables for which significant trends are observed may be dubious. In the extrapolation care should be taken not to move to other failure mode, material model or conditions; e.g. from:

- Ordinary- to high-strength concrete,
- One to another class of steel cross-sections or
- Shear of ordinary-sized concrete beams to shear of deep beams with an arch action

3.4 Probability description of model uncertainty

Conventionally probability models for model uncertainty are preselected as based on accepted reliability modeling practice. This does not only reflect a pragmatic approach, but usually insufficient data to derive an appropriate distribution statistically.
As a first approximation a normal distribution represents a conservative approach for determining the low-er tail of model uncertainty for resistance functions; whilst the two-parameter lognormal distribution should be more realistic but somewhat un-conservative. If sufficient data is available to make a reasonable estimate of the skewness of model uncertainty, the general or three-parameter lognormal distribution (Holicky (2013)) provides

a more realistic option.
The primary focus of the assessment of model uncertainty θ is to reflect its contribution to the reliability performance of the model as characterized by the dispersion of the distribution function ($\sigma\theta$). However the systematic effect or bias as expressed by the mean value of θ ($\mu\theta$) can also have a significant effect. Ideally θ should be unbiased; pragmatically the model should intentionally include a limited degree of conservative bias ($\mu\theta > 1$); the occurrence of an un-conservative bias ($\mu\theta < 1$) is evidence that model development is not necessarily reliably pragmatic.

3.5 Application

Although the primary focus of the paper is the quantification of model uncertainty as such, some guidelines on its subsequent application in deriving an appropriate design verification format can also be formulated. An initial indication of the implications of the relative importance of model uncertainty as discussed above not only serves as guide for the assessment of θ, but also for its application.
As before the case of dominating model uncertainty is considered in particular. Evidently a partial factor for model uncertainty should be included explicitly in the design format. This is required not only for the purpose of transparency but also due to the ineffectiveness of partial factors for basic variables to include provision for model uncertainty.
The need for the explicit treatment of model uncertainty is generally limited to specific situations, such as the shear resistance for structural concrete with stirrups. Provision for an appropriate partial factor for model uncertainty should then be limited to this model, rather than as part of a general scheme of partial factors, such as for all failure modes for structural concrete. It may even be pragmatic to treat such cases separately in terms of partial resistance factors; the resistance factors should then be based on model uncertainty, with nominal adjustment for the basic variables.
Parametric assessment of the influence of model uncertainty as done for the statistical assessment can pro-vide useful insight in the reliability performance of the function. This could serve as basis for the reassessment of the function as such. Various strategies could be considered for improved model uncertainty performance. The range of application of the model may be limited or divided into sub-ranges to allow for differentiated adjustment of the model partial factor (Holicky et al. (2013)). More fundamental measures include adjustment of the model to improve the correspondence between experimental measurement and prediction, improving the level of approximation or considering an alternative approach as basis for the model, Mensah et al. (2013a,b).
Application of model uncertainty may differ for new and existing structures due to the following reasons:

1. In structural design costs of safety measures such as increasing the amount of reinforcing steel are smaller compared to strengthening of an existing structure. That is why it may be affordable to design using a model with greater model uncertainty and accept a more conservative solution.
2. Available measurements may often lead to reduction of uncertainties related to resistance and permanent action effects when assessing existing structures. The sensitivity factors for these variables decrease whilst sensitivity factors for model

uncertainties increase, fib SAG 7 (August 2014).

Based on these arguments improvements of the model and related costs can then be justified for an existing structure as the strengthening is expansive and model uncertainties play a significant role in the reliability assessment. Several strategies can be adopted when improvement of the model is needed:

- Reduction of model uncertainty by using a more advanced model; however, in some cases this step should be taken with caution as the advanced model can require input data that are difficult to obtain directly,
- Updating uncertainty in the accepted model by tests valid for a specific case; as an example models for resistance of iron columns are in general associated with great dispersion of model uncertainty as real resistances are affected by a type of iron and processes of execution that cannot be exactly described by a single model; when several columns from an analyzed structure can be tested, outcomes of these may significantly enhance the estimate of uncertainty in the resistance model.

4 Concluding remarks

Description of uncertainties related to resistance and load effect models can be a crucial problem of reliability analyses. The present study focused on uncertainties in resistance models reveals that:

- Model uncertainty should be carefully treated particularly for cases when modelling of a physical process is impossible or difficult; in such cases model uncertainty often dominates structural reliability,
- The model uncertainty should be related to test uncertainties, real structural conditions and to computational models under consideration,
- The scope of application of the model should be clearly identified; an example is the uncertainty in shear resistance of reinforced concrete beams, depending on presence of special shear reinforcement and amount of longitudinal reinforcement,
- In common cases real resistance can be estimated as a product of the model uncertainty and resistance obtained by the model, lognormal distribution often provides an appropriate probabilistic description of mod-el uncertainty,
- The assessment of model uncertainty consists of characterization of the assessment, compilation of a data-base of model uncertainty observations, statistical assessment of the dataset, derivation of a suitable probabilistic model and application of the model,
- Application of model uncertainty may differ for new and existing structures.

The proposed approach seems to offer better understanding of the uncertainties in resistance models and enables the specification of their real characteristics.

Acknowledgements

This study is partly an outcome of the research project P105/12/2051, supported by the Czech Science Foundation.

References

[1] Allaix, D.L., Carbone, V.I. & Mancini, G. 2013. Global safety format for non-linear analysis of reinforced concrete.

[2] Byfield, M. & Nethercot, D.A. 1998. An Analysis of the True Bending Strength of Steel Beams. Proceedings of the Institution of Civil Engineers-Structures and Buildings 128(2): 188-197.

[3] Cervenka, V. 2013. Reliability-based non-linear analysis according to fib Model Code 2010. Structural Concrete 14(1): 19-28. Dithinde, M., Phoon, K., De Wet, M. & Retief, J. 2011. Characterization of Model Uncertainty in the Static Pile Design Formula. Journal of Geotechnical and Geoenvironmental Engineering 137(1): 70-85.

[4] Dithinde, M. & Retief, J.V. 2013. Pile design practice in southern Africa Part I: Resistance statistics. Journal of the South African Institution of Civil Engineering 55(1): 60-71.

[5] Ditlevsen, O. & Madsen, H.O. 1996. Structural Reliability Methods. Chichester: John Wiley & Sons. fib SAG 7 August 2014. Partial Factor Methods for Existing Structures (draft). fib. .

[6] Helmerich, R., Kühn, B. & Nussbaumer, A. 2007. Assessment of existing steel structures. A guideline for estimation of the remaining fatigue life. Structure and Infrastructure Engineering 3(3): 245-255.

[7] Holicky, M. 2013. Introduction to Probability and Statistics for Engineers. Heidelberg: Springer.

[8] Holicky, M., Sykora, M., Barnardo-Vijloen, C., Mensah, K.K. & Retief, J.V. 2013. Model Uncertainties in Reliability Analysis of Reinforced Concrete Structures. In A. Zingoni (ed.), Proc. SEMC 2013, University of Cape Town, 2-4 September 2013. Millpress.

[9] Huber, U.A. 2005. Reliability of Reinforced Concrete Shear Resistance (MSc thesis). Stellenbosch: Department of Civil Engineer-ing, University of Stellenbosch, Stellenbosch, South Africa.

[10] JCSS 2001a. JCSS Probabilistic Model Code. Joint Committee on Structural Safety. <www.jcss.byg.dtu.dk>.

[11] JCSS 2001b. Probabilistic Assessment of Existing Structures. Joint Committee on Structural Safety, RILEM Publications S.A.R.L. Mensah, K.K. 2012. Reliability Assessment of Structural Concrete with Special Reference to Shear Resistance (MSc thesis). Stel-lenbosch, South Africa: University of Stellenbosch.

[12] Mensah et al. (2013a) Mensah, K.K., Retief, J.V. & Barnardo-Viljoen, C. 2013.

Reliability based application of Eurocode 2's variable strut inclination method for shear. In G. Deodatis, B.R. Ellingwood & D.M. Frangopol (eds.), Safety, Reliability, Risk and Life-Cycle Performance of Structures and Infrastructures - Proceedings of the 11th International Conference on Structural Safety and Reliability, ICOSSAR 2013, New York, 16-20 June 2013. Leiden: CRC Press/Balkema.

[13] Mensah et al. (2013b) Mensah, K.K., Retief, J.V. & Barnardo-Vijloen, C. 2013. A comparison of the variable strut inclination and alternative stirrup design methods. In A. Zingoni (ed.), Proc. SEMC 2013, Cape Town, 2-4 September 2013. Leiden: CRC Press/Balkema.

[14] Schlune, H., Plos, M. & Gylltoft, K. 2011. Safety formats for nonlinear analysis tested on concrete beams subjected to shear forces and bending moments. Engineering Structures 33(8): 2350-2356.

[15] Song, J., Kang, W., Kim, K.S. & Jung, S. 2010. Probabilistic shear strength models for reinforced concrete beams without shear reinforcement. Structural Engineering and Mechanics 34(1): 15-38.

[16] Sykora et al. (2013a) Sykora, M., Cervenka, V. & Holicky, M. 2013. Uncertainties of resistance models for reinforced concrete structures. In D. Marian, I. Leviathan & A.N. Dancygier (eds.), Proc. fib Symposium Tel Aviv 2013, Tel Aviv, 22-24 April 2013. Tel Aviv: Technion.

[17] Sykora et al. (2013b) Sykora, M., Holicky, M. & Krejsa, J. 2013. Model Uncertainty for Shear Resistance of Reinforced Concrete Beams with Shear Reinforcement According to EN 1992-1-1. Transactions of the VSB - Technical University of Ostrava, Civil Engineering Series 23(2): 150-159.

[18] Sykora, M., Holicky, M., Prieto, M. & Tanner, P. 2014. Uncertainties in resistance models for sound and corrosion-damaged RC structures according to EN 1992-1-1 (accepted for publication). Materials and Structures. DOI: 10.1617/s11527-014-0409-1.

Reducing forecast uncertainty by using observations in geotechnical engineering

Maximilian Huber

Deltares, Unit GEO
Researcher & consultant
Bussinesqweg 1, 2629 HV Delft, City, The Netherlands
maximilian.huber@deltares.nl

Abstract
Especially in geotechnical engineering a high level of uncertainty in the design of structures is present. Standards and guidelines recommend the observational method for projects with a high level of uncertainty and when the geotechnical behaviour is difficult to predict. However, this design approach is based on engineering judgement in combination of deterministic approaches, which are adapted sequentially whenever new observations are available. This formulates the need for a sound framework to quantify forecast uncertainty. The contributions explained the sequential data assimilation concept, which can reduce the forecast uncertainty by using observations. A case study on the application of this methodology on a simple example showed the principle of the proposed methodology.

1 Introduction

Design and construction of geotechnical structures often involves a wide range of uncertainties, which are generally associated with the interpretations and assessment of geotechnical properties form a set of data. Eurocode 7 [2] recommends to use the observational method (OM) in projects with a high level of uncertainty and when the geotechnical behaviour is difficult to predict. This design approach enables the engineer to address the uncertainties by continuously predicting, observing and altering the design during construction [12].

Since Peck [11] first formulated the design philosophy of the OM, the method has been contentiously refined and improved. The major principles of the OM are to initially assess acceptable limits of behaviour and the range of possible behaviour for a structure, subsequently followed by monitoring and evaluation of the actual behaviour. During the design phase, it is of great importance that prospective deviations in geotechnical behaviour and associated failure mechanisms are identified so that appropriate actions can be devised in an early stage of the design process. In case of deviation from initial assessments and established limits during construction, actions have to be preformed according to the plan elaborated in the design phase.

Up to now, the OM is based purely on expert judgement and on a deterministic design approach [5, 11, 12, 9, 13]; recently, some tried to incorporate the uncertainty of the soil properties using standard statistical approaches in a Bayesian framework as given in [14]. However, the variability of the simulation model is not considered explicitly and the uncertainties of the observations are not taken into account because they are considered as small in comparison to the subsoil uncertainty.

In this contribution, I provide a statistical framework, which can consider both uncertainties of the subsoil and of the observations. Moreover, I show that we can also incorporate the observations in the probabilistic analysis of a complex geotechnical problem. Additionally, I show how to quantify the forecast uncertainty based on methods from numerical weather prediction. The possibilities and limitations of this approach are discussed in a case study, which shall help the reader to grasp the basic ideas more clearly. At the end of this contributions there is a summary and conclusion for future research steps.

2 Combination of uncertain observations and probabilistic forecasts

Apart from geotechnical engineering, uncertainties in model parameters are an especially dominant source of uncertainty for e.g. hydrological models and models in numerical weather prediction.

2.1 Review of data assimilation methods

Data assimilation methods can take advantage of measurements whenever they are available and are thus useful in both online and offline applications. These methods have more flexibility in dealing with time-variant parameters, compared with batch calibration methods. Some sequential calibration methods also explicitly address uncertainties in input data and model structures. As described in detail by Evensen [4], frequently used data assimilation methods include variational and sequential method.

2.1.1 Variational data assimilation

Four dimensional variational data assimilation (4D-Var), is a method of estimating the set of parameters by optimizing the fit between the solution of the model and a set of observations, which the model is meant to predict. The procedure of adjusting the parameters until the model 'best predicts' the observables, is known as optimization. The 'four dimensional' nature of 4D-Var reflects the fact that the observation set spans not only three dimensional space, but also a time domain.

The approach of this inverse modelling technique is to find the initial conditions of a model, such as to minimize some scalar quantity J. The cost or penalty function $J[x]$ is a functional of the state vector $\mathbf{x}$ and is defined to be a global measure of the simultaneous misfit between $\mathbf{x}$, the current guess of the true model state, and two independent 'versions' of the atmospheric representation. One of these versions is that according to the observations themselves, and the other is taken from a model forecast. The latest observations are contained in the vector $\mathbf{y}$.

We can now proceed to define a form of which simultaneously penalizes a bad fit between the model state $\mathbf{x}$ and the background, and the model state and the predicted observations, given in equation (1).

The usual form of the objective function J is given in the following equation:

$$J[\mathbf{x}] = \frac{1}{2}(\mathbf{x_B} - \mathbf{x})^{\mathrm{T}} \mathbf{B^{-1}} (\mathbf{x_B} - \mathbf{x}) + \frac{\mathbf{1}}{\mathbf{2}} \sum_{\mathbf{t=0}}^{\mathbf{\Delta t}} \left(\mathbf{y}(t) - \mathbf{H_t^0}[\mathbf{x}(t)]\right)^{\mathrm{T}} \mathbf{E^{-1}} \left(\mathbf{y}(t) - \mathbf{H_t^0}[\mathbf{x}(t)]\right) \quad (1)$$

where here and in the remainder of this report, the model state $\mathbf{x}$ applies to the initial time $t = 0$ (defined to be at the start of the current assimilation cycle) unless explicitly labelled otherwise. Other symbols are the following: $\mathbf{B}$ is the background error covariance matrix, $\mathbf{y}(t)$ is the set of observations made at time t, $\mathbf{H_t^0}[\mathbf{x}(t)]$ is the part of the forward model which predicts the observations based on the model's current state, and $\mathbf{E}$ is the observational error covariance matrix. The vector $\mathbf{y}(\mathbf{t}) - \mathbf{H_t^0}[\mathbf{x}(\mathbf{t})]$ is known as a residual.

One has made various assumptions when writing down this cost function. Firstly, it is assumed that the errors are unbiased and Gaussian. Another assumption is that the model is 'perfect' over the assimilation period.

This cost function is minimized in order to get the single state parameters and the initial conditions of the given system.

3D-VAR stands for the variational data assimilation, in which - during a particular assimilation period - no account is taken of the time that observations are taken. The three dimensions are spatial. 4D-VAR stands for variational data assimilation within three space dimensions plus one time dimension.

Evensen [4] reports that the drawback of the variational approaches is the limited applicability. It is reported that it is very difficult do implement and solve the equations of highly non-linear systems. Additionally, a large number of state variables, which are stored in the state vector $\mathbf{x}$, lead to a very large error covariance matrix $\mathbf{B}$ and thus a huge computational effort.

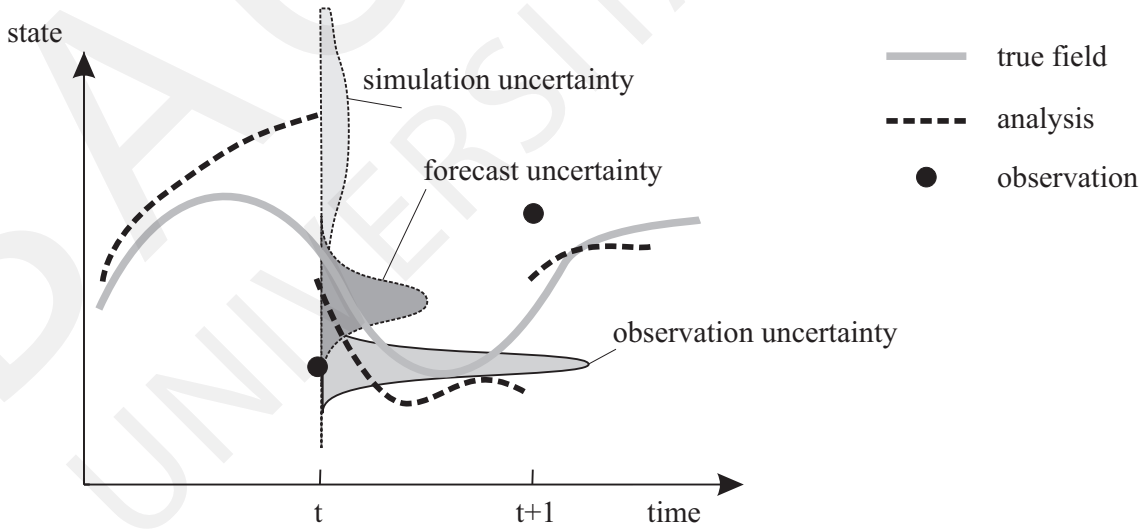

Figure 1: Concept of sequential data assimiliation with the uncertainty of the simulation, the observation and the forecast for a given state.

2.1.2 Sequential data assimilation

Contrary to the sequential methods, which update the model solution every time observations are available, variational methods seek an estimate in space and time where the estimate at a particular time is dependent on both past and future measurements.

2.2 Theoretical background on sequential data assimilation

After its introduction by Evensen [4], the Ensemble Kalman Filter (EnKF) has been widely used in atmospheric, geographic, and oceanic sciences. It was originally proposed as a stochastic or Monte Carlo alternative to the deterministic extended Kalman Filter (EKF) by Evensen [4]. The EnKF was designed to resolve the two major problems related to the use of the EKF with non-linear dynamics in large state spaces, i.e. the use of an approximate closure scheme and the huge computational requirements associated with the storage and forward integration of the error covariance matrix. The EnKF has gained popularity because of its simple conceptual formulation and relative ease of implementation. Furthermore, the computational requirements are affordable and comparable to other popular sophisticated assimilation methods such as the 4D-VAR method.

It was first developed for dynamic state estimation to improve initial conditions for numerical forecasts, and was later applied to model parameter estimation. In EnKF, the posterior estimate $\mathbf{x^a}$, i.e., the analysis is given by

$$\mathbf{x^a} = \mathbf{x^f} + \mathbf{K}\left(\mathbf{y} - \mathbf{H}\mathbf{x^f}\right) \tag{2}$$

and the analysis error covariance $\mathbf{P^a}$ is given by

$$\mathbf{P^a} = (\mathbf{I} - \mathbf{K}\mathbf{H})\ \mathbf{P^f} \tag{3}$$

where $\mathbf{x^f}$ is the prior estimate with n state variables, $\mathbf{y}$ is the observation vector of m observations, $\mathbf{H}$ is the observation operator matrix (dimension $m \times n$) which maps state variables to observations, $\mathbf{I}$ is an identity matrix (dimension $n \times n$), and $\mathbf{P^f}$ is the forecast background error covariance (dimension $n \times n$). The Kalman gain matrix $\mathbf{K}$ (dimension $n \times m$) is defined as

$$\mathbf{K} = \mathbf{P^f}\mathbf{H^T}\left(\mathbf{H}\mathbf{P^f}\mathbf{H^T} + \mathbf{R}\right)^{-1} \tag{4}$$

where $\mathbf{R}$ is the observation error covariance (dimension $m \times m$). $\mathbf{P^f}\mathbf{H^T}$ is the predicted covariance between the states and observed variables, and $\mathbf{H}\mathbf{P^f}\mathbf{H^T}$ is the predicted error covariance of the observed variables; this predicted error covariance is quantifying the forecast uncertainty of the system, which is represented by the state vector $\mathbf{x}$.

3 Case study

3.1 Introduction

This case study demonstrates the possibilities and limitations of sequential data assimilation in geotechnical engineering. For simplicity reasons, I investigates the loading of a

Table 1: Statistical properties of the input ensemble of the paremtetric study A.

Variable	distribution	mean value	COV $= \sigma/\mu$
s	lognormal	0 mm	30 %
η	lognormal	$2.38 \cdot 10^6$ MPa $\cdot$ h	30 %
E_{ref}	lognormal	2,400 MPa	30 %
m	lognormal	0.5	30 %

visco-elastic, non-linear material (e.g. salt), which is simulated by a simple, one dimensional, time dependent non-linear system. This academic example shall help the reader to understand the concept and to be abel to apply it to other problem sets.

3.2 Mechanical system

The visco-elastic material is simulated in the sequel parametric study by the Kelvin-Voigt model and by the Maxwell model. Although these simple approaches are limited in describing e.g. salt or clay, I choose these well known models due to their simplicity.

The Kelvin-Voigt model is described by equation (5).

$$\dot{\epsilon} = \frac{\sigma}{\eta} - \frac{E(\sigma)}{\eta}\epsilon \tag{5}$$

Herein, $\dot{\epsilon}$ is the time increment of strain ϵ under a given load σ and for given viscosity η and a given stiffness E. The stiffness $E(\sigma)$ is dependent on the stress level σ and on the Ohde-exponenet m (equation (6)).

$$E(\sigma) = E_{ref} \cdot \left(\frac{\sigma}{p_{ref}}\right)^m \tag{6}$$

The Maxwell model is defined in equation (7).

$$\dot{\epsilon} = \frac{\dot{\sigma}}{\eta} + \frac{\epsilon}{E(\sigma)} \tag{7}$$

3.3 Parametric study A

The state vector $\mathbf{x} = [\mathrm{s}, \eta, E_{ref}, m]^{\mathrm{T}}$ consists of the calculated settlements s, the viscosity η, the reference stiffness E_{ref} and the Ohde exponent m. Typical values for the material properties of salt are assumed. The mean values μ and the coefficients of variations COV and the corresponding distributions are given in table (1).

Within the EnKF scheme, I choose the Kelvin-Voigt model (equation (5)) as simulation model. This simulation model approximates reality in this case study, which is given by the Maxwell model (equation (7)). Both equations are solved in time by using the well known Runge-Kutta scheme, given in standard mathematical textbooks [1].

The observations are generated by the solving equation (5) using the Runge-Kutta scheme and adding a measurement noise ($\mu_{obs} = 0$ mm, $\sigma_{obs} = 1$ mm).

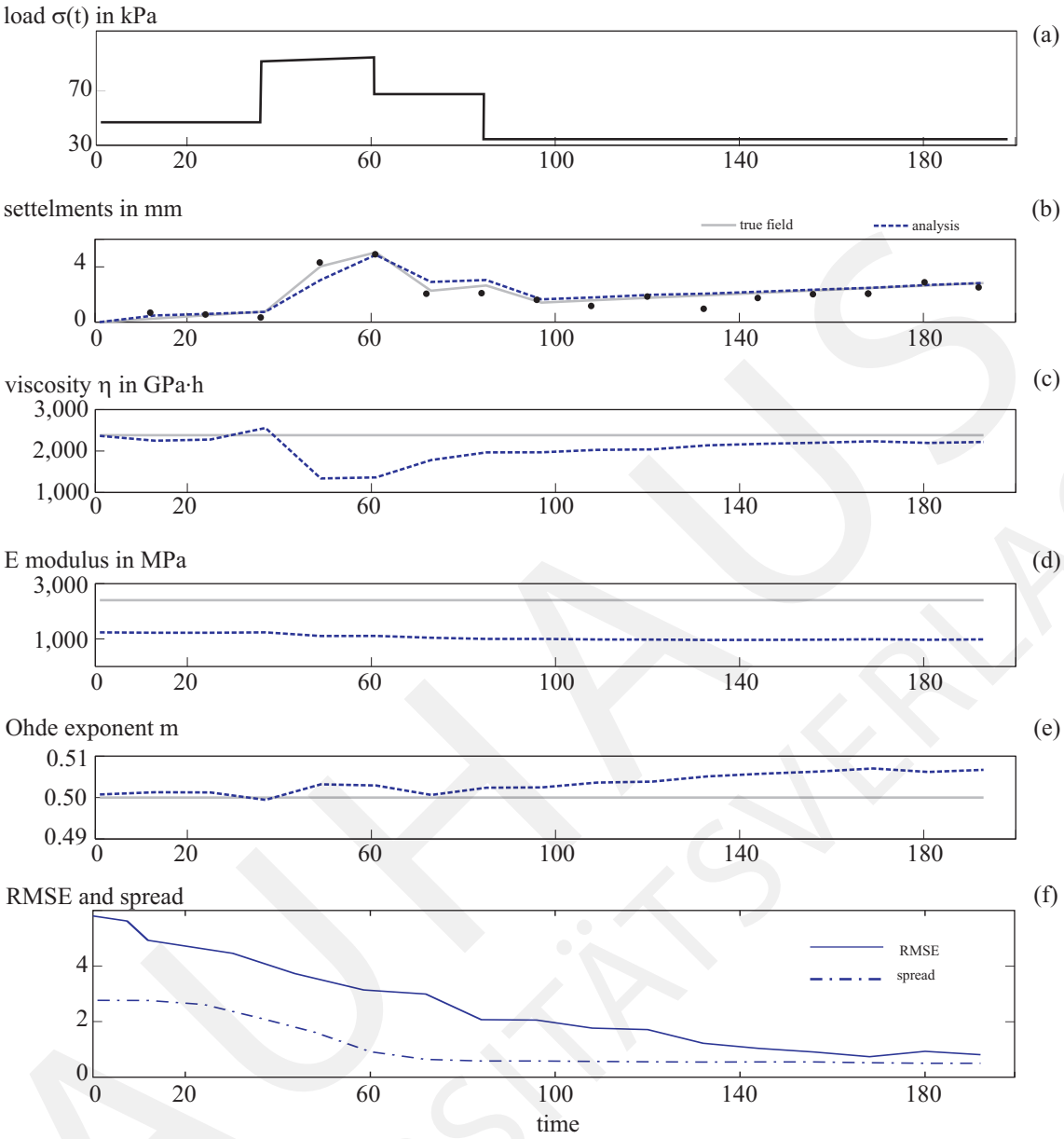

Figure 2: Typical EnKF simulation results showing the true model, the observations and the assimilated properties (a) load $\sigma(t)$, (b) calculated settlements s, (c) viscosity η, (d) reference stiffness E_{ref}, (e) Ohde exponent m; (f) root mean square error between the true model and the assimilated simulations versus time.

Figure 1 visualizes the uncertainty of the simulation, the observation and the forecast for a given state. One can see that the spreading of the simulation is bigger compared to the spreading of the observation. Using the sequential data assimilation, one can reduce the simulation uncertainty significantly and derive the uncertainty of the forecast following the corresponding equation in section 2.2. The results of the time step t is the basis of the simulation of the following time step $t + 1$.

After study figure 1, one can follow the results of the EnKF simulation more easy. In figure 2(a) one can see the load $\sigma(t)$ on one meter of visco-elastic soil, which is changing

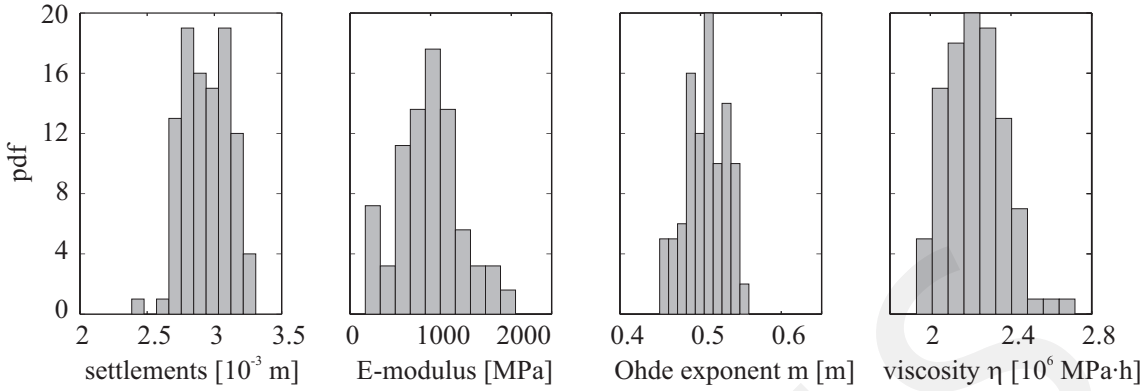

Figure 3: Histograms of the state variables $\mathbf{x} = [\mathrm{s}, \eta, E_{ref}, m]^{\mathrm{T}}$ at t=200.

over time. The single elements of the state vector are plotted in figure 2(b, c, d, e) as results of the sequential data assimilation process. The observation of the settlements in figure 2(b) are used in the EnKF framework. One can clearly see the convergence of the components of the state vector after $t = 180$, which is visualized in figure 2(f) by showing the root mean square error (RMSE). The RMSE is the calculated between the actual state vector and the original values of the true system. One has to keep in mind that this error can not be zero because two different models have been used. This is a normal case in engineering problems, because the true model is never fully known.

In figure 2(a) one can see that the settlements are showing the fastest convergence compared to the other elements of the state vector. It can be seen in figure 2(b) that the viscosity is showing a faster convergence than the stiffness E_{ref} in figure 2(d) or the Ohde exponent m in figure 2(e). By looking to equation (7), one can see that the viscosity η is proportional to the load σ whereas the stiffness is proportional to the change of strains. Therefore it is logical that the stiffness E_{ref} and the Ohde exponent m show a slower convergence than the viscosity. Moreover, one has to keep in mind the variability of the parameters. By looking in table 1, one can see that the viscosity η has a bigger viscosity compared to the stiffness E_{ref} and the Ohde exponent m. In academic case of a full knowledge of the mechanical model, one would have a faster convergence of all parameters.

I visualised the forecast uncertainty in figure 3. The $\mathrm{COV}_{\mathbf{x}}$ of the state variables have reduced. After 200 time steps the settlements have a $\mathrm{COV}_s = 5.11$ %, the viscosity has a $\mathrm{COV}_\eta = 5.86$, the stiffness has a $\mathrm{COV}_{E_{\mathrm{ref}}} = 32.01$ % and the Ohde exponent has $\mathrm{COV}_m = 4.90$ %. The differences in the forecast uncertainties is related to the issues discussed in the paragraph before.

3.4 Parametric study B

Additionally I investigate the influence of the observation variance σ^2_{obs}, the COV of the state vector $\mathrm{COV}_{\mathbf{x}}$ and the ensemble size. The basic configuration is using the observation variance $\sigma^2_{obs} = 0.5 \cdot 10^{-3}$ and the $\mathrm{COV}_{\mathbf{x}}$ of the input ensemble $\mathrm{COV}_{\mathbf{x}} = \left[\mathrm{COV}_s = 30\%, \mathrm{COV}_\eta = 35\%, \mathrm{COV}_{E_{\mathrm{ref}}} = 30\%, \mathrm{COV}_m = 5\%\right]^{\mathrm{T}}$. The input ensemble con-

Table 2: Results of the parametric study B for the variation of the observation variance σ^2_{obs}, the variability of the state vector and the ensemble size.

	COV_s	COV_η	$COV_{E_{ref}}$	COV_m
Observation of the variance σ^2_{obs}				
$2.5 \cdot 10^{-3}$	2.65	3.177	27.86	4.89
$0.5 \cdot 10^{-3}$	5.11	5.86	32.01	4.90
$1.0 \cdot 10^{-3}$	9.66	11.15	32.79	4.91
Scaling of the variances of the state vector				
50%	4.31	4.88	16.41	2.4563
100 %	5.11	5.86	32.01	4.90
Size of the ensemble				
20	6.10	7.03	43.56	5.43
100	5.90	6.53	40.65	4.93
300	5.11	5.86	32.01	4.90

sists of 300 samples. The results given in table 2 summarise the forecast uncertainty at $t = 200$. From these results one can deduce that the reduction of the observation variance σ^2_{obs} is reducing the uncertainty of the forecast uncertainty more than the other investigated parameters. If one scales the variability of the state vector $COV_{\mathbf{x}}$ or changes the size of the ensemble, the influence is less than the effects of reducing the observation variance σ^2_{obs}.

A variation of the time intervals of the observations was not carried out. One can clearly derive from section 2.2 that the forecast uncertainty will reduce if more observations are performed. Due to this reason, I did not investigate this influence.

4 Summary and conclusions

The observational method is commonly used design approach in geotechnical engineering. Studying recent publications on the applications of the observational method [5, 9, 13, 12, 11, 14], one can see the need of a framework provided by the sequential data assimilation methodology.

I show in this contribution the sequential data assimilation scheme, which can be used to reduce the forecast uncertainty by incorporating observations. The principle of this approach is derived and shown in case study. This case study shows a significant reduction of the variability and investigates in a simplified sensitivity analysis the influence of the observation variance, the variability of the state vector and the ensemble size. This shall help the reader to understand the concept of data assimilation to other geotechnical applications and to be aware of the possibilities and limitations of this approach.

Using the experience, which is provided on basis of inverse analysis in several publications [6, 14], one could go the next steps using the sequential data assimilation methodology in engineering. The first steps [7, 10] should be proceeded and the framework of sequential data assimilation has to be extended due to the limitations of the Ensemble Kalman filter

(EnKF): The assumption of normally distributed properties and errors can be misleading in geotechnical problems. In case one wants to use not-normally distributed variables, on can introduce a transformation to lognormal distributions or to aim for more complex approaches (e.g. particle filter or unscented filter) in sequential data assimilation, as described in [3, 8].

References

[1] M. Abramovich and I.A. Stegun. *Handbook of Mathematical Functions with Formulas, Graphs and Mathematical Tables*. Dover, 1974.

[2] CEN. Eurocode 7 Geotechnical design - Part 1: General rules. EN 1997-1:2004, European Committee for Standardization: Brussels, November 2004.

[3] Z. Chen. Bayesian filtering: From Kalman filters to particle filters and beyond. Technical report, McMaster University, 2003.

[4] G. Evensen. *Data assimilation*. Springer, 2007.

[5] R. J. Finno and M. Calvello. Supported excavations: observational method and inverse modeling. *Journal of Geotechnical and Geoenvironmental Engineering*, 131(7):826–836, 2005.

[6] G. Gioda and S. Sakurai. Back analysis procedures for the interpretation of field measurements in geomechanics. *International Journal for Numerical and Analytical Methods in Geomechanics*, 11(6):555–583, 1987.

[7] M. Hoshiya and E. Saito. Structural identification by extended Kalman filter. *Journal of Engineering Mechanics*, 110(12):1757–1770, 1984.

[8] S. J. Julier and J. K. Uhlmann. Unscented filtering and nonlinear estimation. *Proceedings of the IEEE*, 92(3):401–422, 2004.

[9] B. Moritz, H. Goldberger, and P. Schubert. Application of the observational method in heterogeneous rock mass with low overburden. *Felsbau*, 24(1):62–72, 2006.

[10] K. Nakamura, S. Yamamoto, and M. Honda. Sequential data assimilation in geotechnical engineering and its application to seepage analysis. In *Proceedings of the 14th International Conference on Information Fusion (FUSION*, pages 1–6. IEEE, 2011.

[11] R.B. Peck. Advantages and limitations of the observational method in applied soil mechanics. *Geotechnique*, 19(2):171–187, 1969.

[12] A.J. Powderham. The observational method - learning from projects. *Proceedings of the ICE-Geotechnical Engineering*, 155(1):59–69, 2002.

[13] W. Schubert. The development of the observational method. *Geomechanics and Tunnelling*, 1(5):352–357, 2008.

[14] T. H. Wu. 2008 peck lecture: the observational method: case history and models. *Journal of Geotechnical and Geoenvironmental Engineering*, 137(10):862–873, 2011.

Evaluation of a potential mapping using POD

Sylvia Keßler [1], Daniel Kanzler [2], Christoph Gehlen [1].

[1] Centre for Building Materials, TU München, Germany
[2] Federal Institute for Materials Research and Testing, Berlin, Germany

Abstract. An essential part of the evaluation of the capability for a non-destructive testing system (NDT) is defined as "the probability of detecting a defect with a particular size under specified inspection conditions and a defined procedure". The accepted statistical parameter of quantifying this definition is the Probability of Detection (POD). The POD is usually expressed as a function of flaw size (e.g. defect length or defect depth) according to the physical background of the testing system.
One of the most important information for assessment of reinforced concrete structures is the information about the corrosion state. The detection of corroding areas is executed non-destructively with a so-called half-cell potential measurement method. The associated defect size is the anode area. The aim of the paper is the evaluation of half-cell potential measurement method using POD.

1 Introduction

The probabilistic residual service-life prediction of reinforced concrete structures is a powerful tool for an economic condition control of existing structures where corrosion is expected. Chloride induced corrosion is one of the major deterioration mechanism for reinforced concrete structures which is exposed to deicing salt or seawater. As a consequence local loss of steel cross section and subsequent cracking and spalling of the concrete cover could impair the serviceability and if no maintenance is executed also the load bearing capacity of the structure.
The half-cell potential measurement method, also called as potential mapping, is a common used method for detection of reinforcement corrosion in concrete structures non-destructively. This measurement delivers fundamental information for the probabilistic residual service life prediction. But there is a lack of knowledge about the accuracy of corrosion detection.
The evaluation of POD might overcome the lack to make it comparable to the typical NDT methods.

1.1 Basics in determination of the probability of detection

A parametric POD approach based on the physical laws to estimate the reliability of eddy current testing in finding cracks was introduced by Berens [3]. It is nowadays a widespread method in a lot of different industrial branches and used as a characteristic magnitude for quality.
There are two related probabilistic methods for analysing reliability data and producing POD-curves as a function of the flaw size. The first type of data is called "hit/miss" data using the discrete response of the NDT-system. The NDT results are only recorded in

term whether the flaw is detected or not. However, in many NDT-systems there is more information in the NDT response and can be interpreted as the perceived flaw data. The data are continuous response signals (called â). Each type of data - Hit/Miss or signal response - is analysed using different probabilistic models.
The behavior of the signal response of the testing equipment is described in terms of a simplified relationship between the maximum signal (â) and the significant defect parameter causing the signal (a) (Figure 1a). For example, the penetrated length of the defect in radiographic testing, the area perpendicular to the sound field in ultrasonic testing [9], or - in case of eddy current crack testing - the length of the crack [3], are typically used as the main influencing parameters.
This relationship is based on the physical laws of the testing method, and can decrease the amount of data which are necessary for a significant result for the probability of detection. The plotted graph of the data and the abovementioned relationship is called â vs. a graph. The relationship between the signal â and the main defect parameter a is usually required to be linear - directly or after an applied mathematical transformation [10]. This relationship is depicted by a linear line passing through the data values (Figure 1a). In an uncensored way, the linear regression curve, estimated by the mean trend through the data points, rises usually with the size of a. For the POD evaluation, the linear regression describes the mean values of the distribution for each a. E.g. at the cross section with the decision threshold the POD is exactly 50%. For a rising mean trend for a, the POD is also rising with a.
With the deviation, the mean of the data and a defined decision threshold it is possible to calculate the cumulative distribution function of the POD for every parameter status [3]. It is summed up in the POD curve (Figure 1b).

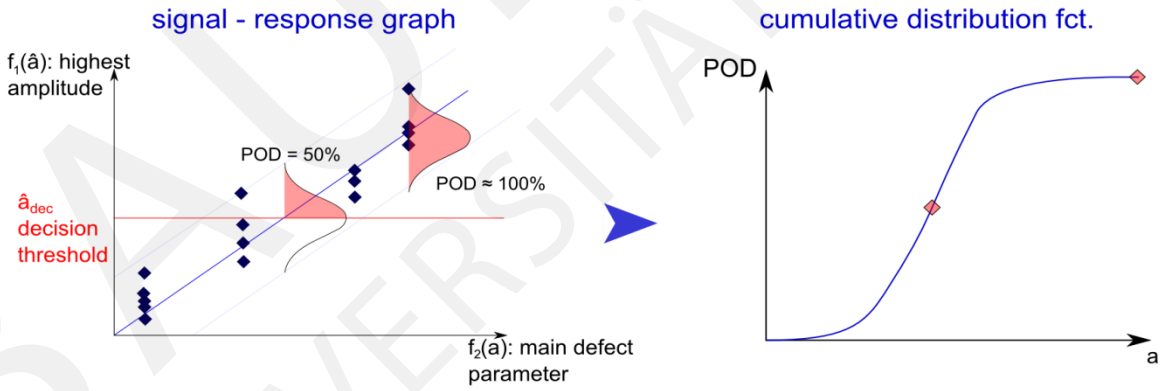

Figure 1: â vs. a-graph (a) and probability of detection curve (b)

Those types of curves were applied for simple cases where it is assumed that the POD of the defect depends only on the defect size and no other influence of the defect or the component is taken into account. In a POD based on experimental data the confidence band is an important and necessary statement. For simulation uncertainties of model parameters were introduced (e.g. PICASSO or MAPOD-Working group). In this case the uncertainty models are still under investigation. Although, both approach to calculate confidence level might lead to different results. In this work, it was waived to calculate no further confidence band than the 50%, shown by the POD curve itself.

1.2 Corrosion detection in reinforced concrete structures

Potential mapping is a measurement method which is able to detect corroding areas non-destructively in reinforced concrete structures. Therefore, potential mapping data are used to check if and where corrosion has started. During potential mapping, the potential difference between an external reference electrode and the reinforcement is measured. A lower potential indicates a higher probability of corrosion. Several guidelines ([10], [5], [1]) contain further information about this measurement method.
Concerning the probabilistic modeling of potential mapping the appropriate defect size is the anode area. This is the section of the reinforcement which is corroding during the measurement. But it is not always the defect size that influences the probability of detection. In addition to that, all influencing factors which are affecting the measurement method itself can have an influence on its reliability. With focus on potential mapping the following influencing factors has to be taken into account: geometry,cover depth, concrete resistivity and grid size [8].
To achieve a probability of detection curve of corrosion detection it is necessary to compare real measurement result with the true corrosion condition state of the reinforcement. The corrosion condition state is only identifiable visually through the removal of the con-crete cover. This is massive intervention in a structure and visual identification of corroding areas is also afflicted with uncertainties. For example, it is unknown if visually identified anode areas were active during the measurement procedure. To exclude this kind of uncertainty a numerical model to estimate the probability of detection of potential mapping is pursued.
Typical construction components, where corrosion can be expected are chloride exposed components like plate§s of a bridge deck or parking decks. Referring to this, the numerical model corresponds to a reinforced deck. The varying defect size, the anode area, is placed in the center of the model. Besides the anode area the following influencing factors are varied according to table Table 1.

Parameter	Unit		Ref
anode A_A	cm^2	0.8, 1.5, 2.3, 3.1, 3.9, 4.7, 5.5, 6.2, 7.0	
resistivity R	Ωm	400	[7]
concrete cover d_c	mm	10, 20, 30, 40, 50	
anodic polarization resistance R_a	Ωm^2	0.5, 1.3, 2.0, 10	[11]
driving potential ΔE	mV	325, 375, 425	[11]
resting potential Anode $\phi_{corr,\,a}$	mV_{SCE}	-540, -600, -630	[2], [6]
resting potential Cathode $\phi_{corr,\,c}$	mV_{SCE}	-175, -225, -225	[2], [6]
cathodic tafel slope β_c	V/dec	120, 285	[11], [4]
exchange current density i_0	$\mu A/cm^2$	0.003, 0.147	[11], [4]

Table 1: Numerical input parameters.

The measurement procedure and the evaluation method influence also the potential mapping and respectively the probability of detection. This dependency can be reflected by the variation of evaluation of the numerical results. Therefore, different grid sizes (5x5cm^2; 15x15cm^2) are considered.

The main factors influencing potential mapping are the concrete resistivity and the grid size [8]. The influence on the POD of potential mapping of these influencing factors has to be evaluated separately.
Each simulation corresponds to one potential field measurement. After the evaluation of the simulation the results in dependence of the threshold potential are compared with the true corrosion condition state. Now, all required data for the analysis of the POD of poten-tial mapping are available.

2 Results for the POD in potential field measurements

The simulation results for the potential field measurement showed that the main defect parameter a is the area of the corrosion. The results for different resistance values and measurement grids should not be handled in one evaluation. In this paper they are be han-dled as different testing procedures and result in different PODs. In Figure 2 the results of the measurement grid of 5x5 cm^2 and 15x15 cm^2 is presented. For the maximum amplitude and signal for the POD evaluation â the signal of the equipment was used. The $E_{negative}$ is the signal dependent on further settings. Therefore, it was decided to use a signal value which is independent of further setting, e.g. the absolute value between $E_{negative}$ and $E_{threshold}$.
The signal â was rising with the area of corrosion a approximately linear, which complies with the linearity requirement of the POD without using any transformation. The deviation of the data values around the main physical law was achieved by introducing the influence of further parameters in the simulation (e.g. R, d_c, R_a, and β_c, i_0) in specific intervals (Table 1). In order to determine a threshold potential $E_{threshold}$ the simulated potentials have to be divided into two probability distributions; one for active and one for passive reinforcement. The passive reinforcement can be regarded as measurement noise. As a threshold potential was chosen the 95% quantile of the active distribution. The decision threshold, the $E_{threshold}$, equaled -0.24 V_{SCE}.

Due to no censored data a least square estimation was used. For the 5x5 grid the R^2 equals 0.89. For the 15x15 grid the R^2 equals 0.85.
The calculation of the POD (Figure 3) is based on the cumulative normal distribution with the estimated distribution parameters on the linearization of â vs. a graph and the decision threshold according to Berens [3]. The normal distribution was assumed; in the future an adequate distribution model will be tested on empirical data.
The intersection of the 90% probability of detection with the cumulative distribution curve was chosen, to use a comparable characteristic for the different methods. The correct procedure would include experimental data and a confidence band. For a first assessment of the method, the $a_{90/50}$ is still a useful number in context with simulated results.

As expected a finer grid size leads to a better detectability of corrosion processes. With a grid size of 5x5 cm^2 anode areas with a size of 1.7 cm^2 are detectable with 50% in 90% of all cases, while for a grid size of 15x15 cm^2 an anode area of 3.5 cm^2 can be indicated. This kind of information is useful to determine the needed grid size in dependence of the re-quirements. The decision threshold is based on the noise and therefore on the

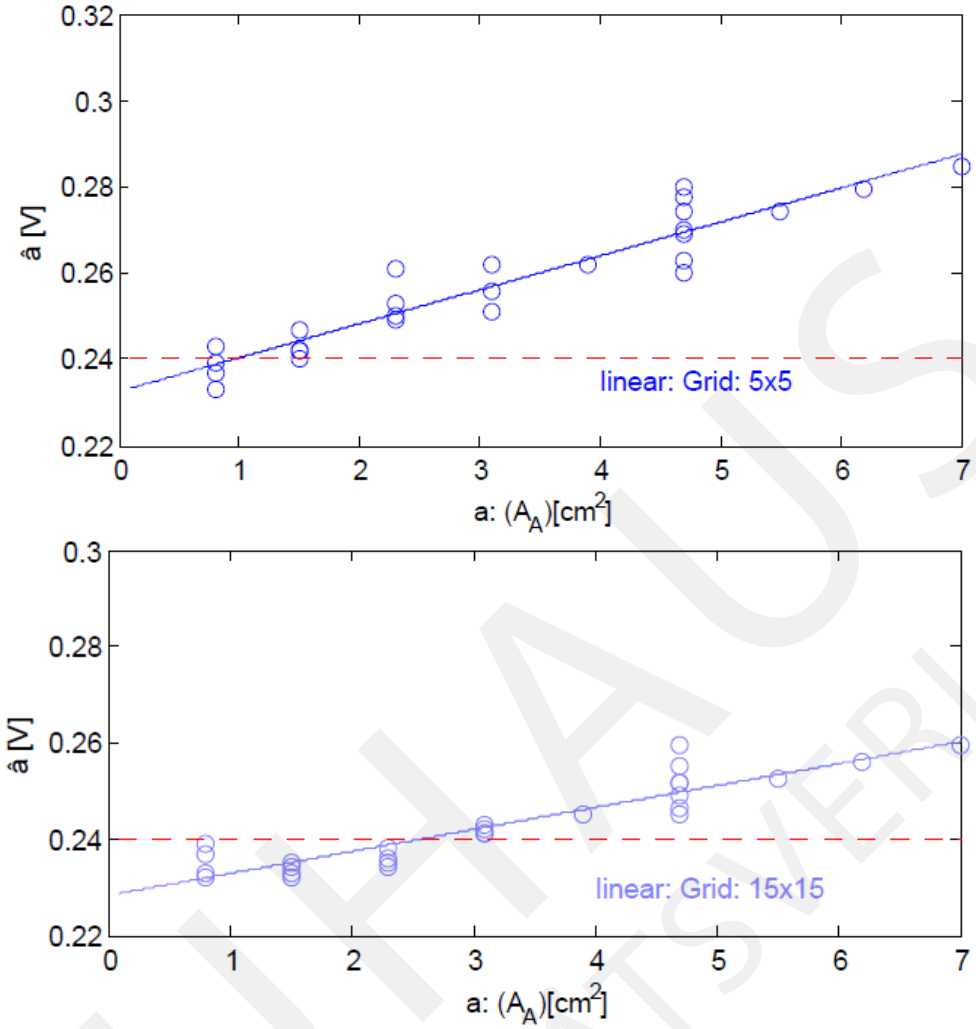

Figure 2: â vs. a-graph for the potential field measurement of corrosion areas in cm^2 with a measurement grid of 5x5 cm^2 (above) 15x15 cm^2 (below); R=400 Ωm

false alarm rate. It was assumed that for both experiments the noise was the same – so the decision threshold will be the same and at the end the false alarm rate is the same. Through the threshold the POD of 5x5 cm^2 crosses the y-axis clearly about 0. Based on the normal distribution the behavior was expected. A higher decision threshold and another distribution model might change this. The uncertainty for the distribution model is higher while going into extreme values. For the aim of a rough overview with the POD it can be accepted, even if the model or the threshold is not exactly chosen, which is an essential future task for real data PODs.

3 Conclusion and Outlook

A numerical approach is presented for evaluating the probability of detection of potential mapping with the â vs. a model. The anode area has the major influence on the POD

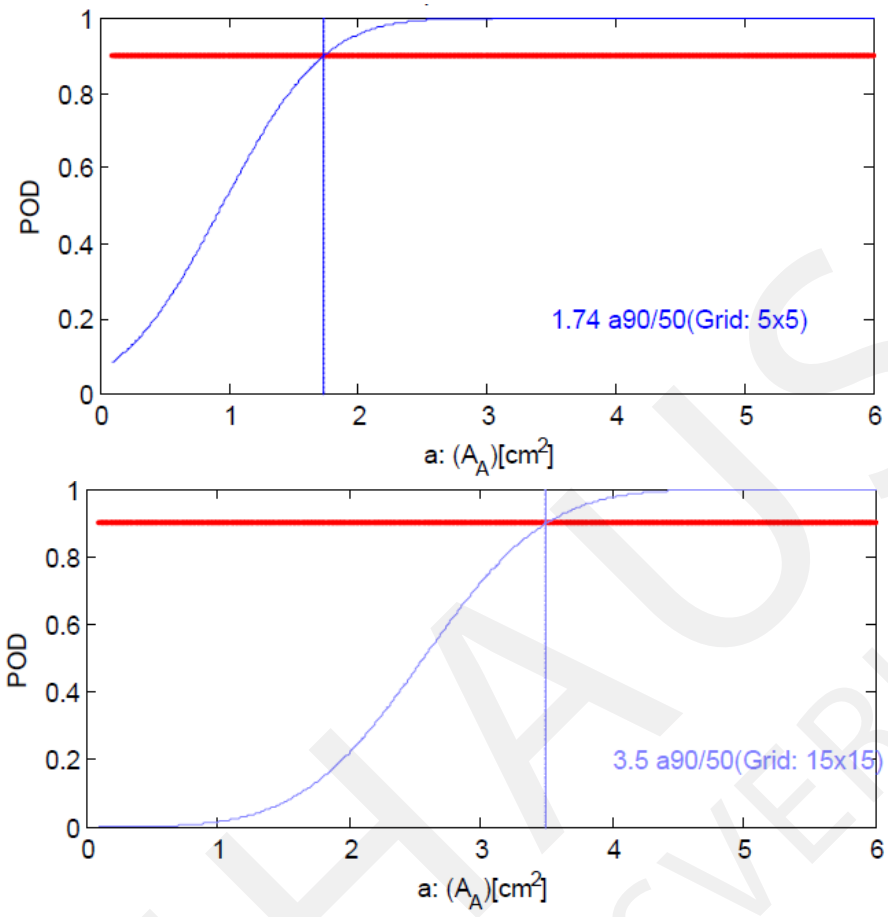

Figure 3: POD-graph for the potential field measurement of corrosion areas in cm^2 with a measurement grid of 5x5 cm^2 (above) 15x15 cm^2 (below); R=400 Ωm

to-gether with the used grid size. With increasing gird sizes decreases the detectable anode area. In the used numerical model the concrete properties like resistivity or concrete cover are totally homogenous. But in reality no concrete has this characteristic. It is assumed that with increasing inhomogeneity the probability of detection decreases.
The results of the â vs. a evaluation based on the simulations showed that the linear regres-sion between anode area and signal can be used. In the future the experimental evaluation of the estimated result should be in the focus. For the experimental data also the evaluation of the used statistical distribution model and the homoscedasticity of the standard deviation should be tested.
In summary the POD is an important tool for the NDT and should be used also for potential mapping to compare with other methods for one task or to evaluate the capability of the method in one particular case.
The confidence band as a characteristic for the reliability evaluation should be based on empirical data, which is a task in the near future. The distribution model and the thresholds for the NDT method should be evaluated for calculating a POD for the potential field measurement in the field.

References

[1] SIA 2006. Durchführung und Interpretation der Potentialfeldmessung an Stahlbetonbauteilen Zürich (in German), 2013.

[2] M. Beck. *Zur Entwicklung der Eigenkorrosion von Stahl in Beton.* Diss., RWTH Aachen, 2010. (German).

[3] Alan P. Berens. *NDE reliability data analysis. ASM International. Metals Handbook*, volume 17. 17 edition, 1989.

[4] M Brem. *Numerische Simulation der Korrosion in Stahlbetonbauteilen.* Diss. eth nr. 15567, Zürich, 2004. (German).

[5] B. Elsener, C. Gulikers, J. Polder R., and M. Raupach. Half-cell potential measurements - potential mapping on reinforced concrete structures. *Materials and Structures*, (36):46–471, 2003.

[6] J. Harnisch. *Zeitabhängige Kenngrößen bei der chloridinduzierten Korrosion.* Diss., RWTH Aachen, 2012. (German).

[7] K. Hornbostel, C.K. Larsen, and M.R. Geiker. Relationship between concrete resistivity and corrosions rate - a literature review. *Proceedings International Conference on Durability of concrete, Trondheim*, 2012.

[8] S Keßler and C. Gehlen. Studie zur Potentialfeldmessung an 40 Jahre alten Stahlbetonbauteilen vom Olympiastadion München - Einfluss des Elektrolytwiderstands und des Messrasters. *Beton- und Stahlbetonbau 108*, 2013. Heft 9 (in German).

[9] C. Müller. et al. Reliability of nondestructive testing (NDT) of the copper canister seal weld. s.l. : Svensk kärnebränslehantering AB, 2006.

[10] C. Sodeikat. Elektrochemische Potentialmessungen zur Detektion von Bewehrungsstahlkorrosion (in German) . DGZfP Merkblatt B3, 2014.

[11] J. Warkus. *Einfluss der Bauteilgeometrie auf die Korrosionsgeschwindigkeit von Stahl in Beton bei Makroelementbildung.* Diss., RWTH Aachen, 2012. (German).

RISK ACCEPTANCE CRITERIA

André Hoffmann, Gerhard Klein, Thorsten Weidl

Department Risk Management
TÜV SÜD Industrie Service GmbH
Westendstraße 199, D-80686 Munich
Germany

1 Introduction

Following the usual definition of risk as combination of the probability of an event and its consequences, the task of risk analyses is to determine systematically the sources of risk and the associated parameters probability and consequence [9]. Risk evaluation is then the process of comparing the risk against given risk criteria to determine the significance of risk [9]. Risk assessment as the overall process of risk analysis and risk evaluation [9] can such be used to demonstrate that specific protection goals for occupational health and safety (hereinafter called OHS) or for the safety of the public and the environment are achieved. This demonstration requires a definition of what risk is acceptable or not. There is a common understanding that the "$\cdots$ risk of suffering harm is an inescapable aspect of living" [6]. On the other hand, the "$\cdots$ progress in the quality of our lives is readily acknowledged but, paradoxically, it has been accompanied by an increased expectation for a society free of involuntary risks$\cdots$ Though people accept that we should continue to take advantage of advances in science and technology, this is moderated by expectations that:

- those responsible for the hazards should ensure that adequate measures are taken to protect people from the harmful consequences that may arise from such hazards;
- the State should be proactive in ensuring that its arrangements for securing the protection of people from risks are adequate and up to date as distinct from reacting to events, and that those arrangements should address, as necessary, the concerns the hazards give rise to." [6].

It follows that risk acceptance is not a scientific exercise, but closely related to risk perception as part of risk communication. The proposals for thresholds of acceptable or tolerable risk as discussed in this paper should be understood as supporting argumentation among experts, not as the suitable way of communication with the community, however; for this purpose we refer to existing literature [20, 4, 3].

This paper is organized as follows: First, we describe the historic development of the concepts of acceptable and tolerable risk, as they are currently and broadly used in different contexts of risk discussions. Next we give an overview of current risk values as used in different countries. Finally, we derive from these values proposals for risk thresholds to be applied for risk analyses.

2 Development of concepts – a short historic overview

The discussion of risk thresholds has a long tradition in the UK and the USA, as well, mainly initiated by the extension of nuclear energy and consequent risk discussion in the mid of the 70s (USA) and early 80s (UK) of the last century. Background of these discussions was the fact that fatalities may occur long time after they were initiated, as it is the case for cancer diseases due to exposure to radioactive substances or direct radiation or carcinogenic substances. In this context the US Supreme Court's benzene decision in 1980 was decisive: "Some risks are plainly acceptable and others are plainly unacceptable. If, for example, the odds are one in a billion that a person will die from cancer by taking a drink of chlorinated water, the risk clearly could not be considered significant. On the other hand, if the odds are one in a thousand that regular inhalation of gasoline vapors that are 2% benzene will be fatal, a reasonable person might well consider the risk significant and take appropriate steps to decrease or eliminate it" (Supreme Court 1980). From this decision, the concept of the de minimis exposition was developed, following the legal principle 'de minimis non curat lex' or simpler: The law does not concern itself with trifles. So 'trifles' or 'negligible risks' are only indirectly characterized by the fact that no "sufficient probability" can be determined. Mere suspicions about possible adverse health effects cannot justify the assumption of a non-negligible risk. The probability of negligible risks was characterized usually in a more or less qualitative way, as e.g. "one in a billion" in the Supreme Court decision cited above.

It was soon recognized that it is necessary to consider also acceptable risks besides negligible risks: There are risks with a quantifiable and justifiable probability which we can consider as inevitable life's risks. Examples are our exposure to the average natural level of radioactivity or to cancerogenic substances in the ambient air due to emissions of cars or industrial activities etc. The target would be then to stay below the thresholds of acceptable risks by controlling emissions, implementing protection measures like PPE or safety instrumented systems (see, e.g., IEC 61508, IEC 61511). But it does not mean that risks are to be avoided at all costs. This was the reason why the Health and Safety at Work etc. Act 1974 introduced the principle of ALARP ('As Low As Reasonably Practicable') in the UK. The definition of 'reasonably practicable' was given as early as 1949 in the important case Edwards vs. National Coal Board where the Court of Appeal stated in the judgement: "Reasonably practicable is a narrower concept than 'physically possible' and implies that a computation must be made$\cdots$ in which the quantum of risk is placed on one scale and the sacrifice involved in the measures necessary for averting the risk (whether in time, trouble or money) is placed on the other and that, if it be shown that there is a gross disproportion between them – the risk being insignificant in relation to sacrifice – the person upon whom the obligation is imposed discharges the onus which is upon him."[1]

For practical implementation, the UK Health and Safety Executive (HSE) suggested to distinguish three areas or regions of risks: "Broadly accepted", "tolerable" and "unaccepted" or "intolerable" risk (Figure 1).

We adopt here the general definitions as proposed by (Kalberlah et al. 2005):

[1] http://en.wikipedia.org/wiki/Edwards_v_National:Coal_Board

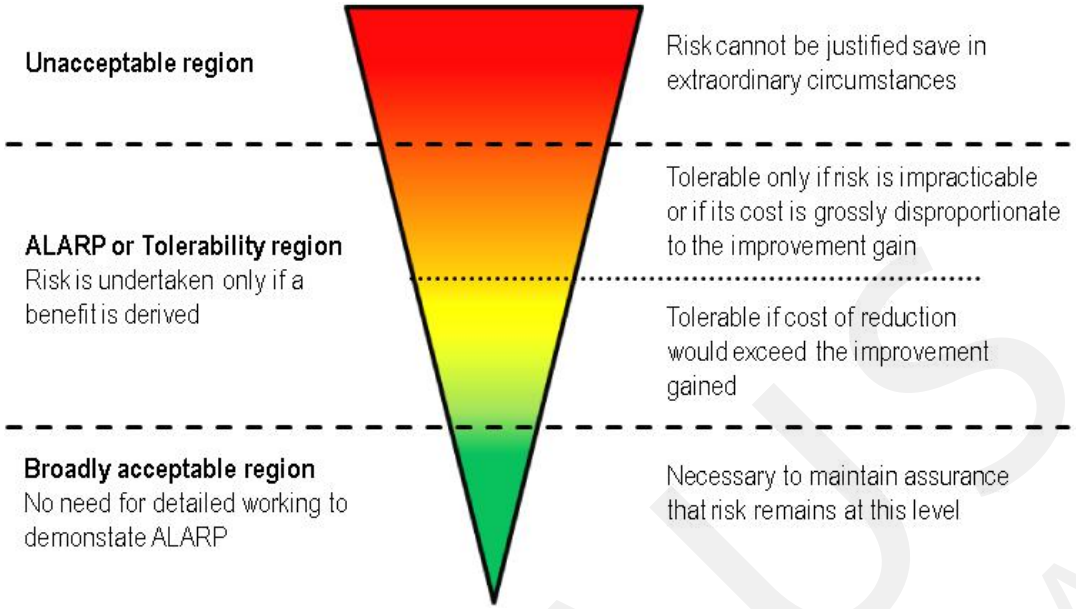

Figure 1: ALARP principle (HSE 2014)

"The "acceptance threshold" defines the transition to a low risk for harmful health effects, which is identical to the German legal term "threshold of concern". Exceeding this acceptance threshold (or threshold of concern) but falling below the danger threshold indicates entry into the region of concern."

The region of concern is identical with the Tolerability region of HSE in Figure 1. In addition, the term "danger threshold" has been introduced:

"The "tolerance threshold" defines the transition to an unacceptable risk for harmful health effects, which is identical to the German legal term "danger threshold" ("sufficient probability for damage to occur"). Exceeding the tolerance threshold indicates entry into the danger region" [10].

Some remarks on these definitions are necessary:

1. ISO/IEC 51 defines "tolerable risk" as a "risk which is accepted in a given context based on the current values of society" and "safety" as "freedom from unacceptable risk". This indicates that there is also no clear distinction between the terms "tolerable" and "acceptable". This is also partly reflected in current standardization as e.g. ANSI/PMMI B155.1-2006 (Safety Requirements for Packaging Machinery and Packaging-Related Converting Machinery) which says: "···"Acceptable risk" and "tolerable risk" are considered as synonymous. Note 1: The expression "acceptable risk" refers to the level at which further risk reduction will not result in significant reduction in risk; or additional expenditures will not result in significant advantage of increased safety highlighted by the authors". Also the British Standard Institution (BSI) replaced the term "tolerable risk" with "acceptable risk" – the goal to be achieved is acceptable risk levels, above these levels and below the threshold of tolerable risk there is need and chance for optimization.

   So we conclude that there is a common understanding of acceptable risk; neverthe-

less the additional definition of a tolerance threshold seems to make sense and should be introduced in future standardization for further clarification (see also chap. 3).

2. "Danger" or "danger threshold" are not a terms generally used in the Anglo-Saxon area. Current standards prefer to refer to "hazard" as "potential source of harm" (e.g. [8]) whereas "danger" can be understood as something like an "actual source of harm" which leads with sufficient probability and in foreseeable future to a harm.
3. One should be very well aware of the meaning of terms like "acceptable" and "tolerable". Society as a whole might tolerate "...to live with a risk so as to secure certain benefits and in the confidence that the risk is one that is worth taking and that it is being properly controlled. However, it does not imply that the risk will be acceptable to everyone, i.e. that everyone would agree without reservation to take the risk or have it imposed on them" [6].

We can summarize our short overview in the following theses:

Acceptance gives not rise to exclusion or limitation of liability

As ANSI/PMMI B155.1-2006 or HSE we think that a level of risk is acceptable when further risk reduction will not result in significant reduction in risk or additional expenditures will not result in significant advantage of increased safety. This has to be proven, however: No matter how the threshold is actually set, for the patient suffering from a severe disease due to his or her exposure to a harmful event the risk has become reality – it's probability is 100%. Usually any adverse event is due to a sequence of causes and effects (technical failures, wrong decisions or other human errors etc.). It must then be demonstrated that all necessary measures and actions have actually been realized to avoid or mitigate that event. It would certainly not be sufficient to refer to an analysis which showed that the risk was below the acceptance threshold and to the simple fact that "probable events are (unfortunately) possible events".

Acceptance requires awareness and/or consent

Acceptance of a risk is based on compliance with the values of society (see above) and therefore requires consent of those who are potentially affected. Since education, training and individual capacities are probably not on the same level for all workers in a chemical plant, e.g., it is questionable whether all workers are fully aware of the risk they seemed to accept and what this means for them. Rather, one could assume that people expect that they avoid risks if they use their protection equipment as required, follow the safety instructions and observe them in a diligent way. We assume that many of these workers are not aware of the argument that they "voluntarily took the risk" or even "accepted higher levels of risk than the public".

Acceptable risk $\neq$ Negligible risk $\neq$ Tolerable risk

From the last paragraph it follows that observing the threshold of acceptable risk is a continuous task of the risk and safety management. Acceptable risks are no trifles, so the

law might and will well concern itself with such risks as soon as harm occurred – they are not negligible. On the other hand, also risks above this threshold can well be tolerable. Significant or unacceptable or intolerable risks are those where a danger will occur with sufficient probability.

3 Tolerable and acceptable risk

3.1 Occupational Health and Safety

Limit values for OHS are usually based on operational experiences (where there might be always a potential for optimization, see above) or general risks of life (see 3.2).

Typical annual fatality rates for workers in different sectors are given for the UK and Germany in Table 1 (called "Tolerability limits for risks entailing fatalities" by HSE):

Known risks at the workplace		Frequency (fatalities per year of Working Lifetime)
Agriculture [1]	3 : 1,000 /WLT [1]	$7.5 * 10^{-5}/a$
Agriculture (not sea fishing) [6]	3 : 1,000 /WLT	$1 : 12,984/a (= 7.7 * 10^{-5}/a)$
Building industry [1]	2 : 1,000 /WLT	$5 * 10^{-5}/a$
Construction [6]	2 : 1,000 /WLT	$1 : 21,438/a (= 4.7 * 10^{-5}0/a)$
Mining [1]	3 : 1,000 /WLT	$7.5 * 10^{-5}/a$
Mining and quarrying (including offshore oil and gas) [6]	3 : 1,000 /WLT	$1 : 14,564 (= 6.9 * 10^{-5}/a)$
Retail [1]	4 : 10,000 /WLT	$1 * 10^{-5}/a$
Service sector [6]	1 : 10,000 /WLT	$1 : 388,565 (= 2.6 * 10^{-6}/a)$

[1] WLT = Working Lifetime = 40 years, assuming 8 hours of exposure per working day) Grey-shaded values are calculated from the originally published values

Table 1: Annual fatality rates in different industries

International regulations for working activities also define acceptance and tolerance thresholds (or analogous quantities) (s.a. [10]):

The situation in the USA is not as clear as in other countries. The Food and Drug Administration (FDA), e.g., proposed a threshold of *de minimis* risks in the order of 1:1,000,000 (one additional fatality in a population of one million exposed persons during a lifetime of 70 years) [18]. On the other hand, most US authorities consider a risk higher than the threshold of $4 * 10^{-4}$ as significant and actually not tolerable (*de manifestis risks*; [18]). For the US authority responsible for OHS (OSHA, Occupational Health and Safety Act) the borderline between "acceptable" and "unacceptable risks" was defined by approx. 1:1,000 [10]. But: "Although OSHA has not articulated a strict definition of significant risk, it has generally used 1:1000 as a benchmark of significance. Labour groups have been concerned that 1 in 1000 has been interpreted by OSHA (and some industry lawyers) as a level of de minimis rather than significant risk. They would like to grant OSHA the flexibility to initiate rule making to reduce residual risk in the range from 1 in 1000 to 1 in 1 Million" [17].

Country	Regulated area	Risk / year	Risk during WLT [1]	Rationale / remark
UK [6]	Working accidents	$1 * 10^{-6}/a$	4 : 100,000/ WLT	Comparison with everyday risks
Netherlands [5]	Exposure to carcinogenic substances	$1 * 10^{-6}/a$	4 : 100,000/ WLT	Target risk, comparison with environmental risks
ICRP [14]	Exposure to radioactivity	$1 * 10^{-4}/a$	4 : 1,000/ WLT	Comparison with accident frequencies in high safety industries
Germany [1]	Exposure to carcinogenic substances	$1 * 10^{-6}/a$	4 : 100,000/ WLT	Valid from 2018 on; until then the risk may be 4 : 10,000/ WLT

[1] WLT = Working Lifetime = 40 years, assuming 8 hours of exposure per working day Grey-shaded values are calculated from the originally published values

Table 2: Acceptance Thresholds for Working Activities in different countries

Country	Regulated area	Risk / year	Risk during WLT [1]	Rationale / remark
UK [6]	Working activity (accidents, radiation)	$1 * 10^{-3}/a$	4 : 100/ WLT	Comparison with everyday risks
Netherlands [5]	Exposure to carcinogenic substances	$1 * 10^{-4}/a$	4 : 1,000/ WLT	Prohibitive risk
ICRP [14]	Exposure to radioactivity	$1 * 10^{-3}/a$	4 : 100/ WLT	Comparison with accident frequencies in different industries
Germany [1]	Exposure to carcinogenic substances	$1 * 10^{-4}/a$	4 : 1,000/ WLT	Comparison with accident frequencies in different industries

[1] WLT = Working Lifetime = 40 years, assuming 8 hours of exposure per working day Grey-shaded values are calculated from the originally published values

Table 3: Tolerance Thresholds for Working Activities in different countries

From Table 2 and Table 3 we note that $\mathbf{1 * 10^{-6}/a}$ is a commonly agreed value for the broadly acceptable risk and $\mathbf{1 * 10^{-4}/a}$ for the tolerable risk. The UK-values and radiation protection for tolerable risk limits are an exception, possibly also due to mutual cross references between the HSE and ICRP publications in the past. Same holds for the OSHA value for "significant risks". Although HSE states that "[in] practice the actual fatality rate for workers in even the most hazardous industries is normally well below the upper limit of a risk of death to any individual of 1 in 1000 per annum for workers..." and ICRP refers to the level of natural radiation for justification (see Table 4) we don't agree with $1 * 10^{-3}/a$ as tolerable limit. $1 * 10^{-6}/a$ can be adopted as reference value for acceptable risk (it should not be called "*de minimis*", however, as FDA did – it is just acceptable, see chap. 2 above). Again we consider the value of ICRP for acceptable risk in radiation protection as considerably too high.

3.2 General population

For the general population, benchmark-setting for acceptable and tolerable risks is more difficult: One has to consider different sensitivities, typically for elder people or children with special sensitivity to genotoxic carcinogenic substances. People must be protected,

but it is a difficult and ongoing process to establish an agreement on the "values of society" [8]. How can we handle this situation?

We all are exposed e.g. to man-made pollution of air, water or soil which are not attributable to a specific single source or to radioactivity of natural origin. In Germany, e.g., the risk of the general population for contracting cancer by the seven most important airborne environmental carcinogens is about 10:10,000 ($1.5 * 10^{-5}/a$ of Lifetime) for urban population and 2:10,000 ($3 * 10^{-6}/a$ of Lifetime) for rural population [1]. A value of 4:10,000 for exposure to multiple substances is intended as a first step of minimizing the risk caused by carcinogenic air pollutants [12].

Different benchmarks can be discussed to define suitable thresholds. The maximum permitted concentrations of carcinogenic substances are usually regulated by several government standards concerning food and environmental matters. "These concentrations have not always been stipulated with respect to an acceptable risk; however, their calculation corresponds to the following risks that are related to the lifetime ... of the general population" [1] and are shown in Table 4:

Exposure by	Risk/ year	Risk during LT [1]
Arsenic in drinking water ($10\mu g/l$)	$7 * 10^{-6}/a$	5 : 10,000/ LT
Dioxin in food ($2pgTeq/kg$)	$4 * 10^{-6}/a$	3 : 10,000/ LT
Diesel soot ($5ngBaP/m^3$)	$3 * 10^{-6}/a$	2 : 10,000/ LT
Cadmium in airborne particles	$3 * 10^{-7}/a$	2 : 100,000/ LT
Natural radiation dose	$1.4 * 10^{-5}/a$	1 : 1,000/ LT

[1] LT = Lifetime = 70 years

Table 4: Risks due to maximum permitted concentrations of carcinogenic substances / natural radioactivity (Germany; [1])

Our daily risks might be remarkably higher if we go by car or spend our leisure time with mountain-climbing and show a large variability:

For the general population, values for acceptable risks have been also defined in different regulations:

With regard to tolerable risk it is necessary to consider not only individual risks (Table 7), but also to consider societal risks, due to the fact that major accidents of a plant can affect many persons.

We understand collective or societal risk as the total risk for the sum of all affected persons in the considered scenario. In contrast to the individual risk, the collective risk involves the total number of all possible victims. In this view, an event with many fatalities is stronger weighted than an event with fewer fatalities. To quantify the collective risk, the so-called F-N curves became largely accepted. They are based on the equation $F(N) = C/N^{\alpha}$. Here, $F(N)$ represents the corresponding frequency with a number of N or more fatalities. C is an absolute term that defines the overall position of the F-N curve for $N = 1$ and corresponds to the individual risk. The so-called risk aversion factor α allows to represent the fact that an event with many victims is less accepted or tolerated the more fatalities could occur [16]. Figure 2 shows two representative examples of F-N-curves from the

	Cause / Activity	Risk of fatalities per year
traffic	Railway	$4.4 \cdots 15 * 10^{-6}/a$
	car drivers	$2.0 \cdots 2.2 * 10^{-4}/a$
	Aircraft (passengers)	$0.67 \cdots 1.2 * 10^{-4}/a$
Leisure activities	Mountain climbing	$1.0 \cdots 2.7 * 10^{-3}/a$
	Parachouting (USA)	$2.0 * 10^{-3}/a$
	Holiday (UK 1990)	$1.0 * 10^{-4}/a$
Everyday life	Fire in buildings	$8.0 * 10^{-6}/a$
	Household activities	$1.0 * 10^{-4}/a$
	Lightning (UK, USA)	$1.0 \cdots 5.0 * 10^{-7}/a$

Table 5: Examples for risks of the general population [16]

Country	Regulated area	Risk / year	Risk during LT [1]	Rationale / remark
UK [6]	Exposure to radioactivity	$1 * 10^{-6}/a$	7 : 100,000/ LT	No other risks causing cancer
Netherlands [5]	Exposure to carcinogenic substances	$1 * 10^{-8}/a$	1 : 1,000,000/ exposure time	Negligible risk
ICRP [14]	Exposure to radioactivity	$1 * 10^{-5}/a$	7 : 10,000/ LT	Comparison with traffic accident frequencies.
Germany [11, 1]	Exposure to carcinogenic substances	$1 * 10^{-6}/a$	1 : 100,000	acceptable risk for a graduated reduction of environmental concentration values

[1] LT = Lifetime = 70 years; for Netherlands 100 years for environmental exposure are assumed
Grey-shaded values are calculated from the originally published values

Table 6: Acceptance Thresholds for General Population in different countries

UK and the Netherlands. The transition area (or ALARP region, see Figure 1) between acceptable and tolerable risk covers two orders of magnitude. Other F-N-curves as they are used in Hong Kong or Switzerland are included in these examples.

It should be noted no risk aversion is taken into account in the UK and in Hong Kong, whereas in the Netherlands and Switzerland a risk aversion factor of two is used. In our opinion there is definitely a risk aversion in the society. We propose to use a risk aversion factor of 1.5 to find an agreement.

The colors used in Figure 3 can be understood as follows (for general population, the

Country	Regulated area	Risk / year	Risk during LT [1]	Rationale / remark
UK [6]	Plant safety, radiation	$1 * 10^{-4}/a$	7 : 1,000/ LT	Fatalities due to accidents
Netherlands [5]	General population (carcinogenic substances)	$1 * 10^{-4}/a$	1 : 1,000,000/ exposure time	Maximum tolerable risk
ICRP [14]	General population (radiation protection)	$1 * 10^{-4}/a$	7 : 1,000/ LT	Comparison with environmental risks and their spread

[1] LT = Lifetime = 70 years; for Netherlands 100 years for environmental exposure are assumed
Grey-shaded values are calculated from the originally published values

Table 7: Tolerance Thresholds for General Population in different countries (individual risk)

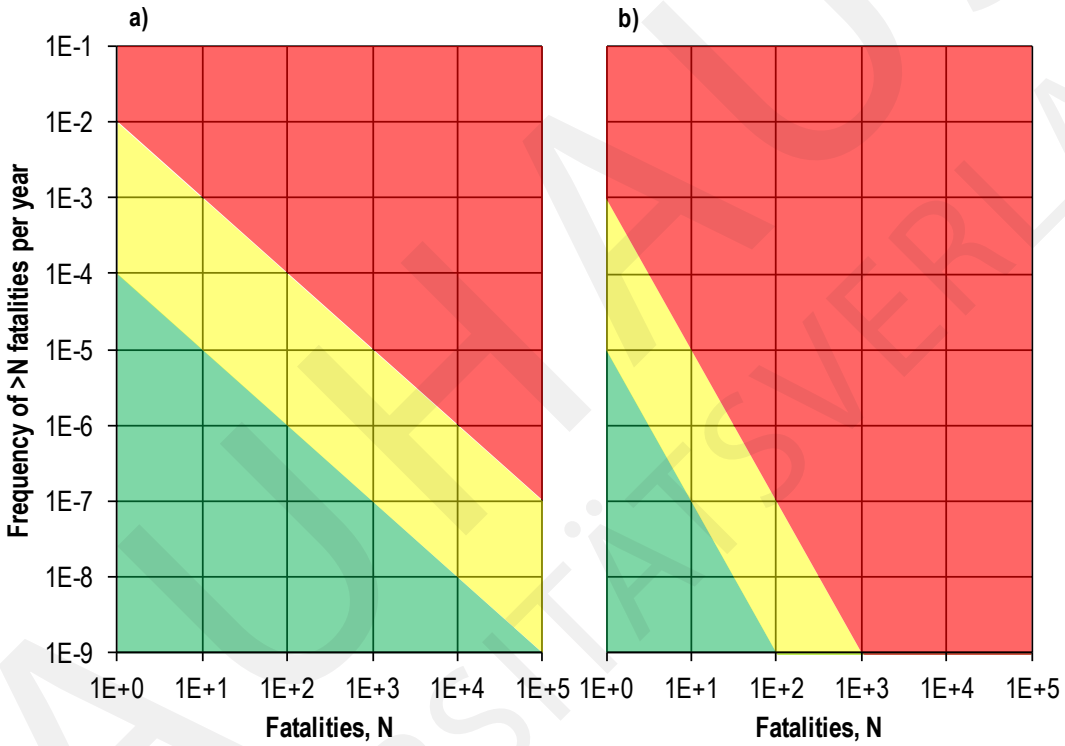

Figure 2: Examples for societal risk criteria in a) United Kingdom (Transport of hazardous goods) and b) the Netherlands (Hazardous facilities) [2]

value for 1 fatality is given):

As can be seen from Table 8, the risk values between OHS and general population differ just by one order of magnitude. This shall reflect the fact that it is debatable whether there should be really a difference in acceptance or tolerance thresholds for workers and the public. If negligible risks shall be also discussed, these values should be below $10^{-7}/a$ for OHS and below $10^{-8}/a$ for the general population. A tolerable risk limit of $10^{-3}/a$ as used by ICRP for OHS in radiation protection seems not to represent the state of the art, however.

Our criteria are based on existing criteria used in different countries in different industrial

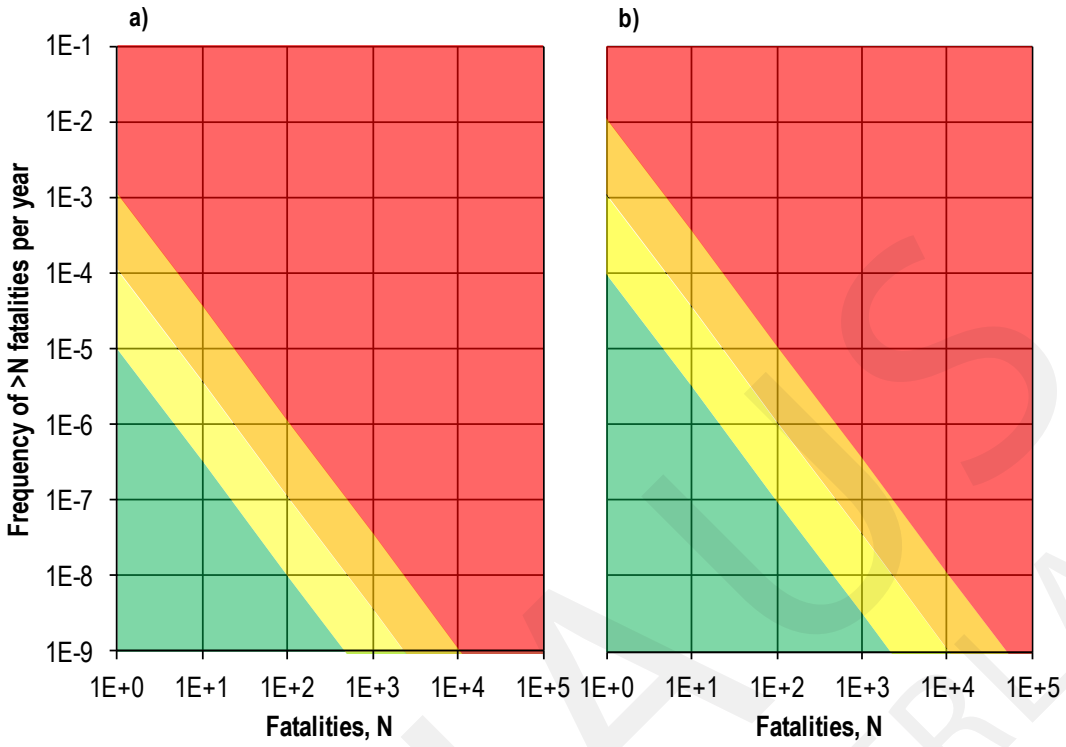

Figure 3: Societal risk criteria proposed by TÜV SÜD related to a) General population and b) OHS.

Risk value $[1/a]$		Evaluation
OHS	General population	
$> 10^{-4}$	$> 10^{-5}$	The risk is unacceptable high. Risk reduction measures have to be initiated immediately.
10^{-5} *to* 10^{-4}	10^{-6} *to* 10^{-5}	The risk is high and it is located in the upper ALARP region. The implementation of well-known risk-reducing measures is highly recommended and it is advised to look for additional risk-reducing measures beyond state of the art.
10^{-6} *to* 10^{-5}	10^{-7} *to* 10^{-6}	The risk is tolerable and in the lower ALARP region. If further measures to reduce the risk are known, they can be examined under cost-benefit aspects. A recommendation to implement such measures is not pronounced.
$< 10^{-6}$	$< 10^{-7}$	The risk is acceptable. There is no action necessary from risk-oriented point of view.

Table 8: Individual risk criteria proposed by TÜV SÜD

sectors and represent the state of the art. We have often used these criteria successfully for different risk analyses and we found that they are in true sense "broadly accepted".

References

[1] AGS (Ausschuss für Gefahrstoffe): TRGS 910 – Risk-related concept of measures for activities involving carcinogenic hazardous substances. Ausgabe: Februar 2014, GMBl 2014 S. 258-270 v. 2.4.2014 [Nr. 12].

[2] Ball, D.. Floyd, P.: Societal Risk - Final report, Health and Safety Executive, 1998.

[3] Covello, V. T.; Sandman, P. M.; Slovic, P.: Risk Communication, Risk Statistics, and Risk Comparisons: A Manual for Plant Managers, Washington DC 1988, http://www.psandman.com/articles/cma-0.htm.

[4] Femers, S.: Zum Umgang mit Risikovergleichen in der öffentlichen Kommunikation, Berlin 2003; http://www.apug.de/archiv/pdf/rk_gutachten_risikovergleiche.pdf.

[5] Health Council of the Netherlands: Guideline for the calculation of risk values for carcinogenic compounds. The Hague: Health Council of the Netherlands, 2012; publication no. 2012/16E.; http://www.gezondheidsraad.nl/sites/default/files/201216EGuideline_for_calculation_risk_carcinogenic_substances.pdf.

[6] HSE, Health & Safety Executive: Reducing Risks, Protecting People, Suffolk, United Kingdom 2001.

[7] HSE, Health and safety Executive: Risk analyses or 'predictive' aspects of comah safety reports guidance for explosives sites - The COMAH Safety Report Process for Predictive Assessment of Explosives Sites, downloaded 2014-08-21, http://www.hse.gov.uk/comah/assessexplosives/intro.htm.

[8] ISO/IEC Guide 51: Safety aspects – Guidelines for their inclusion in standards, 2nd edition 1999.

[9] ISO/IEC Guide 73: Risk Management – Vocabulary – Guidelines for use in standards, 1st edition 2002.

[10] Kalberlah, F.; Bloser, M.; Wachholz, C.: Toleranz- und Akzeptanzschwelle für Gesundheitsrisiken am Arbeitsplatz, BAuA Forschung Projekt F 2010, Dortmund/Berlin/Dresden 2005.

[11] Konietzka, R.: Bewertung und Begrenzung von Umweltrisiken durch krebserzeugende Stoffe, Gefahrstoffe – Reinhaltung der Luft, 68 (2008) Nr. 7/8.

[12] LAI (Länderausschuss für Immissionsschutz): Bericht des Länderausschusses für Immissionsschutz (LAI) „Bewertung von Schadstoffen, für die keine Immissionswerte festgelegt sind - Orientierungswerte für die Sonderfallprüfung und für die Anlagenüber-wachung sowie Zielwerte für die langfristige Luftreinhalteplanung unter besonderer Berücksichtigung der Beurteilung krebserzeugender Luftschadstoffe“ vom 21. September 2004, 61.0-06.

[13] Manuele, F.: Acceptable Risk, Professional Safety, May 2010 http://www.asse.org/professionalsafety/pastissues/055/05/F1Manuel_0510.pdf.

[14] NEA (Nuclear Energy Agency): Evolution of ICRP Recommendations 1977, 1990, 2007 – Changes in Underlying Science and Protection Policy and their Impact on European and UK Domestic Regulation, NEA No. 6920 https://www.oecd-nea.org/rp/reports/2011/nea6920-ICRP-recommendations.pdf.

[15] Paul, H.; Illing, A.: Possible risk considerations for toxic risk assessment. Human and Experimental Toxicology 10 (1991), 3, 215-219 (as cited in Kalberlah et al., 2005).

[16] Proske, D.: Katalog der Risiken – Risiken und ihre Darstellung, self-published, first edition, Dresden 2004.

[17] Sadowitz, M.; Graham, J.D.: A survey of residual cander riks permitted by health, safety and environmental policy. Risk: Health, Safety & Environment 17 (1995), 17-35 (as cited in Kalberlah et al., 2005).

[18] SFK (Störfall-Kommission): Bericht – Risikomanagement im Rahmen Störfall-Verordnung, SFK-GS41, 21.04.2004.

[19] Supreme Court: Industrial Union Dept. v. American Petrol. Inst., 448 U.S. 607 (1980) http://caselaw.lp.findlaw.com/scripts/getcase.pl?court=US&vol=448&invol=607.

[20] Wiedemann, P. M.; et al.: VDI Leitfaden: Risikokommunikation für Unternehmen, VDI 2000; http://www.wiedemannonline.com/blog/wp-content/uploads/2010/09/VDI-Leitfaden-Risikokommunikation1.pdf.

Thermal actions on box girder bridges made of prestressed concrete

Jaroslav Kohoutek; Ngoc Linh Tran; Carl-Alexander Graubner

Institute of Concrete and Masonry Structures, Technical University, Darmstadt
kohoutek@massivbau.tu-darmstadt.de; tran@massivbau.tu-darmstadt.de;
graubner@massivbau.tu-darmstadt.de

Abstract. Thermal actions are decisive for the reliability analysis of statically indeterminate bridge systems, e.g. frame bridges. According to DIN EN 1991-1-5/NA (EC1/NA) [3] temperature effects on the superstructure can be split into constant temperature changes ($T_{N,exp}$; $T_{N,con}$) as well as temperature differences ($T_{M,heat}$; $T_{M,cool}$) between the top and bottom of the superstructure and considered separately. Non-linear effects TE and horizontal temperature differences between the sides of the bridge will be left unconsidered. For constant temperature changes the shade air temperature has a strong influence. Based on climate data from the past 136 years in Germany probability distribution functions (PDF) for shade air temperatures as well as for constant temperature changes are developed which can be used for reliability analysis. For the evaluation of PDFs of temperature differences measurements are carried out over more than six years in a box girder bridge in Hesse. Both – constant temperature changes and temperature differences – correlate to a regression curve which is given in this paper and is suitable for reliability analysis.

Keywords: thermal actions, box girder brides, prestressed concrete, reliability analysis

1 Introduction

1.1 Bridge analysis

Thermal actions are of great importance for design and probability analysis of statically undetermined bridge systems, e.g. continuous beam and frame bridges. Until the 1970's the influence of thermal actions on the superstructure has not been taken into account for bridge design in Germany. Without considering the thermal actions in design, the existing prestressed concrete bridges which were built until the 1970's show a lower than designed lifetime under combined traffic and temperature loading. High fatigue stresses in the pre-stressing steel and the reinforcing steel often occur in these bridges. To evaluate the lifetime of the existing bridges an exact approach for thermal actions should be taken into account. For the accurate evaluation of the existing bridges a full probability analysis is recommended. The detailed probabilistic modelling of thermal actions as well as of other actions is therefore needed. Since the late 1970's the values of thermal actions were investigated, see [9, 8, 6, 4]. Additionally the combination of thermal and other actions were analysed in [4, 5], which were the basis of the actual design code DIN EN 1991-1-5 (EC1) "Actions on structures – Part 1-5 – General actions – Thermal actions" [3].

1.2 Thermal actions

Thermal actions lead to dilatation or contraction of whole structures or parts of structures e.g. carriageways. According to EC1 [2] these temperature effects on bridge decks can be split into four parts and analyzed separately:

- Constant temperature changes ΔT_u. The maximum temperature change is $\Delta T_u = \Delta T_{N,exp}$, the minimum temperature change is $\Delta T_u = \Delta T_{N,con}$ (see Eq. (1) - (3))
- Horizontal, linear temperature changes ΔT_{My}
- Vertical, linear temperature changes ΔT_{Mz} or ΔT_M. In case the top of the bridge deck is warmer than the bottom the maximum value is $\Delta T_{Mz} = \Delta_{TM,heat}$, in case the bottom of the bridge deck is warmer than the top the extreme value is $\Delta T_{Mz} = \Delta T_{M,cool}$
- Nonlinear temperature effects ΔT_E

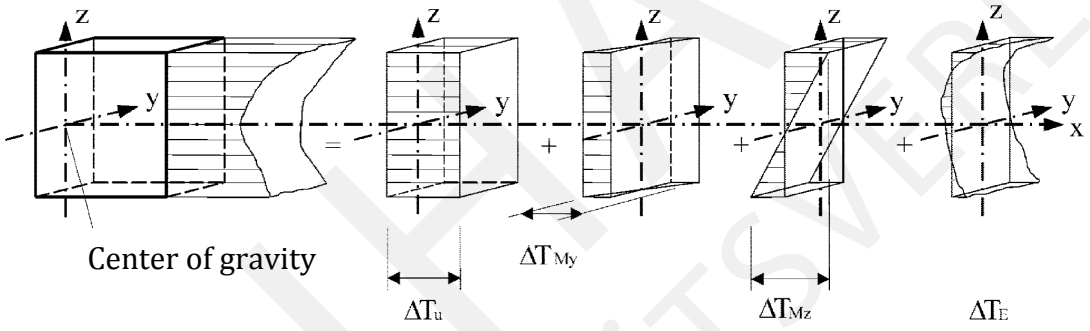

Figure 1: Temperature effects according to EC1 [2], Bild 4.1

According to EC1, 6.1.4.3(1) [2], horizontal, linear temperature changes ΔT_{My} in most cas-es can be left unconsidered. Additionally nonlinear temperature effects ΔT_E will be left disregarded in compliance with EC1/NA, NDP to 6.1.2(2) [3].

$$\Delta T_u = T_e - T_0 \tag{1}$$

$$\Delta T_{N,exp} - T_0 \tag{2}$$

$$\Delta T_{N,con} = T_{e,min} - T_0 \tag{3}$$

with
T_0 = setting up temperature of a structure
T_e = constant temperature of a structure

2 Constant temperature changes

2.1 General

Constant temperature changes influence the bridge expansion and shortening which is decisive for the design of bridge bearings and expansion joints. For integral bridges, thermal expansions and shortenings determine the earth pressures at the abutments which have a strong impact on the probability analysis of the substructures as well as of the superstructure. According to [7] constant temperature changes in bridge decks are caused by the following effects:

- Air temperature changes
- Wind speed
- Global solar radiation as well as absorption ability of the material

Germany has a moderate or oceanic climate affected by the Atlantic Ocean and the Gulf Stream, which helps to sustain somewhat stable and significant higher temperatures than expected in this latitude throughout the year. The prevailing winds are from the west, summers are warm (but not hot) and winters are cool (but not cold). The hours of sunshine in 2013 varied from 1364 hours in Thuringia to 1696 hours in Mecklenburg-Vorpommern according to the Deutscher Wetterdienst DWD (German Weather Service). Several publications show that constant temperature changes are mostly affected by air temperature changes ([9, 7]).

2.2 Shade air temperature

Shade air temperatures in Germany are measured continuously by the DWD and are avail-able since 1876. Fig. 2 shows the location of the weather stations of the DWD (green and white spots). Biased locations (white spots exposed mountains and open sea) haven't been analyzed, because their extreme weather conditions aren't representative for Germa-ny. In this research daily maximum and minimum values of the shade air temperature giving a total of 3,104 million values have been evaluated.

Normal PDFs have no constraints while for probability analysis the knowledge of the minimum and maximum values is compulsory. In Tab. 1 extreme air shade temperatures are displayed. It can be seen that the shade air temperatures vary between $37,8°C$ and $40,2°C$. Further analysis has shown that extremely deep temperatures below 30°C (reached in a total of 9 days in different spots) have a much lower probability of occurrence than 50 years, which is often referred to in design codes e.g. DIN EN 1990 (EC0) [1]. The lowest shade air temperature $37,8°C$ measured in Hüll (part of Wolnzach north of Munich) has to be regarded as a single and not representative event. Therefore the shade air temperature range is set according to Eq. (4), which is also concluded by [5, 7]. The analyzed maximum shade air temperature T_{max} is slightly higher (+3 K) and the minimum shade air temperature T_{min} is reasonably lower (-6 K) than the minimum characteristic value in Eq. (5) according to EC1 [2].

$$T_{min} = -30° \leq T \leq 40° = T_{max} \tag{4}$$

$$T_{min,EC1} = -24° \leq T \leq 37°C = T_{max,EC1} \tag{5}$$

Location	Date	Shade air temperature T
Karlsruhe	2003-08-13	40, 2°C
Karlsruhe	2003-08-09	40, 2°C
Freiburg im Breisgau	2003-08-13	40, 2°C
Gärmersdorf/Oberpfalz	1983-07-27	40, 2°C
Bamberg	1956-02-10	−30, 1°C
Görlitz	1956-02-09	−30, 8°C
Hüll (Wolnzach)	1929-02-12	−37, 8°C
Munich	1942-01-21	−30, 5°C
Nuremberg	1956-02-10	−30, 2°C
Oberstdorf	1956-02-10	−32, 0°C
Straubing	1963-01-18	−32, 0°C
Weiden	1956-02-10	−32, 8°C

Table 1: Extreme shade air temperatures T of Germany (data by DWD)

The following Fig. 3 shows the histogram and normal PDF of the shade air temperature data of all analyzed weather stations while Fig. 4 shows the histogram and normal PDF of the northern, eastern, western and southern federal states of Germany, which are assigned according to Tab. 2. All PDFs are best fit curves of the extreme ranges of the histograms, as these ranges determine the risk of failure in reliability analysis. It can be seen that the various distribution curves in Fig. 4 show only neglectable differences of the mean value μ and standard deviation σ. For further analysis the distribution curve of Fig. 3 is being used.

northern part	eastern part	western part	southern part
Lower Saxony	Brandenburg	North-Rhine-Westphalia	Baden-Württemberg
Schleswig-Holstein	Berlin		Bavaria
Hamburg	Thuringia	Rhineland-Palatinate	
Bremen	Saxony		
Mecklenburg-Vorpommern	Saxony-Anhalt	Saarland	
		Hesse	

Table 2: Parts of Germany

2.3 Constant temperature changes in bridges

As stated in chapter 2.1 constant temperatures in bridge superstructures are influenced by the shade air temperature, solar radiation and wind speed. The effects of solar radiation and wind speeds have been well examined in simulations carried out by [7] and as a result

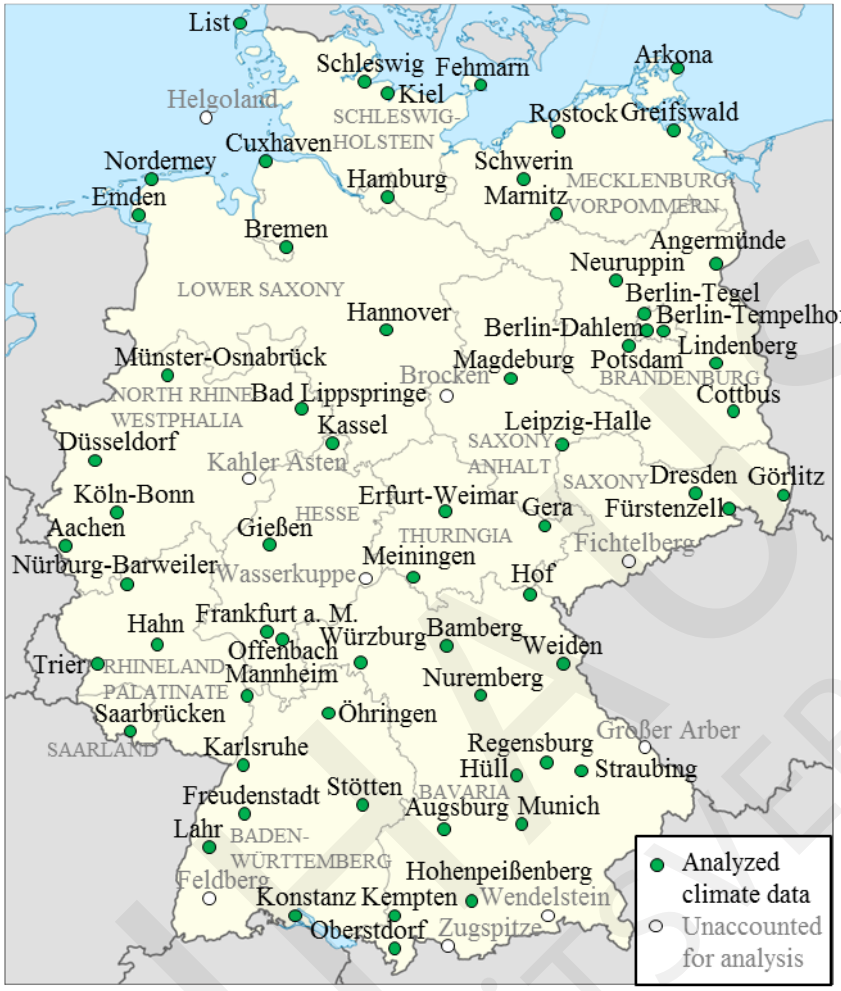

Figure 2: German weather stations of the Deutscher Wetterdienst

a correlation between the minimum T_{min} shade air temperature and the minimum $T_{e,min}$ constant bridge temperature as well as the maximum T_{max} shade air temperature and the maximum $T_{e,max}$ constant bridge temperature has been published, which is expressed in Eq. (6) and Eq. (7) as well as displayed in Fig. 5. Fig. 6 shows the developed histogram and normal PDF of the constant temperature Te in bridge superstructures which is the best fit curve of the extreme ranges of the histograms, as these ranges determine the risk of failure in reliability analysis.

$$T_{e,max} = T_{max} - 2K = 40° - 2K = 38° \tag{6}$$

$$T_{e,min} = T_{min} + 5K = 30° + 5K = -25° \tag{7}$$

The characteristic value of the correlation between the shade air temperature and the constant bridge temperature in the current design code EC1 [3] is given in Eq. (8) and Eq. (9):

$$T_{e,max,EC1} = T_{max,EC1} + 2K = 37°C + 2K = 39°C \tag{8}$$

$$T_{e,min,EC1} = T_{min,EC1} + 8K = -24°C + 8K = -16°C \tag{9}$$

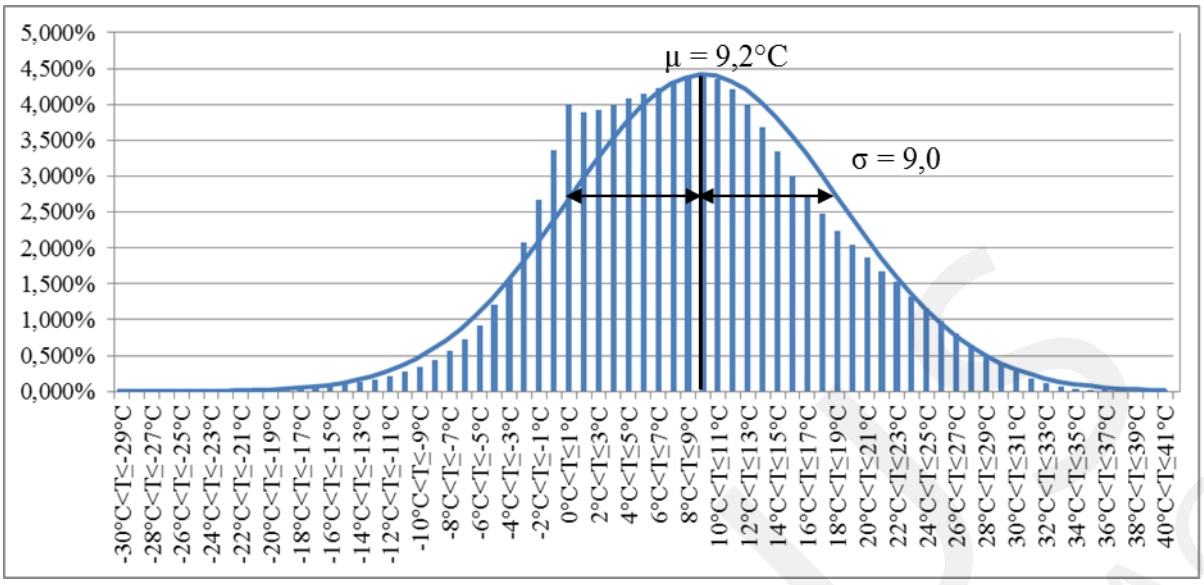

Figure 3: Histogram and normal PDF of the daily maximum and minimum shade air temperatures T of Germany (climate data from the DWD)

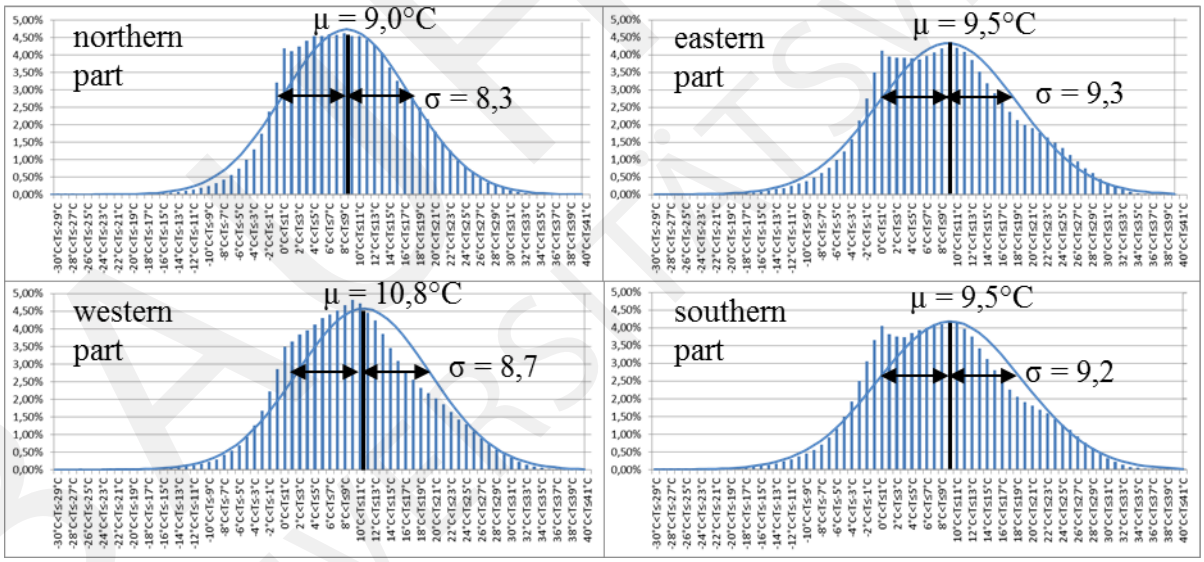

Figure 4: Histogram and normal PDF of the daily maximum and minimum shade air temperatures T of parts of Germany (climate data from the DWD)

It can be seen that the maximum constant temperature Te is almost the same value in EC1 while the minimum temperature differs by -25 – (-16) = -9 K. [7] stated that this differences are covered by the partial safety factor $\gamma = 1,35$ in ultimate limit state.

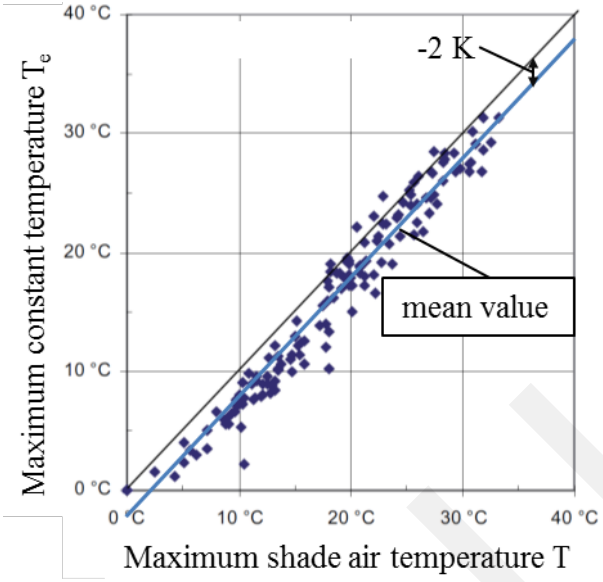

Figure 5: Correlation between the maximum shade air temperature T and the maximum constant bridge temperature Te,max according to [7]

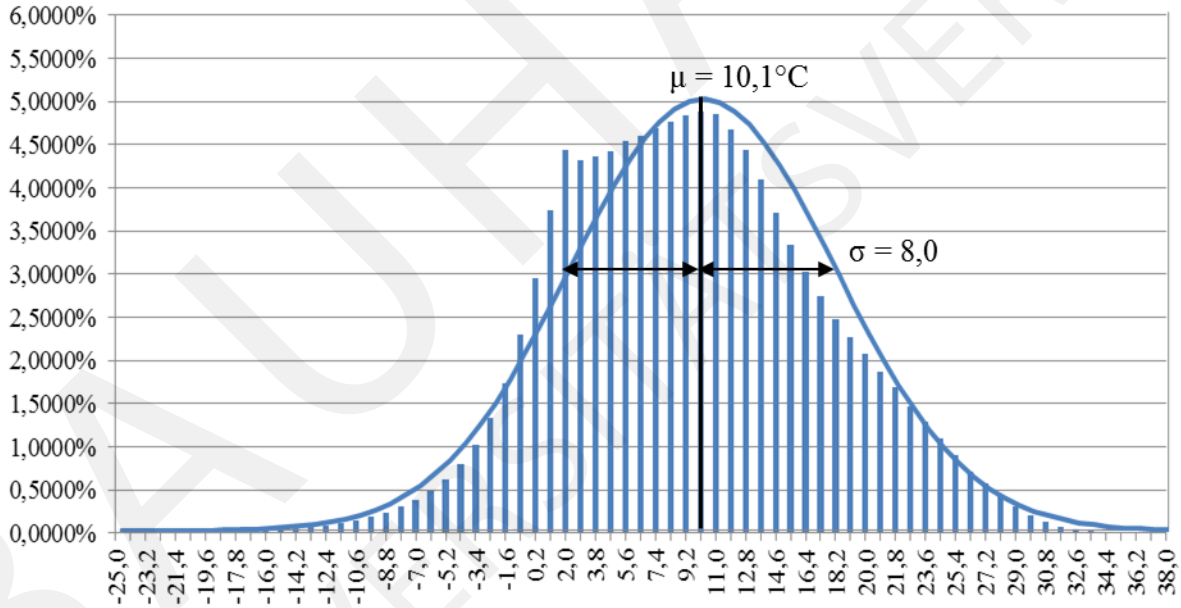

Figure 6: Histogram and normal PDF of the daily maximum and minimum constant bridge temperatures T_e

3 Vertical, linear temperature changes

3.1 Temperature measurements in a prestressed box girder bridge

Solar radiation plays a leading role for vertical, linear temperature changes in bridge decks because the carriageway slab is covered by a layer of dark colored asphalt which absorbs

the rays of light (see [5]). To analyze the vertical linear temperature changes a monitoring system has been installed in a prestressed box girder bridge in the course of motorway A7 near Eichenzell/Döllbach from August 2007 until September 2013. Two temperature sensors were installed inside the concrete; one inside the carriageway slab and one inside the bottom slab (see Fig. 7). Every hour the difference between the temperature of the top and the bottom slab has been analyzed. It has been assumed, that the vertical temperature change follows a linear distribution within the cross-section of the bridge, which is in accordance with EC1/NA, NDP to 6.1.2(2) [3].

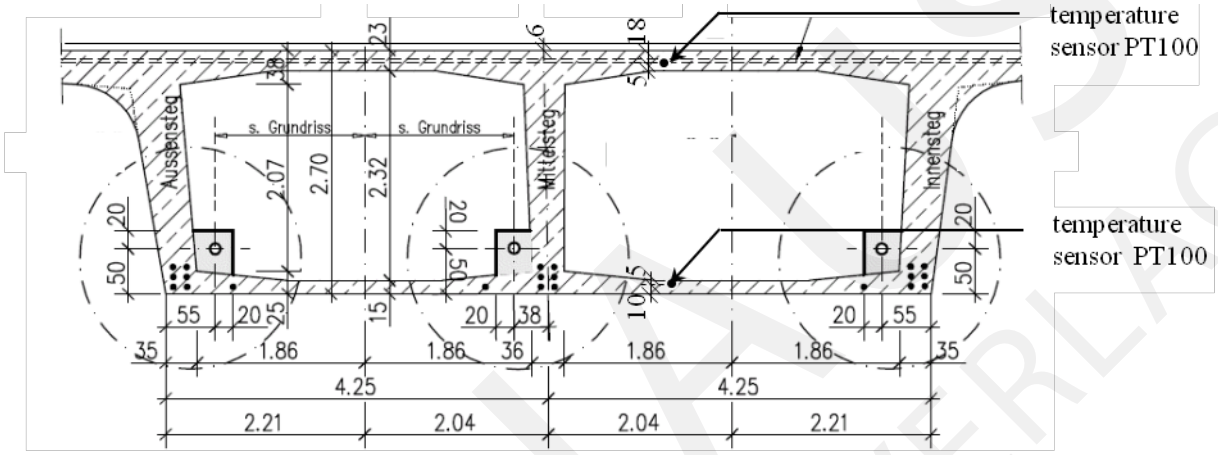

Figure 7: Cross section of the Döllbachtal Bridge (midspan)

In Fig. 8 the evaluation of the hourly temperature difference ΔT_M between the top and the bottom slab is shown. A maximum temperature difference $\Delta T_{M,heat}$ = 8,0 K and a minimum temperature difference $\Delta T_{M,cool}$ = -2,2 K has been recorded over a period of 6 years of observation. The lognormal distribution curve is chosen to reproduce the extreme ranges of the histogram, as these ranges determine the risk of failure in reliability analysis. The equation for the lognormal distribution curve is given in Eq. (10) - Eq. (12). It is obvious that positive values are more likely to occur than negative values, since solar radiation heats mainly the upper slab which has additionally a larger surface than the bottom slab. For this reason an asymmetrical PDF has been chosen.

$$f(x) = \begin{cases} \dfrac{1}{\sqrt{2\cdot\pi}\cdot\sigma_u\cdot(x-x_0)} e^{\left[-\frac{1}{2}\left(\frac{ln(x-x_0)-m_u}{\sigma_u}\right)^2\right]} & x > x_0 \\ 0 & x \le x_0 \end{cases} \tag{10}$$

$$m_u = \ln(\mu - x_0) - \left(\frac{\sigma_u^2}{2}\right) \tag{11}$$

$$\sigma_u = \sqrt{\ln\left(1 + \left(\frac{\sigma}{\mu - x_0}\right)^2\right)} \tag{12}$$

To get the extreme values of the vertical temperature differences [5] used the 3-day instead of the hourly maxima and minima values. The effect of this assumption is shown in Fig.

9. Extreme values have a significantly higher probability of occurrence than in Fig. 8, because the smaller temperature differences within a 3-day observation period are left unconsidered. For design purposes this is a safe assumption.

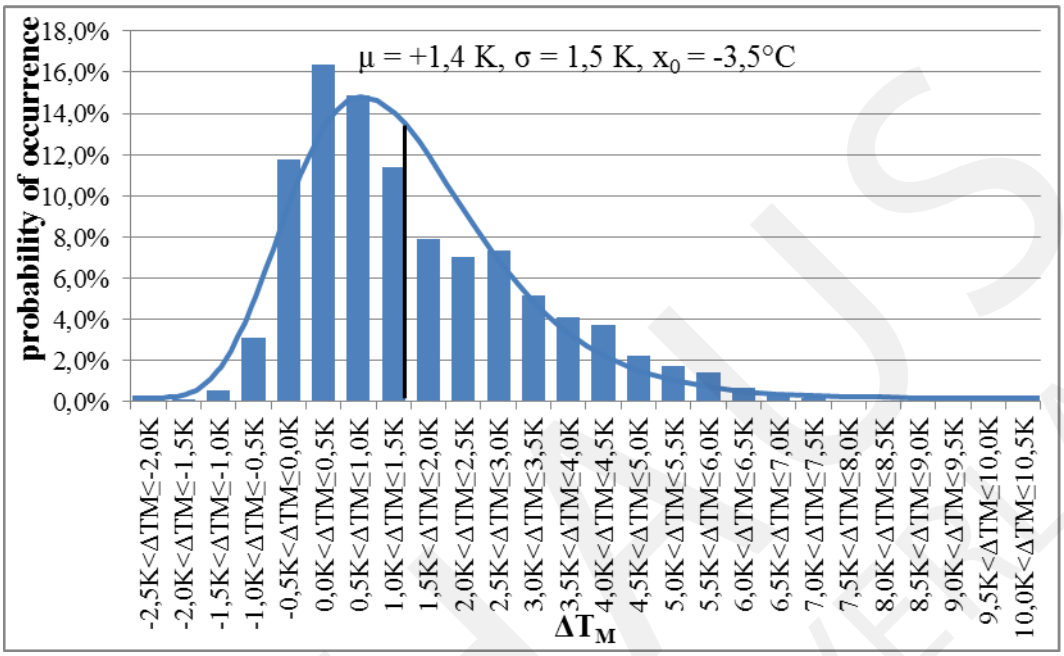

Figure 8: Histogram and lognormal PDF of the vertical linear temperature changes ΔT_M with hourly resolution

Nevertheless Fig. 8 and Fig. 9 show the results of only one single bridge. In order to find a PDF for reliability analysis of concrete bridges, the evaluated extreme values are compared with the values given in the actual design code EC1/NA [3]. The characteristic values given in EC1/NA [3] take into account the thickness (6 cm) of the asphalt pavement (value k_{sur} = 0,94 for maximum temperature difference and k_{sur} = 1,04 for minimum temperature difference) and are presented in Eq. (13) and Eq. (14). It can be stated that both PDFs in Fig. 8 and Fig. 9 are in accordance with the values given in EC1/NA [3]. The characteristic values in EC1/NA [3] take into account a return period of 50 years. Based on the given results for probability analysis a lognormal PDF is recom-mended with the following 2 % value $\Delta T_{M,cool}$ and the 98% value $\Delta T_{M,heat}$, which represent a 50-years return period.

$$k_{sur} \cdot \Delta T_{M,heat} = 0,94 \cdot 10K = 9,4K \tag{13}$$

$$k_{sur} \cdot \Delta T_{m,cool} = 1,04 \cdot (-5) = -5,2K \tag{14}$$

3.2 Correlation between vertical temperature difference and constant temperature

As stated in chapter 2.1 constant temperatures of a bridge superstructure are influenced by the shade air temperatures whereby according to chapter 3.1 the vertical temperature

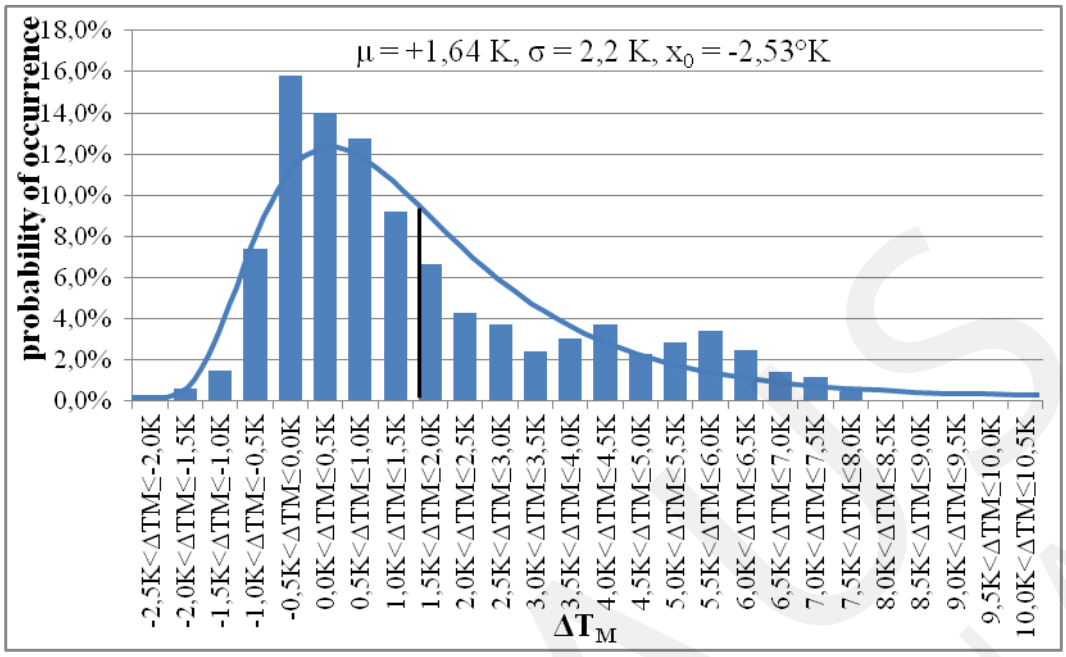

Figure 9: Histogram and lognormal PDF of the 3-day maxima and minima vertical linear temperature changes $\Delta T_{M,heat}$ and $\Delta T_{M,cool}$

differences are mainly influenced by solar radiation. Major positive vertical temperature differences $\Delta T_{M,heat}$ evolve from very high solar radiation during summer where high shade air temperatures are more likely. Negative vertical temperature differences $\Delta T_{M,cool}$ can have many causes, e.g. cooling of the carriageway slab by snowfall or cold rain. The correlation between the vertical temperature differences and the constant temperatures of the Döllbachtal-Bridge is displayed in Fig. 10. The constant temperature was transformed according to Eq. (6) and Eq. (7) from the shade air temperature of the nearest weather station of the DWD in Gießen. The evaluated correlation coefficient $\rho_{Te,\Delta T_M} = 0{,}59$ in Fig. 10 can be used for reliability analysis.

4 Summary

In this paper the impact of thermal actions on bridge superstructures has been analyzed. Based on the data of 65 weather stations of the DWD normal PDFs of the shade air temperatures have been developed for Germany as well as for the northern, eastern, western and southern parts of Germany. After that the PDF of the constant bridge temperatures was deduced from the shade air temperatures. Furthermore temperature measurements inside a prestressed box girder bridge have been evaluated statistically and a lognormal PDF has been derived for the vertical temperature differences. It has been stated that prolonged sampling intervals as were the basis of the actual design codes EC1 [2] increase the probability of extreme values and lead to safe values for the design of bridges. Finally, based on the measured values the correlation between the constant temperatures and the vertical temperature differences has been determined. This research

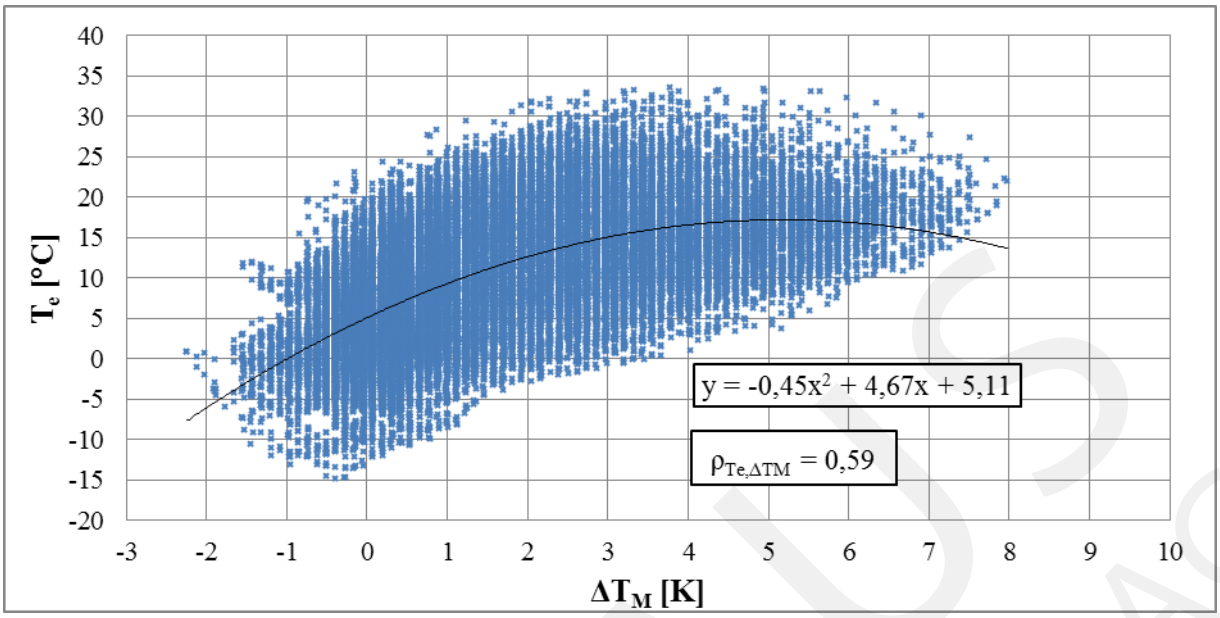

Figure 10: Correlation between the constant temperature Te and the vertical linear temperature difference ΔT_M

wouldn't be possible without the support of Mr. Eberhard Pelke from the road traffic department of Hesse (Hessen Mobil), Mr. Herbert Duda from the engineering office König und Heunisch Planungsgesellschaft mbH & Co. KG in Frankfurt (Main) and Mr. Gerhard Koster, for which the authors want to thank sincerely!

References

[1] DIN EN 1990: Eurocode 0: Grundlagen der Tragwerksplanung; Deutsche Fassung EN 1990:2002 + A1:2005 + A1:2005/AC:2010, Beuth Verlag, Berlin, 2010.

[2] DIN EN 1991-1-5: Eurocode 1: Einwirkungen auf Tragwerke – Teil 1-5: Allgemeine Einwirkungen – Temperatureinwirkungen; Deutsche Fassung EN 1991-1-5:2003 + AC:2009, Beuth Verlag, Berlin, 2010.

[3] DIN EN 1991-1-5/NA: Nationaler Anhang – National festgelegte Parameter – Eurocode 1: Einwirkungen auf Tragwerke– Teil 1-5: Allgemeine Einwirkungen – Temperatureinwirkungen, Beuth Verlag, Berlin, 2010.

[4] Frenzel, B.: Beitrag zur Kombination der Einwirkungen aus Verkehr und Temperatur an Spannbetonbrücken. Dissertation. Hochschule für Architektur und Bauwesen Weimar, Weimar, 1991.

[5] Frenzel, B.; Freundt, U.; König, G.; Mangerig, I.; Merzenich, G.; Novak, B.; Sedlacek, G.; Sukhov, D.: Bestimmung von Kombinationsbeiwerten und -regeln für Einwirkungen auf Brücken. Bundesministerium f|"ur Verkehr, Bonn- Bad Godesberg, 1996.

[6] Mangerig, I.: Klimatische Temperaturbeanspruchung von Stahl- und Stahlverbundbrücken, Dissertation. Institut für Konstruktiven Ingenierbau, Bochum, 1986.

[7] Mangerig, I.; Lichte, U.; Beuchler, S.: Bewertung der Sicherheitsanforderungen von Temperatureinwirkungen auf Brücken. In Stahlbau 79, Heft 3, p. 167–180, 2010.

[8] Zichner, T.; Linse, D.: Temperaturunterschied infolge Witterungseinfluss und Beheizung von massiven Brücken. Vergleichende Untersuchung von Verkehrsregellasten für Straßenbrücken und Ableitung eines verbesserten Lastbildes. Forschung Straßenbau und Straßenverkehrstechnik Heft 212, Bonn-Bad Godesberg, 1976.

[9] Zichner, T.: Temperaturbeanspruchung von massiven Brücken infolge Witterungseinfluß und Beheizung. Dissertation. Technische Hochschule Darmstadt, 1977.

Identification of Residual Stresses in Steel under Uncertain Model Components

Tom Lahmer[1], **Sebastian Bock**[2], **Jörg Hildebrand**[3], **Klaus Gürlebeck**[4]

Faculty of Civil Engineering, Bauhaus University Weimar
Institutes of Structural Mechanics [1], Applied Mathematics [2,4] and Structural Engineering[3]
99423, Weimar, Germany
tom.lahmer@uni-weimar.de[1], sebastian.bock@uni-weimar.de[2],
joerg.hildebrand@uni-weimar.de[3], klaus.guerlebeck@uni-weimar.de[4]

Abstract. We discuss the inverse and ill-posed problem of identifying residual stresses in steel structures. Therefore, steel specimen are subjected to thermal loadings. Due to these loadings deformations occure which are recorded by high resolution laser scanners. The latter serve as input for the inverse problem, where residual stresses are to be recovered. As the inverse problem is ill-posed, it requires regularization, where iteratively regularized fixed-point iterations are applied. Now the quality of the identified stress field depends on a list of parameters, e.g., the choice of the regularization parameters, the noise in the measurements, the error assumed for the definition of stopping criteria, and further uncertainties in other model parameters, like the stiffness of the structure, the thermal expansion coefficient or non-exact geometry.

1 Introduction and State of the Art

During the fabrication of metallic structures residual stresses occur due to the high thermal excitation during the rolling and/or welding process. The residual stresses are generally not known in their location and dimension, however, they lead to strong and un-wanted distortions when the structures are loaded. Closely related to these distortions is the question of the stability of the structure. It is therefore the aim, to reduce the deformations by a process called thermal straightening. The success of this process heavily depends on the prior knowledge of the location and size of the residual stresses. Till know, this straightening process is only possible by well experienced specialists in the field and under high costs. We therefore propose a procedure which allows by inverting a thermo-mechanical problem the identification of the residual stresses and discuss the robustness of the approach w.r.t. uncertainties in the model/experiments.
The solution of inverse problems in the context of partial differential equations allows the reconstruction of distributed physical properties like material parameters or fields of primary or secondary variables, like the residual stresses. In this context, most of the inverse problems are ill-posed, in particular as the stable dependency of the solution from the given data cannot be guaranteed, [2]. The research activities in this field have formulated a series of iterative algorithms to solve nonlinear ill-posed problems in a stable manner, see e.g. [6, 7]. Their applicability to inverse problems in science and engineering has been proved by, e.g. [4, 8, 9]. With respect to the identification of residual stresses there is a set of theoretical investigations [10, 1, 5] and identification results via analytical methods

[12, 13, 14] and numerical approaches [11, 3]. These works have in common that they are solely formulated in a one field problem. Due to the special type of excitation (heating) we are working in a two field area.

2 Thermo-Mechanical Model

The forward problem consists of a series of solution of thermo-mechanical boundary value problems, where the heat source is successively shifted over the structure.

$$\begin{aligned} \rho c_T \frac{\partial T}{\partial t} - \nabla \cdot (\kappa_T \nabla T) &= 0 \quad \text{in } \Omega \times (0, T_{end}] \\ \mathcal{B}^T \left(\mathbf{c}(\mathcal{B}u - \mathbf{m}\beta_T T) \right) &= \mathcal{B}^T \sigma^{eig} \quad \text{in } \Omega \times (0, T_{end}] \\ T(x,t) &= \bar{T}(x,t) \quad \text{on } \Gamma \times (0, T_{end}] \\ T(x, t=0) &= t_0(x) \quad \text{in } \Omega \\ u(x,t) &= 0 \quad \text{on } \Gamma_u \times (0, T_{end}] \\ N^T \mathbf{c} \mathcal{B} u &= 0 \quad \text{on } (\Gamma \setminus \Gamma_u) \times (0, T_{end}] \end{aligned} \tag{1}$$

with

T	temperature
u	displacements
c_T	heat capacity
ρ	density
κ_T	thermal conduction
β_T	thermal expansion
$\mathbf{m}$	$\mathbf{m} = (1,1,1,0,0,0)^T$ (unit vector)
$\mathbf{c}$	stiffness tensor
E	Young's modulus
ν	Poisson ratio
$\mathcal{B}$	strain-displacements differential operator
n	normal vector
N	normal vector for vector fields
σ^{eig}	residual stress

In the experiment an induction heating is considered. However, for the model, to simplify things, the heat excitation is modeled as local surface load assumed to move along the boundary of the structure at a set of discrete positions M. All other parts of the boundary are assumed to be observable by a thermo camera, i.e. why we consider solely Dirichlet boundary conditions for the temperature field.
Mechanically, the structure is supported in two areas, see Figure 1.

The structure has dimensions of 2 m times 0.1 m times 0.05 m. The heat excited part a length of 0.05 m. The support area is assumed to be 0.05 m, too. The material parameters are as follows for the thermal field $\rho = 7.85e3[kg/m^3], c_T = 465[J/kgK]$ and $\kappa = 50[W/mK]$ and for the mechanical field $E = 210e3[MN/m^2], \nu = 0.31$ and $\beta_T = 12e-6$.

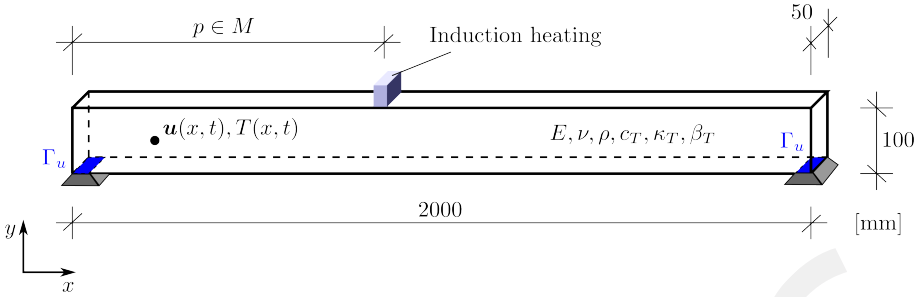

Figure 1: Experimental Setup

The coupled forward problem is assumed to be well-posed by the given initial and boundary conditions. A decomposition of the problem in Eq. 1 leads to a heat equation problem with well defined and compatible initial and boundary conditions. The computed temperature field is assumed to have $T \in L^\infty(0, T, H^1(\Omega))$ regularity. It enters into the mechanical problem as a source term in Eq. 2, which can also be considered to be well-posed.

3 The Inverse Problem

We introduce the following forward operator

$$\begin{aligned} F : X &\rightarrow Y \\ \sigma^{eig} &\mapsto u \end{aligned} \tag{2}$$

which maps residual stresses σ^{eig} to measured displacements u along the boundary $\Gamma = \partial\Omega$ of Ω. For X we assume $H^1(\Omega)$ and for $Y \subseteq L^2((\Omega) \times [0, T])$, i.e. the inverse problem of identifying residual stresses is as ill-posed as one time numerical differentiation. The solution of the nonlinear problem

$$F(\sigma^{eig}) = u^{meas}(x, t)$$

is consequently expected to be ill-posed. The residual stresses are identified by running a derivative-free iteratively regularized Landweber Method

$$\sigma^{eig,k+1,\delta} = \sigma^{eig,k,\delta} + sG^*(F(\sigma^{eig,k,\delta}) - y^\delta) - \alpha_k \sigma^{eig,k,\delta}$$

where s is a well-chosen scaling parameter, G is a locally uniformly bounded operator mapping from X to Y and α_k a series of regularizing parameters. For the latter it is guaranteed, that

$$\lim_{k\to\infty} \frac{\alpha_{k+1}}{\alpha_k} = 0.$$

The y^δ denotes the collection of measured data which are assumed to contain noises which is indicated by the superscript δ. In order to avoid an amplification of noise components in the data, the iterations are stopped according to a discrepancy principle, i.e. when for the first time

$$||F(\sigma^{eig,k+1,\delta}) - y^\delta||_Y \leq \tau\delta$$

Variable	Parameter	Assumed Distribution
δ	true systematic noise	$\mathcal{LN}(-4.1, 0.6)$
$\delta^{assumed}$	assumed systematic noise	$(\delta^{assumed} - \delta)\Delta \sim \mathcal{U}(-0.5; 0.5)$
α_0	initial value of regularizing parameter	$\mathcal{LN}(-1.5, 0.4)$
E	Young's modulus	$\mathcal{N}(210e+03, 0.08 * 210e+03)$
β_T	thermal expansion	$\mathcal{N}(12e-06, 0.08 * 12e-06)$

Table 1: Table of assumed distributions. $\mathcal{LN}$ - Log-Normal, $\mathcal{N}$ - Normal, $\mathcal{U}$ - Uniform.

with $\tau > 1$ and an upper bound δ of the discrepancy between noisy data y^δ and true solution y, i.e. $||y - y^\delta|| \leq \delta$. The true solution is assumed to be obtained from a model fitting 100 percent to the given measurements, an unrealistic situation, though. In the numerical implementation G interpolates in a Finite Element Analysis the nodal values of the displacements to the element mid points values.

3.1 Ill-Posedness

The iterations $\sigma^{eig,k}$ converge to $\sigma^{eig,*}$ in the noise free case with the choice $\alpha = 0$. For already very small noise, slightly more than in the magnitude of 1 per mill of the measured displacements, the solution process becomes unstable, see Figure 2c) and 2d), where the graphs show the convergence in X and Y space for noisy data with and without regularization. Including the proposed regularizing term, i.e. $\alpha_k \neq 0$ and early stopping makes the method robust (see 2a) and 2b)) even for noise levels in the range of 5-10 percent.

4 Uncertainty Analysis

In the sequel we study how different uncertainties in the model and in the algorithmic setup affect the quality of the reconstructed residual fields. We assume, that the following material parameters, boundary conditions and algorithmic parameters are not precisely known and model them therefore as random variables according to the given distributions.

We will now run a series of inverse problems, where key parameters are assumed to be random.

4.1 Systematic Noise

In the theory of inverse and ill-posed problems all data are expected to be contaminated with a systematic noise, where generally estimates like

$$||y - y^\delta||_Y \leq \delta$$

are assumed. The δ measures the distance in Y norm between the true, i.e. the model responses y and the contaminated data y^δ. This contamination may have different sources:

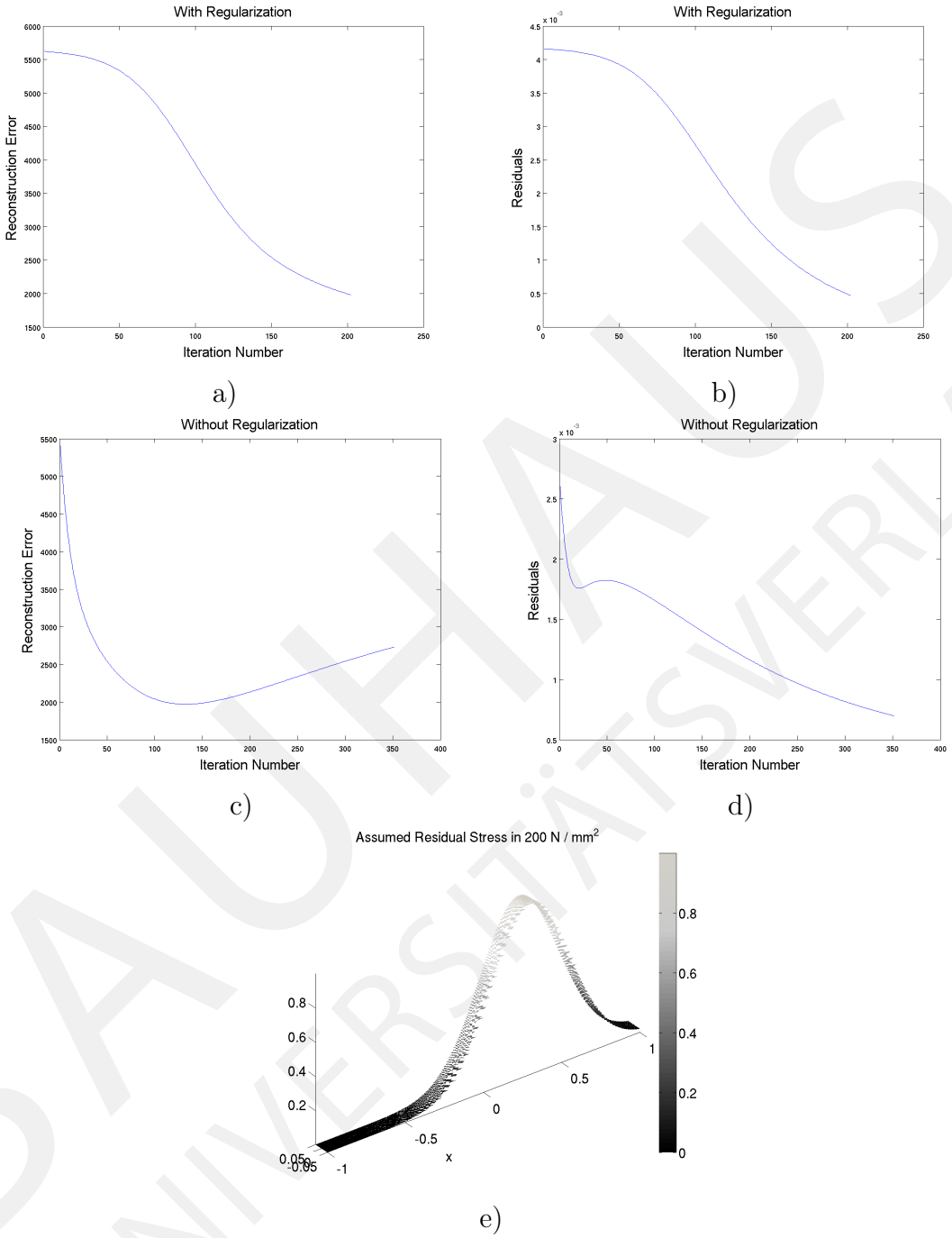

Figure 2: Convergence in X and Y space: a, b) with regularization, c), d) without regularization, Assumed data noise 2%, e) assumed form of residual stress in x-direction.

First, there are errors or uncertainties in the measurements which may have a systematic or random behavior, often a combination of both. Second, model and measurements can never be validated to 100 %, e.g. due to abstractions in the model used. Thus, the systematic error is on the model side and is understood to be the model uncertainty. While generating our synthetic measurements, by forward simulations, we add for every solution of the inverse problem systematic noise according to the distributions given in Table 1. In theory, stopping criteria are formulated in terms of this noise level, i.e.

$$||F(\sigma) - y^{\delta}|| \leq \tau\delta$$

with $\tau > 1$. Here, the engineer or the person experienced with the model may generate a good estimate on the true systematic error, however, this is only an estimate, which in unfortune cases may vary from the real systematic error. If the assumed noise level, let us denote this with $\delta^{assumed}$ is too large, iterations might be stopped to early, reducing the quality of the identified quantitiy. If $\delta^{assumed}$ is too small, the stopping might become active rather late leading to unstable iterations and probably large identification errors. So we will model the true δ and the assumed $\delta^{assumed}$ as two random variables which are correlated to 70%.
Additionally, as we implemented an iteratively regularizing fixed-point method, the question arises, how the initial choice of the regularization parameter α effects the results. We assumed that the initial α follows a log-normal distribution with parameters as in Table 1. During the iterations the regularization parameter is successively reduced as $\alpha_{k+1} = c\alpha_k$ with $c = 0.95$.

4.2 Randomness in constitutive parameters

Besides systematic errors we find random errors in particular in the assumed material properties. The question of interest is, to which extend do wrong assumption in the material properties lead to a reduction of the accuracy of the identified parameters. Exemplarily, we treat the variables of the mechanical problem as random, i.e. the Young's Modulus and the thermal expansion coefficient. Both variables are modelled to follow a normal distribution with a scatter of 8% coefficient of variation.

5 Results

The following scatterplots (Figure 3) visualize the relation between the reconstruction error and the different random input quantities for the inverse problem discussed.

From the results we can conclude that the reconstruction error, which is a quality measure of the identified stress field, is visibly depending on the number of iterations, see Figure 3a. This number is however depending through the discrepancy principle on the noise level assumed, so it supports the message which can be drawn from Figure 3d. The initial value of the regularization parameter seems to have nearly no influence on the reconstructed stress field see Figure 3b. The rather similar plots in 3c and 3d are due to the fact that for δ and $\delta^{assumed}$ a correlation value of 70% is assumed. For other situations, there might be more uncertainty on the true level of systematic noise.

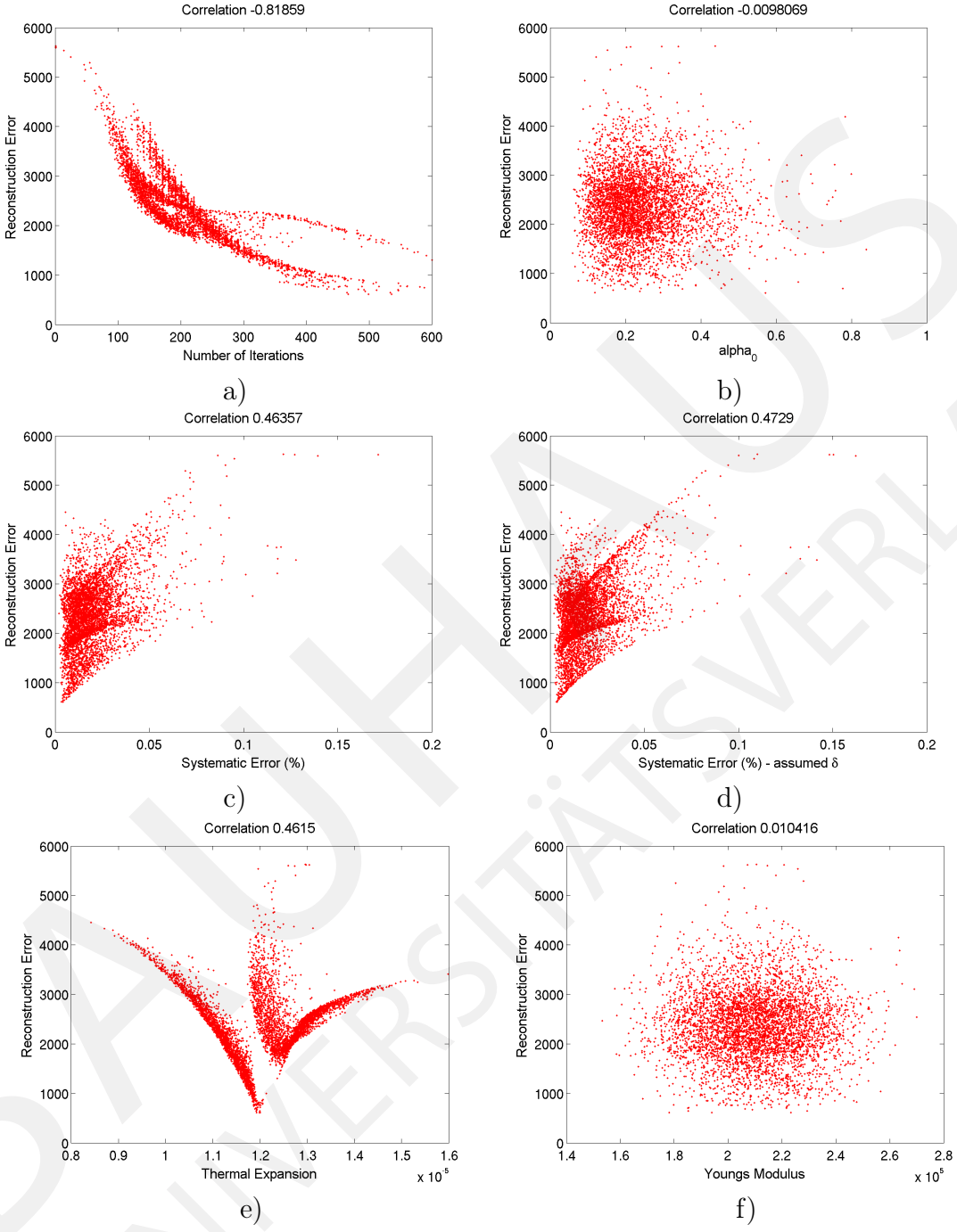

Figure 3: Statistical Analysis. The quality of the reconstructed stresses in dependency of a) the number of iterations, b) the initial value of the regularizing parameter, c) the true systematic error, d) the assumed systematic error $\delta^{assumed}$, e) variations in the thermal expansion coefficient, f) variation in Young's modulus.

From the material parameters, variations in the thermal expansion coefficients have a visible impact on the reconstruction error, while those of the Young's modulus not, see Figure 3e and 3f. Note, that these results can only by generated in this academic example where the true stress field is known. In applications, this is of course not the case and we therefore regard additionally the dependency of the residuals on the different input parameters.

The results of the scatterplots in Figure 4 reveal now the relation between the residuals, i.e. the discrepancy between measurements and simulation, and the different random input quantities. It is clear from theory and implementation that the residuals strongly correlate with the number of iterations and the assumed systematic error, see Figures 4a and 4d. This is also an indicator that the regularisation strategy is working properly as a high number of iterations is only allowed in situations of little systematic noise. From the randomness in material parameters, the thermal expansion has visible effects on the residuals. As in the previous results, also the scatter of α_0 and E do not seem to be influential.

6 Conclusions

A probabilistic analysis of the outcome of an inverse and ill-psed problem helps to detect the sources of uncertainty which may deteriorate the quality of identification results. It is therefore an important step in both model and experimental revision in order to further improve identification results.

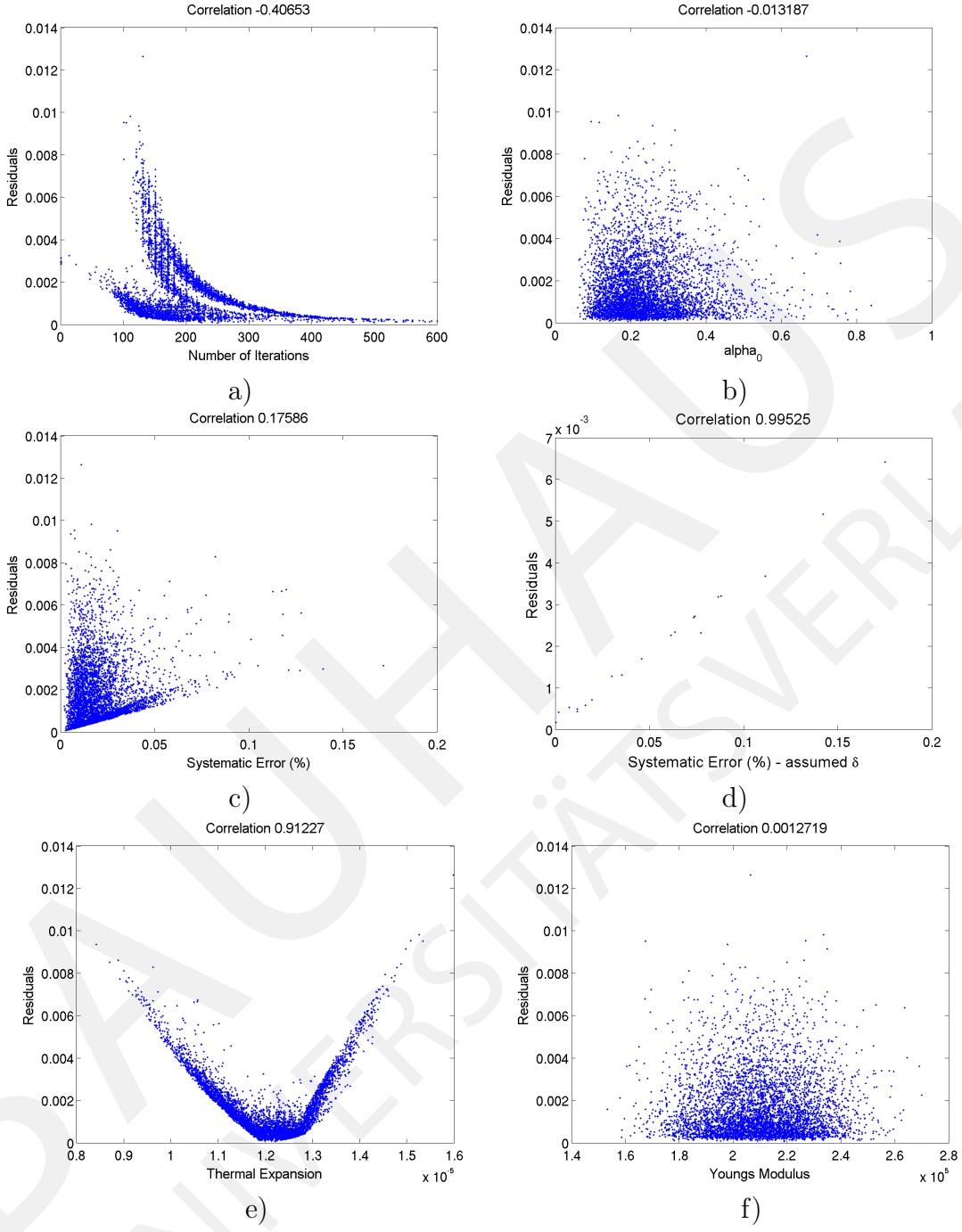

Figure 4: Statistical Analysis. The quality of the residuals in dependency of a) the number of iterations, b) the initial value of the regularizing parameter, c) the true systematic error, d) the assumed systematic error $\delta^{assumed}$, e) variations in the thermal expansion coefficient, f) variation in Young's modulus.

References

[1] H. Egger, H. W. Engl, and M. V. Klibanov. Global uniqueness and hölder stability for recovering a nonlinear source term in a parabolic equation. *Inverse Problems*, 21(1):271, 2005.

[2] H. W. Engl, M. Hanke, and A. Neubauer. *Regularization of Inverse Problems*. Kluwer, Dordrecht, 1996.

[3] R. Fedele, G. Maier, and B. Miller. Identification of elastic stiffness and local stresses in concrete dams by in situ tests and neural networks. *Structure & Infrastructure Engineering: Maintenance, Management, Life-Cycle*, 1(3):165–180, 2005.

[4] M. Hanke. A regularizing levenberg-marquardt scheme, with applications to inverse groundwater filtration problems. *Inverse Problems*, 13(1):79–95, 1997.

[5] V. Isakov, J.-N. Wang, and M. Yamamoto. An inverse problem for a dynamical lame system with residual stress. *SIAM Journal on Mathematical Analysis*, 39(4):1328, 2007.

[6] B. Kaltenbacher, A. Neubauer, and A. G. Ramm. Convergence rates of the continuous regularized Gauss-Newton method. *J. Inv. Ill-Posed Problems*, 10:261–280, 2002.

[7] B. Kaltenbacher, A. Neubauer, and O. Scherzer. *Iterative Regularization Methods for Nonlinear Ill-Posed Problems*. Radon Series on Computational and Applied Mathematics 6. de Gruyter, Berlin - New York, May 2008.

[8] P. Kuegler. Identification of a temperature dependent heat conductivity from single-boundary measurements. *SIAM J. Numer. Anal.*, 41:1543–1563, 2003.

[9] T. Lahmer. Crack identification in hydro-mechanical systems with applications to gravity water dams. *Inverse Problems in Science & Engineering*, 18(8):1083–1101, 2010.

[10] C.-L. Lin and J.-N. Wang. Uniqueness in inverse problems for an elasticity system with residual stress by a single measurement. *Inverse Problems*, 19(4):807, 2003.

[11] A. B. Vieira, D. A. Rade, and A. Scotti. Identification of welding residual stresses in rectangular plates using vibration responses. *Inverse Problems in Science and Engineering*, 14(3):313–331, 2006.

[12] D. Weisz-Patrault, A. Ehrlacher, and N. Legrand. A new sensor for the evaluation of contact stress by inverse analysis during steel strip rolling. *Journal of Materials Processing Technology*, 211(9):1500–1509, 2011.

[13] D. Weisz-Patrault, A. Ehrlacher, and N. Legrand. Evaluation of temperature field and heat flux by inverse analysis during steel strip rolling. *International Journal of Heat and Mass Transfer*, 55(4):629–641, 2012.

[14] D. Weisz-Patrault, A. Ehrlacher, and N. Legrand. Analytical inverse solution for coupled thermoelastic problem for the evaluation of contact stress during steel strip rolling. *Applied Mathematical Modelling*, 37(4):221–2229, 2013.

A probabilistic framework for robust topology optimization of structures sensitive to geometric imperfections

Miche Jansen[1], **Geert Lombaert**[1], **and Mattias Schevenels**[2]

[1]Department of Civil Engineering, KU Leuven
Leuven, Belgium
e-mail: geert.lombaert@bwk.kuleuven.be
[2]Department of Architecture, KU Leuven
Leuven, Belgium
e-mail: mattias.schevenels@asro.kuleuven.be

Abstract. In this paper, design optimization of a shallow arch is performed using the density-based topology optimization method. The design obtained by classical topology optimization is highly sensitive to geometric imperfections when geometric nonlinearity is taken into account. A robust approach to topology optimization is therefore developed in order to find a design that is both efficient and robust.

A Total Lagrangian formulation for large displacements is adopted in order to incorporate geometric nonlinear effects in the topology optimization problem. Robust optimization is considered within a probabilistic framework: geometric imperfections in the design domain are modeled by a vector-valued Gaussian random field, and the variability of the performance is accounted for by minimizing a weighted sum of the mean and standard deviation in the robust optimization problem. During the optimization process the robust objective function is approximated by a second-order perturbation method in order to avoid multiple calls to the nonlinear finite element solver per design iteration.

1 Introduction

Topology optimization [6] is a powerful tool which has been used in various fields of application including civil engineering. The design obtained by classical topology optimization usually forms a very efficient solution for the specific problem at hand. In practice, however, its performance might be strongly reduced because of the uncertain variations inevitably present in the system. In robust optimization, these uncertainties are taken into account in order to find designs which are both efficient and robust. Different sources of uncertainty relevant to civil engineering have been considered in robust topology optimization including variable loads (e.g. [4, 8, 14]), uncertain material properties (e.g. [2, 12]), and geometric imperfections (e.g. [11, 17, 23, 28]).

This paper focuses on robust topology optimization while taking into account geometric imperfections. Imperfections are an important source of uncertainty in many design problems, especially when considering the structural stability and other geometric nonlinear effects. In accordance with the literature on topology optimization of geometric nonlinear structures [9, 10], this work incorporates geometric nonlinear phenomena in the optimization by means of a Total Lagrangian formulation for large displacement mechanics.

Furthermore, while several paradigms to robust optimization exist in the literature [7], a probabilistic approach is adopted in this work: probability distributions are attributed to the uncertainties and the robust performance of a design is assessed in terms of stochastic moments such as the mean and standard deviation. A stochastic perturbation method is developed in order to avoid the necessity of solving multiple instances of the nonlinear equilibrium equations in the robust optimization.

The remainder of this paper is organized as follows. Topology optimization of structures exhibiting geometric nonlinearity is treated in the following section. This method is used in the optimization of a shallow arch whose nominal design turns out to be very sensitive to geometric imperfections. The paper then proceeds with the robust approach to topology optimization: a probabilistic random field model for geometric imperfections is presented, the robust optimization problem is formulated, and a solution strategy based on the stochastic perturbation method is developed. Finally, it is demonstrated how an alternative robust design for the shallow arch can be obtained by means of the robust approach.

2 Topology optimization

2.1 Density based topology optimization

The goal of topology optimization is to find the best material distribution in a design domain Ω for a given set of constraints and boundary conditions. In the optimization of mechanical problems, the design domain Ω is discretized by means of n_e finite elements. The structure is parameterized by assigning a physical material density $\bar{\rho}_e$ to every element in the design domain [6]. The volume densities indicate whether material is present ($\bar{\rho}_e = 1$) or absent ($\bar{\rho}_e = 0$). The volume fraction of the design domain occupied by the structure is therefore expressed as:

$$V = \frac{1}{V_\Omega} \sum_{e=1}^{n_\mathrm{e}} v_e \bar{\rho}_e \tag{1}$$

where v_e is the volume of element e and $V_\Omega = \sum_{e=1}^{n_\mathrm{e}} v_e$ is the volume of the design domain. Since the volume densities are continuous optimization variables, efficient gradient-based optimization algorithms can be used to solve the topology optimization problem. However, intermediate densities ($0 < \bar{\rho}_e < 1$) usually lack a physical interpretation and should be avoided in the optimized design. In the Solid Isotropic Material with Penalization (SIMP) method [5, 22], intermediate densities are therefore penalized in the stiffness interpolation:

$$E_e = E_\mathrm{min} + (E_0 - E_\mathrm{min})\, \bar{\rho}_e^p \tag{2}$$

where E_0 and E_min are the Young's moduli of the material and void phase, respectively. Intermediate densities are made inefficient by selecting the penalization parameter $p > 1$.

Projection filters [16, 24, 30] are used in this paper in order to avoid mesh dependence of the solution and restrict the complexity of the optimized design. The vector of physical densities $\bar{\boldsymbol{\rho}}$ is therefore defined as a function of a new set of design variables $\boldsymbol{\rho} \in \mathbb{R}^{n_\mathrm{e}}$ in

two steps. The design variables ρ_e are first smoothed by a density filter to obtain the intermediate densities $\tilde{\rho}_e$:

$$\tilde{\rho}_e = \frac{\sum_{i=1}^{n_e} \kappa_{ei} v_i \rho_i}{\sum_{i=1}^{n_e} \kappa_{ei} v_i}, \qquad \kappa_{ei} = \max(R - \|\mathbf{x}_e - \mathbf{x}_i\|_2, 0) \tag{3}$$

where $\mathbf{x}_e$ are the coordinates of the center of element e and the filter radius R is related to the desired minimum length scale in the structure.

The smoothing operation (3) removes rapid variations in the design variables, but also introduces unwanted gray transition zones between material and void phase. Gray elements are removed in the second step by projecting the intermediate variables $\tilde{\rho}_e$ using a regularized Heaviside function [16, 28]:

$$\bar{\rho}_e = \frac{\tanh(\beta\eta) + \tanh(\beta(\tilde{\rho}_e - \eta))}{\tanh(\beta\eta) + \tanh(\beta(1 - \eta))} \tag{4}$$

where the parameter β determines the steepness of the function and $\eta \in [0; 1]$ is the threshold value of the projection.

In this paper, the optimization problem is expressed in the form of minimum compliance where the goal is to find the design which minimizes the work done by external forces for a limited amount of material:

$$\begin{aligned} \min_{\boldsymbol{\rho}} \quad & f(\boldsymbol{\rho}) = \mathbf{P}^{\mathsf{T}} \mathbf{u}(\boldsymbol{\rho}) \\ \text{s.t.} \quad & V(\boldsymbol{\rho}) - V_{\max} \leq 0 \\ & \mathbf{0} \leq \boldsymbol{\rho} \leq \mathbf{1} \end{aligned} \tag{5}$$

where the volume fraction $V(\boldsymbol{\rho})$ of the design is limited to a certain value $V_{\max}$. The nodal load vector $\mathbf{P}$ contains the discretized external forces. The nodal displacements $\mathbf{u}$ of the design are determined by means of a finite element analysis. When small strains and displacements are assumed, this amounts to solving the following linear system:

$$\mathbf{g}_{\mathrm{l}}(\boldsymbol{\rho}, \mathbf{u}) = \mathbf{K}(\boldsymbol{\rho})\mathbf{u} - \mathbf{P} = \mathbf{0} \tag{6}$$

The linear stiffness matrix $\mathbf{K}(\boldsymbol{\rho})$ is assembled from the element stiffness matrices $\mathbf{K}_e(\boldsymbol{\rho}) = E_e(\boldsymbol{\rho})\mathbf{K}_e^0$ where $\mathbf{K}_e^0$ is the element stiffness matrix for unit-stiffness.

In order to incorporate geometric nonlinear effects such as buckling and $P - \Delta$ effects, a Total Lagrangian formulation for large displacements is adopted in the following. In this case, the equilibrium equations are written as:

$$\mathbf{g}_{\mathrm{nl}}(\boldsymbol{\rho}, \mathbf{u}) = \mathbf{R}(\boldsymbol{\rho}, \mathbf{u}) - \mathbf{P} = \mathbf{0} \tag{7}$$

The internal force vector $\mathbf{R}$ is expressed as the following integral over the reference configuration of the domain:

$$\mathbf{R}(\boldsymbol{\rho}, \mathbf{u}) = \sum_{e=1}^{n_e} E_e(\boldsymbol{\rho}) \int_{\Omega_e} \mathbf{B}^{\mathsf{T}}(\mathbf{u}) \mathbf{C}^0 \mathbf{E}(\mathbf{u}) \, \mathrm{d}\Omega \tag{8}$$

where $\mathbf{E}$ is the Green-Lagrange strain vector, $\mathbf{B}$ is the strain increment matrix and $\mathbf{C}^0$ the elastic constitutive matrix for unit-stiffness. The reader is referred standard textbooks [29, 31] for more detailed information on this formulation.

Equation (7) is solved by means of the Newton-Raphson method during the design optimization, i.e. the nonlinear displacements for a particular design $\boldsymbol{\rho}$ are determined iteratively by solving a number of local linearizations of the nonlinear system (7):

$$\mathbf{K_T}(\boldsymbol{\rho}, \mathbf{u}^{(k)})\Delta\mathbf{u}^{(k)} = -\mathbf{g}_{\mathrm{nl}}(\boldsymbol{\rho}, \mathbf{u}^{(k)}) \tag{9}$$

where $\Delta\mathbf{u}^{(k)} = \mathbf{u}^{(k+1)} - \mathbf{u}^{(k)}$ is the displacement increment and the tangent stiffness matrix $\mathbf{K_T}$ is defined as the Jacobian of $\mathbf{R}$:

$$\mathbf{K_T}(\boldsymbol{\rho}, \mathbf{u}) = \frac{\partial \mathbf{R}(\boldsymbol{\rho}, \mathbf{u})}{\partial \mathbf{u}} \tag{10}$$

In a nonlinear setting, the objective function $f = \mathbf{P}^{\mathsf{T}}\mathbf{u}$ no longer corresponds to the external work and is commonly referred to as the end-compliance [10]. In the following, nonlinear end-compliance is denoted by f_{nl} and linear compliance by f_{l}.

2.2 Shallow arch

The methodology described in this paper is illustrated in the design of a shallow arch. The design domain and boundary conditions for the problem are shown in figure 1a. The design domain, which spans an angle $\alpha = 30°$ with an inner radius $R_{\mathrm{in}} = 100$ m, outer radius $R_{\mathrm{out}} = 104$ m and out-of-plane thickness $t = 1$ cm, is discretized by 800×60 finite elements. The properties for the material phase are a Young's modulus $E_0 = 200$ GPa and a Poisson's ratio $\nu = 0.3$. The stiffness of the void phase is set to $E_{\min} = 10^{-9}E_0$.

The geometric complexity of the design is limited by means of the projection filter (3)–(4) with a filter radius $R = 0.25$ m, a projection threshold $\eta = 0$ for a minimum length scale in the material phase, and a maximum steepness $\beta = 32$. As is common in topology optimization of geometric nonlinear problems [10], a continuation scheme on the penalization parameter p in the SIMP law (2) is used. The maximum penalization is set to $p = 8$ in order to ensure convergence to nearly discrete designs with the current filter specifications. The design is optimized for minimum end-compliance in case a load $P = 800$ kN is applied and the volume fraction of the design is limited to $V_{\max} = 30$ %. The optimization is performed numerically by means of the method of moving asymptotes [26]. The optimized design is shown in figure 1b.

The stability and nonlinear performance of the design is investigated in the following. The load-displacement curve for the center of the arch at the location of the point load is shown in figure 2a. The equilibrium path is traced using an arc-length algorithm with an orthogonal hyperplane constraint [19]. On the primary equilibrium path, the structural response is initially linear until a limit point is reached at $P = 3628$ kN which corresponds to a snap-through of the arch (fig. 2b). The limit point clearly occurs at a much larger load level than the design load considered in the optimization and so it poses no direct harm for the stability of the design. However, the load-displacement curve of the nominal design also shows an unstable bifurcation point at a much smaller load $P = 1275$ kN

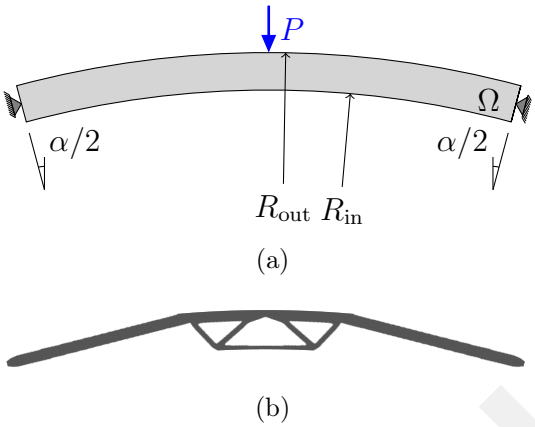

Figure 1: Topology optimization of a shallow arch: (a) design domain and boundary conditions, and (b) optimized nominal design.

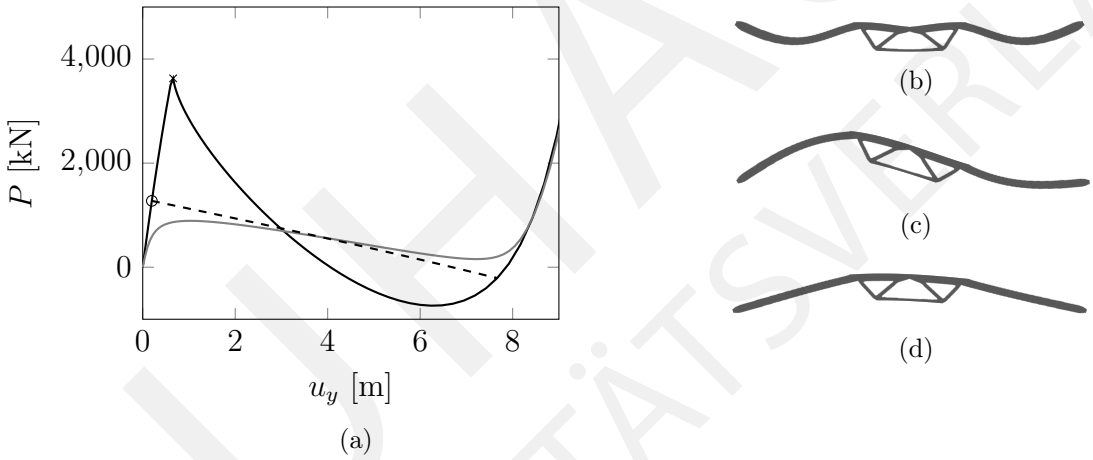

Figure 2: Nonlinear analysis of the nominal arch design: (a) load-displacement curve of the nominal design: the primary path (——) of the perfect nominal design contains a limit point (×) and unstable bifurcation point (○) with bifurcation path (- - -). The limit point corresponds to the snap-through depicted in figure (b) and the bifurcation point to the asymmetrical bifurcation mode in figure (c). The load-displacement curve (——) of the imperfect design in figure (d) is also shown.

as indicated by the dashed line in figure 2a. The corresponding nonlinear bifurcation mode (fig. 2c) is characterized by asymmetric buckling of the outer beams. The stability analysis of the design also has implications on its robustness: the design is particularly sensitive to asymmetric imperfections associated with the unstable bifurcation, even at load levels well below the critical load level. This is illustrated by considering a slightly imperfect design (fig. 2d). The load-displacement curve for this imperfect version is shown as the gray line in figure 2a: the displacements are much larger and the response is clearly nonlinear at load levels far below the critical load.

3 Geometric imperfections

In a probabilistic framework, uncertainties are treated as random variables which are denoted as functions of the probabilistic elementary event θ of the event space Θ.

Geometric imperfections are modeled as a zero-mean Gaussian random field $\mathbf{p}(\mathbf{x}, \theta) : \Omega \times \Theta \to \mathbb{R}^n$. The random imperfections $\mathbf{p}(\mathbf{x}, \theta)$ are added to the coordinates $\mathbf{x}$ of the nominal design:

$$\tilde{\mathbf{x}}(\mathbf{x}, \theta) = \mathbf{x} + \mathbf{p}(\mathbf{x}, \theta) \tag{11}$$

where $\tilde{\mathbf{x}}(\mathbf{x}, \theta)$ are the uncertain material coordinates of the imperfect design. A Gaussian random field is fully characterized by its mean function $\mathbf{m_p}(\mathbf{x})$ and covariance function $\mathbf{C_p}(\mathbf{x}, \mathbf{x}')$:

$$\mathbf{m_p}(\mathbf{x}) = \mathbb{E}\left[\mathbf{p}(\mathbf{x}, \theta)\right] = \mathbf{0} \tag{12}$$

$$\begin{aligned} \mathbf{C_p}(\mathbf{x}, \mathbf{x}') &= \mathrm{Cov}\left[\mathbf{p}(\mathbf{x}, \theta), \mathbf{p}(\mathbf{x}', \theta)\right] \\ &= \mathbb{E}\left[\left(\mathbf{p}(\mathbf{x}, \theta) - \mathbf{m_p}(\mathbf{x})\right)\left(\mathbf{p}(\mathbf{x}', \theta) - \mathbf{m_p}(\mathbf{x}')\right)^{\mathsf{T}}\right] \end{aligned} \tag{13}$$

where $\mathbb{E}$ is the expectation operator. The components of the random vector $\mathbf{p}(\mathbf{x}, \theta)$ are assumed to be uncorrelated in the present study which enables the following representation of the covariance function:

$$\mathbf{C_p}(\mathbf{x}, \mathbf{x}') = \begin{bmatrix} C_{\mathrm{p}_1}(\mathbf{x}, \mathbf{x}') & 0 \\ 0 & C_{\mathrm{p}_2}(\mathbf{x}, \mathbf{x}') \end{bmatrix} \tag{14}$$

A squared exponential covariance function is used for the covariance function C_{p_i} of component p_i of the random vector:

$$C_{\mathrm{p}_i}(\mathbf{x}, \mathbf{x}') = \sigma_{\mathrm{p}_i}^2 \exp\left[-\left(\left(\frac{x - x'}{l_{cx}}\right)^2 + \left(\frac{y - y'}{l_{cy}}\right)^2\right)\right] \tag{15}$$

where σ_{p_i} is the standard deviation of the component p_i of the random field, and l_{cx} and l_{cy} are the correlation lengths of the random field in the directions x and y, respectively.

In the shallow arch problem, the horizontal and vertical components of imperfections are initially described by stationary random fields $p_i(\mathbf{x}, \theta)$ with squared exponential covariance function (15) with $\sigma_{\mathrm{p}_i} = 0.33$ m and $l_{cx} = l_{cy} = 17.45$ m. Furthermore, it is assumed that the structure is placed correctly on the supports, i.e., the geometric imperfections are zero at the location of the supports. Conditional random fields are applied to incorporate these constraints [3, 18]. The conditional distribution of a Gaussian random field given some known values is also Gaussian with a modified mean and covariance function. In case the value of the random field is fixed in a set of points $\{\bar{\mathbf{x}}_i \in \Omega | i \in 1, \ldots, m\}$, the conditional covariance function $\tilde{\mathbf{C}}_\mathbf{p}(\mathbf{x}, \mathbf{x}')$ is expressed as:

$$\begin{aligned} \tilde{\mathbf{C}}_\mathbf{p}(\mathbf{x}, \mathbf{x}') &= \mathrm{Cov}\left[\mathbf{p}(\mathbf{x}, \theta), \mathbf{p}(\mathbf{x}', \theta) | \mathbf{p}(\bar{\mathbf{x}}_i, \theta) = \mathbf{0}\right] \\ &= \mathbf{C_p}(\mathbf{x}, \mathbf{x}') - \mathbf{C}_{\mathbf{p}\bar{\mathbf{p}}}^{\mathsf{T}}(\mathbf{x}) \mathbf{C}_{\bar{\mathbf{p}}\bar{\mathbf{p}}}^{-1} \mathbf{C}_{\mathbf{p}\bar{\mathbf{p}}}(\mathbf{x}') \end{aligned} \tag{16}$$

where $\mathbf{C}_{\mathbf{p}\bar{\mathbf{p}}}(\mathbf{x})$ is the covariance function of $\mathbf{p}(\mathbf{x})$ and $\mathbf{p}(\bar{\mathbf{x}}_i)$ and $\mathbf{C}_{\bar{\mathbf{p}}\bar{\mathbf{p}}}$ is the covariance matrix of $\mathbf{p}(\bar{\mathbf{x}}_i)$. The variance of the conditioned random field is shown in figure 3a which

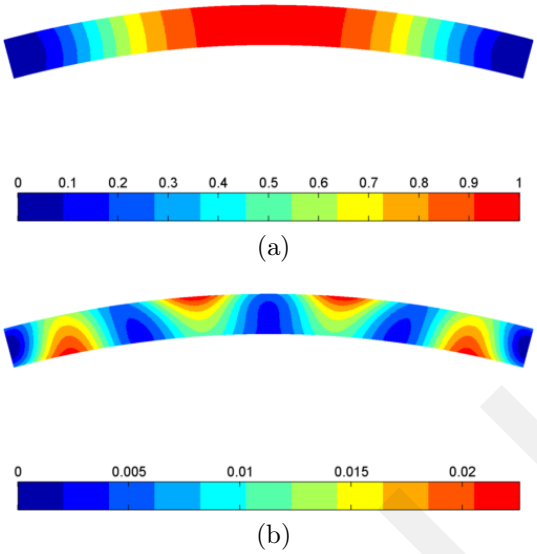

Figure 3: Random field of imperfections for the shallow arch: (a) Normalized variation $C_{\mathrm{p}_i}/\sigma^2_{\mathrm{p}_i}$ of the conditional random field; (b) Normalized error $e_r^2/\sigma^2_{\mathrm{p}_i}$ of the EOLE expansion.

illustrates that the imperfections are small in the areas close to the supports and increase towards the center of the design domain.

A discrete approximation of the Gaussian random field $\mathbf{p}(\mathbf{x}, \theta)$ is established by means of the Expansion Optimal Linear Estimation method (EOLE) which was elaborated by Li and Der Kiureghian [21]. In the EOLE method, the random field is initially only considered in a discrete number of points N in the domain Ω. The random vector corresponding to the values of the random field in these points is a multivariate Gaussian random vector that is decorrelated by means of principal component analysis. At intermediate locations, the random field is approximated by means of the Optimal Linear Estimator (OLE) method. The resulting EOLE expansion is written as a sum of deterministic mode functions $\boldsymbol{\varphi}_k$ multiplied by standard normal random variables $\xi_k(\theta)$, i.e., Equation (11) is approximated as:

$$\tilde{\mathbf{x}}(\mathbf{x}, \theta) \approx \mathbf{x} + \sum_{k=1}^{n_\xi} \boldsymbol{\varphi}_k(\mathbf{x}) \xi_k(\theta) \tag{17}$$

where $n_\xi \leq N$ is the number of modes included in the expansion. The accuracy of the EOLE discretization is quantified by the variance of the error. In the shallow arch problem, a truncated EOLE expansion with $r = 3$ modes for every component p_i is sufficiently accurate since the variance of the error as presented in figure 3b remains smaller than 2.5 %. This leads to a total of $n_\xi = 6$ EOLE modes which are illustrated in figure 4 by applying them to the nominal design.

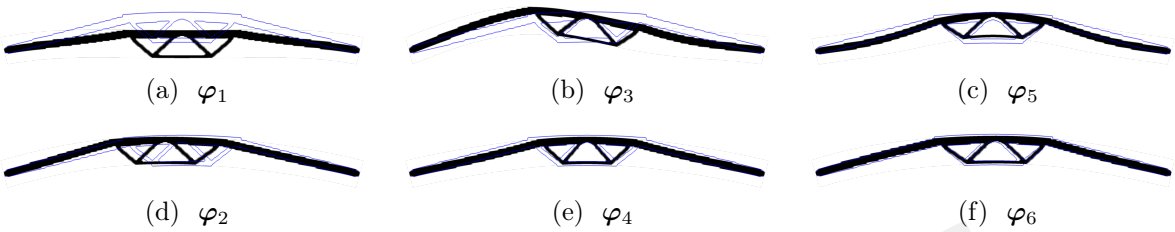

(a) φ_1 (b) φ_3 (c) φ_5

(d) φ_2 (e) φ_4 (f) φ_6

Figure 4: First six EOLE modes of the random field $\mathbf{p}(\mathbf{x}, \theta)$ applied to the nominal arch design.

4 Robust optimization

4.1 Robust optimization problem

When the geometric imperfections in terms of the EOLE expansion (17) are incorporated in the finite element analysis, the equilibrium equations (7) are rewritten as:

$$\mathbf{g}(\boldsymbol{\rho}, \mathbf{u}, \boldsymbol{\xi}) = \mathbf{R}(\boldsymbol{\rho}, \mathbf{u}, \boldsymbol{\xi}) - \mathbf{P} = \mathbf{0} \tag{18}$$

Note that the external load vector $\mathbf{P}$ is assumed to be independent of the imperfections. Equation (18) can be solved in order to express the uncertain displacements $\mathbf{u}(\boldsymbol{\rho}, \boldsymbol{\xi})$ as a function of the design and imperfection variables. Similarly, the uncertain performance $f(\boldsymbol{\rho}, \boldsymbol{\xi})$ also depends on the design variables $\boldsymbol{\rho}$ and the random variables $\boldsymbol{\xi}$. The uncertainties are taken into account in the robust optimization problem by defining the objective function as a weighted sum of the mean m_f and the standard deviation σ_f of the performance:

$$\begin{aligned} &\min_{\boldsymbol{\rho}} \; f_{\mathrm{R}}(\boldsymbol{\rho}) = m_f(\boldsymbol{\rho}) + \omega \sigma_f(\boldsymbol{\rho}) \\ &\text{s.t. } V(\boldsymbol{\rho}) - V_{\max} \leq 0 \\ &\quad \mathbf{0} \leq \boldsymbol{\rho} \leq \mathbf{1} \end{aligned} \tag{19}$$

where the weighting parameter ω is chosen equal to 1 in this study. The mean m_f and standard deviation σ_f of the objective function are defined as:

$$m_f(\boldsymbol{\rho}) = \mathbb{E}\left[f(\boldsymbol{\rho}, \boldsymbol{\xi})\right] \tag{20}$$

$$\sigma_f(\boldsymbol{\rho}) = \sqrt{\mathrm{Var}\left[f(\boldsymbol{\rho}, \boldsymbol{\xi})\right]} = \sqrt{\mathbb{E}\left[\left(f(\boldsymbol{\rho}, \boldsymbol{\xi})\right)^2 - \left(m_f(\boldsymbol{\rho})\right)^2\right]} \tag{21}$$

where $\mathbb{E}$ is the expectation operator.

4.2 Stochastic perturbation method

In order to solve the robust optimization problem, the stochastic moments m_f and σ_f (and their sensitivities) have to be estimated in each design iteration of the optimization algorithm. Various uncertainty quantification techniques can be applied for this purpose [20].

In order to avoid multiple calls to the nonlinear finite element solver per design iteration, a second-order perturbation method [15, 25] is adopted in this work. Note that the $\boldsymbol{\rho}$-dependence of the displacements and performance is dropped for notational convenience in the following, e.g., $\mathbf{u}(\boldsymbol{\rho}, \boldsymbol{\xi})$ is written as $\mathbf{u}(\boldsymbol{\xi})$.

The perturbation method approximates the function $f(\mathbf{u}(\boldsymbol{\xi}))$ by constructing a Taylor series, usually of first- or second-order, in the direction of the random variables $\boldsymbol{\xi}$. The expansion is typically established at the nominal design ($\boldsymbol{\xi} = \mathbf{0}$):

$$f(\mathbf{u}(\boldsymbol{\xi})) \approx f_0 + \sum_{i=1}^{n_\xi} f_{,i}\xi_i + \frac{1}{2}\sum_{i=1}^{n_\xi}\sum_{j=1}^{n_\xi} f_{,ij}\xi_i\xi_j \tag{22}$$

where:

$$f_0 = f(\mathbf{u}(\mathbf{0})) \qquad f_{,i} = \left.\frac{\mathrm{d}f}{\mathrm{d}\xi_i}\right|_{\boldsymbol{\xi}=\mathbf{0}} \qquad f_{,ij} = \left.\frac{\mathrm{d}^2 f}{\mathrm{d}\xi_i \mathrm{d}\xi_j}\right|_{\boldsymbol{\xi}=\mathbf{0}} \tag{23}$$

The computational cost of the perturbation method is governed by the effort related to the computation of the coefficients $(f_0, f_{,i}, f_{,ij})$. An efficient adjoint strategy is presented for this purpose further below.

Once the coefficients $(f_0, f_{,i}, f_{,ij})$ have been computed, the stochastic moments of the quadratic function (22) can be expressed in closed form and are used as estimates for the mean and variance of the actual function $f(\mathbf{u}(\boldsymbol{\xi}))$:

$$\mathrm{E}\left[f\right] \approx \mathrm{E}\left[f\right]_2 = f_0 + \sum_{i=1}^{n_\xi} f_{,i}\mathrm{E}\left[\xi_i\right] + \frac{1}{2}\sum_{i=1}^{n_\xi}\sum_{j=1}^{n_\xi} f_{,ij}\mathrm{E}\left[\xi_i\xi_j\right] \tag{24}$$

$$\mathrm{Var}\left[f\right] \approx \mathrm{Var}\left[f\right]_2 = \mathrm{E}\left[\left(f_0 + \sum_{i=1}^{n_\xi} f_{,i}\xi_i + \frac{1}{2}\sum_{i=1}^{n_\xi}\sum_{j=1}^{n_\xi} f_{,ij}\xi_i\xi_j - \mathrm{E}\left[f\right]_2\right)^2\right] \tag{25}$$

Since $\boldsymbol{\xi}$ is a vector of i.i.d. standard normal random variables, these expressions simplify to:

$$\mathrm{E}\left[f\right]_2 = f_0 + \frac{1}{2}\sum_{i=1}^{n_\xi} f_{,ii} \tag{26}$$

$$\mathrm{Var}\left[f\right]_2 = \sum_{i=1}^{n_\xi} f_{,i}^2 + \frac{1}{2}\sum_{i=1}^{n_\xi}\sum_{j=1}^{n_\xi} f_{,ij}f_{,ji} \tag{27}$$

In the general case of non-Gaussian random variables, additional terms related to higher-order stochastic moments appear in the expression for the variance [7].

The coefficients of the quadratic approximation (22) are computed using the chain rule of differentiation:

$$f_0 = f(\mathbf{u}_0) \tag{28}$$

$$f_{,i} = \frac{\partial f}{\partial \mathbf{u}}\mathbf{u}_{,i} \tag{29}$$

$$f_{,ij} = \mathbf{u}_{,i}^{\mathsf{T}}\frac{\partial^2 f}{\partial \mathbf{u}\partial \mathbf{u}}\mathbf{u}_{,j} + \frac{\partial f}{\partial \mathbf{u}}\mathbf{u}_{,ij} \tag{30}$$

where:

$$\mathbf{u}_0 = \mathbf{u}(\mathbf{0}) \qquad \mathbf{u}_{,i} = \left.\frac{\partial \mathbf{u}}{\partial \xi_i}\right|_{\boldsymbol{\xi}=\mathbf{0}} \qquad \mathbf{u}_{,ij} = \left.\frac{\partial^2 \mathbf{u}}{\partial \xi_i \partial \xi_j}\right|_{\boldsymbol{\xi}=\mathbf{0}} \tag{31}$$

The variables $(\mathbf{u}_0, \mathbf{u}_{,i}, \mathbf{u}_{,ij})$ are found by the differentiation of the nonlinear equilibrium equations (18) in the direction of the random variables:

$$\mathbf{g}_0(\mathbf{u}_0) = \mathbf{R}(\mathbf{u}_0, \mathbf{0}) - \mathbf{P} = \mathbf{0} \tag{32}$$

$$\mathbf{g}_{,i}(\mathbf{u}_0, \mathbf{u}_{,i}) = \mathbf{K_{T0}}\mathbf{u}_{,i} + \frac{\partial \mathbf{R}}{\partial \xi_i} = \mathbf{0} \qquad i = 1, \ldots, n_\xi \tag{33}$$

$$\begin{aligned}\mathbf{g}_{,ij}(\mathbf{u}_0, \mathbf{u}_{,i}, \mathbf{u}_{,j}, \mathbf{u}_{,ij}) = &\mathbf{K_{T0}}\mathbf{u}_{,ij} + \frac{\partial \mathbf{K_T}}{\partial \xi_i}\mathbf{u}_{,j} + \frac{\partial \mathbf{K_T}}{\partial \xi_j}\mathbf{u}_{,i} \\ &+ \frac{\partial^2 \mathbf{R}}{\partial \xi_i \partial \xi_j} + \left(\frac{\partial \mathbf{K_T}}{\partial \mathbf{u}}\mathbf{u}_{,i}\right)\mathbf{u}_{,j} = \mathbf{0} \quad i,j = 1, \ldots, n_\xi\end{aligned} \tag{34}$$

The derivatives of the internal force vector and tangent stiffness matrix such as $\partial \mathbf{R}/\partial \xi_i$ and $\partial \mathbf{K_T}/\partial \xi_i$ correspond to shape variations of the finite element mesh. The computation of these terms is obviously more involved than, e.g., for variable material properties, due to the rather complicated nonlinear dependence of the finite element matrices on the nodal coordinates. In this paper, a semi-analytical approach known from shape optimization [1, 27] is used where the derivatives of the finite element matrices are computed by means of finite differences in order to avoid the tedious derivation of an analytical expression. Similarly, the directional derivatives of $\mathbf{K_T}$ with respect to the displacements are evaluated most easily using finite differences.

The system of equations (32)–(34) should be solved sequentially. The first equation (32) corresponds to the state equation of the nominal system, while the equations (33)–(34) are both linear in the unknowns $\mathbf{u}_{,i}$ and $\mathbf{u}_{,ij}$ with the same coefficient matrix, i.e. the tangent stiffness matrix $\mathbf{K_{T0}} = \partial \mathbf{R}(\mathbf{u}_0, \mathbf{0})/\partial \mathbf{u}$. The perturbation method, therefore, requires only a single factorization of the nominal stiffness matrix $\mathbf{K_{T0}}$ in order to solve the linear system (33)–(34) with $n_\xi + n_\xi^2$ right-hand sides (and actually $(3n_\xi + n_\xi^2)/2$ if symmetry of $\mathbf{u}_{,ij}$ is considered). Hence the increase of the computational cost is proportional to $n_\xi + n_\xi^2$ right-hand side vector assemblies and forward and back substitutions of the factorized stiffness matrix. This method corresponds to a direct differentiation approach [13] since all imperfection sensitivities of the displacement vector are first computed before being utilized in the computation of the sensitivities of the objective function.

When the aim is to quantify the uncertainty of a single output function f, the computational effort of the perturbation method can be further reduced by following an adjoint approach to differentiation. In particular for a second-order Taylor expansion with the coefficients (28)–(30) and the corresponding set of state equations (32)–(34), an adjoint formulation is derived by solving Eq. (34) for $\mathbf{u}_{,ij}$ and implementing the resulting expression into the second-order derivatives $f_{,ij}$:

$$\begin{aligned}f_{,ij} &= \mathbf{u}_{,i}^\mathsf{T}\frac{\partial^2 f}{\partial \mathbf{u}\partial \mathbf{u}}\mathbf{u}_{,j} - \frac{\partial f}{\partial \mathbf{u}}\mathbf{K}_{\mathbf{T0}}^{-1}\left(\frac{\partial \mathbf{K_T}}{\partial \xi_i}\mathbf{u}_{,j} + \frac{\partial \mathbf{K_T}}{\partial \xi_j}\mathbf{u}_{,i} + \frac{\partial^2 \mathbf{R}}{\partial \xi_i \partial \xi_j} + \left(\frac{\partial \mathbf{K_T}}{\partial \mathbf{u}}\mathbf{u}_{,i}\right)\mathbf{u}_{,j}\right) \\ &= \mathbf{u}_{,i}^\mathsf{T}\frac{\partial^2 f}{\partial \mathbf{u}\partial \mathbf{u}}\mathbf{u}_{,j} - \mathbf{v}^\mathsf{T}\left(\frac{\partial \mathbf{K_T}}{\partial \xi_i}\mathbf{u}_{,j} + \frac{\partial \mathbf{K_T}}{\partial \xi_j}\mathbf{u}_{,i} + \frac{\partial^2 \mathbf{R}}{\partial \xi_i \partial \xi_j} + \left(\frac{\partial \mathbf{K_T}}{\partial \mathbf{u}}\mathbf{u}_{,i}\right)\mathbf{u}_{,j}\right)\end{aligned} \tag{35}$$

where the adjoint variable $\mathbf{v}$ is defined as the solution of the following linear system:

$$\mathbf{g}_{\mathrm{a}}(\mathbf{u}_0, \mathbf{v}) = \mathbf{K}_{\mathbf{T}0}^{\mathsf{T}}\mathbf{v} - \left(\frac{\partial f}{\partial \mathbf{u}}\right)^{\mathsf{T}} = \mathbf{0} \tag{36}$$

As a result, the second-order derivatives $f_{,ij}(\mathbf{u}_0, \mathbf{u}_{,i}, \mathbf{v})$ are expressed in terms of the variables $(\mathbf{u}_0, \mathbf{u}_{,i}, \mathbf{v})$ and it is no longer necessary to compute the second-order perturbations $\mathbf{u}_{,ij}$. Since $\mathbf{v}$ represents a single unknown vector, the set of variables $(\mathbf{u}_0, \mathbf{u}_{,i}, \mathbf{v})$ and corresponding set of equations (32)–(33) and (36) grow linearly rather than quadratically with the number n_ξ of random variables.

In order to achieve a similar linear growth in the design sensitivity analysis, it is necessary to consider the sensitivities of the robust objective $f_{\mathrm{R}}(\mathbf{u}_0, \mathbf{u}_{,i}, \mathbf{v})$. The design sensitivities and adjoint equations are derived by introducing the Lagrangian:

$$\hat{f}_{\mathrm{R}}(\mathbf{u}_0, \mathbf{u}_{,i}, \mathbf{v}, \boldsymbol{\lambda}_0, \boldsymbol{\lambda}_i, \boldsymbol{\gamma}) = f_{\mathrm{R}}(\mathbf{u}_0, \mathbf{u}_{,i}, \mathbf{v}) - \boldsymbol{\lambda}_0^{\mathsf{T}}\mathbf{g}_0(\mathbf{u}_0) - \sum_{i=1}^{n_\xi} \boldsymbol{\lambda}_i^{\mathsf{T}}\mathbf{g}_{,i}(\mathbf{u}, \mathbf{u}_{,i}) - \boldsymbol{\gamma}^{\mathsf{T}}\mathbf{g}_{\mathrm{a}}(\mathbf{u}_0, \mathbf{v}) \tag{37}$$

Setting the partial derivatives with respect to the state variables $(\mathbf{u}_0, \mathbf{u}_{,i}, \mathbf{v})$ equal to zero, leads to the following set of adjoint systems:

$$\mathbf{K}_{\mathbf{T}0}\boldsymbol{\gamma} = \left(\frac{\partial f_{\mathrm{R}}}{\partial \mathbf{v}}\right)^{\mathsf{T}} \tag{38}$$

$$\mathbf{K}_{\mathbf{T}0}^{\mathsf{T}}\boldsymbol{\lambda}_i = \left(\frac{\partial f_{\mathrm{R}}}{\partial \mathbf{u}_{,i}}\right)^{\mathsf{T}} \qquad i = 1, \ldots, n_\xi \tag{39}$$

$$\mathbf{K}_{\mathbf{T}0}^{\mathsf{T}}\boldsymbol{\lambda}_0 = \left(\frac{\partial f_{\mathrm{R}}}{\partial \mathbf{u}_0}\right)^{\mathsf{T}} - \sum_{i=1}^{n_\xi} \left(\frac{\mathrm{d}\mathbf{K}_{\mathbf{T}}}{\mathrm{d}\xi_i}\right)^{\mathsf{T}} \boldsymbol{\lambda}_i - \left(\frac{\partial \mathbf{K}_{\mathbf{T}}}{\partial \mathbf{u}}\mathbf{v}\right)^{\mathsf{T}} \boldsymbol{\gamma} \tag{40}$$

where the derivatives of $\mathbf{K}_{\mathbf{T}}$ are understood as:

$$\frac{\mathrm{d}\mathbf{K}_{\mathbf{T}}}{\mathrm{d}\xi_i} = \frac{\partial \mathbf{K}_{\mathbf{T}}}{\partial \mathbf{u}}\mathbf{u}_{,i} + \frac{\partial \mathbf{K}_{\mathbf{T}}}{\partial \xi_i} \tag{41}$$

The design sensitivities of f_{R} correspond to the partial derivatives of the Lagrangian (37) with respect to the design variables:

$$\frac{\mathrm{d}f_{\mathrm{R}}}{\mathrm{d}\boldsymbol{\rho}} = \frac{\partial \hat{f}_{\mathrm{R}}}{\partial \boldsymbol{\rho}} = \frac{\partial f_{\mathrm{R}}}{\partial \boldsymbol{\rho}} - \boldsymbol{\lambda}_0^{\mathsf{T}}\frac{\partial \mathbf{g}_0}{\partial \boldsymbol{\rho}} - \sum_{i=1}^{n_\xi} \boldsymbol{\lambda}_i^{\mathsf{T}}\frac{\partial \mathbf{g}_{,i}}{\partial \boldsymbol{\rho}} - \boldsymbol{\gamma}^{\mathsf{T}}\frac{\partial \mathbf{g}_{\mathrm{a}}}{\partial \boldsymbol{\rho}} \tag{42}$$

It should be noted that although no direct dependence of the performance function $f(\mathbf{u}(\boldsymbol{\rho}, \boldsymbol{\xi}))$ on the design is considered, $\partial f_{\mathrm{R}}/\partial \boldsymbol{\rho}$ is not zero since $f_{,ij}$ is expanded using Eq. (35) in the adjoint approach. In summary, the adjoint approach involves $2 + 2n_\xi$ additional right-hand sides in the linear system with coefficient matrix $\mathbf{K}_{\mathbf{T}0}$ compared to a deterministic function evaluation and sensitivity analysis.

4.3 Shallow arch

The design obtained by solving the robust optimization (19) using the perturbation method is shown in figure 5: this design is clearly more robust and it can be anticipated

Figure 5: Robust design for the shallow arch.

that the critical load of asymmetric buckling is larger due to the reduced slenderness of the outer beams. The performance of the designs is assessed by an elaborate Monte Carlo simulation with 10 000 samples. The results of the different designs are compared in table 1. It can be seen that the nominal design is very sensitive to imperfections as indicated by the large mean $m_{f_{\mathrm{nl}}}$ and standard deviation $\sigma_{f_{\mathrm{nl}}}$ of the nonlinear end-compliance. The sensitivity of the nominal design can be mainly attributed to geometric nonlinear effects related to the unstable bifurcation since the linear statistics $m_{f_{\mathrm{l}}}$ and $\sigma_{f_{\mathrm{l}}}$ of the nominal design are much smaller (and in fact quite similar to those of the robust design). Although the nominal performance f_{nl} of the robust design is slightly worse than for the nominal design, the robust design is less sensitive to geometric imperfections as the statistics $m_{f_{\mathrm{nl}}}$ and $\sigma_{f_{\mathrm{nl}}}$ are much better. Furthermore, the minor differences between linear and nonlinear statistics of the robust design suggest that the imperfections no longer trigger any significant geometric nonlinear behavior in the design.

In order to further illustrate the effect of robust optimization, figure 6 compares the nonlinear end-compliance of the nominal and robust design as a function of the third EOLE mode (the third mode resembles the asymmetric buckling mode and is therefore expected to have a particularly large influence on the structural performance). It can be seen that the nominal performance of the robust design (i.e. at $\xi_3 = 0$) is slightly worse, but the performance of the design is much less affected by geometric imperfections. Finally, it should be noted that the second-order perturbation method proves to be very accurate in the present robust optimization as indicated by the small difference between the estimates $\hat{m}_f$ and $\hat{\sigma}_f$ and the statistics $m_{f_{\mathrm{nl}}}$ and $\sigma_{f_{\mathrm{nl}}}$ in table 1. Furthermore, in figure 6, the quadratic approximation is almost indistinguishable from the actual performance of the robust design. For the nominal design, the quadratic approximation in figure 6 is less accurate which is to be expected as (geometric) nonlinearity is more pronounced in this design.

Design	f_{nl}	$m_{f_{\mathrm{l}}}$	$\sigma_{f_{\mathrm{l}}}$	$\hat{m}_f$	$\hat{\sigma}_f$	$m_{f_{\mathrm{nl}}}$	$\sigma_{f_{\mathrm{nl}}}$	f_{Rnl}
Nominal	97.1	108.1	20.1	/	/	337.3	1033.3	1370.6
Robust	121.1	119.1	11.5	126.3	12.1	126.6	13.1	139.7

Table 1: Results for the optimized shallow arch designs including the nominal nonlinear performance f_{nl}, the mean $m_{f_{\mathrm{l}}}$ and standard deviation $\sigma_{f_{\mathrm{l}}}$ of the linear compliance obtained by a Monte Carlo simulation with 10 000 samples, the estimated statistics at the end of the robust optimization $\hat{m}_f$ and $\hat{\sigma}_f$ and the mean $m_{f_{\mathrm{nl}}}$ and standard deviation $\sigma_{f_{\mathrm{nl}}}$ of the nonlinear end-compliance. All results are in kJ.

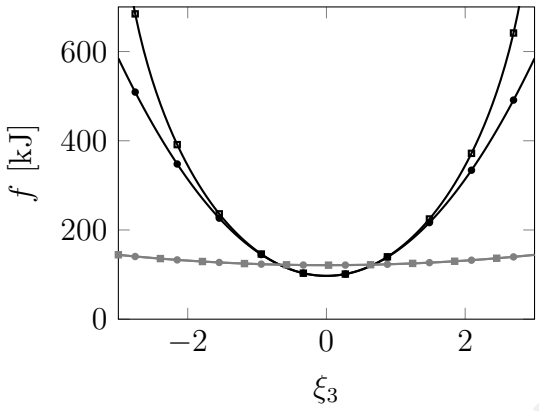

Figure 6: Shallow arch: nonlinear end-compliance of the nominal design (—▪—) and the robust design (—▪—) as a function of the third mode of imperfection φ_3; quadratic approximations by the second-order perturbation method for the nominal design (—•—) and robust design (—•—).

5 Conclusions

Geometric imperfections are an important concern in many design problems and often have a significant impact on the structural performance, especially when geometric nonlinear effects such as buckling and large displacements are taken into account. This paper develops a robust approach to topology optimization in order to obtain well performing designs that are also insensitive to imperfections. The important interaction between geometric imperfections and geometric nonlinearity is taken into account by means of a Total Lagrangian formulation for large displacements.

Robust optimization is performed in a probabilistic framework where spatially varying geometric imperfections are modeled by means of a vector-valued random field in the design domain. The objective function of the robust optimization problem is formulated as a weighted sum of the mean and standard deviation of the structural performance affected by geometric imperfections. These stochastic moments are estimated using a second-order perturbation method during the optimization. Afterwards, the results of the robust optimization are validated by means of an extensive Monte Carlo simulation: it is shown that the perturbation method provides accurate estimates of the uncertain nonlinear performance in this problem. Furthermore, the simulation also demonstrates that despite a slightly worse nominal performance, the robust design is much less sensitive to geometric imperfections.

6 Acknowledgments

The research presented in this paper has been performed within the framework of the KU Leuven - BOF PFV/10/002 OPTEC - Optimization in Engineering Center.

References

[1] S. Arnout, M. Firl, and K.-U. Bletzinger. Parameter free shape and thickness optimisation considering stress response. *Structural and Multidisciplinary Optimization*, 45:801–814, 2012.

[2] A. Asadpoure, M. Tootkaboni, and J.K. Guest. Robust topology optimization of structures with uncertainties in stiffness – Application to truss structures. *Computers & Structures*, 89(11-12):1131–1141, 2011.

[3] M. Baitsch and D. Hartmann. Optimization of slender structures considering geometrical imperfections. *Inverse Problems in Science and Engineering*, 14(6):623–637, 2006.

[4] A. Ben-Tal and A. Nemirovski. Robust truss topology design via semidefinite programming. *SIAM Journal on Optimization*, 7(4):991–1016, 1997.

[5] M.P. Bendsøe. Optimal shape design as a material distribution problem. *Structural and Multidisciplinary Optimization*, 1:193–202, 1989.

[6] M.P. Bendsøe and O. Sigmund. *Topology optimization: Theory, Methods and Applications*. Springer, Berlin, second edition, 2004.

[7] H.G. Beyer and B. Sendhoff. Robust optimization – A comprehensive survey. *Computer Methods in Applied Mechanics and Engineering*, 196(33–34):3190–3218, 2007.

[8] K. Brittain, M. Silva, and D. Tortorelli. Minmax topology optimization. *Structural and Multidisciplinary Optimization*, 45:657–668, 2012.

[9] T.E. Bruns, O. Sigmund, and D.A. Tortorelli. Numerical methods for the topology optimization of structures that exhibit snap-through. *International Journal for Numerical Methods in Engineering*, 55(10):1215–1237, 2002.

[10] T. Buhl, C.B.W. Pedersen, and O. Sigmund. Stiffness design of geometrically nonlinear structures using topology optimization. *Structural and Multidisciplinary Optimization*, 19:93–104, 2000.

[11] S. Chen and W. Chen. A new level-set based approach to shape and topology optimization under geometric uncertainty. *Structural and Multidisciplinary Optimization*, 44:1–18, 2011.

[12] S. Chen, W. Chen, and S. Lee. Level set based robust shape and topology optimization under random field uncertainties. *Structural and Multidisciplinary Optimization*, 41:507–524, 2010.

[13] K.K. Choi and N.H. Kim. *Structural sensitivity analysis and optimization, Volume 1. Linear systems*. Springer, New York, 2005.

[14] P.D. Dunning and H.A. Kim. Robust topology optimization: Minimization of expected and variance of compliance. *AIAA Journal*, 51(11):2656–2664, 2013.

[15] R.G. Ghanem and P.D. Spanos. *Stochastic finite elements: a spectral approach*. Springer-Verlag, New York, 1991.

[16] J.K. Guest, J.H. Prevost, and T. Belytschko. Achieving minimum length scale in topology optimization using nodal design variables and projection functions. *Inter-*

national Journal for Numerical Methods in Engineering, 61(2):238–254, 2004.

[17] M. Jansen, G. Lombaert, M. Diehl, B.S. Lazarov, O. Sigmund, and M. Schevenels. Robust topology optimization accounting for misplacement of material. *Structural and Multidisciplinary Optimization*, 47(3):317–333, 2013.

[18] K. Kolanek and S. Jendo. Random field models of geometrically imperfect structures with "clamped" boundary conditions. *Probabilistic Engineering Mechanics*, 23(2-3):219–226, 2008.

[19] S. Krenk. *Non-linear Modeling and Analysis of Solids and Structures*. Cambridge University Press, 2009.

[20] O.P. Le Maître and O.M. Knio. *Spectral Methods for Uncertainty Quantification: With Applications to Computational Fluid Dynamics*. Scientific Computation. Springer, 2010.

[21] C.C. Li and A. Der Kiureghian. Optimal discretization of random fields. *Journal of Engineering Mechanics*, 119(6):1136–1154, 1993.

[22] G.I.N. Rozvany, M. Zhou, and T. Birker. Generalized shape optimization without homogenization. *Structural and Multidisciplinary Optimization*, 4:250–252, 1992.

[23] M. Schevenels, B.S. Lazarov, and O. Sigmund. Robust topology optimization accounting for spatially varying manufacturing errors. *Computer Methods in Applied Mechanics and Engineering*, 200(49-52):3613–3627, 2011.

[24] O. Sigmund. Morphology-based black and white filters for topology optimization. *Structural and Multidisciplinary Optimization*, 33(4–5):401–424, 2007.

[25] B. Sudret and A. Der Kiureghian. Stochastic finite element methods and reliability – A state-of-the-art report. Report UCB/SEMM-2000/08, Department of Civil & Environmental Engineering, University of California, Berkeley, November 2000.

[26] K. Svanberg. The method of moving asymptotes – A new method for structural optimization. *International Journal for Numerical Methods in Engineering*, 24:359–373, 1987.

[27] D.A. Tortorelli and P. Michaleris. Design sensitivity analysis: Overview and review. *Inverse Problems in Engineering*, 1(1):71–105, 1994.

[28] F. Wang, B.S. Lazarov, and O. Sigmund. On projection methods, convergence and robust formulations in topology optimization. *Structural and Multidisciplinary Optimization*, 43:767–784, 2011.

[29] P. Wriggers. *Nonlinear Finite Element Methods*. Springer-Verlag Berlin Heidelberg, 2008.

[30] S. Xu, Y. Cai, and G. Cheng. Volume preserving nonlinear density filter based on Heaviside functions. *Structural and Multidisciplinary Optimization*, 41:495–505, 2010.

[31] O.C. Zienkiewicz and R.L. Taylor. *The finite element method, Volume 2: solid mechanics*. Butterworth-Heinemann, Oxford, United Kingdom, fifth edition, 2000.

Modeling the effect of random environmental influences on stochastic creep in concrete members

Reybrouck N., Maes M. A., Caspeele R., Criel P. and Taerwe L.

Department of Structural Engineering
Ghent University,
Ghent, Belgium
nicky.reybrouck@ugent.be

Abstract. The most significant contribution to the variability of long-term creep for in-situ structural concrete members stems from the effect of environmental influences. Many of these external processes are both seasonal and random. Specifically, ambient temperature, relative humidity, and wind are key factors with regard to creep response. But the influencing factors also include the time of casting/construction, the severity and the extent of seasonality, the exposure characteristics of the concrete member, the geographic location of the structure together with its prevailing meteorological regime, and the correlation between temperature and humidity. In order to investigate the impact of these various factors on the net macroscopic creep coefficient used in analysis and design, a discretized 2D physical model is developed, formulated in terms of combined heat transfer and moisture diffusion. The "local" strain response throughout the structural element in space/time is then transformed to a section-wide temporal creep response. The analysis model is then subject to both seasonal and stochastic processes for the triplet variables: ambient temperature, ambient relative humidity, and ambient wind conditions. By modifying various main meteorological features, construction time, dimensional/exposure variables, and stochastic process parameters, we are able to estimate the sectional creep response and, most importantly, the resulting net uncertainty regarding creep as a function of time.

1 Introduction

The stress and strain in a concrete section is subject to change for a long period of time due to the effect of creep. For a sustained applied stress on the concrete section, the strain will gradually increase with time. The magnitude of the concrete deformation depends upon the applied stress, the age of concrete at loading, the concrete quality, the shape of the concrete member and the environment in which it is kept. In this paper the dependence of creep on the environmental parameters is further investigated by including the effect of the ambient relative humidity and the temperature. The temperature has an effect on the maturity of concrete and the moisture content plays an important role in the creep deformation of concrete. The ambient temperature and relative humidity are strongly correlated and both need to be simultaneously accounted for in the analysis. A finite element model was developed to determine the creep deformation of a concrete section due to the varying environmental effects. The model consists of a rectangular mesh and matching boundary conditions to simulate the behavior of the concrete. The effects that are included are diffusivity, convection and radiation of heat and diffusion and

surface transition of moisture. Instantaneous elastic and time-dependent strains caused by shrinkage and creep arise when a concrete section is subject to an axial load. Due to the effects of environmental influences the spatial creep is non-uniform. However, the section remains plane after deformation based on the hypothesis of Navier-Bernoulli, so that internal self-equilibrating stresses arise in the concrete section [7]. Analysis of heat and moisture flow in a body is generally a three-dimensional problem. For a concrete slab or wall it can be simplified by treating the problem as a one- or two-dimensional problem. The temperature and moisture fields are assumed to be constant over the element length, but variable over the cross-section.

2 Environmental parameters

Measured environmental data such as temperature variation T, wind direction, wind velocity, precipitation, and relative humidity RH can be obtained from numerous weather stations at different locations, for example as made available at Weather Underground [12]. Some basic statistics which are of interest to this contribution are provided in Table 1 by choosing three different specific locations:

- Brussels, Belgium (oceanic climate)
- Dubai, United Arab Emirates (hot desert climate)
- Calgary, Canada (boreal climate, cold winter, hot summer)

		Brussels	Calgary	Dubai
Temperature	Min	-10	-32	14
[°C]	Avg ± std	11 ± 6.4	4.8 ± 10.2	29 ± 6.2
	Max	30	25	41
Rel. hum.	Min	39	19	14
[%]	Avg ± std	77.3 ± 10	62 ± 15.5	52 ± 13.4
	Max	99	100	87
Wind speed	Min	2	0	3
[km/h]	Avg ± std	12 ± 6.2	12 ± 5.3	10.1 ± 3.3
	Max	40	47	32

Table 1: Information about daily means in the period 2001-2011

The temperature, relative humidity and wind speed as function of time for Brussels are shown in Figure 1, Figure 2 and Figure 3 respectively.

The ambient temperature has a clear sinusoidal component. To account for seasonal variations of temperature a sinusoidal variation with superposed noise is proposed by [3] as:

$$\overline{T(t)} = \frac{(T_{max} + T_{min})}{2} + \frac{(T_{max} - T_{min})}{2} \sin(2\pi t) \tag{1}$$

The time-dependent data temperature consists of this sinusoidal variation with an additional stochastic noise:

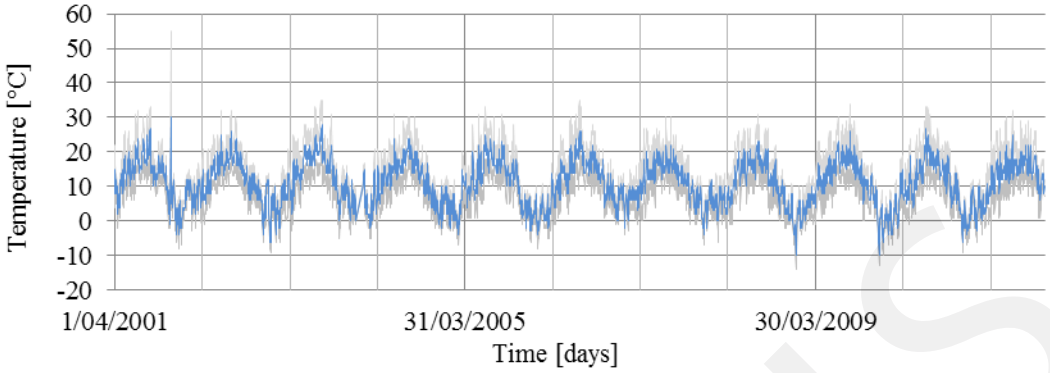

Figure 1: Example: Temperature (Min, Avg, Max) as function of time (Brussels, BE, period 2001-2011, wunderground)

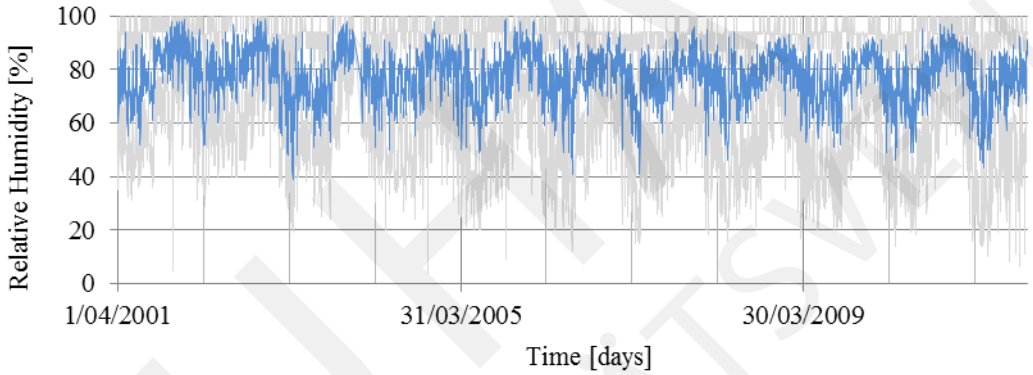

Figure 2: Example: Relative humidity (Min, Avg, Max) as function of time (Brussels, BE, period 2001-2011, wunderground)

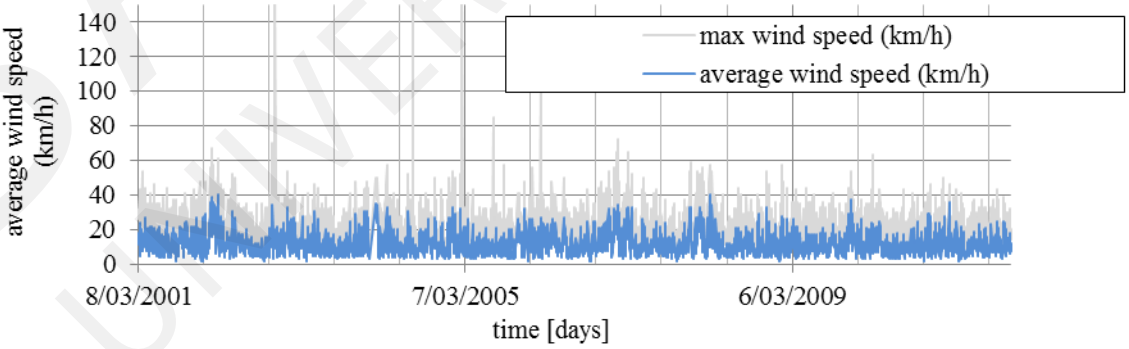

Figure 3: Example: Wind speed (Avg, Max) as function of time (Brussels, BE, period 2001-2011, wunderground)

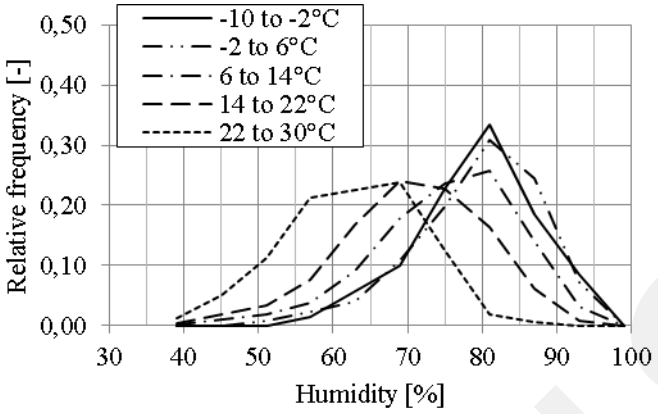

Figure 4: Conditional histogram of RH given T (Brussels, BE, period 2001-2011)

$$T(t) = \overline{T(t)} + T_{scatter}(t) \tag{2}$$

The noise $T_{scatter}(t)$ can be modeled using different methods. For example, the Karhunen-Loéve expansion [6], a renewal pulse process [10], or a simplified least-squares fitting sine, etc. The ambient temperature and the relative humidity are correlated. A conditional histogram of the relative humidity given different corresponding temperatures is shown in Figure 4. It can be observed that increasing ambient temperatures correspond to decreasing values of relative humidity.

3 2D-Model Concrete response

3.1 Model

Immediately after casting, a concrete element goes through a critical period associated with the evolution and dispersal of its heat of hydration, its initial drying and the environment it is exposed to. As the concrete grows older it is subject to long-term changes (annual atmospheric variations). The concrete element is hence subject to heat and moisture flows. The environmental boundary conditions will govern the thermal and hygral distributions in a concrete section and a parabolic diffusion equation is used to simulate the 2-D flow in a cross-section. Heat and moisture transport take place in a plane perpendicular to the mid-plane of the element. The distribution resulting from the environment is identical for all cross-sections. The combined effect of continuously changing boundary conditions and the nonlinear process of moisture diffusion require a numerical analysis.

Possible variables influencing the final concrete response are:

- Environmental variables: RH, T, wind speed
- Geographical location
- Material properties: hydration heat, creep, temperature expansion
- Dimensional variables: depth, width, height, span

- Time of casting and loading

The formulas for creep and Young's modulus of concrete are given by NBN EN 1992-1-1 [1]. The concrete deformation due to a gradually changing load can be calculated using the Age-Adjusted Effective Modulus Method [8]. The free creep deformations are non-uniform. Eigenstresses originate from incompatibility of free strains caused by non-uniform creep within one section. The free strain cannot develop and must be neutralized by a normal force N, bending moment M and internal self-equilibrating stress-distribution in the cross-section.

3.2 Thermal diffusion

Transient heat transfer analysis is used to determine the temperature variation within the concrete section in function of time. The partial differential equations describing the temperature in this cross section is defined by the Fourier equation taking into account the heat source provided by the hydration of the cement and is given by:

$$\rho C_p \frac{\partial T}{\partial t} = k\nabla^2 T + q_v \tag{3}$$

where ρ = material density (kg/m^3); k = thermal conductivity (W/mK); C_p = specific heat of concrete (J/kgK); and q_v = the rate of heat production (W/m^3). The chemical hydration reaction of cement generates heat over the curing period. The development of the heat of hydration q_v at the early ages of the concrete is dependent on the chemical composition of cement paste and temperature. The rate of heat of hydration per unit volume q_v is given by:

$$q_v = \rho\lambda Q_\infty e^{-\lambda t_E} 2^{0.08(T_i - 20°C)} \tag{4}$$

where Q = heat development by hydration (J/kg); Q_∞ = limiting heat (J/kg); λ = heat development constant (s^{-1}); and t_E = equivalent reaction time taking account of the time during which the temperature differs from the standard temperature 20°C (s). Heat is transferred from the boundary faces of the cross section by convection and radiation. The heat transfer between the concrete surface and the environment consists of convection and Boltzman-type radiation. The surface heat flow is the sum of surface convection flow and emission of radiant heat. Convection and radiation heat transfer are assumed to take place between the faces of the concrete and a specified ambient temperature. This will allow a sensitivity study of wind, convection and radiation. Because radiation is included, the problem is nonlinear. The amount of heat transferred from each face per unit area due to convection is defined as:

$$Q_{conv} = h_c(T - T_a) \tag{5}$$

where T_a = ambient temperature (K); T = temperature at a particular x and y location on the concrete surface (K); and h_c = specified convection coefficient (W/m^{2}K).

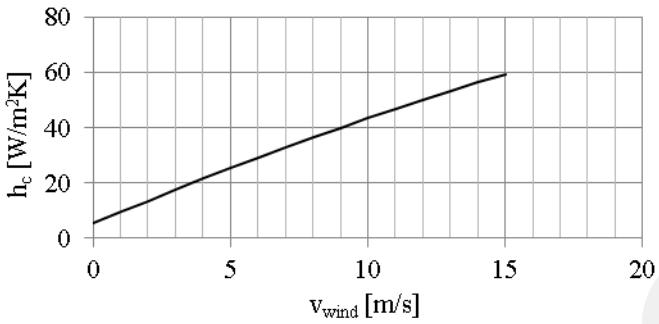

Figure 5: Convection coefficient as function of wind speed

The magnitude of the thermal surface convection factor h_c depends on the wind speed. An estimate for the specific convection coefficient h_{conv} based on the wind speed is given as illustrated in Figure 5 by Bentz [9].

The amount of heat transferred from each face per unit area due to radiation is:

$$Q_r = \epsilon C_S (T^4 - T_a^4) \tag{6}$$

where ϵ = emissivity coefficient applied to the radiant heat transfer between the face of the concrete and the surrounding air (-); and C_s = Stefan-Boltzmann constant (W/m^2K^4). The values are shown in Table 2. The surface heat flow is equal to the sum of the surface convection flow and the emission of radiant heat. The effects that were excluded from the thermal analysis are solar radiation on the concrete surface (sun and cloud cover: solar radiation intensity and absorptivity on a concrete surface).

3.3 Moisture diffusion

The analysis is performed by solving partial differential equations. The moisture diffusion depends strongly on the moisture content and temperature and is thus non-linear. The moisture diffusion coefficient drops from 100% for wet concrete to 10% for 50% moisture content in the concrete [5]. The 2D-nonlinear moisture diffusion equation is expressed by Su-Tae et al. [11] as:

$$\frac{\partial h}{\partial t} = \nabla \cdot (D_s(h,T) \nabla h) \tag{7}$$

where h = pore relative humidity (-); and D_s = moisture diffusion coefficient (m^2/s).

The moisture diffusion coefficient D_s is dependent on the relative humidity and temperature. For isothermal conditions, the moisture diffusion coefficient is influenced by the pore relative humidity taken into account according to Model Code 90 [2] and permeability on the temperature according to BAZANT and NAJJAR [4]. The equation is expressed as:

$$D_s(h,T) = \frac{3.6 \cdot 10^{-6}}{f_{ck} \backslash 10} (\alpha + \frac{1-\alpha}{1 + (\frac{1-h}{1-h_c})^n}) exp[\frac{Q_h}{R}(\frac{1}{273+20} - \frac{1}{273+T})] \tag{8}$$

Parameter	Symbol	Value	Unit
material density (in Eq 3)	ρ	2200	kg/m^3
thermal conductivity (in Eq 3)	k	2	W/mK
specific heat (in Eq 5)	C_p	960	J/kgK
limiting heat (in Eq 5)	Q_∞	320	kJ/kg
heat development	λ	8.0×10^{-6}	1/s
convection coefficient	h_{conv}	10	W/m^{2}K
emissivity of the face	ϵ	0.9	-
coefficient α (in Eq 9)	α	0.05	-
coefficient h_c (in Eq 9)	h_c	0.75	-
coefficient Q_h/R (in Eq 9)	Q_h/R	2500	K
coefficient n (in Eq 9)	n	15	-
coefficient β (in Eq 9)	β	30×10^{-9}	m/s

Table 2: Assumptions for the constants used in the described formulas

For the boundary condition of moisture, it is necessary to correlate the surface moisture with the ambient humidity. The transfer of moisture between the exposed concrete surface and surrounding air of relative humidity is described by Su-Tae et al. [11] as:

$$D_s(h,T)\frac{\partial h}{\partial z} = \beta(h_a - h_s) \tag{9}$$

where β = hygral surface transition coefficient (quantifies several moisture transition mechanisms) (m/s); h_a = environmental humidity (-); and h_s = relative humidity on the exposed surface (-). The values considered for these parameters are also given in Table 2.

Sink and source effects of hydration drying and carbonation wetting are considered to make a negligible contribution and are omitted. At the end of the wetting period (wet curing) $h = 1$ at t_0 is assumed.

Both space and time are discretized. The Forward Difference scheme is used for the time derivative. The equation has a second-order derivative in space. As an improvement the Crank–Nicolson method is used for solving the diffusion equation numerically. It is a second-order method in space and it is implicit in time.

4 Analysis

4.1 Analysis steps

The analysis is performed in a quasi-deterministic manner using recorded daily weather data as the boundary condition for the coupled moisture and heat transfer analysis. This provides the creep strain as a function of time for any given geometry and ambient conditions. The uncertainty of the creep process in the concrete element with exposed surfaces is captured by using different casting periods.

Finally a table is generated defining modified parameters for temperature and relative

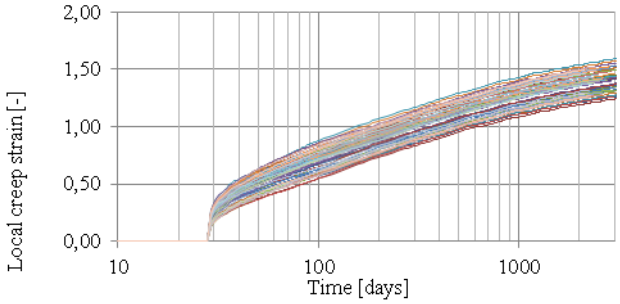

Figure 6: Local creep, different casting periods (example for Belgium)

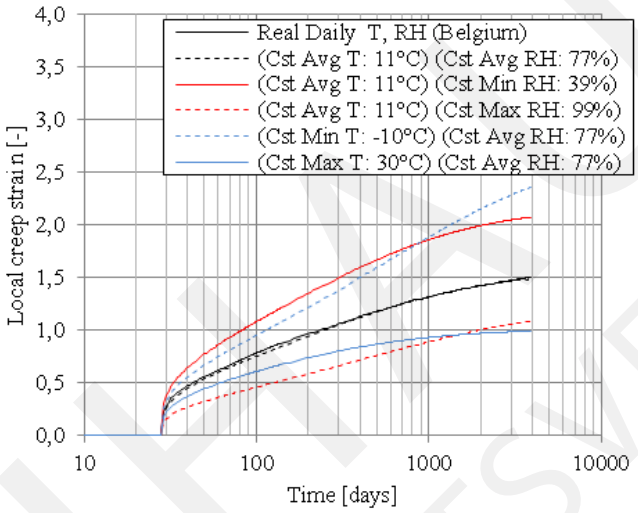

Figure 7: Effect of different constant parameters on local creep strain

humidity for a given location and casting date. This method allows the designer to include the ambient conditions in a simplified but more accurate manner using commonly used creep equations such as those provided in Eurocode and Model Code.

4.2 Results

Based upon the obtained data of relative humidity and temperature as function of time, creep strains can be estimated. For example, the local creep of a cross section with a moisture content which is constant in space but variable in time and temperature equal to the surrounding environmental conditions is shown in Figure 6. The figure represents many different casting times. The different casting times have a significant effect on the final creep and result in variations in long term creep strains up to 30%.

The extreme values for temperature or relative humidity are compared in Figure 7:

The expected creep increases with decreasing ambient temperature and relative humidity. The local creep strain depends on the location (for an equal casting day at March 2001 and loaded at 28days). This is shown in Figure 8 where the effect of diffusion is included.

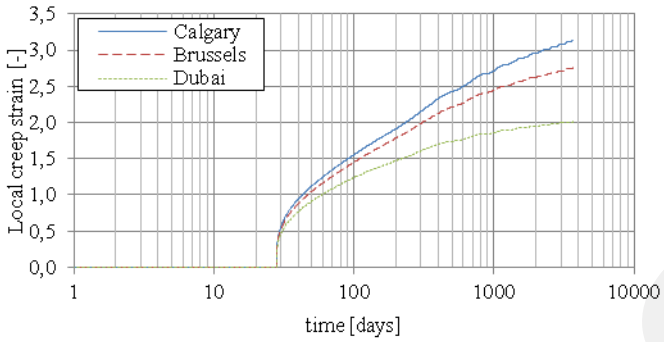

Figure 8: Influence of geographical location (for same casting days) on local creep strain.

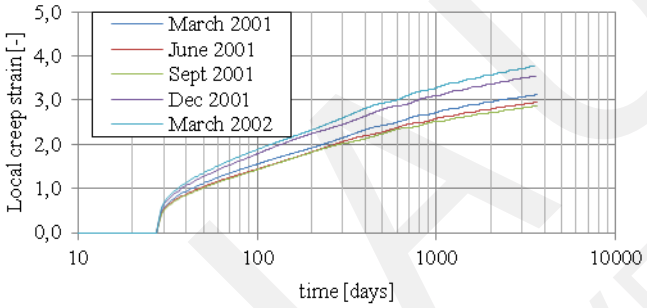

Figure 9: Influence of different time of casting (Calgary, CA)

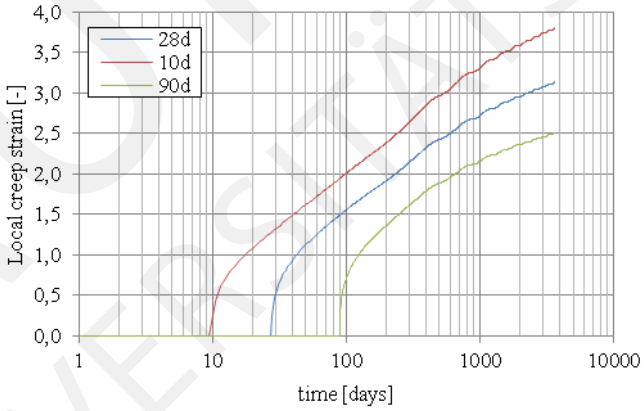

Figure 10: Influence of different loading times (Calgary, CA)

For a given geographic location, the creep also depends on the time of casting, as shown in Figure 9, and on the different loading times, as shown in Figure 10.

Table 3 can be used to determine constant replacement values for temperature and relative humidity that result in creep strain histories equivalent to those resulting from the full time history data. Least squares methods are to detect the "best fit" values given in Table 3.

	Belgium	Calgary	Dubai		Belgium	Dubai
2 Jan	10°C, 76%	6°C, 50%	27°C, 54%	6 Jul	14°C, 78%	26°C, 62%
17 Jan	10°C, 74%	5°C, 50%	27°C, 52%	21 Jul	15°C, 78%	31°C, 52%
1 Feb	9°C, 74%	6°C, 46%	28°C, 48%	5 Aug	14°C, 80%	29°C, 58%
16 Feb	11°C, 70%	6°C, 46%	29°C, 44%	20 Aug	13°C, 82%	32°C, 52%
8 Mar	11°C, 70%	4°C, 52%	27°C, 48%	4 Sep	14°C, 82%	28°C, 62%
23 Mar	10°C, 72%	3°C, 56%	28°C, 46%	19 Sep	14°C, 82%	28°C, 62%
7 Apr	11°C, 72%	4°C, 56%	29°C, 44%	4 Okt	12°C, 84%	27°C, 64%
22 Apr	12°C, 72%	6°C, 54%	28°C, 48%	19 Okt	13°C, 82%	29°C, 58%
7 May	12°C, 74%	5°C, 60%	27°C, 52%	3 Nov	12°C, 82%	31°C, 52%
22 May	12°C, 76%	4°C, 66%	26°C, 56%	18 Nov	12°C, 80%	27°C, 60%
6 Jun	13°C, 76%	5°C, 66%	26°C, 58%	3 Dec	10°C, 80%	27°C, 58%
21 Jun	13°C, 78%	6°C, 66%	26°C, 60%	18 Dec	10°C, 78%	27°C, 56%

Table 3: Constant replacement values for temperature and relative humidity corresponding to different casting periods.

5 Conclusions

The 2D model is used to make a prediction of the creep deformation as function of time using a history of ambient temperature and relative humidity as function of time. The intention of the analysis is to use the results of computer simulations to provide evidence of the relative importance of various parameters. Many of the simulations gave similar results and showed little influence on the creep strain. The following conclusions are made:

- Different combinations of boundary conditions (exposed or insulated) give similar results for an equal environment time history.
- The effect of wind on temperature gradients can be neglected because the concrete is fully adjusted to the ambient temperature within several hours for normal specimen sizes.
- The creep response depends significantly on the time of casting and the geographic location where differences of 30% in long term creep are possible.
- The major part of creep deformation occurs during the first months after applying the load.
- The thermal response D_T (approximately 10^{-6} m/s^2) is approximately 10^4 times faster compared to the moisture diffusion D_S (approximately 10^{-10} m/s^2) in concrete. Thick sections are observed to dry out quickly in the first few months at the surface but the inner core seems to remain moist for a long time. The nonlinearity of moisture diffusion is responsible for this effect. The dry outer layers cause a drastic decrease in diffusivity so that the moist core of the structure is surrounded by a skin becoming gradually more impermeable.

References

[1] *NBN EN 1992-1-1 2005.* European Committee for standardization, 2006.

[2] Model Code 90. *CEB-FIB Model Code 1990. design code.* Comite Euro-International du Beton, 1993.

[3] Sanchez-Silva M. Bressolette P. Schoefs F Bastidas-Arteaga E., Chateauneuf A. A comprehensive probabilistic model of chloride ingress in unsaturated concrete. *Engineering Structures, Vol. 33, p. 720-730.*, 2010.

[4] Najjar L. J. Bazant Z. P. Nonlinear water diffusion in nonsaturated concrete. *Materiaux et constructions, Vol. 5, p. 18.*, 1972.

[5] Wittmann F. H. Bazant Z. P. *Creep and Shrinkage in Concrete Structures.* John Wiley and Sons, 1982.

[6] Bucher C. *Computational Analysis of Randomness in Structural Mechanics.* New York, CRC Press., 2009.

[7] Elbadry M. Ghali A., Favre R. *Concrete Structures Stresses and Deformations.* London, Spon Press, 2002.

[8] Bazant Z. P. Prediction of concrete creep effects using age-adjusted effective modulus method. *Journal of the American Concrete Institute, Vol. 69, p. 212-217.*, 1972.

[9] Bentz D. P. A computer model to predict the surface temperature and time-of-wetness of concrete pavements and bridge decks. *National Institute of Standars and Technologiy*, 2000.

[10] Taerwe L. R. Detection of inherent heterogeneities in cement strength records by means of segmentation. *American Society for Testing and Materials, p. 25.*, 1987.

[11] Yun L. Yon-Dong P. Jin-Keun K. Su-Tae K., Jeong-Su K. Moisture diffusivity of early age concrete considering temperature and porosity. *Journal of Civil Engineering, 2012, p. 179-188.*, 2011.

[12] Weather Underground. *Weather for Everyone [Online].* wunderground.com, 2014.

Increasing the Robustness of Bayesian Analysis for the Reliability Assessment of Existing Structures

F. Marsili[(1)], P. Croce[(2)], L. Eckfeldt,[(1)]

[(1)]Institute for Building Material, Concrete Construction and Fire protection (iBMB), Concrete Construction Department - Technische Universität Braunschweig, Beethovenstraße 52, 38106 Braunschweig - D

[(2)]Department of Civil and Industrial Engineering – Structural Division – Univ. of Pisa - I

francesca.marsili@unifi.it

Abstract. The reliability assessment of existing structures is usually carried out applying partial factor method. As in most cases the complexity of the problem is beyond traditional assessment procedures, probabilistic methods are often invoked in order to estimate the actual probability of failure. Nonetheless a factor that should be considered is the potential bias arising with the refinement of probabilistic models: in effect, the outcome of reliability assessment will be dependable only if the potential bias is negligible. In this paper a procedure that increases the robustness of probabilistic methods and Bayesian updating techniques for the reliability assessment of existing structures is presented. The procedure will be especially devoted to historical buildings.

1 Introduction

Due to environmental, economic and socio-political reasons, significance and field of application of existing structures assessments' extend rapidly, also in view of preservation of cultural heritage. Despite assessment of existing buildings and design of new buildings differ in many aspects, in them basic variables are handled similarly through partial factors. On the other hand, considering that an increase of the safety level is usually more costly for an existing structure than for a new one, which is still in the design phase, and that the partial factor method is generally a safe-sided approach, in the assessment of existing structures particular attention should be devoted to avoid unnecessary expensive interventions, that, in case of heritage buildings, also entail a loss of the related and predominant cultural value.

Probabilistic methods are often invoked in order to perform more 'realistic' reliability assessment. Those methods have been widely implemented in the mechanical and aeronautical branch of engineering, where the components, which are mass-produced, are manufactured under the same conditions and can be tested repeatedly till to failure. On the contrary, reliability of civil structures is deeply influenced by the site specific conditions in which they are built: in effect, they are single and usually unique products, that cannot be tested to destruction and whose collapse is infrequent and often associated to human errors. Moreover, these aspects are further emphasized in historical buildings, designed according to experience and tradition.

In the following the procedure for performing a probabilistic reliability assessment is reviewed and its limits are highlighted, especially when it is applied to heritage structures.

The main contribution of this paper is the development of a flow chart for planning test and inspection on historical buildings aiming to increase the robustness of probabilistic methods and Bayesian updating techniques for the reliability assessment of existing structures.

2 Procedure for performing a probabilistic reliability assessment

- Establishment of the limit states to be considered;

A limit state is a distinct condition separating satisfactory and unsatisfactory states of a structure. Two fundamentally types of limit states are recognized: ultimate limit states and serviceability limit states. Ultimate limit states are associated with collapse and other form of structural failure, while serviceability limit states correspond to conditions of normal use (deflections, vibration, cracks).

- Identification of failure modes that could lead to the limit states;

A component, or a system, may fail a limit state in any of a number of failure modes. Modes of failure include mechanism such as: *yielding, bursting, ovality, bending, buckling, creep, ratcheting, de-lamination, denting, fatigue, fracture, corrosion, erosion, environmental cracking, excessive displacement, excessive vibration.*

- Construction of limit state functions;

The limit state criterion must be expressed in terms of a performance function that is a function of basic variables equals to zero at the corresponding limit state. The basic variables that should be considered are: *dimensions of the structural elements, load characteristics, material properties, model uncertainties.*
The fundamental case of the theory of structural reliability is the analysis of the simple requirements that the action effect E is smaller than resistance R.

$$E < R$$

This condition leads to the fundamental forms of the limit state functions that are [7]:

$$G = R - E = 0 \text{ or } Z = R/E = 1,$$

being G the so-called safety margin and Z the so called safety factor. Both E and R are generally random variables and it is necessary to accept the fact that the limit state may be exceeded with a certain probability. The essential object of the reliability theory is to assess the probability of failure p_f:

$$p_f = P[G < 0] = P[R - E < 0] \text{ or, equivalently, } p_f = P[Z < 1] = P[R/E < 1]$$

A simplified estimate of the failure probability p_f in construction engineering can be obtained through the reliability index β.
When E and R are normally distributed β is exactly given by

$$\beta = \frac{\mu_R - \mu_E}{\sqrt{\sigma_R^2 - 2\rho_{RE}\sigma_R\sigma_E + \sigma_E^2}} = \frac{\mu_G}{\sigma_G}$$

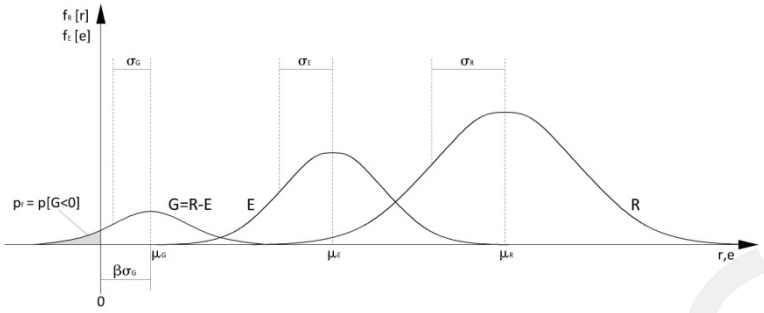

Figure 1: Definition of probability of failure p_f and reliability index β.

where μ_R, μ_E and μ_G are the mean values of R, E and G, respectively, σ_R, σ_E and σ_G are the standard deviations of R, E and G, respectively, and ρ_{RE} is the correlation coefficient of R and E, which is nil for uncorrelated variables. When, instead, E and R are log-normally distributed β is exactly given by

$$\beta = \frac{\ln(mr_R) - \ln(m_E)}{\sqrt{\ln(1+V_R^2) - 2\rho_{RE}\sqrt{\ln(1+V_R^2)\ln(1+V_E^2)} + \ln(1+V_E^2)}}$$

where m_R, m_E and m_G are the medians of R, E and G, respectively, V_R, V_E and V_G are the variation coefficients of R, E and G, respectively, and $\rho_R E$ is the correlation coefficient of R and E. Limit states can be defined for components part of the structure or for the complete structural system.

- Definition of internal forces

A basic requirement of a probabilistic reliability assessment is the definition of internal forces. Internal forces mainly depend on 2 variables: the action and the *transfer function* that converts action in internal forces. The definition of *transfer functions* requires the identification of the structural scheme and actual properties of structural elements.

- Data analysis and the construction of appropriate probability distribution functions: Bayesian updating techniques;

Determining the appropriate pdf and its parameters for basic variables is one of the most difficult and crucial task in the reliability assessment of existing structures.
One significant difference to be considered assessing existing buildings and assessing new ones is that while existing buildings belong to the physical world, in the design stage new ones belong to the ideal world. Clearly, at the end of the erection phase, the actual reliability of a new structure can be greater or lesser than the theoretical reliability estimated in the design phase: this is the natural outcome of all the uncertainties accompanying the erection phase itself. But an existing structure is much more than a structure just built, since it is also the result of the time passage, in one word of its history, in which aging, deterioration, environmental influences and human interventions modify the actual reliability level during the time.
When assessing an existing building is a general principle that actual characteristic of basic variables should be considered. It follows that detailed assessment should be based on material testing, determination of action and structural properties [7].
One relevant challenge in assessing existing structures is what to do with information

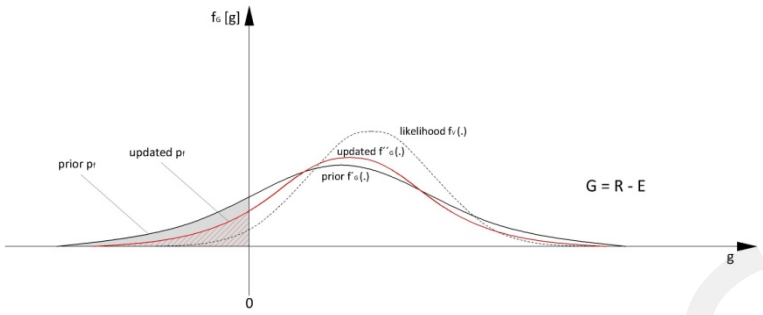

Figure 2: Prior p_f and updated p_f as modified by new information fv(.).

obtained and how to employ it in a probabilistic framework. If additional information has been gathered, the knowledge implicit in that information might be applied to improve, or update, previous estimate of structural reliability. The framework for doing this is Bayesian statistic, which uses Bayes Theorem [15]. The concept can be illustrated quite simply for the updating of pdf of G.
If $f'_G(.)$ represents the a priori (conditional) pdf of G, and $f_v(.)$ represent the (conditional) PDF based on new data, the *posteriori* or updated pdf $f''_G(.)$ is as shown.

The type of information available can be, for instance: survival after a significant overloading, material characteristics from different sources, capacity by proof loading, static and dynamic response to controlled loading, known geometry, damage and deterioration, known actions, known human intervention. It is possible to update the pdf of basic variables or the pdf of events. In both cases the refining process will then lead to an updated PDF of p_f.

- Evaluation of failure probabilities: notional, realistic and actuarial probability of failure;

A probability of failure calculated for the purpose of code development and calibration is based on conventional model and we usually refer to it as notional. When notional probabilities are evaluated quantities are omitted either intentionally (e.g. human error) or unintentionally because of a lack of data or a full understanding of the structural scheme. Instead, if probabilities are estimated on the basis of a set of modeling assumptions consistent with realistic aspects of the real structural behavior, the calculated probability will represent the true degree of belief and it will be a true Bayesian probability. Some authors referred to it as 'realistic' probability of failure [18]. However, in many cases, it is not necessary to remove all the layers of conservatism and realistically model all aspects of behavior. It should be noted that neither notional nor realistic probability of failure are sufficient for the purpose of risk based optimization, that it should be based on 'actuarial' or 'true' probability of failure. A true probability must be estimated using realistic probabilistic models and they must be validated with regard to observed probabilities of failure.

- Assessment of the result.

The goal for reliability analysis is to document that the target reliability is achieved. Target reliabilities are based on calibration and optimization and reflect the 'accepted'

level of risk in terms of possible failure consequences in a given reference time period. The accepted level of risk is a complicated societal issue because it depends both on the risks associated with other human activities and on the actual probability of failure of built heritage and it is normally the result of political choices in the framework of more general safety policy.

3 Limits of probabilistic methods for the reliability assessment of existing structures

3.1 General consideration

Different kinds of uncertainties are associated at each step of the procedure that may be classified regarding their source. Some examples are: *inherent, measurements, statistical and model uncertainty*. With the last one we especially refer to the epistemic uncertainty associated with the choice of the models that are implemented in a reliability assessment. Model uncertainty is due to imperfections and idealization made in physical model formulation for load and resistance as well as in the choice of the probability distribution representing the uncertainty in basic variables. For a population of structure, it is possible to assess the bias arising from model uncertainty, and treat it as a random variable in the reliability assessment. However, for any particular structure, model uncertainty manifests as a model bias. The bias especially arises from the epistemic uncertainties associated with the refinement of the 'realistic' model. Among the others, examples of possible model bias are: *ambiguity in the definition of limit states, misunderstanding failure modes; misunderstanding the structural scheme; disregarding system effects; wrong estimation of variables dependency; arbitrariness in the choice of the probability distribution; acquisition of data that is not relevant for the structure*. The reliability assessment of a particular structure will be dependable only if the potential bias due to epistemic uncertainties is negligible [18]. Therefore the fundamental limitation of probabilistic methods stems from modeling issues, and strategies aimed to reduce the related uncertainties have to be proposed in order to limit potential errors, and widen the range of applicability of those methods in the reliability assessment of existing structures.

3.2 Challenges in applying probabilistic methods to historical building

The bias can be particularly great in case of historical structures. With historical buildings we refer to important monuments but also to vernacular heritage, mainly made of masonry and wood. Applying probabilistic methods to those structures is particularly difficult because:

1. They are designed according to empirical bases instead of formal design approach and recognized theories or normative prescription;
2. The probabilistic description of the material properties is affected by great uncertainties, for example due to the heterogeneity and to the composite nature of ma-

sonry or the wood anisotropy; the acquisition of data is also a complicated process [19];

3. Transfer functions are affected by great uncertainties; it is possible to recognize 3 sources of randomness:
   - The actual behavior is represented by means of an ideal model, for example using de Saint-Venant theory, disregarding local effects or stress concentrations, considering theoretical restraints and theoretical dimensions and disregarding dimensional tolerances and unavoidable error in executions. This is an intrinsic source of randomness also presents in new structures, but it has a special impact in this framework because classical theory cannot be easily applied;
   - Structures are complex, with no distinction between decorative and structural elements, characterized by dependency among the elements and a high degree of indeterminacy;
   - Alteration may have occurred to the structure.

However several authors applied probabilistic methods for the assessment of existing historical structures [1], [8], [17], [19], [21]. Nonetheless a probabilistic approach depending on a lot of random variable is difficult to govern and often becomes unreliable. Therefore a clear understanding of the structural scheme is the first step toward the reduction of at least the last source of uncertainty, as well as the uncertainty related to internal forces.

3.3 Main source of model uncertainty: structural alteration

Uncertainty in the structural scheme is especially great if the structure has been altered over the course of the years. With structural alteration we referred to:

- Modifications to the structural scheme;
- Deterioration processes.

A good example of a structure that has been subjected to different kind of alterations is briefly described below; for further details it is referred to [2]. It is an old wooden roof structure that belongs to a building in Munich erected in 1615. The preliminary assessment reveals that connections are decaying or broken and the floors are affected by big deformations. Analyzing damages and deformations it was possible to reconstruct the history of the roof since its erection.
At the beginning damages occurred due to a leak in the roof. Some joints were destroyed and failed, and the entire roof settled into an inclined position. In order to stop the movements, a vertical truss was added: the element took the vertical loads, but it was not able to take the horizontal thrust. Therefore a new mechanism originated, leading to additional damage. In order to prevent further deformation, struts were built with the aim of supporting the middle of the span. Due to the struts, forces in the suspension structure changed from tension to compression. The joints which were not designed to take compression forces fell apart.
Modification and degradation are seldom documented and not easy detectable. Furthermore, as it is clear from the example, they usually have a great impact on the structural integrity, leading to weak points and structural defects. Disregarding those anomalies

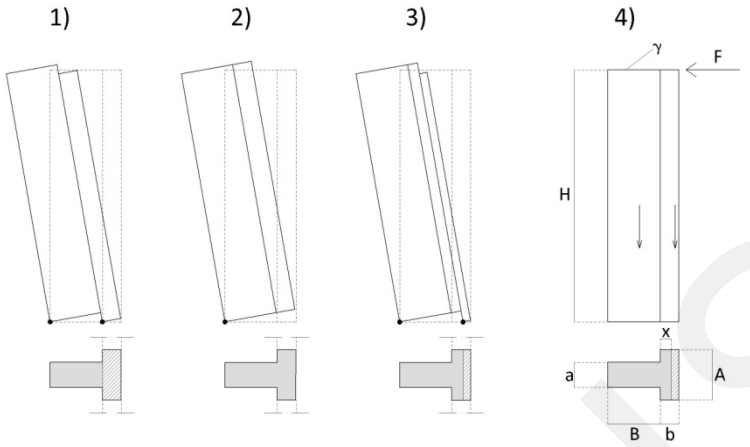

Figure 3: Possible failure modes in case of: 1) No connection; 2) Total connection; 3) Partial connection. In 4) the parameters considered in the sensitivity analysis are represented.

entails a misunderstanding of the structural scheme that leads to an unacceptable error in the reliability assessment. Therefore, a preliminary careful examination of the structure is necessary to understand the actual structural behavior and to diagnose correctly possible cause of failure.

3.4 Example: the impact of model uncertainty due to a structural alteration on the reliability assessment

An example of a frequent structural alteration is presented below; for further details it referred to [9]. It is the case of a masonry chapel from the 18th century whose walls have been reinforced later with counterforts. The method of bonding with counterforts may significantly vary, therefore the behavior of a compound buttress under the force transmitted from the vault is uncertain as well. A sensitivity analysis has been carried out, considering three different bonding conditions between the buttress and the wall, at which correspond three different failure modes:

1. No connection: this is a limit case, where the counterfort is considered as simply added to the wall: the buttress and the wall rotate independently around the respective external base vertex, so that the common boundaries slide without friction;
2. Total connection: this is another limit case, where the whole system rotates around the external base vertex of the counterfort;
3. Partial connection: this situation is simulated considering that a portion of the wall rotates together with the counterfort around external base vertex of the counterfort itself.

The assumption that part of the wall is well bonded to the buttress, so that it may collaborate to the stability, appears rational. The key question is the length x of well-bonded wall that should be assumed. Therefore a parametric study showing the impact

of the parameter x on the reliability assessment has been arranged and developed using COMREL. The following parametric limit state has been considered:

$$G(x) = \left[\gamma a \frac{B^2}{2} + \gamma x A(B + \frac{x}{2}) + \gamma A \frac{(b-x)^2}{2} - F\right] H$$

The deterministic parameters are a, representing the width of the buttress, A, representing the width of the wall, b, representing the thickness of the wall, while stochastic variables are B, representing the height of the buttress, γ, the specific weight of the material, and F, which the horizontal force applied at the top element. Assumptions regarding their probability distribution have been made according to [12]. The model for the load F consider both the uncertainties in the thrust transmitted by the vault and uncertainties in the location of the thrust itself, so that the reliability level can be assumed independent on the height H, which can be assumed as deterministic.

Variable	**Distribution**	μ_x	V_x
F (kg)	Normal	10000	0,18
B (m)	Normal	2,5	0,1
γ (kg/m^3)	Normal	2500	0,08

Table 1: Stochastic variables.

Constant	
a (m)	1,2
A (m)	2,4
b (m)	0,9
H (m)	5,3

Table 2: Deterministic values.

Results reveal that the considered parameter x has a dramatic impact on the reliability assessment: as x increase from zero to the wall thickness b, the reliability index β ranges from around 0,7, corresponding to a probability of failure $p_f \approx 0,242$, to $4,2$, corresponding to a probability of failure $p_f \approx 1,33 \cdot 10^{(-5)}$. These results confirm that, to obtain dependable estimate of the structural reliability, it is necessary both to recognize the actual behavior of the structure, also taking into account structural alterations, and to evaluate accurately model uncertainty.

4 Flow chart for planning test and inspection on the structure

The flow chart represents an extension of the ISO 13822 general flow for the assessment of existing structures when a detailed evaluation is required [11]. A detailed reliability

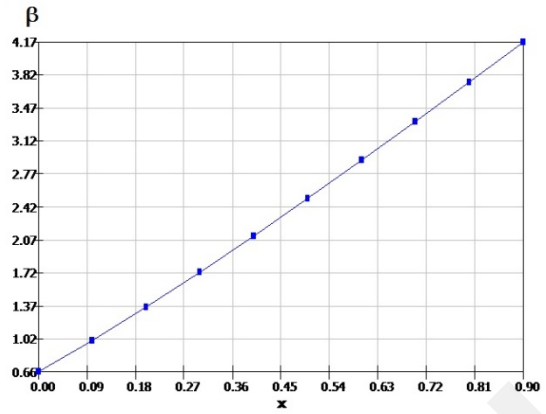

Figure 4: Variation of the reliability index β with the parameter x.

assessment can be carried out regarding several circumstances [7]. The reliability assessment of the whole structure is considered as a general scope; anyhow, in some cases local assessment may suffice depending on particular situation. The extension, which is especially devoted to assess historical heritage but can be applied to all existing structures, has been developed according to the following principles:
The extension can be applied to all existing buildings, but it is especially devoted to historical structures. The extension has been developed according to the following principles:

1. The main source of error in the reliability assessment of existing structures is represented by disregarding defects due to structural alterations. If defects are not recognized, the reliability assessment is not dependable.
2. Destructive tests (DTs) endanger both the cultural value and the structural integrity of the building; therefore they should not be performed. Minor destructive tests (MDTs) can be performed assuming that critical elements for the structural stability have been recognized.

The flow chart represents a process for planning extensive inspections and tests on the structure. According to ISO 13822 flow chart, also this extension is conceived as iterative process. The process starts with non-destructive tests (NDTs), going ahead with MDTs; at the same time, an increasing understanding of the structure, of crucial elements and defects will be achieved.
Along the flow chart structural models and analysis will be exploited not only to assess the structural reliability but also to plan investigation. The process of modelling and analysis, always not trivial, is particularly complex in case of historical buildings. It is important to underline that:

1. The choice of models and analysis is influenced by several constraints, e.g. cost, need of experience, level of accuracy required, availability of input data, need of validation, information sought etc.
2. Simpler model and analysis should be implemented to assess the system behaviour. Then local assessment will be carried out with more advanced numerical tools. Often comprehensive answers can only be obtained only through a combined approach. For more details it is referred to [13] and [6].

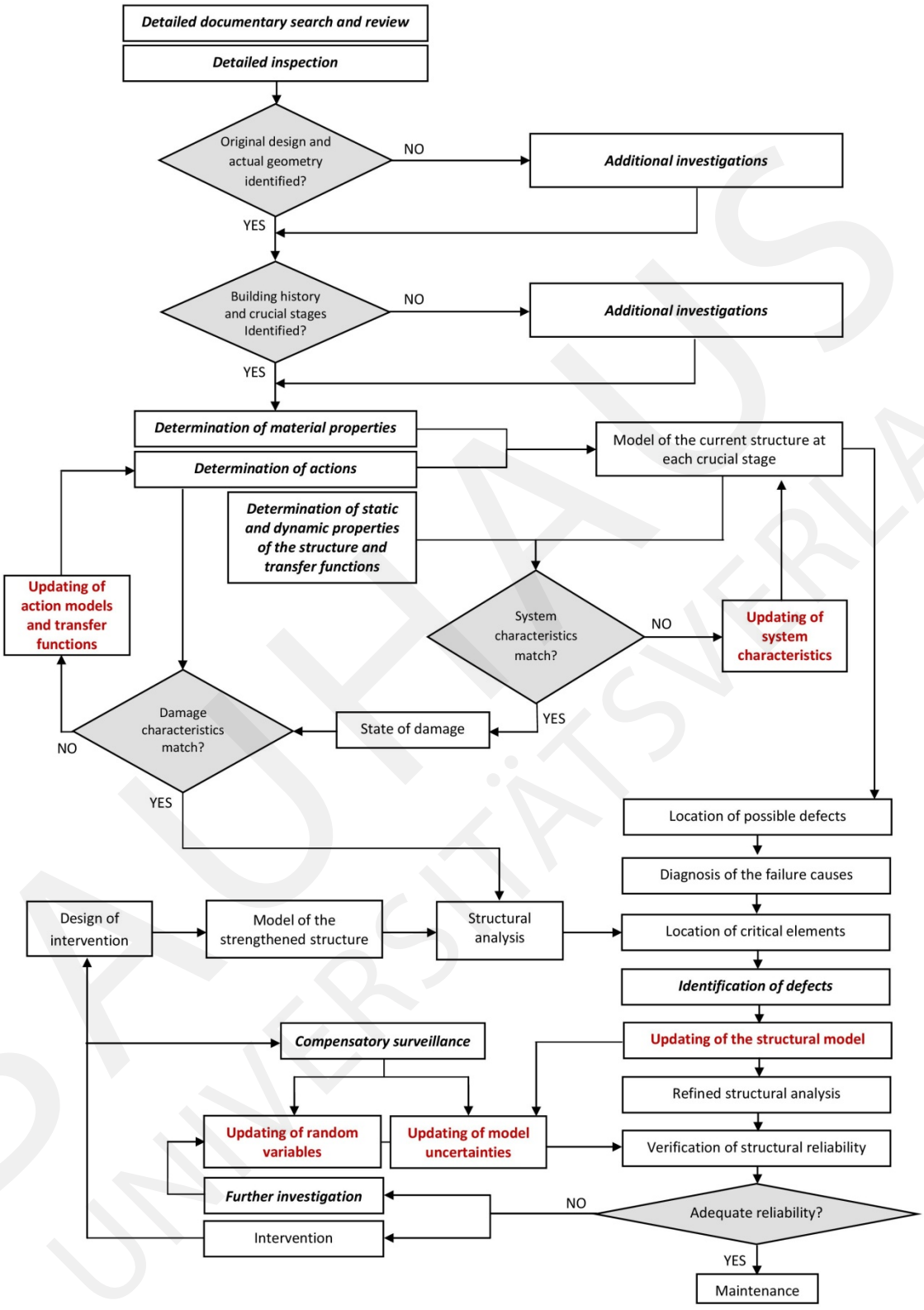

Figure 5: Flow chart for planning investigation on existing structures.

It is possible to articulate the procedure for collecting information in 5 steps, regarding the purpose of each investigation campaign. In the following each stage is analysed, and some specification are given. Some possible examples of specific objects, and the related investigation techniques, regarding masonry historical buildings are then listed in a summary table.

- Step 1: Determination of the historical evolution of the building

As a starting point the original state of the building has to be defined. In case of existing building designed using formal design approach, it is possible to arrive at the so called *simulated original design*, or redesigning the structure considering original drawings, methodologies and Code [6]. If the building has been designed on empirical bases, it is more difficult to define the original design. However a deep knowledge of construction techniques commonly used in that period may help in identifying the original structural condition and appearance. It should be emphasized that old buildings are hardly structurally sound and they usually exhibit an enormous degree of improvisation. Therefore retracing the original design of the structure helps to address first inspection and determine earlier defects.
Researches should then focus on documented and observed structural alteration. Deterioration mechanism, as well as maintenance and restoration, seldom reported, should be identified. It is important also to notice cosmetic maintenance that could hide degradation characteristics and bring to an erroneous perception of the structural reliability. The historical evolution of the building has to be reconstructed and the relevant stages should be defined. Theoretical studies, like the development of numerical models describing the behaviour of the structure at each stage, should be carried out, if necessary. The goal is to determine causes and effects of damage and degradation process, as well as motivation of structural modifications and their impact on the structure.

- Step 2: Determination of the current structure

This step is articulated in 2 phases. The first phase is the determination of current material properties and actions. Investigation should especially be made in order to define the type of soil and the quality of the material. A powerful methodology to determine masonry properties based on visual inspection is proposed in [5]. Deterioration models which describe the future performance of the structure should be determined based on investigation and experience with similar structures.
The second phase is the determination of structural properties performing static or dynamic load tests. Results of dynamic tests may be used not only to identify the model of the structure and thus to improve the evaluation of the response of the structure to loads and external actions, but also the occurrence and the evolution of damage in structural members or in the whole structure. For further details it is referred to [6].

- Step 3: Identification of defects

Defects will be identified according to a cross-check procedure, based on the location of critical elements and the location of possible defects.
The definition of the historical evolution of the building could point out where alterations

may have occurred, and therefore where more accurate observations have to be concentrated. At the same time the system analysis reveals which members are crucial for the structural integrity. A critical element is an element whose failure would start a chain reaction of successive failures that would take down a structure. Critical element depends on the following system properties: redundancy, damage tolerance, robustness. According to [16], it is possible to measure the contribution of each member to the overall structural integrity; for crucial elements it is important to guarantee higher reliability level and reduced model uncertainties. Therefore critical member will be deeply investigated, especially if alteration may have affected them. Difficult problems can be solved by the complementary use of MDTs and NDTs, but particular care should be paid in planning the MDTs to avoid damages and reliability reduction of these crucial elements; in many cases NDTs have to be used in alternative. Precautionary measures have to be arranged if the investigation may endanger the safety of the element. Some typical defects are listed in the summary table together with the best combination of tests able to detect them [4].

- Step 4: Reduction of uncertainties in the probability distribution of basic variables

The first reliability analysis is performed for the most critical elements using default probabilistic models of action effects and resistance. If the structural safety of those areas is not verified, further evaluation is possible based on improved load and resistance models. Those models will be improved through the collection of site data. Results reveal which parameters can be most effectively updated, and therefore where more refined investigation should focus on [22].

- Step 5: Compensatory surveillance

When reliability is not verified it is possible to arrange compensatory surveillance measures that ensure the continued use of a structure for a given bearing capacity. Those measures can be recurring – e.g. time interval recurring inspections, recurring load test – or continuous – e.g. threshold value monitoring, weight control. Then compensatory surveillance will result in a safety gain that can be quantified implementing several methods [20].

4.1 Application of Bayesian updating techniques to investigation results

Along the flow chart Bayesian updating techniques are often invoked in order to implement investigation results in a probabilistic framework. In the flow chart 4 different updating stages are recognized:

- Updating of system characteristics

Dynamic test results must verify model output. If the model output compares favourably to physical evidence, the model acquires credibility. However, if significant deviations are found, model calibration procedures may then be implemented. In [3] both the structural model and the probability model describing the accuracy of the structural model's pre-

	Object of the investigation	Investigation techniques
Detailed documentary search and review	Original drawing, design documentation, design methodology; Codes valid in the period where the structure was designed, documented alterations, actions (earthquakes, flooding, fire etc.).	Archive study, study of database gathering information about comparable structure.
Detailed inspection	Geometry of the structure; damage (out of plumb, deformations, crack pattern etc.); observed degradation, modification, maintenance and repair intervention.	Visual inspection, geometrical surveys, photogrammetry, monitoring techniques (mechanical instruments - e.g. crack meter, removable deformometer; electronic monitoring – e.g. trasducers, data acquisition system).
Determination of material properties and actions	Shape of masonry units; connection among masonry leaf; uniformity of masonry bond; quality of mortar; arrangement of vertical joints; arrangements of horizontal row.	Study of literature, study of database gathering information about comparable structure, visual inspection, geometrical surveys.
Determination of static and dynamic properties of the structure and transfer functions	Stiffness of floors and balcony.	Load tests.
	Stiffness, natural period, modes of vibrations, damping, amplitude of vibrations.	Dynamic tests. (Disturbance: wind, traffic, earthquakes, forced action induced by impact or vibrators. Monitoring techniques: seismoters, accelerometers, remote radar interferometric measurements of displacements and vibrations).
dentification of defects	Surveys of structural damages connected to typical cracks.	Flat jack, sonic and radar test.
	Presence of multiple leaf walls or detachment of layers.	Endoscopic surveys, dismantlement of small part of the section.
	Presence of inclusions and voids.	Thermographic survey if they are at small distance from the surface, otherwise sonic and radar test, georadar.
	Moisture.	Radar test, termographic survey, power drilling method.
Further investigation	State of stress; modulus of elasticity; coefficient of lateral deformations; masonry elements and mortar chemical, physical and mechanical properties; morphology of the wall cross section.	Flat jack, double flat jack, dismantlement of small part of the wall, endoscopic surveys, samplings of masonry elements and mortars, laboratory test.
Compensatory surveillance	Action, deformations, cracks depth and length, displacements, eccentricities.	Monitoring techniques (e.g. fibre optic sensor technology).

Table 3: Objects of the investigation and investigation techniques for a masonry structure.

dicted response are updated using test data. This is done by applying Bayes' theorem to update probability models and quantify modelling uncertainties.

- Updating of action models

If the building to be assessed is affected by some damage, it is often desirable to identify the magnitude of those forces in order to learn for future events. The damaged structure may be used as a 'measurement device'. This should involve a modelling of the uncertainty of the state of the structure, as to express the variation deemed possible for the environmental forces. Concerning the environmental forces, there is a common agreement that a Bayesian setting is adequate. This means assigning so-called a priori probabilities to actions, based on the usually extensive knowledge on how they are generated – e.g. storms, floods, earthquakes. Then a posteriori information will be obtained through Bayesian updating, as new information is included. In this step testing and updating is performed numerically; then numerical results maybe compared to the estimated state of damaged structure [14].

- Updating of the structural model and model uncertainties

This stage is very akin to the system identification, this time not of the global structure but of a part of it. The updating process of both the structural model and the related

uncertainty is carried out considering investigation results aimed at detect hidden defects. The model uncertainty can be quantified by performing a sensitivity analysis regarding the uncertain model parameters or by (qualitative) professional judgment.

- Updating of random variables

If after the first assessment uncertainty is still too large, especially when deciding if it is safe or not, further testing may be required. Parameters of the distributions are initially modelled by prior distribution functions. Observations of realisations of random variables are used to update prior distribution functions by the application of the Bayes theorem, and transformed into posterior distribution functions. It is also possible to perform a posterior analysis for a given test plan before results have been obtained, assuming that results will follow the prior probabilistic model. This type of analysis is called pre-posterior and it is implemented in order to plan the number of tests and at the same time minimize the overall cost [7].

5 Conclusion

A probabilistic approach that depends on several random variables is difficult to handle and often it becomes unreliable. This is the reason why probabilistic methods should be carefully applied to existing buildings and especially heritage structures, affected by numerous uncertainties. The main source of model uncertainties is represented by structural alteration, referring with this term to structural modification, also due to human intervention, and degradation phenomena. Investigations and tests should be aimed to detect hidden defects especially in those elements that are crucial for the structural integrity, and reduce uncertainty in the models. A flow chart for planning test and inspection on the structure has been proposed; along the flow chart, Bayesian updating techniques have been exploited with the aim of including investigation results in a probabilistic framework and obtaining more 'realistic' probability of failure. The definition of the historical evolution is a multidisciplinary task [10] that assumes a paramount role in detecting hidden defects; it is also important for developing appropriate repair concepts.

6 Acknowledgements

The authors would like to thank Dr. Ing. Christina Krafczyk (TU Braunschweig), Dr. Antonio Becchi (Max Planck Institute for the History of Science, Berlin), Prof. Dr. Hermann G. Matthies (TU Braunschweig), Dr. Noémi Friedman (TU Braunschweig), Ing. Corinna Siegert (TU Braunschweig), Prof. Santiago Huerta (Polytechnic University of Madrid) for their collaboration.

References

[1] Anzani A., Garavaglia E., Binda L., Long term damage of historic masonry: a prob-

abilistic model, Construction and Building Materials 23, 713-724, 2009.

[2] Barthel R., Maus H., Analysis and repair of historical roof structures: two examples, two different concepts, Proceedings of the First International Congress on Construction History, Madrid, 2003.

[3] Beck J.L., Katafygiotis L.S., Updating models and their uncertainties. I: Bayesian Statistical Framework, Journal of Engineering Mechanics, April 1998.

[4] Binda L., Saisi A., Application of NDTs to the diagnosis of Historic Structures, Non-Destructive testing in Civil Engineering, Nantes, June 2009.

[5] Borri A., De Maria A., Indice di Qualità Muraria (IQM) e sue applicazioni nell'ambito delle NTC 2008, L'Edilizia, Ed. De Lettera, 2009.

[6] Croce P., Holicky M., Operational methods for the assessment of existing structures, Tipografia Editrice Pisana, 2013.

[7] Diamantidis D., Holicky M., Innovative methods for the assessment of existing structures, Czech Technical University in Prague, Klokner Institute, 2012.

[8] Garavaglia E., Gianni A., Molina C., Reliability of Porous Materials: Two Stochastic Approaches, Journal of Materials in Civil Engineering, Asce, September/October 2004.

[9] Huerta S., The safety of masonry buttresses, Engineering History and Heritage, 163, Pages 3-24, Febraury 2010.

[10] ICOMOS, The Venice Charters, International Charters for the Conservation and Restoration of Monuments and Sites, International Council on Monuments and Sites, 1964.

[11] ISO 13822, Basis for design of structures - Assessment of existing structures, ISO, Geneva, Switzerland, 2001.

[12] JCSS 2011. JCSS Probabilistic model code, Joint Committee on Structural Safety, Zurich, 2011.

[13] Laurenco P.B., Computations on historic masonry structures, Prog. Struct. Eng. Mater. 4, 301–319, 2002.

[14] Matthies H.G., Structural damage and risk assessment and uncertainty quantification, proceedings NATO-ARW, Springer, 2008.

[15] Melchers R.E., Structural reliability analysis and prediction, John Wiley and Sons, 1999.

[16] Nafday A.M., Consequence-based structural design approach for black swan events, Structural Safety 33 (2011) 108–114. .

[17] Proske D., van Gelder P., Safety of Historical Stone Arch Bridges, Springer, 2009.

[18] Reid S., Calculation and interpretation of realistic probability of failure, Ships and Offshore Structures, 4(3), 197-205, 2009.

[19] Schuremans L., Assessing the Safety of Existing Structures using a Reliability Based Framework: Possibilities and Limitations, restoration of Buildings and Monuments, Bauinstandsetzen und Baudenkmalpflege Vol. 12, No 1, 1–16, 2006.

[20] Siegert C., Eckfeldt L., Empelmann M., Approaches to quantify the safety gain for existing concrete bridges due to surveillance. In: Proceedings of the 5th International Conference on Structural Engineering, Mechanics and Computation (SEMC 2013); Kapstadt, Südafrika, 02.-04, September 2013.

[21] Sykora M., Cejka T., Holicky M., Witzany J., Probabilistic model for compressive strength of historic masonry, Safety, Reliability and Risk Analysis: Beyond the Horizon – Steenbergen et al. (Eds), 2014.

[22] Tanner P., Interaction between planning, execution and evaluation of tests, IABSE Report, 1997.

Experience-Based Assessment of Yield Displacement Estimates for Reinforced Concrete Walls

Samira Marzban, Jochen Schwarz, Lars Abrahamczyk

Research Training Group 1462
Faculty of Civil Engineering, Bauhaus-Universität Weimar
Berkaer Str. 9, 99423, Weimar, Germany
samira.marzban@uni-weimar.de

Abstract. Experimental data is a a rich source of information for studies on structural behavior. Also, a characteristic property to be studied in structural force-deformation relationship is the yield point. So, in this study, we used the experimental data collected in a database on reinforced concrete walls to investigate different methods available in the literature for the calculation of the yield displacement. The database was originally created for model quality evaluation purposes to which the present study belongs.

1 Introduction

Strength and deformation components are well known as convenient response parameters to be used in performance-based analysis/design. A characteristic point in the strength-deformation relationship of a structure under seismic loading is where the global yield happens. i.e. where a major loss in the stiffness occurs. Yield point has become a crucial part of many simplified seismic design procedures. This specifically includes methods involving simplification of multi-degree of freedom systems to single-degree of freedom systems. The simplification process normally takes advantage of some linearization method ([1] for instance) which indeed requires a simplified definition of the yield point. Since this point characterizes the idealized force-deformation relationship (or the capacity curve), careful attention should be paid to its definition. As a result, many researchers have focused on yield displacement calculations. Paulay et al. [8], for instance, estimated the yield curvature in terms of the ϵ_y the yield strain of the steel at the extreme fiber and ϵ_{ce} the corresponding elastic concrete compression strain on the opposite edge of the wall. Obviously, this estimation relies on the local response of the concrete and the steel which might not always be accessible.
A large number of methods have been introduced to estimate the yield displacement based on the global response. Majority of such methods, specifically those addressed in design codes, rely on bilinearization techniques. ATC40 [1], for example, recommends to bilinearize the force-deformation relationship by an elastic branch followed by an inclined post-yield branch. The post-yield stiffness is found through minimizing the difference between the area under the main curve and its idealization. The intersection is known to be the global yield point. In contrast to ATC40, FEMA273 [2] suggests a secant stiffness through 60% of the yield strength for the first branch. The rest of the procedure, though, is the same as that of the ATC40. An application and a comparison of some of the code-recommended methods can be found in [4, 5].

As an application of the relation proposed in [9], Kazaz et al. [6] calculated the yield displacement for several RC walls in a parametric study. As a result, they derived empirical formulations for the calculation of the yield deformation components in terms of the influential parameters.
Having reviewed all the above sources, it is clear that a lot of work has been devoted to the calculation of the yield displacement for RC walls. However, probabilistic assessment of the available methods still requires further studies. In this study, we aim at assessing a selected number of the aforementioned methods applied to RC walls. To achieve this goal, the data collected on RC walls for *experience-based model quality evaluation of RC walls* was used. The yield displacement of the database walls was calculated according to the chosen methods and the results were compared through uncertainty analysis.

2 Yield Displacement Estimates

A considerable number of the existing methods for yield displacement calculation, used normally in practical design, rely on bilinearization techniques. Such methods tend to idealize the nonlinear force-deformation relationship and result in simple estimates of the yield displacement. Since methods of this kind are quite popular, specifically in design codes, we chose three of them to perform an assessment study. The methods, as shown in Figure 1, included the method proposed by Paulay and Priestley [8] and the methods recommended by ATC40 [1] and FEMA273 [2]. Along with the aforementioned methods, two empirical relationships introduced by Priestley et al. [9] and Kazaz et al. [6] were used to compute the yield displacement. In what follows, a brief description of each method is provided.

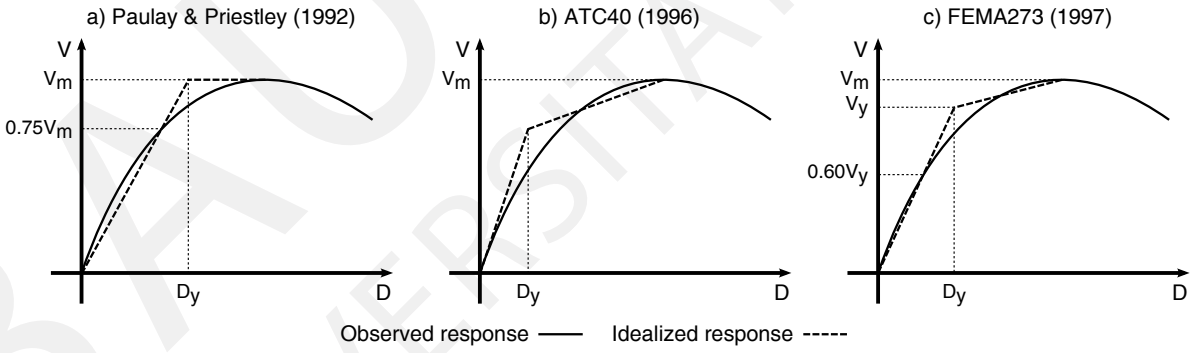

Figure 1: Studied bilinearization methods for yield displacement estimation.

2.1 Paulay & Priestley (1992)

In 1992, Paulay & Priestley [8] suggested the effective secant stiffness to 75% of the ideal yield strength for the elastic branch of the idealized force-deformation curve. Their model assumed a zero post-yield stiffness (See Figure 1a). According to them, the procedure for the calculation of the secant stiffness was introduced to allow for a reliable computation of the interstory drifts in the design process.

2.2 ATC40 (1996)

Later in 1996, as part of the capacity spectrum method for the design of structures, ATC40 [1] recommended to idealize the the capacity curve by a bilinear curve. The code recommended to use the initial stiffness of the force-deformation relationship as the elastic stiffness to the yield point for the idealized curve (See Figure 1b). The post-yield stiffness had to be found based on the equal energy absorption criterion. This concept dictates that the energy absorbed by the real and idealized systems should be identical i.e. the area under the real and the idealized curves should be equal.

2.3 FEMA273 (1997)

FEMA273 [2], introduced a bilinearization technique mainly to determine the structural period. The stiffness of the elastic branch was found such that the idealized curve intersects with the real curve at 60% of the yield strength (See Figure 1c). The stiffness of the plastic branch was specified by minimizing the difference between the areas under the curves. Again here, the equal energy absorption concept was used.

2.4 Priestley et al. (2007)

Priestley et al. [9] developed simplified relationships as approximations of the yield displacement for the sake of displacement-based design of structures. The relationships addressed several structural types including RC walls. Equation (1) conditions the yield curvature of the wall on its length (L_w) and the yield strain of the flexural reinforcement (ϵ_y). It should be noted that in the present study the yield displacement estimation techniques were investigated. Therefore, the yield curvature was converted to the yield displacement by assuming a uniform distribution of the curvature over $0.5L_w$ along the height of the wall.

$$\phi_y = 2.0(\epsilon_y / L_w) \tag{1}$$

2.5 Kazaz et al. (2012)

In a recent study in 2012, Kazaz et al. [6] proposed empirical relationships for deformation limits of RC walls based on parametric numerical analysis. The parameters included the shear-span-to-wall-length ratio, wall length, axial load ratio, normalized shear stress, the amount of horizontal web reinforcement, and the amount of longitudinal reinforcement at the confined boundary of the wall. Influential parameters were chosen according to the correlation coefficients and used to generate a regression model. Equation (2) expresses the yield drift ratio in terms of the wall length (L_w) and the longitudinal boundary reinforcement ratio (ρ_b).

$$\Delta_y = 0.125(e^{-0.116L_w})(\rho_b^{0.225})) \tag{2}$$

3 Experience-Based Database of RC Structural Walls

As mentioned before, the database was developed for model quality evaluation purposes. It includes nearly 300 wall specimens from about 48 sources (See Table 1 in [7]). Based on the FEMA356 [3] definition, walls with aspect ratios less than 1.5 were considered as squat which accounted for the majority of the walls (68%). Walls with aspect ratios more than 3.0 were considered as slender according to the same guidelines. Only 5% of the walls fell in this category. The rest of the walls were assumed to be transition walls with aspect ratios between 1.5 and 3 (27% of the walls). In order to fulfill the purpose of the database development, several input/output parameters were recorded for each specimen. The input parameters included geometry, material, reinforcement layout and loading properties of the walls. Three parameters defined the geometrical properties, namely, H/L the wall aspect ratio and A_b/A (L_b/L) the boundary area (length) ratio. The reinforcement layout was characterized through A_{svw}/A_w web vertical, $A_{shw}/s_w t_w$ web horizontal, A_{svb}/A_b boundary vertical and $A_{shb}/s_b t_b$ boundary horizontal reinforcement ratios. The concrete compressive strength f'_c and the reinforcement yield strength f_y determined the material properties. Finally, the axial loading ratio was specified by $P/(f'_c.A)$.
In the above terms: A_b, A_w and A are the boundary, web and total areas, respectively. A_{svw} and A_{shw} (A_{svb} and A_{shb}) denote, in the same order, the web (boundary) vertical and horizontal reinforcement areas. s_w and s_b are the horizontal reinforcement spacing in the web and boundary, respectively. The other parameters are presented schematically in Figure 2.

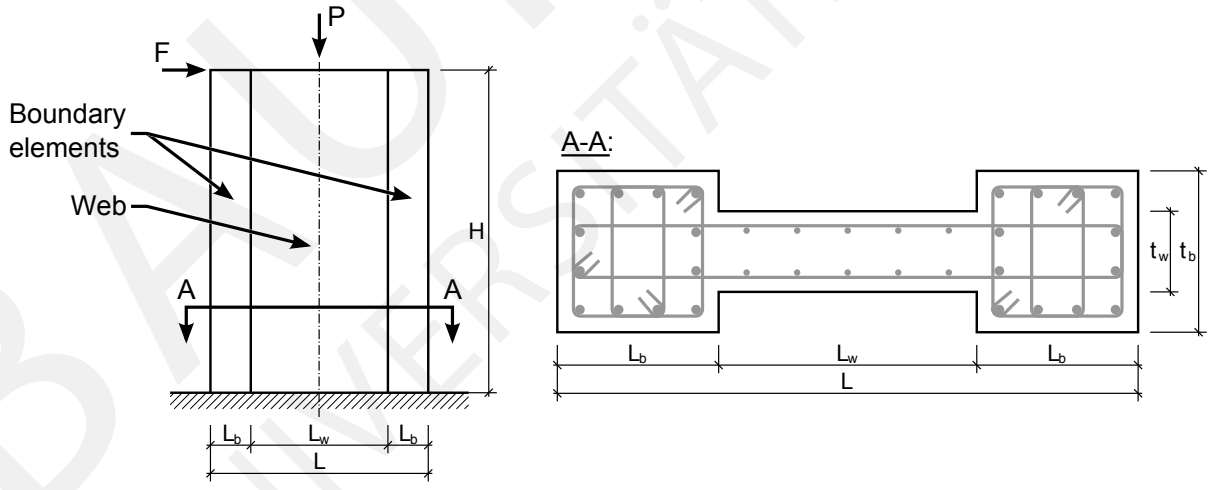

Figure 2: Schematic of the studied walls and the corresponding parameters.

It should be noted that in the present study only the results from 136 walls, comprising of 41% transition and 56% squat walls, are discussed. Table 1 presents the 5% and 95% quantiles for the recorded parameters of these walls.

Table 1: 5% and 95% Quantiles of the studied parameter ranges.

	Squat walls		Transition walls	
	Quantile			
Parameters	5%	95%	5%	95%
1. Aspect ratio	0.5	1.4	1.8	3.0
2. Boundary area ratio	0.00	0.55	0.00	0.59
3. Boundary length ratio	0.00	0.40	0.00	0.43
4. Web vertical reinforcement ratio	0.0000	0.0158	0.0021	0.0150
5. Web horizontal reinforcement ratio	0.0013	0.0110	0.0024	0.0160
6. Boundary vertical reinforcement ratio	0.0000	0.0830	0.0000	0.0922
7. Boundary horizontal reinforcement ratio	0.0000	0.0227	0.0000	0.0382
8. Concrete compressive strength [MPa]	15.6	46.3	20.2	63.7
9. Steel yield strength [MPa]	294.2	664.1	216.0	753.0
10. Axial load ratio	0.00	0.14	0.00	0.24

For each wall in the database the force-deformation relationship was also recorded as the main output. Various output parameters (such as the yield/ultimate point, ductility and so forth) could be derived from the mentioned relationships. Such parameters characterize the behavior of RC walls. Therefore, their study leads to a better understanding of this behavior. Here, we focus on the yield displacement calculation based on the selected methods described in the previous section. More information regarding the database can be found in [7].

4 Discussion of the Results

As mentioned before, five different methods of calculating the yield displacement were applied to the RC walls collected in the database. For the bilinearization methods, the backbone force-deformation curves were used to find the idealized bilinear curves and the corresponding corner yield points. During the application of the method by Paulay & Priestley [8] the ideal yield strength was assumed to be equal to the maximum strength of the specimens. In case of the methods based on formulations, the yield displacements were calculated by replacing the variable parameters by the values taken from the database.
Figure 3 shows the studied force-deformation curves along with the computed yield points. Two different categories can be observed, in this figure, based on how the methods estimate the yield displacement. In the first category, including Paulay & Priestley [8] and FEMA273 [2], the estimated yield displacements are in the vicinity of where a sever stiffness reduction occurs i.e. the global yielding location. In the second category, however, the results are not only limited to specific drift ratios but also unrelated to the global yield point. Methods based on the formula from Priestley et al. [9] and Kazaz et al. [6] fall in this category. The aforementioned misleading estimation could be due to the fact that such formulations disregard parameters that might affect yielding. The method based on ATC40, can be considered in between the two defined categories. Although, its results seem to follow a pattern in a bounded range, the method generally fails because of underestimation.

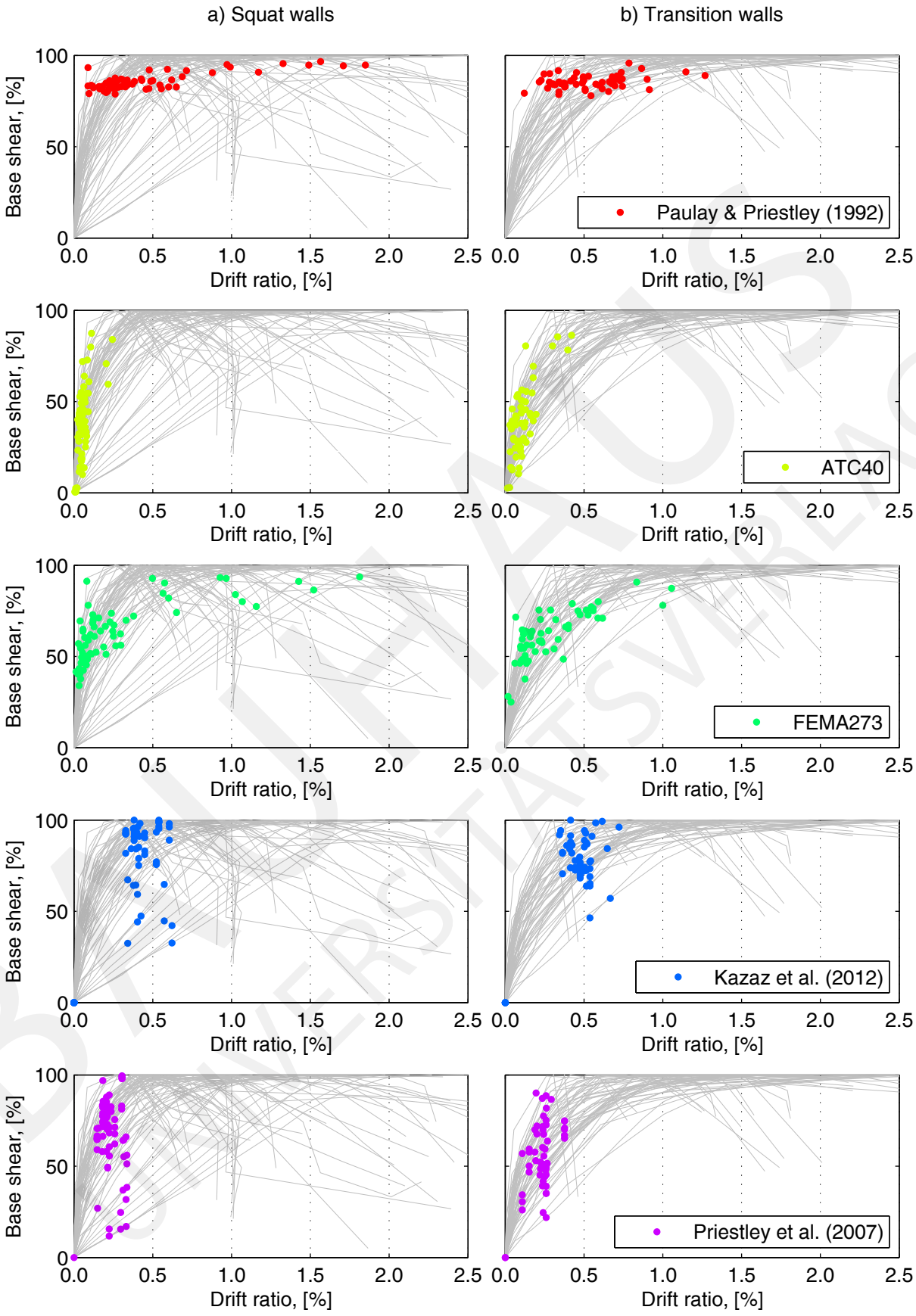

Figure 3: Yield point located based on the studied methods (Base shear is normalized to the maximum shear for each wall).

In order to investigate the uncertainty properties of the methods each parameter range was divided into three slices of equal probability. This is an step in performing variance-based sensitivity analysis by direct approximation of the means. In each slice the mean value and the variance of the samples were calculated. Figure 4 shows the distribution of the means along the parameter ranges. The corresponding standard deviations are presented in Tables 2 and 3. Figure 4 clearly shows that not only the methods have quite different behaviors along the parameter ranges but also their differences depend on the parameter value. Taking the boundary vertical reinforcement as an example, we can see that convergence of the methods in the smaller values of the parameter is considerably more than in the larger values. In addition to Figure 4, Tables 2 and 3 provide some interesting information. According to these tables, for instance, the two underestimating methods, namely ATC40 and Priestley et al. (2007), have the least scatter along all the parameters. Such uncertainty/sensitivity properties can be used to rank the models based on their competency. This is the topic of a future publication.

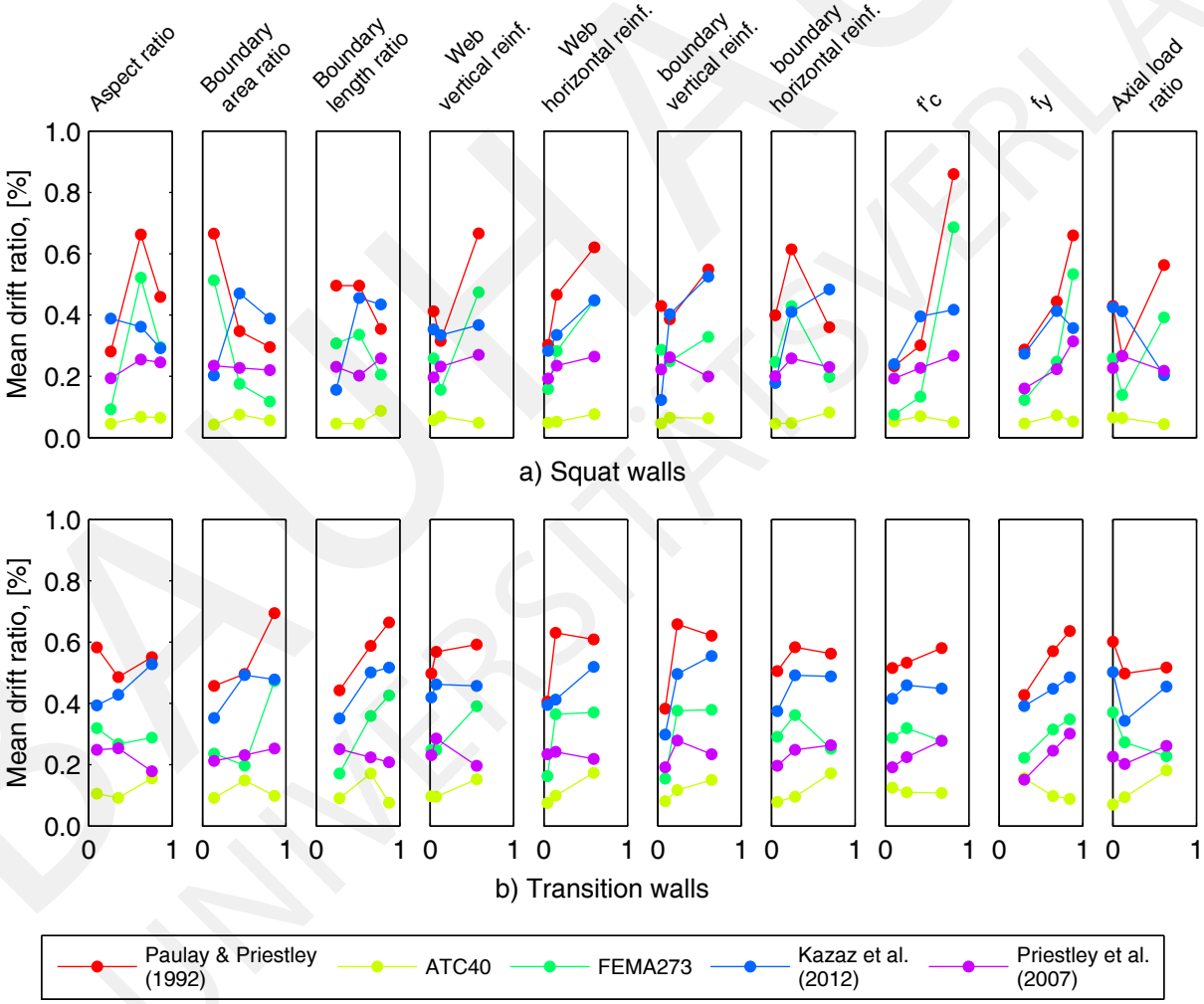

Figure 4: Distribution of the average yield displacement along the studied parameter ranges (Parameter ranges are normalized to fit in the [0 1] interval. Actual parameter ranges are presented in Table 1).

Table 2: Standard deviation of the yield displacement for the squat walls along the parameter ranges, [%].

	Three slices along the parameter range:														
	Paulay			ATC40			FEMA273			Kazaz			Priestley		
Para.	1	2	3	1	2	3	1	2	3	1	2	3	1	2	3
1	0.1	0.6	0.2	0.0	0.1	0.0	0.1	0.6	0.3	0.2	0.2	0.2	0.0	0.1	0.1
2	0.5	0.2	0.1	0.0	0.1	0.0	0.5	0.2	0.1	0.2	0.1	0.0	0.1	0.1	0.0
3	0.4	0.5	0.2	0.0	0.0	0.1	0.4	0.5	0.2	0.2	0.1	0.1	0.1	0.1	0.0
4	0.4	0.2	0.4	0.1	0.0	0.0	0.4	0.2	0.4	0.2	0.2	0.2	0.1	0.1	0.1
5	0.2	0.4	0.5	0.0	0.0	0.1	0.2	0.4	0.5	0.2	0.2	0.1	0.1	0.1	0.1
6	0.5	0.3	0.4	0.0	0.0	0.1	0.4	0.3	0.5	0.2	0.0	0.1	0.1	0.1	0.1
7	0.4	0.5	0.2	0.0	0.0	0.1	0.4	0.5	0.2	0.2	0.1	0.1	0.1	0.0	0.1
8	0.1	0.2	0.5	0.0	0.1	0.0	0.0	0.1	0.5	0.3	0.1	0.2	0.1	0.0	0.1
9	0.2	0.4	0.5	0.0	0.1	0.0	0.1	0.4	0.5	0.3	0.2	0.1	0.0	0.0	0.0
10	0.2	0.3	0.6	0.1	0.0	0.0	0.3	0.2	0.6	0.1	0.1	0.3	0.1	0.1	0.1

Parameters

1: Aspect ratio
2: Boundary area ratio
3: Boundary length ratio
4: Web vertical reinforcement ratio
5: Web horizontal reinforcement ratio
6: Boundary vertical reinforcement ratio
7: Boundary horizontal reinforcement ratio
8: Concrete compressive strength [MPa]
9: Steel yield strength [MPa]
10: Axial load ratio

Table 3: Standard deviation of the yield displacement for the transition walls along the parameter ranges, [%].

	Three slices along the parameter range:														
	Paulay			ATC40			FEMA273			Kazaz			Priestley		
Para.	1	2	3	1	2	3	1	2	3	1	2	3	1	2	3
1	0.2	0.2	0.3	0.0	0.0	0.1	0.3	0.2	0.2	0.2	0.1	0.2	0.1	0.0	0.1
2	0.3	0.2	0.2	0.1	0.1	0.0	0.2	0.1	0.2	0.3	0.1	0.1	0.1	0.1	0.0
3	0.2	0.2	0.2	0.0	0.1	0.0	0.2	0.2	0.3	0.2	0.1	0.0	0.1	0.0	0.1
4	0.2	0.3	0.2	0.1	0.0	0.1	0.2	0.3	0.3	0.2	0.1	0.2	0.1	0.1	0.1
5	0.1	0.2	0.2	0.0	0.0	0.1	0.1	0.3	0.2	0.1	0.2	0.2	0.1	0.1	0.0
6	0.1	0.2	0.2	0.0	0.1	0.1	0.1	0.3	0.2	0.2	0.0	0.1	0.1	0.1	0.1
7	0.3	0.3	0.1	0.0	0.0	0.1	0.3	0.3	0.2	0.2	0.1	0.1	0.1	0.0	0.1
8	0.3	0.3	0.1	0.1	0.1	0.0	0.2	0.3	0.2	0.2	0.1	0.1	0.1	0.1	0.1
9	0.2	0.3	0.2	0.1	0.1	0.0	0.1	0.3	0.3	0.3	0.1	0.1	0.1	0.0	0.1
10	0.2	0.3	0.2	0.0	0.0	0.1	0.3	0.2	0.2	0.1	0.2	0.2	0.1	0.1	0.1

Parameters

1: Aspect ratio
2: Boundary area ratio
3: Boundary length ratio
4: Web vertical reinforcement ratio
5: Web horizontal reinforcement ratio
6: Boundary vertical reinforcement ratio
7: Boundary horizontal reinforcement ratio
8: Concrete compressive strength [MPa]
9: Steel yield strength [MPa]
10: Axial load ratio

5 Conclusions

The yield displacement was computed according to five different methods for a collection of RC walls which belonged to an experience-based database. Comparison of the methods based on the data taken from experience-based database facilitates the reliability and quality assessment of the methods. Comparison of the results from different methods revealed that the methods based on the global response are more successful in predicting the global yielding phenomena. These methods are mainly working with bilinearization techniques. The methods based on local response tend to estimate the same yield drift ratios for different walls which can be far from the physical yielding. This might be a result of ignoring several parameters in the formation of the relationship for yield displacement calculation.

References

[1] ATC-40: Seismic Evaluation and Retrofit of Concrete Buildings, 1996.

[2] FEMA273: NEHRP Guidelines for the Seismic Rehabilitation of Buildings, 1997.

[3] FEMA356: Prestandard and Commentary for the Seismic Rehabilitation of Buildings, 2000.

[4] M. M. Ibrahim. *Linear and Nonlinear Flexural Siffness Models for Concrete Walls in High-Rise Buildings*. PhD thesis, University of British Columbia, 2000.

[5] K. KADAŞ. Influence of Idealized Pushover Curves on Seismic Response. Master's thesis, Middle East Technical University, 2006.

[6] I. Kazaz, P. Gulkan, and A. Yakut. Deformation Limits for Structural Walls with Confined Boundaries. *Earthquake Spectra*, 28(3):1019–1046, 2012.

[7] S. Marzban, A. Almasi, and J. Schwarz. Reinforced Concrete Structural Wall Database Development for Model Validation. In *2nd European Conference on Earthquake Engineering and Seismology*, Istanbul, Turkey, August 25-29 2014.

[8] T. Paulay and M. J. N. Priestley. *Seismic Design of Reinforced Concrete and Masonry Buildings*. John Wiley & Sons, 1992.

[9] M. J. N. Priestley, G. M. Calvi, and M. J. Kowalsky. *Displacement-Based Seismic Design of Structures*. IUSS Press, Pavia, Italy, 2007.

Probabilistic design of relief wells systems as piping mitigation measure.

Carlos Miranda[1,2*], **Ana Teixeira**[2+], **Maximilian Huber**[2++], **Timo Schweckendiek**[1,2**]

[1] Delft University of Technology, Delft, The Netherlands
[2] Deltares, Delft, The Netherlands
*Carlos.Miranda@deltares.nl
+ Ana.Teixeira@deltares.nl
++ Maximilian.Huber@deltares.nl
** Timo.Schweckendiek@deltares.nl

Abstract Nowadays there is an on-going discussion about piping safety for dikes in the Netherlands. Relief wells represent an attractive solution as mitigation measure against piping, saving hinterland space. Nevertheless, they have been disregarded due to the uncertainties in its performance over its life cycle. The aim of this contribution is to demonstrate a probabilistic design of relief wells systems using fully and approximated probabilistic methods. We compare the results with the reliability target for piping as set in the Netherlands. For this purpose, statistical parameters of the influencing variables were studied, using collected data from existing projects or field observations in the Netherlands. Within this, we used the the design approach for relief wells, as proposed by U.S. Army Corps of Engineers.

1 Introduction

Netherlands is historically known for its continuous battle against flooding. The Netherlands has 3,600 km of dikes and dunes. These primary flood defences given in figure 1 are evaluated every five years. According to the last assessment of primary flood defences in 2013 [3], 680 km of dikes do not fulfil these given safety requirements.

Piping is a type of regressive erosion underneath a dike. This erosion process starts downstream and progresses upstream until it reaches the water source (e.g. river), creating pipes underneath the structure, which could lead to its collapse.

Up to now, design methods have been based on the use of semi-probabilistic safety factors for load and resistance parameters. These different safety factors are based on expert knowledge or probabilistic analyses on an acceptable low probability of failure. Latest developments in reliability (probabilistic) based design and the possibility to perform numerous computations allow introducing uncertainties from all the involved variables into the performance functions. This allows determining the probability of failure of the system, which will lead towards a more "rational" design, without the need of safety factors, which sometimes are not specified on design codes.

This contribution focuses on the probabilistic based design of relief wells. This includes the basics for the design of relief wells, the discussion of the limitations and strength of the proposed approach and a case study at the end of this contribution.

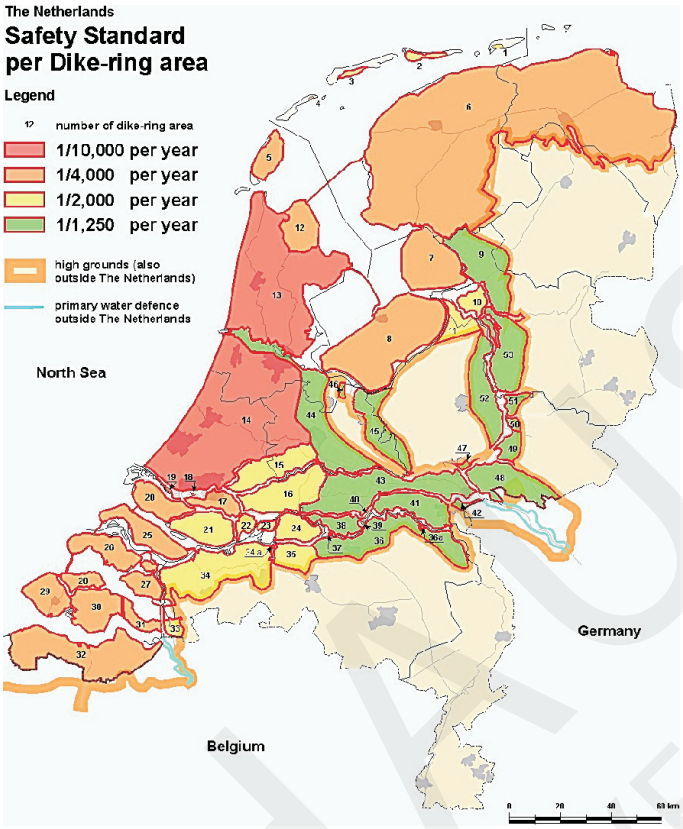

Figure 1: Safety standards per dike ring area in the Netherlands, [9].

2 Relief wells

Relief wells are drainage systems in confined aquifers as shown in figure 2; relief wells are one of the possible mitigation measure against failure due to the piping mechanism. They consist of a riser pipe drilled in the soil through the impervious strata until the previous strata, allowing the underwater to reach the free surface, relieving the pore water pressure. Screens and filters are needed in order to avoid loss of coarse fine material and prevent clogging, which can lead to a decrease in wells' efficiency. A system of partially or fully penetrated wells is needed in order to obtain a reduced ground-water level and to ensure an allowable level. The goal of this design is to find the position of such wells in order to acquire the design requirements.

2.1 Design approach for relief wells

In general, one can distinguish between two system of relief wells: the fully penetrated wells in figure 3 (a) and the partially penetrated wells in figure 3 (b). We assume that the drawdown of the hydraulic head in relief wells is in accordance to Dupuit Forchheimer assumption [1]. In the case of fully penetrated wells in figure 3 (a) the maximum hinterland head will always occur midway between wells. For partially penetrated wells in figure 3 (b) the efficiency is reduced through a smaller available flow discharge. Additionally, partial

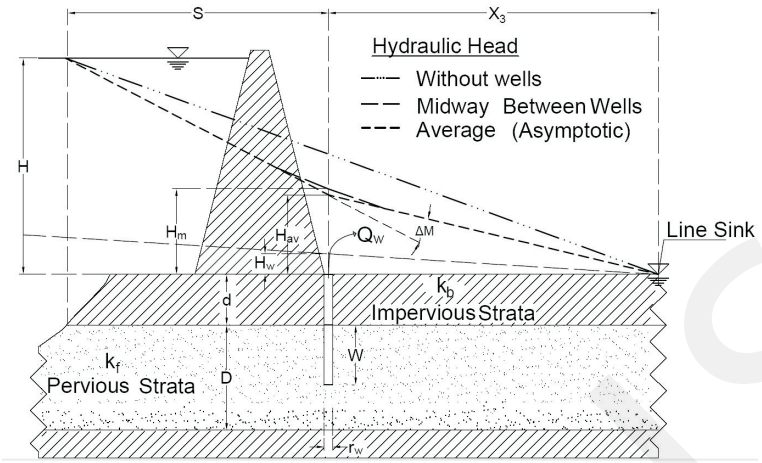

Figure 2: Nomenclature for relief wells system.

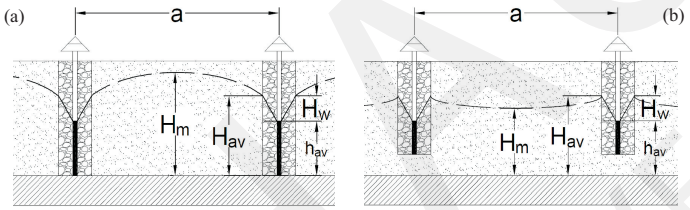

Figure 3: Hydraulic head in relief wells system for fully penetrated wells (a) and partially penetrated wells (b).

penetration induces a vertical flow and increases the velocity in the vicinity of the well; this increases the head losses. This effect decreases while moving away from the well and leads the maximum head to be on wells' plane.

We use the semi-empirical method, which is proposed by USACE [11], to evaluate the potential at the exit point in a multiple well systems. The procedure and formulas to apply are described in detail at [5]. We consider the head at well's plane H_{av} and the head between wells H_m given in equation 1 and 2, which are used to calculate net seepage slope ΔM. Figures 2 and 3 shows the head at well's plane H_{av} and the head between wells H_m for fully and partially penetrated wells.

$$H_{av} = a \cdot \Delta M \cdot \theta_a + H_w \tag{1}$$

$$H_m = a \cdot \Delta M \cdot \theta_m + H_w \tag{2}$$

$$\Delta M = f(H, H_{av}, S, X_3) \tag{3}$$

In equation 1 and 2 a refers to the well spacing given in figure 3. The net seepage slope (ΔM) is defined as the difference between the slope formed in front of the well; from ΔH and H_{av} , and the hinterland slope in figure 2. θ_a and θ_m are the so called well factors which are function of: D/a, W/D and a/r_w. The hydraulic heads (H_{av} and H_m) are

corrected by adding the well losses H_w. The rest of the involved variables are given in the appendix.

2.2 Limitations of USACE method

Using the proposed USACE method for the design of relief wells, one has to keep the limitations of this approach in mind. The main limitation of the USACE method is the assumption of laminar flow. According to [1], we also assume 1 as a maximum Reynolds number value, which is a safe limit taking into account that the Reynolds number is highly sensitive to sand characteristic diameter. The method shows for practical application a limitation due to well factors which were determined for a given range of the ratio between well spacing (a) and aquifer's thickness ($0.25 < D/a < 4$); this limits to find the solution in between those limits. These losses can be estimated from experimental data, given in [10].

3 Probabilistic design of relief wells system

In order to reduce the complexity of the given system of relief wells, we consider only heave and uplift in the sequel case studies. The probability of failure of the system P_f is, therefore, a parallel system of the probability of failure for uplift $P_{f,u}$ and for heave $P_{f,h}$ given in equation 4. We do not consider piping because there is not a method to consider this mechanism when drainage systems are applied.

$$P_f = P_{fu} \cap P_{fh} \tag{4}$$

We use the FORM and the Monte-Carlo approach for the case of piping mechanism under a dike.

3.1 Limit state functions

The limit state function defines the ultimate state of a mechanism, which is the boundary between desirable and undesirable performance of the mechanism considered. High water pressure in the sand layer under the impervious strata (blanket) can cause uplifting and even cracking of this layer. The limit state function for uplift is defined by the difference of resistance, which is the vertical effective stress at the bottom of the cover layer, and the load, which is the average head of the well H_{av} and the average head between wells H_m (equation 5). Heave can only occur, if the vertical gradient at the exit point exceeds the critical value for heave i_c. The limit state equation compares the critical gradient for heave and the existing vertical gradient on the blanket as given in equation 6.

$$Z_u = \frac{d \cdot (\gamma_s - \gamma_{water})}{\gamma_{water}} - \max\{H_{av}, H_m\} \tag{5}$$

$$Z_h = i_c - \frac{\max\{H_{av}, H_m\}}{d} \tag{6}$$

We use equation 7 within the Monte-Carlo approach for the simulation of the combination of uplift and heave.

$$Z_{u+h} = \max\{Z_u, Z_h\} > 0 \tag{7}$$

Additionally, we use the established Hohenbichler Rackwitz approach [2] to combine the uplift and heave mechanism within FORM.

3.2 Random variables

The basis for random variables are given in [4] and [6,7]. We assume the gravity acceleration g, the well radius r_w, the well thickness t_p and the specific weight of the water γ_w as deterministic variables. We summarize the random variables with type of distribution, mean value and standard deviation in table 1.

3.3 Target reliability for piping

In order to obtain a probabilistic design we set our target based on the reliability of the system. Reliability is a measure of the probability that our system does not fail. The reliability index is defined as:

$$\beta = -\Phi^{-1}(P_f) \tag{8}$$

Herein,β is the reliability index, Φ^{-1} is the inverse of the standard normal cumulative distribution function, and P_f is the probability of failure of our system.

Dikes are usually long structures, which are influenced by longitudinal spatial variations. This spatial variation is considered via the length effect. The length effect is defined

Table 1: Distribution type of the random variables, mean values μ, standard deviations σ used for the design of the relief wells system in case study A and case study B.

	pdf	Case study A		Case study B	
		μ	σ	μ	σ
γ_{cover} [kN/m^3]	normal	16.00	1.60	17.10	1.70
γ_w [kN/m^3]	determ.	10.00	-	10.00	-
d [m]	lognormal	3.00	0.15	4.11	1.23
D [m]	normal	26.30	5.05	9.30	3.00
k_f [m/s]	lognormal	$1.74{\cdot}10^{-4}$	$3.29{\cdot}10^{-4}$	$5.79\ {\cdot}10^{-4}$	$7.56{\cdot}10^{-4}$
k_b [m/s]	lognormal	$1.16{\cdot}10^{-6}$	$1.16{\cdot}10^{-6}$	$1.16{\cdot}10^{-6}$	$1.16{\cdot}10^{-6}$
h_r [m]	Gumbel	-3.79	0.30	-8.45	0.30
h_p [m]	normal	4.30	0.25	8.70	0.10
H_e [m]	lognormal	0.05	0.05	0.05	0.05
S [m]	normal	28.50	3.42	22.86	2.29
C [-]	normal	125	10	125	10
r_w [m]	normal	0.15	0.00	0.15	0.00
i_c [-]	lognormal	0.70	0.10	0.70	0.10

as the increase of the failure probability with the length of the dike due to imperfect correlations and/or independence between different cross sections and/or elements [8]. This indicates that decrease of the system reliability with the increase of its length. In order to be able to perform a probabilistic design, the reliability target has to be defined. Different researches [8] developed the formulation presented on equation 9 for translating dike ring requirement 1 into a (local) cross section safety requirement for piping and uplift.

$$P_{adm,loc} = \frac{0.1 \cdot P_{adm,ring}}{1 + \frac{\alpha}{l_{eq}} * L_{dr,s}} \tag{9}$$

Herein, $P_{adm,loc}$ stands for the local admissible failure probability, $P_{adm,ring}$ for the admissible failure probability for the dike ring requirements, $\frac{\alpha}{l_{eq}}$ is the length effect factor, and $L_{dr,s}$ is the length of the dike that is sensitive to the considered mechanism. Among others, [8] reports the ratio is $\alpha/l_{eq} = 0.0028$ for piping and $\alpha/l_{eq} = 0.0045$ for uplift.

4 Case studies

In this section we investigate the design of relief wells within a probabilistic based design framework in two case studies. We selected a cross section located in dike ring 36 for case study A and and a cross section in dike ring 52 for case study B, given in figure 1. The data for these two locations are given in table 1. One can derive from figure 1 that both locations have a required probability of failure of $1/1,250$ years. For both, 10 km of the dike stretches, which are sensitive to piping are considered and one can calculate the target reliability $\beta_{adm,loc} = 4.5$ using equation 9. We investigate several combinations of well spacing and well penetration in order to cover all possible combinations. We show the results of case study A and B in figure 4. The reliability index β is plotted as contour lines among the possible combinations of well spacing a and well penetration W/D, delimiting zones with equal reliability target. From the results we can derive that large ratios W/D

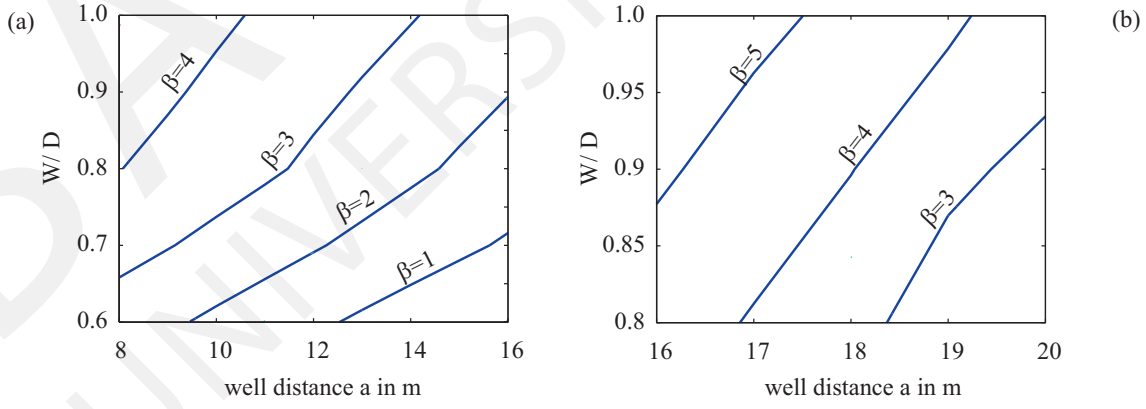

Figure 4: Ratio of well penetration W and thickness of the aquifer D in relation to the well distances a for different reliability indices β for case study A (a) and case study B (b).

and small well distances a show high reliability indices. For the investigated cases one

can see that in case of a reliability index $\beta \geq 4.5$ fully penetration is needed (figure 4).

The FORM-sensitivity factors α^2 for the investigated cases are given in figure 5. We present them grouped on basis of W/D and show them for two different ratios of D/a. It can be observed that there is a significant scatter among the sensitivity factors. From figure 5 (a) and (d) we can observe that for partial well penetration the blanket permeability is the driven variable. For fully penetration, entrance losses are the driven variable. On the other hand, in 5 (d), larger well spacing, blanket and aquifer permeability's are the driven variables despite well penetration. In case of having small well spacing one can see in 5 (b) that the influence of the specific weight of the blanket is lower than when having larger well spacing.

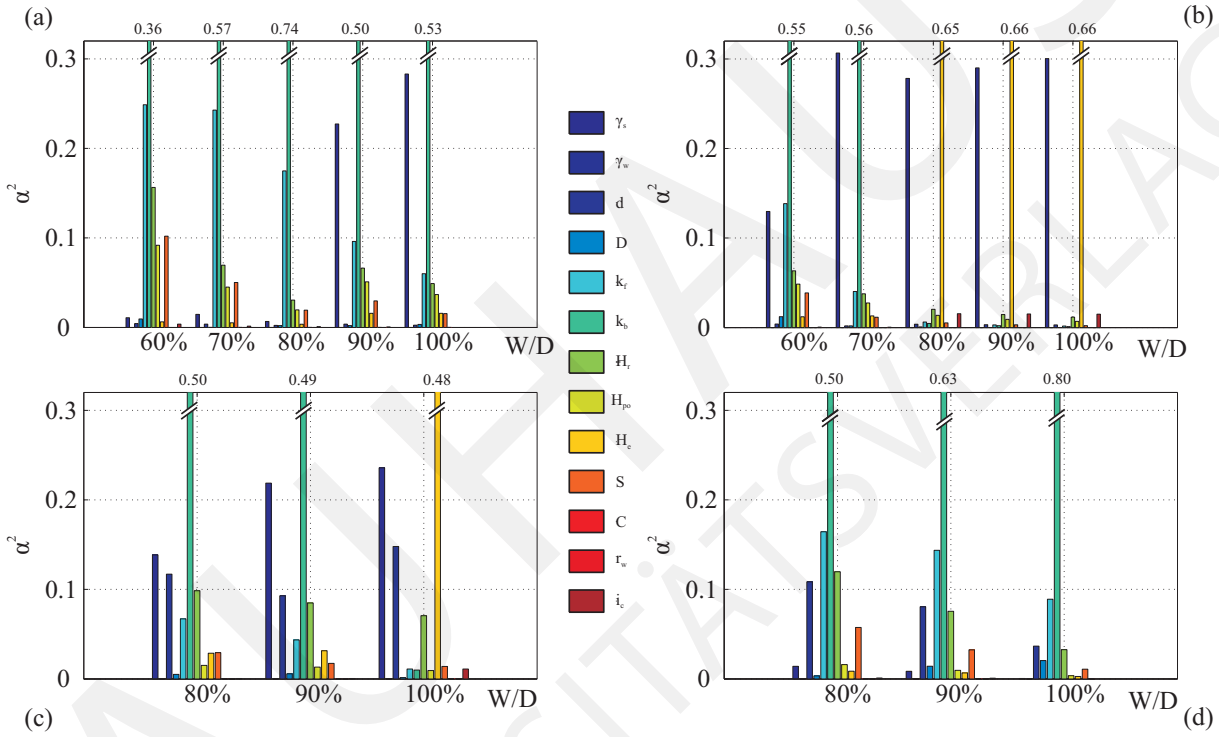

Figure 5: Sensitivity factors for cases for different well penetration D/a =1.6 in case study A (a), D/a =2.6 in case study A (b), D/a =0.6 in case study B (c) and D/a =0.46 in case study B (d).

5 Conclusions

This contribution presents the application of a probabilistic design of relief wells for piping mitigation solution. Within this, we use the USACE relief wells' design procedure in the framework of a probabilistic based design. Herein, the length effect due to the soil spatial variability is considered, as well as the combination of the sub-failure modes heave and uplift as a parallel system to achieve piping failure. Two case studies were investigated, and each uncertainty studied to identify which are the most important and influential in the evaluation of the performance of relief wells. FORM-sensitivity coefficients show that,

using USACE method, the blanket and the aquifer permeability, as well as the hydraulic losses, are the dominant variables (from the 'load' side). However, a high discrepancy between these sensitivity coefficients was found for 'strength' side in partially and fully penetrated wells. As result of the reliability analysis, graphs like 4 shows the appropriate combinations of the design variables which fulfil our safety requirements. The optimum alternative should then be chosen after a cost analysis optimization, the core of such analysis can be found in [5].

References

[1] R. A. Barron. Mathematical theory of partially penetrating relief wells. Technical report, US Army Engineer Waterways Experiment Station, 1982.

[2] M. Hohenbichler and R. Rackwitz. First-order concepts in system reliability. *Structural Safety*, 1(3):177–188, 1983.

[3] Inspectie Verkeer en Waterstaat. Assessment of primary flood defences in The Netherlands. Technical report, Inspectie Verkeer en Waterstaat, 2006.

[4] R. Jongejan, B. Maaskant, W. ter Horst, and N. Harry F. Havinga. The vnk2-project: a fully probabilistic risk analysis for all major levee systems in the netherlands. *IAHS Publ*, 357:75–85, 2013.

[5] C. Miranda. Probabilistic design of relief wells as piping mitigation measure. Master's thesis, Delft University of Technology, 2014.

[6] K.-K. Phoon and F.H. Kulhawy. Characterization of geotechnical variability. *Canadian Geotechnical Journal*, 36:612–624, 1999.

[7] K.-K. Phoon and F.H. Kulhawy. Evaluation of geotechnical property variabaility. *Canadian Geotechnical Journal*, 36:625–639, 1999.

[8] T. Schweckendiek. Target reliabilities and partial factors for flood defenses in the netherlands. In P. Arnold, G.A. Fenton, and M. A. Hicks, editors, *Modern Geotechnical Design Codes of Practice*, pages 311 – 328. IOS Press, 2012.

[9] Technical Advisory Committee for Flood Defences (TAW). Fundamentals on water defences. Technical report, Technical Advisory Committee for Flood Defences (TAW), 1998.

[10] U.S. Army Corps of Engineers. Design, construction and maintenance of relief wells. Technical report, USACE, 1992.

[11] US Army Corps of Engineers, editor. *Seepage Analysis and Control for Dams: Engineering and Design*, volume 1110. U.S. Army Corps of Engineers, 1993.

Probabilistic Modelling of Radionuclide Transport Evaluation for Geological Disposal in Meuse/Haute-Marne, France

Sitakanta Mohanty, Stuart Stothoff, Michael Muller

Southwest Research Institute
6220 Culebra Road
San Antonio, Texas, USA 78228
smohanty@swri.org

Marc Bourgeois, Amelie de Hoyos, Gregory Mathieu, Delphine Pellegrini

Institut de Radioprotection et de Sûreté Nucléaire
PRP-DGE/SEDRAN/BERIS
BP 17, 92262 Fontenay-aux-Roses Cedex, France
gregory.mathieu@irsn.fr

Abstract. This paper presents a probabilistic framework, referred to as the MC-MELODIE hydrologic flow and contaminant transport code, for analyzing flow and transport behavior in the context of intermediate-level long-lived waste and high level waste disposal foreseen in a deep geological formation at the Meuse/Haute-Marne site in France. The flow and transport framework includes geological features, detailed drifts, and shaft/ramp configurations in the host formation. One-million-year probabilistic simulations, considering normal and altered evolution scenarios, showed ∼5 to 6 orders of magnitude variation in peak activity fluxes, with peaks occurring mainly in a few hundreds of thousands of years. Scatter plots and regression equations revealed that only a few sampled parameters contribute significantly to the uncertainty in peak activity fluxes.

1 Introduction

In December 2005, the French national radioactive waste management agency (Andra) presented to the French government the results of a feasibility study for a radioactive waste disposal facility (i.e., repository) for intermediate-level, long-lived waste (IL-LLW) and high level waste (HLW) in a deep geological formation at the Meuse/Haute-Marne (MHM) site in France [2, 1], called the "Cigéo project." The 2005 study was later updated to take into account, notably, a revision of the architecture design and additional knowledge acquired on the host formation's properties [3]. In support of its technical reviews of this project, the French institute for radiological protection and nuclear safety (IRSN) has carried out extensive but focused field-scale experimental and modelling studies [6, 7].

The disposal facility, consisting of a natural and an engineered system, is proposed to be located in the argillaceous Callovo-Oxfordian (COx) formation. Andra's reports [2, 1] describe the COx as a low-permeability formation that is homogeneous over a large area, has few to no faults, and has very low water flow. The overlying and underlying limestone formations are reported to have low permeability and rather slow water flow

rates. These characteristics are expected to prevail over a 250-km^2 area called the "zone de transposition".

Mined openings in the low-permeability host formation can represent preferential flow paths. The engineered system isolates waste containers from water flow using low-permeability clayey materials, among other features. Such materials, if emplaced at the entrance of the disposal cells (cell seals and plugs), in the drifts (drift seals), and in the shafts and ramps at the level of the top of the COx formation (shaft and ramp seals), could minimize water flow along the axes of the engineered components of the disposal facility. Limiting such a flow would, in turn, limit and delay the release and transport of radionuclides to and through the shafts and ramps, and thus to the surface.

The current probabilistic modelling study aims at consolidating the deterministic modelling approach commonly used in France, allowing verification that the various scenarios considered in radionuclide migration modelling account for various possible situations as well as for the remaining uncertainties. In fact, the knowledge of a repository's hydrologic system is inherently uncertain given, for example, the space scale of concern and the heterogeneity of the various parameters to be characterized. The outcome of any hydrologic modelling is thus linked to this uncertainty. The cause–effect relationship between the hydrologic system's calculated performance and input parameter uncertainties must be understood. Probabilistic analyses, especially those based on Monte Carlo (MC) methods, can be effectively used as an avenue to understand trends and relationships in the model outputs resulting from the uncertainty and variability in the input data. Such trends may not be easily discerned from deterministic simulations.

Most probabilistic models rely on variants of the MC method because of the flexibilities that MC methods offer: (i) the process or performance model complexity is not a limitation, (ii) the performance function model does not need to be modified, (iii) large parameter uncertainties can be propagated through the performance function model, (iv) the full model output range is available for deriving statistics, and (v) any sampling-based sensitivity analysis technique (e.g., regression-based methods) can readily be applied to the results.

The objective of the current study is, therefore, to augment the deterministic IRSN flow and transport models into a MC-based probabilistic framework model that calculates an envelope of model outputs as opposed to a single model output. This paper (i) describes the "MC-MELODIE" software used and the resulting probabilistic framework model developed by IRSN with assistance from the Center for Nuclear Waste Regulatory Analyses (CNWRA®) of Southwest Research Institute® (SwRI®), (ii) illustrates the analysis approach, and (iii) presents selected preliminary results.

2 IRSN'S MELODIE flow and transport model

The combined characteristics of the radionuclides, host formation, and engineered barrier system are expected to control activity releases from the waste packages to the surrounding formations. Total activity release from a failed waste package will likely depend on the interplay between diffusion rates, solubility limits, and decay rates. IRSN uses the MELODIE software to simulate radionuclide transport within the COx host formation.

IRSN also uses the MELODIE software to simulate flow and radionuclide transport at a much larger scale, using calculated releases from the COx model described below as a source term applied to a few grid cells. Although the MC-MELODIE approach considers the nested models simultaneously; the present work focuses on just the COx model for simplicity.

MELODIE Software

IRSN's hydrologic flow and transport conceptualization is embodied in the MELODIE software, a numerical tool developed by IRSN [4]. It is specifically developed for long-term assessment of surface and subsurface radioactive waste repositories. MELODIE models fluid flow and contaminant transport in porous media in 2 or 3 spatial dimensions (2D or 3D). The software is designed to model a disposal site factoring in the main physical and chemical characteristics. These are represented in simplified form, adapted to large scales of time and space required for simulation. MELODIE assumes Darcy flow and the transport model handles advection, diffusion, solubility, retention (retardation factor), and radioactive decay chains.

COx Model

The COx model embodies details of the repository, including the shaft and ramp area (Figure 3). In fact, IRSN developed a simplified representation of the facility to focus on the IL-LLW zone, which is closest to the two shafts and two ramps. The overall domain includes a 135-m thick COx host formation block that is 3 km by 2.6 km in the horizontal. The repository is represented by 86 cells receiving radioactive waste. Each cell is a $10 \times 10 \times 530$ m drift. Waste packages are emplaced in the central 450 m of each drift, then the drift is backfilled and sealed at its end with a 40-m plug. Each drift is assumed to be surrounded by an excavation damaged zone (EDZ - where the permeability is significantly larger than the undisturbed COx) grading into a micro-fissured zone (where the permeability is slightly larger than the undisturbed COx), as shown in Figure 1 and Table 1. Backfilled access drifts connect the 86 cells to a set of two backfilled ramps and two backfilled shafts, which connect the facility to the surface. Due to the mineralogy of the upper part of the COx formation (higher carbonate content), a micro-fissured zone is expected to appear around the ramp and shaft seals, but an EDZ is not expected to appear.

Boundary conditions include (i) a no-flow boundary on the four lateral sides and (ii) zero activity concentration at the bottom and top faces. These top and bottom boundary conditions maximize radionuclide releases to the overlying and underlying aquifers. At the COx scale, the focus is primarily on two transfer pathways: (i) diffusive transport through the host formation, and (ii) advective transport through the drifts to the exits of the ramps and shafts. The source term is conservatively assumed to consist of one radionuclide (I-129) instantaneously released in all 86 cells, primarily to understand the transport behavior. I-129 is considered soluble and non-sorbing in all the porous media. The repository and surrounding host formation are discretized into 2,001,391 node points and 11,404,800 tetrahedral elements.

The parameters defining this system include the flow and transport properties of (i) the COx host formation and (ii) the engineered system, as well as the hydraulic gradient across the COx (for vertical upward flow). The COx flow and transport parameters include permeability, kinematic porosity, and diffusion coefficient. The engineered system

parameters include permeability, kinematic porosity, and diffusion coefficient associated with drift, shaft and ramp backfill, concrete, seals, EDZ, and micro-fissured zone. Table 1 presents the values for the COx model's input parameters.

3 MC-MELODIE

As described previously, MC-MELODIE is an MC-method-based probabilistic framework that propagates model input parameter uncertainty and obtains an envelope of model responses (i.e., the output of the performance function representing the hydrologic system). The MC framework uses the MELODIE code for computing flow and transport as the performance function. Each run of MELODIE in the MC-MELODIE framework is a deterministic run. Consequently, each deterministic run is that of a computationally intensive detailed hydrologic flow and transport model that involves the numerical solution of a system of partial differential equations. The MELODIE infrastructure remains unchanged in the MC runs except that its parameters (or models, if specified) are changed from realization to realization.

Sampling: The COx model simulation is computationally intensive, therefore MC-MELODIE uses the Latin Hypercube Sampling (LHS) method [5] as a substitute for the conventional MC method, which can be prohibitively expensive because of its requirement for a large number of realizations (i.e., deterministic model runs) to obtain stable results. LHS's sampling scheme promises to give the same level of coverage of the parameter uncertainty range as the simple sampling of the conventional MC method, but with far fewer realizations (e.g., 100 realizations in the current study).

Selection of Input Parameters: MC-MELODIE includes a variety of statistical distribution functions to represent parametric uncertainty. However, since the deterministic model has a large number of input parameters, constant values are assigned to parameters that are well characterized (less uncertain), are known to have negligible variability, or are known to minimally affect model outputs. For the current study, it was determined whether a constant value or a specific probability distribution function was assigned to a model parameter on the basis of qualitative reasoning, Andra's published parameter values [2, 1], and IRSN's past experience gained through field studies and deterministic sensitivity analysis studies [6, 7]. As Table 1 shows, the probability distribution functions in the system model reflect the stochastic nature of the permeability values and the diffusion coefficient for COx and selected zones associated with the engineered system.

The objective of the sensitivity study was to understand system behavior when using combinations of conservative values deduced from extrema in the distribution ranges. In the end, a total of 5 out of 26 parameters were randomly sampled from specified probability distribution functions. None of the sampled parameters were specified as partially correlated to another sampled parameter; this approach can yield physical inconsistencies and must be kept in mind when interpreting the calculation's preliminary results.

4 Results and discussion

Probabilistic results were obtained from a 100-realization MC simulation with LHS sampling. This sample size was considered to be sufficiently large to give stable results for 5 sampled parameters (i.e., the same trends that one would obtain with a larger number of realizations) while maintaining computational efficiency. Each realization of MC-MELODIE was a one-million-year simulation. The 100 realizations allowed testing parameter extremes and parameter combinations for their potential to cause a simulation to fail. Given the extreme values used, the MELODIE software demonstrated strong robustness.

The MC-MELODIE code is typically operated using two simulations for each realization of the parameters: (i) a steady-state flow simulation and (ii) a transient transport simulation. The COx model is run in this dual-simulation mode. The average run time for the COx model was 1.38 hr on a system with a Hex-core Xeon 5680 64-bit Westmere processor with a core frequency of 3.33 GHz.

In order to understand the behavior of the disposal facility, radionuclide releases are quantified at the outlets of the COx model. On the one hand, activity fluxes (reported in Bq/yr) are estimated at the top and bottom of the COx to evaluate the amount of radionuclides transferred, primarily by diffusion, from the waste packages to these boundaries through the rock; this allows evaluation of the capability of the COx to limit and delay the radionuclide plume to the surrounding aquifers. On the other hand, activity fluxes are assessed at the outlets of the shafts and ramps in order to quantify the amount of radionuclides transferred through the drifts, primarily by advective transport. This allows evaluation of the contribution of the seals to radionuclide transfer to the aquifers, depending on hydraulic flows induced by variations of parameter combinations. An "altered" scenario was also considered that assumes the seals are totally ineffective.

Several approaches for analyzing the simulation results based on scatterplots and regressions were applied to help identify sensitivities and identify likely consequences. To understand the sensitivity of the hydrologic model of the repository site to the input parameters, scatter plots of individual sample parameter versus model output were examined visually as well as mathematically (i.e., through the computation of regression coefficients) to determine which parameters have significant effects on the model prediction of activity flux. If there is a discernible pattern (i.e., slope) in the scatter plot of the values of a sampled input parameter and the corresponding model output values, then the pattern indicates a certain influence of that input parameter on the output. Peak activity flux in terms of magnitude and time of appearance was used as the performance metric for identifying parameter influence on the model outputs.

Six release surfaces were tracked: the top and bottom of the COx and the top of the two shafts and two ramps (Figure 2). The Top and Bottom pathway fluxes show a little over one order of magnitude variation in the activity flux from various realizations. Within each realization, the Top pathway has a slightly larger magnitude than the Bottom pathway, consistent with diffusion-dominated transport slightly modified by the upward flow through the COx. Figure 2 also shows that the peak activity fluxes for the Top and Bottom pathways occur predominantly during the period from 100,000 to 1,000,000 yr. The regression slopes suggest that only a few of these parameters contribute significantly to

the uncertainty in peak activity flux. Fluxes calculated for the Top and Bottom pathways most strongly correlate to the diffusion coefficient in the COx (Figure 3). Other parameters that showed influence, to a much lesser degree, are the permeability of the COx and the vertical upward flow. A few peaks appear before 100,000 yr due to combinations of low porosity values and high diffusivity values in the COx, which are physically inconsistent, leading to an overestimation in the diffusive transport in the host formation.

The shaft and ramp pathway fluxes show a variation of 4 and 6 orders of magnitude, respectively (see Figure 2 for peak flux). The ramp pathways show the lowest activity flux, with the shaft pathway activity fluxes approximately one order of magnitude larger, due to the additional distance for radionuclide transfer to the ramp exit in comparison with the shaft exit. The Top and Bottom pathway activity fluxes are 5 to 6 orders of magnitude greater than the activity fluxes through the ramp and shaft pathways. Hence, the Top and Bottom activity fluxes clearly dominate. The peak activity fluxes for the ramp and shaft fluxes occur over a wider range than for the Top and Bottom pathways, and show a large dependence on seal permeability (see Figure 3). Activity fluxes may peak as early as 20,000 yr when the seal permeability is very large (corresponding to an altered scenario for which the seals are considered ineffective). However, most of the realizations with very small seal permeability have the activity fluxes still increasing at 1,000,000 yr.

The results show that the shaft and ramp fluxes are dependent on the COx permeability as well as on the vertical upward gradient (i.e., COx providing water in the drifts), notably for large seal permeability. The shaft and ramp pathway fluxes also show a small negative dependence on the COx diffusion coefficient. This negative dependence arises from a competition for the available I-129 between advective transport in the engineered pathways and the much larger total diffusive flux in the host formation. Finally, the correlation between shaft and ramp pathway fluxes and the input parameters is poorer than the correlation with the host formation's diffusivity. Factors that may reduce the correlation include: (i) the small values of shaft and ramp pathway fluxes relative to the competing host formation's flux, leading to a loss of precision; and (ii) the coarse resolution of diffusion pathways in the drift seals and EDZ, leading to numerical inaccuracy.

As stated previously, a set of 100 Monte Carlo realizations was considered adequate for the current analyses. The parameters showing poor regression fit (e.g., $R^2 < 0.5$) as such validate our intuition. However, larger LHS sample sets or the Bootstrap method could be used in the future to determine if the R^2 values for the parameters will improve.

5 Conclusions

MC-MELODIE was successfully developed as a probabilistic, detailed, and computationally intensive hydrologic flow and contaminant transport model. By providing an avenue for including the full range of uncertainty in parameters, this framework model is capable of assessing the performance of the hydrologic system under a combination of conservative and realistic conditions. The model was successfully used to (i) understand the relationships between the envelope of model output values and the range of input value combinations and (ii) determine which parameters significantly influence flow and trans-

port in the hydrologic system. The probabilistic approach has been helpful in (i) testing the deterministic model for resiliency against extreme parameter values and (ii) adjusting numerical criteria accordingly to avoid code failures. The COx model showed, considering normal and altered evolution scenarios, <2 orders of magnitude variation in peak activity fluxes through the host rock and ∼5 to 6 orders of magnitude variation through engineered features. Peak fluxes occur mainly in a few hundreds of thousands of years, and are typically 1 to 6 orders of magnitude smaller in the engineered features than in the host rock. Scatter plots and regression equations identified a few sampled parameters contributing significantly to the uncertainty in peak activity fluxes, particularly the diffusion coefficient in the COx. A future paper will highlight other sensitivity analysis methods applied for identifying parameters significant to activity flux.

References

[1] Andra. "Dossier 2005 Argile. Synthesis: Evaluation of the Feasibility of a Geological Repository in an Argillaceous Formation." 2005b.

[2] Andra. "Dossier 2005 Argile. Tome: Safety Evaluation of a Geological Repository." 2005a.

[3] Andra. "Stockage réversible profond – étape 2009: options de sûreté du stockage en formation géologique profonde." 2009.

[4] Bourgeois, M. "MELODIE—Modèle d'Évaluation à Long Terme des Déchets Irradiants Enterrés–Notice Théorique 2002." IRSN/DPRE/SERGD/02-13. 2002.

[5] Iman, R.L., and M.J. Shortencarier. NUREG/CR–3624, SAND83-2365, "A FORTRAN Program and User's Guide for the Generation of Latin Hypercube and Random Samples for Use With Computer Models." Washington, DC: U.S. Nuclear Regulatory Commission. March 1984.

[6] IRSN. "Avis de l'IRSN sur la faisabilité d'un stockage géologique de déchets radioactifs en formation argileuse - Dossier 2005 argile." 2006. http://www.irsn.fr/FR/expertise/rapports_gp/gp-dechets/Pages/Avis-IRSN-Dossier-2005-Argile.aspx.

[7] IRSN. "Rapport sur l'examen mené par l'IRSN du «dossier 2009 »de l'Andra relatif au projet de stockage de déchets radioactifs HA-MAVL en couche géologique profonde." 2010. http://www.irsn.fr/FR/expertise/rapports_gp/gp-dechets/Pages/rapport-IRSN-Dossier2009-Andra-stockage-HA-MAVL.aspx.

Material	Porosity	Hydraulic Conductivity (m/yr)	Diffusion Coefficient (m^2/yr)	Dispersivity (m)	
				Longitudinal	Transverse
COx host formation	0.09	$\log T[3.15 \times 10^{-7}, 1.58 \times 10^{-5}, 3.15 \times 10^{-5}]^*$	$\log N[2.5 \times 10^{-4}, 1.58 \times 10^{-2}]$	6	0.6
	—	Vertical-to-horizontal ratio of 0.5	—		
EDZ	0.1	$\log T[3.15 \times 10^{-3}, 0.157, 3.15]$	2.21×10^{-3}	10	1
Micro-fissured zone	0.1	3.15×10^{-4}	2.21×10^{-3}	10	1
Seals	0.18	$\log T[3.15 \times 10^{-4}, 3.15 \times 10^{-4}, 3.15 \times 10^{-1}]$	3.15×10^{-3}	4	0.4
Backfill	0.1	$\log U[3.15 \times 10^{-1}, 3.15 \times 10^{1}]$	6.31×10^{-2}	10	1

* $\log U[] = log\text{–}uniform[min, max]$; $\log T[] = log\text{–}triangular[min, peak, max]$; $\log N[] = log\text{–}normal[min, max]$. Min and max are the 0.1 and 99.9 percentile values, respectively.

Table 1: Flow and Transport Properties for the Normal and Altered Cases

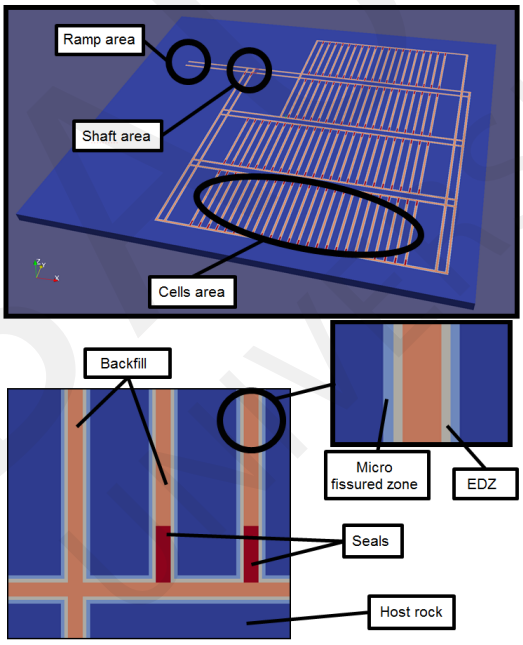

Figure 1: Layout of the COx model.

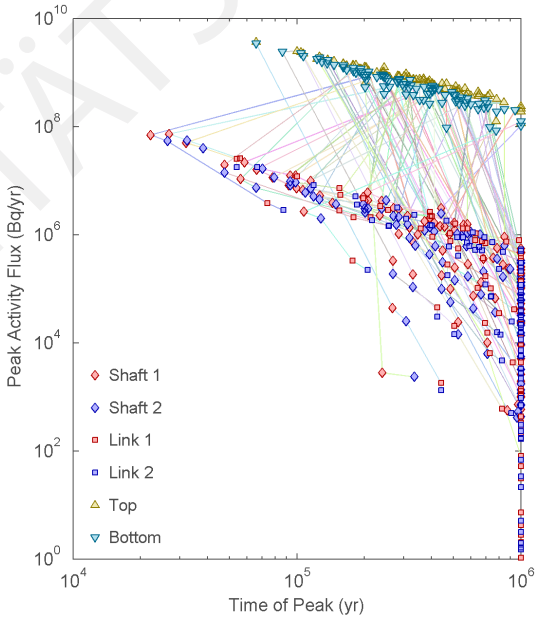

Figure 2: Peak Activity Release for Each Realization and Pathway. The Six Pathways for Each Realization Are Connected With a Colored Line.

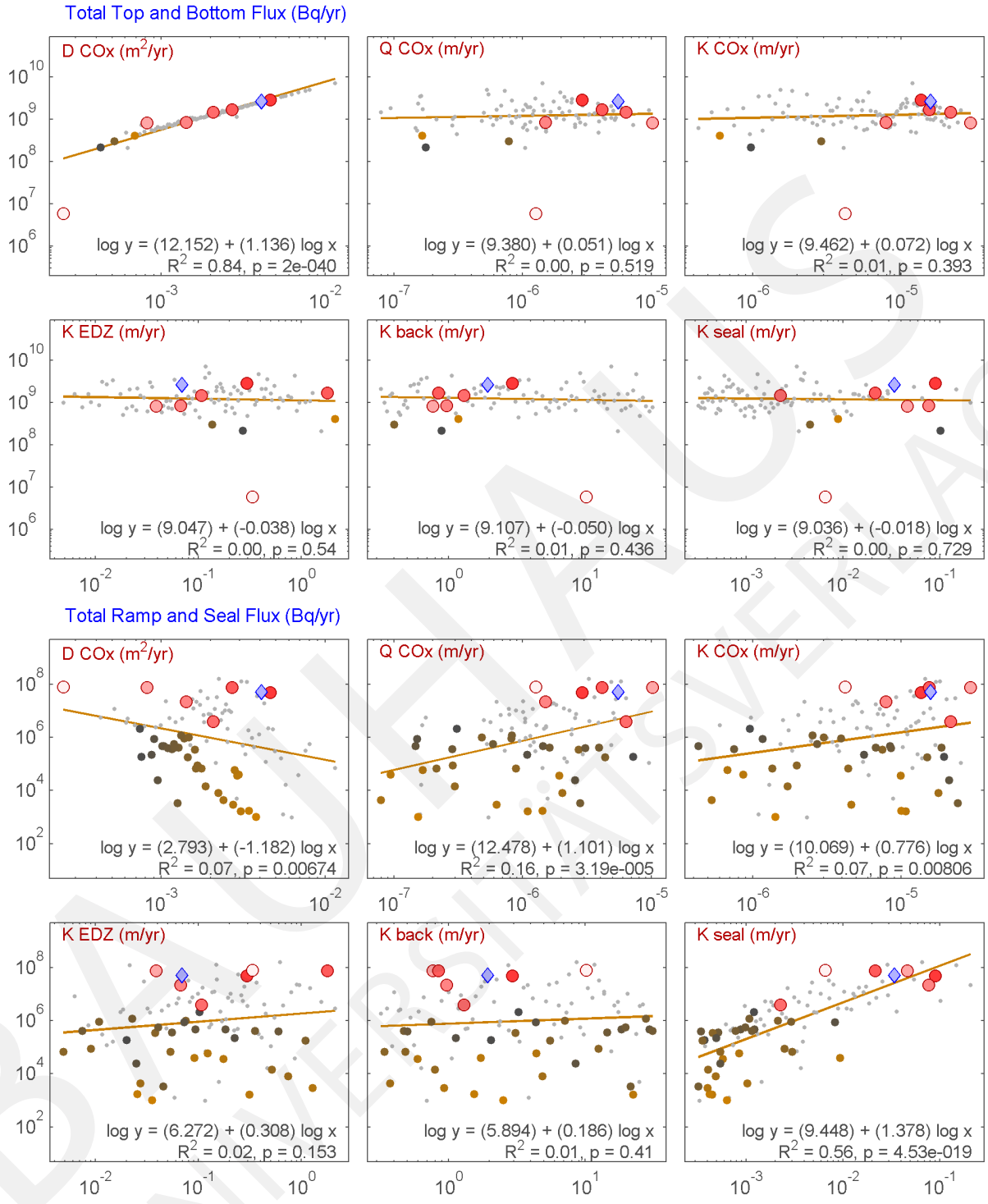

Figure 3: Scatter plots along with regression fits of COx model parameter *(diff: diffusion coefficient in the COx; Q COx: vertical upward gradient; KCOx: permeability in the COx; K EDZ: permeability in the EDZ; K back: permeability in the backfill; K seal: permeability in the seals)* with the flux (y axis values) from the Top and Bottom pathways (top figures) and Shaft and Ramp pathways (bottom figures). Each figure includes the equation for the regression line.

Reliability of Measurement Results for Materials Testing

H.B. Motra, J. Hildebrand, A.D. Osburg, T. Lahmer

Research Training Group 1462,
Bauhaus-Universität Weimar
Berkaer Str. 9, 99425, Weimar, Germany
frank.scheiber@uni-weimar.de

Abstract. In civil engineering experimental models are used for the parameter identification, validation/verification of numerical models and study of the behaviour of reality. All these activities are strongly connected with the development of experimental activity, where measurement has a fundamental role. Experimental models are usually support the development of mathematical models and provide measurement results with acceptable quality.
This paper presents a methodology for the quality evaluation of experimental results. It also suggests a generalization of standard approaches for characterizing experimental uncertainty that carefully distinguishes and retains separate different forms of uncertainty. In particular, the probabilistic approach can provide significant information during the evaluation process. Therefore, methods for predicting the uncertainty, sensitivity, and reliability are proposed for quality evaluation of experimental results. Furthermore, different uncertainties are to be taken into consideration when comparing different experimental models with different level of complexity. For this purpose, different approaches for predicting these uncertainties are implemented. Their contribution to the reliability of materials testing are illustrated. From this study it can be concluded that the presented methodology provides mathematical and computational tool and is able to quantify the model uncertainty. Moreover, it is useful to improve measurement processes to promote quality and capacity with decision-making.
Keywords: Measurement uncertainty, Metrology, Model quality, Quality, Reliability

1 Introduction

The civil engineering activities cover a wide and diversified range of domains, each one dealing with specific issues where the experimental and monitoring components often play an important role. In recent years, rapid change has been made in materials technology, and the trend is set to continue with substantial investments being made world-wide in materials development, processing and applications. The use of modern materials pervades all of industry and has a strong influence on its competitiveness. However, to convert these materials into competitive engineering products, the designer requires access to appropriate design methodologies that specify material property requirements. The need for reliable design data generated becomes crucial [7, 15]. Furthermore, quantitative assessment of materials behaviour and performance is essential to achieve quality and reliability of products [11]. Materials measurements have an important and widespread impact.

Experimental models are fundamental for guaranteeing the quality of scientific and industrial activities. The results of such measurements must be valid, comparable, and reproducible; and their uncertainty is the quantitative measurement that expresses the quality of such results. There are always variations of influences to measurements that are not under full control. Each measurement has an uncertainty resulting from these variation. Quantifying the measurement uncertainty provides important information about the reliability of measurement results and allows a comparison of different measurement settings. However, there is a lack of a methodology for the quantitative assessment of the quality of the results of experimental model and their exemplary implementation.

The conventional uncertainty analysis by the Root Sum Square (RSS) method is ofte n difficult in complex systems and requires approximation at each stage of processing, placing serious doubts on the validity of the results. In accordance with the ISO/IEC 17025:1999 [2] standard, all calibrations or testing laboratories must have and apply procedures to evaluate uncertainty in measurement as a guarantee of their technical competence. In order to perform this evaluation, the ISO 98:1995 guide commonly known as the "Guide to the expression of uncertainty in measurement" JCGM 100) [2] has been widely used and accepted by the metrological accreditation organization. A variety of supplements to GUM are being developed, which will progressively enter into effect. In the first of these supplements (GUM S1) [3], an alternative procedure is described for the calculation of uncertainties: the Monte Carlo Method (MCM). These include non-symmetric measurement uncertainty distributions, non-linearity within the measurement system, input dependency and systematic bias. The main elements of the formalism were originally put forward by Weise et al.[9]. Later, the procedure was succinctly outlined by [5] and focused on its relation to MCM described in [3]. Ref. [6] explained similarities and differences between the GUM and GUM S1 approaches. Recently, there have been many papers that apply a Bayesian updating to the evaluation of measurement uncertainty, e.g., [4, 9] and books [8, 10] discuss on issues relevant to these general evaluation method. The approach introduces a state of knowledge distribution about the quantity on interest and is derived from prior information about the quantity as well as other influence quantity and measured data, using probabilistic inversion or, inverse uncertainty evaluation [14].

This study is presented to create calculation methodology for determining the result of measurement concerning tensile mechanical properties and their respective uncertainties. The methodology has a systematic application associated with advanced metrology concepts, aiming to a guarantee of metrological reliability to the results of the tensile properties, as well as the possibility of implementation in industrial laboratories, researches centers and related tensile test firm. Uncertainty in calculating the correct values and the reduction of the value, it is achieved indicator of the quality test results.

This paper introduces how to express the reliability of of measurement results referring the concept of metrological traceability and associated measurement uncertainty.

2 Experimental Study

Tensile test results of a steel is defined as the relation between stress σ imposed on material and strain ε response of the material. In this study, a electro-mechanical testing

machine 250 kN maximum was used. The force accuracy class of the machine is $\pm 0.5\%$, deformation accuracy of the machine is $\pm 0.5\%$ displacement resolution 0.001 mm with respect to EN ISO 7500-1 standard. Clip-on extensometer of class 0.5 (EN ISO 9542) is used and has fixed gage length 50 mm, attached to a test specimen to measure elongation or strain as the load is applied. For 0.5 class extensometer, calibration protocol provides the total bias error of 1% or 25 μm, whichever is the greater, and this can lead to significant errors at the low strain over which the mechanical properties are measured. The test specimens were rods prepared from same material. Their dimensions were prepared according to the tensile testing standard EN ISO 6892-1 [1] for metals. To get reliable results five test specimens were tested. All samples were tested under identical testing protocols. The test speeds were selected 1.2 mm/min. All tests were performed at 23 °C ± 1 °C temperature. The sample dimensions are measured using the vernier calliper with an accuracy of ± 0.02 mm, with resolution of 0.01 mm, repeatability of ± 0.02 mm, with flatness ± 0.005 mm, Parallelism of ± 0.008 mm, and rounding accuracy of ± 0.1 mm.

3 Uncertainty Analyis

Generally, uncertainties in experimental data can be divided into two categories: systematic and random errors. It is a common assumption in this type of models (linear and nonlinear regression) involving experimental measurements that the error sources are mainly random and independent with no constant background errors (systematic errors). However, from comparisons of different experimental data sources evidence is often found of significant bias or calibration errors. The uncertainty analysis approach presented in this work is based on the analysis of cumulative probability distributions for output variables of the models involved taking into account the effect of both types of errors. Figure 1 shows possible components which causes sources of uncertainties. The probability distributions are obtained by performing Monte Carlo simulation coupled with appropriate definitions for the random and systematic errors.

3.1 Uncertainty Propagation in Measurement Models

Propagation of uncertainty discuss types and step of measurement uncertainty and ways to quantify them, shown in Figure 2, based on [2, 3].

Methods used for evaluation of measurement uncertainties are based on the concept of a measurement equation:

$$Y = f(X_1, X_2..., X_N). \tag{1}$$

The input quantities X_i are all those that have an influence on the result of the measurement, including correction factors as well as quantities that take into account other variability sources. The output quantity is the measurand Y. The GUM characterize quantities using a normal (Gaussian) distribution, which allows measurement uncertainty to be delimited by means of a coverage interval. Data consist of the estimates $x_i = (x_1, x_2, ..., x_N)$ and associated standard uncertainties $\mu = (\mu_1, .., \mu_N)$. The functional relation between the output quantity Y and the input quantities X_i must be linearized

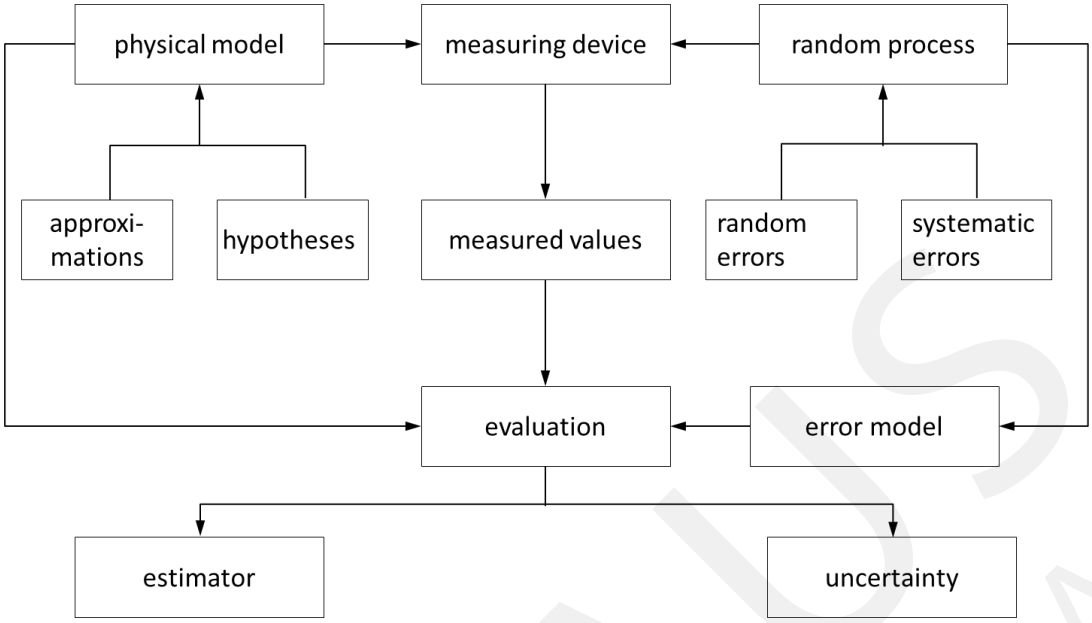

Figure 1: Different possible components of physical modeling and related uncertainty

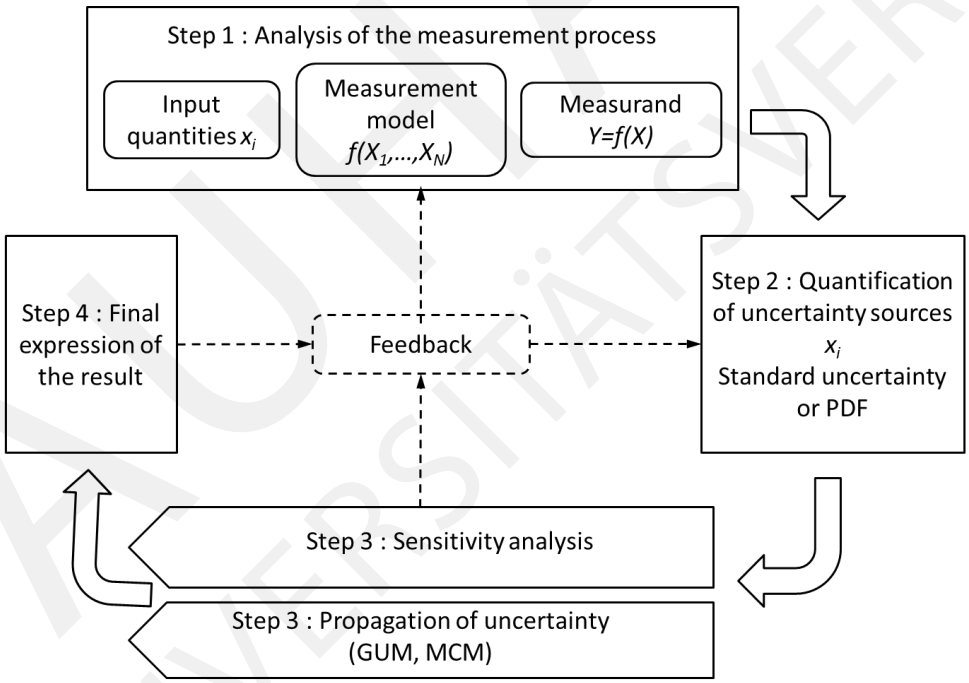

Figure 2: The general method to evaluate measurement uncertainty based on [3]

by approximating it through the first order terms of the Taylor series in a neighborhood of its estimates x_i, denoted by a lower case letter:

$$Y = f(X_1, X_2..., X_N) \cong y = f(x_1, x_2..., x_N) + \sum_{i=1}^{N} c_i X_i, \tag{2}$$

where the coefficients c_i are known as sensitivity coefficients:

$$c_i = \left. \frac{\partial f(X_1, X2_2, ..., X_N)}{\partial X_i} \right|_{x_1, x_2 ..., x_N}, \tag{3}$$

Once linearized, it is possible to use the law of propagation of uncertainty (LPU) [2, 3]:

$$\mu_s^2(y) = \sum_{i=1}^{N} \left(\frac{\partial f}{\partial x_i} \right) \mu_s^2(x_i) + 2 \sum_{i=1}^{N-1} \sum_{j=i+1}^{N} \left(\frac{\partial f}{\partial x_i} \frac{\partial f}{\partial x_j} \right) \mu(x_i, x_j). \tag{4}$$

where $\left(\frac{\partial f}{\partial x_i} \right)$ is the sensitivity coefficient, m degree of freedom and N is the number of input in measurement model and $u(x_i, , x_j)$ are the possible covariances between them. Sensitivity coefficients measure of how much change is produced in the measured by changes in an input quantity. Mathematically, sensitivity coefficients are obtained from partial derivatives of the model function f with respect to the input quantities. In particular, the sensitivity coefficient c_i of the input quantity x_i is given by which expresses mathematically how much f changes given an infinitesimal change in x_i.

Estimation of measurement uncertainty of tested bar for specified materials depends on several error sources such as [12, 13, 14]

- measurement of test bar dimensions;
- measurement of tensile force;
- test temperature and loading rates in successive stages of tests;
- the method of gripping the test piece and axiality of the application of the force;
- the testing machine characteristics (stiffness, drive, control and method of operation);
- human and software errors associated with determination of the tensile properties;
- the material in homogeneity that exists even within a single processed batch obtained from a single melt of material.

The first two error sources that are measurement of test bar dimensions and measurement of tensile force have already been added into the measurement uncertainty calculations. The calculations of other effects are very difficult due to the determination of all influencing parameters. Instead of uncertainty calculations for all listed error sources, the standard deviation of the test results can be used to calculate the measurement uncertainty of all other parameters mentioned in the listed error sources. The test data covers the influencing parameters.

As an example of a random uncertainty evaluation, consider an input quantity X_i whose value is estimated from n independent observations $X_{i,k}$ of X_i obtained under the same conditions of measurement. In this case the input estimate x_i is usually the sample mean:

$$x_i = \bar{X}_i = \frac{1}{n} \sum_{k=1}^{n} X_{i,k} \tag{5}$$

and the standard uncertainty $\mu(x_i)$ to be associated with x_i is the estimated standard

deviation of the mean:

$$\mu(x_i) = s(\bar{X}_i) = \frac{1}{n(n-1)} \sum_{k=1}^{n} (X_{i,k} - \bar{X}_i)^{1/2}. \tag{6}$$

Also statistical analysis of the test results was done with the purpose of assessing their reliability. The uncertainty calculations were made by using different references [2, 3, 12, 13, 14]. The uncertainty in measurements of the test parameter is calculated by standard distribution formula.

$$\mu_A = s(\bar{X}_i) = \mu_{rep} \tag{7}$$

Then, combined uncertainty ($U_{combined}$) can be calculated then measurement uncertainty for output quantities as shown below;

$$\mu_{combined} = \sqrt{\mu^2(y) + \mu_{rep}^2} \tag{8}$$

The uncertainty of measurement is expressed as an expanded uncertainty with coverage factor (see [3], which is depends upon the degree of freedom). The expanded uncertainty of measurement is stated as the standard uncertainty of measurement multiplied by the coverage factor $k = 2$, which for a normal distribution corresponds to a coverage probability of approximately 95%.

$$U_E = k * \mu_{combined}. \tag{9}$$

4 Sample Calculation

The test result of the five test of rectangular specimen tested and result of sample calculation of tensile properties are given in Table 1. The calculation of measurement uncertainties of the test results using equation from (1) to (8) and given in Table 2.

Table 1: Tensile test results for strucutural steel specimen.

Specimen Nr.	Thickness t, (mm)	Width b, (mm)	Cross-section area ,A (mm^2)	Tensile force F, (kN)	Tensile strength (MPa)
1	8.515	19.752	168.188	84.304	501.250
2	8.439	19.873	167.712	84.044	501.120
3	8.353	19.716	163.957	74.865	456.615
4	8.582	19.851	169.210	79.940	472.430
5	8.513	19.851	169.008	79.971	473.180
$\overline{X}$	8.480	19.764	167.613	80.608	480.919

The standard uncertainty with respect to force (μ_F) is directly taken from calibration certificate of material testing machine and uncertainty associated with caliper is also taken from calibration certification of the caliper. The average thickness of the test specimen is 8.480 mm, the average width is 19.764 mm, the average maximum force if 80.608 kN

and the average tensile strength is 480.919 MPa. The tensile strength and uncertainty in the result of tensile test are shown in Tables 1 and 2 as (480.919 ± 10.10) MPa.

Sample calculation shows that all of the uncertainty sources including dimensions of the specimen, cross-section area, uncertainty of caliper, applied forces, repeatability of the test results and related sensitivity coefficients calculated and they are important input quantities for tensile strength model. In other words, its need more precise control over safety factors; again, this is related to the reliability of test data. Reducing the scattering range as well as increasing the comparability of data could be achieved through establishing evaluation system since poor data reliability is partly due to an improper uncertainty quantification.

Table 2: Calculation of sensitivity coefficients and uncertainties of the tensile testing.

c_F	c_A	c_{AC}	μ_σ	U_E
$1/mm^2$	N/mm^4	mm	N/mm^2	GPa
0.000041	-0.48	20.15	2.95	-
μ_F	μ_A	μ_{AC}	μ_{rep}	
$0(N)$	mm^2	mm^2	N/mm^2	-
411.18	20.15	0.03	5.80	10.10

where, c_F is the sensitivity coefficient for applied force measurement; c_A is the sensitivity coefficient for cross-section measurement of test specimen; c_{AC} is the sensitivity coefficient for cross-section measurement of test specimen (c_{AC} = t + b, t = thickness of specimen, b = width of specimen); μ_F is the measurement uncertainty of applied force taken directly from calibration certificates of machine; μ_A is the measurement uncertainty of cross-section of test specimen and μ_{AC} is the measurement uncertainty of cross-section of specimen associate with thickness and width.

The result of a measurement of a physical quantity it is a value attribute to a measurand by measurement. When a result is informed, it should be indicated, clearly, if the same refers to an indication, the uncorrected result, the correlated result or to the medium value of several measurements and, complete expression on its measurement uncertainty. In the case study, the results presented to proceed refer to the medium value of the several obtained measurements of the studied mechanical properties, that is, the value of Modulus of elasticity, yield strength, tensile strength elongation at maximum force and elongation at fracture, added of information of its measurement uncertainty, for a probability coverage of 95%. The Table 3 presents tahe value of the results of the measurement of the mechanical properties of the strucural steel of IPE400. The variation in modulus of elasticity expressed by the 3.30%, yield strength 2.74%, tensile strength 2.10%, which is acceptable limit. It is good practice in any test procedure to quote the uncertainties associated with the measurement itself, but this is not always carried out and steel rarely reported. For the tensile test of steel it is reasonably atraightforward to make some estimate of the uncertainties associated with the test method.

Table 3: Tensile test results for strucutural steel specimen.

Mechanical properties	Symbol	Results	Uncertainty,% $k = 2$
Modulus of elasticity	E	201.10 GPa	$\pm$6.61 GPa
Yield strength	YS	351.16 MPa	$\pm$9.64 MPa
Tensile strength	R_m	480.91 MPa	$\pm$10.10 MPa
% Elongation at Maximum force	A_{gt}	20.60%	$\pm$0.53%
% Total elongation fracture	A_t	34.96%	$\pm$4.21%

5 Conclusions

An approach based on GUM was developed to analyze the effect of systematic and random errors on computer models involving experimental measurements. The results from the case studies presented show that the approach is able to distinguish which error type has the dominant contribution to the total error on the uncertainty propagation through the measurement model. It was shown that systematic errors present in experimental measurements can play a very significant role in uncertainty propagation, an effect that is traditionally ignored when estimating and using physical properties. Additionally, it was observed that the effect of random and systematic errors on the uncertainty propagation is additive, meaning that the error type with the largest effect clearly defines the uncertainty propagated to the output variables of the model. In general, experimentalists have not been concerned enough about systematic errors when reporting experimental or observable data. It is found that these systematic errors are significant sources of uncertainty and that more attention should be given to estimating them and using them in uncertainty and sensitivity analyses.

This study shows effect of quality and uniformity of specimen and also error caused by operator has a definite effect on total measurement uncertainty in most material tensile testing. In addition to specimen, approved testing method, steady force measuring system and periodically calibrated machine lowers the total measurement uncertainty.

Competent laboratories know the quality of their testing methods and the uncertainty associated with the results. Measurement uncertainty is therefore an essential quality feature for testing methods. Others, such as repeatability, reproducibility, robustness and selectivity are also important for the characterisation of the overall quality of a testing method.

In this study was to presents a methodology for determining the result of measurement concerning tensile mechanical properties and their respective uncertainties. Such methodology, which has a possible systematic application, is associated with advanced metrology concepts, aiming a guarantee of metrological reliability to the results of the tensile properties, as well as the possibility of implementation in industrial laboratories, researches centers and in the Testing Laboratory Network.

Thus, metrology probabilistic approach has mathematical and computational tools particularly suited to improve the quality of measurement thus fulfilling the growing technological demands of the modern society.

Acknowledgment

This research is supported by the German Research Foundation (DFG) via research training group "Assessment of Coupled Experimental and Numerical Partial Models in Structural Engineering (GRK 1462)", which is gratefully acknowledged by the authors.

References

[1] EN ISO 6892-1. *International Standard, Metallic materials-Tensile testing-Part 1: technique of test at room temperature.* ISO, 2009.

[2] IFCC-ILAC ISO IUPAC IUPAP BIPM, IEC and OIML. *Evaluation of measurement data - Guide to the expression of uncertainty in measurement. Joint Committee for Guides in Metrology.* JCGM, Geneva, 2008.

[3] IFCC-ILAC ISO IUPAC IUPAP BIPM, IEC and OIML. *Evaluation of measurement data - Supplement 1 to the Guide to the expression of uncertainty in measurement - Propagation of distributions using a Monte Carlo method. Joint Committee for Guides in Metrology.* JCGM, Geneva, 2008.

[4] B. Toman C. Elster. Bayesian uncertainty analysis under prior ignorance of the measurand versus analysis using the supplement 1 to the guide: a comparison. *Metrologia*, 46:261–266, 2009.

[5] M.G. Cox C. Elster, W. Wöger. Draft gum supplement 1 and bayesian analysis . *Metrologia*, 44:31–40, 2007.

[6] C. Elster G. Wübbeler, M. Krystek. Elster, evaluation of measurement uncertainty and its numerical calculation by a monte carlo method meas . *Measurement Science and Technology*, 19, 2008.

[7] H.C. Frey J. Zheng. Quantitative analysis of variability and uncertainty with known measurement error . *Methodology and case study*, 25(3):663–675, 2005.

[8] F.T. Jaynes. *Probability Theory: The Logic of Science.* Cambridge: Cambridge University Press, 2003.

[9] W. Woeger K. Weise. A bayesian theory of measurement uncertainty . *Measurement Science and Technology*, 4(1):1–11, 1993.

[10] I. Lira. *Evaluating the Uncertainty of Measurement.* Institute of Physics Publishing, Bristol, 2002.

[11] H.B. Motra, A. Dimmig-Osburg, and J. Hildebrand. Evaluation of experimental measurement uncertainty in engineering properties of pcc samples . *Journal of Civil Engineering Research*, 3(3):104–113, 2013.

[12] H.B. Motra, J. Hildebrand, and A. Dimmig-Osburg. Assessment of strain measurement techniques to characterize mechanical properties of structural steel . *Engineering Science and Technology, an International Journal*, Accepted for publication, 2014.

[13] H.B. Motra, J. Hildebrand, and A. Dimmig-Osburg. linfluence of specimen dimensions and orientations on the tensile properties of structural steel. *Material Testing*, (Submitted), 2014.

[14] H.B. Motra, J. Hildebrand, A. Dimmig-Osburg, and H. Stutz. A probabilistic method for quality evaluation of experiments in civil engineering. *Measurement, Journal of the International Measurement Confederation (IMEKO)*, Submitted, 2014.

[15] W.B. Whiting V.R. Vasquez. Accounting for both random errors and systematic errors in uncertainty propagation analysis of computer models involving experimental measurements with monte carlo methods . *Risk Analysis*, 25(6):1669–1681, 2005.

Identifying time-dependent changes in design discharges by means of stochastic time-series approaches

Christoph Mudersbach[1,2], Jens Bender[2,3], Fabian Netzel[1]

[1] Bochum University of Applied Sciences, Institute for Water and Environment, Lennershofstr. 140, 44801 Bochum, E-Mail: christoph.mudersbach@hs-bochum.de

[2] wbu consulting Ingenieurgesellschaft mbH, Schelderberg 16a, 57072 Siegen, E-Mail: bender@wbu-consulting.de

[3] University of Siegen, Research Institute for Water and Environment, Paul-Bonatz-Str. 9-11, 57076 Siegen

Abstract

Within this investigation, we focused on analyses of the discharge data of the gauge Neu Darchau (Elbe River), which is the most downstream discharge gauge of the Elbe River before it becomes an estuary. We followed the questions, if the discharge characteristics of the Elbe River have changed over the last decades and how much the design discharges (i.e. HQ100) are affected by the latest extreme events in 2002, 2006, 2011 and 2013. Hence, we conducted (i) trend estimations for different flood indicators, (ii) an assessment of time-dependencies of the design discharge HQ100 by using extreme value statistics with both block maxima and peak-over-threshold approaches and (iii) an estimation of confidence levels for the time-dependent behavior of the design discharges by means of Monte-Carlo simulations using autoregressive models. For the majority of the flood indicators an increase in the HQ100 level over the last decades can be stated. The 2013 event leads to a remarkable jump in the HQ100 events in all flood indicators. No HQ100 level exceeds the upper (or lower) confidence band, thus no statistically significant changes can be stated at the 90%-level. However, for many flood indicators there is clear tendency towards the upper confidence bands.

1 Introduction

During the last decades several severe floods occurred in different river basins in Germany (e.g. 1993 and 1995 Rhine; 1997 Odra; 1999, 2001, 2006 and 2013 Danube, 2002, 2006, 2011 and 2013 Elbe) [21]. In a public perception there seems to be a trend to more frequent hydrological extreme events resulting in a rising flood hazard.

Within this investigation, we focus on detailed analyses of the discharge data of the gauge Neu Darchau (Elbe River). The gauge Neu Darchau is the most downstream discharge gauge of the Elbe River before it becomes an estuary (Fig. 1). The gauge is considered as a benchmark for the total discharge of the Elbe River [25]. Thus, the discharge statistics of this gauge is of special importance for all designing purposes downstream this location.

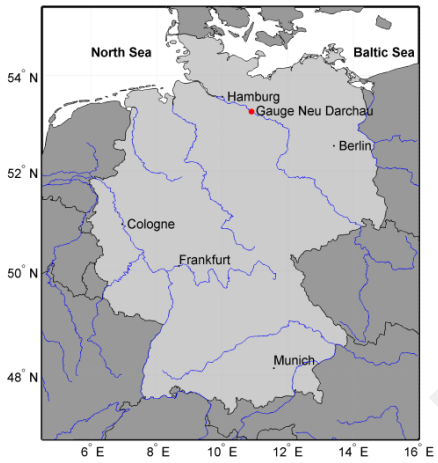

Fig. 1: Location of the gauge Neu Darchau.

For the determination of design discharges, traditionally a stationary behaviour of the flood regime is assumed and has to be assured. The severe flood events on 23 August 2002 ($Q_{\text{Neu Darchau}} = 3410$ m^3/s), 9 April 2006 ($Q_{\text{Neu Darchau}} = 3590$ m^3/s), 23 January 2011 ($Q_{\text{Neu Darchau}} = 3593$ m^3/s), and 11 June 2013 ($Q_{\text{Neu Darchau}} = 4070$ m^3/s) may lead to the assumption, that more frequent extreme events are likely or at least a period with a clustering of floods occurs. While the floods in 2006 and 2011 occurred within the typical flood period (December – May), the severe floods in 2002 and 2013 occurred during summer. It is worthwhile to mention, that the 2013 event is a new record, i.e. this value is higher than all values observed before.

Thus, the questions arise if the discharge characteristics of the Elbe River have changed over the last decades and how much the design discharges (i.e. the 100-yr return discharge) are affected by the latest extreme events in 2002, 2006, 2011, and 2013?

Many recent studies focussed on trend estimations in flood magnitude, frequency and seasonality of European or German rivers (e.g. [18, 19, 21, 22, 3, 26, 4] ; Mudelsee, 2004; Petrow et al., 2009; Petrow and Merz, 2009; Beurton and Thieken, 2009; Stahl et al., 2010; Bormann et al., 2011). Mudelsee et al. (2003) investigated discharge data sets from the Elbe and Odra River for the past 80 to 150 years. For the Elbe River (gauge Dresden), they found a decreasing trend in winter floods, while summer floods do not show any significant trend.

Mudelsee (2004) analysed extreme floods in central Europe (namely the Elbe and Odra River) over the past 500 years. In this context he focused on so-called Vb-cyclones, which are responsible for heavy rainfall events in central Europe, especially in the summer period. Based on the used data sets he find for both the Elbe and Odra River significantly decreasing trends in winter flood risk and no significant trends in summer flood risk during the twentieth century.

Petrow und Merz (2009) investigated flood time series for 145 discharge gauges in Germany in the period of 1952 to 2002. For trend estimates, they studied eight flood indicators such as annual maximum daily mean discharge, seasonal annual maximum daily mean discharge for winter and summer season, peak-over-threshold magnitude and others. The locations

of the gauges are more or less equally distributed over Germany. The individual names of gauges are not listed in their paper, but looking at the plotted maps it is obvious, that the gauge Neu Darchau was one of the analysed sites. For most flood indicators they found no significant trends for the gauge Neu Darchau as for most gauges in the north-eastern region of Germany, while a considerable fraction of basins in other German locations show upward trends. Analysing at the seasonal behaviour, they found larger changes for winter periods compared to summer periods.

Beurton and Thieken (2009) investigated the seasonal distribution of annual maximum floods at 481 gauge stations across Germany. As a result, they created a map with three regions representing homogeneous flood regimes. The Elbe River belongs to the so called cluster B, which covers most parts of Germany. This flood regime is characterized by spring and winter floods. In comparison to Cluster A (mainly westerly regions of Germany), the maximum in December is shifted to March. However, winter is the most important season for flooding.

In a recent study Stahl et al. (2010) investigated discharge trends from 441 small catchments in 15 countries across Europe. Small catchments are defined as areas not exceeding an area of 1000 km^2. Thus, no data sets from the middle or lower Elbe River were used. The investigated catchments in the easterly regions show negative trends in annual discharges and positive trends for the winter season.

Bormann et al. (2011) conducted a spatial analysis of German discharge and flood stage data. They used 78 gauges and most of the data sets do not show any significant trends in any of the considered flood parameters. Looking more into detail, non-uniform trends along the Elbe River were detected. The gauge Dresden shows a decreasing trend in the annual maximum discharge of -3.9 $m^3/s/a$ from 1852 to 2005. The downstream located gauge of Wittenberg shows an increasing trend of 11.96 $m^3/s/a$ from 1950 to 2003, whereas the gauge of Neu Darchau does not exhibit any significant trend from 1874 to 2005. However, the authors emphasize the strong dependence of the trend on the underlying record length.

Interannual and decadal oscillations as well as correlations between discharge, precipitation and other meteorological forcings (e.g. NAO) in the Elbe River basin are investigated more in detail in recent years (e.g. Markovic, 2006; Kropp and Schellnhuber, 2011). In analysing different Elbe River discharge time series from gauge Dresden to the downstream gauge Neu Darchau, Markovic (2006) identified statistically significant low frequency oscillations with periods of 7.1 yrs and 10-14 yrs occurring additionally to the seasonal cycle, indicating the occurrence of extended dry and wet cycles. In Kropp and Schellnhuber (2011), numerous authors addressed long-term correlations in hydro-meteorological variables showing that many discharge records in Europe and Germany are characterized by such effects.

Interestingly, although the extreme values are of major importance for river training, flood risk management and design purposes there is a lack of publications covering the aspect of changes in extreme flood quantiles (e.g. HQ100). In this paper we would like to make a contribution to close this gap.

In order to gain the above mentioned objectives we conduct the following steps (constrained to the gauge Neu Darchau):

- trend estimations for different flood indicators
- assessment of time-dependent changes in design discharges (flood quantile HQ100) by using extreme value statistics with both, block maxima (Generalized Extreme Value distribution, GEV) and peak-over-threshold (Generalized Pareto distribution, GPD) approach
- an estimation of confidence levels for the time-dependent behavior of the design discharges by means of Monte-Carlo simulations using autoregressive models.

2 Data

2.1 Daily mean discharge data

For this study, discharge data from the gauge Neu Darchau at Elbe location 536.4 km (Fig. 1) were obtained from the Water and Shipping Office Lauenburg (WSA Lauenburg), which is the official gauge operator. The records comprise daily mean discharge values from 1 November 1874 to 31 October 2013 (hydrological year in Germany: 1 November to 31 October), resulting in a time series covering 139 years without any gaps. The discharge measurements operate regularly since 1874 without any discontinuities. Since 1 November 1997 data with a resolution in time of 15 minutes are available. Prior to that, several measurements per day (not equally distributed) are the basis for the daily mean discharge data. Since the catchment size amounts to 131,950 km^3, these daily measurements are also suitable to compute representative daily mean discharge data.

The most extreme flood in the official data set is on 25 March 1888 with HHQ = 4400 m^3/s. Since it was a severe winter flood, it is known that during this event river icing occurred in the Elbe River which significantly influenced the flood stage measurement at gauge Neu Darchau (WSA Lauenburg, 2012) due to backwater effects. Hence, the dedicated discharge of 4400 m^3/s is also affected by river icing. For this flood event the WSA Lauenburg provides a corrected peak discharge of 2310 m^3/s on 24 March 1888 instead of 4400 m^3/s on 25 March 1888 (Rölver, 2012), which allows for the incorrect flood stage measurement. Although the corrected discharge is not officially fixed, we decided to use this corrected value instead of the original value, since the original–and obviously incorrect–value would significantly affect the extreme value statistics. Figure 2 illustrates the corrected daily mean discharge series at gauge Neu Darchau from 1875 to 2013. Even if the latest extreme events in 2002, 2006, 2011, and 2013 are very noticeable, the time series reveals that extreme floods already occurred in a comparable magnitude in former years. The overall mean of the daily mean discharge from 1875 to 2013 (hydrological years) amounts to MQ = 710 m^3/s with a standard deviation of s = 446 m^3/s. The linear trend with a standard error is 0.05 ± 0.05 $m^3/s/yr$, which is a non-significant trend at the 95% confidence level. In addition, we fitted a non-linear function to the time series, using locally weighted scatterplot smoothing (LOWESS). The applied LOWESS function fits simple models to localized subsets of the data using linear least-squares fitting and a first-degree polynomial (Cleveland, 1981). The LOWESS results with a filter span of 10 years illustrate, that the series can be intersected into two periods. A first one from 1875 to about 1920, where a rather small variance exists, followed by a period up to

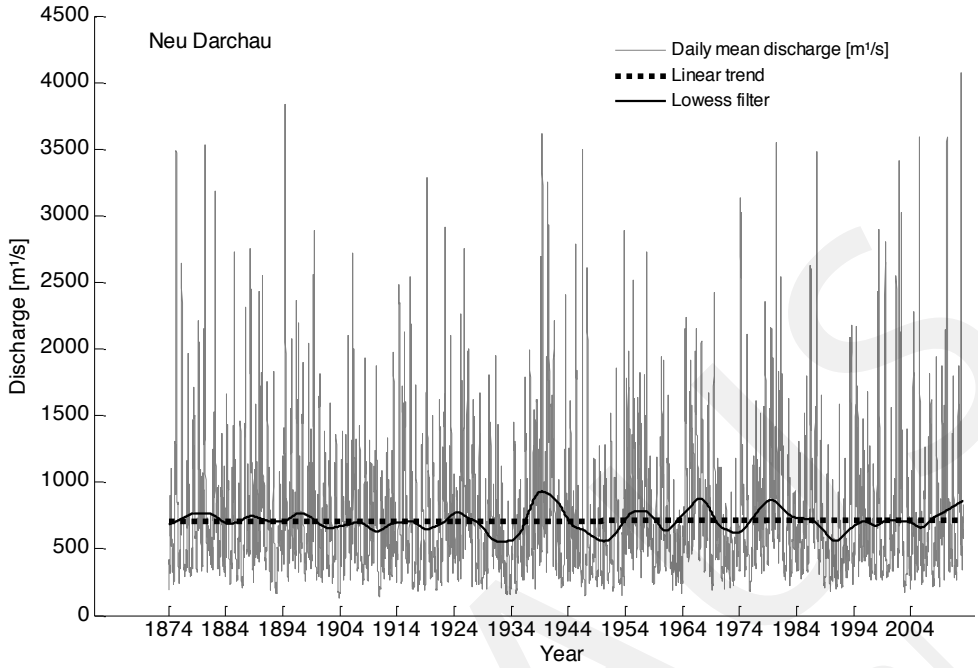

Fig. 2: Daily mean discharge at gauge Neu Darchau from 1875 to 2013 with linear and non-linear trend (LOWESS, span = 10 yrs).

the end with higher magnitudes. Interannual or decadal variations in discharges may be explained to a certain extend by the North Atlantic Oscillation (NAO) (Villarini et al., 2011; Kingston et al., 2006; Pociask-Karteczka 2006).

2.2 Flood indicators

Six flood indicators were analysed in this study using both, the block maxima and the peak-over-threshold approach. The most common flood indicator in flood trend studies is the annual maximum discharge, i.e. the largest daily mean discharge that occurs in each hydrological year. This flood indicator is labelled as AMF. The annual maxima approach has extensively been used in the past (e.g. Acero et al., 2011). However, it can be a wasteful method if further data of extremes are available (Coles, 2001). Conversely, if no extreme flood occurs within a year, the maximum value will still be selected. To overcome these shortcomings, some alternative approaches came up in hydrological statistics. The most prominent methods are the r-largest approach (e.g. Smith, 1986; Coles, 2001) and the peak-over-threshold (POT) approach (e.g. Leadbetter, 1991; Bayliss and Jones, 1993; Coles, 2001).

In the r-largest approach, not only the annual maximum values (r = 1) are considered in the sample, but e.g. the two (r = 2) or three (r = 3) largest annual values. The advantages and disadvantages of this method are obvious. Given a year with several extreme floods, using the r-largest method extends the data basis by including more of the available information concerning extreme discharge events. In contrast, if a year has

no major floods, using the r-largest approach still considers the r-largest events of this year within the sample.

Discharge datasets can exhibit dependencies that are related to the same event that caused these floods. By creating a sample of the r-largest values per year, one has to ensure independence of the selected events, which means that the events should have a certain distance in time (declustering time). Following Svensson et al. (2005), we use a declustering time of 20 days, since the catchment area of the gauge Neu Darchau is >100.000 km^3. In this study we compute the annual r-largest samples considering the r = 2 and r = 3 largest events per year, hereafter referred to as AMFr2 and AMFr3.

The POT approach (also known as partial duration series) provides a more flexible representation of floods compared to the AMF approach, since it accounts for stochastically and unequally distributed occurrences of floods. A POT sample is created using all values exceeding a predefined threshold u. The main advantage of the POT approach is therefore the consideration of all severe floods within a flood intensive year, while years with no extreme events are neglected. Thus, a POT time series captures more information concerning the entire flood characteristics of a river than using AMF. The key challenge of the POT approach, however, is the threshold selection, since statistical methods (e.g. extreme value distribution) may react very sensitive to different thresholds. Selecting suitable thresholds is therefore a complex task representing the main difficulty associated with the POT approach (Lang et al., 1999). Additionally, the independence of the individual events has to be assured as well.

Lang et al. (1999) reviewed some threshold selection techniques. An important factor in the threshold selection is the mean number N of events per year. They recommend that there should be at least a mean number of floods of N = 2 or 3 per year. A common threshold selection criteria is to use a standard frequency factor f, so that the threshold can be estimated from the daily mean discharge series Q by:

$$u = \mu_Q + f \cdot \sigma_Q$$

where μ_Q and σ_Q are the mean and standard deviation of the daily mean discharge series Q, respectively. Rosbjerg and Madsen (1992) prefer to use a standard frequency factor of f = 3, but take care for the condition N > 2.

For the daily mean discharge data of gauge Neu Darchau Table 1 shows a compilation of a range of standard frequency factors, thresholds and the resulting mean number of floods per year. Since the factor 3 results in less than 1 value per year (not shown), we reject this factor. Instead we use the standard frequency factors f = 0.78, f = 1.20 and f = 2.18, which lead to a mean number of floods per year of N = 3, N = 2, and N = 1, respectively. Hence, we name the partial series as POT-0.78, POT-1.23, and POT-2.18. Note: Even if the POT-0.78 series has in mean 3 flood events per year, the series is not equal to AMFr3. The same is true for the other samples.

The trend analyses of the different flood indicators show, that there is no evidence for any long-term trend in the flood indicators. All trend values are not significant, with the exception of the POT-0.78 series at the 1σ-level.

Standard frequency factor f	**Threshold U**	**(Mean) number of floods per year N**	**Name**	**Trend with standard error (1875-2013)**
0.78	1060 m^3/s	3	POT-0.78	1.00 ± 0.68 $m^3/s/yr$
1.23	1260 m^3/s	2	POT-1.23	0.68 ± 0.79 $m^3/s/yr$
2.18	1685 m^3/s	1	POT-2.18	0.11 ± 1.05 $m^3/s/yr$
-	-	1	AMF	0.08 ± 1.10 $m^3/s/yr$
-	-	2	AMFr2	0.09 ± 1.10 $m^3/s/yr$
-	-	3	AMFr3	0.10 ± 0.89 $m^3/s/yr$

Table 1: Compilation of thresholds, standard frequency factors and the resulting number of floods per year for the six flood indicators at gauge Neu Darchau based on daily mean discharge data

3 Extreme value methods

Nowadays, the Generalized Extreme Value distribution (GEV) and the Generalized Pareto distribution (GPD) have established as the main distribution functions for extreme value statistics (e.g. Coles, 2001). A series of block maxima is described by the GEV which is defined as

$$\mathrm{GEV} = \exp\left(-\left(1+\xi\left(\frac{(z-\mu)}{\sigma}\right)\right)^{\frac{-1}{\xi}}\right)$$

with the location parameter μ, the scale parameter σ, the shape parameter ξ and the block maxima values considered, denoted as z. This formula combines the Gumbel, Fréchet and Weibull families into one single family. Each family has a location μ and a scale parameter σ while the Fréchet and the Weibull families additionally have a shape parameter ξ (Coles, 2001).

The use of POT methods is based on the GPD. The GPD encompasses a number of common extreme functions (Hawkes et al., 2008) and is defined as

$$\mathrm{GPD} = 1-\left(1+\frac{\xi y}{\widetilde{\sigma}}\right)^{\frac{1}{\xi}}$$

with

$$\widetilde{\sigma} = \sigma + \xi\,(u-\mu)$$

with the location parameter μ , the scale parameter σ, the shape parameter ξ and threshold value (Coles, 2001).

The parameter estimation method in this paper is maximum likelihood estimation (MLE) for all model parameters (Smith, 1986; Hosking and Wallis, 1997; Davison and Smith, 1990). The MLE is a general and flexible method to estimate the unknown parameters of a distribution (Coles, 2001). However, according to Katz et al. (2002), the performance

of MLE can be extremely erratic for small samples ($n \leq 25$), especially when estimating extreme quantiles of the GEV distribution.

As introduced in Section 1 we try to clarify, if the extreme floods in 2002, 2006, 2011 and 2013 affect the extreme value statistics and if design discharges for engineering tasks (i.e. HQ100) have changed over the last decades. Time-dependent changes in extreme value statistics can be investigated using a non-stationary extreme value approach (e.g. Mendez et al., 2007; Mudersbach and Jensen, 2010). However, until now the non-stationary methods are not common in hydrological practice. Thus, we use a quasi non-stationary extreme value approach in order to analyse the influence of single extreme events on the extreme value statistics. The quasi non-stationary approach is based on the above mentioned stationary extreme value distributions (i.e. GEV and GPD) and a stepwise analysis of different time series lengths. Firstly, stationary extreme value statistics are computed for a time period from 1875 to 1950. Afterwards, the time series is extended step by step by one year until the entire time series from 1875 to 2013 is analysed. This procedure reflects the real situation in statistical or engineering practice, where design values have to be steadily verified due to new data. The whole process is shown in Fig. 3 (left).

As a result of the quasi non-stationary method time series of the HQ100 for the different flood indicators will appear. Only with these information one can assess if any time-dependent behaviour is existing, but the question which can not be answered is, if the observed changes are significant or not. To do so, we need appropriate confidence bands for the HQ100 time series. The basic idea is now the following: Having a large set of synthetic daily mean discharge data of the gauge Neu Darchau, we are able to compare the calculated HQ100 levels from the original series with quantiles of the HQ100 values calculated from the large synthetic data set. Thus, we simulate a large data set of synthetic daily mean discharges by using autoregressive models. Therefore, we first have to detrend the original time series of Neu Darchau. Then, we have to remove the saisonal cycle and transform the data in order to get normally distributed residuals (e.g. Maidment, 1993). Afterwards an AR-model can be fitted to the data. In our case we found an AR2-model to be the best fit to the data so that the basic equation for the AR2-model is:

$$Q_t = aQ_{t-1} + bQ_{t-2} + \epsilon_t$$

Using this AR2-model we can simulate a large number of synthetic time series. Due to limited computer capacity we simulated 100 synthetic time series. For all synthetic time series the same analyses as for the original discharge time series is repeated. For calculating the confidence bands we chose the 90% quantile of the resulting HQ100 time series. Details of the procedure are shown in Fig. 3 (right).

4 Results

Figure 4 illustrates the results of the quasi non-stationary extreme value analysis for the six flood indicators POT-0.78, POT-1.23, POT-2.18, AMF, AMFr2, and AMFr3. The black thick lines represent the time-dependent development of the HQ100 values for each

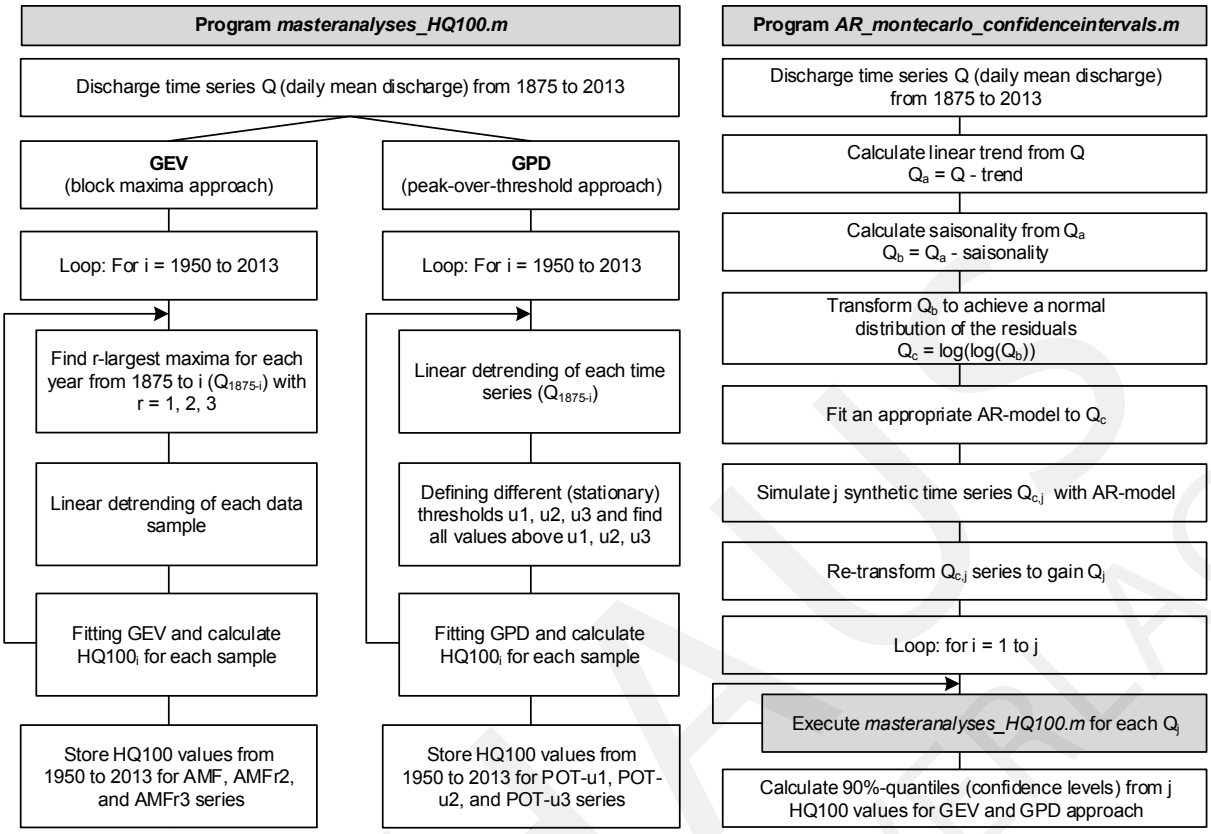

Fig. 3: Analysis process of the quasi non-stationary extreme value method (left) and for the confidence bands using Monte-Carlo simulations (right).

time span. This means, the first value plotted at the year 1950 is the HQ100 value resulting from 1875 to 1950. The next value, plotted at 1951, results from the time series 1875 to 1951 and so on. The red lines display the 90% confidence bands calculated by means of the Monte-Carlo simulations.

Results from analysing the POT-0.78 time series with the GPD show a decreasing development of the HQ100 from 1950 to about 2000 and a slight increase until 2013. However, there is a convergence to the upper confidence band. With respect to the POT-1.23 results, the general development is comparable, whereas the whole results are approx. 200 m^3/s lower. The POT-2.18 results indicate a more or less stationary behaviour until 2010 and a sharp increase until 2013. The GEV analyses (AMF, AMFr2, AMFr3) do show similar characteristics. From 1950 to about 1980 a decrease can be observed and from 1980 to 2013 an increase is visible. Noteworthy is the sharp increase from 2012 to 2013.

With respect to the extreme events in 2002, 2006, and 2011 it can be stated, that those events do not lead to extraordinary changes in the HQ100 events. Nevertheless, in the majority of the flood indicators an increase in the HQ100 levels over the last decades can be stated. The 2013 event leads to a remarkable jump in the HQ100 events in all flood indicators. Comparing the absolute values of the HQ100 events one can see that the more data a flood indicator contain (e.g. POT-0.78 and AMFr3) the higher the HQ100 values are.

To answer the question if there are any statistically significant changes in the HQ100 levels the confidence bounds can be used. No HQ100 level exceeds the upper (or lower) confidence band, thus no statistically significant changes can be stated at the 90%-level. However, for many flood indicators there is clear tendency towards the upper confidence band, which might be exceeded if one or more new extreme events will occur.

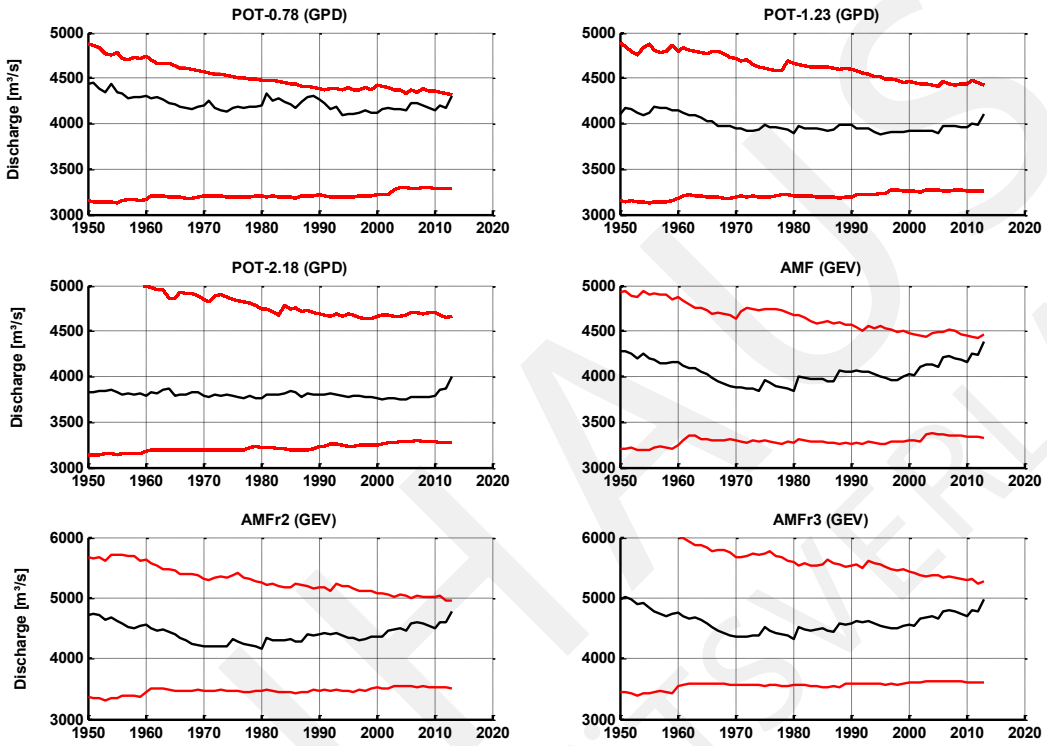

Fig. 4: Time-dependent HQ100 levels of discharge (thick black line) at gauge Neu Darchau from 1950 to 2013 for different flood indicators. The red lines refer to the 90% confidence bands.

5 Conclusions

The main objective of this paper was to answer the questions, if the discharge characteristics of the Elbe River have changed over the last decades and how much the design discharges (i.e. HQ100) are affected by the latest extreme events in 2002, 2006, 2011, and 2013.

For the majority of the flood indicators an increase in the HQ100 levels over the last decades can be stated. The 2013 event leads to a remarkable jump in the HQ100 events in all flood indicators. No HQ100 level exceeds the upper (or lower) confidence band, thus no statistically significant changes can be stated at the 90%-level. However, for many flood indicators there is clear tendency towards the upper confidence bands. The results obtained within this investigation for the gauge Neu Darchau are not unrestricted transferable to more upstream located gauges (e.g. Dresden) due to differences in the

catchment size, runoff concentration time and specific discharge.

Acknowledgements

We highly acknowledge the Waterways and Shipping Administration of the Federal Government for providing discharge data of gauge Neu Darchau.

References

[1] Acero, F.J., Garcia, J.A., and Cruz Gallego, M.: Peaks-over threshold study of trends in extreme rainfall over the Iberian, Peninsula, J. Climate 24, 1089–1105, 2011.

[2] Bayliss, A.C., and Jones, R.C.: Peaks-over-threshold flood database: Summary statistics and seasonality. Report No. 121. Institute of Hydrology: Wallingford, 1993.

[3] Beurton, S., and Thieken, A.H.: Seasonality of floods in Germany. Hydrological Sciences Journal 54 (1): 62–76, 2009.

[4] Bormann, H., Pinter,N., and Elfert, S.: Hydrological signatures of flood trends on German rivers: Flood frequencies, flood heights and specific stages. Journal of Hydrology 404 (1-2): 50–66, 2011.

[5] Cleveland, W. S. (1981) LOWESS: A program for smoothing scatterplots by robust locally weighted regression. The American Statistician 35, 54.

[6] Coles, S.: An Introduction to Statistical Modeling of Extreme Values. Springer-Verlag: New-York, 2001.

[7] Davison, A.C., and Smith, R.L.: Models for exceedances over high thresholds (with discussion). Journal of the Royal Statistical Society B 52: 393- 442, 1990.

[8] Hawkes, P.J., Gonzalez-Marco, D., Sánchez-Arcilla, A., and Prinos, P.: Best practice for the estimation of extremes: A review. Journal of Hydraulic Research 46 (Extra Issue 2): 324–332, 2008.

[9] Hosking, J.R.M., Wallis, J.R.: Regional frequency analysis. Cambridge University-Press: Cambridge, 1997.

[10] Katz, R.W., Parlange, M.B., and Naveau, P.: Statistics of extremes in hydrology. Advances in Water Resources 25: 1287–1304, 2002.

[11] Kingston, D.G., Lawler, D.M., and McGregor, G.R.: Linkages between atmospheric circulation, climate and streamflow in the northern North Atlantic: research prospects. Progress in Physical Geography 30 (2): 143–174, 2006.

[12] Kropp, J.P., and Schellnhuber, H.J.: In Extremis. Disruptive Events and Trends in Climate and Hydrology. Springer-Verlag: Berlin, 2011.

[13] Lang, M. Ouarda, T .B.M.J., and Bobée, B.: Towards operational guidelines for over-threshold modeling. Journal of Hydrology 225: 103–117. DOI:10.1016/S0022-1694(99)00167-5, 1999.

[14] Leadbetter, M.R.: On a basis for 'Peaks over Threshold modeling. Statistics & Probability Letters 12: 357–362, 1991.

[15] Maidment, D.: Handbook of Hydrology, McGraw-Hill, New York, 1993.

[16] Markovic, D.: Interannual and interdecadal oscillations in hydrological variables: Sources and modeling of the persistence in the Elbe River Basin. Dissertation: University of Kassel, 2006.

[17] Mendez, F., Menendez, M., Luceno, A., and Losada, I.J.: Analyzing monthly extreme sea levels with a time-dependent GEV Model. Journal of Atmospheric and Oceanic Technology 24: 894-911, 2007.

[18] Mudelsee, M., Börngen, M., Tetzlaff, G., Grünewald, U.: No upward trends in the occurrence of extreme floods in central Europe. Nature 425: 166–169, 2003.

[19] Mudelsee ,M.: Extreme floods in central Europe over the past 500 years: Role of cyclone pathway "Zugstrasse Vb". Journal of Geophysical Research 109 (D23). 2004.

[20] Mudersbach, C., and Jensen, J.: Non-stationary extreme value analysis of annual maximum water levels for designing coastal structures at the German North Sea coastline. Journal of Flood Risk Management 3 (1): 52–62, 2010.

[21] Petrow, T., Merz, B.: Trends in flood magnitude, frequency and seasonality in Germany in the period 1951–2002. Journal of Hydrology 371 (1-4): 129–141, 2009.

[22] Petrow, T., Zimmer, J., Merz, B.: Changes in the flood hazard in Germany through changing frequency and persistence of circulation patterns. National Hazards Earth System Sciences 9 (4): 1409–1423, 2009.

[23] Pociask-Karteczka, J.: River Hydrology and the North Atlantic Oscillation: A General Review. AMBIO: A Journal of the Human Environment 35 (6):312–314, 2006.

[24] Rosbjerg, D., and Madsen, H.: On the choice of threshold level in partial durations series. XVII Nordic Hydrological Conference, Alta, Norway, NHP Rep no. 30: 604–615, 1992.

[25] Rölver, N.: Discharge on 24/25 March 1888 at gauge Neu Darchau. WSA Lauenburg. pers. Comm, 2012.

[26] Smith, R.L. Extreme Value Theory Based On The Largest Annual Events. Journal of Hydrology 86: 27–43, 1986.

Fourier Integral Operators in Stochastic Structural Analysis

Michael Oberguggenberger, Martin Schwarz

Institute of Basic Sciences in Engineering Science
Unit of Engineering Mathematics
Faculty of Engineering Science
University of Innsbruck,
Technikerstr. 13, A-6020 Innsbruck, Austria
michael.oberguggenberger@uibk.ac.at

Abstract. The goal of this programmatic paper is to propose a novel method of analyzing the effects and propagation of disturbances in engineering structures in the presence of spatially distributed random imperfections. The applicative targets are reliability analysis, damage detection, system identification, and calibration of models in the presence of randomly perturbed structures in elasticity and strength of materials. The set-up applies to wave propagation in random media, i.e., materials with stochastically varying properties. The approach will consist in representing the dynamic response of the structure by means of stochastic Fourier integral operators. That is, the random variations of the structural parameters are not modelled directly, but represented by stochastic terms in an asymptotic approximation to the solution. In this way, the stochastic characteristics of the response can be explicitly calculated. Having calibrated the stochastic response parameters to the given data, predictions about the future behavior as well as the underlying structural parameters can be made. The proposed research is in its initial phase.

1 Introduction

One of the most prominent tasks in engineering fields, such as civil or aerospace engineering, is the assessment of the reliability of the designed structure. The reliability depends on the loads, to which the structure will be subjected, and its material and/or geometric properties. Both kinds of input come with uncertainty, either due to lack of knowledge about the future usage or through production imperfections or progressing damage.

In civil engineering, modelling the uncertainties by probabilistic methods has become the standard for more than twenty years. The response of an engineering structure is generally described by means of an input-output function, often given by a numerical model. The *direct* problem consists of determining the stochastic variations of the output, given randomly perturbed input parameters. The *inverse* problem consists of determining the properties of the input parameters, given error prone measurements of the output. A stochastic structural theory has to be able to address both questions.

Random fields constitute the established mathematical tool to describe random spatial variations of material or geometric properties of a structure [5]. Applications in elastostatics and reliability are abundant [6, 7, 8]. In the dynamic case, stochastic processes have been in use for describing driving forces in stochastic structural mechanics. These noise processes are usually applied to systems whose material properties are deterministic. The

same applies to the well established methods of damage detection e.g. by Lamb waves, state space and time series methods, which are used to detect changes in the properties of otherwise deterministically given structures. However, few methods are available in the case of dynamically excited structures with random field coefficients. Only in the special case of randomly layered media, i.e. media which are smooth between randomly placed interfaces, an elaborate theory is available [2].

Wave propagation and propagation of disturbances in random media with continuously varying random fields has hardly been addressed so far. The reason for this gap can be found in the mathematical theory of partial differential equations with random field coefficients. Indeed, the realizations of the random fields commonly in use in elastostatics do not have the degree of smoothness required to construct solutions in the propagation case. This makes it impossible to investigate the stochastic characteristics of the solutions, which would be required to study the influence on the reliability of the structure, to detect material parameters, or to model damage on a continuous level. A further obstacle is that the dependence of the response on the coefficients of a differential equation is generally nonlinear, even if the equation is linear. Thus the effects of a stochastic perturbation of otherwise smooth coefficients can hardly be tracked explicitly.

The goal of the research[1] presented here is to close this gap and develop and implement a new method for the description of the time-dependent behavior of structures with randomly perturbed material and geometric properties. We propose to cast the structural response in the form of a Fourier integral operator and to shift the stochastic modelling from the coefficients to stochastic building blocks of the Fourier integral operator. A Fourier integral operator consists of an exponential term containing the phase function (which describes the propagation geometry) and an amplitude. Applied to initial data, an approximate solution of the system of partial differential equations describing the wave propagation is obtained.

The direct approach would start from the equation and a stochastic model of its coefficients, and consist of computing the phase function and amplitude. In our approach, we will start from a stochastic model of the phase function and amplitude and model the stochastic structural response with the aid of the Fourier integral operator. Since neither the stochastic models of the coefficients nor the ones of the phase function and amplitude are known a priori, but have to be determined by data fitting, the new approach appears as justified as the old approach. However, the big advantage of the Fourier integral operator approach is that explicit formulas for the stochastic properties of the response can be computed, like its autocovariance function, which can then readily be compared with measurement data.

As the research is in its initial phase, the purpose of this presentation is programmatic – no concrete results can be given at this stage. In Section 2, the concepts will be elaborated in more detail. Section 3 contains the description of a simple model from elastodynamics and should demonstrate why the new methods will aid in solving the stochastic direct and inverse problems. Section 4 addresses the case of a one-dimensional transport equation, in which case first explicit results can be demonstrated.

[1]Project No. 4602529, "Fourier Integral Operators in Stochastic Structural Analysis", Bridge Program, The Austrian Research Promotion Agency (FFG), together with INTALES Engineering Solutions, Natters, Austria, start in October 2014.

2 The general set-up

To describe the intended methods, consider the equilibrium equations in linear elasticity theory

$$\rho\frac{\partial^2 u_i}{\partial t^2} - \sum_{j,k,l}\frac{\partial}{\partial x_j}c_{ijkl}\frac{\partial u_l}{\partial x_k} = f_i, \quad i = 1,2,3$$

as a typical, simple example or, more generally, hyperbolic systems of the form

$$\frac{\partial \mathbf{u}}{\partial t} = \sum_{j=1}^{m}\mathbf{A}_j(t,x)\frac{\partial \mathbf{u}}{\partial x_j} + \mathbf{B}(t,x)\mathbf{u} + \mathbf{f}(t,x), \tag{1}$$

to be solved for the unknown functions $\mathbf{u}(t,x) = (u_1(t,x), \cdots, u_n(t,x))$. Here t denotes time, x is an m-dimensional space variable, and $\mathbf{A}_j$, $\mathbf{B}$ are $(n \times n)$-matrices.

The main concern will be that the coefficients are random functions of their arguments, i.e., random fields. Random fields are described by means of their autocorrelation function, which is dictated by the data and the available stochastic models. Indeed, a random field R is a stochastic process in space. More precisely, it assigns to every point x in space a random variable $R(x)$. The random field is determined by the finite dimensional, joint probability distributions of the random variables $R(x_1), \ldots, R(x_n)$ for all choices of finitely many points $x_1, \ldots, x_n$. If the random field is Gaussian, it suffices to know the expectation values $\mathrm{E}(R(x))$ and the covariances $\mathrm{COV}(R(x), R(y))$. If the random field is assumed stationary and homogeneous, the expectation value is constant, $\mu \equiv \mathrm{E}(R(x))$, and the covariance is given by an autocovariance function $\Gamma(d) = \mathrm{COV}(R(x), R(y))$ which depends only on the distance $d = |x - y|$. Often, parametrized autocovariance functions of the form $\Gamma(d) = \sigma^2\gamma(d)$ are used, with typical autocorrelation functions $\gamma(d) = \exp\big(-|d|/\tau\big)$ or $\gamma(d) = \exp\big(-d^2/\tau^2\big)$, the field variance σ^2 and the correlation length τ as parameters.

It is important to note that Gaussian fields of this type have continuous, but not necessarily differentiable realizations. Existing mathematical theory provides no solution concept for hyperbolic equations such as (1), if the coefficients are not differentiable up to a certain higher order.

The starting point for this research is the fact that in the case of deterministic, smooth coefficients, the solution to equations like (1) can be written as a sum of Fourier integral operators

$$u(t,x) = \frac{1}{(2\pi)^m}\iint \mathrm{e}^{i\phi(t,x,y,\xi)}a(t,x,y,\xi)u_0(y)\,\mathrm{d}y\mathrm{d}\xi \tag{2}$$

applied to the initial data u_0 (possibly up to a smooth error term). The phase function ϕ, which carries the propagation geometry of the problem, and the amplitude a can be computed from the coefficients of the partial differential equation by solving the so-called eikonal equation and an infinite asymptotic recursion. Apart from the mentioned fact that smoothness of the coefficients is required for the computation of the amplitude and phase, it is practically impossible to track the stochastic properties of the coefficients through these calculations. On the other hand, if the stochastic properties of the amplitude and phase are known, it is much easier to compute the stochastic properties of the solution through the representation (2).

Thus, instead of starting with a stochastic model of the material parameters and computing the stochastic solution, a stochastic asymptotic form of the prospective solution is proposed which then is fitted to the material properties. The program can be summarized as follows:

- Start with a stochastic process model of the phase function and the amplitude, more precisely, a stochastic perturbation of the mean field model. For this, a wealth of stochastic processes is available.
- Introduce scale and regularization parameters in the stochastic perturbation that can be adjusted to the concrete application.
- Construct asymptotic solutions to (1) using formula (2) and determine their stochastic properties.
- Fit those solutions to the specific data in the structural engineering application.
- Draw conclusions about the structural model by studying the changes of the parameters in the fitted asymptotic solutions.
- At this stage, the behavior of the structure can be investigated by usual methods, as e.g. Monte Carlo simulation using the asymptotic solutions. Further, the underlying structural and material parameters can be identified. Following changes in the parameters admits, e.g., damage detection.

3 Indications for longitudinal waves in beams

At this stage, the exemplification of our approach and our target in a simple example will be helpful. This will be followed by an account of the requirements for the envisaged full problem. The example concerns longitudinal vibrations of an elastic, semi-infinite beam. The displacement $u(t,x)$ satisfies the wave equation

$$\rho(x)\partial_t^2 u(t,x) - E\partial_x^2 u(t,x) = 0$$

for $x > 0$, with the density $\rho(x)$ and the modulus of elasticity E.[2] We assume that driving conditions $u(0,t)$, $\partial_x u(0,t)$ have been recorded at the endpoint $x = 0$ for all times t. The sound speed is $\sqrt{E/\rho(x)}$; for notational convenience, we denote its reciprocal by $c(x) = \sqrt{\rho(x)/E}$. Separating the propagating directions by $v = (\partial_x - c(x)\partial_t)u$, $w = (\partial_x + c(x)\partial_t)u$ leads to the coupled system of first order equations

$$(\partial_x + c(x)\partial_t + b(x))v = -b(x)w \quad (3)$$

$$(\partial_x - c(x)\partial_t - b(x))w = b(x)v \quad (4)$$

with $b(x) = c'(x)/2c(x)$, and data $v(0,t) = v_0(t)$, $w(0,t) = w_0(t)$ given at $x = 0$. The propagation geometry is given by the characteristic curves, which in the general case of a space and time dependent coefficient $c(t,x)$ are obtained as solutions of the differential equation

$$\frac{\mathrm{d}}{\mathrm{d}y}\alpha(x,t,y) = c(\alpha(x,t,y),y), \quad \alpha(x,t,x) = t. \quad (5)$$

[2]To shorten the notation, we write $\partial_t = \frac{\partial}{\partial t}$, $\partial_t^2 = \frac{\partial^2}{\partial t^2}$ etc. for the partial derivatives in the sequel.

In the special case under consideration, they are simply given by $\alpha(x,t,y) = t - \int_y^x c(z)\,\mathrm{d}z$. Introducing the phase function ϕ and the amplitude a – in terms of the language of Fourier integral operators – by

$$\phi(t,x,\xi) = \alpha(x,t,0)\xi, \quad a(t,x,y) = \exp\big(-\int_y^x b(z)\,\mathrm{d}z\big),$$

the first component v satisfies the integral equation

$$v(t,x) = \frac{1}{2\pi}\int_{-\infty}^{\infty} \mathrm{e}^{\mathrm{i}\,\phi(t,x,\xi)} a(t,x,0)\widehat{v_0}(\xi)\,\mathrm{d}\xi - \int_0^x a(t,x,y)b(y)w(\alpha(x,t,y),y)\,\mathrm{d}y, \qquad (6)$$

where $\widehat{v_0}$ denotes the Fourier transform of v_0, and similarly for the second component w. The first term in this equation is a classical Fourier integral operator.

Turning to the stochastic case, assume that the deterministic coefficient $c(x)$ is perturbed by some stochastic component, say of the form $c(x) + R(t,x)$ with a random field $R(t,x)$. An immediate obstacle arises, namely, the characteristic equation (5) is only solvable if the realizations of the random field are sufficiently regular, which is typically not the case. Even if the characteristic equation can be solved, the phase function ϕ and the amplitude a are nonlinear functions of the noise term $R(t,x)$ and not known explicitly – thus the stochastic properties of the Fourier integral operator in the solution formula are not tractable, in general.

In our approach we plan to circumvent these problems by introducing the noise not in the coefficient $c(x)$, but rather in the representation of the solution. That is, the phase function is assumed to be of the form $\phi(t,x,\xi) + X(t,x,\xi,\sigma,\tau,\varepsilon)$ where $\phi(t,x,\xi)$ is the deterministic part (possibly from the unperturbed deterministic system) and $X(x,t,\xi) = X(t,x,\xi,\sigma,\tau,\varepsilon)$ denotes a family of mean zero stationary stochastic processes with variance σ^2, correlation length τ (possibly vector valued in the non-isotropic case) and a further parameter ε (which is meant for scaling and/or regularizing the paths of the process). Similarly, the amplitude may be perturbed in such a way or kept deterministic in a first order approximation.

In the next step, this stochastic phase function is introduced in the integral equations for v and w – for the purpose of exposition, the amplitude (and the initial data) is kept deterministic here. Taking the expectation in Equation (6) leads to terms of the form

$$\mathrm{E}\left(\int_{-\infty}^{\infty} \mathrm{e}^{\mathrm{i}\left(\phi(t,x,\xi)+X(t,x,\xi)\right)} a(t,x,0)\widehat{v_0}(\xi)\,\mathrm{d}\xi\right) = \int_{-\infty}^{\infty} \mathrm{e}^{\mathrm{i}\,\phi(t,x,\xi)}\mathrm{E}\left(\mathrm{e}^{\mathrm{i}\,X(t,x,\xi)}\right) a(t,x,0)\widehat{v_0}(\xi)\,\mathrm{d}\xi.$$

But $\mathrm{E}\big(\mathrm{e}^{\mathrm{i}\,X(t,x,\xi)}\big)$ is the characteristic function of the noise process, hence known (and containing parameters σ,τ,ε to be adjusted later). The expectation value of the second integral in (6) will contain cross correlation terms that might be handled by a perturbation expansion, say, with respect to the variance $\sigma^2 \to 0$. Noting that the second integral in (6) can also be rewritten as a Fourier integral operator, the procedure should result in an integral equation for $\mathrm{E}(v(t,x))$ and $\mathrm{E}(w(x,t))$ or at least an approximate integral identity for small σ. A similar computation can be evoked to obtain the autocorrelation and the cross-correlation functions of $v(t,x)$ and $w(t,x)$.

Details of the procedure have yet to be worked out. Further, for applicative purposes, handling two and three space dimensions as well as more general systems will be mandatory. In the general case, separating the components requires pseudodifferential operators (one-way wave equations) and the full power of Fourier integral operators [1, 3, 4].

4 Proof of concept: transport equations

In order to further illuminate the intended approach, we detail the example of a scalar transport equation with random coefficient, which constitutes the simplest type of a hyperbolic equation. In this case, the difficulties of a coupled system as in (3) do not arise, and we are in the position to present a complete solution. The initial value problem for the general transport equation in m space dimensions with source term is of the form

$$\begin{aligned} &\partial_t u + \textstyle\sum_{j=1}^m c_j(t,x)\partial_{x_j} u = b(t,x)u \\ &u(0,x) = u_0(x). \end{aligned} \tag{7}$$

Rather than discussing the general Fourier integral operator representation, which can be found in [4], we focus on the simpler, but prototypical one-dimensional case without source term and propagation speed depending on x only:

$$\begin{aligned} &\partial_t u + c(x)\partial_x u = 0 \\ &u(0,x) = u_0(x), \end{aligned} \tag{8}$$

The characteristic curves are obtained as solutions to

$$\frac{\mathrm{d}}{\mathrm{d}s}\beta(x,t,s) = c(\beta(x,t,s)), \qquad \beta(x,t,t) = x.$$

(Note the interchange of the roles of x in t as compared to (5).) This differential equation can be readily solved by separation of variables, resulting in

$$\beta(x,t,s) = C^{-1}\big(C(x) + s - t\big) \quad \text{with} \quad C(y) = \int \frac{\mathrm{d}y}{c(y)}.$$

The solution can be explicitly expressed as

$$u(t,x) = u_0(\beta(x,t,0)) = u_0\big(C^{-1}\big(C(x) - t\big)\big).$$

Again, if we want to compute the expectation value of $u(x,t)$, we would have to know the law of $C^{-1}\big(C(x) - t\big)$. This is practically impossible and thus demonstrates one of the obstacles in the direct approach. As noted earlier, the solution can be written in terms of a Fourier integral operator

$$u(t,x) = \frac{1}{2\pi}\int_{-\infty}^{\infty} \mathrm{e}^{\mathrm{i}\,\phi(t,x,\xi)}\widehat{u_0}(\xi)\,\mathrm{d}\xi$$

with

$$\phi(t,x,\xi) = \beta(x,t,0)\xi.$$

In this formulation, the law of $C^{-1}\big(C(x) - t\big)$ is still needed. To elaborate our proposed alternative approach, assume first that $c(x) = c_0 + \varepsilon R(t,x)$, a small random perturbation

of a constant propagation speed c_0. Then $\beta(x,t,0) = x - c_0 t + \varepsilon S(t,x) + \mathcal{O}(\varepsilon^2)$ where $S(t,x)$ still has an unknown distribution. As proposed, let us replace $\varepsilon S(t,x)$ by a random process $X(x,t) = X(t,x,\sigma,\tau,\varepsilon)$ of a certain law with parameters to be fitted by model calibration. Then the expression for $u(t,x)$ takes the form

$$u(t,x) \approx U(t,x) = \frac{1}{2\pi}\int_{-\infty}^{\infty} \mathrm{e}^{\mathrm{i}\,(x-c_0 t)\xi}\mathrm{e}^{\mathrm{i}\,X(t,x)\xi}\widehat{u_0}(\xi)\,\mathrm{d}\xi.$$

In this form, we achieve control over the stochastic properties of the prospective solutions. Indeed, if $X(t,x)$ is a stationary mean zero Gaussian process with variance σ^2, we compute the expectation value of $U(t,x)$ by

$$\mathrm{E}\big(U(t,x)\big) = \frac{1}{2\pi}\int_{-\infty}^{\infty} \mathrm{e}^{\mathrm{i}\,(x-c_0 t)\xi}\mathrm{E}\Big(\mathrm{e}^{\mathrm{i}\,X(t,x)\xi}\Big)\widehat{u_0}(\xi)\,\mathrm{d}\xi = \frac{1}{2\pi}\int_{-\infty}^{\infty} \mathrm{e}^{\mathrm{i}\,(x-c_0 t)\xi}\mathrm{e}^{-\sigma^2\xi^2/2}\widehat{u_0}(\xi)\,\mathrm{d}\xi.$$

Noting that the inverse Fourier transform of a product becomes convolution, it is seen that $\mathrm{E}(U(t,x))$ is the convolution of the initial data $u_0(y)$ with the Gaussian kernel $\exp(-y^2/2\sigma^2)/\sqrt{2\pi}\sigma$, evaluated at $y = x - c_0 t$. Similarly, the second moments of the response at different points can be computed to

$$\begin{aligned}
&\mathrm{E}\big(U(t_1,x_1)\overline{U}(t_2,x_2)\big)\\
&= \frac{1}{(2\pi)^2}\int_{-\infty}^{\infty}\int_{-\infty}^{\infty} \mathrm{e}^{\mathrm{i}\,(x_1-c_0t_1)\xi-\mathrm{i}\,(x_2-c_0t_2)\eta}\mathrm{E}\Big(\mathrm{e}^{\mathrm{i}\,X(t_1,x_1)\xi-\mathrm{i}\,X(t_2,x_2)\eta}\Big)\widehat{u_0}(\xi)\overline{\widehat{u_0}}(\eta)\,\mathrm{d}\xi\,\mathrm{d}\eta\\
&= \frac{1}{(2\pi)^2}\int_{-\infty}^{\infty}\int_{-\infty}^{\infty} \mathrm{e}^{\mathrm{i}\,(x_1-c_0t_1)\xi+\mathrm{i}\,(x_2-c_0t_2)\eta}\mathrm{E}\Big(\mathrm{e}^{\mathrm{i}\,X(t_1,x_1)\xi+\mathrm{i}\,X(t_2,x_2)\eta}\Big)\widehat{u_0}(\xi)\widehat{u_0}(\eta)\,\mathrm{d}\xi\,\mathrm{d}\eta.
\end{aligned}$$

Here the bar denotes complex conjugation, and we have used the fact that $\overline{\widehat{u_0}}(\eta) = \widehat{u_0}(-\eta)$. We observe that $X(t_1,x_1)\xi + X(t_2,x_2)\eta$ is a mean zero Gaussian variable with variance

$$\mathrm{E}\big((X(t_1,x_1)\xi + X(t_2,x_2)\eta)^2\big) = \sigma^2\xi^2 + \sigma^2\eta^2 + 2\sigma^2\xi\eta\gamma\big(d(t_1,x_1,t_2,x_2)\big),$$

where $\gamma(d)$ is the autocorrelation function of $X(t_1,x_1)$ and $X(t_2,x_2)$, which also depends on the correlation length τ, and $d(t_1,x_1,t_2,x_2)$ is some distance measure between points (t_1,x_1) and (t_2,x_2). Thus

$$\mathrm{E}\Big(\mathrm{e}^{\mathrm{i}\,X(t_1,x_1)\xi+\mathrm{i}\,X(t_2,x_2)\eta}\Big) = \mathrm{e}^{-\frac{1}{2}\left(\sigma^2\xi^2+\sigma^2\eta^2+2\sigma^2\xi\eta\gamma(d(t_1,x_1,t_2,x_2))\right)}$$

and it is seen that $\mathrm{E}\big(U(t_1,x_1)\overline{U}(t_2,x_2)\big)$ is obtained by convolution of $u_0(z_1)u_0(z_2)$ with a two-dimensional Gaussian kernel with covariance matrix

$$\begin{bmatrix} \sigma^2 & \sigma^2\gamma(d(t_1,x_1,t_2,x_2))\\ \sigma^2\gamma(d(t_1,x_1,t_2,x_2)) & \sigma^2, \end{bmatrix}$$

evaluated at $z_1 = x_1 - c_0 t_1$, $z_2 = x_2 - c_0 t_2$, hence explicitly known.

Finally, a sample of measurement data at N points of time and space can be used to estimate the empirical autocovariance function of the response $u(t,x)$, which in turn can be used to determine the parameters σ,τ,ε in the stochastic part of the phase function.

5 Conclusion

In the course of a research project just initiated, the development of a new approach to modelling partial differential equations for wave propagation with random field coefficients is proposed. The novelty lies in developing and implementing a stochastic theory of Fourier integral operators and in placing the stochastic dependence into the phase function and amplitude, rather than into the material parameters. The research will result in a new parametric representation of the stochastic solutions and will admit (a) modelling continuously varying material or geometric properties in imperfect or damaged materials; (b) determining the influence of stochastic perturbations on the dynamic system response; (c) performing reliability and sensitivity analysis for a wider class of engineering problems than currently available; (d) identifying system parameters. The resulting strategy should provide new paths to damage detection, modal analysis in the presence of stochastic noise, parameter identification, sensitivity analysis and reliability analysis. Details have yet to be worked out. This presentation aimed at presenting the concepts and showing the feasibility of the approach in two simple examples.

References

[1] M.V. de Hoop, G. Hörmann, M. Oberguggenberger. Evolution systems for paraxial wave equations of Schrödinger-type with non-smooth coefficients. *Journal of Differential Equations* 245, 1413–1432, 2008.

[2] J.-P. Fouque, J. Garnier, G. Papanicolaou, K. Sølna. *Wave propagation and time reversal in randomly layered media.* Springer, New York, 2007.

[3] C. Garetto, G. Hörmann, M. Oberguggenberger. Generalized oscillatory integrals and Fourier integral operators. *Proceedings of the Edinburgh Mathematical Society* 52, 351–386, 2009.

[4] C. Garetto, M. Oberguggenberger. Generalised Fourier integral operator methods for hyperbolic equations with singularities, *Proceedings of the Edinburgh Mathematical Society* 57, 423–463, 2014.

[5] R.G. Ghanem, P.D. Spanos. *Stochastic finite elements: a spectral approach.* Springer-Verlag, New York, 1991.

[6] O.P. Le Maître, O.M. Knio. *Spectral methods for uncertainty quantification. With applications to computational fluid dynamics.* Springer, New York, 2010.

[7] H.G. Matthies. Stochastic finite elements: Computational approaches to stochastic partial differential equations. *Zeitschrift für Angewandte Mathematik und Mechanik* 88, 849–873, 2008.

[8] C.A. Schenk, G.I. Schuëller. *Uncertainty Assessment of Large Finite Element Systems.* Springer, Berlin, 2005.

Estimation of uncertainties in probabilistic seismic hazard analysis

Mathias Raschke

Stolze-Schrey-Str.1,
65195 Wiesbaden, Germany
+49 611 98819561
MathiasRaschke@t-online.de

Abstract. Buildings and technical facilities are designed against earthquakes. The corresponding design load depends on the local seismic hazard. The latter is described by the relation between local earthquake impact and its average of the annual exceedance frequency. This annual exceedance function (AEF) is mostly estimated by a probabilistic seismic hazard analysis (PSHA) and includes estimation uncertainties (estimation error) as every estimation does. An attempt is made to quantify these uncertainties by the logic tree approach in the PSHA. Therein, AEFs are computed for different parameter combinations of the sub-models such as magnitude distributions, seismicity in the geo-space and ground motion relations. The parameters are selected and weighted by experts.

We criticise the logic tree approach from the statistical point of view and introduce an alternative statistical approach for the estimation of the uncertainties in the PSHA. Therein, we also combine different parameter values for the sub-models. But these are realizations of the random distributions that model the confidence intervals of the parameter estimations. We demonstrate by numerical experiments that our approach works well. It can be evaluated scientifically by the tools of mathematical statistics.

1 Introduction

The level of local seismic shaking intensity is estimated for modern building codes and the earthquake-resistant design of industrial facilities by probabilistic seismic hazard analysis (PSHA). This is part of seismology and earthquake engineering. The goal of the PSHA is the estimation of the annual exceedance function (AEF), $\lambda(y,s)$, for a defined site s that describes the average exceedance rate (frequency, reciprocal return period) of a random shaking intensity Y at site s with $Y > y$ for very rare events. There are different formulations for $\lambda(y,s)$. Cornell (1968) introduced the first comprehensive PSHA. A large number of papers about concrete PSHAs and the corresponding methodology have been published in the last decades (e.g. McGuire, 1993; Bommer and Scherbaum, 2008). A very general formulation for the AEF is (Raschke, 2014)

$$\lambda(y,s) = \int_t v(t) \int_{X_E} f_E(X_E,t)\Big(1 - F_y\Big(y; E(Y(s)) = g\big(X_{E,s,t}\big), V(Y(s)) = g^2\big(X_{E,s,t}\big)V(\epsilon)\Big)\Big)dX_E dt \quad (1)$$

with location vector t of source allocations, parameter vector X_E of the quake and event density v of at point t, the ground motion relation g (GMR; also called the attenuation function and ground motion prediction equation), the cumulative distribution function

(CDF) F_y of Y with variance $V(.)$ and expectation $E(.)$. One possible regression model of the ground motion relation is

$$Y = \epsilon g(X),\ E(Y) = g(X), E(\epsilon) = 1, V(Y) = V(\epsilon)g^2(X), \tag{2}$$

The vector X of the predicting variables include X_E of Eq.(1) and the distance $d = |s-t|$. The error component is ϵ and determines the characteristic of F_y in Eq.(1).

There are many different formulations for Eq.(1) and (2). Eq.(1) is often expressed by a sum of integrals for the different source regions with homogeny seismicity (e.g., [9]). Moreover, the integration over the geographic space can be replaced by integration over the source distance and its probability distribution. We prefer Eq.(1) because it is more oriented to the formulations of random fields (e.g., [8]) and the area-equivalence can be only discovered and explained by Eq.(1) [12].

All or most parameters of Eq.(1) and (2) are estimated statistically. This results in estimation errors (standard errors, uncertainties). A large problem in PSHA is the quantification of the estimation error of $\lambda(y, s)$ respectively of y for a defined value of $\lambda(y, s)$ in the sense of a quantile estimation [18] that is caused by the propagated errors. We discuss the popular logic tree approach for the quantification of the estimation error of the AEF in the next section. We then introduce a statistical approach for the quantification of the estimation error and demonstrate the functionality of this approach by numerical research in section 4. In the final section, we summarize the results.

2 The conventional quantification of the estimation uncertainty of the PSHA

The estimation error of a PSHA is frequently quantified by the logic tree according to McGuire (1993). It is now popular and very often used (see, e.g., [2]). Therein, different variants of model components are considered according to Fig.1. This includes different single parameters: for example the maximum magnitude m_{max}, also called the upper bound magnitude, and different sub models, for example the source regions or the GMR. A separate weighting $w*_{,i}$ is applied at each branching of the tree. The sum of the weightings per branching is 1. At the end, there are a large number of combinations of variants of the model components. The AEF $\lambda_j(y, s)$ is computed for each combination. The corresponding weighting $w_{j,all}$ is defined in Fig.1. The sum of these final weightings is again 1. The final estimation for the AEF can be the mean according this weighting or a kind of pseudo-median or pseudo-quantile. The weightings are frequently derived by expert opinion. There is an attempt to quantify weightings for the GMR more objectively with the values from the likelihood function [16], but some important rules of statistical model selection are not considered sufficiently therein [13]. The logic tree approach is also considered for and applied to further natural hazards (e.g., [17, 1]).

We reject the logic-tree approach basically because it is not a method conforming to mathematical statistics. In detail:

- We cannot really compute the standard error and a statistical confidence interval by the logic tree.

- We cannot estimate an objective estimation error by subjective weightings.
- It is an unproved doctrine without the possibility of falsification.
- The estimation errors of the single parameters and components such as maximum magnitude or GMR are not considered in the logic tree although they influence the exactness of the estimation of the AEF.

The error estimation according to the logic tree approach is not really a quantification of the estimation error according to mathematical statistics. Nevertheless, the statistical terms 'confidence interval' or 'median' are applied. We reject this application of statistical terms and suggest calling it 'pseudo-quantile' or 'pseudo-median' to clarify the difference. The quantification of the logic tree is a sensitivity analysis according to Grünthal and Wahlström [6]. We support differentiating between the logic tree and actual uncertainty quantification in the sense of mathematical statistics, but a sensitivity analysis should quantify explicitly the influence of each parameter. We present a mathematical definition of sensitivity in the following section. Unfortunately, we cannot suggest a description of the logic-tree approach according to mathematical statistics as it differs too much from the rules and methods of mathematical statistics.

We underline that we do not exclude expert opinion from science. The economic development of the following year can be estimated by expert opinion. These opinions can then be validated scientifically by the actual development occurring next year. Falsification is possible in this situation. But we cannot validate the results of a PSHA with a logic tree in the same way because we estimate the hazard of local shaking for return periods of hundreds or thousands of years.

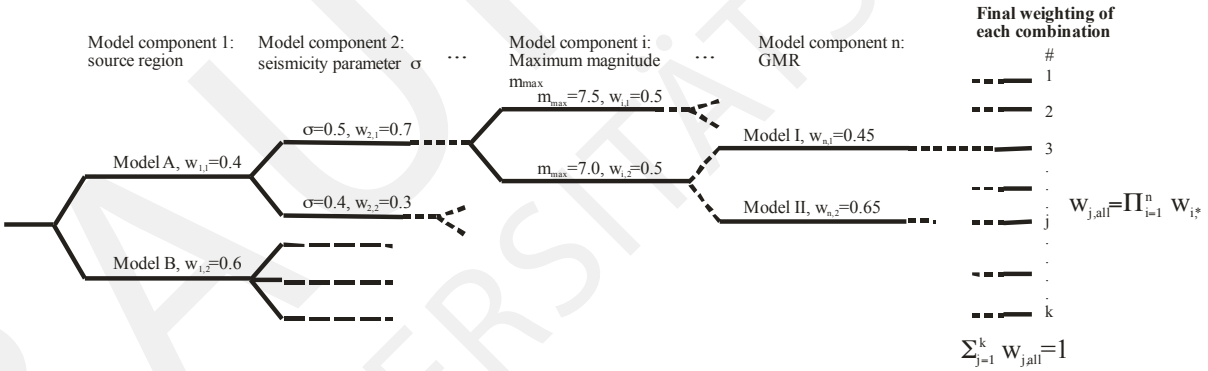

Figure 1: Scheme of the logic tree.

3 The new approach for the quantification of the estimation error in the PSHA

There is a useful and popular tool in mathematical statistics that is called the delta method or delta theorem ([5], chapter 3). It means that the maximum likelihood estimation of ϕ is $\hat{\phi}_0 = p(\hat{\Theta}_0)$ for a statistical model with parameter vector Θ and the scalar function $\phi = p(\Theta)$. The value ϕ is the exceedance frequency in our case and function

p is the entire PSHA model. The estimation error of $\hat{\phi}_0$, respectively the estimation variance, can also be derived from the estimation error of $\hat{\Theta}$ by using the Nabla operator ∇. The confidence interval can be constructed by the normal distribution with (see, e.g., [3], section 2.6.4)

$$\hat{\phi}_0 \; N(\phi_0, V_\phi) \tag{3a}$$

$$V_\phi = \nabla\phi^T V_0 \nabla\phi, \text{ and} \tag{3b}$$

$$\nabla\phi = \left[\frac{\partial\phi}{\partial\Theta_1}, \cdots, \frac{\partial\phi}{\partial\Theta_i}, \cdots, \frac{\partial\phi}{\partial\Theta_k}\right]^T. \tag{3c}$$

The number of elements in Θ is k. The sensitivity of $\hat{\phi}_0$ in relation to a parameter Θ_i is obviously determined by Eq.(3c). This is also our mathematical definition of sensitivity.

We cannot directly apply the delta method for the PSHA as the numerical burden would be very large if we computed the confidence range of y in $\lambda(y, s)$. Moreover, a PSHA can include a large number of parameters. Last but not least, not every parameter estimation is normally distributed. The estimation of the maximum magnitude can be exponentially distributed [11] in the case of the truncated exponential distribution. Nevertheless, we can apply the principal idea of the delta method according to the procedure of Fig.2. We estimate in the first step the parameters of the PSHA model, including the estimation errors and the dependencies between the estimated parameters. We then point estimate the AEF in step 2. In addition, we generate realisation for the parameters by Monte Carlo simulations according to the distribution of the estimation errors of step 1. The AEF is computed for each realization of the parameter vector in step 4. In the last step, the error propagation from step 1 to step 2 can be computed by analysing the set of AEFs from step 5. Their variances are equal to the error variances (square of the standard error/standard deviation) of the AEF of step 2. The accurateness of the procedure depends on the number of simulations in step 3.

We demonstrate the functionality of the approach by a simple, fictive example in the following section. The numerical research is also the possibility for the falsification of our approach.

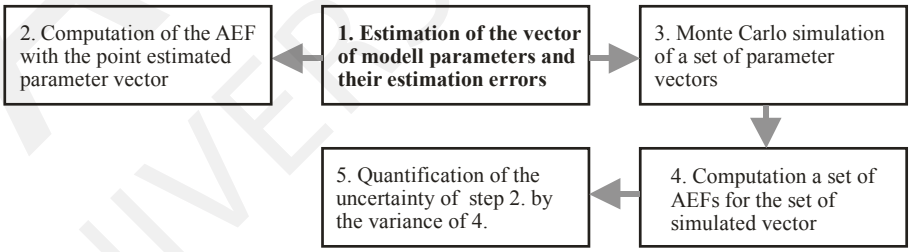

Figure 2: Scheme of a PSHA with computation of the estimation error.

4 A numerical example

We construct the reality for our example and define its 'actual' parameters. The considered site is in a source region with uniform seismicity according to Fig.2a. The average

numbers of earthquakes in this region is η for random magnitudes $M \geq 4$ and corresponds to $v(t)$ in Eq.(1) with

$$\eta = 300^2 v(t) \tag{4}$$

The magnitude distribution is modelled by the truncated exponential distribution [4] and is shown in Fig.2b. It has a maximum magnitude $m_{max} = 7$ in our example. The CDF is

$$F(m) = \frac{1 - \exp(-(m - m_{min})/\sigma)}{1 - \exp(-(m - m_{max})/\sigma)} \tag{5}$$

The 'actual' circular GMR $g(X)$ of the point sources is formulated with for the peak ground acceleration (PGA, $[cm/s^2]$; d and h [km]) and normally distributed residuals ξ

$$\ln(Y) = g^*(X) + \xi, E(\ln(Y)) = g^*(X), V(\ln(Y)) = V(\xi), E(\xi) = 0 \tag{6a}$$

$$g^*(X) = \Theta_0 + \Theta_1 m + \Theta_2 \ln\left(\sqrt{d^2 + h^2}\right) + \Theta_3 \sqrt{d^2 + h^2}, X = (h, d, m) \tag{6a}$$

$$g(Y) = E(Y) = \exp\left(g^*(X) + V(\xi)/2\right) \tag{6a}$$

The GMR is pictured in Fig.3c. The random hypocentre depth H is log-normally distributed. We list the relevant information about the parameters such as their actual values, their samples and references for their inference in Tab.1.

Para-meter	Actual value	Description	Equation	Estimation method and error distribution (confidence range)	Sample (size n)
σ	0.4348	magnitude distribution	5	simplified according to exponential distribution [7]	n=40
m_{max}	7	maximum magnitude	5	[10, 11]	Maximum of 600 years
η	1	average annual number of earthquake $M \geq 4$ in the region	4	parameter estimation for the Poisson distribution [15]	Observed number $M \geq 4$ of 100 years
Θ_0	4.7	GMR	6	[14]	n=300
Θ_1	0.6	GMR	6	[14]	n=300
Θ_2	-1.1	GMR	6	[14]	n=300
Θ_3	-5	GMR	6	[14]	n=300
$V(\xi)$	0.25	GMR, residual variance	6	[14]	n=300
$E(H)$	10	Expectation of hypocentre depth	-	[7, 15]	n=300
$V(H)$	36	Variance of hypocentre depth	-	[7, 15]	n=300

Table 1: Parameters, the actual values of the example, sample sizes and estimation

We simulate 1000 samples for our constructed reality and estimate the parameters according to step 1 in Fig.2. We then compute the AEF with the point estimations according to step 2. Therein, we define the values of $\lambda(y, s)$ and compute the corresponding value of y.

Furthermore, we generate parameters by Monte Carlo simulations (step 3) and compute the corresponding AEFs (step 4). We do these 20 times for each of the 1000 samples of the 'real world' and estimate the estimation variance each time. We can now evaluate the suggested procedure by a comparison between the variance of a 1000 AEF of the point

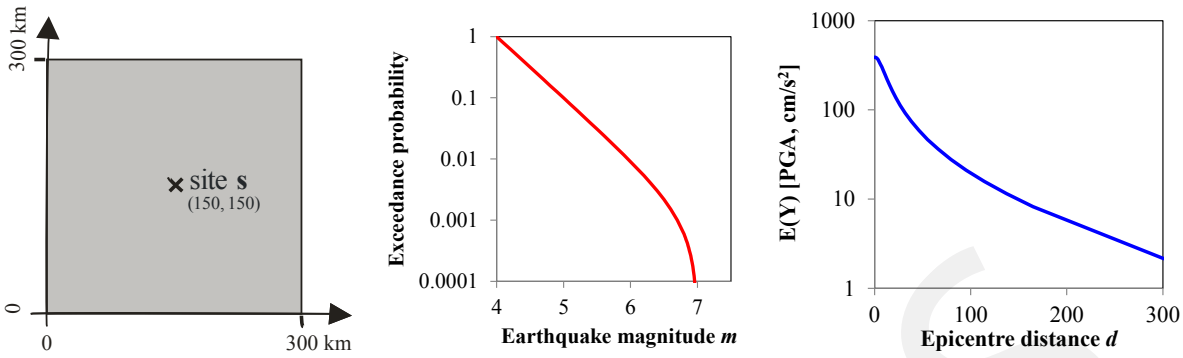

a b c

Figure 3: Constructed example: 3a) analysed site and source region, 3b) magnitude distribution, 3c) GMR (h=10km, m=6).

estimations (step 2) and the average of all estimated error variances for step 5. We show this comparison in Fig. 3a. There is a very good accordance for exceedance frequencies smaller than 1/1000. The average of the estimated error variances is a bit larger for larger exceedance frequencies. This could be caused by the decreasing exactness of our computation for decreasing exceedance frequency. We apply a Monte Carlo simulation similar to the stochastic integral to compute the AEF.

We also compare the 'actual' AEF with the average of the point estimations (step 2) and the average of the averages of the AEFs of step 4 in Fig. 3b. There are differences for exceedance frequencies larger than 1/1000.

The construction of confidence ranges is not investigated in detail. But we have briefly researched the distribution of the estimated values of y for $\lambda(y, s) = 1/1000$. The result is depicted in Fig.2c. The confidence ranges obviously should be constructed with a log-normal distribution rather than with a normal distribution.

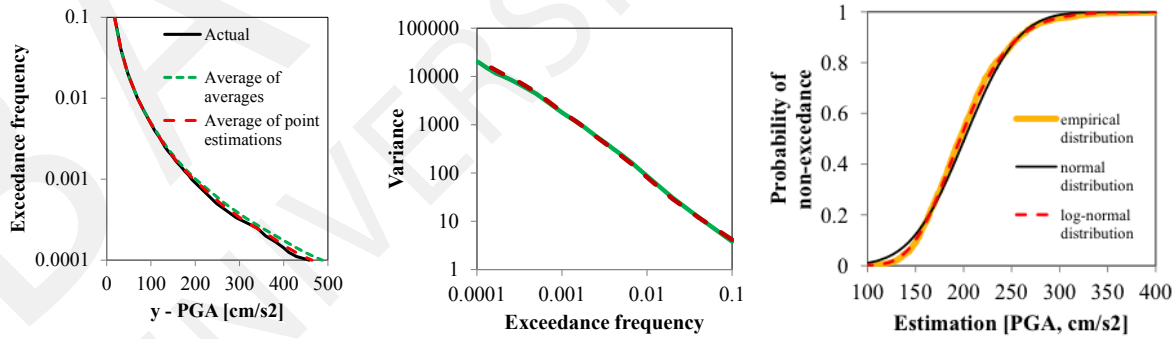

a b c

Figure 4: Results of the PSHA for the example in Fig.3 a) AEF, b) variance of the estimation errors of y for defined exceedance frequencies (green line – variance of the point estimations of step 2, red line – average of the 1000 estimated variances of step 5), c) distribution of estimated y for $\lambda(y, s) = 1/1000$.

5 Conclusions

We have criticised the logic-tree approach for the quantification of the uncertainty of the PSHA and have suggested a new approach for the quantification of the estimation error that is strongly oriented to the delta method from mathematical statistics. We have shown by the numerical example that our approach works. It also could be falsified if it is not correct. In this way, it fulfils a principal scientific standard. This cannot be claimed for the logic-tree approach.

We suggest further research in this field to verify and improve our approach and to extend it. The correct construction of the confidence interval should be the goal of future research.

References

[1] Annaka, T., Satake, K., Sakakiyama, T., Yanagisawa, K., Shuto, N. (2007): Logic-tree Approach for Probabilistic Tsunami Hazard Analysis and its Applications to the Japanese Coasts. Pure and Applied Geophysics 164:577-592.

[2] Bommer, J.J., Scherbaum, F. (2008): The Use and Misuse of Logic Trees in Probabilistic Seismic Hazard Analysis. Earthquake Spectra 24:997-1009.

[3] Coles, S. (2001): An introduction to statistical modeling of extreme values. Springer, London.

[4] Cosentino, P., Ficarra, V., Luzio, D. (1977): Truncated exponential frequency-magnitude relationship in earthquake statistics. Bulletin of the Seismological Society of America 67: 1615-1623.

[5] DasGupta, A. (2008): Asymptotic theory of statistics and probability. Springer Texts in statistics, Spinger, New York.

[6] Grünthal, G., Wahlström, R. (2001): Sensitivity of parameters for probabilistic seismic hazard analysis using a logic tree approach. Journal of Earthquake Engineering 5:309-328.

[7] Johnson, N.L., Kotz, S., Balakrishnan, N. (1994): Continuous univariate distributions – Vol.I. 2nd ed., Wiley, New York.

[8] Kabluchko, Z., Schlather, M., de Haan, L. (2009): Stationary max-stable random fields associated to negative definite functions. The Annals of Probability 37:2042–2065.

[9] McGuire, R.K. (1993): Computation of seismic hazard. Anali di Geofisica, 36:181-200.

[10] Pisarenko, V.F., Lyubushin, A.A., Lysenko, V.B., Golubeva, T.V. (1996): Statistical estimation of seismic hazard parameters: maximum possible magnitude and related parameters. Bulletin of the Seismological Society of America 86: 691-700.

[11] Raschke, M. (2012): Inference for the truncated exponential distribution. Stochastic Environmental Research and Risk Assessment 26: 127-138.

[12] Raschke, M. (2013): Statistical modelling of ground motion relations for seismic hazard analysis. Journal of Seismology 17:1157-1182.

[13] Raschke, M. (2014): Insufficient statistical model development of ground motion relations for regions with low seismicity. Bulletin of the Seismological Society of America 104:1002-1005.

[14] Rawlings, J.O., Pantula, S.G., Dickey, D.A. (1998): Applied Regression Analysis: A Research Tool. 2nd Ed. Springer: New York.

[15] Rinne, H. (2008): Taschenbuch der Statistik (German, Pocketbook of statistics). 4st ed., Verlag Harri Deutsch, Frankfurt am Main.

[16] Scherbaum, F., E. Delavaud, and C. Riggelsen (2009): Model selection in seismic hazard analysis: an information-theoretic perspective. Bulletin of the Seismological Society of America 99:3234-3247.

[17] Thieken, A., Merz, B., Kreibich, H., Apel, H. (2006): Methods for flood risk assessment: Concepts and challenges. International Workshop on Flash Floods in Urban Areas, Muscat – Sultanate of Oman, 4-6 September 2006.

[18] Upton, G., Cook, I. (2008): A dictionary of statistics. 2nd rev. Ed., Oxford University Press.

Comparison of different model-based design of experiment approaches under moderate errors

Ina Reichert, Peter Olney, Tom Lahmer

Research Training Group 1462,
Faculty of Civil Engineering
Bauhaus-University Weimar,
Berkaer Str. 9, 99425 Weimar, Germany
ina.reichert@uni-weimar.de

Abstract. Performing experiments on and monitoring of civil engineering structures has become more common in recent years for state determination of both aging and newly built modern structures. Before conducting experiments it is always useful to determine the best achievable sensor positions by optimal design of experiments. In this case, model-based design procedures, driven by numerical simulations, are used to find the optimal sensor locations even before the construction of a building. Through the use of a finite element model, measurement results are created artificially by adding two different types of errors: random errors and systematic errors. In order to determine the optimal design, two different methods are used: one based on the Fisher Information Matrix by applying the D-optimality criterion and the other one by reducing the mean-squared error between the true and the estimated solution. A tower-like structure, modeled as a one dimensional cantilever column and discretized using standard beam elements, serves as an application example to compare the presented methods. The results highlight advantages and disadvantages for each method as well as the ability to include different types of errors for the determination of sensor positions.

1 Introduction

To understand processes which happen in reality it is always useful to conduct experiments and take measurements. Preliminary investigations concerning the measurement to be taken are requiered in order to make the experiments as efficient as possible. The basics in Design of Experiments go back to the 1920's "where statistically based methods of experimentation based on the factorial designs" [7] were invented. Since that time a lot of improvements concerning finding the optimal design of experiments were made, but mainly not applied to civil engineering problems. A short review about developed methods is given in the following paragraph.

The Fisher Information Matrix (FIM) M goes back to Ronald Fisher who defined the inverse of M as the lower boundary of the covariance matrix of the parameters [1]. M is computed by the sensitivities of the forward operator of the problem and an optimal design can be found by the use of any optimality criterion which can be found in literature, e.g. [1, 9]. Uciński uses in [9] a Fisher Information Matrix $M(s)$ which depends on the sensor positions s.
While in the publications of Haber, Tenorio and Horesh a bias for ill-posed problems exists, the optimal design is found by minimizing the mean squared error, MSE, [5]. A

similar approach is used by Bardow [2] where the "expected total error, ETE" which is the difference "between the Tikhonov estimate and the true function" is being minimized. This leads to a trade-off between the bias and the variance regarding the expected error. In [2] also a comparison between his approach and the E-optimality criterion used on the FIM is given. The outcome of Haber et. al. [5] is included in the research of Lahmer [6] which also uses the minimization of the MSE. In his work he also uses the FIM to minimize the variances of the parameters by comparing different criteria for optimal design.

For the approach by using the FIM it is missing that systematic errors can not be taken into account. It can only deal with random errors which in most cases follow a normal distribution with zero mean and a constant standard deviation. One step further can be taken by minimizing the MSE, because in this case the error consists of one term for the bias and one for the variance.
This work dedicates itself to the comparison of both approaches while it is considering the optimal sensor positioning on a tower-like structure related to civil engineering as the test example where both methods are going to be verified.

2 Model based design of experiments

Numerical modeling and simulation of structures can be approached in a number of different ways with the inclusion of many sub or partial models. The selection of the appropriate model or models and corresponding complexity must be undertaken by the design or inspection engineer subject to experience or strategic procedures, e.g. see [8]. Experiments and monitoring of structures bridges the gap between physically measured reality and numerical simulations. Generally the design of experiments is necessary to reduce the uncertainties and errors which are obtained by conducting any experiment. Finally the selection of sensor types, their positioning and sampling rate should be optimized by a method for DoE and updated by a numerical model of the examined structure.

2.1 Types of errors

The two types of errors considered are systematic and random, which are both inherent in measurement data originating from various sources. As described in [3], the total error in measurement data can be written as:

$$\delta_i = \beta_i + \varepsilon_i \tag{1}$$

where β represents the systematic or bias error, and ε represents the random error. The error terms are given by a value relative to δ_i for β_i and $\varepsilon_i = \mathcal{N}(0, \sigma^2)$, a normally distributed random variable with zero mean and variance σ^2. For example, the systematic error could come from a poor calibration or too strong of an abstraction during the model building process, while the random error can have a number of sources including phenomena such as cable noise observed in wired monitoring systems. A fictitious measurement time history u is created by adding the total error to the model response y:

$$u(x, t_i) = y(x, t_i) + \delta_i \tag{2}$$

where x and t correspond to the spatial and temporal domains respectively.

2.2 Optimal sensor positions using Fisher Information Matrix

As described in Uciński [9], the Fisher Information Matrix, FIM, can be derived using the Cramér-Rao inequality as a lower bound estimate of the covariance matrix of parameters. This leads to a probabilistic definition of optimal sensor placement. Most simulations of civil engineering structures use deterministic models and methods, therefore this original form of the FIM cannot be used directly for the design of experiments. In order to relate numerical model responses and parameters to measurement on structures, certain assumptions are necessary. A basic assumption is that the numerical model sufficiently represents the considered structure. The most common approach is to consider the numerical model response as a measured response by the addition of noise. When this noise is taken as a random variable with a probability distribution, then a relation between the probabilities and model responses can be made. Considering this along with spatially uncorrelated errors [9], the FIM becomes

$$M = \frac{1}{\sigma^2} \sum_{j=1}^{n^{\text{sens}}} \int_0^{t_f} \left(\frac{\partial y(\theta, x^j, t)}{\partial \theta} \right)^{\mathrm{T}} \left(\frac{\partial y(\theta, x^j, t)}{\partial \theta} \right) \mathrm{d}t \tag{3}$$

where y solves the forward problem, θ are the parameters of interest, x is the spatial variable and t is the temporal one, the measurements are taken over a finite time interval, t_f. The standard deviation of the measurement error is σ, constant for all measurement locations.

From this brief overview, it becomes immediately clear that only random errors can be considered directly with the FIM, a potential disadvantage when systematic errors are large. Different criteria exist for evaluating and comparing FIMs, which also may return different results as to which sensor configuration is optimal. As described in [9], optimal sensor positioning should minimize some real-valued function, J. One example is the D-optimality criterion:

$$J(M) = \det(M^{-1}). \tag{4}$$

While many other criteria exist and there is still some debate about which one is the best to use, an advantage of the D-optimality condition is that it is independent of the scaling of the parameters (units) [4]. This criterion will be used in this discussion for these and other reasons. This choice is immaterial as long as it is consistent when the comparison is made between measurement setups.

2.3 Optimal sensor positions using mean-squared errors

This second method is using the minimization of the difference between the "exact" solution for the parameters θ and its estimate $\hat{\theta}$. Therefore first the form of the data has to be defined, assuming a linear relation between model input and output. In this case the data u consists of the "exact" solution y and an error term δ which is described by equation 2, where $\delta = \beta + \varepsilon$ can describe both, either a systematic (β) or a random (ε) error as explained in 2.1. As we do not know the true structure of the systematic error β, it is here considered as a relative error to the "exact" value and ε represents a normal distribution with zero mean and known variances σ^2. The question is now how to setup

an experiment that leads to the best approximation of the unknown vector of parameters θ. Firstly, a sufficient number of experiments has to be chosen. In the well-posed case, with which we are dealing in this article, the number of experiments or in this case sensors n^{sens} has to hold the inequality $n^{\text{sens}} \geq n$. [5]
Coming back to the optimization problem a cost function has to be set up. This leads to the usage of the mean-squared error (MSE) which is expressed by

$$\mathbf{MSE}(\hat{\theta}) = \mathrm{E}\|\hat{\theta} - \theta\|^2 \tag{5}$$

and which should be minimized by

$$\min \mathrm{E}\|\hat{\theta} - \theta\|^2 \tag{6}$$

as written in [2] to find the optimal experimental design.
After the number of sensors is defined, the optimal postions have to be found. The method which is used in this paper deals only with artificial measurements, which means that two different types of noise are added to the "real" measurement which is not corrupted by any kind of noise and is gained by solving a finite element approach.
This way we take a model response y and add a random error on the one hand and a systematic error on the other hand to get the measured data u. This leads to the noise corrupted terms

$$u^{\text{rand}}(\theta, x^j, t_i) = y(\theta, x^j, t_i) + \varepsilon \quad \text{and} \tag{7}$$

$$u^{\text{sys}}(\theta, x^j, t_i) = y(\theta, x^j, t_i) + \beta \quad \text{respectively,} \tag{8}$$

which depend on the parameters θ, the sensor postions x^j and the time t_i. The corresponding cost functions that depend on the parameters θ and which should be minimized are expressed by

$$\min_{\theta} J^{\text{rand}}(\theta, x^j, t_i) = \min_{\theta} \sum_{j=1}^{n^{\text{sens}}} \left(y(\theta, x^j, t_i) - u^{\text{rand}}(\theta, x^j, t_i)\right)^2 \quad \text{and} \tag{9}$$

$$\min_{\theta} J^{\text{sys}}(\theta, x^j, t_i) = \min_{\theta} \sum_{j=1}^{n^{\text{sens}}} \left(y(\theta, x^j, t_i) - u^{\text{sys}}(\theta, x^j, t_i)\right)^2. \tag{10}$$

After a certain number of iteration steps the gained parameters serve as the estimated ones $\hat{\theta}$ and lead to the mean-squared error given by

$$\mathbf{MSE}(\hat{\theta}, x^j) = \|\hat{\theta}(x^j) - \theta(x^j)\|^2. \tag{11}$$

The value of the MSE is then used as the selection criteria for finding the best sensor positions. This means that the best sensor positions x^j are, where the mean-squared error is minimal.

3 Application on a tower-like structure

3.1 Numerical model

In order to compare the results from applying the two different design of experiment strategies introduced, a tower-like structure is considered as depicted in Figure 1. The

tower is separated into three equal length sections each corresponding to a different material with Young's modulus, E_i. Although three materials are modeled, the density is kept constant at 2550 kg/m^3. A finite element model using nine Bernoulli beam elements of equal length (3 per material) is used to model the structure. Modal damping is kept at 5% for all modes in the discretized system. A dynamic simulation is computed using an initial displacement followed by a free vibration response. Design of the input loading for optimal experiments is outside the scope of this paper.

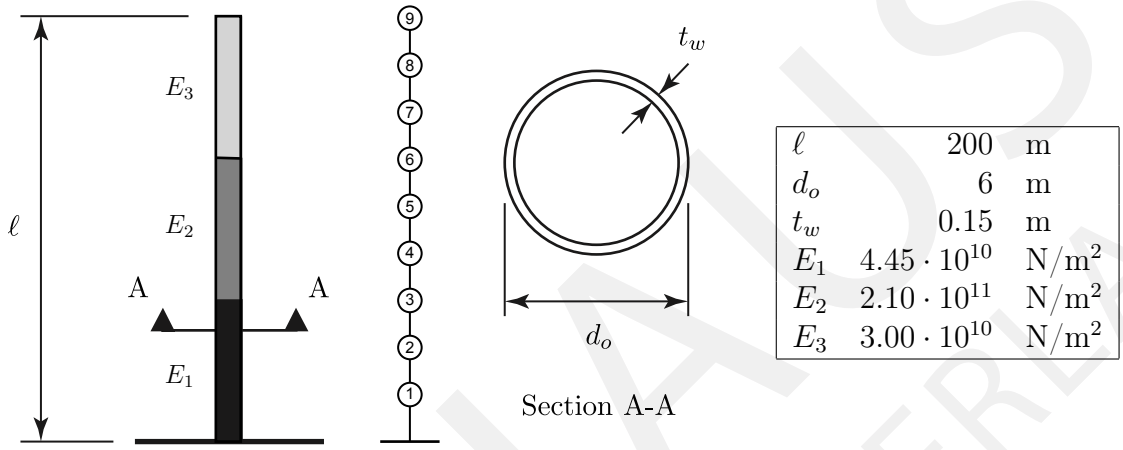

ℓ	200	m
d_o	6	m
t_w	0.15	m
E_1	$4.45 \cdot 10^{10}$	N/m^2
E_2	$2.10 \cdot 10^{11}$	N/m^2
E_3	$3.00 \cdot 10^{10}$	N/m^2

Figure 1: Sketch of the cantilever beam with discrete sensor positions, cross section A-A and values of the material properties

Acceleration time histories taken at specific locations x^j and corrupted by the afore mentioned two types of noise are considered as the measurement data. The random error is hereby represented by a normal distribution $\varepsilon_i = \mathcal{N}(0, \sigma^2)$ with zero mean and the standard deviation $\sigma = 0.005$. For the systematic error a relative description is used, so the systematic error is 5% of the exact value of the acceleration time history.

As we are dealing with the model response on discrete positions x^j, the optimal sensor postions are found by evaluating all combinations of three sensors n^{sens} at nine possible positions n^{pos}. Applying the combinatorial equation

$$\frac{n^{\text{pos}}!}{n^{\text{sens}}!\,(n^{\text{pos}} - n^{\text{sens}})!}, \tag{12}$$

we get 84 combinations which have to be calculated. Their values of the D-optimality criterion and respectively the mean-squared error are serving for sorting the sensor setups in order to gain the best one.

3.2 Results: Comparison between FIM and MSE

The comparison of the results of both methods are shown in the tables 1 and 2. Where there is depicted the best, second best and worst value for the D-optimality criterion of the Fisher Information Matrix, FIM, on one side and the values of the mean-squared error, MSE, corresponding to this particular design of sensors on the other side and the

rows below vice versa. In table 1 the comparison for the random error and in table 2 the one for the systematic one is given.

Table 1: **Random error:** Overview of normalized values of D-optimality criterion of FIM and MSE (Opt. Crit.) for the two best and the worst design corresponding to each method and their values for the other method respectively

	FIM		MSE	
Design	Opt. Crit.	Rank	Opt. Crit.	Rank
[5 8 9]	0.010	1	0.527	30
[4 8 9]	0.010	2	0.384	4
[1 2 3]	1.000	84	0.494	18
[2 5 7]	0.153	44	0.202	1
[2 5 8]	0.120	36	0.332	2
[4 6 7]	0.129	41	1.000	84

Table 2: **Systematic error:** Overview of normalized values of D-optimality criterion of FIM and MSE (Opt. Crit.) for the two best and the worst design corresponding to each method and their values for the other method respectively

	FIM		MSE	
Design	Opt. Crit.	Rank	Opt. Crit.	Rank
[5 8 9]	0.010	1	0.545	58
[4 8 9]	0.010	2	0.545	57
[1 2 3]	1.000	84	0.777	83
[1 2 9]	0.097	30	0.520	1
[1 3 9]	0.343	76	0.520	2
[1 2 4]	0.162	51	1.000	84

4 Discussion and conclusions

The comparison showed that the FIM and MSE optimal placement methods give different results. For the FIM, the ranks and normalized values of the possible designs are independent of the two types of errors considered. However, the MSE showed that the differences in the considered errors can be accounted for resulting in alternative optimal designs. When comparing the same designs between the two methods, the corresponding ranks and normalized values are scattered; no relation can be observed between the best of one method when computed by the other. The relative normalized values are also in different proximities of the best designs.

While these differences can be observed, this information is not sufficient to say one method is better than the other. The MSE method is a far more computational intensive

procedure since the model must be computed for each iteration of an updating optimization for every set of sensor positions. On the other hand, the FIM only requires that the model be computed a few times (twice the number of parameters) in order to approximate the partial derivatives. From the theoretical background, it is apparent that the FIM method is limited to random errors whereas the MSE method can take into account both random and systematic errors, which can be seen in the results, because the systematic error does not effect the optimal sensor positions when using the FIM. Since the type and amount of error actually results in different designs, an accurate description of the error in measurement system is necessary. In addition, a compatible measure for the quality of the measurement setup is necessary due to the fact that optimality criteria are different. Both of these aspects as well as the investigation of the influence of the number of iterations for MSE and the introduction of the sigma-point method will be the subject of further work.

References

[1] Hans Bandemer and Andreas Bellmann. *Statistische Versuchsplanung*. BG Teubner, 1994.

[2] André Bardow. Optimal experimental design for ill-posed problems. In *16th European Symposium on Computer Aided Process Engineering and 9th International Symposium on Process Systems Engineering*, pages 173–178, Amsterdam, 2006. Elsevier.

[3] HW Coleman and WG Steele Jr. *Experimentation and uncertainty analysis for engineers*. John Wiley and Sons, 1989.

[4] Graham C. Goodwin and Robert L. Payne. *Dynamic system identification: experiment design and data analysis*. Academic press, 1977.

[5] Eldad Haber, Lior Horesh, and Luis Tenorio. Numerical methods for the design of large-scale nonlinear discrete ill-posed inverse problems. *Inverse Problems*, 26(2):025002, 2010.

[6] Tom Lahmer. Optimal experimental design for nonlinear ill-posed problems applied to gravity dams. *Inverse Problems*, 27(12):125005, 2011.

[7] LM Lye. Design of experiments in civil engineering: Are we still in the 1920s. In *Proceedings of the 30th Annual Conference of the Canadian Society for Civil Engineering, Montreal, Quebec, June*, 2002.

[8] Thomas Most. Assessment of structural simulation models by estimating uncertainties due to model selection and model simplification. *Computers & Structures*, 89(17):1664–1672, 2011.

[9] Dariusz Uciński. *Optimal measurement methods for distributed parameter system identification*. CRC Press, 2005.

Model Coupling in Structural Engineering Application

Frank Scheiber, Hem Bahadur Motra, Dmitrii Legatiuk, Frank Werner

Research Training Group 1462,
Bauhaus-Universität Weimar
Berkaer Str. 9, 99425, Weimar, Germany
frank.scheiber@uni-weimar.de

Abstract. The paper shows an approach for the coupling of mathematical and physical models in the abstraction process of structural engineering models. Based on the uncertainty quantification in both types of models, weighting factors for the model combination are determined. The more certain a model is, the more it is taken into account in the coupled model. So the coupling approach gives the possibility to verify the accuracy of the used models and to adjust the coupled model to be more precise in predicting physical reality. By usage of the academic example of a cantilever beam, the applicability of the approach is demonstrated.

Keywords: model abstraction, model uncertainties, model coupling

1 Introduction

In the field of structural engineering, the subject of model quality evaluation and model error estimation has become more and more important [1], [11], [14] during the past decade. This is mainly due to the fact that, objects in structural engineering are mostly unique structures. The design process is done only by usage of mathematical abstraction models. Hence, the uncertainty in these models must be reduced to a minimum to make sure that the design criteria given by currently relevant codes, e.g. Eurocode 3 [5], can be maintained without safety concerns. Since current structural systems become more and more complex and challenging, the design only based on mathematical models is sometimes not possible. Experimental investigations will be necessary to determine the physical behavior of materials or structural parts and couple them with numerical calculations [15]. The goal of structural engineering, to achieve a certain reliability and safety, is still in the focus of all investigations and current research.
In accordance to Figure 1, models can be basically separated in two types, mathematical and physical models. They are part of the abstraction process of a considered system. On one side, the mathematical models can consist of numerical or analytical descriptions [17] and will be used in virtual simulations. On the other side, physical models consist of real structural parts, which are physically present. Thereby, physical models may be divided into two subgroups: experiments and monitoring. Experiments are characterized by the definition of boundary conditions, loading, model abstraction and model scaling by the user. In monitoring, measurements were done on real structures with respect to true system input scenarios and the related system responses. For this, the system will not be changed in the characteristics and no structural restrictions occur. In contrast to the system under consideration, the monitoring is also still a model, since only a limited number of model input and output variables can be determined during the measurement process. But, this model is based on the real system under consideration.

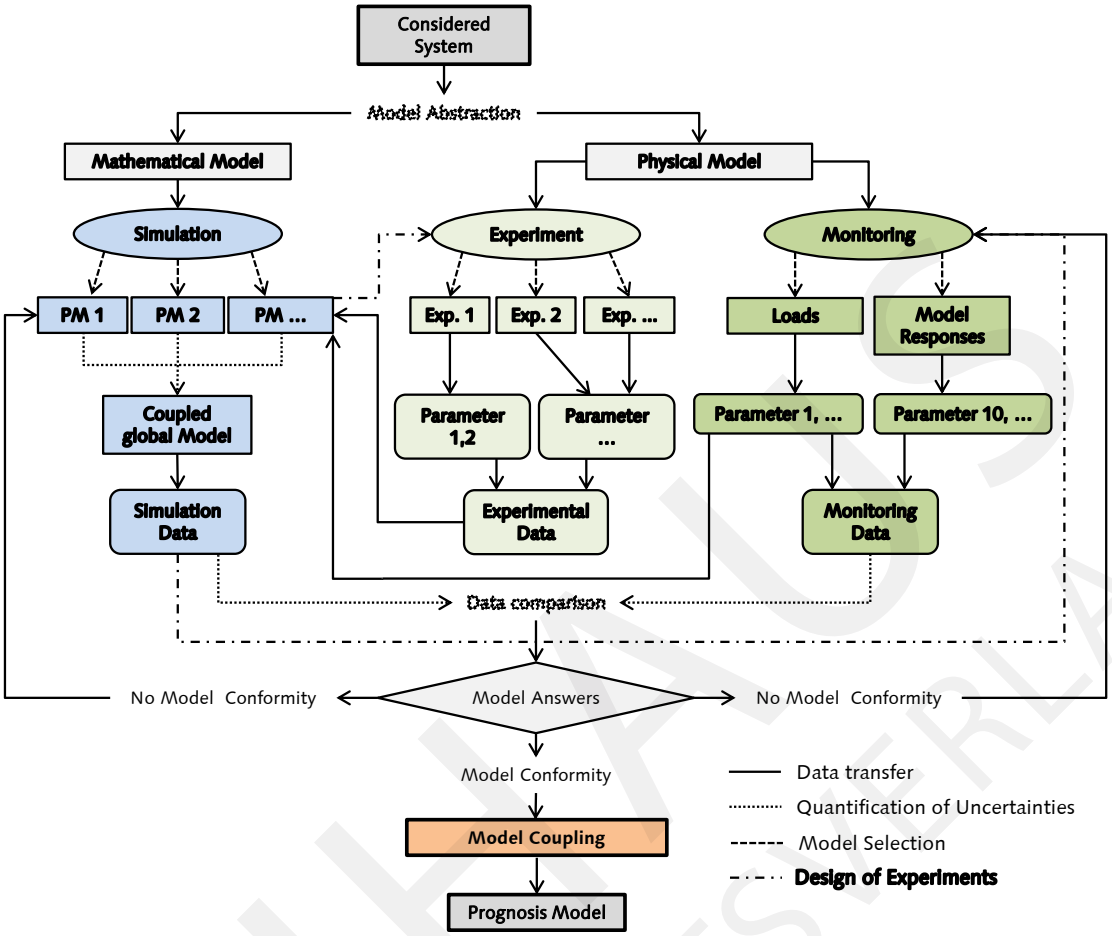

Figure 1: Flowchart of model abstraction and coupling process

To achieve a high quality of mathematical structural design models, there are several approaches for the quality evaluation process available. Most commonly, they are based on the validation to real measurements, which can be done with different methods. The method of model validation [12] or the model assessment by usage of Bayesian theories [2], [7] are the most famous. Since the main content of this paper refers to the coupling of mathematical and physical models, the available measured data in this case can not be used for the evaluation process of the mathematical model. The measurements are required for the coupling process only. Therefore, an evaluation process purely based on mathematical model data has to be used. Different approaches are available in common literature [8], [11], [14].

The quality of a coupled mathematical-physical model strongly depends on the quality of its parts, i.e. the quality assessment of mathematical and physical model has to be performed separately based on the uncertainty calculation for both models. This means that, for the mathematical model the total uncertainty, consisting of model and parameter uncertainty, has to be minimized (see Figure 2). Therefore, the model complexity is the important factor. The more complex a model is, the more phenomena will be considered and this reduces the model uncertainty. In return, however, the number of parameters and thus the parameter uncertainty will be increased. So, there must be a balance between model and parameter uncertainty to find the point for lowest total uncertainty. Limita-

tions in the optimal model combination come from the model robustness also, which takes the usability of the model into account. Robustness therefor is specified as a restriction of the deviations in the output data, which is often necessary in the estimation of highly nonlinear phenomenas. Depending on the range of the important parameters, there are often limitations in the model applicability. These may lead to high scattering in the model responses, which can not be explained by the input variations.

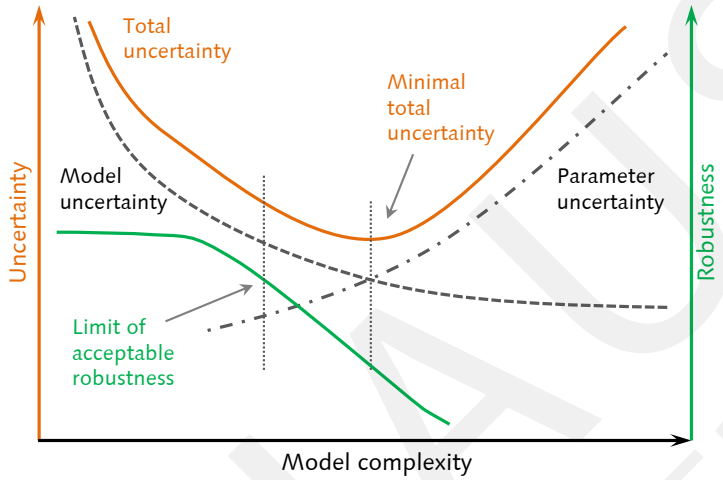

Figure 2: Relationship between model complexity, uncertainty and robustness

A measurement or observed data can unknowingly be very close to the unknown value of the measurand, thus having a negligible error; however, it may have a large uncertainty. Since the exact value of a measurand can never be evaluated, error is an abstract concept, which can never be quantified. However, uncertainty is a measure that can be and should be quantified for every measurement. For this reason, in this study, measurement uncertainty associated with the characterization of material parameters and deflection of beam can be calculated in accordance with GUM [3], a classical approach and GUMS1 [4], Bayesian paradigm.

Some approaches for the combination and coupling of mathematical and physical models are available in literature. One is the hybrid procedure from Laermann [9]. But, currently no approach considering mathematical and physical model uncertainty in the coupling process is presented. Thus, in this paper, a methodology for the quantitative assessment of the quality of the results of measurements and mathematical models as well as developed method of hybrid coupled physical-numerical model are presented. Basis is the academic example of a cantilever beam under vertical loading. For simplification, the experimental investigations will be done virtually. By usage of the exact analytical solution, the determination of real model responses is possible with a minimum of effort.

2 Uncertainty based model coupling

The following approach for the assessment of model coupling is based on the uncertainty quantification in the output parameters of the mathematical and physical models. The polynomial regression analysis [10] as a fundamental response surface method for the

output data is basic for the determination of the uncertainties. So, the output data uncertainties can be determined by the variation of the model responses which are given by:

$$\varepsilon_M(Y) = |\tilde{m}(Y) - \mu_M(Y)| \qquad \varepsilon_P(Y) = |\tilde{p}(Y) - \mu_p(Y)|, \tag{1}$$

where $\tilde{m}(Y)$ and $\tilde{p}(Y)$ are responses of the mathematical and physical models, $\mu_M(Y)$ and $\mu_p(Y)$ are corresponding results of the polynomial response surfaces. For the coupling process, all sources of uncertainties have to be taken into account, so the model evaluation processes for the mathematical and physical models are fundamental. According to equation (1), the so called total difference between the response surfaces of the mathematical and physical model is introduced as follows:

$$\varepsilon_T(Y) = |\mu_M(Y) - \mu_P(Y)|, \tag{2}$$

which estimates the deviation in the mean values of mathematical and physical model response. To use the given models for the coupling approach, there must be a so called model conformity. That means, the models must be able to match the other model answer, at least partially. This can be determined by usage of the model uncertainties and the total difference between the models as follows:

$$\epsilon_T(Y) \leq \epsilon_M(Y) + \epsilon_P(Y), \qquad \epsilon_T(Y) > \epsilon_M(Y) + \epsilon_P(Y). \tag{3}$$

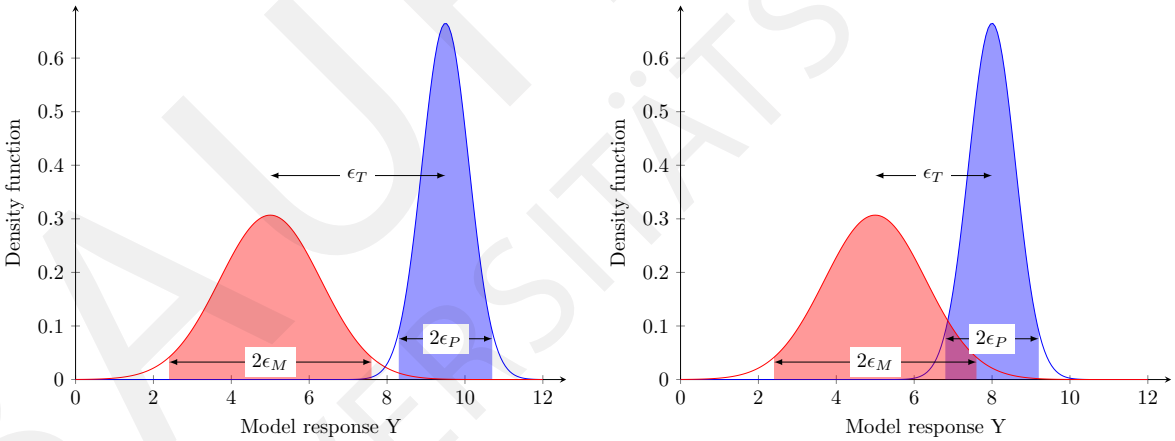

(a) No conformity (b) Partial conformity

Figure 3: Model uncertainties and related model conformity

If the used models have partial model conformity, then there is still a space of coincidence in the model results. The coupling approach has the objective, that the most suitable accurate model answer of the considered system can be described by mathematical and physical model and is therefore located inside of the overlapping model answer space. By usage of the determined model uncertainties, the coupling of the models will be based on weighting factors:

$$\delta_n = 1 - \frac{\epsilon_n}{\sum_{n=1}^{N} \epsilon_n}, \tag{4}$$

where n is the number of the model and N is the amount of all models which will be used for the coupling process. At least two models (one mathematical and one physical model) are required. For multiple mathematical or physical models, the coupling process is also valid. Related to the weighting factors, the response of the new coupled model function can be determined by:

$$\mu_c = \frac{\sum_{n=1}^{N} \delta_n * \mu_n}{N}. \tag{5}$$

Through regression analysis, this response can be determined by a polynomial equation, which describes the coupled model response. By parameter optimization, the mathematical model can be used for the determination of the specific model input parameters to represent this response. Thus, the mathematical model considering the fixed input parameters is able to be used for further investigations on the structural behavior of the considered system.

3 Application - Cantilever beam

3.1 System

For the application of the shown model coupling approach, the example of a cantilever beam is used. The system consists of a rectangular hollow cross section 120x120x10 mm with a length of 1.5 m. The material of the beam is steel S355 according to [5]. Thereby the considered system is similar to practical applications in structural steel engineering. The cantilever beam is loaded by a load of 25 kN distributed over a small area near the end point. By the given dimensions and loading, the considered system reacts in the range of elastic system capacity. So the deviation in the output data is limited. By nonlinear system capacity, the mathematical model output will become high deviations, which leads to model robustness problems. Thereby the deviations in the output data increase significantly by an increase of the load. The fluctuations in the output data can not be described by the variations of the input data anymore. By the definition of a rectangular hollow cross section the phenomenon of structural failure in a sway mode can be neglected, only vertical displacement occurs and will be considered as objective function in the coupling approach. By loading up to plastic deformations,

For simplification, the experimental investigations will be done virtually, by usage of an analytical solution. Unknown scattering in the responses, as usual in measurements, is generated by fluctuations in the implemented load over time.

3.2 Mathematical model

Related to the considered system, the mathematical model abstraction will be done by a parametrized numerical model, consisting of quadratic 3-node beam elements. According to the fact that all material and system parameters in real objects are scattering values, the numerical simulations are performed by usage of normal distributed input parameters according to current literature [13], which are shown in Table 1.

Table 1: Scattering input parameters for numerical model

Parameter	Mean	COV
Young's modulus $[GPa]$	210	0.03
profile height $[m]$	0.12	0.01
profile width $[m]$	0.12	0.01
profile thickness $[m]$	0.01	0.02
Density $[kg/m^3]$	7850	-

The application of model quality analysis for the available numerical models has been shown, that the influences of the different partial models on the objective function of vertical displacement can be neglected. For the given loading in the range of elastic material capacity, geometrical and physical linear, as well as nonlinear models will predict the same model response. So, the model uncertainty related to the abstraction process can be determined as zero, the only uncertainty in the mathematical model responses is caused by the scattering model input parameters and is directly related to the scattering in the model output parameters. That means, the less complex models lead to less parameter uncertainty and thus to less total uncertainty. For consideration of the scattering in the model input parameters, 500 samples were generated by advanced Latin Hypercube Sampling [6], in order to achieve a good parameter distribution. Calculations were done over the full time range with maximum time steps of 0.1 $[s]$, to get impressions of the influences of the scattering on the model output.

3.3 Physical model

To illustrate the proposed strategy for the model coupling, a virtual physical model for a cantilever beam is considered. The idea behind this model is to use the analytical solution for a cantilever beam for the considered loading case, and simulate by this analytical solution results of an experiment. Displacements $u(x,t)$ of points of the beam can be described in framework of the Bernoulli-Euler beam theory by the following non-homogeneous partial differential equation:

$$\rho\, A\, \frac{\partial^2 u}{\partial t^2} + E\, I\, \frac{\partial^4 u}{\partial x^4} = f(x,t), \quad x \in (0, L), \tag{6}$$

where A is the area of a cross-section, ρ is the density, E is the Young's modulus, I is the moment of inertia. All calculations will be performed with the following set of the parameters:

$$\begin{array}{ll} L = 1.5 \text{ m}, & \rho = 7850 \text{ kg/m}^3, \\ A = 4.25 \cdot 10^{-3} \text{ m}^2, & I = 8.43 \cdot 10^{-7} \text{ m}^4, \\ E = 210 \text{ GPa}. & \end{array} \tag{7}$$

The boundary conditions for the cantilever beam are given by:

$$\begin{array}{rcl} u \mid_{x=0} & = & 0, \quad \dfrac{\partial^2 u}{\partial x^2} \mid_{x=L} \; = \; 0, \\ \frac{\partial u}{\partial x} \mid_{x=0} & = & 0, \quad \dfrac{\partial^3 u}{\partial x^3} \mid_{x=L} \; = \; 0. \end{array} \tag{8}$$

The problem will be solved with the homogeneous initial conditions:

$$u \mid_{t=0} = 0, \quad \frac{\partial u}{\partial t} \mid_{t=0} = 0. \tag{9}$$

The excitation force $f(x,t)$ in (6) has the following form:

$$f(x,t) = h_1(x)h_2(t), \tag{10}$$

where:

$$h_1(x) = \begin{cases} 0, & \text{for } x < L_1, \\ -\dfrac{25}{L_2 - L_1} \text{ kN/m}, & \text{for } L_1 \leq x \leq L_2, \\ 0, & \text{for } L_2 < x < L, \end{cases} \tag{11}$$

for $0 < L_1 < L_2 < L$, and:

$$h_2(t) = \begin{cases} t + \frac{1}{10}\sin(150\,t), & \text{for } 0 < t < 1, \\ 1 + \frac{1}{10}\sin(150\,t), & \text{for } 1 \leq t < \infty, \end{cases} \tag{12}$$

where the function $h_2(t)$ contains terms representing a "noise" which is always present in real measurements.

The initial boundary value problem (6)-(10) will be solved by the method of separation of variables. Only some important steps of this method will be mentioned here, the details of the method can be found in [16]. The solution of the beam equation (6) can be represented in the form of the Fourier series as follows:

$$u(x,t) = \sum_{n=1}^{\infty} X_n(x)a_n(t), \tag{13}$$

where $X_n(x)$ are eigenfunctions of the differential equation, and $a_n(t)$ are modal coefficients. Taking into account the boundary conditions (8), the initial conditions (9) and the excitation force (10), the displacements $u(x,t)$ of points of the beam can be described as follows:

$$u(x,t) = \sum_{n=1}^{\infty} \frac{X_n(x)}{\omega_n\,\rho\,A} \left(\int_0^L h_1(x)\,X_n(x)dx \right) \left(\int_0^t h_2(\tau)\sin\left[\omega_n\,(t-\tau)\right] d\tau \right). \tag{14}$$

3.4 Model responses and coupling

In Figure 4 the model responses of both models, numerical and physical, are shown. For the numerical model the scattering model responses are plotted representative at nine time steps. This gives a better overview on both model results.

It can be observed that, with increasing load, the influences of the scattering in the model input parameters on the numerical model results are also increasing. The physical model shows a more constant scattering in the results. Under full load, the scattering is increased by changes in the loading, which is with respect to real measurements. By use

of polynomial regression, the corresponding response surfaces for the considered models can be determined by:

$$\mu(X) = \sum_{i=1}^{n+1} a_i x^{n+1-i}, \tag{15}$$

which are also shown in Figure 4. These response surfaces describe the mean values of the considered models over time and will be used for the next steps of the uncertainty estimation. In accordance to the described coupling approach, the basic model uncertainties are calculated as follows:

$$\varepsilon_M(Y) = \sum_{i=0}^{T} |\tilde{m}(Y_i) - \mu_M(Y_i)| = \pm 2,2[mm], \tag{16}$$

$$\varepsilon_P(Y) = \sum_{i=0}^{T} |\tilde{p}(Y_i) - \mu_p(Y_i)| = \pm 3,8[mm], \tag{17}$$

It shows that, the scattering in the physical model response is much higher than the scattering in the mathematical model response. In order to check the applicability of the coupling approach, the total difference between the models will be used:

$$\varepsilon_T(Y) = \sum_{i=0}^{T} |\mu_M(Y_i) - \mu_P(Y_i)| = 1,25[mm]. \tag{18}$$

With a smaller total difference than the mathematical and physical model uncertainty, the models have at least partial model conformity. The model output ranges are overlapping each other, which means both models are able to represent the system behavior in the model coupling zone. Thus, the models can be used for further investigations. By usage of the calculated averages of model uncertainties from both models, the weighting factors

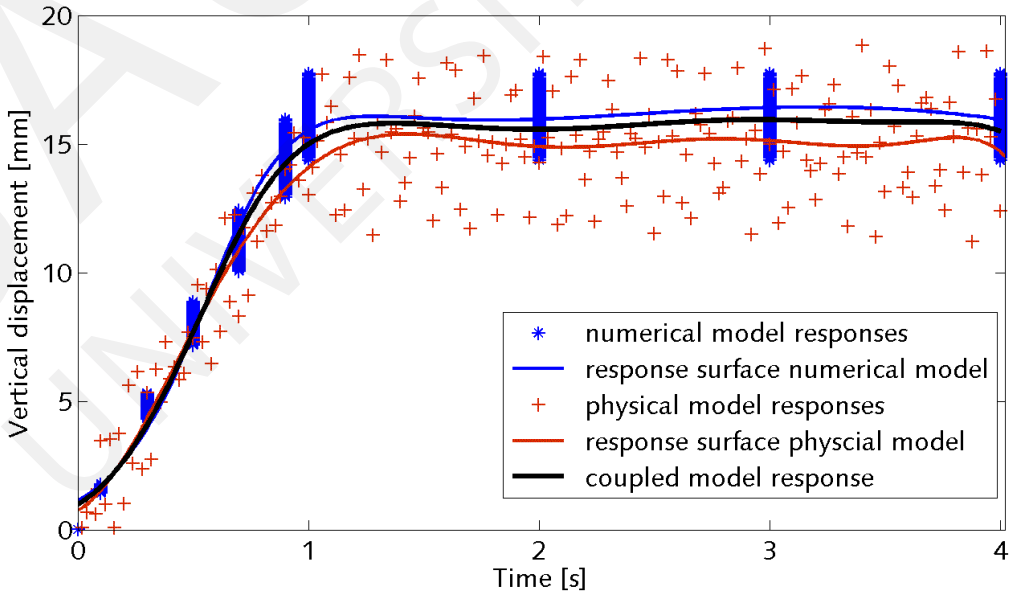

Figure 4: Model outputs, response surfaces and coupled model response surface

are:

$$\delta_M = 1 - \frac{\epsilon_M}{\epsilon_M + \epsilon_P} = 0.633 \qquad \delta_P = 1 - \frac{\epsilon_P}{\epsilon_P + \epsilon_M} = 0.366 \tag{19}$$

So, the numerical model with less model uncertainty will be used with 63.3 % for the model coupling. The more uncertain physical model will be only considered with 36.6 % in the coupled model. By the use of coupling equation 5, the coupled model function shown in Figure 4 is determined. For further investigations and predictions of the system behavior under other conditions, the optimal model input parameters for the coupled model can be determined by parameter optimization. Therefore, the evaluated mathematical model will be used. By checking the model conformity, the applicability for the parameter optimization was also checked.

4 Conclusions

A method for the uncertainty based coupling of mathematical and physical models in structural engineering is discussed. By usage of available model evaluation approaches from current literature, the model evaluation process was introduced. The models were checked for sources of uncertainties and the total uncertainties were determined. Based on the determined model uncertainties, weighting factors were created to consider certain models as the main part of the coupled model. By model conformity check, the coincidence of the model responses was proved. For further investigations, the coupled model was created. Furthermore a check of the model robustness can be determined by a check of the first derivation of the model responses. The bigger the differences over the loading process and the higher the variance between the considered models, the lower the robustness. For the successful use of the coupling approach, the objective function of the coupled model has the highest importance. In the next step, the usability of the shown coupling approach will be checked on a real structural example including more than one objective function. Also the limitations due to model robustness problems will be investigated within an example.

Acknowledgment

This research is supported by the German Research Foundation (DFG) via research training group "Assessment of Coupled Experimental and Numerical Partial Models in Structural Engineering (GRK 1462)", which is gratefully acknowledged by the authors.

References

[1] U.S. Enviromental Protection Agency. *Guidance on the Development, Evaluation, and Application of Environmental Models.* Washington DC, 2009.

[2] I. Babuška, F. Nobile, and R. Tempone. A systematic approach to model validation based on bayesian updates and prediction related rejection criteria. *Computer Methods in Applied Mechanics and Engineering*, 197(29-32):2517–2539, 2008.

[3] IFCC ILAC ISO IUPAC IUPAP BIPM, IEC and OIML. *Evaluation of measurement data Ű Guide to the expression of uncertainty in measurement. Joint Committee for Guides in Metrology.* JCGM, Geneva, 2008.

[4] IFCC ILAC ISO IUPAC IUPAP BIPM, IEC and OIML. *Evaluation of measurement data Ű Supplement 1 to the Guide to the expression of uncertainty in measurement - Propagation of distributions using a Monte Carlo method. Joint Committee for Guides in Metrology.* JCGM, Geneva, 2008.

[5] DIN Deutsches Institut für Normung e. V. *Eurocode 3: Bemessung und Konstruktion von Stahlbauten Ű Teil 1-1: Allgemeine Bemessungsregeln und Regeln für den Hochbau.* Beuth Verlag, 2010.

[6] D.E. Huntington and C.S. Lyrintzis. Improvements to and limitations of latin hypercube sampling. *Probabilistic Engineering Mechanics*, 13(4):245–253, 1998.

[7] H. Keitel, A. Dimmig-Osburg, L. Vandewalle, and L. Schueremans. Selecting creep model using bayesian methods. *Materials and Structures*, 45, 2012.

[8] H. Keitel, G. Karaki, T. Lahmer, S. Nikulla, and V. Zabel. Evaluation of coupled partial models in structural engineering using graph theory and sensitivity analysis. *Engineering Structures*, 33(12):3726–3736, 2011.

[9] K.-H. Laermann. Hybrid techniques in experimental solid mechanics. In K.-H. Laermann, editor, *Optical methods in experimental solid mechanics*, volume 403 of *CISM courses and lectures / International Centre for Mechanical Sciences*, pages 1–72. Springer, Wien and New York, 2000.

[10] D.C. Montgomery and G.C. Runger. *Applied statistics and probability for engineers.* Wiley, New York, 3rd edition, 2003.

[11] T. Most. Assessment of structural simulation models by estimating uncertainties due to model selection and model simplification. *Computers & Structures*, 89(17-18):1664–1672, 2011.

[12] W.L. Oberkampf, T.G. Trucano, and C. Hirsch. *Verification, Validation, and Predictive Capability in Computational Engineering and Physics.* U.S. DEO, Washington D.C., 2003.

[13] JCSS Joint Committee on Structural Safety. *Probabilistic Model Code (Part 1-3).* 12th draft edition, 2001.

[14] M. Reuter and F. Werner. Evaluation of complex engineering models using model quality analysis. *Engineering Structures*, 42:410–419, 2012.

[15] W. Scheufler, S. Burghard, O. Fischer, and C. Braun. Beurteilung der wirkungsweise von adaptiven seildämpfern im brückenbau durch kopplung von numerischer simulation und experiment. *Beton- und Stahlbetonbau*, 108(2):116–123, 2013.

[16] A.N. Tikhonov and A.A. Samarskii. *Equations of Mathematical Physics.* Dover Publications, New-York, 1963.

[17] K. Velten. *Mathematical modeling and simulation: Introduction for scientists and engineers.* Wiley-VCH, Weinheim, 2009.

Extension of Latin Hypercube samples while maintaining the correlation structure

Robin Schmidt, Matthias Voigt, Konrad Vogeler

Chair of Turbomachinery and Jet Propulsion
Institute of Fluid Mechanics
Research associate
Faculty of Mechanical Science and Engineering
Technische Universität Dresden
01062, Dresden, Germany
robin.schmidt@tu-dresden.de

Abstract. Due to its variance reducing properties compared with random sampling, Latin Hypercube sampling (LHS) is frequently used in Monte Carlo methods for the probabilistic analysis of a system. An extension of the sample size is created in the case of the LHS only by doubling its size. Especially with large samples and the perpetuation of an existing correlation structure this can become a drawback of LHS.

This paper presents an engineering approach to the multiple extension of a Latin Hypercube sample. The objective is to extent the sample size but to keep the number of realizations small. It is of particular importance that the present approach is able to maintain the correlations between the input variables in the probabilistic analysis. The quality of the statistical measures as well as the correlation setting is discussed and evaluated by means of simple example cases. By comparative analyses with LHS without modifications, a benchmark of the method is performed. Subsequently the method is applied to the sensitivity analysis of the aerodynamic performance of a two-stage high pressure compressor.

Nomenclature

D^*	largest negative distance between discrete and continuous pdf
D	critical K-S value
$\hat{D}$	K-S value
F	continuous pdf
I	interval for LHS realization
k	number of random variables
l	level
n_g	group size eLHS
n_{sim}	sample size LHS
r	correlation coefficient
$\tilde{r}$	rank correlation coefficient
R^2	coefficient of determination
P	probability
X	random variable
CoI	coefficient of importance
CoD_{CV}	coefficient of determination with cross-validation
LHS	Latin Hypercube sampling
eLHS	extended Latin Hypercube sampling
MCS	Monte Carlo simulation
RP	Restricted Pairing
SCR	sample to coefficient ratio

1 Introduction

The sensitivity analysis allows for an evaluation of the influence of uncertainties in the input variables and model parameters on the output quantities. Thereby Monte Carlo methods are frequently used. These have the advantage of being robust and easy to use. Within the Monte Carlo simulation (MCS), the sampling method forms the core. Through sampling a mapping of the continuous input variables in discrete implementations is achieved. In addition to random sampling (Simple Random sampling) a variety of adapted sampling methods, see e. g. Beachkofski [1], Helton et al. [6] or Saltelli et al. [17], are used. Great popularity enjoys the Latin Hypercube Sampling (LHS), which in comparison to Simple Random Sampling (SRS) can reduce the size of the used sample while maintaining the statistical significance. A comparison of LHS against SRS was done for example by Manteufel [12]. The method of LHS was first proposed by McKay et al. [13] and further developed among others by Iman et al. [8]. Compared to SRS, the method is characterized by a reduction of the variance. Thereby mean value as well as the distribution function can be estimated unbiased. The bias in the estimation of the variance is low and associated with a significantly lower sampling variability [6].

A drawback of the Latin Hypercube sampling is the strict procedure for the generation of the realizations and the associated limitations in the extension of the sample. Merely a doubling of the sample is simple to implement, since only this maintains the LHS design.

The results of a Monte Carlo simulation as for example sensitivities or robustness measures mostly are in the form of point estimators available. The statistical quality of these estimators can only be determined after completion of a Monte Carlo simulation by using confidence intervals. If the quality is is not sufficiently, the carried out deterministic calculations must be discarded and a new MCS with a larger sample size must be performed. This approach is especially with time-consuming and therefore very "expensive" deterministic calculations doubtful. In the literature, various methods for extending a Latin Hypercube sampling are described.

Pleming and Manteufel use in [14] a level-group approach, where in each level a certain number of groups can be added. After an initial LHS design is created, an equal number of realizations in the form of a group is added. Thereby the initial bins are considered. A certain number of groups is necessary to maintain the LHS design in each level. In the work of Pleming and Manteufel the realizations are set at fixed bin fractions, similar to the Descriptive sampling, and not uniformly distributed on the bin. The approach can be combined with an algorithm for correlation or discrepancy control.

Vorechovskỳ pursued in [19] an approach consisting of an exponent and a base value, from which the added realizations follow. Two methods: LLHS and HSLHS are presented, which differ with respect to the calculation rule and the base value. Also, the Descriptive Sampling approach is used, since each realization is set at the median of the corresponding interval. A disadvantage of the LLHS is the deviation from the LHS design, which results in a grouping around the mean. If all existing realizations are considered the HSLHS yields in a LHS design, however each extension by itself is not a LHS design.

Sallaberry et. al [16] chose an approach for the extension of the LHS by doubling the sample, however thereby it is possible to reach an existing correlation structure without

the use of a subsequent correlation control procedure.

A method for extending a Latin Hypercube Samples should ideally have the following features:

- The concept of the LHS design should be maintained. At least it should be possible to achieve a LHS design at a certain step.
- The extension of the sample should be as variable as possible.
- The correlation adjustment is possible within the method or with an additional method.

The first two criteria act usually in opposite directions. A further reasonable feature can be:

- Each extension is a separate LHS design in the same parameter space.

The paper includes the following sections. After a brief description of the LHS, Chapter 3 presents an method to extend a Latin Hypercube sampling. The method is linked to a correlation control algorithm. Subsequent the performance of the extension method is shown on a simple example. In Chapter 4 the extension method is applied to the sensitivity study of the influence of geometrical manufacturing tolerances on the performance of a 2-stage high-pressure compressor.

2 Latin Hypercube Sampling

First the algorithm of the Latin Hypercube sampling should be briefly introduced to illustrate the method of extended Latin Hypercube Sampling (eLHS) afterwards. In Latin Hypercube sampling each continuous distribution of the input variables is divided into equiprobable strata or bins. For a sample X_n of the random variable X with $n = 1, ..., n_{sim}$ the probability of each strata is given by $P_n = 1/n_{sim}$. Hence, follow the intervals I_n in which the realization are located. The calculation of the intervals is performed in the present work by numerical integration of the respective probability density function. The realization n is set uniformly distributed in the interval I_n. For asymptotically expiring functions such as the normal distribution, with no assigned bounds, the realization of the left-most and right-most interval I_1 and $I_{n_{sim}}$ is assigned with the value which corresponds to the centroid of an equivalent triangle on the abscissa. This differs from the approach of the LHS, but improves the reproduction of such distributions significantly. The algorithm described has to be repeated for all k input variables.

Subsequently, the implementations have to be assembled according to their dependence or independence. To obtain independent realizations, Iman and Conover used in [8] the approach to choose the intervals by k permutations of the numbers $(1, ..., n_{sim})$. For the generation of dependent variables with a given correlation structure Iman and Conover [7] presented the Restricted Pairing (RP). An adaptation of the method in the form of an repetitive sequence is shown in the work of Dandekar et al. [4]. Also, in the present work the RP method is used iteratively, based on the concept of Dandekar et al.. The correlation structure is adjusted about three hierarchized iteration loops and a stopping criterion according to Voigt [18] based on the maximum correlation error is used. It should

be noted that in this work the relations between k input variables are solely set in the form of correlations, which is not a complete description of the dependence structure in a mathematical sense.

3 Extended Latin Hypercube Sampling

3.1 Methodology

The presented extended Latin Hypercube sampling (eLHS) is based on the choice of two parameters: level l and group size n_g. It is assumed that still no sample exists. The approach is to select a small group size, such as the number of input variables k + 5 realizations, and reach the desired number of realizations n_{sim} by repetition l times. Is a probabilistic simulation already given, the number of realizations respectively simulations corresponds to the group size. If no sample exists, level 0 corresponds to a Latin Hypercube sampling and is generated according to the method described in Chapter 2. The in level 0 used intervals are henceforth referred to as the root intervals I_n^*, the sample itself as the root sample. Subsequently the correlation of the variables is set with the above presented iterative Restricted Pairing. Note, the Restricted Pairing can only be applied if the group size n_g exceeds the number of variables.

The eLHS works with a doubling of the intervals I_n. However, this is only required if no free intervals are available. In each expansion step respectively level n_g realizations are added. One new realization is chosen per root interval. Is more than one free interval per root interval available, the selection of the interval is based on the largest negative distance D^* between continuous and discrete distribution function.

$$D^* = \min_{1 \le i \le n_{sim}} \left(\frac{i}{n_{sim}} - F(y_i) \right) \tag{1}$$

The value D^* is a measure of the lack of realizations in the probability distribution function or density function and is derived from the Kolmogorov–Smirnov test. The method of extending the sample is depicted in Figure 1.

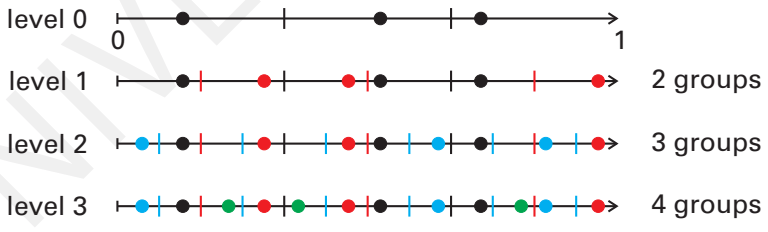

Figure 1: Example with group size of 3 and 3 levels

In the first level, the root sample is doubled and the new realizations (in red) are assigned to the free intervals. In the second level again a further doubling of the root sample takes place, but now there are two free intervals per root interval available. By using D^*,

the respective intervals are selected. In the third level the free intervals are filled up (in green), no duplication takes place.

The setting of the correlation of the newly added realizations is performed using the iterative Restricted Pairing after the generation of the realizations in each level. The entire procedure is shown in Figure 2. Sallaberry et al. [16] show that two samples with the same correlation structure in turn lead to a similar correlation structure when they are joined together. In the presented procedure the whole sample is tested, after adjusting the correlations of the new realizations and joining them with the existing sample. The correlation adjustment of the new realizations is repeated until predefined stop criteria are met. Three criteria are applied. On the one hand the maximum correlation error, on the other hand the minimal Euclidean distance L of the realizations and a value G, which expresses in physical analogy the sum of the repulsive forces upon considering the realizations as electrically charged particles. A detailed description of L and G can be found in Liefvendahl & Stocki [11].

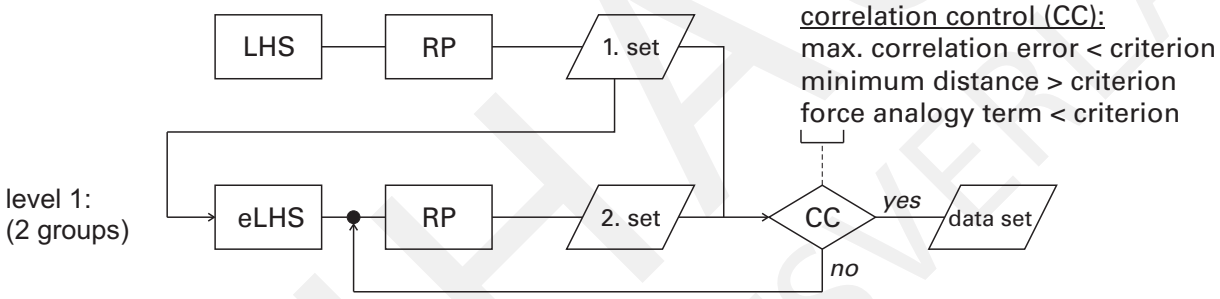

Figure 2: Correlation adjustment

Later on in this work, the generation of random numbers as well as the control of the correlation is always denoted by the term eLHS.

3.2 Evaluation of the eLHS

For the evaluation of the eLHS two standard normal distributed random variables are generated according to the experimental matrix in table 1. For each test point the correlation values of $r = [0, 0.25, 0.5, 0.75, 0.99]^T$ are examined. This results in a $3 \times 8 \times 5$ experimental matrix.

To compare the eLHS with the LHS the following samples were generated.

$$n_{sim} = [15, 20, 30, 40, 50, 60, 65, 80, 100, 120, 130, 160, 200, 240, 260, 320]^T \tag{2}$$

Therein the same correlation values as for the eLHS are used. This results in a 16×5 experimental matrix. Each test point of the two experimental matrices was repeated 1000 times. The eLHS will now be tested against the LHS regarding the correlation between the random variables, the reproduction of the distribution function by means of the K-S test and the reproduction of the mean value as well as the standard deviation. The comparison is done with the mean values based on the 1000 repetitions.

level (group)	group size		
	5	10	20
3	15	30	60
4	20	40	80
6	30	60	120
8	40	80	160
10	50	100	200
12	60	120	240
13	65	130	260
16	80	160	320

Table 1: Experimental matrix eLHS

3.2.1 Correlation of the input values

The comparison in terms of correlation of the random variables is carried out based on the mean absolute error between the predetermined and actual realized correlation coefficient. The rank correlation coefficient $\tilde{r}$ according to Spearman is always used for the correlation coefficient realized.

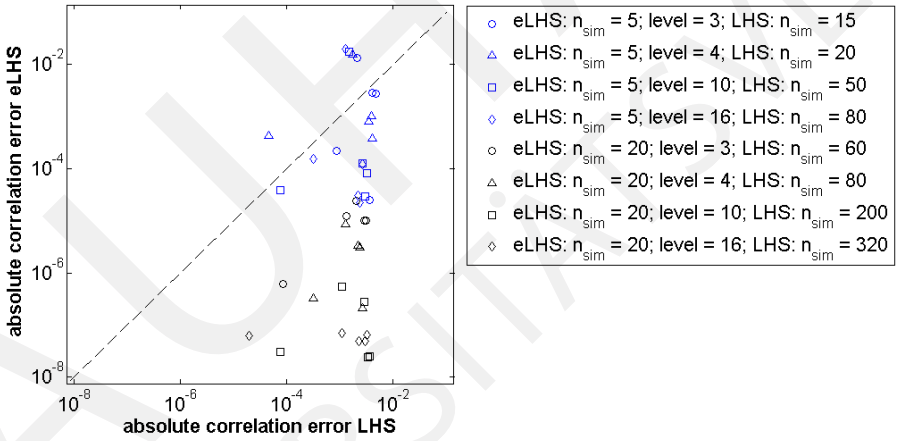

Figure 3: Comparison of LOG absolute correlation error for LHS and eLHS

Figure 3 shows for the group size of $n_g = 5$ and 20 an overview of four different levels $l = [3, 4, 10, 16]^T$ and their comparable LHS sampling. By a comparable LHS sample the same number of realizations n_{sim} as in the eLHS sample is meant. Generally it can be observed that the iterative Restricted Pairing leads to very low mean absolute correlation errors of maximal 10^{-2} for LHS and eLHS. The correlation error of the eLHS is in the majority of cases located below that one of the LHS, since most of the values are below the diagonal line. Only for a small number of realizations $n_g = 5$ and a high correlation value $r = 0.99$ larger mean absolute correlation errors occur for the eLHS. That is shown in detail on the left side of figure 4. Over the predetermined correlation value the mean absolute correlation error of comparable eLHS and LHS is plotted. For high correlation values at low group size, the correlation control algorithm is not able to deliver the same

performance for the eLHS as for the LHS with correspondingly l times higher number of realizations. Pleming et al. [14] therefore proposes to choose the size of the sample four times the number of variables when applying Restricted Pairing.

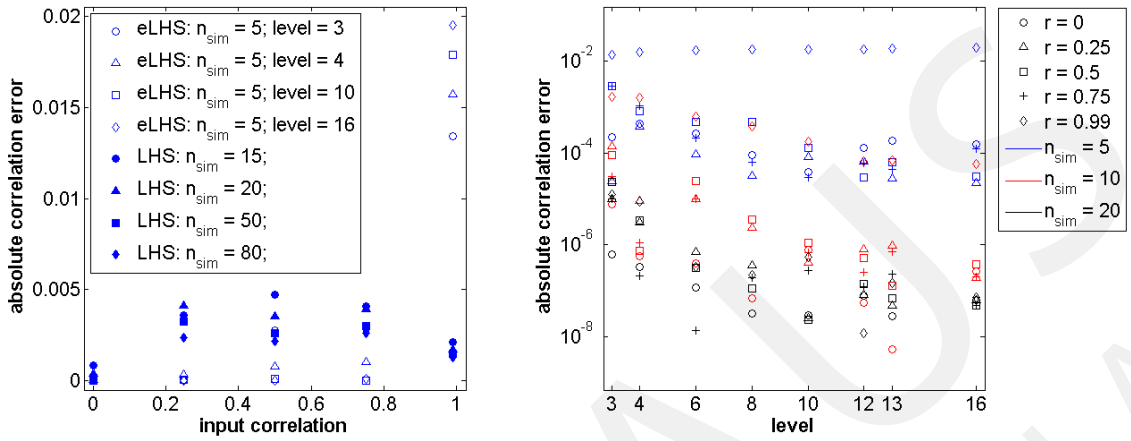

Figure 4: left: Absolute correlation error for $n_g = 5$; right: Number of Levels against LOG absolute correlation error for eLHS

On the right side of figure 4, a comparison of the various group sizes and level is shown for the mean absolute correlation error. A distinction is made within the five computed correlation values. Once again it becomes clear that the samples with low group size and high correlation coefficient result in the highest deviation. Comparing the samples with a group size of $n_g = 10$, the largest absolute correlation error also arises from high correlations of $r = 0.99$. At a group size of $n_g = 20$, and thus 10 times the number of variables, this event no longer occurs. With increasing group size, and thus variability of each level the mean absolute correlation error decreases. An increase in the number of levels mostly also results in a decrease of the error. Based on the conducted experiment only trends can be shown for the influence of the level on the correlation value, here further investigations have to be conducted.

3.2.2 Reproduction of the distribution function

The discussion of the reconstruction of the distribution function is performed using the Kolmogorov-Smirnov test and the resulting value $\hat{D}$.

$$\hat{D} = \max_{1 \le i \le n_{sim}} \left| F(y_i) - \frac{i}{n_{sim}} \right| \tag{3}$$

The Kolmogorov-Smirnov test can be used to check whether a discrete distribution function corresponds to a particular distribution in the form of a continuous distribution function F. In the experiment the distributions of the input variables are known.

Figure 5 shows the mean K-S value over the number of levels for three selected representative parameter combinations. The error bars represent the standard deviation of the value resulting from 1000 repetitions. The progression of $\hat{D}$ for the three parameter

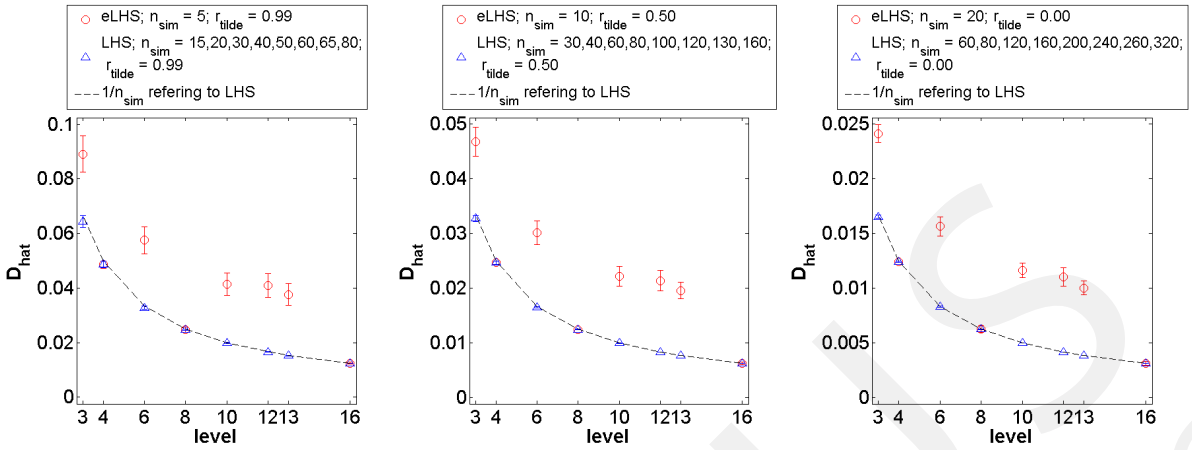

Figure 5: Mean K-S-value vs number of level

combinations are very similar. As was to be expected, $\hat{D}$ decreases with increasing sample size and group size. The K-S values of the level 4, 8 and 16 correspond to those of the LHS. These levels have no free intervals I_n. Due to the free intervals at the other levels, errors arise compared to the LHS which are visible in a worse K-S value. Also, the variability of the K-S values increase. The worst mean K-S value occurs for a group size of $n_g = 5$ and level 3 with $\hat{D} = 0.0891$. A reference value for the assessment derives from the critical value D. It applies to random events and thus actually only for random sampling. At a significance level of $\alpha = 0.05$ and a sample of $n_{sim} = 15$, the value for D is 0.338 (taken from [15]). Thus $\hat{D}$ is smaller than D. In the case of a random sampling the hypothesis to accept the distribution as a standard normal distribution would therefore be approved. A comparison of the eLHS with random sampling (Simple Random Sampling) is still pending.

For a LHS the maximum occurring error with respect to the K-S value is $1/n_{sim}$ and is achieved if a realization of the sample is located on the edge of an interval I_n. The depicted threshold of $1/n_{sim}$ is slightly above the average K-S value of the LHS with 1000 repetitions. This demonstrates that very often a realization of the sample is placed near the interval borders, even in small samples.

The correlation of the random variable has no effect on the reproduction of the distribution function.

3.2.3 Reproduction of the mean value and standard deviation

The mean of one of the two generated random variables over the number of levels for three parameter combinations is shown in figure 6. The mean is again obtained by averaging from 1000 repetitions. Error bars show the standard deviation of the averaged value.

As for the reproduction of the distribution function the mean values for eLHS and LHS of level 4, 8 and 16 lie closely one upon the other. Also, the associated scatter in the form of the standard deviation can be compared. There are no vacant intervals at this level and the eLHS corresponds to a LHS concerning the assignment of the intervals I_n.

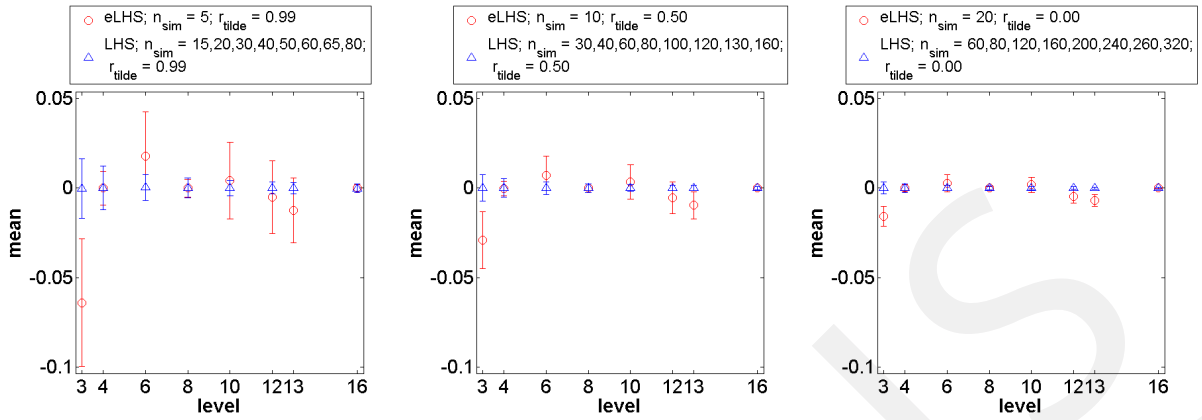

Figure 6: Mean value over the number of levels

The other levels show deviations which decrease with increasing group size (from left to right). A characteristic shape of the deviations appears by comparing the three group sizes. It results from the allocation of intervals. Based on D^* for realization X_n the new realization is always added in the interval below X_n. An exception only arises if:

$$|D^*| = |F(y_i) - 1| \text{ with } i = n_{sim} \tag{4}$$

Then the interval above the highest realization is chosen. In level 3 exist two free intervals per root interval, but only one is used. In the root interval I_1 the free interval below the smallest realization is assigned. However, the free interval above the largest realization in the root interval $I_{n_{sim}}$ stays empty. Thus, the mean of the eLHS is shifted to smaller values. In level 6, there are three free intervals per root interval, however, only one will be assigned. In the root interval $I^*_{n_{sim}}$ above the largest realization remains only one vacant interval, whereas two vacant intervals remain below the smallest realization in the root interval I^*_1. Thus, the mean of the eLHS is shifted to larger values. All other shifts of the eLHS mean value can be explained in the same manner.

The reproduction of the standard deviation depending on the number of levels and group size is shown in figure 7. The corresponding standard deviation of the standard deviation is plotted in the form of error bars, and results from the 1000 repetitions of the sampling. The deviation of the LHS with respect to the target value decreases asymptotically with increasing number of realizations and approaches from above the target value.

Unlike the mean value, the mean standard deviations of eLHS and LHS do not lie on top of each other in the levels 4 and 8. This can approximately be achieved at level 16. The deviations to the LHS decrease with increasing group size. In the level 4 and 8, the eLHS underestimates the target value significantly, whereas the LHS overestimates the value. The occurring scatter of the standard deviation in these levels is comparable. The reason for the underestimation of the target value is the generation algorithm for the new smallest and largest realization. As stated above, in the used LHS algorithm for asymptotically expiring functions with no assigned bounds, the realization of the left-most and right-most interval I_1 and $I_{n_{sim}}$ is assigned with the value which corresponds to the

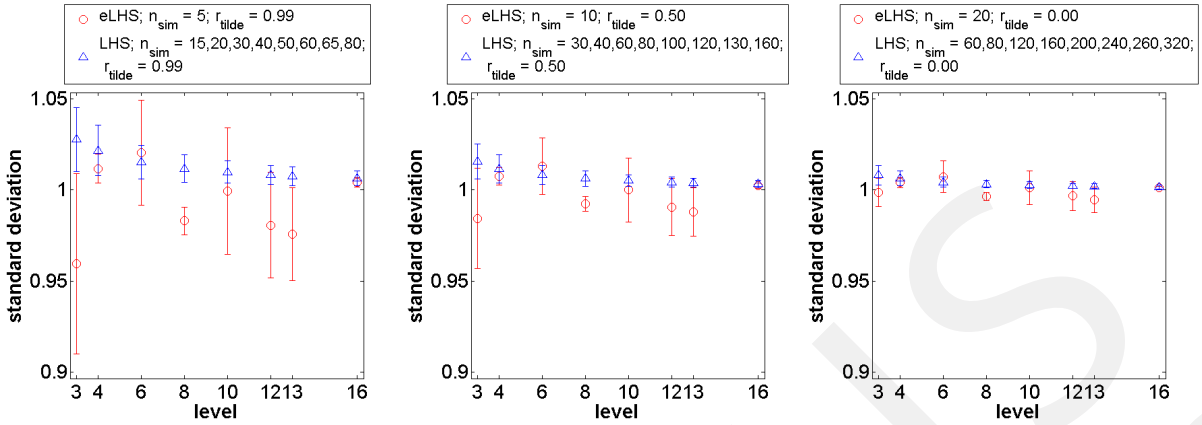

Figure 7: Standard deviation over the number of level

centroid of an equivalent triangle on the abscissa. This also applies to new realizations in the new intervals I_1 and $I_{n_{sim}}$ in each extension step, which results in an underestimation of the standard deviation. If free intervals are available after an extension step, as in the levels 3, 6, 12 and 13, the interval assignment comes to bear as discussed for the mean value. Deviations to the target value and increased scatter arise. These are reduced with increasing group size.

As well as for the reproduction of the distribution function, the correlation value does not affect the reproduction of mean and standard deviation.

4 Sensitivity analysis of a two-stage high pressure compressor

The application of the method of the previous chapters is carried out by the sensitivity analysis of a two-stage high-pressure compressor. Thereby, the possibilities of the eLHS should be in the foreground.

The deterministic CFD calculation of the two-stage compressor was provided by the Rolls-Royce Deutschland Ltd & Co KG. The compressor consists of two blade and two stator rows, as shown in figure 8, and is part of an jet engine high pressure compressor. The cantileverd stators were modeled with hub gap and casing fillets, the rotors with tip gap and hub fillet respectively. The calculation of the deterministic numerical model was performed with the Hydra Suite of Rolls-Royce Deutschland Ltd & Co KG. The automated grid generation was done with the program Padram also provided by Rolls-Royce Deutschland Ltd & Co KG. No adjustments of the grid were made for the different realizations, always the same grid setup was used. The boundary and initial conditions are given by radial profiles. At the inlet these are the total temperature, total pressure, radial and tangential flow angle and the Spalart-variable. At the outlet a mass flow is specified. The data transfer between the blocks is done by mixing planes.

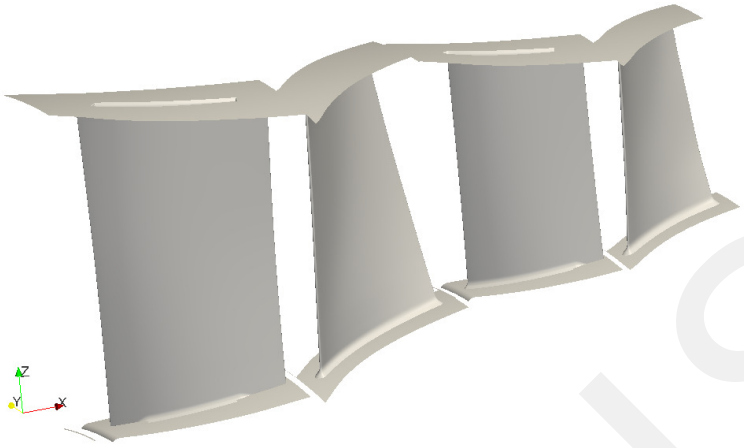

Figure 8: 2 Stage compressor

The parameterization of the airfoil is based on the physical parameters used by Heinze et al. [5]. The geometry variations were only applied to the first rotor. Therefore the delta-parameter model of Lange et al. [9] was used. It was shown in [10], that in the construction of compressor blades due to the high correlation of the airfoil parameters in radial direction only one averaging section in spanwise direction is sufficiently accurate. This results in 14 parameters for the entire airfoil and one parameter for the radius of the fillet. An overview of the used parameters is given in figure 9 and table 2.

symbol	description
ax_{pos}	axial position of the leading edge point
tan_{pos}	tangential position of the leading edge point
c	chord length
γ	stagger angle
α_{LE}	angle at leading edge
α_{TE}	angle at trailing edge
t_{max}	maximum thickness
x_{tmax}	position of maximum thickness
w_{max}	maximum camber
x_{wmax}	position of maximum camber
a_{TE}	large semi axis of the trailing edge ellipse
b_{TE}	small semi axis of the trailing edge ellipse
a_{LE}	large semi axis of the leading edge ellipse
b_{LE}	small semi axis of the leading edge ellipse
$fillet$	fillet radius

Table 2: Description of the geometric parameters

The sensitivity analysis was conducted using the Monte Carlo simulation. As sampling method, eLHS was applied in combination with the iterative Restricted Pairing. Based on typical geometric variations for compressor blades due to manufacturing variability, the

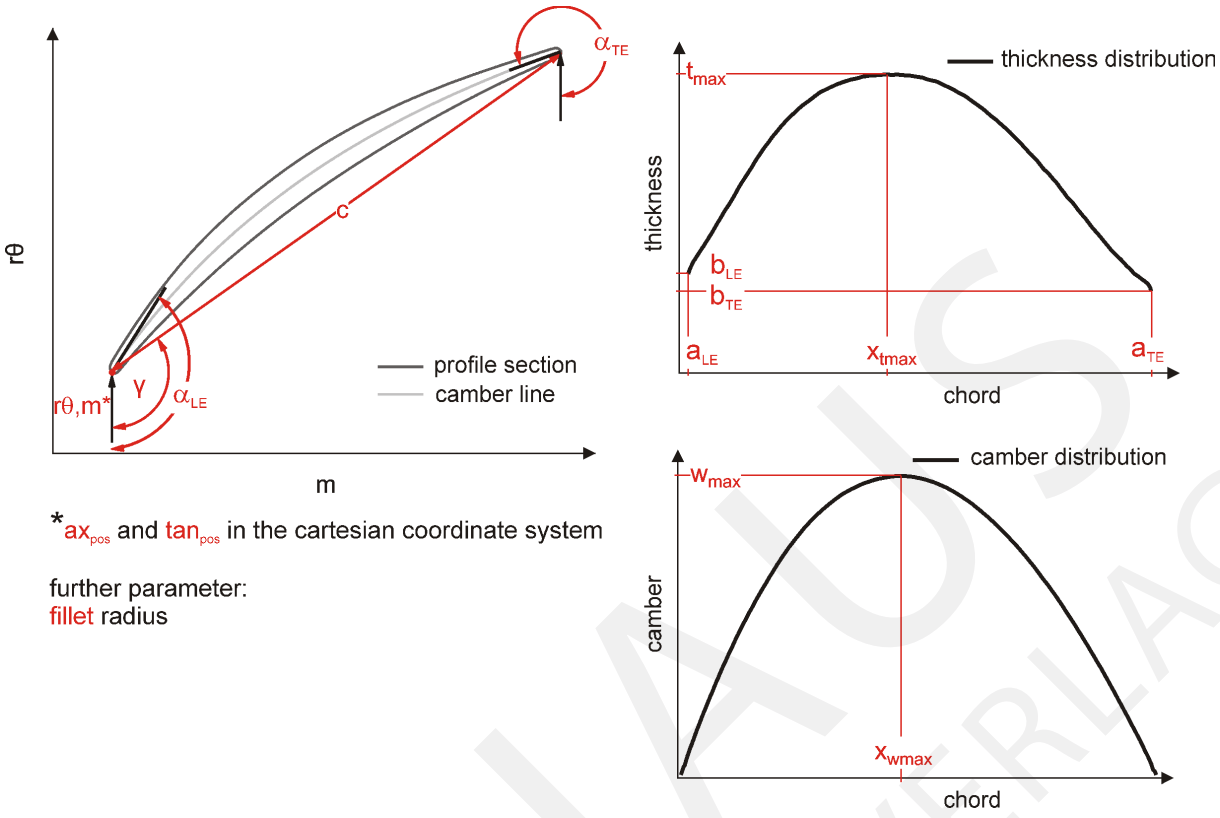

Figure 9: Geometric parameters

probability distributions of the 14 parameters were approximated by normal distributions. The relationship between the parameters is specified by correlation coefficients. The probabilistic simulation was started with a sample of a group size of $n_g = 30$ realizations. Subsequently another 3 groups were added up to level 4 which ultimately yielded in 120 realizations. The time to generate the random numbers amounted to 144.5 minutes on one CPU of a Intel® Core— i7 computer at 3.4 GHz and 24 GB RAM. Within the MCS led seven deterministic calculations to no solution. One of them belonged to level 1, two to level 2, two to level 3 and two to level 4.

In a first step, the sensitivities to the input variables will be described on the basis of Spearman's rank correlation coefficient. The result quantity is the isentropic compressor efficiency of the two-stage compressor. It compares an actual conversion of energy in the form of the polytropic compressor work at a given pressure ratio with an ideal conversion of energy in the form of the isentropic compressor work at a given compressor pressure ratio. The rank correlation coefficient can describe linear and monotonic nonlinear relationships. In case of a simple MCS without eLHS only one condition is known and a comparison of the rank correlation coefficient with increasing sample size is only achievable by a new MCS. Only with the eLHS the statistical quality can be verified after each level and a decision on the further course of the calculation can be taken. Figure 10 shows in pie charts for the level 1 and 4 the rank correlation coefficients between the isentropic compressor efficiency and the input variables.

Within the 7 most important input parameters for the isentropic compressor efficiency

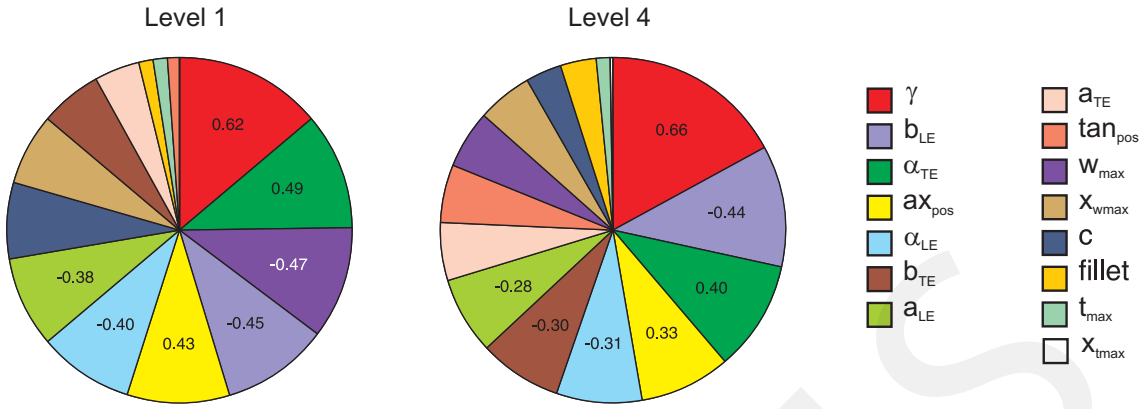

Figure 10: Pie chart for isentropic compressor efficiency

a shift in the ranking and magnitude of the values occurs from level 1 to level 4. Six of these values are already recognized in level 1, but the rank correlation coefficient between isentropic compressor efficiency and maximum camber shifts to smaller values and moved down in the ranking.

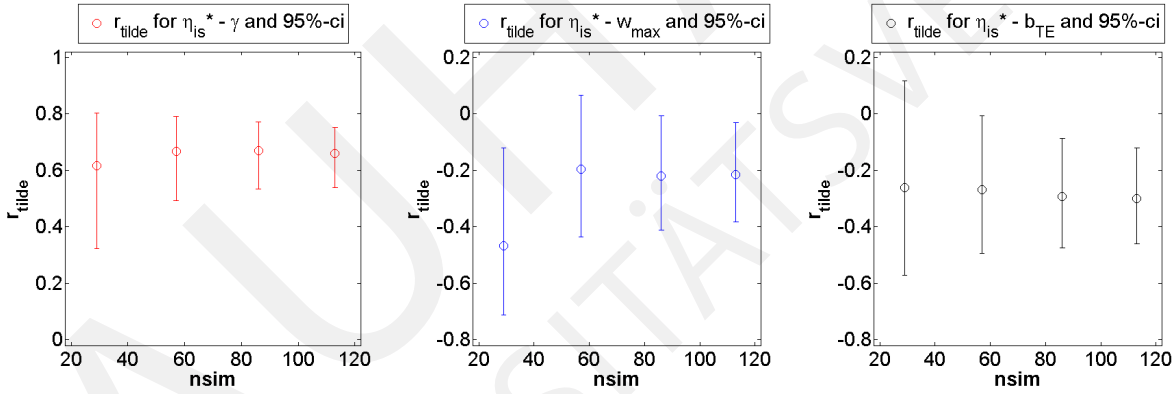

Figure 11: Rank correlation coefficient and 95% confidence interval

For three selected rank correlation coefficients, figure 11 shows a detailed presentation of the magnitude of the coefficient over the size of the sample and thus the level. Furthermore, the figure shows the 95% confidence interval of the rank correlation. The calculation of the confidence interval was performed using Fisher's z-transformation and was taken from [15].

In level 1 the stagger angle is the most influential input variable based on the rank correlation coefficient. With an increase of the stagger angle the efficiency increases. The confidence interval shows the stagger angle with a 95 percent probability always in a positive region. With increasing number of realizations and thus level, this statement is clarified and the stagger angle remains the most influential input variable. With respect to the influence of the stagger angle, the simulation could be stopped after level 2.

The maximum camber is the third most important input variable in level 1. Based on the rank correlation coefficient the efficiency decreases with an increase in the maximum

camber. The confidence interval is located entirely in the negative range of the rank correlation coefficient, however, it stretches over a range of very small negative values of -0.12 up to very large negative values of -0.71. In level 2 the value of the rank correlation coefficient increases towards zero. Due to this, the size of the confidence interval hardly changed. The maximum camber can still have no or a negative impact on the efficiency. At level 3 and 4, the value of the rank correlation coefficient decreases slightly and the confidence interval is reduced. With a slight negative correlation the influence of the maximum camber moves downward in the ranking of the most important input variables so that it is only the tenth most important input variable in level 4.

An opposite behavior is shown for the influence of the small semi axis of the trailing edge ellipse. The value of the rank correlation coefficient with approximately 0.3 hardly changes with increasing level. The correlation is low, an increase in the thickness of the trailing edge of the profile is followed by a small reduction in the efficiency. However in level 1 the range of the confidence interval reaches from 0.12 to -0.57 so that the effects of the input variable are not clearly assignable. With an increase of the sample, the confidence interval is reduced and the statistical quality or significance of the rank correlation coefficient rises. With respect to the rank-correlation coefficient of the small semi axis of the trailing edge ellipse, the simulation may have been stopped after Level 3.

The input variables of the MCS are correlated with each other, so are mutually dependent. A sensitivity analysis based on the correlation coefficient is difficult due to the problematic assessment of cause and effect. A statistical measure which is unaffected by low input variable correlations and is able to assess the sensitivities of the result quantities on the input variables is represented by the coefficient of importance (CoI) [3]. The CoI is based on modified response surfaces and is calculated with the coefficients of determination R^2 [15] by:

$$CoI_{i,j} = R_j^2 - R_{i,j}^2 \tag{5}$$

For the determination of R_i^2 of an input quantity X_i to a result quantity X_j all terms that contain the quantity X_i are omitted from the response surface which describes X_j. Depending on the used response surface, the CoI also describes relationships of higher order. To use the CoI, the system behavior must be sufficiently accurate reflected by the response surface. An assessment of the quality of the response surface can be performed with the cross-validation.

Level	1	2	3	4
SCR	1.813	3.563	5.375	7.063
R^2	0.958	0.913	0.915	0.899
CoD_{MCCV}	0.748	0.834	0.876	0.865
average R^2 - CoD_{MCCV}	0.853	0.874	0.895	0.882

Table 3: Parameter of the response surfaces

The cross-validation is based on separate data sets for the calculation and evaluation of the regression model. For this purpose the sample respectively the supporting points of

the response surface is divided into training and validation realizations. In this work, the Monte Carlo cross-validation (MCCV) by Beschorner [2] was used. The splitting ratio amounted to 0.85 and the number of runs was 1000.

In the following, the sensitivities of the input variable to the result quantity total pressure ratio will be displayed using the CoI. The total pressure ratio refers to the increase in pressure which the two-stage compressor provides. The system behavior has been approximated with a first order polynomial without mixed terms in each level. Table 3 shows the achieved coefficients of determination, coefficients of prognosis (CoD_{MCCV}) due to the cross-validation and their average. Further, the ratio (SCR) of sample size to the needed coefficients of the response surface is presented.

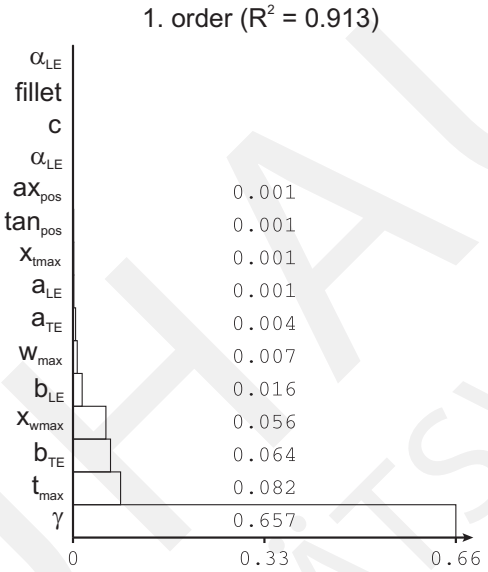

Figure 12: CoI bar chart for total pressure ratio at level 2

R^2 and CoD_{MCCV} differ yet distinctly from one another in level 1. From [2] it is known that at low SCR, the CoD_{MCCV} underestimates the quality of the response surface, whereas the R^2 overestimates it. A prediction of the possible achievable quality of the response surface is provided by the average of R^2 and CoD_{MCCV}. Since in level 1 a possible improvement of the CoD_{MCCV} of 0.1 is available, the LHS is extended and another group of realizations is added. Thus, the SCR rises, the R^2 decreases, the CoD_{MCCV} also increases and the spacing between R^2 and CoD_{MCCV} is reduced. The average of R^2 and CoD_{MCCV} changed only slightly. The potential for an improvement with a further extension is significantly less. In case of a practical application the extension would be terminated at this point and the CoI calculation could be carried out. In the level 3 and 4 the values of R^2 and CoD_{MCCV} approach further to each other. The potential for improvement with an extension of the sample is low, a saturation occurs.

From the response surface of the level 2 the coefficients of importance were calculated and shown in figure 12. The stagger angle is the dominant input variable with respect to the total pressure ratio. An extension of the sample leads only to negligible changes in the CoI.

5 Conclusion

The paper presents a method to extend a Latin Hypercube sampling with further realizations. If the extension is considered before the start of a probabilistic simulation, the presented approach achieves the biggest advantages over LHS. The desired number of realizations can then be realized by repeated extension. The method does not maintain the LHS design in each level, however, thus a more variable extension is achieved. If at a certain level all intervals are occupied, the extended sample corresponds to a LHS. Each extension represents an LHS design for itself. This makes it possible to investigate an application of the t-statistics on l extensions in further analyzes. The setting of the correlation as a measure of relationship between the random variables was realized by an iterative Restricted Pairing. It was demonstrated, that the application of an iterative RP leads to low deviations from the target correlation for LHS and eLHS despite small number of realizations.

The comparison of eLHS against LHS showed that the deviation from the LHS design cause errors in the reproduction of the distribution function and of the statistical measures mean and standard deviation. If all intervals are occupied, the representation of the distribution function and the mean value corresponds to that one of a LHS. The standard deviation is underestimated by the extension method. However, with increasing group size and levels the deviation to the target values decreases.

The benefit of an extension method has been shown by the sensitivity analysis of the performance of a two-stage high-pressure compressor under scattering geometry. As a result of the variable configuration of the probabilistic analysis with the sample extension method it is possible to use the statistical quality, e.g. confidence intervals, of certain statistical measures as a criterion for an abortion. The extension results in an increased gain of information from the probabilistic analysis. Based on the sensitivity analysis using the rank correlation coefficient and coefficient of importance the practical application of the extension method was shown.

Acknowledgment

The research leading to these results has received funding from the European Union's Seventh Framework Program for research, technological development and demonstration under grant agreement number ACP3-GA-2013-605036. Moreover, the authors would like to thank Rolls–Royce Deutschland Ltd & Co KG for the provision of the deterministic model and the support for questions.

References

[1] Brian Beachkofski and Ramana V. Grandhi. *Confidence Interval Minimization Through Experimental Design.* PhD thesis, Wright State University; Ohio Center of Excellence for Product Reliability and Optimization, 2004.

[2] André Beschorner, Matthias Voigt, and Konrad Vogeler. Monte carlo cross-validation

for response surface benchmark (to be published). In *Proceedings of the 12th International Probabilistic Workshop*, Weimar, 2014. International Probabilistic Workshop.

[3] Christian Bucher. *Computational Analysis of Randomness in Structural Mechanics*, volume 3 of *Structures and Infrastructures Series*. CRC Press, May 2009.

[4] Ramesh A. Dandekar, Michael Cohen, and Nancy Kirkendall. Sensitive micro data protection using latin hypercube sampling technique. In *Inference Control in Statistical Databases*, page 117–125. Springer, 2002.

[5] Kay Heinze, Marcus Meyer, Jens Scharfenstein, Matthias Voigt, and Konrad Vogeler. A parametric model for probabilistic analysis of turbine blades considering real geometric effects. *CEAS Aeronautical Journal*, 5(1):41–51, 2014.

[6] J.C. Helton and F.J. Davis. Latin hypercube sampling and the propagation of uncertainty in analyses of complex systems. *Reliability Engineering & System Safety*, 81(1):23–69, July 2003.

[7] Ronald L. Iman and W. J. Conover. A distribution-free approach to inducing rank correlation among input variables. *Communications in Statistics - Simulation and Computation*, 11(3):311–334, January 1982.

[8] Ronald L. Iman and W.J. Conover. Small sample sensitivity analysis techniques for computer models with an application to risk assessment. *Communications in Statistics - Theory and Methods*, 9(17):1749–1842, January 1980.

[9] Alexander Lange, Konrad Vogeler, Volker Gümmer, Henner Schrapp, and Carsten Clemen. Introduction of a parameter based compressor blade model for considering measured geometry uncertainties in numerical simulation. In *ASME Turbo Expo 2009: Power for Land, Sea, and Air*, page 1113–1123. American Society of Mechanical Engineers, 2009.

[10] Alexander Lange, Matthias Voigt, Konrad Vogeler, Henner Schrapp, Erik Johann, and Volker Gümmer. Probabilistic CFD simulation of a high-pressure compressor stage taking manufacturing variability into account. In *ASME Turbo Expo 2010: Power for Land, Sea, and Air*, page 617–628. American Society of Mechanical Engineers, 2010.

[11] M. Liefvendahl and R. Stocki. A study on algorithms for optimization of latin hypercubes. *Journal of Statistical Planning and Inference*, 136(9):3231–3247, September 2006.

[12] Randall D. Manteufel. Evaluating the convergence of latin hypercube sampling. In *41st AIAA/ASME/ASCE/AHS/ASC Structures, Structural Dynamics and Materials Conference*, 2000.

[13] M. D. McKay, R. J. Beckman, and W. J. Conover. A comparison of three methods for selecting values of input variables in the analysis of output from a computer code. *Technometrics*, 42(1):55–61, 1979.

[14] Jason Brant Pleming and Randall D. Manteufel. Replicated latin hypercube sampling. In *46th AIAA/ASME/ASCE/AHS/ASC Structures, Structural Dynamics and Materials Conference*. University of Texas at San Antonio, 2005.

[15] L. Sachs and J. Hedderich. *Angewandte Statistik*. Springer, 13 edition, 2009.

[16] C.J. Sallaberry, J.C. Helton, and S.C. Hora. Extension of latin hypercube samples with correlated variables. *Reliability Engineering & System Safety*, 93(7):1047–1059, July 2008.

[17] A. Saltelli, K. Chan, and E. M. Scott. *Sensitivity Analysis*. John Wiley & Sons, Chichester New York Weinheim Brisbane Singapore Toronto, 2000.

[18] Matthias Voigt. *Probabilistische Simulation des strukturmechanischen Verhaltens von Turbinenschaufeln*. PhD thesis, Technische Universität Dresden, 2010.

[19] Miroslav Vorechovskỳ. Extension of sample size in latin hypercube sampling with correlated variables. In *4th International Workshop on Reliable Engineering Computing*, 2010.

Risk-Informed Decision Making on Protective Measures for Highway Bridges

M. Sykora[1], **D. Diamantidis**[2], **M. Holicky**[1], **R. Lenner**[3] & **P. MaŇas**[4]

[1]Klokner Institute, Czech Technical University in Prague, Czech Republic
[2]Faculty of Civil Engineering, OTH Regensburg, Germany
[3]Department of Civil Engineering, Stellenbosch University, South Africa
[4]Faculty of Military Technology, University of Defence, Czech Republic

Abstract. The European road network has a vital importance for the European economy. Many infrastructures linked to the network are permanently aging and deteriorating. Even smaller disruptions due to traffic restrictions or failure of some elements of the network may result in high consequences. The protection of such'critical' infrastructures should be based on considerations of significant hazards affecting the system. Bridges and tunnels are perceived as the most vulnerable components of the road network. In this study assessments of individual highway bridges exposed to accidental situations are discussed from a general point of view. A methodology of the risk-informed decision making based on Bayesian networks is developed. From an economic point of view the objective is to minimize the total working-life cost (risk) of the bridge. The decision parameter(s) to be optimised may represent resistance in the case of upgrading, stand-off distance, properties of energy absorbing shields etc. Total structural costs consist of initial, in-service costs and consequences of structural failure. For risk analysis use of Bayesian networks is advocated. The present study shows that decisions concerning protective measures can be based on the risk-based optimisation of the expected costs. Actions to be considered in the assessment may include normal and accidental (natural or man-made) ones. Protective measures may comprise restriction of physical access, detection efforts, security planning and coordination, and construction modifications improving structural robustness.

Keywords: risk-informed decision making, economic optimisation, highway bridges, accidental situations.

1 Introduction

The European road network has a vital importance for the European economy. Even smaller disruptions due to traffic restrictions or failure of some elements of the network may result in high consequences and negative environmental impacts [1]. In such a case the network and its major components are classified as a "critical infrastructure (object)" that can be defined according to the European Directive 2008/114/EC [2] as:

an asset, system or part thereof which is essential for the maintenance of vital societal functions, health, safety, security, economic or social well-being of people, and the disruption or destruction of which would have a significant impact in a state as a result of the failure to maintain those functions.

The Communication [1] indicates that the protection of critical infrastructure is to be based on an all-hazards approach; recognising the threat from terrorism as a priority.

Cost–benefit and other risk studies are deemed to be useful particularly for low probability–high consequence events where public safety is a key criterion for decision making [22].

Bridges are perceived as the most vulnerable components of the road network [3]. While single bridges can fail under particular structural damage or loads, the overall network performance is more likely to be affected by events that may have impact on many bridges of the network, for example by loading due to earthquakes or floods.

Assessments of individual bridges are discussed from a general point of view in this study. Methodology of the risk optimisation based on Bayesian network, applied previously for analyses of flooding [9] is adapted for highway bridges exposed to accidental situations.

It is noted that the terminology is adopted from Eurocodes [6, 7] and other European documents [25, 1].

2 Identifying critical bridges

The following aspects should be taken into account when selecting critical bridges [21]:

- location in urban environment,
- conventional construction type,
- possible traffic bottleneck formation,
- large bridge over the sea,
- landmark bridge,
- historical and cultural aspects,
- difficulty to rebuild bridge,
- significance due to traffic volume.

Detailed procedure for the identification of possible critical bridges is provided in [21]. The failure consequences can be seen as an appropriate indicator of the importance of a bridge [25]. The legislation of the Czech Republic provides several criteria for identification of critical infrastructures. For example the object is considered as critical when it is essential for the maintenance of vital societal functions, health, safety, security, economic or social well-being of people, and its malfunction affects more than 125 000 persons. Primarily based on this criterion, most bridges on highways, motorways and main routes are considered as critical.

3 Principles of risk-informed decision making

The basis for risk-informed decision making is provided considering the latest draft of ISO/DIS 2394:2014. The decision making should in principle aim at the solution minimising risks, considering possible events and their unfavourable consequences. Such events are often caused by extreme hazards including flooding. Adequate hazard scenarios and relevant occurrence probabilities need to be estimated [23, 17], often on the basis of expert

assessments and judgements.

When for mutually independent hazard situations H_i the failure F of the component given a particular hazard situation H_i occurs with the conditional probability $P(F|H_i)$, then the total probability of failure P_f is given by the law of total probability as:

$$P_f = \sum_i P(F|H_i)P(H_i) \tag{1}$$

The conditional probabilities $P(F|H-i)$ are determined by analyses of the hazard scenarios H_i. Thereby, one-year reference period is normally considered. The situations H_i may lead to several events E_{ij} (e.g. excessive cracking, failure of a structural member, collapse of the bridge) with adverse consequences C_{ij} that are commonly expressed in monetary units. The total annual risk R corresponding to the hazard situations H_i can be expressed as:

$$R = \sum_{ij} C_{ij}P(E_{ij}|H_i)P(H_i) \tag{2}$$

If the acceptable risk R_t [16] is specified, the bridge or its structural members can be assessed on the basis of the inequality $R < R_t$. When the criterion of acceptable risks is not fulfilled, it is necessary to modify the system by appropriate interventions aiming at the reduction of probability of occurrence of adverse events (protective measures) or at the reduction of their consequences (mitigation measures). Further information on the probabilistic risk analysis can be obtained from [23, 16, 14].

From an economic point of view the objective is to minimize the total working-life cost of the bridge. For simplification consider hereafter assessment of the cost efficiency of a single protective measure (the presented procedure can be readily extended for decisions concerning several protective measures).

The decision parameter(s) d to be optimised may represent resistance in the case of strengthening, stand-off distance, properties of energy absorbing shields etc. The parameter may be continuous, discrete or attain a single value. In general the costs of a selected measure consist of:

- cost C_0 independent of the decision parameter (e.g. costs related to surveys, design, economic losses due to traffic interruptions),
- marginal cost C_m per unit of the decision parameter.

The failure consequences C_f can be estimated on the basis of the total annual risk R. Since the main reason for the existence of civil infrastructures is public interest, failure consequences need to include all societal losses, see Section 5.

For consistency, all the costs need to be expressed on a common basis. Costs of the measure are normally specified in a present value. All the expected failure costs that may occur within a reference period should thus be likewise estimated in the present worth. Assuming almost independent failure events in subsequent years and small probabilities $P(H_i)$, the expected failure cost related to a reference period t_{ref} (in years) can be estimated as [11]

$$E[C_f(t_{ref}, d)] \approx R(d)[1 - 1/(1+q)^{t_{ref}}]/[1 - 1/(1+q)] = R(d)Q(q, t_{ref}) \tag{3}$$

where q = annual discount rate (e.g. 0.03, an average long-run value of the real annual discount rate in European countries during the last years, however this rate is currently lower); and Q = time factor. The expected total costs C_{tot} can now be expressed as (omitting the symbol of expectation for convenience of notation):

$$\text{Measure applied:} \quad C_{tot}(t_{ref}; d) \approx C_0 + C_m d + R(d)Q(q, t_{ref}) \tag{4a}$$

$$\text{No measure:} \quad C_{tot}(t_{ref}) = R(nomeasure)Q(q, t_{ref}) \tag{4b}$$

From eqn. (4a) the optimum value of the decision parameter d_{opt} (the optimum measure) can be assessed:

$$minimum_d C_{tot}(t_{ref}; d) = C_{tot}(t_{ref}; d_{opt} \tag{5}$$

The considered measure is consequently rejected when the total cost according to eqn. (4b) is less than the total cost of the optimum upgrade.

Apparently a more complex cost model would consider costs of inspections, maintenance, upgrades and other life-cycle costs. However, in most cases this extension hardly affects the optimum measures mitigating risks in accidental situations.

4 Risk optimisation using Bayesian networks

4.1 Advantages of Bayesian networks

The risk of various technical systems in hazard situations can be analysed using the standard techniques such as fault trees, event trees, cause-consequence method, Bayesian (causal) networks and Petri networks [23]. Fault trees cannot directly accommodate dependent basic events, which may be a serious limitation for civil engineering applications. In principle event trees can deal with such dependencies; however this requires great care during event-tree construction [8]. Moreover both methods suffer from the difficulty in updating based on new information. Petri Nets provide a powerful platform, but the evaluation often takes basis in Monte Carlo simulations requiring considerable computational demands [20]. These drawbacks can be reduced by the use of Bayesian probabilistic networks with discrete nodes, supplemented by decision and utility nodes [19].

With regard to practical applications Bayesian networks facilitate [10]:

- break down of a complex task (system of structural elements) into smaller sub-tasks (foundations, piers, super-structure) that can be analysed separately by different experts,
- illustrative interpretation of knowledge concerning structural elements based on results of measurements and expert appraisals,
- consideration of uncertainties related to action effects, material and geometrical properties, and also to the applied theoretical models (so-called model uncertainties),
- modelling of complicated dependencies amongst initiation events of actions, their effects, structural properties and effects of protective measures,

- updating of results when new information becomes available for example related to action or resistance parameters.

The analysis of Bayesian network is based on the specification of conditional probabilities of nodes under assumption of information on other nodes (in the direction of casual links). The analysis is based on the concept of conditional probabilities and the theory of probability. Detail information can be found for example in [23, 19, 12].

4.2 Example of the network

Figure 1 shows an example of the Bayesian network (influence diagram) that may provide a general basis for a particular assessment. Note that the network is significantly simplified and has to be modified to reflect specific conditions of an analysed structure and considered accidental situations. In practical applications each random node may represent a subsystem and additional utility nodes may be needed. The following nodes are included in Figure 1:

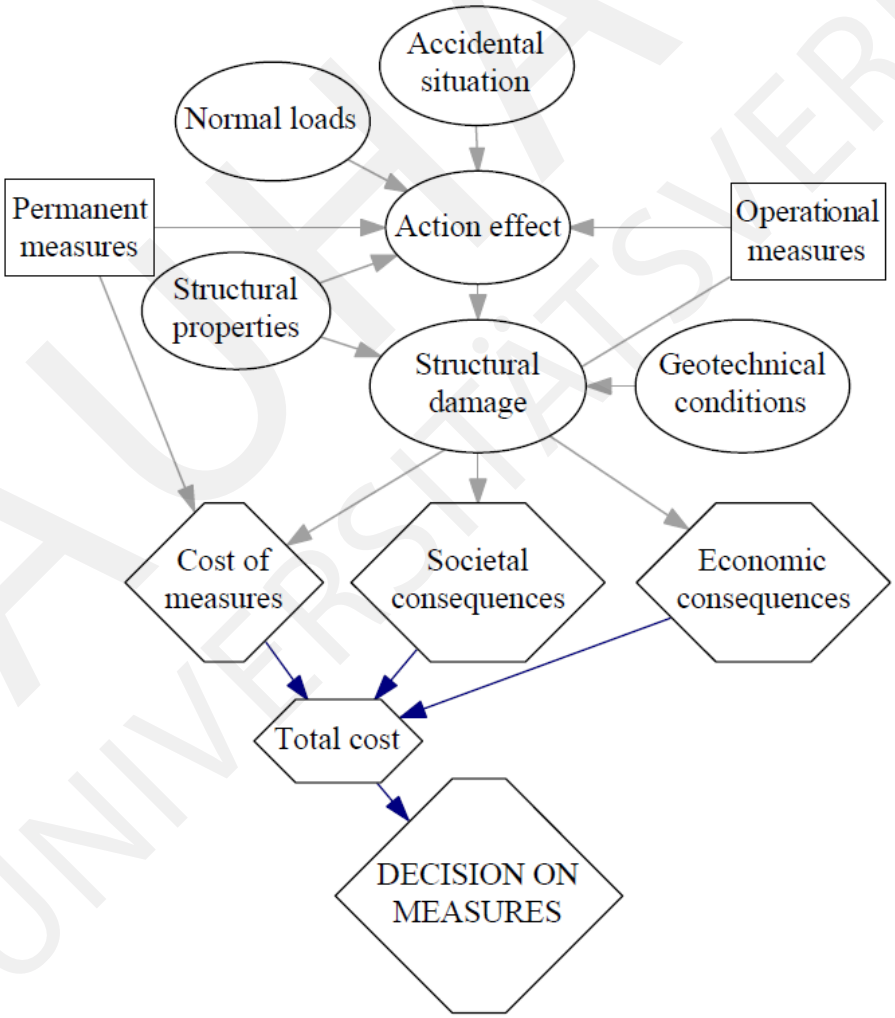

Figure 1: Example of the Bayesian network.

- chance nodes - Accidental situation, Action effect, Structural damage, Geotechnical conditions, and Structural properties,
- decision nodes - Permanent and Operational measures,
- utility nodes - Cost of measures, Societal and Economic consequences, and Total cost.

Directional arrows, interconnecting all the nodes, indicate the causal links between parent and children nodes.

Given an accidental situation, the action effects depend on accepted protective measures and may lead to structural malfunction due to damage, local failures, partial or total collapse of the bridge. This is covered in the network by the random node Structural damage. Probability of structural damage and its extent may depend on geotechnical conditions and structural properties.

Structural damage may result in societal and economic consequences. The utility node Societal consequences describes the human consequences in terms of expected number of fatalities and injuries per year due to the structural collapse and is related to a monetary value through a compensation cost for a fatality, which may be approximated by the so-called societal value of statistical life; see ISO/DIS 2394:2014 or [12].

5 Modelling of selected nodes

Bridges may be exposed to the following actions [27]:

- normal actions due to self weight, traffic, temperature or wind,
- accidental (natural) actions such as earthquake, landslide, hurricane and tornado, avalanche, rock fall, flood and tsunami,
- accidental (manmade – malicious or unconscious) actions such as explosion, fire, impact of vehicle or projectile, mining settlement,
- human errors - design error, material flaw, construction error, misuse, lack of maintenance.

The model of an accidental action takes into account the annual probability of occurrence of the accidental situation and in some cases the conditional probability of the occurrence accidental action itself (e.g. success rate in the case of blast terrorist attack). This information may be gained from experts, scenario analysis and statistical analysis of available data [24]. Limited statistical information concerning these probabilities can be found in [22].

Guidance for the development of probabilistic models of accidental action effects is provided in [28]; for instance models for earthquake, impact load and fire are discussed in [15] and blast loading in [18]. Damage on the bridge exposed to normal and accidental loads is then estimated on the basis of system modelling considering the effects of applied protective measures. Overview of possible consequences is provided in [21]:

- direct consequences resulting directly from the structural damage, examples include:

  - fatalities or injuries due to structural collapse, blast pressure or secondary projectiles (concrete, steel, glass),
  - economic losses due to cost of rehabilitation or rebuilding, cost of damaged vehicles,
- indirect consequences describing other impacts on the society, for instance:
  - fatalities or injuries due to malfunction of the bridge (e.g. in an emergency situation),
  - losses due to detours, traffic delays, loss of tolls, losses of local businesses affected by malfunction of the bridge,
  - environmental impacts such as air pollution, energy use or fuel consumption,
  - psychological consequences including loss of reputation or undue changes in professional practice,
  - infrastructure interdependency costs.

Injuries and fatalities often expressed in terms of compensation costs or increased insurance (see ISO/DIS 2394:2014). Indications for quantification of failure consequences are provided in [13, 26].

Permanent or operational protective measures may include [2]:

- restriction of physical access (barriers, security officers to control access, eliminated parking near critical structures, landscaping to increase standoff distance),
- surveillance and detection efforts (inspections, warning that the bridge is being monitored, enhanced lighting, motion sensors, removal of overgrown vegetation),
- security planning and coordination (security plans to identify critical components and establish their protection, emergency telephones, means for rerouting traffic to enable access of emergency vehicles, restricted access after span failure),
- structural modifications (protection of lower parts of cables on cable-stayed and suspension bridges, reinforce welds and bolted connections to ensure plastic capacity, use of energy absorbing bolts to strengthen connections and reduce deformations, alternate load paths).

It is noted that efficiency has to be assessed for the considered measures. For instance investments into motion sensors may decrease needs for the restriction of physical access. The control of access by guards is often ineffective since they can be intentionally distracted by secondary attacks. For blast attacks stand-off distance is a key parameter and can be hardly replaced by protective walls.

6 Case studies under development

The presented methodology is at present being applied in two case studies that have been selected considering the criteria outlined in Section 2:

- highway bridge built over an existing bridge forming a ‘double-deck’ bridge (Figure 2):

  - the highway bridge is vulnerable to a terrorist attack due to accessibility provided by the rarely used bottom bridge,
  - malfunction of the upper bridge requires long detours of highway traffic on local roads, implying significant failure consequences and enhancing attractiveness of the bridge as a target,

- highway bridge over a wide and deep valley (Figure 3):
  - the piers of the bridge are accessible by local roads and can be exposed to a blast attack or impact,
  - the height of the piers complicates repair of main girders of the bridge increasing significantly failure consequences,
  - petrol station located nearby the bridge can be a target in order to damage highway, with a significant impact due to exceptionally long detours for lorries.

Figure 2: 'Double-deck' bridge.

Figure 3: Highway bridge over a wide and deep valley.

The aim of the case studies is to provide background information for decisions concerning protective measures against a blast attack. Key steps of each study can be described as follows:

- three scenarios are considered – different amounts of an explosive charge transported by a van, small lorry and lorry with a trailer,

- several protective measures such as closure of the local roads providing access to the bridges are identified and costs related to these measures are estimated,
- the probability of the attack, depending on the amount of the charge, is a study parameter; it is assumed that this probability is provided by a relevant authority, - given the attack, probability of a 'successful' attack is determined on the basis of available data,
- given the successful attack, probabilistic analysis of the blast action and its effect on a bridge is conducted considering effects of protective measures and consequently the probability of bridge failure is determined,
- direct and follow-up (indirect)consequences of failure are estimated,
- risks for various alternatives of the attack and protective measures are analysed and optimal solutions are provided considering different probabilities of the attack.

7 Discussion

Risk and cost-benefit considerations provide important insights into how security measures should perform based on their effect on risk reduction and their total lifetime costs [24]. A risk-averse attitude in which severe consequences are more weighed is commonly accepted in decision-making [5]. Despite this, a risk-neutral attitude is suggested in this study to obtain the most efficient option in terms of the expected life cycle cost.

Highway and road authorities and network managers may be more interested in the risks of a whole network rather than to the risks of an individual bridge. In this case the methodology proposed here should be extended similarly as proposed in [4].

8 Concluding remarks

Bridges in accidental situations represent the most vulnerable components of road networks. It is shown that decisions concerning selection of protective measures can be based on the risk-based optimisation of the expected total costs. Actions to be considered in the assessment may include normal and accidental (natural or manmade) loads and effects of human errors. Potential protective measures should include restriction of physical access, detection efforts, security planning and coordination, and construction modifications aiming to improve structural robustness. It appears that the probabilistic cost optimisation in conjunction with Bayesian networks provide an effective tool for decisions concerning the selection of appropriate protective measures for bridges endangered by various types of hazards.

Acknowledgements

The study is based on outcomes of the research project VG20122015089 supported by the Ministry of the Interior of the Czech Republic.

References

[1] Commission of the European Communities, Communication from the Commission on a European Programme for Critical Infrastucture Protection COM 2006786,pp. 13, 2006.

[2] Berrick, C.A., Highway Infrastructure: Federal Efforts to Strengthen Security Should be Better Coordinated and Targeted on the Nation's Most Critical Highway Infrastructure, DIANE Publishing Company: 2009.

[3] Bocchini, P. & Frangopol, D.M., A stochastic computational framework for the joint transportation network fragility analysis and traffic flow distribution under extreme events. Probabilistic Engineering Mechanics, 26(2), pp. 182-193, 2011.

[4] Bocchini, P. & Frangopol, D.M., Generalized bridge network performance analysis with correlation and time-variant reliability. Structural Safety, 33(2), pp. 155-164, 2011.

[5] Cha, E.J. & Ellingwood, B.R., Risk-averse decision-making for civil infrastructure exposed to low-probability, high-consequence events. Reliability Engineering & System Safety, 104 pp. 27-35, 2012.

[6] EN 1990, Eurocode - Basis of structural design, CEN: Brussels, pp. 87, 2002.

[7] EN 1991-1-7, Eurocode 1: Actions on structures - Part 1-7: General actions - Accidental actions, CEN: Brussels, 2006.

[8] Faber, M.H. & Stewart, M.G., Risk assessment for civil engineering facilities: critical overview and discussion. Reliability Engineering & System Safety, 80(2), pp. 173-184, 2003.

[9] Holicky, M. & Sykora, M., Assessment of Flooding Risk to Cultural Heritage in Historic Sites. Journal of Performance of Constructed Facilities, 24(5), pp. 432-438, 2010.

[10] Holicky, M., Markova, J. & Sykora, M., Forensic assessment of a bridge downfall using Bayesian networks. Engineering Failure Analysis, 30(0), pp. 1-9, 2013.

[11] Holicky, M., Optimisation of the target reliability for temporary structures. Civil Engineering and Environmental Systems, pp. 1-10, 2012.

[12] Holicky, M., Probabilistic risk optimization of road tunnels. Structural Safety, 31(3), pp. 260-266, 2009.

[13] Imam, B.M. & Chryssanthopoulos, M.K., Causes and Consequences of Metallic Bridge Failures. Structural Engineering International, 22(1), pp. 93-98, 2012.

[14] ISO 13824, Bases for design of structures - General principles on risk assessment of systems involving structures, ISO TC98/SC2: Geneve, Switzerland, pp. 43, 2009.

[15] JCSS, JCSS Probabilistic Model Code, Joint Committee on Structural Safety: Zurich, 2011.

[16] JCSS, Risk Assessment in Engineering - Principles, System Representation & Risk Criteria, Joint Committee on Structural Safety: Zurich, pp. 35, 2008.

[17] Melchers, R.E., Structural Reliability Analysis and Prediction, John Wiley & Sons

Ltd.: Chichester, England, pp. 437, 2001.

[18] Netherton, M.D. & Stewart, M.G., Blast load variability and accuracy of blast load prediction models. International Journal of Protective Structures, 1(4), pp. 543-570, 2010.

[19] Nielsen, T.D. & Jensen, F.V., Bayesian Networks and Decision Graphs, Springer: Berlin, pp. 448, 2007.

[20] Nishijima, K., Maes, M.A., Goyet, J. & Faber, M.H., Constrained optimization of component reliabilities in complex systems. Structural Safety, 31(2), pp. 168-178, 2009.

[21] SeRoN, Risk Assessment (Deliverable D500), The SeRoN Consortium, pp. 110, 2012.

[22] Stewart, M., Risk-informed decision support for assessing the costs and benefits of counter-terrorism protective measures for infrastructure. International Journal of Critical Infrastructure Protection, 3(1), pp. 29-40, 2010.

[23] Stewart, M.G. & Melchers, R.E., Probabilistic Risk Assessment of Engineering Systems, Springer: Berlin, pp. 288, 1997.

[24] Stewart, M.G. & Mueller, J., Terror, Security, and Money: Balancing the Risks, Benefits, and Costs of Critical Infrastructue Protection. Proceedings of Reliability Engineering Computing REC2012, eds. M. Vorechovsky, V. Sadilek V, S. Seitl, V. Vesely, R.l. Muhanna & R.l. Mullen, Brno University of Technology , Brno, pp. 513-533,2012.

[25] The European parliament and the Council, COUNCIL DIRECTIVE 2008/114/EC on the identification and designation of European critical infrastructures and the assessment of the need to improve their protection, Official Journal of the European Union Brussels, pp. 8, 2008.

[26] Thoft-Christensen, P., Life-cycle cost-benefit (LCCB) analysis of bridges from a user and social point of view. Structure and Infrastructure Engineering, 5(1), pp. 49-57, 2009.

[27] Vrouwenvelder, T., Leira, B.J. & Sykora, M., Modelling of Hazards. Structural Engineering International, 22(1), pp. 73-78, 2012.

[28] Vrouwenvelder, T., Stochastic modelling of extreme action events in structural engineering. Probabilistic Engineering Mechanics, 15(1), pp. 109-117, 2000.

Determination of Design Ground Motions for Important Structures in Performance-based Earthquake Engineering

Tsuyoshi Takada

Professor
Graduate School of Engineering,
The University of Tokyo,
7-3-1, Hongou, Bunkyo-ku, Tokyo, Japan 113-8656
takada@load.arch.t.u-tokyo.ac.jp

Abstract. This paper, focusing on how to determine design ground motions (DGMs) on important structures that require dynamic response analyses to meet performance requirements, proposes technically sound and practically reasonable procedures with close linkage with the design point concept in a structural reliability theory. Several procedures, some of them recently proposed by the author, are presented with numerical output results and discussion are made from applications for performance-based framework of seismic design.

Keywords. Structural reliability, design point, design ground motion, time histories, performance-based seismic design.

1 Introduction

Performance-based design has been highlighted in the last two decades in the field of earthquake engineering [9]. Its great emphasis is placed not only on clear description of required performances to structures, but also on quantification of their requirement level. The design based on the performance requirements is understood as the limit state design, which originates from Europe. Much effort for the theoretical development and for implementation of the design method have been made in Europe and, eventually the results are now reflected into the form of ISO documents and EUROCODE.

Therefore, the limit state design concept has been proposed so far and currently this concept matches the same concept of the performance-based design ([5], [9]). In the limit state design (LSD), design limit states are usually classified into the ultimate and serviceability limit states, and the former is closely related to load bearing capacity and ductility of buildings as a whole under extreme loading conditions rather than individual structural members, while the latter focuses on functionality and inconvenience due to building damage during normal use of buildings.

It then leads that the seismic design load or the magnitude of the design load for the particular limit state should be different among all performance required in the design. For example, in a seismic design, an appropriate level of the seismic design load should be determined on the basis of performance requirement. In addition to the magnitude of the seismic load, more relevant parameters specifying the detail seismic design load such as the spectral content, the duration time of the ground motions, etc. are needed, all of

which come from detailed information of earthquake sources. Ultimate description of the seismic design load on structures is given in the form of time histories, so called design ground motions (DGMs), which are effectively used for dynamic response analyses with structural models.

In this context, it is presented in this paper how the DGMs can be determined for seismic design of structures in the framework of the performance-based design, and that there are historically several concept and methods to determine DGMs (time-histories) in a probabilistic approach and demonstrated are the recent advancements made by the author.

2 Design Point Concept in Structural Reliability Theory

2.1 Checking Point in Structural Reliability Theory

For a general limit state function, the first-order second-moment (FOSM) theory gives us a checking point or a beta-point in a standard normal space, which is the shortest distance of the approximated hyper-plane of the limit state function from the origin, or the point of greatest probability density (or maximum likelihood point), as is seen in Fig.1 ([1]; [3]; [10]). Equivalently, the value of each variable corresponding to the checking point P can be understood as the most adequate value for the limit state of interest for the specified condition.

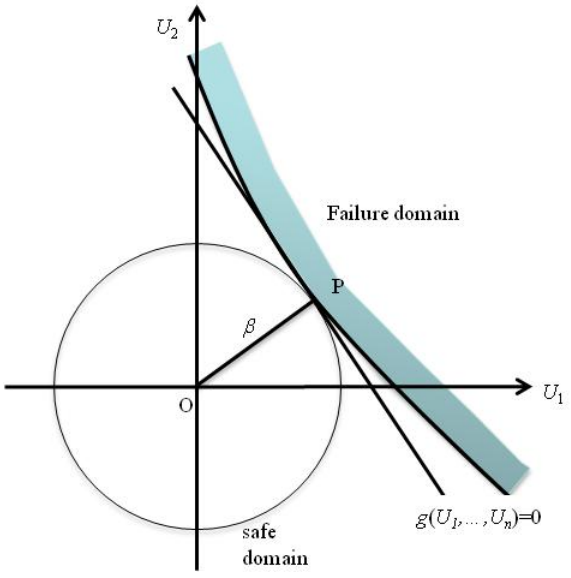

Figure 1: Concept of checking point

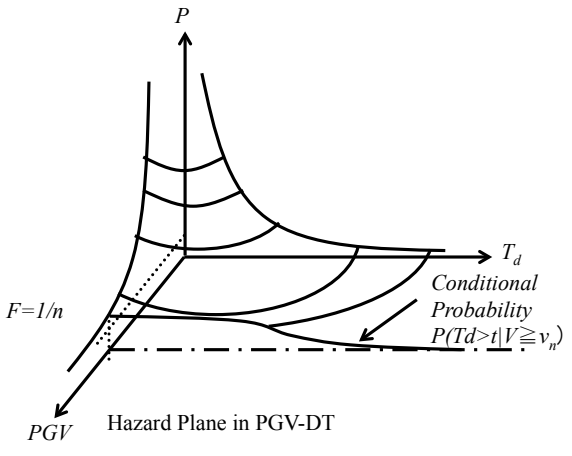

Figure 2: Seismic hazard plane

2.2 Design Format based on Design Point

In a design situation, given a limit state function with random parameters to be determined under the condition of the specified reliability index β_T or an allowable probability

of failure P_{fa}, the design point P in the normal space gives a design format as in the following LRFD (Load and Resistance Factor Design) format, which has been used in north America, same as the partial safety factor format in Europe [5].

$$\phi R_n \geq \sum_i \gamma_i S_{ni} \tag{1}$$

where ϕ, γ_i are resistance and load factors, respectively, which are function of β_T and statistical property of random variables involved, and R_n is a nominal resistance, S_{ni} is mostly the representative values of the load i. ϕR_n and $\gamma_i S_{ni}$ are so called, "design resistance" and "design loads". Therefore, the design load varies according to the required reliability index and statistics of the random variables for the given limit state. The higher β_T provides the larger design load and the less design resistance.

It directly leads that the seismic design load to a structure must be directly linked to the reliability requirement for a concerned limit state. Although the magnitude of seismic design load is often given in terms of the return period value in the performance-based earthquake engineering [9], the design load expressed by the product of the load factor and the representative value of the load $\gamma_i S_{ni}$ can easily be converted into the equivalent return period value.

3 DGM for Seismic Design

To accurately characterize seismic GMs for dynamic response analyses of structures, it is essential to adequately specify the following four basic properties of earthquake GMs; their maximum amplitude, spectral content, duration time and temporal change of time series. It is possible to generate synthesized design ground motions by properly taking into account of the above basic properties. Although the current probabilistic seismic hazard analysis (PSHA) has given a design basis in terms of seismic hazard map or curves, it can estimate only scalar quantity of GMs such as PGA, PGV, spectral response, but cannot produce any information that is needed to capture all the above basic properties of GMs. Due to this methodological shortcoming of the PSHA, design ground motions cannot be generated directly based on the results from the conventional PSHA [2].

It is a goal to evaluate all of those four basic properties simultaneously and reasonably based on the results from the PSHA. In the first step, it is shown in the author's paper [11] that by focusing on both PGV and the duration time (DT) of future ground motions, the joint probability density function (JPDF) is formulated in the framework of the probabilistic seismic hazard analysis. Figure 2 illustrates the seismic hazard plane in PGV and DT, from which the two parameters are determined under the given exceedance probability. Figure 3 shows examples of DGMs (acceleration time histories) for different locations in Japan with return periods 75 and 250 years. Then, a method to carry out a bi-variate PSHA that can simultaneously predict both PGV and DT is suggested in the reference.

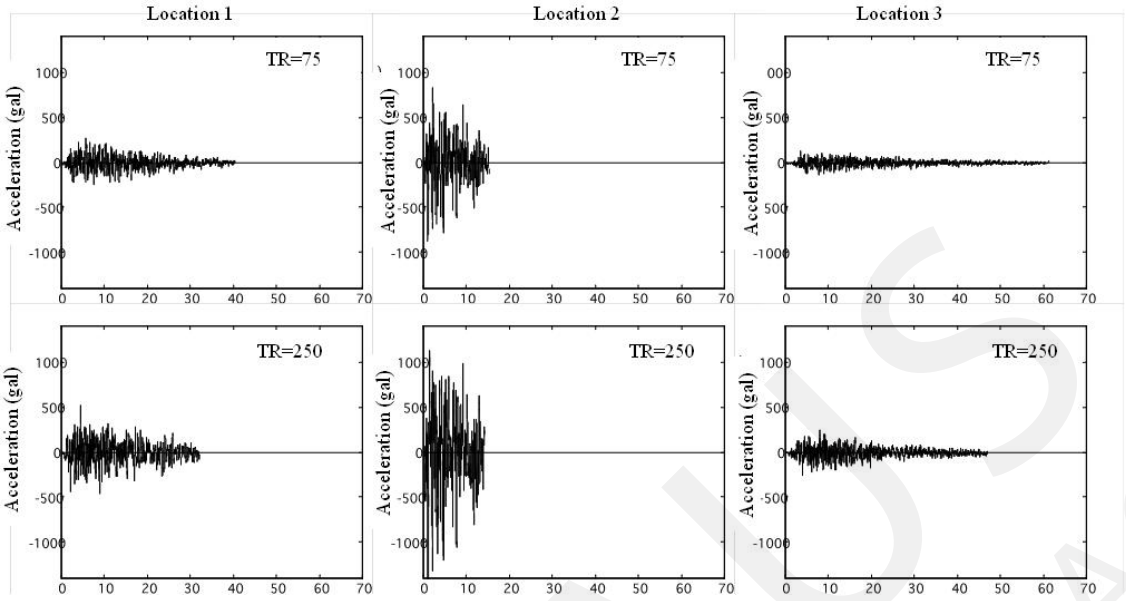

Figure 3: Examples of generated GMs (Takada and Obuchi, 2005)

3.1 DGM based on Multi-variate PSHA

3.2 Concept of Controling Earthquakes based on Deaggregation of PSHA Results

One of the most important issues in the seismic design of structures as well as in the earthquake disaster mitigation policy-making is what kind of earthquakes have to be taken into consideration. These selected earthquakes are called "Scenario earthquakes" or "controlling earthquakes", which are specified deterministically or probabilistically. How large earthquakes should be adopted, of course, depends on the target risk level which varies among structures with different importance.

For the selection of such earthquakes on probabilistic basis, it should not only take account of likelihood of earthquake events, but also is based on quantitative measures. The PSHA can estimate the probability distribution of the earthquake ground motion intensity not earthquakes themselves, but the only disadvantage of this assessment was said to be that it lacks of the concept of "earthquakes [6]". To remedy this shortcomings, the procedures to select the earthquakes corresponding to the specified risk or exceedance probability have been developed, and these selected earthquakes are called "controlling earthquakes ([7]; [6])" or "hazard-consistent earthquakes [4]". Both of the procedures are based on deaggregation of a specified point on the seismic hazard curve, and these methods have been fully adopted as a siting criterion in the US nuclear regulatory and Japanese practice [13]. McGuire (1993) called this deaggregation process as "Closing loop", which implies that there is a definite linkage between the probabilistic ground motion intensity and possible earthquakes thus selected.

Once the earthquakes are selected, which are characterized in terms of their source magnitude and distance, more advanced up-to-date simulation techniques from their sources

can be applied to them to accommodate more realistic earthquake information to be used for seismic designs and earthquake disaster mitigation.

Herein, an earthquake magnitude M, a source distance R and a parameter representing the uncertainty of a GM attenuation law ϵ are assumed to be random variables. Now, an attenuation law, in general, takes the following form.

$$Y = Y(M, R, \epsilon) \tag{2}$$

where Y denotes the intensity of earthquake ground motion of a site, such as peak ground acceleration (PGA), peak ground velocity (PGV) or spectral response, etc.

Since the point on the hazard curve consists the sum of statistical contribution of different source magnitudes and distances, therefore, the point, inversely can be decomposed into the contributions of each different source magnitudes and its distance. This decomposition process is called “deaggregation” of the seismic hazard curve. Figure 4 shows schematic diagram of how to determine magnitude, distance and epsilon, which appear in the limit satate function associated with the GM intensity,

$$G(M, R, \epsilon) = y - Y(M, R, \epsilon) \tag{3}$$

once the M, R, ϵ are determined, basic earthquake source information can be obtained, from which GM time histories can be generated. The author’s paper studies several possible procedures for determination of these parameters based on the structural reliability theory [12].

4 Recent Advancements of DGM based on PSHA

4.1 DGM Selction from SWI (Seismic Wave Inventory)

The great number of records have been accumulated in Japan after the 1995 Kobe earthquake at the observation network, which is called “K-NET”. The author proposes to directly use these observed records without processing the records for future ground motion prediction. In the past, in order to achieve a new ground motion attenuation relationship from the observed records, some intensity measures such as PGA, PGV or spectral acceleration are of major concern, all of which are well known as not sufficiently effective indicators to represent earthquake destructiveness. In this respect, the author proposed a wave database, so called "seismic wave inventory (SWI)", in which all observed records are tagged in terms of earthquake magnitudes, source-site distances, soil category, etc., as is seen in Fig. 5 [15].

The SWI can play the same role as the conventional ground motion attenuation laws since all records have their attributes such as an earthquake magnitude, distance and other attributes. In the reference [14], it is presented that a set of GMs corresponding to a target return periods can be easily selected from the inventory. As numerical examples, GMs with difference return periods are selected.

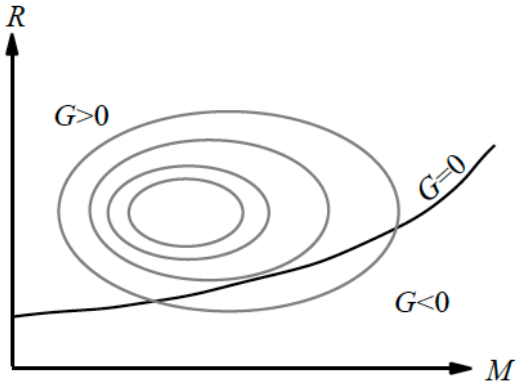

Figure 4: LS function and JPDF

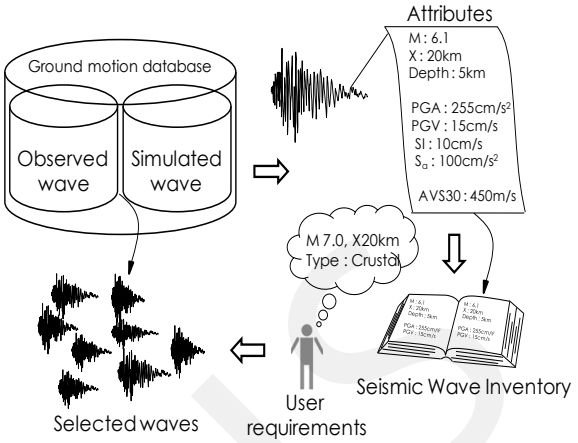

Figure 5: Concept of Seismic Wave Inventory

Figures 6 and 7 show selected GMs with the return periods 500 and 5000 years, which are determined from the PGV hazard curve of the PSHA. Selected GMs are two types; actually observed records in black waves and the ones simulated based on physical fault models in gray. Several types of earthquakes with different magnitudes and distances are selected, all of which, however, produce the same amount of PGV at a site of interest. In Fig. 7, only simulated waves are selected since there are no such observed records with high PGV of 55 kines. Figures 8 and 9 show the contribution of selected earthquakes in a M-R plane. It can be seen that near-field earthquakes with higher magnitudes have much contribution to the amount of PGV.

4.2 DGM based on Physics-based simulations

Here, the author proposes a methodology to generate a set of ground motions that are consistent with the seismic hazard of the target site since there has been theoretical development of physics-based simulation technique in the last two decades (Boore et al. (1983), Kamae et al. (1991), Irikura et al. (1997)). A set of generated GMs are expected to be used for safety assessment and seismic design of important structures such as nuclear power plants.

For generating GMs, several fault models containing stochastic parameters of seismic sources characteristics are set in each group of seismic sources that are divided by region, magnitude, and distance [8]. In the following Monte Carlo Simulation, the GMs are repeatedly generated one by one for each fault where realization values for stochastic parameters are given in the way that realization values are randomly set according to the corresponding distribution of stochastic parameters, under the constraint that PGA of the generated GMs fall within the specified range, e.g., from 700 to 1100 gals in this case. Figure 10 shows the generated GMs from different earthquake categories, whose PGA are within the same range.

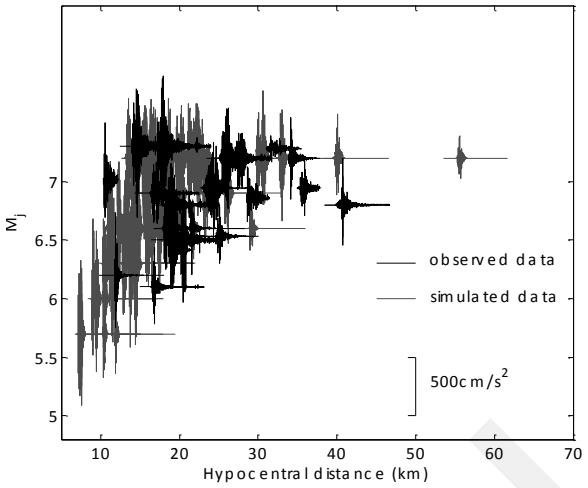

Figure 6: Selected GMs (TR=500yrs)

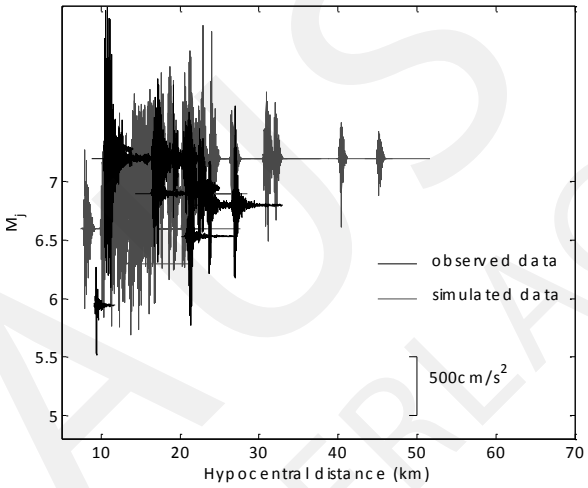

Figure 7: Selected GMs (TR=5000yrs)

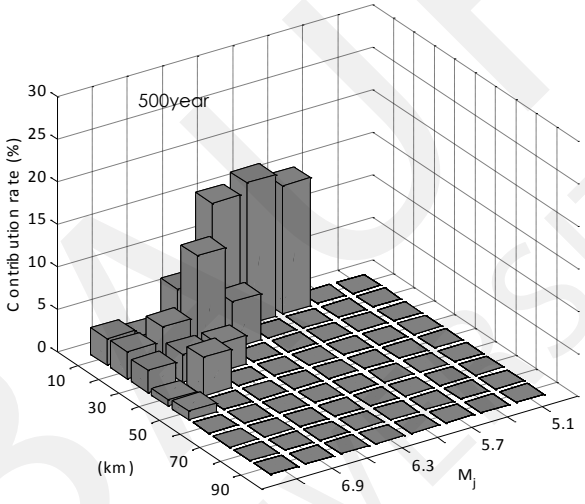

Figure 8: Contribution of earthquakes (TR=500yrs)

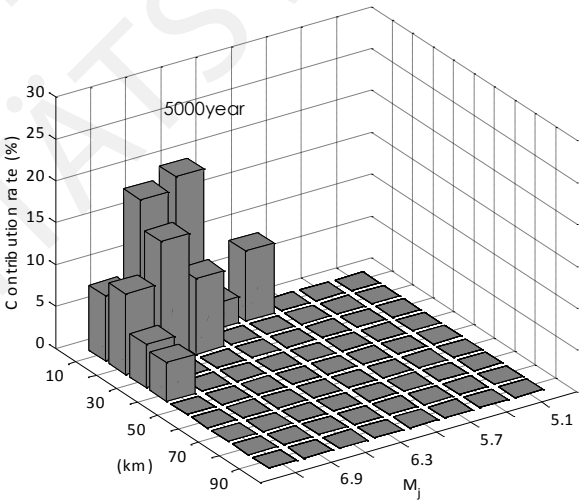

Figure 9: Contribution of earthquakes (TR=5000yrs)

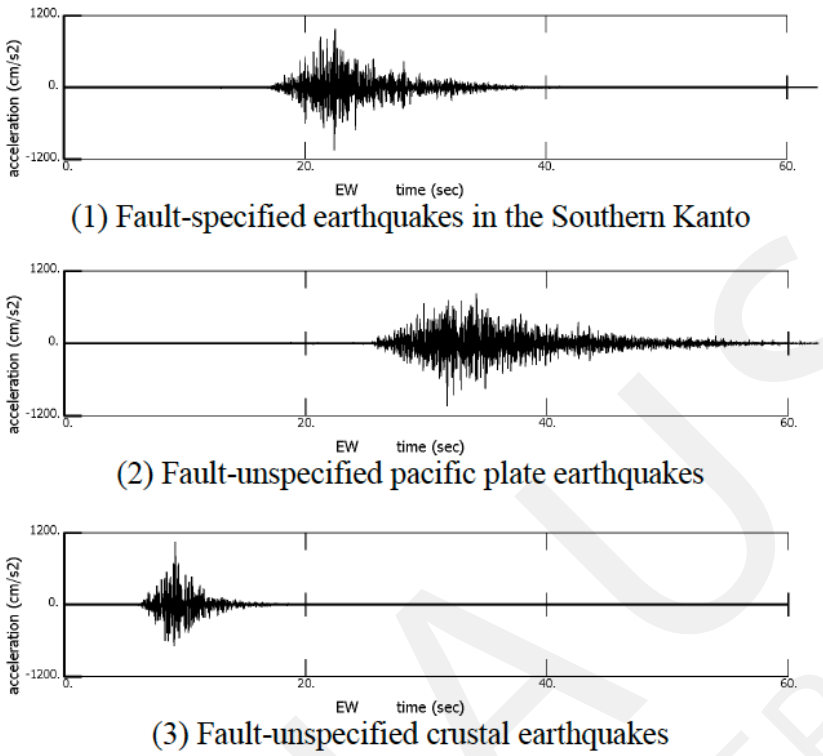

Figure 10: Examples of generated GMs based on physics-based fault models

5 Conclusions and Future Research Subjects

The DGMs used for dynamic response analyses of important structures should be directly linked with performance requirements. The performance requirements imply the performance category required and its quantitative basis for a particular structure. This paper presents the determination procedures of DGMs with the concept of the design point in a structural reliability theory and demonstrates the recent advancements made by the author. The proposed procedure needs further improvement in order to reflect more realistic features of GMs in the framework of performance-based earthquake engineering.

References

[1] A H-S Ang and W H Tang. *Probability concepts in engineering planning and design*. John Wiley & Sons, Inc, 1984.

[2] C A Cornell. Engineering seismic risk analysis. *Bulletin of the Seismological Society of America*, 58(5):1583–1606, 1968.

[3] A M Hasofer and N C Lind. Exact and invariant second-moment code format. *Journal of the Engineering Mechanics Division*, 100(1):829–844, 1978.

[4] Y Ishikawa and H Kameda. Hazard-consistent magnitude and distance for extended seismic risk analysis. *ICOSSAR'93*, pages 2139–2146, 1994.

[5] ISO 2394:1998 General Principle on Reliability of Structure, 1998.

[6] R K McGuire. Probabilistic seismic hazard analysis and design earthquakes: closing the loop. *Bulletin of the Seismological Society of America*, 85(5):1275–1284, 1993.

[7] R K McGuire and K M Shedlock. Statistical uncertainties in seismic hazard evaluations in the united states. *Bulletin of the Seismological Society of America*, 71(4):1287–1308, 1981.

[8] A Nishida, S Igarashi, S Sakamoto, Y Uchiyama, Y Yamamoto, K Muramatsu, and T Takada. Characteristics of simulated ground motions consistent with seismic hazard. *Transaction of SMiRT22*, 08 2013.

[9] Vision 2000 SEAOC. Performance based earthquake engineering of buildings. *Sacramento, CA*, 1995.

[10] M Shinozuka. Basic analysis of structural safety. *Journal of Structural Engineering*, 109(3):721–740, 1983.

[11] T Takada and M Obuchi. Joint pdf of ground motion intensity and duration time and its applications. *J. of Structural construction and engineering*, (589), 2005. (in Japanese).

[12] T Takada, S Ochi, and J Kanda. Probability-based determination of design earthquakes. In *Probabilistic Safety Assessment and Management (PSAM6): Proceedings of the 6th International Conference on Probabilistic Safety Assessment and Management*, 2002.

[13] T Takada, T Okumura, J Hirose, K Muramatsu, S Taki, and K Ishii. Probabilistic scenario earthquakes for seismic design–comparison of two identification procedures. In *Proceedings of the OECD/NEA Workshop on Seismic Risk, NEA/CSNI*, 1999.

[14] T Takada, K Tanaka, and T Itoi. New methodology for wave-based probabilistic seismic hazard analysis. 2013.

[15] K Tanaka and T Takada. Empirical selection method for ground motion for prediction from observed earthquake record inventory. *J. of Structural construction and engineering*, (646):2219–2225, 2009. (in Japanese).

Reliability analysis of HSC and UHPC columns

Ngoc Linh Tran

Institute for Concrete and Masonry Structures
Technische Universitaet Darmstadt
Germany
tran@massivbau.tu-darmstadt.de

Abstract.

With the use of high and ultra-high strength materials reinforced concrete columns in building structures are being more and more slender. Material properties and geometric parameters are significant sensitive to load bearing capacity of the columns. This paper presents a numerical stochastic analysis of slender reinforced concrete columns. An effective method for considering the random field of reinforced concrete column, which based on response surface method, is applied. Spatial variability of material is taken into account. Hereby the tensile strength, compression strength and elastic modulus of concrete are special interested due to their large deviations. A parameter study is conducted to point out the critical regions of structural reliability for the reinforced concrete columns.

Keywords: reinforced concrete columns, spatial variability, random field, response surface method.

1 Introduction

The success of developing ultrahigh-performance concrete (UHPC) in the early 1990s allows an extension of application field of reinforced concrete constructions. Meanwhile concrete technological developments have allowed production of UHPC with a compressive strength of more than $150 N/mm^2$. Consequently, the cross-sectional dimensions required for highly stressed compression members can be reduced. This positive development increased the trend to even more slender and but likelier also to buckle structural systems. Under certain conditions, it is to be expected that the safety level of such construction elements decreases. A detailed stochastic modelling as well as a full probabilistic analysis can give the answer for this problem.

In the view of structural analysis, concrete properties show a large randomness and spatial variability in structure, especially by fibre concrete. By using assumption of homogenous material properties without considering their spatial variability the failure positions of structural members are fixed. For a pinned-column under eccentric compression load a failure is located at the middle of the column, where the maximal moment is always found. Experimental results showed that real columns have failures in range of $\frac{1}{3}$ length of the column at the middle [5], meaning that the simple assumption cannot reflect fully the true behaviour of the structure. To overcome the drawback of this assumption, it is necessary to consider the randomness and spatial variability of structural properties in reliability analysis. In this case, the concrete properties are especially interested.

In this paper, a reliability analysis of high strength and ultra-high performance fibre reinforced concrete columns under eccentric load is presented, in which the spatial variability of concrete properties are taken into account. The influence of the spatial variability of the concrete properties on structural reliability is analysed. A comparison with the use of homogeneous material hypotheses is also presented.

2 Experimental tests on slender columns

2.1 General

Accompanying the numerical calculations, experimental tests were carried out on slender columns. Determining load bearing capacity of the columns, randomness and spatial variability of concrete properties is the goal of these tests. To test columns with a high ratio slenderness ratio ($\lambda \geq 80$) the cross-sectional dimensions have to be relatively small (h/b/l = 12cm/12cm/278cm) due to the capacity of the laboratory's mechanical equipment. The columns are loaded in a position-controlled component test by a hydraulic cylinder. During the test, deflections and compressions of reinforcement, concrete and structural system are measured with strain gauges and displacement sensors at more than 20 measuring points. In addition to these tests, investigations on compressive strength, flexural strength and modulus of elasticity of UHPC were carried out. The correlation and spatial variability of concrete properties are also studied. To determine the influence of geometry on the spatial variability of material properties, reinforced concrete columns with different cross-sectional dimensions and cross-sectional forms are investigated.

2.2 Test results

In order to adequately estimate the model uncertainties, the number of samples should be maximized. Because of this, more than 10 columns were tested at TU Darmstadt. Figure 1 illustrates a slender column in different loading states of 300, 518 and 330 kN as well as the force-deflection-relationship of the experimental test.

Figure 2 illustrates the axial force of the hydraulic cylinder dependent on axial compression of the column for NSC and UHPC. It is clear that the maximum axial force of the UHPC column is higher than that of the same column type made of NSC. Much more interesting is that, also in the case of fibre-reinforced UHPC, system behaviour can be characterized as brittle. Hence, the nearly linear trend of the axial force-compression-relationship confirms the doubts about an increasing risk of failure due to less ductile system behaviour. More detailed results of the load bearing tests can be found in [5].

At the moment, the study of spatial variability of concrete properties is being carried out at the institute of concrete and masonry, TU Darmstadt. After taking concrete samples out from the reinforced concrete columns by boring, the samples are tested to determine their mechanical properties. By UHPRC columns, the fibre distribution and orientation are also analysed by using the computer-tomography and optical analysis measurement methods.

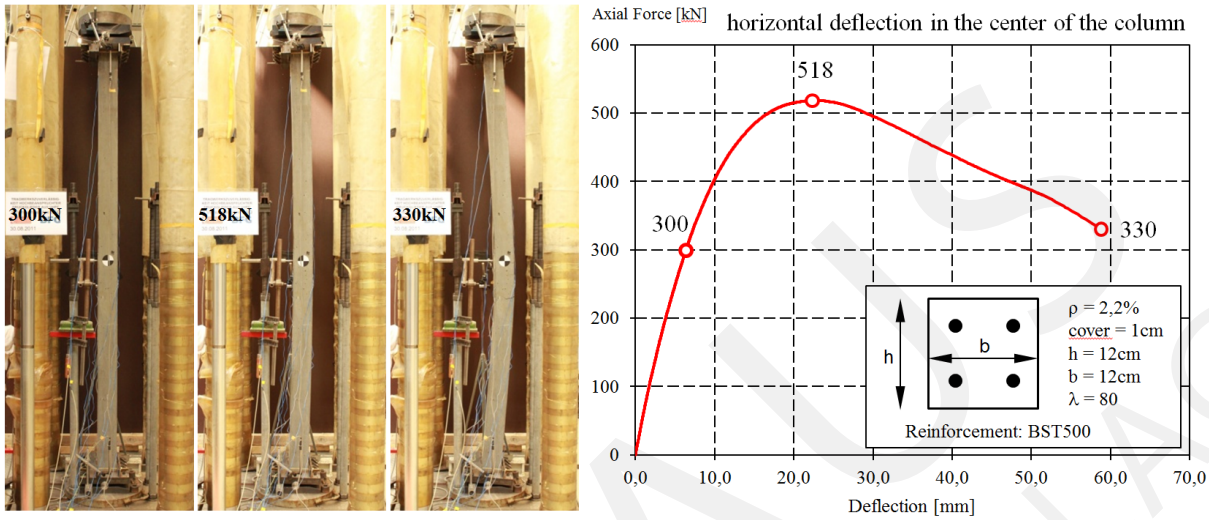

Figure 1: Slender UHPC column in different loading states

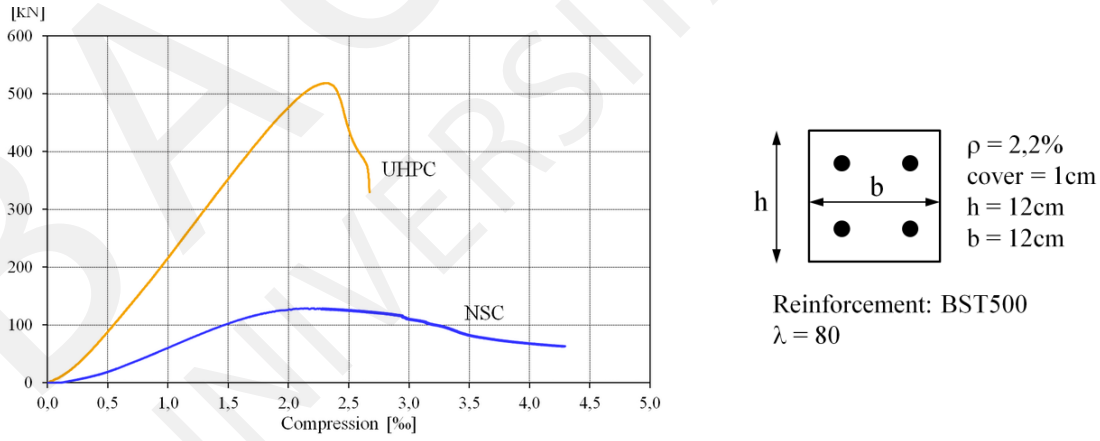

Figure 2: Behaviour of NSC and UHPC column

3 Structural Modelling and Analysis

For analysis of the reinforced concrete columns, a combined method which was developed in [9] is used. In this method, the structure system is divided into a finite number of beam elements. Because the sectional stiffness of each element generally depends on the load state, this stiffness is not constant at every position of element. To determine exactly the relationship between load and displacement, the beam element is divided into some small segments and the transfer matrix method is used for calculating. Each segment has equal cross-section stiffness and this stiffness is determined by using a section calculation algorithm, which is based on stress integration. To create stiffness matrix and load vector of elements, the dis- placement method is used in combination with the transfer matrix method. The computation of the whole structure system is carried out with the use of the Newton-Raphson method and tangent stiffness matrixes (see Fig. 3). The method considers also the nonlinear geometry effect of the structure. Nonlinear material analysis is carried out in process of calculating section. This analysis is based on the predefined realistic stress-strain curves of concrete and steel, which has already been integrated in some structural codes, such as CEB-FIP, Eurocode 2. Effects of softening, cracking of concrete are also considered following Quast's approach [8]. The calculation method was implemented in the program STAB3D, which is specially designed for analysis of reinforced concrete columns.

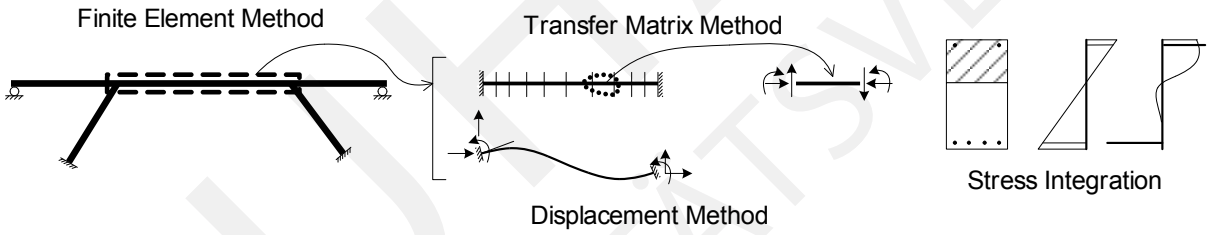

Figure 3: Combined method

To take into account the spatial variability of concrete properties, generated random properties are set to all structural sections. Hereby only the variability in the long direction of the column is considered. On cross section, concrete properties are assumed to be constant.

4 Probabilistic Modelling

4.1 Random variables

Based on the results of experimental tests which was already reported in [5] and suggestions according to the Probabilistic Model Code [9], a summary of the investigated basic variables is given in Table 1 for both normal concrete and UHPC. To determine the design load, the nonlinear analysis method according to Eurocode 2 is applied. The global factor of resistance $\gamma_R = 1.3$ is used.

Properties	Var.	Expression	Type	Unit	μXi	σXi	V_{Xi}
Concrete EC2							
compression strength	f_c	$f_{ck} + 8$	LN	N/mm^2	-	5,0	-
tensile strength	f_{ct}	$\alpha_{ct} \cdot (f_c - 8)^{2/3}$ for $f_c \leq 58$ $2,12 \cdot \ln(1 + f_c/10$ for $f_c > 58$		N/mm^2	-	-	-
tensile strength factor	α_{ct}	determined	LN	-	0,30	-	0,30
elastic modulus	E_c	$22000 \cdot \ln(1 + f_c/10)^{0,3}$	LN	N/mm^2	-	-	0,15
Concrete M2Q							
compression strength	f_c	$f_{ck} \cdot (1 + 0,06 \cdot 1,645)$	LN	N/mm^2	164,8	-	0,06
tensile strength	f_{ct}	$\alpha_{ct} \cdot f_c^{2/3}$		N/mm^2	13,5	2,0	-
tensile strength factor	α_{ct}	determined	LN	-	0,45	-	0,15
elastic modulus	E_c	$\alpha_{Ec} \cdot f_e^{1/3}$		N/mm^2	51260	2510	-
elastic modulus factor	α_{Ec}	determined	LN	-	9350	-	0,10
Reinforcement							
yield strength	f_y	$1,1 \cdot f_{yk}$	LN	N/mm^2	550	33	0,06
ultimate yield strength	f_u	$1,05 \cdot f_y$		N/mm^2	578	-	-
elastic modulus	E_s	determined	D	N/mm^2	200000	-	-
Geometry							
length	l	-	D	m	-	-	-
width	b	-	N	m	bm	0,005	-
height	h	-	N	m	hm	0,005	-
concrete cover thickness	c	-	N	m	cnom	0,005	-
steel diameter	d_s	-	N	m	dsm	-	0,02
eccentricity	e	-	D	m	-	-	-
Load							
dead load	G	$G_m = G_m = \frac{R_d}{\gamma_G + Q_k/G_k \cdot \gamma_Q}$	N	kN		-	0,10
live load	Q	$Q_m = \frac{R_d - G_k \cdot \gamma_G}{1,746 \cdot \gamma_Q}$	Gumbel	kN		-	0,40
Model uncertainty	θ	determined	LN	-	1,0	-	0,10

Table 1: Parameters of basic variables

Although model uncertainty was determined and reported in [5] with mean value 1.0 and variance coefficient 0.07 by using the calculation program STAB3D for column analysis, in this study, the variance coefficient with value 0.10 of the model uncertainty was taken according to [7].

4.2 Random fields

Randomness and spatial variability of structural properties is a natural phenomenon, which have a big influence on structural behaviour and should be taken into account in reliability analysis of the structure. For reinforced concrete columns, the elastic modulus and tensile strength of concrete are very sensitive to the load bearing capacity, especially when fibers are used in concrete. In the model, the strength random field is homogeneous and isotropic. That means the local distribution is identical in all points of the structure. The following correlation function is used in this study:

$$\rho_{UU}(x_1, x_2) = e^{-(\frac{x_1 - x_2}{L})^2} \tag{1}$$

where L is the correlation length. If L = 0 the properties are not correlated ($\rho_{UU}(x_1, x_2) = 0$) and when L tends to infinity the correlation is perfect ($\rho_{UU}(x_1, x_2) = 1$). In the case

of very large L, the random field is reduced to random variable. According to [4] the correlation length is about 1 m for plan structural members and 5 m for columns. In [3] the correlation length for reinforced concrete column is $L = 6h_m$, with h_m representing the mean height of the column cross section. In this paper the correlation length L = 3m is chosen for all studied concrete properties.

On the other hand, the concrete properties are correlated each other. For modelling the random variables, a correlation matrix for concrete materials in reference to [2] is adopted. Hereby only the tensile strength and the elastic modulus are uncorrelated (see Tab.1).

	f_c	f_{ct}	E_c
f_c	1	0.4	0.3
f_{ct}	0.4	1	0
E_c	0.3	0	1

Table 2: Correlation matrix of concrete materials [2]

In this study, the reinforced concrete column is divided into 30 segments as well as 31 sections. Each segment has 3 basic variables describing concrete properties: compression strength, tensile strength and elastic modulus. The number of basic variables describing concrete properties for whole column is 93. The concrete properties are correlated on section and along the column. To generate the random values, all correlated random variables can be converted to uncorrelated random variables using eigenvalue decomposition of the covariance matrix. For convenience in calculation, random variables are normalized with zero mean value. The covariance matrix C_{XX} can be expressed though eigenvectors matrix ψ and eigenvalue matrix λ as follows:

$$C_{XX} = \psi \cdot \mathrm{diag}\{\lambda_i\} \cdot \psi^T \tag{2}$$

Therefore, standard random variables X_0 are calculated through uncorrelated random variable Y using following transformation:

$$X = \psi \cdot Y \tag{3}$$

Here, the independent random variables Y have Gauss distribution. The associated standard deviations are calculated from the eigenvalues.

$$Y_i \sim N(0; \sqrt{\lambda_i}) \tag{4}$$

By strong correlation only some random variables Y with large standard deviations can describe very well the random variables X. In this case, we can significantly reduce number of required random variables Y. As a result, calculation time for probabilistic analysis is also reduced.

In general, for basic variables with non-Gaussian distributions a Nataf-model proposed by Liu and Der Kiureghian [6] for transforming non-Gaussian multivariate distribution into standardized Gaussian distribution can be used. In this study, the concrete properties

have lognormal distribution. A simple transformation from lognormal distribution to normal distribution is expressed as follows:

$$X_{0i} = \frac{\ln X_i - \ln \mu_i}{s_i} = \frac{1}{s_i} \ln \left(\frac{X_i}{\mu_i} \right) \tag{5}$$

Here are $\mu = \ln \left(\overline{X} / \sqrt{1 + v_x^2} \right)$ and $s = \sqrt{\ln(1 + v_x^2)}$ with mean value $\overline{X}$ and covariance v_x.

According to [1], by positive correlation coefficient and especially with covariance coefficient up to 0.4 there is only a very small difference between original and adjusted correlation of two correlated log-normal variables using the Nataf model. This is also confirmed by Vorechovský in [10]. Hence, in this study the original covariance matrix C_{XX} is used also for transformed values.

5 Reliability analysis

5.1 Analysis methods

Performing a reliability analysis of high-dimensional nonlinear problems with implicit response functions is always a big challenge. If the analysis of each sample requires much computation time, numerical methods such as Crude Monte Carlo Simulation (CMCS), adaptive importance sampling (AIS) maybe not effective enough and in many cases is not feasible. Response surface method (RSM) overcomes the disadvantages of these methods. The main idea of RSM is approximating the limit state surface of studied structure, namely response surface, to convert the implicit problems into problems with explicit response function, which can be easily solved by popular methods. In this paper load bearing capacity presenting limit state surface of the structure is polynomial approximated as following:

$$R(x) = a_0 + \sum_{i=1}^{n} b_i \cdot \left(\frac{x_i - x_i^*}{k \cdot \sigma_i} \right) + \sum_{i=1}^{n} c_i \cdot \left(\frac{x_i - x_i^*}{k \cdot \sigma_i} \right)^2 \tag{6}$$

Here are n number of variables related to resistance of structure,

$x(x_1, x_2, ..., x_n)$ any point of response surface, also vector of variables,

$x^*(x_1^*, x_2^*, ..., x_n^*)$ referent point, also design point when adaption of RS is used,

σ_i standard deviation of variable i,

k factor controlling the study range, can be set with value of 3. If an adaption of response surface is used, this factor should be changed to 1 for local analysis.

$a_0, b_i, c_i, i = 1..n$ constants,can be easily determined by solving $(2n + 1)$ equations with selection $\left(\frac{x_i - x_i^*}{k \cdot \sigma_i} = 0\right)$ and $\left(\frac{x_i - x_i^*}{k \cdot \sigma_i} = 0\right)$.

Algorithm of RSM with the polynomial approximation presented above was implemented in the probabilistic analysis program ANNA, which was also developed by author. The program ANNA is coupled with the structural analysis program STAB3D to perform reliability analysis for reinforced concrete frame structures.

5.2 Results

5.2.1 Comparison of RSM and AIS method

To illustrate the effective of the response surface method, a reinforced concrete column with cross section 40 cm x 40 cm and slenderness of 80 made of concrete C100/115 under eccentric load was studied. The column is analysed in some cases of reinforcement ratios and eccentricities to consider different nonlinearity situations. The reliability analysis was carried out using RSM as well as the AIS method as a reference.

Reinf.Ratio	$\rho_s = 1.0\%$				$\rho_s = 2.0\%$			
Eccentricity	$e/h = 0.1$		$e/h = 2.0$		$e/h = 0.1$		$e/h = 2.0$	
$N_d(kN)$	4303		146.4		6393		383.1	
Method	*AIS*	*RSM*	*AIS*	*RSM*	*AIS*	*RSM*	*AIS*	*RSM*
p	4.7×10^{-4}	4.9×10^{-4}	1.3×10^{-6}	1.6×10^{-6}	5.8×10^{-4}	5.6×10^{-4}	2.0×10^{-5}	2.4×10^{-5}
β	3.305	3.296	4.703	4.654	3.249	3.258	4.110	4.064
n_{Sim}	15000	21	15000	21	15000	21	15000	21
$T_{cal}(sec)$	436	9	507	7	486	9	479	6
$Note: T_{cal}(CrudeMonte - CarloSimulationwith 2.0 \times 10^{10} samples, approximated) \approx 21 years$								
Computer used for all analysis: Processor Intel ®Core i7-2600 CPU @ 3.4GHz, 8GB RAM								

Table 3: Comparison of numerical analysis results

By controlling of maximal static error fewer than 10% the analysis shows that there is a very small difference in calculation results between two calculation methods (see Tab. 3). Requiring only few structural simulations, which are used for finding the limit state of structure, the response surface method gives a very efficient performance on reliability analysis. At same quality of analysis results, the calculation time required in case of using RSM is reduced about 50 times when compared with AIS method. It is also seen that the chosen polynomial approximation reflects very well the limit state surface of reinforced concrete columns. In this case, no adaptation of response surface is required.

This result shows the computational efficiency of the response surface method in reliability analysis of reinforced concrete columns. In the next calculations only analysis results with the use of RSM are presented.

5.2.2 Failure zone of columns

As described in the chapter 1, due to the spatial variability of concrete properties the failure position is not fixed at the middle of column. To illustrate the failure zone, a reinforced concrete column under eccentric compression load was analysed. In this example,

only concrete tensile strength was considered for random field. Monte Carlo method was used to capture possible positions of failures. Two values of correlation length (L = 0 and L = 1m) are used to investigate its influence on failure position of the reinforced concrete col- umn. In case of zero correlation length, the failure zone dominates on about half of the column length. The failure zone is significant shortened by the correlation length L = 1m.

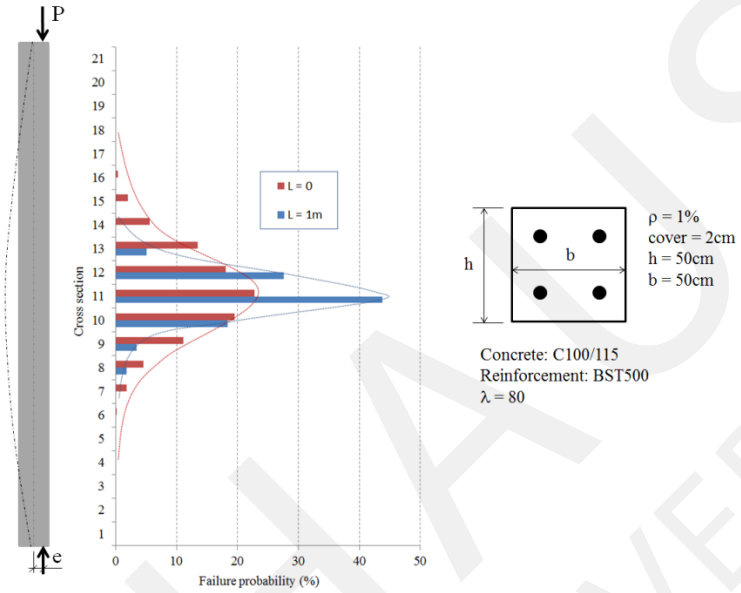

Figure 4: Failure probability of sections along the column

5.2.3 Reliability of columns

Fib. 5 shows results of reliability analysis of two columns made of HSC and UHPC with slenderness ratio 80. The analysis is carried out for two cases of consideration: with and without random field. In general, calculated safety index is small by small relative eccentricity and increases to the maximal value at the eccentricity of about 0,5h. From this point, the safety index is relative unchanged independent on the eccentricity (see Fig. 5). The reason for that is by small eccentricity the scattering of resistance is large. Column collapses due to concrete failure in compression and due to buckling. With larger scattering than that of concrete strength, the elasticity modulus has a very large influence on the reliability of the column (see Fig. 6a). By large eccentricity where a bending failure is dominated, only tensile strength of concrete has big sensitivity factor on the resistance side (see Fig. 6b).

For HSC columns, the considering of random field gives a significant larger calculated ?-value than in the simplified case (see Fig. 5a), while by UHPC columns both results are nearly the same (see Fig. 5b). This is resulted from the different scattering of HSC and UHPC parameters. In this study, the elastic modulus of normal concrete hat a variance coefficient of 0.15 while by UHPC (M2Q) this value is only 0.10. This means, by small variability of material properties, the influence of random filed on the structural reliability can be neglected.

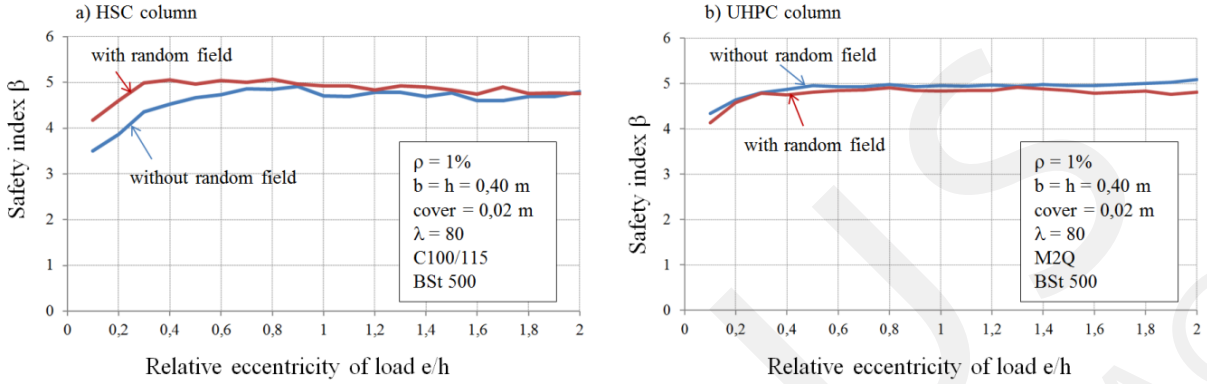

Figure 5: Reliability of columns depending on eccentricity of load

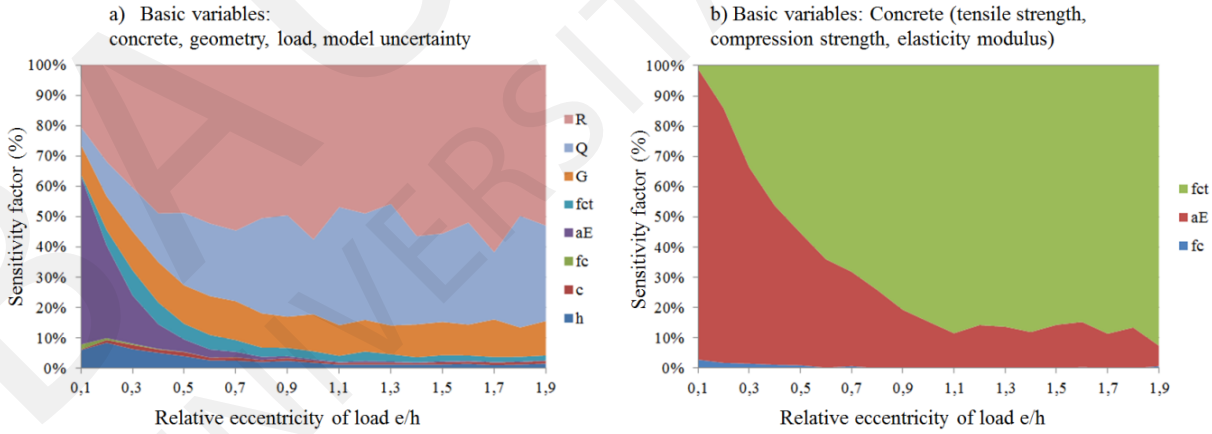

Figure 6: Sensitivity factors by HSC column made of C100/115

6 Conclusions

A probabilistic modelling and reliability analysis of load bearing capacity of concrete columns made of high strength concrete and ultra-high strength concrete were presented. In this study, the random fields of concrete properties were especially considered. Not only spatial correla- tions of each random field but also the cross correlations among random variables were taken into account. Concrete properties were modelled as homogeneous Gaussian random fields. The nonlinear structural analysis was carried out by using finite frame elements with nonlinear ma- terial model for concrete and consideration of theory 2^{th} order for the whole column.

The Monte Carlo method was employed to obtain failure probability distribution of column along its length. For reliability analysis of reinforced concrete columns different methods in- cluding the importance sampling method and the response surface method were used. Ob- tained results were compared to show the efficiencies of the analysis methods. Although a simple function was used to describe structural response surface, the response surface method shows in this case of reinforced concrete columns the most calculation efficiency.

Comparison results of full and simplified reliability analyses of column made of HSC and UHPC have shown that the spatial variations of concrete properties should be taken into ac- count to get a realistic estimation of structural reliability. If quality of concrete is well con- trolled, such as in the case of UHPC, the influence of spatial variation on reliability of columns is reduced. In this case, a simplified reliability analysis could be used.

Additionally, the correlation length has also a significant effect on reliability of the columns. Due to lacking of experimental results, the analysis in this study was carried out with an as- sumption of L = 3m. In the next step, a full reliability analysis of UHPC columns using exper- imental results of spatial variation of UHPC properties is carried out. Based on the obtained results, further suggestions for design can be made.

References

[1] C Bucher. *Computational Analysis of Randomness in Structural Mechanics,*. Taylor and Francis Group, London, UK., 2009.

[2] Somodíková M.; Dolezel J.; Lehký D. *Probabilistic load bearing capacity assess- ment of posttensioned composite bridge*. Proceedings of the 11th International Probabilistic Workshop, Brno, 2013.

[3] José Milton de Araújo. Probabilistic analysis of reinforced concrete columns. *Advances in Engineering Software, Elsevier*, pages 871–879, 2002.

[4] E. Erdem. *Probabilistisch basierte Auslegung stahlfasermodifizierter Betonbauteile auf experimenteller Grundlage, DIssertation*. PhD thesis, Ruhr-Universität Bochum, 2002.

[5] M. Heimann. *Tragwerkszuverlässigkeit hochbeanspruchter Druckglieder aus ultrahochfestem Beton*. PhD thesis, TU Darmstadt, 2013.

[6] P. Der Kiureghian A. Liu. Multivariate distribution models with prescribed marginals and covariances. *Probab Eng Mech*, 1:105–111, 1986.

[7] JCSS Probabilistic Model Code Part 3 Resistance Models. Joint committee of structural safety, 2001.

[8] U. Quast. *Rechenansätze in Form einer Spannungsdehnungsbeziehung für das Mitwirken des Betons in der gerissenen Zugzone von Stahlbetonquerschnitten.* Institut für Baustoffe, Massivbau und Brandschutz der Technische Universität Braunschweig, 1980.

[9] N.L. Tran. *Berechnungsmodell zur vereinfachten Abschätzung des Ermüdungsverhaltens von Federplatten bei Fertigträgerbrücken, Dissertation.* PhD thesis, TU Darmstadt, 2011.

[10] M. Vorechovský. Simulation of simply cross correlated random fields by series expansion methods. *Structural Safety 30, Elsevier*, pages 337–363, 2008.

Reliability-based equivalent ISO 834 fire duration for the Eurocode parametric fire curve and comparison with the EN 1991-1-2 equivalency rules

R. Van Coile, R. Caspeele, L. Taerwe

Ghent University,
Department of Structural Engineering,
Ghent, Belgium
Ruben.VanCoile@UGent.be

Abstract. The implications of performance based design for structural fire safety are investigated by comparing the reliability of concrete slabs exposed to both standard fires and natural fires. Through this comparison an equivalent standard fire duration is defined, which is found to be more severe than the equivalency rules given in Eurocode.

1 Introduction

Two opposing trends have been observed with respect to structural fire safety. On the one hand large disasters and fire accidents have been strengthening the perception that structural fire safety is important, while on the other hand deviations from severe standard fire curves towards less severe natural fires have been promoted by the increasingly popular concept of performance based design.

In the performance based design concept, design solutions are deemed acceptable when performance requirements are met. Defining these requirements is however very difficult and therefore equivalency with the old prescriptive designs is often a requirement in countries which have not yet adopted a fully performance based approach. For structural fire safety this implies a safety level during exposure to natural fires which is at least as high as the safety level during exposure to the standard fire curve of the prescriptive design concept. This does however introduce many practical difficulties as the safety level obtained with the prescriptive rules is not explicitly known and reliability calculations can be both too time-consuming and too complex for applications by practitioners. Therefore, the reliability during exposure to both standard and natural fires has to be assessed and a method for equivalency has to be developed. This equivalency should allow to relate a natural fire to a standard fire duration, while meeting the criterion of equivalent safety. As a first step the applicability of the equivalency formula given in the Eurocode is evaluated.

2 Fire curves according to the Eurocode and the equivalent standard fire concept

For the European Union, the ISO 834 fire is the standard fire curve applied in prescriptive design rules for structural fire safety [2]. However, EN 1991-1-2 also provides a temperature-time curve for natural fires in Annex A, and even an equivalency formula

relating natural fires to an equivalent ISO 834 standard fire duration in Annex F. The natural fire curve is a function of the fire load density q representing the total energy which can be released by combustion, the opening factor O representing the amount of ventilation, and the geometry of the compartment. The ISO 834 standard fire and a number of natural fires are visualized in Figure 1, and in Figure 2 the equivalent standard fire duration according to the Eurocode formula of Annex F is visualized. For both graphs and in the following sections a square room was assumed, since this is the most severe situation for a given floor area A_f, and concrete thermal properties were used.

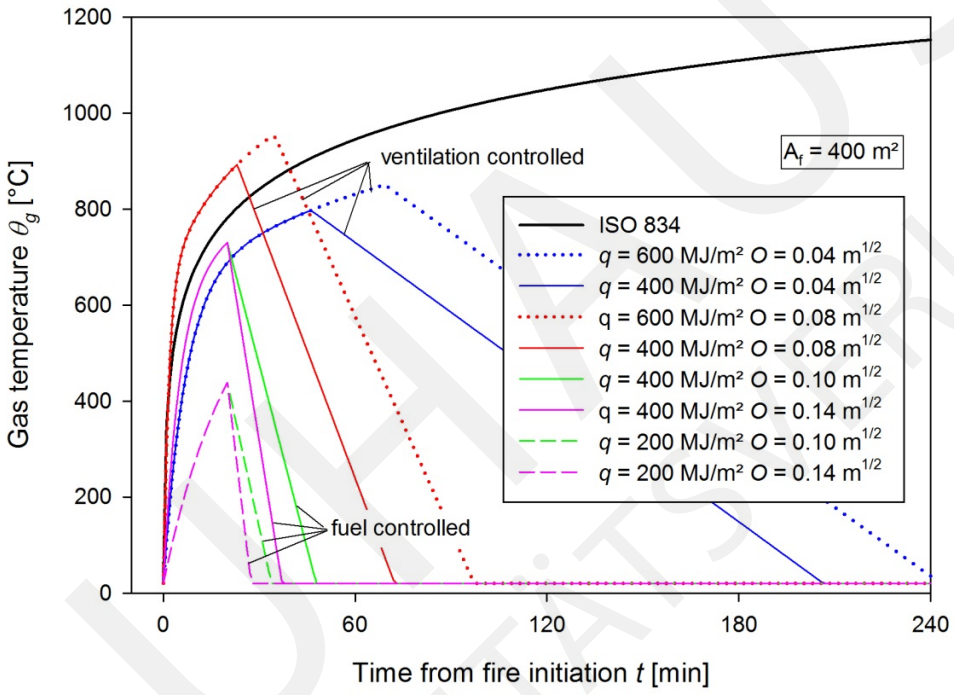

Figure 1: ISO 834 standard fire and EN 1991-1-2 natural fire curve for different q and O ($A_f = 400m^2$, $H = 3m$).

The fire curves in Figure 1 indicate how for a ventilation controlled fire an increase in the opening factor O results in a faster and higher fire growth, but also in an earlier start of the cooling phase. This effect of increasing O is valid until the fire becomes fuel controlled. Once the fire is fuel controlled, O only governs the steepness of the decay phase. The fire load density q on the other hand positively influences the peak of the fire curve. Furthermore, the ratio of q to O governs whether the fire is fuel or ventilation controlled through a linear limit criterion [2].

For a given room height H and averaged opening height h_{eq} the equivalency curves in Figure 2 shift only a little when changing the compartment area A_f (except for very small compartments $< 100m^2$). As $t_{ISO,eq}$ is a linear function of the fire load density, linear interpolation can be used to find $t_{ISO,eq}$ for intermediate values of q.

The equivalent standard fire allows to apply known test results for standard fire situations to a wide range of natural fires and to determine which construction products can be

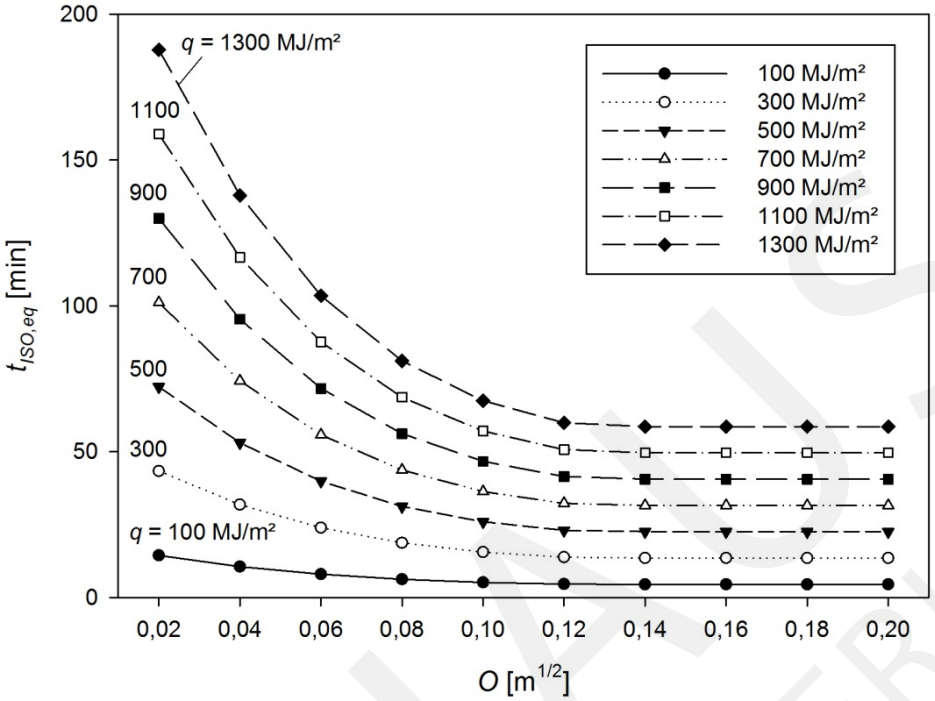

Figure 2: Equivalent ISO 834 standard fire duration $t_{ISO,eq}$ according to EN 1991-1-2, as a function of q and O ($A_f = 400m^2$, $H = 3m$, $h_{eq} = 1.7m$).

applied in the design given their structural fire resistance classification (R-value) which relates to the standard fire. As such it is a very practical concept. However, it is a priori unclear whether the Eurocode formula is conservative from the perspective of structural safety.

3 Reliability of concrete slabs exposed to natural fires and reliability-based equivalent standard fire duration

As mentioned earlier, an equivalent solution should provide at least the same safety level as provided through the prescriptive rules. Therefore, the reliability of concrete slabs exposed to both the standard fire and natural fires is investigated using the calculation concepts described in [6] and using a mixed-lognormal approximation for the bending moment capacity, as derived in [5]. The investigated slab configuration is given in Table 1.

The characteristic values of the bending moment induced by the permanent load and the imposed load (i.e. M_{Gk} and M_{Qk}) are defined through equations 1 and 2. This calculation concept allows to evaluate the reliability of individual structural elements, without requiring additional assumptions with respect to the current and future use of

Property	Symbol	Distribution	μ	σ
concrete compressive strength at $20°C$ [MPa] ($f_{ck} = 42MPa$)	$f_c, 20$	Lognormal	60	9
reinforcement yield stress at $20°C$ [MPa] ($f_{yk} = 500MPa$)	$f_y, 20$	Lognormal	581.4	40.7
slab thickness [mm]	h	Deterministic	200	-
slab unit width [mm]	b	Deterministic	1000	-
horizontal reinforcement axis distance [mm]	s	Deterministic	100	-
concrete cover [mm]	c	Beta	35	5
reinforcement area [mm^2]	A_s	Normal	$A_{s,nom}$	$0.02A_{s,nom}$
bending moment induced by the permanent load [kNm]	M_G	Normal	M_{Gk}	$0.1M_{Gk}$
bending moment induced by the imposed load [kNm]	M_Q	Gumbel (5-year reference period)	$0.2M_Q$	$0.22M_{Qk}$
model uncertainty for the resistance effect [-]	K_R	Lognormal	1.1	0.11
model uncertainty for the load effect [-]	K_E	Lognormal	1.0	0.10

Table 1: Characteristics of the example slab configuration: property description, symbol, stochastic distribution, mean value μ and standard deviation σ.

the structure.

$$\chi = \frac{q_k}{q_k + g_k} = \frac{M_{Qk}}{M_{Qk} + M_{Gk}} \tag{1}$$

$$M_{Gk} = \frac{M_{Rd}}{max\left\{\left(\gamma_G + \psi_0\gamma_Q\frac{\chi}{1-\chi}\right); \left(\xi\gamma_G + \gamma_Q\frac{\chi}{1-\chi}\right)\right\}} \tag{2}$$

with χ the load ratio, g_k the characteristic value of the permanent load effect, q_k the characteristic value of the imposed load effect, M_{Gk} the bending moment induced by the characteristic value of the permanent load, M_{Qk} the bending moment induced by the characteristic value of the variable load, γ_G the partial factor for the permanent load, ξ a reduction factor for unfavourable permanent loads, γ_Q the partial factor for the variable load, and ψ_0 a combination factor.

The reliability index during fire $\beta_{fi,t}$ is calculated by a FORM analysis for the limit state function 3, for a load ratio χ of 0.5 and the stochastic models of Table 1, with $M_{R,fi,t}$ the bending moment capacity during fire, as derived in [5]. Equation 2 is evaluated with $\gamma_G = 1.35$, $\gamma_Q = 1.5$ and $\psi_0 = 0.7$ (i.e. for residential areas, office areas, congregation areas shopping areas and traffic areas, [1]). Results for different combinations of O and q are visualized in Figure 3 and Figure 4 for $A_f = 400m^2$ and $H = 3m$.

$$Z = K_R M_{R,fi,t} - K_E(M_G + M_Q) \tag{3}$$

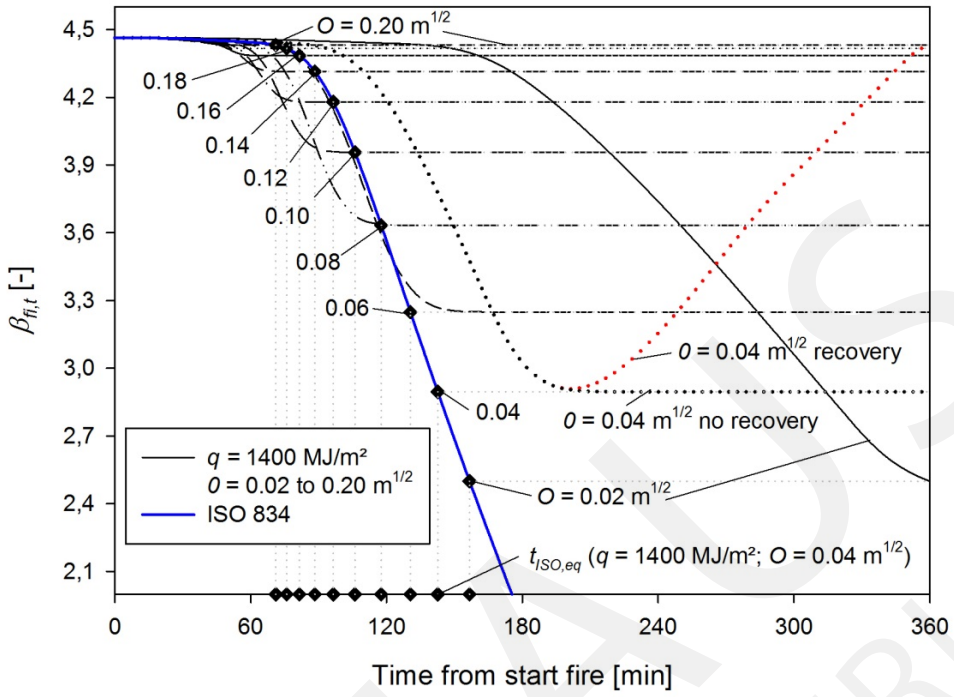

Figure 3: Reliability $\beta_{fi,t}$ for the concrete slab of Table 1 exposed to the ISO 834 standard fire curve and the EN 1991-1-2 parametric fire curve ($q = 1400\ MJ/m^2$, O every $0.02m^{1/2}$ from 0.02 to $0.20m^{1/2}$).

In both Figure 3 and Figure 4, an alternative result for the combination $q = 1400MJ/m^2$ and $O = 0.04m^{1/2}$ is visualized which rises again after approximately 200 minutes. This alternative represents the reliability obtained when considering recovery of the reinforcement strength properties in the cooling phase. Although a strength recovery after fire exposure has been described in literature [4], it is reasonable to assume that this strength recovery is not instantaneous. More importantly, if immediate strength recovery is taken into account, the minimum value of $\beta_{fi,t}$ will be overestimated due to the stochastic nature of amongst others the concrete cover.

The obtained minimum value of the reliability index is further denoted as β_{min}, and defines a reliability-based equivalent ISO 834 standard fire duration as the time of exposure to the ISO fire for which the same reliability is found, i.e. β_{min} is projected on the reliability curve associated with exposure to the ISO 834 fire. These projections are visualized in Figure 3 and Figure 4 by the diamond-shaped dots and define an equivalent standard fire duration $t_{ISO,eq}$ through a second projection on the (horizontal) time axis. An overview of the results is given in Figure 5.

4 Comparison with Eurocode equivalency formula

As visualized above in Figure 2, EN 1992-1-2 gives a deterministic formula to relate an equivalent ISO 834 fire duration to a given parametric fire. The equivalent standard fire

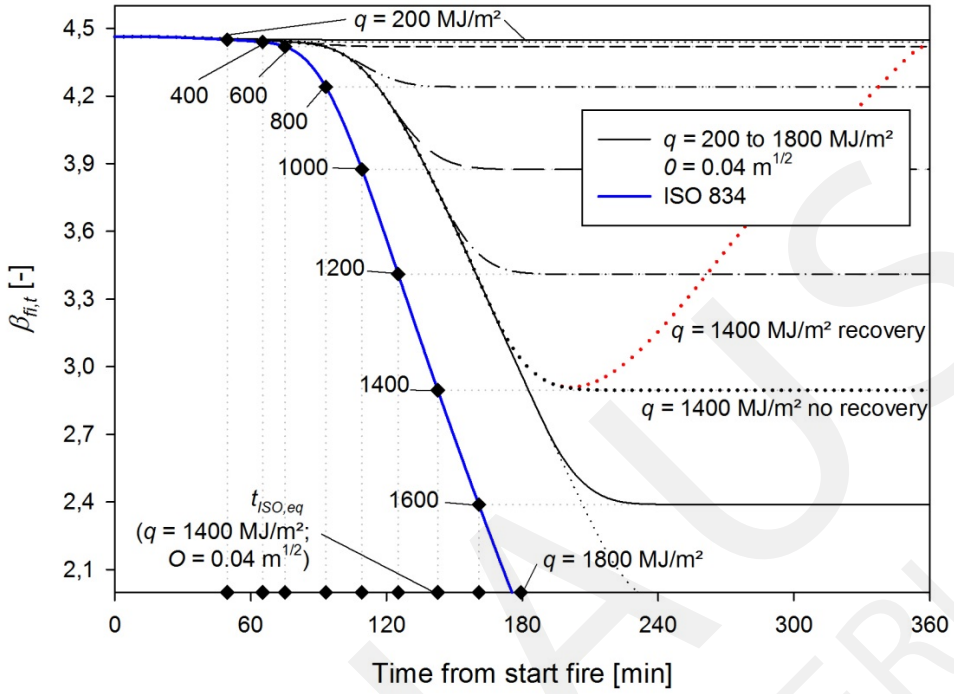

Figure 4: Reliability $\beta_{fi,t}$ for the concrete slab of Table 1 exposed to the ISO 834 standard fire curve and the EN 1991-1-2 parametric fire curve (q = every $200 MJ/m^2$ from 200 to $1800 MJ/m^2$, $O = 0.04 m^{1/2}$).

duration $t_{ISO,eq}$ according to EN 1991-1-2 (Figure 2) is found to be non-conservative for most combinations of q and O, as visualized in Figure 6 for a limited dataset. Only when both the opening factor O is small and the fire load q is large, the Eurocode formula can be considered conservative.

5 Influence of a larger standard deviation for the concrete cover

While the equivalency formula of EN 1991-1-2 is deterministic, the reliability-based approach is capable to take into account the effect of increased or reduced uncertainty with respect to the basic variables. As the influence of the standard deviation σ_c of the concrete cover has been stressed for example in [6], its effect on $t_{ISO,eq}$ is investigated.

If a larger standard deviation of the concrete cover is for example witnessed in an existing structure, this larger σ_c should be taken into account when determining the reliability $\beta_{fi,t}$ during exposure to the parametric fire curve. However, it can be a priori less obvious whether this larger standard deviation of the concrete cover should also be considered when determining the reference curve for exposure to the ISO 834 standard fire curve. If the larger σ_c is considered for the reference curve as well, both will give lower reliabili-

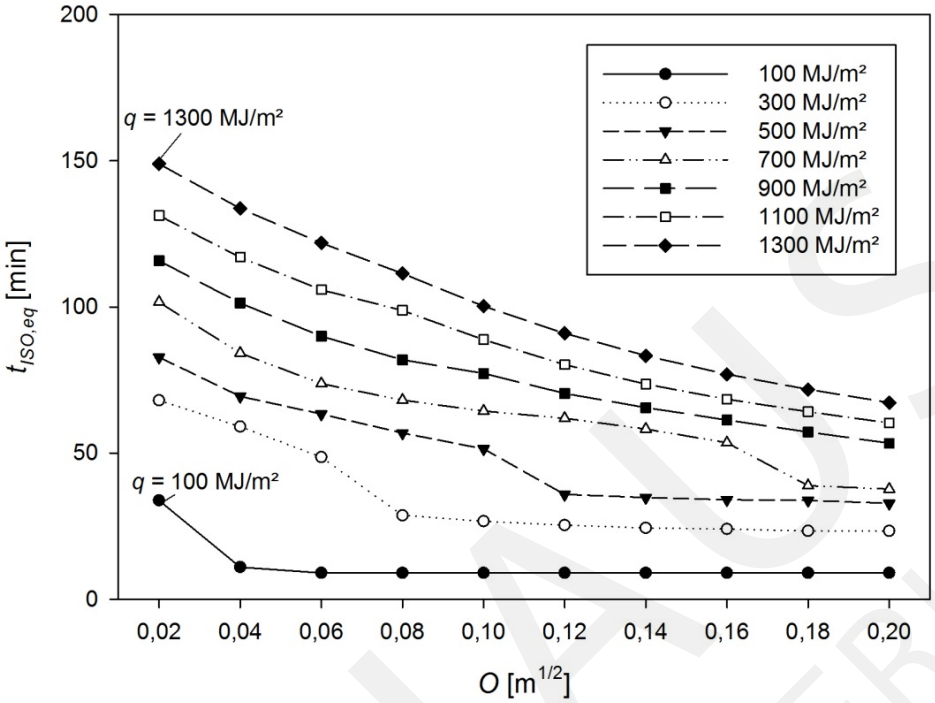

Figure 5: Reliability-based equivalent ISO 834 standard fire duration $t_{ISO,eq}$, as a function of q and O ($A_f = 400m^2$, $H = 3m$, $h_{eq} = 1.7m$, slab characteristics as given in Table 1).

ties, and therefore the ISO 834 fire duration $t_{ISO,eq}$ for which β_{min} is obtained will not differ much from the result in case of a common standard deviation σ_c. If this $t_{ISO,eq}$ is subsequently used to prove that the slab has adequate fire resistance considering the tabulated requirements in EN 1992-1-2 [3] for the nominal concrete cover (mean value), a lower reliability will be accepted than (implicitly) foreseen by the Eurocode (considering a common value for σ_c). In this case the reference curve should therefore be calculated with common uncertainties for the basic variables. However, if the increased uncertainty for the concrete cover would be incorporated in a second phase, for example by provisions in the Eurocode related to the ISO 834 standard fire, the increased concrete cover standard deviation should be considered for the reference reliability curve as well.

As no guidelines with respect to the standard deviation of the concrete cover are given in EN 1992-1-2, the first option is chosen in which the reference ISO 834 reliability is determined for a standard slab (with standard probability density functions for the basic parameters and associated common value for σ_c). These considerations are important as the increased σ_c results in a lower reliability (see [6]), which should be taken into account in a performance based calculation, for example by a larger $t_{ISO,eq}$ as determined in Figure 7 for the slab configuration of Table 1 where $\sigma_c = 10mm$.

As can be expected, Figure 7 indicates that the Eurocode equivalency formula is clearly not conservative in case of an increased standard deviation of the concrete cover. Conse-

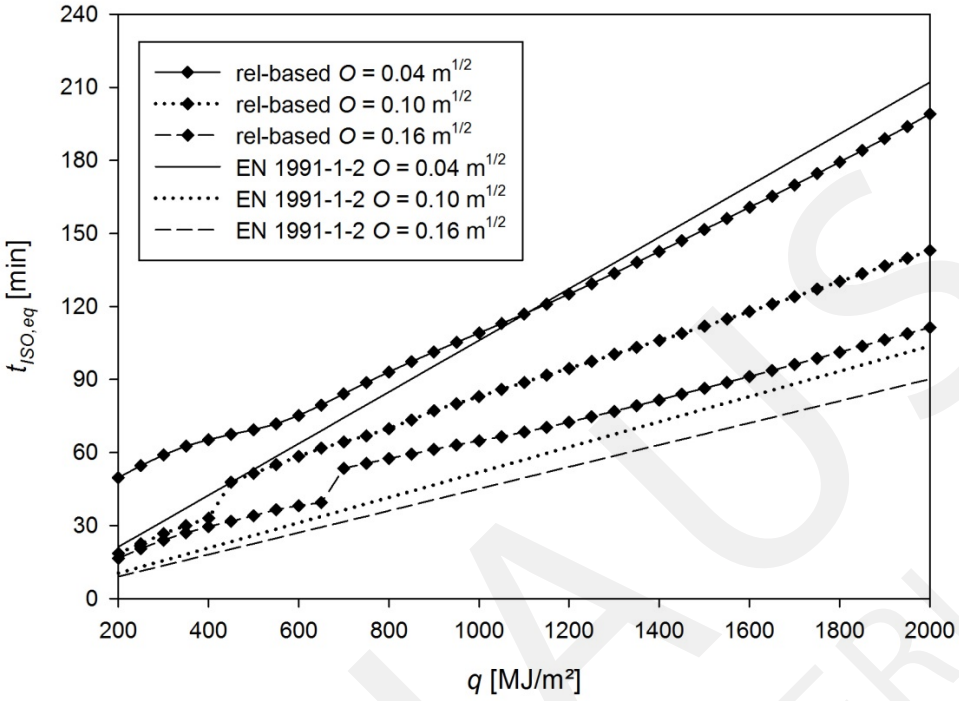

Figure 6: Comparison of $t_{ISO,eq}$ according to EN 1991-1-2, and according to the concept of equivalent reliability (for the results of Figure 5).

quently, it is in this situation not acceptable to use the Eurocode equivalency formula to determine the $t_{ISO,eq}$ to be applied in conjunction with the tabulated data of EN 1992-1-2 [3] to determine the required nominal concrete cover. However, no results have been determined for smaller fire load densities as the configuration with $\sigma_c = 10mm$ has a slightly smaller reliability at the start of the fire than when $\sigma_c = 5mm$. Consequently, for less severe fires, this small deviation affects the results. For more severe fires, the reliability-based approach as described above can be applied.

6 Conclusions

The reliability of concrete slabs exposed to fire is evaluated for both the ISO 834 standard fire and the parametric fire curves of EN 1991-1-2. Applying a criterion of equal performance in terms of reliability index, the minimum reliability obtained during exposure to a parametric fire is unambiguously related to an equivalent ISO 834 standard fire duration. These equivalent fire durations are used to evaluate the equivalency rule given in EN 1991-1-2. The Eurocode equivalency is found to be non-conservative, except when both small opening factors and large fire load densities occur together. The non-conservative nature of the Eurocode equivalency formula is even more pronounced in case of an increased standard deviation of the concrete cover.

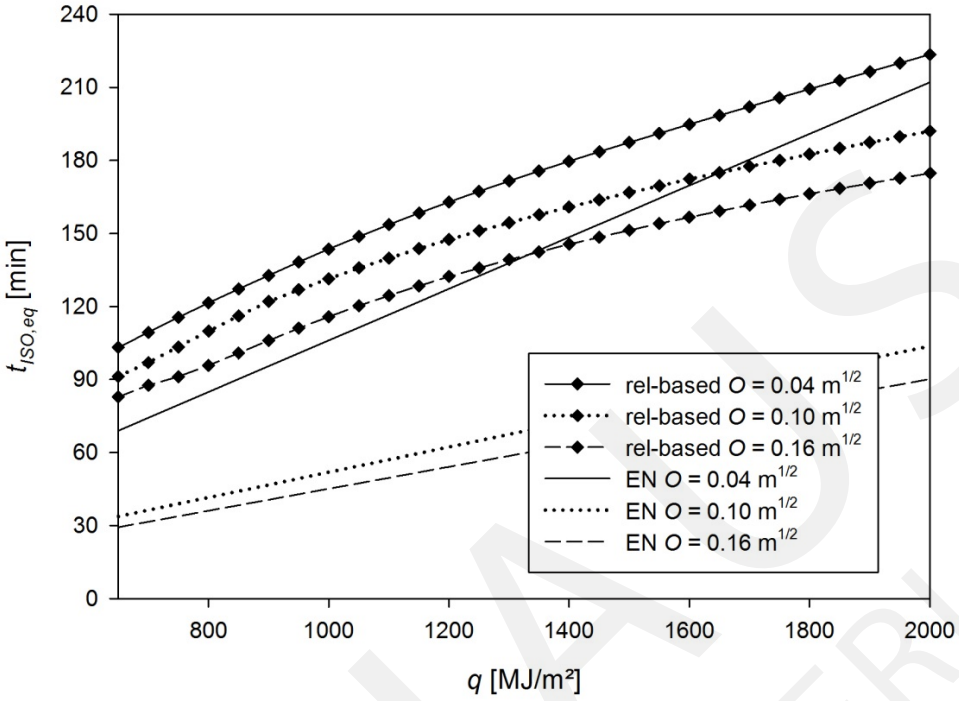

Figure 7: Comparison of $t_{ISO,eq}$ according to EN 1991-1-2, and according to the concept of equivalent reliability ($\sigma_c = 10mm$ for $\beta_{fi,t}$ of the parametric fire).

References

[1] CEN EN 1990. *Basis of structural design.* European Standard, 2002.

[2] CEN EN 1991-1-2:. *Actions on structures – Part 1–2: General actions – Actions on structures exposed to fire.* European Standard, 2002.

[3] CEN EN 1992-1-2. *Design of concrete structures: Part 1–2: General rules – Structural fire design.* European Standard, 2004.

[4] L. Taerwe, P. Bamonte, K. Both, J.-F. Denoël, U. Diederichs, J.-C. Dotreppe, R. Felicetti, J. Fellinger, J.M. Franssen, P.G. Gambarova, N.P. Hoj, T. Lennon, A. Meda, Y. Msaad, J. Ozbolt, G. Periskic, P. Riva, F. Robert, and A. Van Acker. *Fire Design of Concrete Structures: Structural Behaviour and Assessment: State-of-art Report*, volume 46. FIB-Féd. Int. du Béton, 2008.

[5] R Van Coile, R Caspeele, and L Taerwe. The mixed lognormal distribution for a more precise assessment of the reliability of concrete slabs exposed to fire. Amsterdam (30/09-2/10), 2013.

[6] R. Van Coile, R. Caspeele, and L. Taerwe. Reliability-based evaluation of the inherent safety presumptions in common fire safety design. *Engineering Structures*, 77:181–192, 2014.

Reliability of thin-walled single screwed connections in cold-formed steel against tilt-and-bearing failure

Mr. R van Wyk, Dr. C Viljoen

Department of Civil Engineering,
University of Stellenbosch,
2014, South Africa

Abstract. The South African National Standard for the structural use of cold-formed steel [9] provides design provisions for screwed connections. Through reliability analyses, including assessment of the model factor through experimental work, the reliability of such connections in tilt-and bearing is established. Model factors with mean values close to one and small standard deviations confirm the adequacy of the prediction model. High reliability index values confirm a conservative design formulation across a range of plate thicknesses and –strengths.

1 Introduction

The South African (SA) housing industry has, for many years, primarily been dealing with masonry and timber as the go-to building materials for wall- and roof construction respectively. In 2006, light, thin and economical Cold-Formed Steel (CFS) was introduced to the SA market as an alternative. Shaped and formed at ambient temperature, CFS members originate from flat steel sheets. Used in the primary and secondary framing of walls, floors and roofing systems, the method of connecting two or more CFS members depends on the connection purpose. Where bolts are generally used for anchorage and bolting to thicker members with a high load demand, screws are used for a lower load demand and thinner members [1].

The first specification for the design of light gage steel structural members was published by the AISI, already in the 1940's. It was updated regularly and the 1968 edition of the American Specifications formed the basis for the first Australian standard (AS 1538) in 1974. The South-African national standard for the structural use of CFS structures [9] was in turn adopted from the AZ/NZS 4600:2500 with various national modifications made regarding the geometry and material properties of CFS members [4]. SANS 10162-2 provides capacity prediction models for screwed connections which are designed against shear failure of the screw(s), section tear-out, net section failure and tilt-and-bearing failure ([1]; [3]).

2 Connections in tilt-and bearing

Previous studies [7] showed that, when connecting relatively thin members, connection capacity is typically determined by the tilt-and-bearing type failure mode. This failure mode is caused by the extreme thinness of the connected members that induces an eccentric shear load on the screw, causing it to tilt. Equation 1 gives the nominal capacity

for screwed connections with equally thick members expected to fail in screw tilting and hole bearing, with tilting the dominant contributor towards failure, according to SANS 10162-2. The design capacity V_d is obtained by multiplying the nominal capacity V_b by a capacity reduction factor of $\phi = 0.5$.

$$V_b = 4.2\sqrt{t^3 d_f f_u} \tag{1}$$

where t is the thickness of the connected members, d_f the nominal screw diameter and f_u the ultimate tensile strength of the connected members.

3 Reliability

3.1 Background

The reliability theory is typically used to assess the adequacy of structural performance by accounting for variability and/or uncertainties in the parameters that influence performance in order to quantify its probability of failure. Probabilistic design methods are based on the condition that the reliability index of a structure β should exceed the specified target reliability β_t. The reliability index β is directly related to the probability of failure and is defined as the negative value of a standardised random variable corresponding to the probability of failure, i.e.$\beta = -\Phi_N^{-1}(p_f)$.

If structural failure can be defined as a structure not being able to resist the applied actions, the performance function or limit state can be expressed as $G = R - E$, where the resistance R and load E is considered as random variables and failure is assumed to occur when $E > R$, i.e. when $G < 0$ [5]. The probability of failure $p_f = p(G < 0)$ may be assessed using reliability methods such as the First Order Reliability Method (FORM).

Variability of parameters that influence performance may be due to natural randomness of materials and loads or to uncertainty, including uncertainty contained in prediction models due to simplifications, unclear definitions or inadequate formulations. Such model uncertainties [6] may be quantified by comparisons with other more involved models that represent a closer representation of reality or (preferably) by comparison with collected data from experimental work.

EN 1990 allows for separate consideration of resistance reliability and that of load effect. To this end sensitivity factors α_R and α_E are provided to quantify their respective contributions to overall reliability, so that the target resistance reliability index becomes $\beta_{t,R} = \alpha_R \beta_t = 0,8\beta_t$.

3.2 Formulation for tilt-and bearing resistance

Considering only the provisions for resistance, the structure is assumed safe if the actual connection capacity V_{actual} exceed the design capacity. The performance function is thus defined as

$$G = V_{actual} - V_d \tag{2}$$

The design capacity V_d is computed deterministically based on the design provisions of SANS 10160-2. Equation 1 may be used as an unbiased prediction model for connection capacity if nominal values are replaced with unbiased estimates. A model factor θ accounts for the uncertainties associated to the prediction model, so that

$$V_{actual} = \theta_{(\mu,\sigma)} * V_{predicated} \tag{3}$$

The unbiased estimate $V_{predicated}$ may be a deterministic value based on measured parameter values, as was used for the model factor estimation in Section 3.3.1 or may be probabilistic, as obtained through probabilistic descriptions of the material and geometric parameters. In the latter case, Equation 2 becomes

$$G = \theta_{\mu,\sigma} * 4.2\sqrt{t^3_{\mu,\sigma} d_{f,(\mu,\sigma)}} f_{u,(\mu,\sigma)-V_d} \tag{4}$$

3.3 Probabilistic parameter description

3.3.1 Model factor

The model factor is defined as the ratio of actual connection capacity over the unbiased predicted capacity.

$$\theta = \frac{V_{actual}}{V_{predicted}} \tag{5}$$

The actual connection capacity is determined by testing, with the corresponding unbiased prediction based on Equation 1, but calculated using measured parameter values instead of nominal (biased) values.

To this end experimental work was necessary: Measurements were made of the plate thicknesses and screw diameters and tensile tests were performed to obtain the tensile strength used in the capacity predictions. In addition, connection capacity tests were performed to obtain the actual connection capacities. The tests are discussed in more detail in Section 4.

Testing of 132 screwed connections resulted in the same number of model factor estimates, allowing the model factor to be expressed as a random variable best approximated by a Normal distribution, and with an average and standard deviation of 1.05 and 0.055 respectively.

3.3.2 Tensile strength, thickness and screw diameter

The uncertainties associated with the material strength- and geometric parameters were accounted for by modelling each with an appropriate probabilistic distribution model, based on tensile tests and physical measurements which are discussed in Section 4.2. As advised by expert literature ([5]; [2]) the geometric parameters (thickness and screw diameter) were modelled with normal distributions and the tensile strength with a log-normal distribution. The statistical moments for connections made of 550 MPa steel with plate thickness 0.8 mm and a nominal screw diameter of 4.8 mm are provided in Table 1, including the associated model factor values.

Variable	Average μ	Standard deviation σ	Coefficient of variation (%)	Distribution
θ	1.050	0.055	5.2	Normal
$t(mm)$	0.765	0.007	0.92	Normal
$d_f(mm)$	4.790	0.049	1.0	Normal
f_{MPa}	657.7	70.49	10.7	Log-normal

Table 1: Statistical properties of input parameters

3.4 Target reliability measure

In South Africa the target reliability index for connections is $\beta_t = 4,5$ (SABS 2011).Correspondingly, the target resistance reliability is $\beta_{t,R} = 0,8 * 4,5 = 3,6$ [5].

3.5 Reliability analysis

A reliability analysis was performed for the tilt-and bearing resistance of a typical connection made of 550 MPa steel with plate thickness 0.8 mm and a nominal screw diameter of 4.8 mm designed according to SANS 10162-2. Equations 2 to 4 and the statistical properties in Table 1 formed the basis of the FORM analysis.

The computed resistance reliability index β_R must exceed the specified target value of $\beta_{t,R} = 3.6$ for the connection to be considered sufficiently reliable.
FORM sensitivity factors indicate the relative contribution of probabilistically described parameters to the computed reliability. The analysis results are discussed in Section 5.

4 Experimental work and measurements

CFS sections with a sheet thickness of 0.8 mm and steel grade of 550 MPa is the most frequently used in South Africa and thus primarily considered in the current experimental investigation. This investigation included the capacity testing of connections, tensile strength tests and geometrical measurements, with the purpose of determining the model factors. All tests were executed according to standardised procedures as set out in respective national standards. SANS 4998 details the tensile tests and Appendix F of SANS 10162-2 the connection capacity tests.

4.1 Connection capacity tests

The connection specimen consisted of two equally sized flat steel strips joined by lapping the ends and fastened through the centre of the lapped area with a 4.8 mm diameter self-tapping screw. The dimensions of the specimen are shown in Figure 1.

A uniform shear load that passed through the centroid of the connection was applied using a Zwick/250 test machine with a hydraulic clamping system and end plates. This

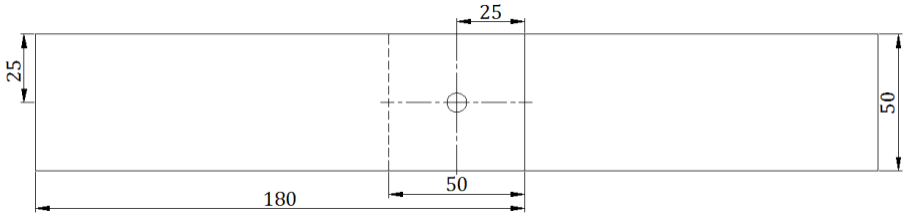

Figure 1: Connection test specimen

machine's lower platform moves up or down relative to the upper platform, applying either a tensile or compression force. The tensile (connection in shear) force was applied at a strain rate of 0.03 mm per second and the connection capacity was taken as the highest force reached prior to a 6mm displacement.

The failure mode observed for all 132 screwed specimens was a combination of screw-tilting and hole-bearing with the former the dominant contributor. Figure 2 illustrates the observed failure mode. As the shear force was applied, the steel strips underwent some bearing, but as the force increased, the screw started to tilt and eventually started to pull out. The pull out was caused by the force not being pure shear anymore, but rather a combination of shear and tension. It is important to note that the ultimate force was reached before any pulling out occurred.

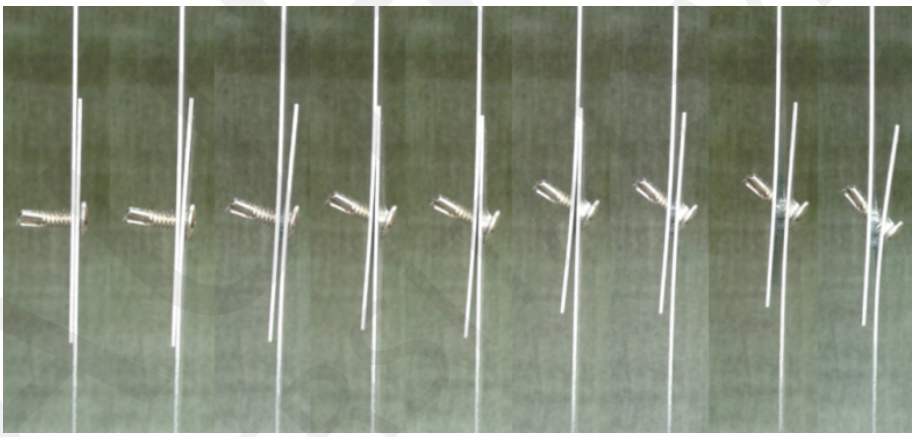

Figure 2: Observed connection failure

4.2 Tensile tests and measurements

The tensile steel strength, nominal screw diameter and the plate thickness had to be obtained for each specimen, in order to calculate an unbiased estimate of the connection capacity on which to base the model factor calculation (Section 3.3.1). Both the screw diameter and thickness were physically measured for each test specimen, before testing. As it was impossible to measure the tensile strength of the exact connection specimen that still had to be tested for its capacity, the tensile tests were performed on typical dog-bone shaped tensile test specimen.

Unfortunately, for practical reasons and due to supplier constraints, all specimens were cut from only four different steel coils. Variability of strength and thickness within a single coil was very low, with coefficients of variation typically less than 1.0%. The average of three tensile test results per coil was found to adequately represent the coil strength. Variability of tensile strength thus stem mainly from differences in steel strength from coil to coil.

Average values from each of the coils, of the thickness and tensile strength respectively, were used as four sample points to calculate representative averages and standard deviations for the overall thickness and tensile strength random variables of 0.8 mm, 550 MPa steel. The obtained values are reported in Table 1 and show acceptable agreement with expected ranges of 1 to 4% and 7 to 10% respectively for the coefficients of variation from literature [5].

5 Reliability results and discussion

A reliability analysis was performed for the tilt-and bearing resistance of a typical connection made of 550 MPa steel with plate thickness 0.8 mm and a nominal screw diameter of 4.8 mm designed according to SANS 10162-2. Equations 2 to 4 and the statistical properties in Table 1 formed the basis of the FORM analysis. Table 2 presents the results of the analysis.

Reliability Index (β): 8.3		Failure probability: $4.2e^{-17}$
Variable	Design value μ	Sensitivity factor
Tensile strength	309 MPa	-0.84
Model factor	0.81	-0.53
Screw diameter	4.77 mm	-0.04
Base metal thickness	0.76 mm	-0.11

Table 2: Reliability analysis results

The computed reliability index of $\beta = 8.3$ far exceed the target value of $\beta_{t,R} = 3.6$, which implies that the design formulation for this typical screw connection according to the SANS 10162-2 is highly conservative.

During design, a capacity reduction factor of $\phi = 0.5$ is applied to the nominal connection capacity. The application of this factor was identified as the primary reason for the significant conservatism. The influence of this factor is made clear in Figure 3 where the tested capacities are plotted together with the nominal and design capacities. The range denoted as (a) represents the conservative bias achieved through the use of nominal values and other conservative limitations where (b) is an additional conservative bias achieved by applying the capacity reduction factor.

The sensitivity factors show that, as far as the relative contributions to reliability by probabilistically described variables go, the tensile strength and model factor dominate. Theoretically plate thickness and screw diameter may be treated deterministically in further investigations, without introducing significant error in the reliability estimates.

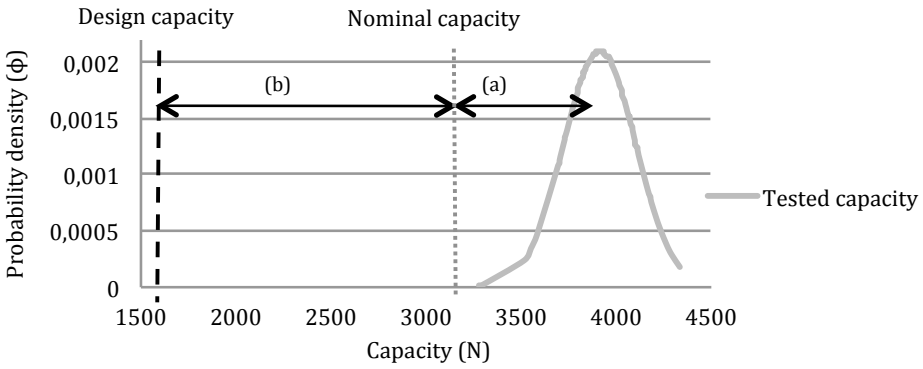

Figure 3: Influence of capacity reduction factor

Thus far, only the analysis of the 0.8mm, 550MPa connection configuration was discussed. However, connections with a wider range of steel thicknesses (0.58mm and 1.0 mm) and strengths (230 MPa and 300 MPa) were considered in a similar way. Table 3 reports these results.

Configuration	Model Factor (θ_μ)	Reliability Index (β)
0.58 mm, 550 MPa	1.01	9.15
1.0 mm, 300 MPa	1.2	8.4
0.8 mm, 230 MPa	1.25	8.84

Table 3: Reliability indices and average model factors of other configurations

The computed reliability indices confirm the highly conservative nature of SANS 10162-2 design provisions for typical screw connections in tilt-and-bearing.

The model factors obtained based on the ratios of experimental- over predicted capacities showed some interesting trends. Model factors increased with increased plate thickness and reduced with increased steel strength, as shown in Figure 4. Standard deviations of the model factors were low, between 0.05 and 0.08 for the different configurations.

In the light of the model factor trend depicted in Figure 4a, one would expect lower reliability estimates for 0.58mm, 550MPa configuration than what was obtained for the 0.8mm, 550MPa. Likewise, in the light of the model factor trend depicted in Figure 4b, one would expect lower reliability estimates for 0.8mm, 550MPa configuration than what was obtained for the 0.8mm, 230MPa. This however was not the case, largely due to appropriate provisions in SANS 10162-2 to increase reliability for plate thicknesses and strength where the model factor trends toward a value less than one. Clause 1.5.1.4 of SANS 10162-2 requires the following modifications in the calculation of the design capacity when 550 MPa grade steel is used in plate thicknesses less than 0.6 mm or 0.9 mm respectively:

- For 550 MPa grade steel with a thickness less than 0.9 mm, the steel strength used in the design calculations must be taken as the smallest of 495 MPa or 90% of the specified strength value.

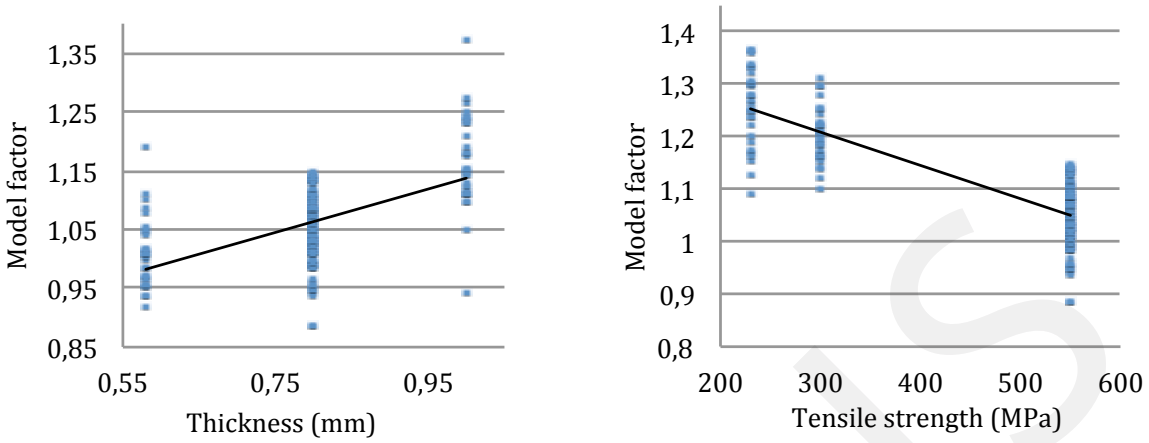

(a) Model factor vs Thickness

(b) Model factor vs Tensile strength

Figure 4: Model factor trends

- For 550 MPa grade steel with a thickness less than 0.6 mm, the steel strength used in the design calculations must be taken as the smallest of 410 MPa or 75% of the specified strength value.

It is known that high strength plates have very little ductility, especially when the plates are thin. This was confirmed by tensile test measurements for these configurations, where the yield- and ultimate strength barely differed.

6 Conclusion

Reliability analysis of typical cold formed steel connections, expected to fail in tilt-and-bearing, indicated high levels of conservatism in the design formulation of SANS 10160-2 and its parent standard AS/NZS 4600. A number of typical configurations with different plate thicknesses and steel strength achieved reliability index values of $\beta > 8$. The application of a capacity reduction factor of $\phi = 0.5$ to the nominal capacity proved to be the main contributor to conservatism. There may be scope to increase this factor to obtain reliability closer to the target of $\beta_t = 3.6$ if economic benefit can be derived from such a calibration.

Unbiased predictions based on the standards' prediction model compared well with experimentally determined capacities, with average model factors (ratio of actual over predicted capacity) between 1.01 and 1.25 and standard deviations between 0.05 and 0.08. Model factors increased with increased plate thickness and decreased with increased steel strength.

Very thin high strength plates have low ductility with little difference between the yield- and ultimate strength. Limitations of the nominal steel strength in design capacity computations for these ensure adequate conservatism, adjusting for the trend towards non-conservative unbiased predictions.

References

[1] D. Allen. History of cold formed steel. *Structural magazine*, pages 28–32, November 2006.

[2] JCSS Probabilistic Model Code. Part 1, basis of design. *Probabilistic Model. Joint Committee on Structural Safety*, 2000.

[3] G.J. Hancock. *Design of Cold-formed Steel Structures: To Australian/New Zealand Standard AS/NZS 4600: 2005*. Australian Steel Institute, 2007.

[4] G.J. Hancock, T. Murray, and D.S. Ellifrit. *Cold-Formed Steel Structures to the AISI Specification*. Civil and Environmental Engineering. CRC Press, Sydney, 2001.

[5] M. Holickỳ. *Reliability analysis for structural design*. SUN MeDIA, 2009.

[6] M. Holicky, M. Sykora, C. Barnardo-Viljoen, K.K. Mensah, and J.V. Retief. Model uncertainties in reliability analysis of reinforced concrete structures. 2013. Paper presented at CEMC2013.

[7] C.A. Rogers and G.J. Hancock. Screwed connection tests of thin g550 and g300 sheet steels. *Journal of Structural Engineering*, 125:128:129–136, 1999.

[8] SABS. Sana 10160-1. *SABS Standards division*, 2011.

[9] SABS. Sans 10162-2. *SABS*, 2011.

Assessment of the ice throw and ice fall risks nearby wind energy installations

Thorsten Weidl, Michaela Kaposvari

Department Risk Management
TÜV SÜD Industrie Service GmbH,
Westendstraße 199, 80686, Munich, Germany
thorsten.weidl@tuev-sued.de

Abstract. TÜV SÜD implemented a simulation model to determine the possibly affected area around a wind turbine subject to ice fall and a following procedure to quantify and assess this risk.

The ice fall calculation uses average local wind conditions such as the sectoral distribution of wind speed and direction at the desired location to perform Monte-Carlo-simulations for defined scenarios which are only distinguished by the properties of the ice piece to fall off.

Based on the results of this calculation it has to be decided whether or not a detailed risk analysis has to be performed. This depends on the before mentioned affected area and the local situation, e.g. special objects such as parking areas, streets or motorways, paths or ways just for pedestrians within the hazardous area around the planned wind turbine.

Once the decision is made that a detailed risk assessment is necessary, for each planned wind turbine and each object of interest a complex investigation is initiated. This consist of the severity judgement on the one hand, based on the Probit function, and of the frequency of being hit by a piece of ice on the other hand, which is based on the results of the ice fall expertise and developed farther to assess the risk as accurate as possible. Due to the complexity of the situation this method is still being continuously improved.

One of the central tasks performing the risk analysis is a proper classification of the objects defined in the expertise with respect to the potential presence of people there, which is the major influencing factor of the risk.

We will give a survey of the state of the art for risk analyses of ice throw and ice fall, a description of the method how we use it today and an outlook of how we plan to improve the method in the future.

1 Introduction

Wind energy is the leading source of renewable energy in Germany, supporting the ambitious targets for moving towards a nuclear free and carbon free generation profile. As Germany is densely populated the building of new wind parks is subject to a quite complex approval procedure. One important topic during this planning and approval stage is the assessment of the risk of ice throw and ice fall near wind energy installations.

Wind turbines in Germany are not allowed to operate during ice formation on rotor blades, the installation of a functional detection system for icing combined with the subsequent

shut-down of the turbine has to be confirmed in the approval process. Residual risk of ice fall from stopped turbines has to be investigated depending on the local situation, especially when special objects are located nearby.

TÜV SÜD implemented a procedure for project developers planning on-shore wind parks to meet the demands of the German authorities regarding the risk of ice throw and ice fall.

At this point a distinction between the definition ice throw and ice fall has to be made. The difference between these two is such that ice throw considers a spinning wind turbine, ice fall indicates either a stopped wind turbine or a turbine in idling mode. For the approval process in Germany ice fall is of interest, nevertheless the simulation can consider both cases – ice throw and ice fall – by using the wind turbine specific rotational speed.

2 Ice fall Simulation

The ice fall simulations (Monte-Carlo-Simulations) are performed for four different scenarios:

- Scenario A: rime ice with a mass of 90 g
- Scenario B: rime ice with a mass of 240 g
- Scenario C: clear ice with a mass of 70 g
- Scenario D: clear ice with a mass of 180 g

To achieve a suitable convergence at the relevant objects of interest (e.g. streets or paths) we use 5'000'000 iterations for each simulation as a fixed value for each project. It is currently not clear if competitive analytical methods are able to solve this problem, but in our ongoing process of improvement this will be checked.

These four scenarios were identified based on characteristic ice formation processes with assumed proportions as well as on the consequence expected when pieces of ice accelerate while falling from a height of 140 m to the ground (i.e. typical hub height of a wind turbine). As shown in the following chapter, the masses chosen for the simulation define the lower and the upper boundary of consequences:

- 90 g rime ice and 70 g clear ice: beginning of slight injuries
- 240 g rime ice and 180 g clear ice: fatality has to be assumed

The simulations are performed under consideration of:

- hub height
- rotor diameter
- rotor revolution
- ice properties
- wind properties.

For the wind properties a wind rose and a distribution of the wind speed (the Weibull distribution can be esteemed as a common standard which describes the behaviour of wind

speed as accurate as possible) are produced using meteorological data of local weather stations near the planned wind park or data of wind measurements, if available. For a reliable conclusion of the simulation results the input wind distribution should be as representative as possible for the turbine site. Depending on the representativeness between the site of meteorological data and the planned wind park an uncertainty analysis on the input data of wind properties is performed, which is leading to a slight increase in the occurrence of higher wind speeds in the sectoral distribution and thus to conservative results with respect to safety issues.

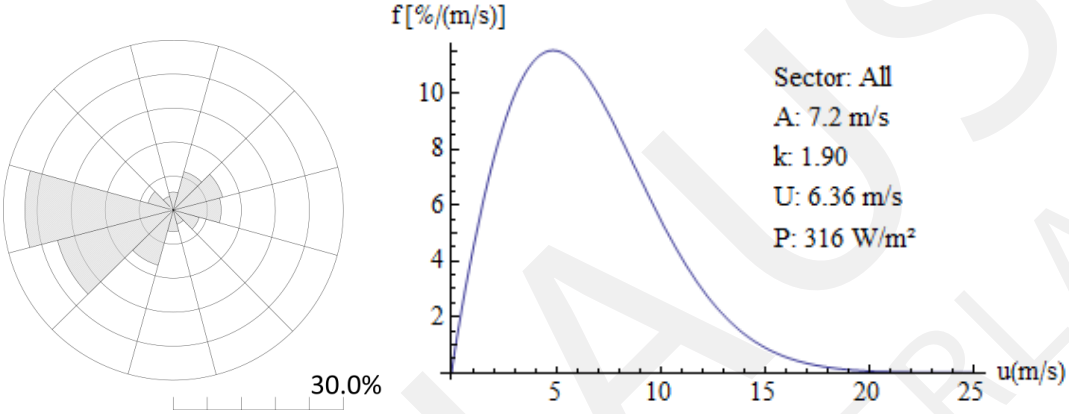

Figure 1: Example for a wind rose and Weibull distribution (distribution of wind speed occurrences) as used for the ice fall simulations.

Based on these input data, the simulation of the x, y and z acceleration of the considered ice pieces can be performed using the equation system of motion:

$$M\acute{x} = \frac{-1}{2}\rho\, C_D A(\acute{x} - U)W \tag{1}$$

$$M\acute{y} = \frac{-1}{2}\rho\, C_D A\acute{y}W \tag{2}$$

$$M\acute{z} = -Mg - \frac{1}{2}\rho\, C_D A\acute{z}W \tag{3}$$

with:

M = mass of ice piece
ρ = density of air
C_D = drag coefficient
U = wind speed at hub height
A = cross-sectional area of ice piece
W = relative wind speed = $\sqrt{(\acute{x} - U)^2 + \acute{y}^2 + \acute{z}^2}$
g = gravitational acceleration

For each scenario 5‘000‘000 iterations are performed, whereby each iteration means a hit of an ice piece on a flat surface with the wind turbine in the centre. The surface is divided into areas of 5 m times 5 m, and for each such area the number of the hits out of the 5 Mio simulations is accumulated. The final result of the simulations is the area theoretically affected by ice fall or ice throw.

Within each iteration, the current wind regime, i.e. wind speed and wind direction, and the radial and azimuthal position of the ice fragment on the rotor blade are randomly chosen, with respect to the original distribution of wind speed and direction. The exact simulation result respectively the outlier hits, which are caused by high wind speeds with a low occurrence frequency, are not accurately reproducible. However these individual hits are not significant in the critical risk assessment. The ice fall affected area appears through the simulation of 5 Mio iterations and according to the Monte Carlo method as a stable distribution.

In the calculation of the trajectory of the falling ice piece a rotation of the fragment is included, which exposes different cross-sections along with different drag coefficient to allow for a more realistic simulation.

A result of such a simulation is exemplarily shown for scenario C in the following Figure 2. The colouring shows for each cell the total amount of hits by an ice fragment within the performed iterations. The site of the wind turbine is located in the centre of the grid pattern. Range rings in the distances of the rotor radius of the turbine as well as of 100 m and 200 m are shown for better orientation. The results of the ice fall simulations

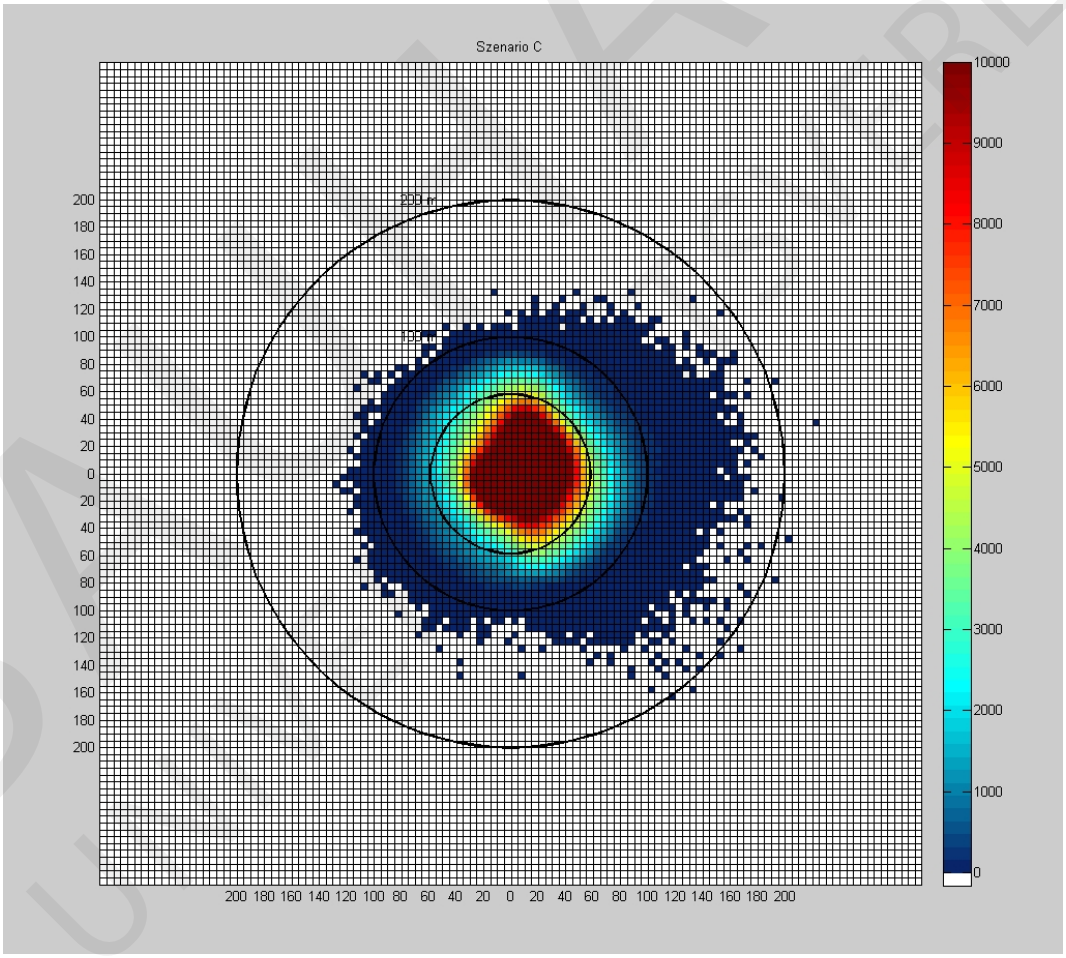

Figure 2: Example of the result of an ice fall simulation according to the input wind regime. The wind turbine is located in the centre of the grid pattern. The colouring shows the amount of hits per cell.

are finally transferred to a topographical map, in order to investigate whether roads, footways, paths or other objects of interest are affected by ice pieces (example see in Figure 3). Based on the calculated frequency of hits respective of the objects of interest a decision has to be made, if and for which objects a risk assessment has to be performed. In the example of Figure 3 one broader road and three footways would have to be taken into account for the risk assessment.

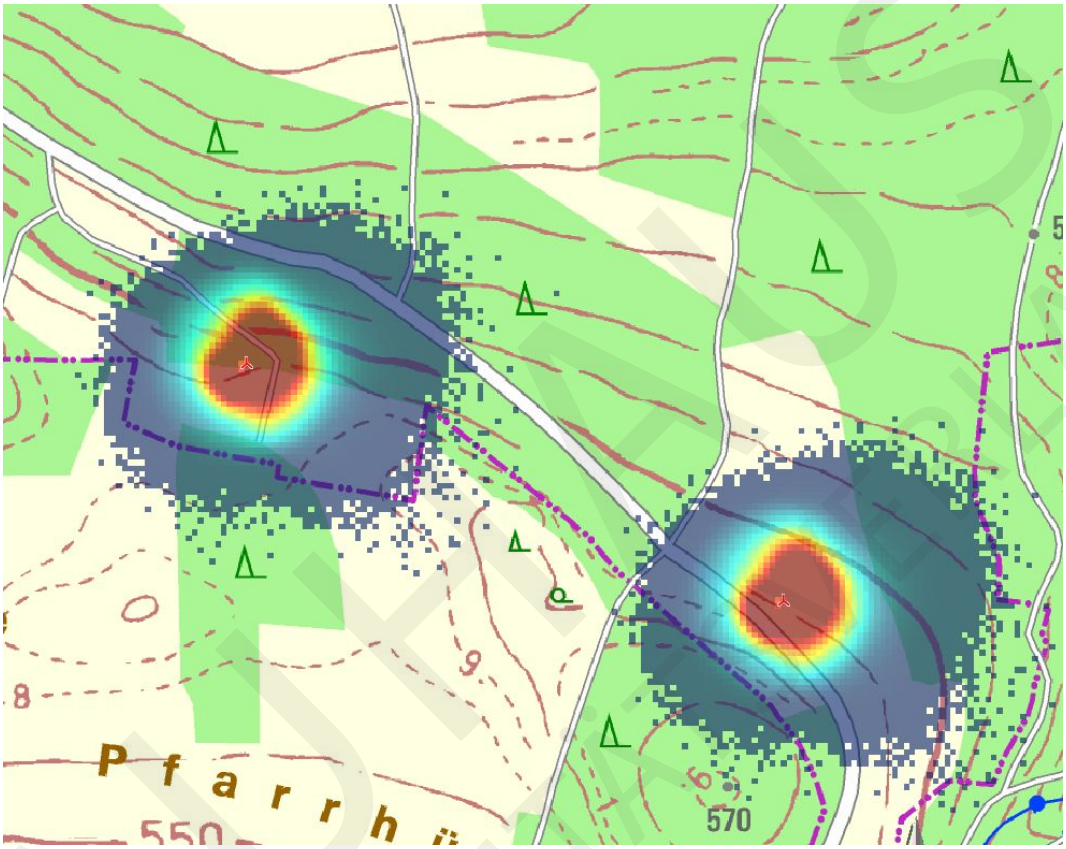

Figure 3: Projection of simulation results to a topographical map, example with two wind turbines surrounded of several paths and roads.

3 Determining the extent of damage C

For determining the extent of damage, the so-called probit function is used. The probit function is defined by

$$Pr = -17.56 + 5.3 \cdot \ln S \tag{4}$$

with $S = \frac{1}{2}mv^2$ as the kinetical energy of the ice pieces.

Using Table 1 the extent of damage can be estimated.

Example:
If the value of the probit function is 5.99, the calculated value of the extent of damage is

%	0.00	1.00	2.00	3.00	4.00	5.00	6.00	7.00	8.00	9.00
0	-	2.67	2.95	3.12	3.25	3.36	3.45	3.52	3.59	3.66
10	3.72	3.77	3.82	3.90	3.92	3.96	4.01	4.05	4.08	4.12
20	4.16	4.19	4.23	4.26	4.29	4.33	4.36	4.39	4.42	4.45
30	4.48	4.50	4.53	4.56	4.59	4.61	4.64	4.67	4.69	4.72
40	4.75	4.77	4.80	4.82	4.85	4.87	4.90	4.92	4.95	4.97
50	5.00	5.03	5.05	5.08	5.10	5.13	5.15	5.18	5.20	5.23
60	5.25	5.28	5.31	5.33	5.36	5.39	5.41	5.44	5.47	5.50
70	5.52	5.55	5.58	5.61	5.64	5.67	5.71	5.74	5.77	5.81
80	5.84	5.88	5.92	5.95	5.99	6.04	6.08	6.13	6.18	6.23
90	6.28	6.34	6.41	6.48	6.55	6.64	6.75	6.88	7.05	7.33
99	7.33	7.37	7.41	7.46	7.51	7.58	7.65	7.75	7.88	8.09

Table 1: Relation between value of the probit function and quantitative extent of damage.

0.84 (84%), where the first digit is taken from the row and the second digit is taken from the column. This quantitative approach considers the following relation:

- Quantitative value of 1: fatality
- Quantitative value of 0.1: severe injury
- Quantitative value of 0.01: slight injury

Based on this calculation the thresholds for the masses for the four scenarios A to D for slight injuries and fatalities can be calculated.

4 Determining the frequency P

In an assessment of the WECO Project (Wind Energy Production in Cold Climate) the icefall of a wind turbine WEA near the mountain Gütsch in Switzerland was observed. Here the number of the fallen ice pieces has been counted [2].

During a stage of three years a total number of 200 ice pieces has been counted [2]. As it has to be assumed that not all the ice pieces from the testing turbine have been found, because they broke at the crash on the ground, it is further assumed that a number of 200 ice pieces per year is more realistic. Furthermore this number is set into relation to the radius of the rotor blades. (z. B. 20 m radius in [2] and 200 ice pieces results in 600 ice pieces at a radius of 60 m).

So the results of the icefall simulation (relative frequency) can be transferred into an absolute frequency of hits in a $5m \times 5m$ square per year. Considering a relevant cross-section area ($0,04m^2$ for the head of pedestrians an $2m^2$ for the windscreen of cars) and assuming an average speed of 5 km/h for pedestrians and 60 km/h for cars the total probability of being hit by an ice piece while crossing one of these $5m \times 5m$ squares can be calculated.

Expositon
The resulting individual risk for each scenario for pedestrians is calculated by estimating the exposition (time per year in the hazardous area) by categorization of the ways and paths for pedestrians in reference to their expected usage. This categorization is one of the main tasks within the risk assessment and is performed using available information of the local authorities, on-site visits and aerial views (e. g. from Google Earth). Te resulting Categorization is shown in Table 2. For cars on the roads the collective risk

Category	Meaning
Regularly used way	This way is – due to its size, its accessibility and its position to villages and towns – assumed to be used regularly. This means, it has to be assumed that this way is used by one and the same jogger or pedestrian at each day we assume ice fall conditions.
Sporadic used way	For this kind of way not all of the attributes above are applicable. So leads e. g. a higher distance to villages or a worse accessibility to the assumption that this way is not used at each day by joggers or pedestrians.
Seldom used way	These are ways, which can be clearly identified as ways from the aerial view, but which are definitely not used as a main ways and which conditions allows the conclusion that it is used seldom.
Usually not used way	Ways which can be rarely identified as such from the aerial view, which are a lot of kilometres away from the next buildings or which are identified as blind alleys are seen as usually not used.

Table 2: Categorization of ways and paths in reference to their expected usage

is calculated. Therefore the risk of one commuter (exposition at each of the 20 days of assumed icefall condition [3]) is calculated and then multiplied with the total number of cars assumed on this road per day. For cars a risk reduction factor of 0.1 is assumed to consider the protective effect of the car itself.

5 Calculating the risk

Finally the risk for each scenario is calculated by adding the risks of the 5mx5m squares which are touched by the way (actually a line in the main orientation using the minimum distance is used, but the more precise method is planned). For the risk the following equation is used:

$$R_{scenario\,i} = C_{scenario\,i} \cdot P_{scenario\,i} \tag{5}$$

Considering that each scenario will have more or less the same probability, the overall risk can be calculated to

$$R = 0.25 \cdot \sum_{i=A\,to\,D} C_{Szenario\,i} \cdot P_{Szenario\,i} \tag{6}$$

6 Results

The calculated result is transferred into a diagram similar to the one shown in Figure 2 and Figure 3. In this diagram the simulated number of hits in the $5m \times 5m$ squares is replaced by the risk crossing one of these squares considering exposition, probability of being hit and the calculated consequence. The colouring is set to the usually used colouring defined by the international risk acceptance criteria (see [4]). For our risk assessment maps from the open source project openstreetmaps are used. An example of such a result, including ways and paths for pedestrians as well as a road is shown in the following

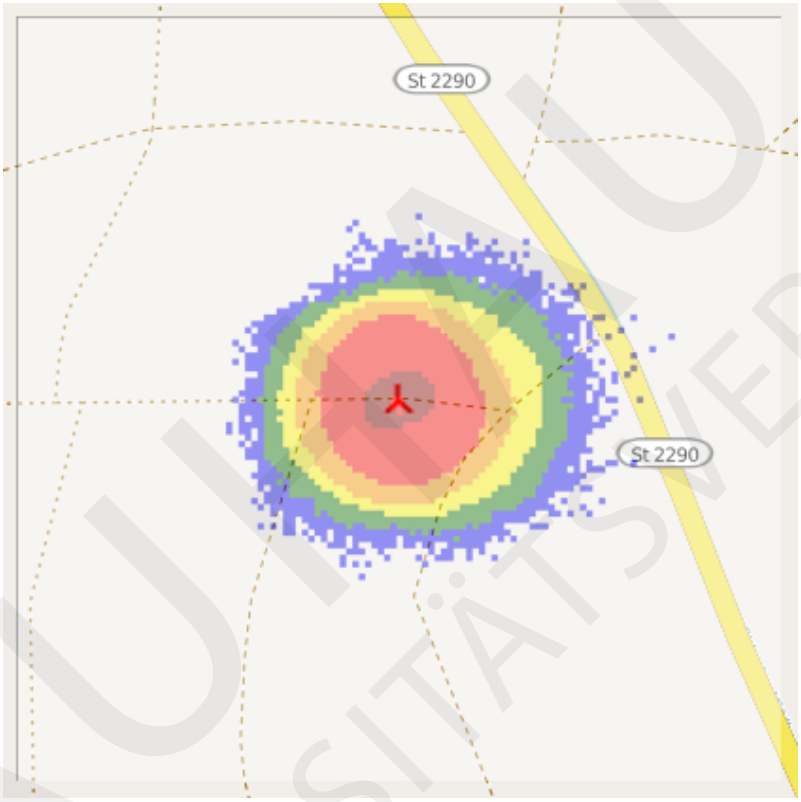

Figure 4: Example for a graphical representation of the result.

Usually a different cascade of measures is proposed by used, dependent of the calculated risk:

Ways and paths for pedestrians

- Negligible risk: no specific measures, general warning signs.
- Acceptable risk: no specific measures, general warning signs
- Tolerable risk: specific warning signs near the wind turbine, if possible closing of the way during winter.
- High risk: specific warning signs near the wind turbine, mandatory closing of the way during winter.
- Unacceptable risk: Movement of the wind turbine to another site.

Roads

- The collective risk has to be identified at least as tolerable risk. If not, the intended position for the wind turbine is not possible (nevertheless we have made assessments where roads are closed during winter and the wind turbine stays at the intended position)

7 Conclusion

The procedure to calculate the ice fall risks shown in the chapters 3 2 to 54 was based on the result of the Monte-Carlo-Simulation shown in chapter 21. Earlier approaches with analytical methods have been far away from the reality as it was known from observations, e. g. mentioned in [2].

The necessity of this kind of assessment was triggered by the needs of the industry to find new sites for wind turbines, as more or less hazard free sites are not longer available in Germany. So, triggered by requirements of the local authorities, ice fall simulation and the subsequent risk assessment have become a permanent demand for the approval process of wind turbines in Germany.

This method was developed from 2006 until today and it is still a process of steady learning. But, as our company offers this service from its early beginnings and develops it further with each new project, the method shown defines momentary the state-of-the-art in science and technology.

In the future we will implement some smaller improvements, as for example a closer junction between Monte-Carlo-Simulation and risk assessment, as well as long-term planned improvements like e. g. a backwards simulation of the results shown in figure 3 to achieve more precise results to be less attackable by the authorities or opponents of wind energy. Furthermore new findings regarding size of ice pieces or frequency of ice fall conditions are considered in our model as soon as we gain knowledge therefrom.

References

[1] S Biswas, P Taylor, and J Salmon. A model of ice throw trajectories from wind turbines. *Wind Energy*, 15(7):889–901, 2012.

[2] R Cattin. *Alpine Test Site Gütsch Handbuch und Fachtagung, Schlussbericht*. Bundesamt für Energie, Bern, 2008.

[3] H DOBESCH, G KURY, HV TRAN, and S ZACH. Das windenergiepotential vorarlbergs - endbericht. *Endbericht. Wien*, 2003.

[4] Hoffmann et. al. Risk acceptance criteria. *12th International Probabilistic Workshop*, 2014.

[5] Committee for the Prevention of Disasters. *Guidelines for Quantitative Risk Assessment: Purple Book*. CPR 18E. Directorate-General for Social Affairs and Employment, 1999.

Sensitivity Analysis of Strengthened RC Beams with Stochastically Distributed Material Properties

Jörg Weselek, Ulrich Häußler-Combe

Institute of Concrete Structures
Department of Civil Engineering
Technische Universität Dresden
01062 Dresden
Germany
Joerg.Weselek@tu-dresden.de

Abstract. The utilization of textile reinforced concrete is a promising approach to increase the load capacities of reinforced concrete elements nowadays. To reach an adequate safety level an appropriate numerical model should be found which regards several effects on those capacities. Scattering effects, especially those of material properties, are responsible for uncertainties which have to be considered by all means. Therefore in the present contribution a mathematical construct named random fields to model fluctuating material properties is introduced. They require a sufficient amount of samples which could be compared with trials of the structures in laboratories. The generation of the samples is realized within a Monte Carlo simulation. Furthermore a sensitivity analysis is performed to determine the influence of the apparently dominating property of random fields called correlation length.

1 Introduction

When the successive deterioration of buildings becomes critical, an effective method to extend their lifespans using existing structures is sought. The adoption of textile reinforced concrete could be an adequate technique for those needs. But before it can be safely applied, an appropriate safety level should be confirmed. A common way to reach this aim is the execution of a reliable analysis. On the resistence-side various scattering and uncertain properties of materials and the geometry of the structure needs to be considered. Therefore in this contribution major material properties, compressive and tensile strengths, are modelled as scattering distributions along the length of a bending beam which is loaded until it fails. These fluctuating properties are modelled with random fields. The application of these requires a multiple numerical test execution due to their random characteristics. This need is achieved by using the well-known Monte Carlo method.

In a previous work ([17]) the authors applied various numerical methods ([16, 6, 15]) to perform Monte Carlo simulations on the, later presented, numerical model. Thereby the correlation length, which specifies the influences of randomly determined strength values and their vicinity, was declared to be an important property of the random fields and an assumed addional material property respectively.

Thus the dependence of the correlation length on the bending load capacity of RC beams is investigated. The method of Sobol' (see [14]) as a quantitative method of sensitivity

analysis is used for this purpose. The results of the simulation appear to indicate the influence of the evaluated input variables. In our case these are the correlation lengths of the two uncorrelated random fields and the standard deviation of their input distributions, realized with a Gaussian distributed random variable.

2 Flexural Strengthening of Reinforced Concrete Beams by Textile Reinforced Concrete

Textile reinforced concrete (TRC) is a composite material. The function of tensile strengthening is taken over by orthogonally oriented rovings within technical textiles. In comparison to ordinary reinforced concrete, these textiles substitute the steel reinforcement. To ensure sufficient bond properties a fine-grained concrete must be used. As part of the collaborative research centre (SFB) 528 the Technische Universität Dresden investigated the advantages of textile reinforcement for strengthenings of pre-loaded concrete structures (see e.g. [9]). To understand the applied upcoming numerical model a brief summary of the main content of [17] regarding strengthening of concrete beams is given in the following. The explanations relate to the most common procedures and combinations of materials and do not claim to be complete.

2.1 Composition and Characteristics of TRC

Usually the TRC is applicated at highly stressed structures by the lamination technique (see [9]). An example of a retrofitted cross-section is shown at the right side in figure 1. The several layers need only a thickness of 3 millimeters each. The mentioned researches had proven, that carbon has the most promissing properties for those purposes. However it must be noted, that a roving and the textiles embedded in the fine-grained concrete lead to other values for the respective tensile strength. By reason of the complicated bond-mechanisms the values cannot be converted into each other. Therefore special tensile specimens and test setups were developed to determine the stress-strain-relations of the final strengthening structures (see [8, 6]). Newer researches suggest a linear relation with a limited tensile strain. A comparatively high corresponding average ultimate strength of approximatelly $1900 MN/m^2$ can be reached with the present composites. The potential of those applications for strengthening for flexural bending was demonstrated in many experiments (see e.g. [3]). An improvement of the bearing load capacity up to 300 percent is possible with only one strengthening layer made by carbon rovings.

3 Numerical Model for a Retrofitted RC Beam

3.1 Static System

The single-span beam, which is shown in figure 1, is based on a test setup according to the general type approval for strengthenings with TRC [1]. The chosen system is

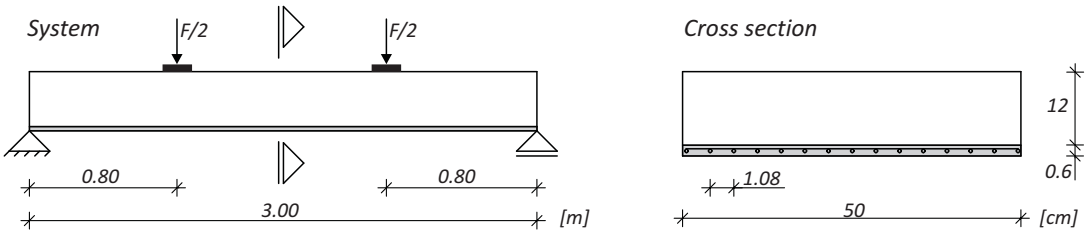

Figure 1: Static System based on Test Setup of [1]

equipped with one strengthening layer for the sake of simplicity and the related properties of the reinforcements can be deduced from table 1. The accumulated cross-section area of the TRC layers results from the clearance between the rovings in load-carrying direction and needs to be multiplied by the width of the beam cross-section. To consider softening behaviours the shown loading is applied path-controlled until the system fails.

Table 1: Geometric Properties of Reinforcements

	Unit	Value
Steel Reinforcement		
Rebar Diameter ⌀	mm	6.0
Number of Rebars		5
Cross Section Area A_{s1}	cm^2	1.414
Textile Reinforcement		
Roving Cross Section Area $A_{t,1}$	mm^2	1.833
Number of Rovings per Meter	$\frac{1}{m}$	92
Accumulated Cross Section Area $A_{t,a}$	mm^2	84.318

Table 2: Relevant Material Characteristics

	Unit	Value
Concrete		
Young's Modulus E_c	MN/m^2	31000.0
Compressive Strength f_c	MN/m^2	28.0
Strain at peak stress ϵ_{c2}		-0.0021
Nominal ultimate strain ϵ_{cu2}		-0.0035
Steel Reinforcement		
Young's Modulus E_s	MN/m^2	200000.0
Yield Strength f_y	MN/m^2	560.0
Tensile Strength $f_{t,cal}$	MN/m^2	588.0
Ultimate Strain ϵ_{su}		0.025
Textile Reinforcement		
Young's Modulus E_t	MN/m^2	220000.0
Tensile Strength f_{tu}	MN/m^2	1872.2
Ultimate Strain ϵ_{tu}		0.0085

3.2 Finite Element Model

ConFem, a software which has been developed at the Intitute of Concrete Structures, is used to calculate the described system. The FEA-program provides an enhanced two-node 2D-beam element type based on the theory of Bernoulli. It also allows the integration of steel as well as textile reinforcements. Furthermore the structure was divided into 120 elements of the same length. This configuration is detailed enough to generate precise results with a reasonable computational cost for calculation.

3.3 Materials and Internal Force Equilibrium

For the ordinary concrete in the compression zone a parabolic-rectangular stress-strain relation according to the standard [5] is applied. Furthermore to absorb tension the material is not considered. Solely the reinforcements transfer the tensile forces. Thereby a bilinear elastic-plastic constitutive relation considering hardening is applied for steel

reinforcement (see [5]). As mentioned above a linear-elastic material law with an ultimate strain ϵ_{tu}, respectivelly a limited tensile strength f_{tu} is adopted for TRC. Further information and notations about relevant deterministic material properties can be found in table 2. To find the internal force equilibrium of any cross-section an amplified model based on [5] is applied. It regards different limit states where failure occurs in the simulation. Thereby the ultimate compressive strain $|\epsilon_c|$ of concrete in the zone of pressure and the tensile failure strain of steel ϵ_{su} represent the well-known limit states, while the tensile failure of TRC ϵ_{tu} has to be added. It also occurs in the tension zone of the cross-section. The described model yields a non-linear system, which requires an incrementally-iterative calculation to find the solution of the internal equilibrium.

4 Stochastically Distributed Material Properties

To model reality more accurate, we assume that the material properties or more precisely the strengths fluctuate along the geometry of a structure, in our case along the length of an RC beam. For a mathematical description, this can be achieved by using random fields. It should also be possible to consider dependences of one point with its immediate neighborhood. Due to the limited scope of this contribution there will be only brief explainations for random variables and fields in the following. These are based on [7, 16] and [17].

4.1 Random Variables

For our investistigation we are using continuous probability distributions to describe the spatial scattering of the compressive strength of concrete and the tensile strength of the textile reinforcement layer. A realisation y of the random variable Y is assumed as a real-valued number. The cumulative distribution function (CDF) $F(y)$ declares the probability P that Y takes a value lower than y. The probability density function (PDF) $f(y)$ is obtained by differentiation of $F(y)$ and its shape characterizes the distribution (type). The mean value μ_y and the standard deviation σ_y define a normally distributed random variable. The covariance σ_{yz} expresses the relationship between realisations of different random variables Y and Z. For further explanations see e.g. [2].

4.2 Spatial Influence of Material Properties

As mentioned along the longitudinal axis of the investigated beam the compressive strength of concrete and textile tensile strength are assumed as scattering values. For one of those strength distributions assuming two different realisations y_1, y_2 of identical random variables at two positions x_1, x_2 the covariance $\sigma_{y_1y_2}$ can be adopted for the spatial influences. The well-known bell-shaped *autocorrelation function* (see eq. (1)) is commonly used to describe it. It depends on the distance $|x_1 - x_2|$ and the standard deviations of the random variables. Because of its decisive impact the correlation length $L_{corr,x}$ deserves special consideration. The influence on the distributions of the realisations along the length of the beam is shown in figure 6 of [17]. Several samples of strength

distributions with different correlation length can be obtained. L_{corr} needs to be added as a material parameter.

$$\sigma_{Y_1,Y_2}(x_1,x_2) = \sigma_{y_1}\sigma_{y_2}e^{-\left(\frac{|x_1-x_2|}{L_{corr,x}}\right)^2} \tag{1}$$

In the current standards [5] scattering material properties are integrated by means of characteristic values. For the compressive strength of concrete they represent the 5 percent quantile of a random variable which is assumed as a normal distribution. For concrete of the strength class C20/25 the standard deviation σ_y can be derived by using the characteristic strength $f_{ck} = 20\frac{MN}{m^2}$ and the mean value $\mu_y = 28\frac{MN}{m^2}$. A precise derivation of these values is given in [17].

One part of the quoted general type approval is the specification of the scattering strength properties of TRC. To determine the characteristics for f_{tu} a probabilistic analysis as a Monte Carlo simulation was performed. The mean value $\mu_y = 1872.2\frac{MN}{m^2}$ and standard deviation $\sigma_y = 148.52\frac{MN}{m^2}$ assuming a normal distribution were determined.

4.3 Random Fields within a Monte Carlo Simulation

Within a Monte Carlo simulation it is possible to generate deterministic samples with randomly distributed input variables. Thereby each sample represents a retrofitted RC beam with discretizised curves for the compressive strength of concrete and textile tensile strength. Determining all strength values on the integration points over the sample population two uncorrelated random fields (one for each strength distribution) can be established. Assembling all spatial fluctuations a so-called autocorrelation matrix P is introduced. It is quadratic and stores all autocovariance functions (eq. (1)) for all related locations. Subsequently its dimension $n_{rv}\,\mathrm{x}\,n_{rv}$ is derived from the number of integration points n_{rv}. Using the *Karhunen-Loéve expansion* a decomposition of P into eigenvectors Ψ and eigenvalues λ can be facilitated. By solving the standard eigenvalue problem $P\Psi = \lambda\Psi$ ([7]) the calculation effort can be minimized without loss of crucial information. Thus a realisation can be expressed by eq. (2).

$$S = \sum_{i=1}^{n_{rv}} \sqrt{\lambda_i}\xi\psi_i \tag{2}$$

where S expresses a sample for each random variable Y and ξ are standard Gaussian random numbers. For more details about the procedure see [15, 16].

At the beginning of this section the generating of a Monte Carlo population was mentioned. So a series of realisations for each material property has to be compiled, i.e. in our case $2 \cdot n_{set}$. Where n_{set} represents the population size. Each of them consists n_{rv} realisations of ξ, which are in turn determined by the well-known latin hypercube sampling method.

After the calculation of n_{set} RC beams with scattering material properties using ConFem it is possible to display the frequency distribution of the bending load capacity for each failed structure. Two of those diagrams can be found in [17]. Subsequently for the frequency distribution a distribution type with its properties can be derived by e.g. kernel density estimators (see [2]).

5 Sensitivity Analysis and Method of Sobol'

As explained in [12] a determination which variation of sources effects the variation of the output can be derived by a sensitivity analysis. Thereby quantitative and qualitative methods are destinguished. This contribution focused on the quantitive and withal a variance-based method namely the Method of Sobol' (see [14]).

5.1 Correlation Ratio and Variance-Based Methods

Regardless of the model properties variance-based methods allows a quantitative assessment of global sensitivity-indices ([13]). I.e. from a mathematical point of view a closed system is not neccessary, which is important because of the used iterative FE-model for the calculations. Eq. (3)([12]) shows the correlation ratio η^2 and describes a variance-based sensitivity indicator.

$$\eta^2 = \frac{Var_X[E(Y|x)]}{Var[Y]} \tag{3}$$

where $Var_X[E(Y|x)]$ represents the variance of the conditional expectation (VCE) for Y and $Var[Y]$ is the output variance. The former one is gained by a variance decomposition and measures the importance of the inputs x (see [12, chap. 8.2]). For the discrete case the correlation ratio needs to be estimated. I.e. for each input factor x_i the VCE is estimated. For further information we recommend the lecture of [12, chap. 8].

5.2 Sensitivity and Total Effect Indices

First order sensitivity indices or - briefer expressed - sensitivity indices S_i allow the identification of the additivity of a system and the estimation of priority of the input values. Whereas the total effect indices S_{Ti} are more reliable for the investigation of the overall effect of each single factor (see [12]).

To determine the indices several simulations are neccessary. Each value of the input variables can be stored in a sample matrix X. Within it a column represents the generated realisations for one input variable. Furthermore the number of lines expresses the sample size n of the sensitivity analysis. For the evaluations of the first order and total effect indices matrix X has to be combined by another matrix with the same size. The result of this combinations are in the former case k (number of input variables) matrices X', where the column of the input variables is the same like in X. For the total effect indices in turn only the column of the investigated input variable differs.

This yields an overall computational effort of $n(2k + 1)$ simulations. To determine the effect of the specific input variable equation (3) needs to be solved $2k$-times. Scrambled Sobol' LP_τ sequences (see [11]) were used to generate samples for the different input matrices.

6 Results and Discussion

As mentioned in the introduction the dependence of four input variables on the output variables is investigated. The latter ones are the mean value and the standard deviation of the assumed normal distribution of frequency distributions of the Monte Carlo simulation. 1000 samples as the population size of each MC simulation were calculated. The sample size of the sensitivity analysis was chosen with $n = 40$. This number was derived from the recommendation in [13] with respect to the reference manual of SimLab[1] for a minimum of 10-times the amount of input variables. Consequently this yields 360000 simulations which need to be performed by ConFem.

Table 3: Sobol' sensitivity indices

	S_i	μ_{M_u}	σ_{M_u}	S_{Ti}	μ_{M_u}	σ_{M_u}
$L_{corr,f_{cu}}$		−0.282	0.77		182.50	1.76
$L_{corr,f_{tu}}$		−0.946	0.88		11.07	0.44
$\sigma_{f_{cu}}$		−1.576	2.25		18.91	0.62
$\sigma_{f_{tu}}$		−0.852	0.57		8.96	0.12

The results, especially the negative ones in the first column, indicates that the sample size for the sensitivity analysis was not chosen in a sufficient range. By involving the studies of e.g. [13] for the convergence behaviour of various methods, it can be assumed that the results will stabilize with increasing the sample size. With respect to that fact an interpretation of the non-negative results will not lead to new knowledge about the influences and the dependences of the individual factors due to the complicated non-linear model which was described and investigated.

7 Conclusion and Outlook

The novel strengthening technique of TRC has been investigating for 15 years at the Technische Universität Dresden. To ensure the commonly-used high safety level a relative high partial safety factor of approximately 2.0 must be applied. The first step to evaluate which input variables have high impact on that factor which expresses several uncertainties was presented in this contribution. A sensitivity analysis was executed using a non-linear FE-model which was derived from a current general type approval [1]. Furthermore the aim of involving spatial scattering properties was realized with the use of random fields. Hence the impact of the assumed dominating input variable called correlation length which describes the influence of random realisations of strength values by their vicinity could not be determined.

However, the results suggest that the described model do not fit the applied method for the sensitivity analysis. Also other approaches should be regarded to investigate the presented numerical model with its characteristics due to its high complexity. Therefore the work of Morris [10] and some methods based on this (e.g. [4]) should deserve attention in the future. Another approach could be the simplification of the model. In this context the investigations of Hartig ([6]) for uniaxial tensile behaviour of TRC could be considered.

[1]This reference was not available while writing this contribution.

References

[1] Abz. z-31.10-182 "Verfahren zur Verstärkung von Stahlbeton mit TUDALIT (Textilbewehrter Beton)", 6. juni 2014.

[2] K. Bosch. *Statistik-Taschenbuch*. Oldenbourg, München [u.a.], 1992.

[3] A. Bösche. *Möglichkeiten zur Steigerung der Biegetragfähigkeit von Beton- und Stahlbetonbauteilen durch den Einsatz textiler Bewehrungen Ansatz für ein Bemessungsmodell*. PhD thesis, TU Dresden, Fakultät Bauingenieurwesen, Dresden, 2007.

[4] Francesca Campolongo, Jessica Cariboni, and Andrea Saltelli. An effective screening design for sensitivity analysis of large models. *Environ. Model. Softw.*, 22(10):1509–1518, October 2007.

[5] EN. *EN 1992-1-1 Eurocode 2: Design of concrete structures - Part 1-1: General ruels and rules for buildings*, Brussels, 2005. CEN.

[6] J.U. Hartig. *Numerical investigations on the uniaxial tensile behaviour of Textile Reinforced Concrete*. PhD thesis, Technische Universität Dresden, Fakultät Bauingenieurwesen, Dresden, 2011.

[7] U. Häussler-Combe and J. Hartig. Rissbildung von Stahlbeton bei streuender Betonzugfestigkeit. *Bauingenieur*, 85(11):460–470, 2010.

[8] F. Jesse. *Tragverhalten von Filamentgarnen in zementgebundener Matrix*. PhD thesis, Technische Universität Dresden, Fakultät Bauingenieurwesen, Dresden, 2004.

[9] F. Jesse and M. Curbach. *Verstärken mit Textilbeton*, volume 1. Ernst & Sohn, Berlin, November 2009.

[10] Max D. Morris. Factorial sampling plans for preliminary computational experiments. *Technometrics*, 33(2):161–174, April 1991.

[11] Art B. Owen. Scrambled net variance for integrals of smooth functions. *The Annals of Statistics*, 25(4):1541–1562, 08 1997.

[12] A. Saltelli. *Sensitivity analysis*. Wiley, paperback ed. edition, 2008.

[13] V. Schwieger. *Nicht-lineare Sensitivitatsanalyse gezeigt an Beispielen zu bewegten Objekten*. Bayrische Akad. der Wiss. München, 2005.

[14] I. M. Sobol'. Sensitivity analysis for non linear mathematical models. *Math. Model. Compu. Exp. 1*, 1:407–414, 1993.

[15] B. Sudret and Armen Der Kiureghian. *Stochastic finite element methods and reliability: a state-of-the-art report*. Department of Civil and Environmental Engineering, University of California, 2000.

[16] Miroslav Vořechovský. Simulation of simply cross correlated random fields by series expansion methods. *Structural safety*, 30(4):337–363, 2008.

[17] J. Weselek and U. Häussler-Combe. Bending Load Capacity of Strengthened RC Beams with Stochastically Distributed Material Properties. In *Proceedings of EURO-C 2010, 24-27 March 2014, St. Anton am Arlberg, Austria*, 2014.

Probability Density Evolution Equation For Probability Dissipated System

Jie Li [1] and Jun Xu[1,2]
[1]School of Civil Engineering
Tongji University, 1239 Siping Road, Shanghai 200092, P.R.China
[2]Department of Civil and Environmental Engineering
Rice University, 6100 Main Street, Houston, Texas,77005, USA
E-mail: lijie@tongji.edu.cn, 86xujun@tongji.edu.cn

Abstract: Reliability related problems can be evaluated from the point of view of probability dissipated system. The principle of probability preservation is firstly investigated by state space description with consideration of the dissipated probability, where a coupled partial differential equation that governs the probability density evolution process of a probability dissipative system is derived. However, it is pity that the high-(say more than 4) dimensional partial differential equation is so far intractable because all state variables are coupled for general non-linear system. Instead, the principle of probability preservation is revisited by random event description, where the dissipated probability relies on the physical dynamic response. Therefore, the generalized density evolution equation for probability dissipated (GDEE-PD) system can be naturally formulated, which is possible to extract the probabilistic information of concerned single physical quantity, which is numerically feasible, after probability dissipation. Taking an integral over the remaining probability density functions after probability dissipation will give the remaining probabilities. Different physical mechanisms can be introduced into GDEE-PD as the triggering forces of probability dissipation, which leads to different types of reliability problems. For example, if strength failure criterion is considered to cause probability dissipation, the remaining probability after probability dissipation is the dynamic reliability; if the dynamic instability of structures induces probability dissipation, the dissipated probability is the unstable probability and thus the remaining is the stable reliability. Numerical example is carried out to illustrate the probability dissipated system based methodology for reliability analysis of structures.

Keywords: reliability, the principle of probability preservation, probability-dissipative system, probability density evolution equation

1. Introduction

The first-passage reliability assessment of structures always involves with a probability dissipated system. The recent years has seen great development in stochastic dynamics from the point of view of probability conservative systems, for example, the classical Liouville equation[1], the celebrated Fokker-Planck-Kolmogorov equation[2-4] and the Dostupuv-Pugachev equation[5] can be derived by employing the state space description of the principle of preservation of

probability[6, 7]. However, solutions, even the numerical ones to these equations are usually unavailable when the complex system is taken into account. Owing to the inherent complexity of solving these equations, a governing partial differential equation with respect to the evolutionary probability density function of stochastic response, which is applicable to general stochastic dynamic system, is of great necessity. The principle of probability preservation is revisited from the perspective of random event description, therefore a generalized density evolution equation (GDEE) is derived accordingly, which can extract the probabilistic information of any concerned quantity[8]. Besides, the GDEE is a one-dimensional partial differential equation, which is practically solvable with application of numerical themes. The method based on the GDEE is called the probability density evolution method (PDEM), which indeed degrades the difficulty of stochastic dynamic response analysis of complex nonlinear systems.

As is mentioned, the stochastic dynamic response can be predicted from the probability preserved system, nevertheless, the dynamic reliability problems are still an open challenge with consideration of the limitation of the probability preserved system. As a matter of fact, the probability dissipated system should be paid great attention to for assessing the dynamic reliability, which embodies the more general sense of stochastic dynamic system where the probability preserved system can be regarded as the special case of the probability dissipated system. Thus, the probability density evolution equation for the probability dissipated system must be well investigated.

The purpose of the present paper is to derive the probability density evolution equation for probability dissipated system and show the applications in dynamic reliability problems.

2. Probability Density Evolution Equation for Probability Dissipated System

2.1 Derivation of the probability density evolution equation for probability dissipated system from the state space description

Consider a n-dimensional dynamical system with random initial conditions, namely

$$\dot{\mathbf{Y}} = \mathbf{A}\left(\mathbf{Y},t\right), \qquad \mathbf{Y}\left(t_0\right) = \mathbf{Y}_0 \tag{1}$$

where $\mathbf{Y} = \left(Y_1, Y_2, ..., Y_n\right)^T$ is the n-order state vector, $\mathbf{Y}_0 = \left(Y_{1,0}, Y_{2,0}, ..., Y_{n,0}\right)^T$ is the initial condition vector, $\mathbf{A}\left(\cdot\right)$ is the deterministic operator.

Let us consider the fixed domain D_{fixed} with boundary ∂D_{fixed} in the state space, which is fixed in a time-variant velocity field determined by $\mathbf{v} = \mathbf{A}(\mathbf{y},\mathbf{t})$. The probability dissipation is assumed to happen in such domain, where the probability dissipated domain is denoted as D_a. Therefore, the principle of preservation of probability says that: in any arbitrary fixed domain in the state space, the increment of probability during a time interval $[t, t+\Delta t]$ is equal to the probability transited through the bound minus the dissipated probability during the same time interval[6]. Mathematically, the above statement can be expressed as

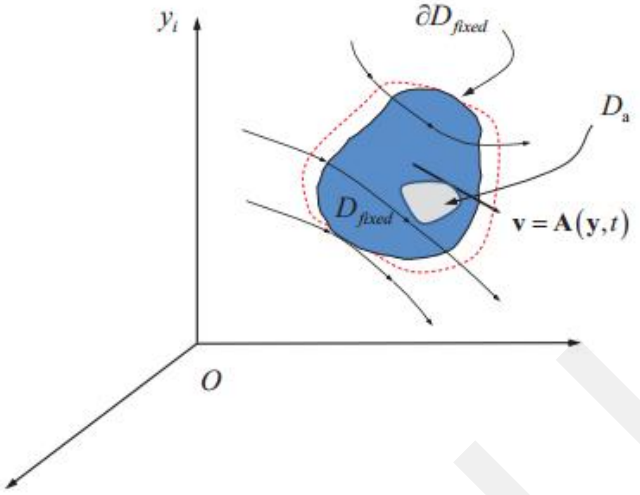

Figure 1 State space description

$$\Delta_{[t,t+\Delta t]}P_{D_{fixed}} = \Delta_{[t,t+\Delta t]}P_{\partial D_{fixed}} - \delta P \tag{2}$$

where $\Delta_{[t,t+\Delta t]}P_{D_{fixed}}$ is the increment of probability over D_{fixed}, $\Delta_{[t,t+\Delta t]}P_{\partial D_{fixed}}$ is the probability transited through the boundary ∂D_{fixed}, δP is the dissipated probability during the same time interval

$$\delta P = -\mathcal{H}\left(\mathbf{Y}(t)\right)\left[\int_{D_a}\int_{t}^{t+\Delta t}\tilde{p}_{\mathbf{Y}}\left(\mathbf{y},t\right)dtd\mathbf{y}\right] \tag{3}$$

where $\mathcal{H}$ is the probability dissipation indicator, defined as

$$\mathcal{H}\left(\mathbf{Y}(t)\right) = \begin{cases} 0 & \mathbf{Y}(t) \notin D_a \\ 1 & \mathbf{Y}(t) \in D_a \end{cases} \tag{4}$$

and $\tilde{p}_{\mathbf{Y}}\left(\mathbf{y},t\right)$ is the average PDF dissipated in the time interval

$$\tilde{p}_{\mathbf{Y}}\left(\mathbf{y},t\right) = \frac{p_{\mathbf{Y}}\left(\mathbf{y},t\right)}{\Delta t} \tag{5}$$

when $\Delta t \to 0$, we have

$$\lim_{\Delta t\to 0}\tilde{p}_{\mathbf{Y}}\left(\mathbf{y},t\right) = p_{\mathbf{Y}}\left(\mathbf{y},t\right) \tag{6}$$

In Eq. (2), the increment of probability can be rewritten as

$$\begin{aligned}\Delta_{[t,t+\Delta t]}P_{D_{fixed}} &= \int_{D_{fixed}} p_{\mathbf{Y}}\left(\mathbf{y},t+\Delta t\right)d\mathbf{y} - \int_{D_{fixed}} p_{\mathbf{Y}}\left(\mathbf{y},t\right)d\mathbf{y} \\ &= \int_{D_{fixed}}\int_{t}^{t+\Delta t}\frac{\partial p_{\mathbf{Y}}\left(\mathbf{y},t\right)}{\partial t}dtd\mathbf{y}\end{aligned} \tag{7}$$

and the probability transited through the boundary is

$$\Delta_{[t,t+dt]}P_{\partial D_{fixed}} = -\int_{t}^{t+\Delta t}\int_{\partial D_{fixed}} p_{\mathbf{Y}}\left(\mathbf{y},t\right)(\mathbf{v}dt)\cdot\mathbf{n}dS \tag{8}$$

where $\mathbf{n}$ is the unit outward normal vector of the boundary ∂D_{fixed}, dS is the unit area on the boundary. According to the divergence theorem[9], Eq.(8) can be rearranged as

$$\begin{aligned}&\int_t^{t+\Delta t}\int_{\partial D_{fixed}} p_{\mathbf{Y}}(\mathbf{y},t)(\mathbf{v}dt)\cdot\mathbf{n}dS=\int_t^{t+\Delta t}\int_{\partial D_{fixed}} p_{\mathbf{Y}}(\mathbf{y},t)\mathbf{A}(\mathbf{y},t)\cdot\mathbf{n}dSdt\\&=\int_t^{t+\Delta t}\int_{D_{fixed}}\frac{\partial\left[p_{\mathbf{Y}}(\mathbf{y},t)\mathbf{A}(\mathbf{y},t)\right]}{\partial\mathbf{y}}d\mathbf{y}dt\\&=\int_t^{t+\Delta t}\int_{D_{fixed}}\sum_{l=1}^{m}\frac{\partial\left[p_{Y_l}(y_l,t)A(y_l,t)\right]}{\partial y_l}d\mathbf{y}dt\end{aligned}\tag{9}$$

Substituting Eqs. (7), (9) and (3) into Eq. (2) and noting the arbitrariness of $[t,t+\Delta t]$, we have

$$\begin{aligned}&\int_{D_{fixed}}\frac{\partial p_{\mathbf{Y}}(\mathbf{y},t)}{\partial t}d\mathbf{y}+\int_{D_{fixed}}\sum_{l=1}^{m}\frac{\partial\left[p_{Y_l}(y_l,t)A(y_l,t)\right]}{\partial y_l}d\mathbf{y}\\&=-\mathcal{H}(\mathbf{Y}(t))\int_{D_a}\tilde{p}_{\mathbf{Y}}(\mathbf{y},t)d\mathbf{y}\end{aligned}\tag{10}$$

Further, if $D_a=D_{fixed}$ and letting $\Delta t\to 0$, Eq. (10) immediately leads to

$$\frac{\partial p_{\mathbf{Y}}(\mathbf{y},t)}{\partial t}+\sum_{l=1}^{m}\frac{\partial\left[p_{Y_l}(y_l,t)A(y_l,t)\right]}{\partial y_l}=-\mathcal{H}(\mathbf{Y}(t))p_{\mathbf{Y}}(\mathbf{y},t)\tag{11}$$

which can be called the probability density evolution equation for probability dissipated system (PDEE-PD) from the state space description. It should be noted that when $\mathbf{Y}(t)\notin D_a$ always holds, $\mathcal{H}(\mathbf{Y}(t))\equiv 0$, meaning a probability preserved system is interested, Eq. (11) reduces to be the classical Liouville equation.

Actually, the PDEE-PD can also be derived directly from the standpoint of Taylor expansion. The state vector at the time instant $t+\Delta t$, namely, $\mathbf{Y}(t+\Delta t)$ can be regarded as

$$\mathbf{Y}(t+\Delta t)=\mathbf{Y}(t)+\mathbf{A}(\mathbf{Y},t)\Delta t+O(\Delta t)\tag{12}$$

Let

$$\tilde{\mathbf{y}}=\mathbf{y}(t+\Delta t)=\mathbf{y}(t)+\mathbf{A}(\mathbf{y},t)\Delta t+O(\Delta t)\tag{13}$$

For a probability dissipated system, the following relationship exists

$$p_{\mathbf{Y}}(\tilde{\mathbf{y}},t+\Delta t)d\tilde{\mathbf{y}}=p_{\mathbf{Y}}(\mathbf{y},t)d\mathbf{y}-\mathcal{H}(\mathbf{Y}(t))\tilde{p}_{\mathbf{Y}}(\mathbf{y},t)\Delta t d\mathbf{y}\tag{14}$$

Differentiating Eq. (13) yields

$$d\tilde{\mathbf{y}}=|J|d\mathbf{y}=\left[1+\sum_{l=1}^{m}\frac{\partial A_l(\mathbf{y},t)}{\partial y_l}\Delta t\right]d\mathbf{y}\tag{15}$$

where J is the Jacobian.

Expanding $p_{\mathbf{Y}}(\tilde{\mathbf{y}},t+\Delta t)$ at $p_{\mathbf{Y}}(\mathbf{y},t)$ gives

$$p_{\mathbf{Y}}(\tilde{\mathbf{y}},t+\Delta t)=p_{\mathbf{Y}}(\mathbf{y},t)+\frac{\partial p_{\mathbf{Y}}(\mathbf{y},t)}{\partial\mathbf{y}}(\tilde{\mathbf{y}}-\mathbf{y})+\frac{\partial p_{\mathbf{Y}}(\mathbf{y},t)}{\partial t}(t+\Delta t-t)+.\tag{16}$$

the first-order approximation of which reads

$$p_{\mathbf{Y}}\left(\tilde{\mathbf{y}},t+\Delta t\right)=p_{\mathbf{Y}}\left(\mathbf{y},t\right)+\sum_{l=1}^{m}\frac{\partial p_{\mathbf{Y}}\left(\mathbf{y},t\right)}{\partial y_l}\mathbf{A}\left(\mathbf{y},t\right)\Delta t+\frac{\partial p_{\mathbf{Y}}\left(\mathbf{y},t\right)}{\partial t}\Delta t \tag{17}$$

Substituting Eqs. (15) and (17) into Eq. (14), we have

$$\begin{aligned}&\left[p_{\mathbf{Y}}\left(\mathbf{y},t\right)+\sum_{l=1}^{m}\frac{\partial p_{\mathbf{Y}}\left(\mathbf{y},t\right)}{\partial y_l}\mathbf{A}\left(\mathbf{y},t\right)\Delta t+\frac{\partial p_{\mathbf{Y}}\left(\mathbf{y},t\right)}{\partial t}\Delta t\right]\left[1+\sum_{l=1}^{m}\frac{\partial A_l\left(\mathbf{y},t\right)}{\partial y_l}\Delta t\right]d\mathbf{y}\\&=p_{\mathbf{Y}}\left(\mathbf{y},t\right)d\mathbf{y}-\mathcal{H}\left(\mathbf{Y}(t)\right)\tilde{p}_{\mathbf{Y}}\left(\mathbf{y},t\right)\Delta t d\mathbf{y}\end{aligned} \tag{18}$$

Expanding Eq. (18) goes to

$$\begin{aligned}&\left\{p_{\mathbf{Y}}\left(\mathbf{y},t\right)+\left[\sum_{l=1}^{m}\frac{\partial p_{\mathbf{Y}}\left(\mathbf{y},t\right)}{\partial y_l}\mathbf{A}\left(\mathbf{y},t\right)+\frac{\partial p_{\mathbf{Y}}\left(\mathbf{y},t\right)}{\partial t}+\sum_{l=1}^{m}\frac{\partial A_l\left(\mathbf{y},t\right)}{\partial y_l}p_{\mathbf{Y}}\left(\mathbf{y},t\right)\right]\Delta t\right\}d\mathbf{y}+O\left(\Delta t\right)\\&=p_{\mathbf{Y}}\left(\mathbf{y},t\right)d\mathbf{y}-\mathcal{H}\left(\mathbf{Y}(t)\right)\tilde{p}_{\mathbf{Y}}\left(\mathbf{y},t\right)\Delta t d\mathbf{y}\end{aligned} \tag{19}$$

Omitting the high order term of Δt and letting $\Delta t\to 0$, we have ,

$$\frac{\partial p_{\mathbf{Y}}\left(\mathbf{y},t\right)}{\partial t}+\sum_{l=1}^{m}\frac{\partial p_{\mathbf{Y}}\left(\mathbf{y},t\right)}{\partial y_l}\mathbf{A}\left(\mathbf{y},t\right)+\sum_{l=1}^{m}\frac{\partial A_l\left(\mathbf{y},t\right)}{\partial y_l}p_{\mathbf{Y}}\left(\mathbf{y},t\right)=-\mathcal{H}\left(\mathbf{Y}(t)\right)p_{\mathbf{Y}}\left(\mathbf{y},t\right) \tag{20}$$

where the relationship in Eq. (6) is actually embedded when $\Delta t\to 0$. Rearranging Eq. (20) gives

$$\frac{\partial p_{\mathbf{Y}}\left(\mathbf{y},t\right)}{\partial t}+\sum_{l=1}^{m}\frac{\partial\left[p_{\mathbf{Y}}\left(\mathbf{y},t\right)A_l\left(\mathbf{y},t\right)\right]}{\partial y_l}=-\mathcal{H}\left(\mathbf{Y}(t)\right)p_{\mathbf{Y}}\left(\mathbf{y},t\right) \tag{21}$$

It should be noted Eq. (21) is a multiple-dimensional partial differential equation, which is impractically solvable due to the coupling of all the state variables. When randomness is involved in, say, the excitation, the corresponding governing PDEE-PD can also be derived similarly. Besides, it is worth pointing out that probability dissipation is associated closely with the dynamical system, that is, the probability dissipation must relate to a specific physical mechanism.

2.2 Probability density evolution equation for probability dissipated system from the random event description

The stochastic dynamic system can also be represented as

$$\dot{\mathbf{Y}}=\mathbf{A}\left(\mathbf{Y},\boldsymbol{\Theta},t\right) \tag{22}$$

where $\boldsymbol{\Theta}=\left(\Theta_1,\Theta_2,...,\Theta_s\right)$ are the random variables involved in the external excitation, the system parameters and the initial conditions.

A random event description of Eq. (22), say the solution to Eq. (22) is unique, existent and continuously dependent on $\boldsymbol{\Theta}$, can be employed

$$Y_l\left(t\right)=H_l\left(\boldsymbol{\Theta},t\right);\qquad l=1,2,...,m \tag{23}$$

where Y_l is the lth component of $\mathbf{Y}$ and the velocity is given by

$$\dot{Y}_l\left(t\right)=h_l\left(\boldsymbol{\Theta},t\right);\qquad l=1,2,...,m \tag{24}$$

It is noted that all the randomness involved in $Y_l(t)$ comes from $\boldsymbol{\Theta}$, and the joint PDF of the augmented system $\left(Y_l(t),\boldsymbol{\Theta}\right)$ can be represented as $p_{Y_l\boldsymbol{\Theta}}\left(y_l,\boldsymbol{\theta},t\right)$. The dissipated probability can be expressed as

$$\delta P=-\mathcal{H}\left(Y_l(t)\right)\left[\int_{\Omega_l\times\Omega_{\boldsymbol{\Theta}}} p_{Y_l\boldsymbol{\Theta}}\left(y_l,\boldsymbol{\theta},t\right)dy_l d\boldsymbol{\theta}\right] \tag{25}$$

Likewise, the average joint PDF during the time interval $\left[t,t+\Delta t\right]$ is

$$\tilde{p}_{Y_l\boldsymbol{\Theta}}\left(y_l,\boldsymbol{\theta},t\right)=\frac{p_{Y_l\boldsymbol{\Theta}}\left(y_l,\boldsymbol{\theta},t\right)}{\Delta t} \tag{26}$$

and

$$\lim_{\Delta t\to 0}\tilde{p}_{Y_l\boldsymbol{\Theta}}\left(y_l,\boldsymbol{\theta},t\right)=p_{Y_l\boldsymbol{\Theta}}\left(y_l,\boldsymbol{\theta},t\right) \tag{27}$$

Therefore, the dissipated probability can be rewritten as

$$\delta P=-\mathcal{H}\left(Y_l(t)\right)\left[\int_{\Omega_l\times\Omega_{\boldsymbol{\Theta}}} \tilde{p}_{Y_l\boldsymbol{\Theta}}\left(y_l,\boldsymbol{\theta},t\right)\Delta t dy_l d\boldsymbol{\theta}\right] \tag{28}$$

Likewise, $Y_l(t+\Delta t)$ can be transformed from $Y_l(t)$

$$Y_l\left(t+\Delta t\right)=Y_l\left(t\right)+H_l\left(\boldsymbol{\Theta},t\right)\Delta t+O\left(\Delta t\right) \tag{29}$$

and the joint PDF of $\left(Y_l\left(t+\Delta t\right),\boldsymbol{\Theta}\right)$ is denoted as $p_{Y_l\boldsymbol{\Theta}}\left(\tilde{y}_l,\tilde{\boldsymbol{\theta}},t+\Delta t\right)$, where

$$\tilde{y}_l=y_l\left(t+\Delta t\right)=y_l\left(t\right)+h_l\left(\boldsymbol{\theta},t\right)\Delta t+O\left(\Delta t\right) \tag{30}$$

$$\tilde{\boldsymbol{\theta}}=\boldsymbol{\theta}\left(t+\Delta t\right) \tag{31}$$

Following a process analogous to Eq. (16), we have

$$\begin{aligned} &p_{Y_l\boldsymbol{\Theta}}\left(\tilde{y}_l,\tilde{\boldsymbol{\theta}},t+\Delta t\right)\\ &=p_{Y_l\boldsymbol{\Theta}}\left(y_l,\boldsymbol{\theta},t\right)+\frac{\partial p_{Y_l\boldsymbol{\Theta}}\left(y_l,\boldsymbol{\theta},t\right)}{\partial y_l}\left(\tilde{y}_l-y_l\right)+\frac{\partial p_{Y_l\boldsymbol{\Theta}}\left(y_l,\boldsymbol{\theta},t\right)}{\partial\boldsymbol{\theta}}\left(\tilde{\boldsymbol{\theta}}-\boldsymbol{\theta}\right)\\ &\quad+\frac{\partial p_{Y_l\boldsymbol{\Theta}}\left(y_l,\boldsymbol{\theta},t\right)}{\partial t}\left(t+\Delta t-t\right)\\ &=p_{Y_l\boldsymbol{\Theta}}\left(y_l,\boldsymbol{\theta},t\right)+\frac{\partial p_{Y_l\boldsymbol{\Theta}}\left(y_l,\boldsymbol{\theta},t\right)}{\partial y_l}\left(h_l\left(\boldsymbol{\theta},t\right)\Delta t+O\left(\Delta t\right)\right)+\frac{\partial p_{Y_l\boldsymbol{\Theta}}\left(y_l,\boldsymbol{\theta},t\right)}{\partial t}\Delta t \end{aligned} \tag{32}$$

where $\dot{\boldsymbol{\Theta}}$ is time invariant, thus, $\tilde{\boldsymbol{\theta}}-\boldsymbol{\theta}=0$. Eq. (32) can further be represented to be

$$p_{Y_l\boldsymbol{\Theta}}\left(\tilde{y}_l,\tilde{\boldsymbol{\theta}},t+\Delta t\right)=p_{Y_l\boldsymbol{\Theta}}\left(y_l,\boldsymbol{\theta},t\right)+\frac{\partial p_{Y_l\boldsymbol{\Theta}}\left(y_l,\boldsymbol{\theta},t\right)}{\partial y_l}h_l\left(\boldsymbol{\theta},t\right)\Delta t+\frac{\partial p_{Y_l\boldsymbol{\Theta}}\left(y_l,\boldsymbol{\theta},t\right)}{\partial t}\Delta t \tag{33}$$

where the high-order term of Δt is omitted.

For a probability dissipated system during the time interval $\left[t,t+\Delta t\right]$, there exists

$$p_{Y_l\boldsymbol{\Theta}}\left(\tilde{y}_l,\tilde{\boldsymbol{\theta}},t+\Delta t\right)d\left(\tilde{y}_l,\tilde{\boldsymbol{\theta}}\right)=p_{Y_l\boldsymbol{\Theta}}\left(y_l,\boldsymbol{\theta},t\right)d\left(y_l,\boldsymbol{\theta}\right)-\mathcal{H}\left(Y_l(t)\right)\tilde{p}_{Y_l\boldsymbol{\Theta}}\left(y_l,\boldsymbol{\theta},t\right)\Delta t d\left(y_l,\boldsymbol{\theta}\right) \tag{34}$$

where

$$d\left(\tilde{y}_l,\tilde{\boldsymbol{\theta}}\right)=\left|J\right|d\left(y_l,\boldsymbol{\theta}\right)=\left[\frac{\partial\left(\tilde{y}_l,\tilde{\boldsymbol{\theta}}\right)}{\partial\left(y_l,\theta_j\right)}\right]dy_l \qquad j=1,2,...,s \tag{35}$$

s is the total number of random variables involved in $\boldsymbol{\theta}$. It is proved that $\left|J\right|=1$.

Substituting Eq. (33) into Eq. (35) and letting $\Delta t\to 0$, we have

$$\frac{\partial p_{Y_l\boldsymbol{\Theta}}\left(y_l,\boldsymbol{\theta},t\right)}{\partial t}+h_l\left(\boldsymbol{\theta},t\right)\frac{\partial p_{Y_l\boldsymbol{\Theta}}\left(y_l,\boldsymbol{\theta},t\right)}{\partial y_l}=-\mathcal{H}\left(Y_l(t)\right)p_{Y_l\boldsymbol{\Theta}}\left(y_l,\boldsymbol{\theta},t\right) \tag{36}$$

which can be called the generalized density evolution equation for probability dissipated system (GDEE-PD) from the random event description. It is noted that the GDEE-PD is a one-dimensional partial differential equation relevant with the concerned physical quantity, the solution to which is easy to obtain. In addition, different physical mechanism can be introduced to trigger the probability dissipation, such as

$$\frac{\partial p_{Y_l\boldsymbol{\Theta}}\left(y_l,\boldsymbol{\theta},t\right)}{\partial t}+h_l\left(\boldsymbol{\theta},t\right)\frac{\partial p_{Y_l\boldsymbol{\Theta}}\left(y_l,\boldsymbol{\theta},t\right)}{\partial y_l}=-\mathcal{H}\left(Z(t)\right)p_{Y_l\boldsymbol{\Theta}}\left(y_l,\boldsymbol{\theta},t\right) \tag{37}$$

where $Z(t)$ is the interested physical quantity that results in probability dissipation. This characteristic provides a possibility to investigate different kinds of reliability /failure probability problems in engineering, in which each specific failure mechanism can be treated as the driven force of probability dissipation and the remaining probability is the reliability of need.

For instance, if one is interested in the probability of strength failure, $Z(t)$ can be adopted as the stress at the key section or the displacement; if the reliability of stability is of great concern, $Z(t)=S\left(t\right)$ where $S\left(t\right)$ is the stability function that identifies the stability state of structures[10] and $S\left(t\right)\geq 0$ indicates dynamic stability of structures; moreover, some complex failure mode, e.g. the stable strength failure with consideration of instability can also be introduced to trigger the corresponding probability dissipation and investigate the failure probability, the GDEE-PD for which could be expressed as

$$\frac{\partial p_{Y_l\boldsymbol{\Theta}}\left(y_l,\boldsymbol{\theta},t\right)}{\partial t}+h_l\left(\boldsymbol{\theta},t\right)\frac{\partial p_{Y_l\boldsymbol{\Theta}}\left(y_l,\boldsymbol{\theta},t\right)}{\partial y_l}=-\left\{\left[1-\mathcal{H}\left(S(t)\right)\right]\cdot\mathcal{H}\left(Y_l(t)\right)\right\}p_{Y_l\boldsymbol{\Theta}}\left(y_l,\boldsymbol{\theta},t\right) \tag{38}$$

where

$$\mathcal{H}\left(S(t)\right)=\begin{cases}0 & S\left(t\right)\geq 0\\ 1 & S\left(t\right)<0\end{cases} \tag{39}$$

herein, only if $S(t)\geq 0$ and $Y_l(t)$ is in the failure domain (probability dissipation domain) $\left\{\left[1-\mathcal{H}\left(S(t)\right)\right]\cdot\mathcal{H}\left(Y_l(t)\right)\right\}=1$ manifests the probability dissipation occurs when the strength criterion is violated on the premise that the structure keeps stable.

Under the initial condition

$$p_{Y_l\boldsymbol{\Theta}}\left(y_l,\boldsymbol{\theta},t\right)\Big|_{t=t_0}=\delta\left(y_l-y_{l,0}\right)p_{\boldsymbol{\Theta}}\left(\boldsymbol{\theta}\right) \tag{40}$$

the GDEE-PD can be solved, and the remaining probability after the probability dissipation is

$$R(t)=\int_{-\infty}^{+\infty}\int_{\Omega_{\Theta}} p_{Y_l\Theta}(y_l,\boldsymbol{\theta},t)dy_l d\boldsymbol{\theta} \tag{41}$$

and the reliability is the remaining probability at the final time instant.

3. Illustrating Example

A 17-storey controlled frame structure is adopted to illustrate the GDEE-PD for evaluating the reliability or the failure probability. The equation of motion can be expressed as

$$\mathbf{M}\ddot{\mathbf{Y}}(t)+\mathbf{C}\dot{\mathbf{Y}}(t)+\mathbf{K}\mathbf{Y}(t)=\mathbf{F}(t)+\mathbf{s}(t) \tag{42}$$

where $\mathbf{M}$, $\mathbf{C}$ and $\mathbf{K}$ are the 17×17 mass, damping and stiffness matrices, respectively, the mass and the stiffness of each storey are denoted as m and k, which are normal random variables; $\mathbf{Y}(t)$, $\dot{\mathbf{Y}}(t)$ and $\ddot{\mathbf{Y}}(t)$ are the 17×1 displacement, velocity and acceleration vectors; $\mathbf{F}(t)$ is the 17×1 external excitation vector; $\mathbf{s}(t)$ denotes the 17×1 control force vector; Rayleigh damping is adopted as $\mathbf{C}=\beta_1\mathbf{M}+\beta_2\mathbf{K}$; the visco-elastic damper described by the fractional model are deployed between the 0-1, 1-2, 2-3, 5-6, 10-11, 12-13, 14-15, 15-16 storey, where the control force of each damper $f_i(t)$ can be expressed as

$$f_i(t)=k_{ve}Y_i(t)+c_{ve}D^{\alpha}\langle Y_i(t)\rangle \tag{43}$$

where $D^{\alpha}\langle\cdot\rangle$ is the fractional derivative operator, k_{ve} and c_{ve} are the controller parameters, respectively.

The stochastic external excitation is assumed to be

$$\mathbf{F}(t)=-\mathbf{M}\mathbf{I}\xi_1\ddot{x}_{El\_NS}(t) \tag{44}$$

where $\ddot{x}_{El\_NS}(t)$ denotes the El centrol acceleration(N-S component), ξ_1 is the amplitude of the ground motion, which is a random variable with normal distribution, $\mathbf{I}=(1,1,\ldots,1)^T$ is the 17×1 column vector.

The parameters of the system are listed in Table 1.

Table 1 The parameters

Parameter	m	k	β_1	β_2	α	k_{ve}	c_{ve}	ξ_1
Mean	19300kg	897064kN/m	0.0093	0.1006	0.55	35000kN/m	63000kNs/m	3
C.O.V.	0.2	0.2	0	0	0	0	0	0.2

note: C.O.V stands for coefficient of variation for short.

The stochastic dynamic response analysis is firstly performed by PDEM, where the probabilistic response of the top displacement is shown in Figure 1. Correspondingly, the remaining probabilistic response after the probability dissipation, which is governed by the GDEE-PD, is depicted in Figure 2 when the probability dissipated condition is adopted as

$$|Y_{17}(t)|<0.40m \tag{45}$$

where $\left|Y_{17}(t)\right|$ is the top displacement.

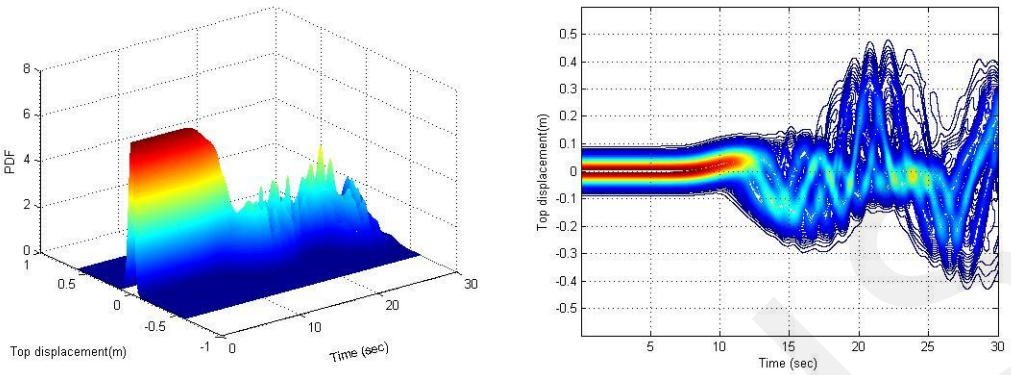

(a) PDF surface (b) PDF contour

Figure 1 PDF evolution of probability preserved system

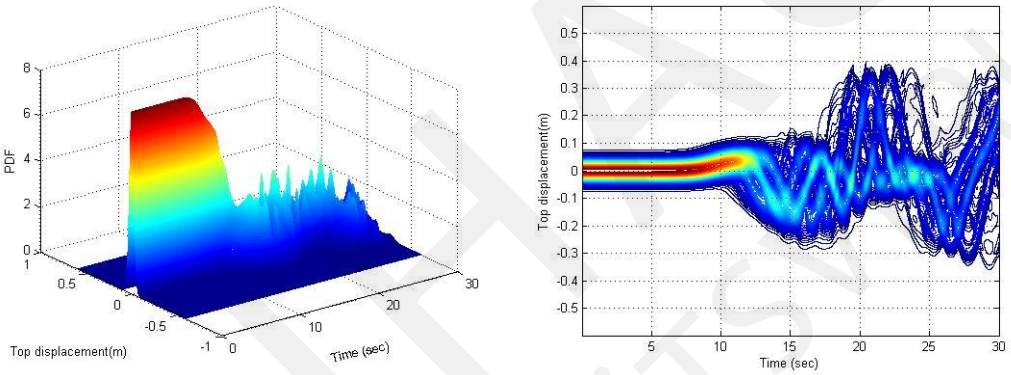

(a) PDF surface (b) PDF contour

Figure 2 PDF evolution of probability dissipated system

It is seen from the comparison that the probability dissipation has a strong influence on the evolutionary PDF, where the distribution range of the PDF after the probability dissipation is obviously narrower and the peak value is lower than those of the probability preserved system, shown in Figure 3.

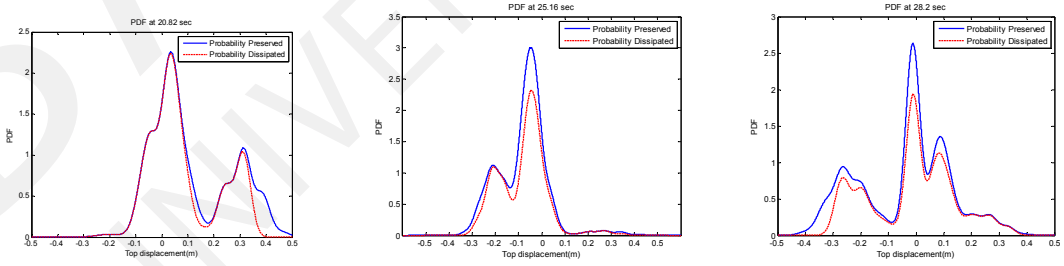

(a) 20.82 s (b) 25.16 s (c) 28.2 s

Figure 3 Typical PDFs at three time instants

Taking an integral over the remaining evolutionary PDFs after the probability dissipation gives the remaining probabilities at each time instant. In this case, the remaining probability at the end is the dynamic reliability when the probability dissipated condition is adopted as the safety criterion, which is pictured in Figure 4.

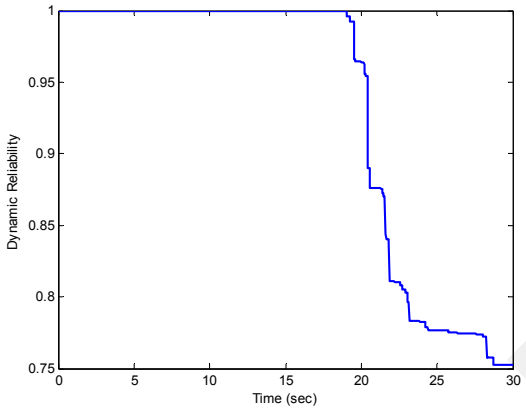

Figure 4 Dynamic reliability assessment

By using the probability dissipated system, the reliability of dynamic stability of structures can also be assessed. In this example, the time delay $\tau = 0.05s$ is considered in the controller, which may have a deleterious effect on the stability of the controlled structure. A newly developed energetic criterion for identifying dynamic instability of structures is employed as the physical mechanism for triggering the probability dissipation, thus, the remaining probability is the reliability of dynamic stability. Figure 5 pictures two typical samples of the top displacement together with the corresponding stability function process. It is seen that dynamic instability of the controlled structure is inevitable due to the time delay inherent in the controllers.

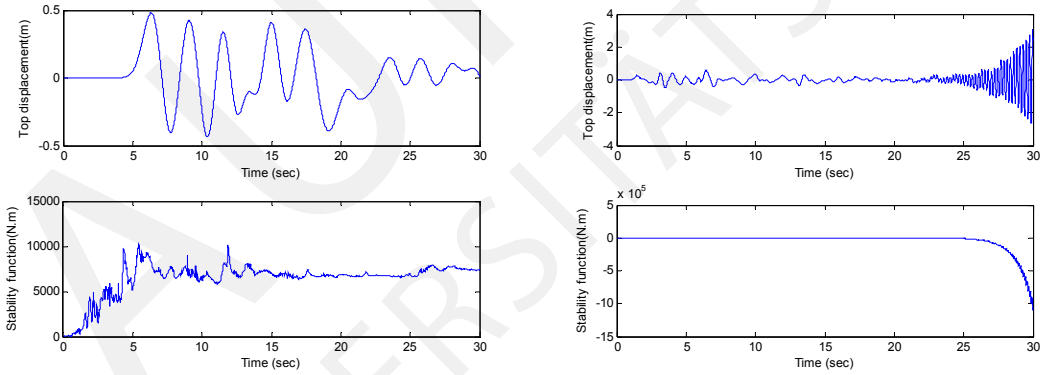

(a) stable motion (b) Unstable motion

Figure 5 Typical samples of the controlled structure with time delay

The remaining PDF evolution contour of the top displacement after the instability induced probability dissipation is shown in Figure 6(a). Clearly, the time delay in the controller even deteriorates the structural performance when the structure is of stability. Consequently, the remaining probability is the reliability of dynamic stability, as is shown in Figure 6(b). Further, the strength failure mechanism in the stable domain can also be introduced to study the probability of strength failure with consideration of dynamic instability of structures. Similarly, the probability evolution contour of the top displacement after the probability dissipation can be obtained via GDEE-PD, which is depicted in Figure 7(a) when $\left|Y_{17}(t)\right| < 0.40m$ is taken as the strength criterion in the stable domain, and the failure probability of losing strength is

the dissipated probability pictured in Figure 7(b). Compared to Figure 4, it is noted that the failure probability increases when the structure is stable because of the time delay effect in the controller. Therefore, the reliability of dynamic stability and the failure probability provides a comprehensive probabilistic understanding of the controlled structure with time delay.

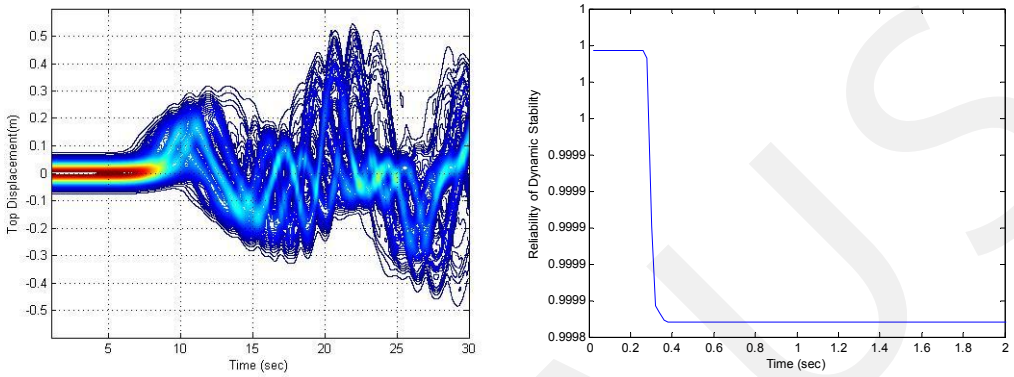

(a) Remaining PDF contour (b) Reliability of dynamic stability

Figure 6 Probability dissipation of instability induced probability dissipation

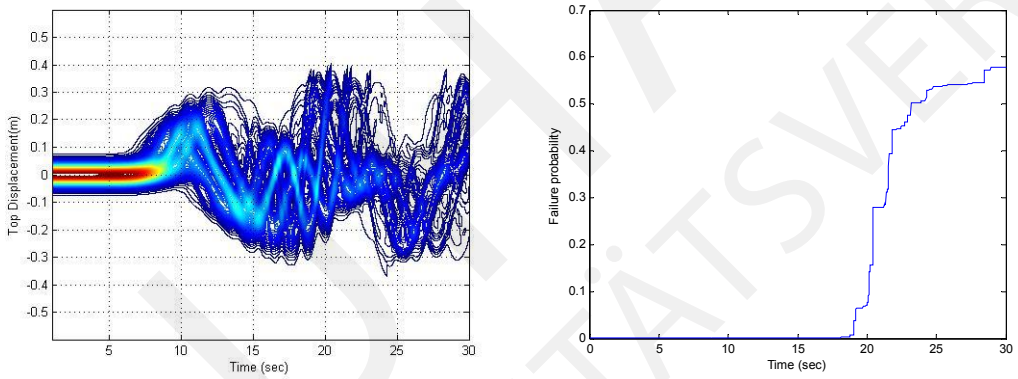

(a) Remaining PDF contour (b) Failure probability

Figure 7 Probability dissipation of strength failure in the stable domain induced probability dissipation

4. Concluding Remarks

In the present paper, the probability density evolution equations for the probability dissipated system are derived according to state space description and random event description of the principle of preservation of probability, respectively. It is demonstrated that the GDEE-PD is able to capture the instantaneous PDF evolutionary process of any concerned physical quantity after probability dissipation, where different physical mechanisms of structural failure can be introduced as the triggering forces of probability dissipation. The reliability or the failure probability is then evaluated straightforwardly by integrating the remaining PDF evolutionary process. This allows us to ensure the structural safety in a probabilistic way with consideration of many different failure modes by applying the probability density evolution equation for probability dissipated system.

Acknowledgement

The supports of the National Natural Science Foundation of China (Grant Nos. 51261120374 and 91315301), the State Key Laboratory of Disaster Reduction in Civil Engineering and the China Scholarship Council are highly appreciated.

Reference:

[1] Syski, R. Stochastic differential equations. in *Modern nonlinear equations* 1967, McGrawHill. chapter 8

[2] Fokker, A. Die mittlere energie rotierender elektrischer dipole im strahlungsfeld. Annalen der Physik, 1914, Vol.348(5):810-820.

[3] Plank, M. Ueber einen satz der statistichen dynamik und eine erweiterung in der quantumtheorie. Journal, 1917:324-341.

[4] Kolmogoroff, A. Über die analytischen methoden in der wahrscheinlichkeitsrechnung. Mathematische Annalen, 1931, Vol.104(1):415-458.

[5] Dostupov, B., Pugachev, V. The equation for the integral of a system of ordinary differential equations containing random parameters. Automatika i Telemekhanika, 1957, Vol.18:620-630.

[6] Chen, J.-B., Li, J. A note on the principle of preservation of probability and probability density evolution equation. Probabilistic Engineering Mechanics, 2009, Vol.24(1):51-59.

[7] Li, J., Chen, J.B. The principle of preservation of probability and the generalized density evolution equation. Structural Safety, 2008, Vol.30(1):65-77.

[8] Li, J., Chen, J.B. Stochastic dynamics of structures. John Wiley & Sons, 2009.

[9] Korn, G., Korn, T. Mathematical handbook for scientists and engineers, 1968. McGraw-HillNew York:23-24.

[10] Xu, J., Li, J. An energetic criterion for dynamic instability of structures under arbitrary excitations. International Journal of Structural Stability and Dynamics, Vol.15(2): doi: 10.1142 /S02194 55 414500436.

The effect of load on the spatial variability of soil properties

Pengtao Zhu[1*], **Maximilian Huber**[2+], **Karl-Josef Witt**[1**]

[1]Bauhaus-Universität Weimar,
Coudraystrasse 11c, 99423, Weimar, Germany
[*]pengtao.zhu@uni-weimar.de
[**]kj.witt@uni-weimar.de
[2]Deltares, Delft, The Netherlands
[+]maximilian.huber@deltares.nl

Abstract: The spatial correlation length of soil properties is an important parameter to quantify the inherent spatial variability of soil. Since void ratio is a key parameter of soil, the effect of loading on the spatial correlation length of void ratio based on the Monte Carlo simulation was investigated. Firstly, 1D random fields of void ratio with a specific correlation length were generated using the Markov correlation function. Secondly, we simulated a loading process by using an advanced constitutive model and analysed the changes in the pattern of the random fields by means of geostatistical approaches. The results show a decrease of the spatial correlation with increasing load. The results of this concept shows good results and contributes to the explanation of spatial variability of soil properties due to loading and unloading cycles.

Keyword: correlation length; hypoplasticity; spatial soil variability; soil heterogeneity

1 Introduction

Soils are geological materials formed by weathering, erosion and sedimentation processes and, save for residual soils, transported by physical means to their present locations. They have been subjected to various stresses, pore fluids, and physical and chemical changes. Thus, it is hardly surprising that the physical properties of soils vary from place to place [11, 16]. These variations are known as uncertainty. The uncertainties and their importance in natural soil have long been appreciated. Although it is truly difficult to embrace uncertainty directly and easily due to its complexity in geotechnical issues, great efforts have been undertaken in this area. Uncertainty in geotechnical engineering can be categorized into epistemic and aleatoric uncertainty [10]. Epistemic uncertainty consists of model uncertainty and measurement uncertainty while aleatoric uncertainty consists of physical uncertainty, which is also known as inherent uncertainty; it is a natural randomness of a quantity, which cannot be reduced by increasing site investigation [6]. The spatial correlation of soil properties is referred in standard geotechnical and geostatistical literature as correlation length, as explained in Huber [11].

While emphasizing the importance of soil variability and spatial soil variability [12], various researchers [11, 14] quantify the correlation length using in-situ experiments. It is proven in various studies that the horizontal spatial correlation length can be separated from the vertical spatial correlation length [11, 15], this is taken into account in different

studies [9, 11]. Amongst others, Fenton & Griffiths [7] use the Random Finite Element Method (RFEM) to quantify the effect of changing spatial correlation length in various standard geotechnical problems. However, the effects of a loading process on the spatial correlation of soil properties have not been investigated according to the knowledge of the authors, which is in the focus of this contribution.

2 Methodology

We employ different techniques form geostatistics, mathematics and soil mechanics to study the effects of a loading process on the spatial correlation of soil properties. Herein, we use the Random Finite Element Method for the simulation of the effects of spatial correlated soil properties; the non-linear soil behaviour is considered by an advanced constitutive model.

2.1 Simulation of non-linear soil behaviour

We model the soil behaviour by an advanced constitutive model. The hypoplastic model is a constitutive soil model developed for granular materials based on hypoplasticity theory [3, 8].

It is an eight-parameter model with void ratio a state variable, given in equation (1).

$$\mathring{\boldsymbol{\sigma}} = f_s[\mathbf{L}(\hat{\boldsymbol{\sigma}}, \mathbf{D}) + f_d \mathbf{N}(\hat{\boldsymbol{\sigma}}) \|\mathbf{D}\|] \tag{1}$$

Herein $\mathring{\boldsymbol{\sigma}}$ is the stress ratio, the scalar factors f_s and f_d take into account the influence of mean pressure and density, $\mathbf{D}$ is the stretching ratio. The forth order tensor $\mathbf{L}$ is linear with respect to $\mathbf{D}$, the second order tensor $\mathbf{N}$ is non-linear with respect to $\mathbf{D}$, and $\hat{\sigma} = \sigma / \mathrm{tr}\,(\sigma)$.

2.2 Random Finite Element Method

The Random Finite Element Method (RFEM) is a robust method for the quantification of the effects of spatially distributed properties in engineering. Fenton & Griffiths [7] have applied this to various non-linear problems in geotechnical engineering.

For this reason, we use RFEM to study the effects of loading on the spatial correlation of soil properties. We use random fields, which are generated by the well-known Cholesky decomposition [4], for the representation of the void ratio, a key parameter in the description of soil behaviour. The spatial correlation of the void ratio is described by a spherical correlation function. Theses random fields are used as input in a non-linear finite element calculation.

2.3 Evaluation of the change in the spatial dependence

After each step in loading we analyse the spatial dependence of the void ratio. Following standard geostatistical textbooks [4], we use the correlation length to quantify this spatial dependence. The correlation length is the distance within which the property values have a relatively strong correlation. We use the experimental variogram given in equation 2 to derive the correlation length.

$$\gamma(\mathbf{h}) = \frac{\mathbf{1}}{\mathbf{2}\ n\,(\mathbf{h})} \sum [\mathbf{z}(\mathbf{x}) - \mathbf{z}(\mathbf{x}+\mathbf{h})]^{\mathbf{2}} \tag{2}$$

where $n(\mathbf{h})$ is the count of pairs of points separated by the mutual distance $\mathbf{h}$ between the property values $z(\mathbf{x})$ at the location $\mathbf{x}$.

We use the well-known weighted least squares methodology to calculate the correlation lengths in order to compare the results of the experimental variograms. Apart from this, we chose the weighted least squares fitting of different theoretical variograms to the experimental variograms [5]. By using the theoretical variogram, we weight the values of the variogram near the origin provide more important information [2] than the other values and the precision of the variogram decreases with an increase of the distance. Three commonly used theoretical variogram models are used for this issue. The spherical model, exponential model and Gaussian model are given in equation 3, 4 and 5.

$$\gamma_z(\mathbf{h}) = \begin{cases} c_0[\frac{3}{2}\frac{\mathbf{h}}{a_0} - \frac{1}{2}(\frac{\mathbf{h}}{a_0})^3] & \text{for } \mathbf{h} \leq \mathbf{a_0} \\ c_0 & \text{for } \mathbf{h} > a_0 \end{cases} \tag{3}$$

$$\gamma_z(\mathbf{h}) = c_0 \left[\mathbf{1} - \exp\left(-\frac{\mathbf{h}}{a_0}\right)\right] \tag{4}$$

$$\gamma_z(\mathbf{h}) = c_0 \left[\mathbf{1} - \exp\left(-\frac{\mathbf{h^2}}{{a_0}^{\mathbf{2}}}\right)\right] \tag{5}$$

We use N, $N/\mathbf{h^2}$, $N/(\gamma(\mathbf{h}))^{\mathbf{2}}$ as weights for the weighted least squares fitting of the theoretical variograms; herein, is N the number of point pairs, h the distance and $\gamma(\mathbf{h})$ the semivariogram.

We use the Akaike information criterion (AIC) [1] to verify the best weight and the most appropriate theoretical variogram model. The AIC provides a means for model selection through evaluating the relative quality of statistical models, for a given set of data. It is defined by a finite sample set n:

$$\mathrm{AIC} = n \cdot \ln(L) + 2 \cdot k \tag{6}$$

where k is the number of parameters used in the statistical model and L is the maximum value of the likelihood function for the estimated model. AIC measures the loss of information caused by fitting an incorrect model to the data. Therefore given a set of different models for the data, the best model has the minimum AIC value. The AIC can be rewritten for a fitting by the weighted least square method.

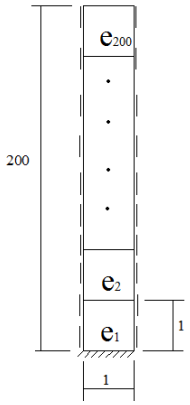

Figure 1: Discretisation of the one-dimensional FEM subsoil model.

$$\mathrm{AIC} = n \cdot \ln(\frac{\mathrm{WRSS}}{n} + 2k) \tag{7}$$

The weighted residual sum of the squares (WRSS) is:

$$\mathrm{WRSS} = \sum_{i=1}^{n} w_i^2 \left(\hat{\gamma}\left(\mathbf{h_i}\right) - \gamma\left(\mathbf{h_i}\right)\right)^2 \tag{8}$$

where $\hat{\gamma}\left(\mathbf{h_i}\right)$ is the semivariance estimate of the theoretical semivariance $\gamma\left(\mathbf{h_i}\right)$ at the i^{th} mutual distance.

3 Case study

3.1 Random Finite Element Method

We investigate the proposed methodology on a one dimensional model. The model is a 200 m deep weightless sand slice with a width of 1 m as is shown in figure 1. It is equally divided into 200 square elements with a length of 1 m; every square will be assigned a void ratio which is from a random field. Then a pressure will be put on the top of the sand slice, and the Gudehus-Bauer hypoplastic model is used here to simulate the loading process. We list the parameters of this model in table 1.

The random fiels represent the void ratio $\mathrm{e_{d0}}$ and have a mean value $\mu = 0.7$ m, standard deviation $\sigma = 0.1$ m and correlation length $= 10$ m are generated within a Matlab environment using Cholesky decomposition. The correlation length follows an exponential variogam model.

Table 1: Input parameters of the hypoplastic model.

$\varphi_c(^\circ)$	$h_s(MPa)$	n	α	β	e_{i0}	e_{d0}	e_{c0}
22.6	659	0.214	0.45	2	1.20	0.30	0.82

Table 2: Mean AIC values from different theoretical variogram models and different weights.

	spherical variogram	exponential variogram	Gaussian variogram
N	-147.7	-155.6	-137.9
$N/(\gamma(\mathbf{h}))^\mathbf{2}$	808.6	780.4	1043.8
$N/(\mathbf{h})^\mathbf{2}$	**-556.9**	**-560.7**	-480.0

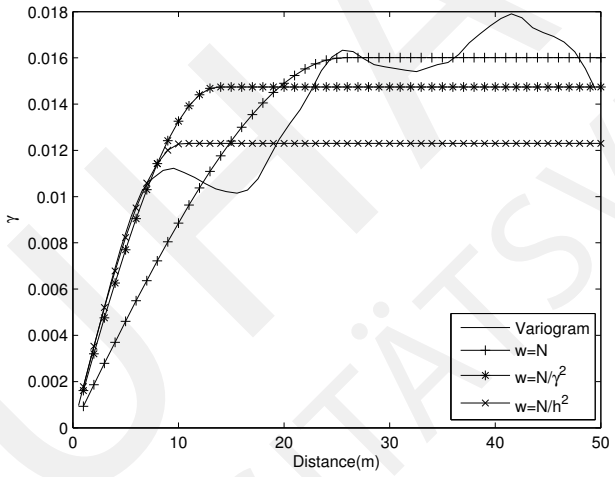

Figure 2: Comparison of the using different weights for WLS fitting of three theoretical variograms.

3.2 Analysing the RFEM results

3000 original void ratio data sets are used here in order to get the mean value of AIC. Table 2 is the result of the mean AIC from different weights of the weighted least square method and different theoretical variogram models.

The spherical model with $w = N/h2$ is adopted because it fits the slope near the origin best as is seen in Figure 2, compared with the other models and weights, and the AIC value from spherical model ($w = N/h^2$) does not differ too much compared with the least value which is from exponential model ($w = N/h^2$).

We use the software libary R with the GSTAT [13] package to calculate the experimental

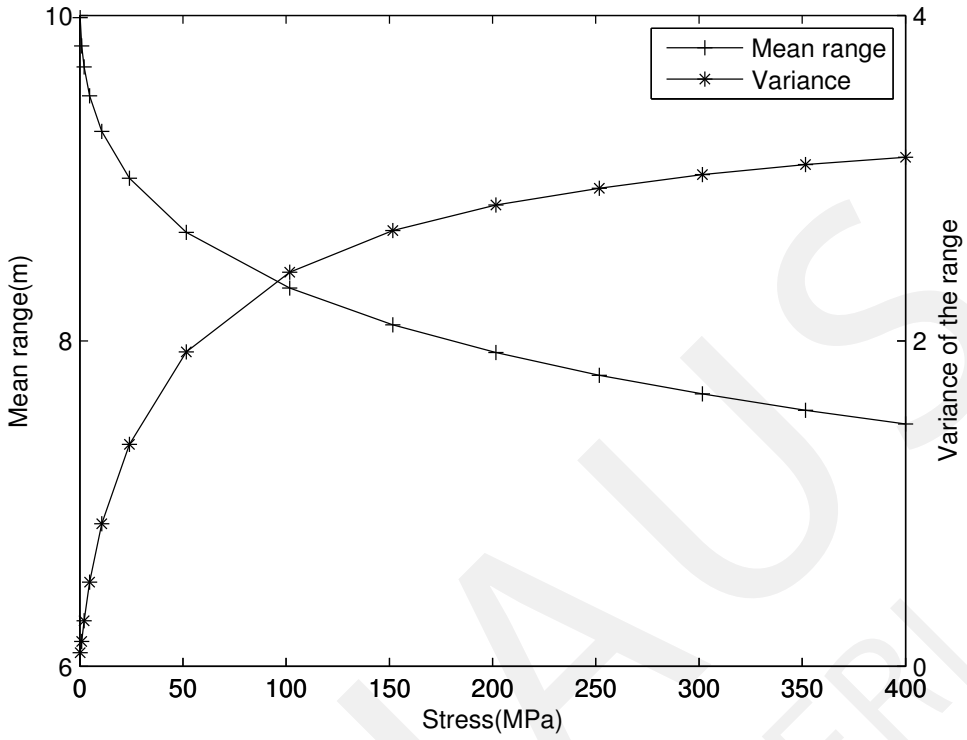

Figure 3: Mean value and variance of the correlation length for different stress levels.

variogram and to fit the theoretical variogram.

The relation between the stress and both the mean range, and the variance of the range can be seen from figure 3. It is clearly that the mean correlation length (mean range) of soil void ratio decreases as the increase of the stress during loading with a log-normal distribution given in figure 4. When a stress of $\sigma = 25$ MPa is putting on the top of soil, the correlation length reduces quickly from $\theta = 10$ m to approximately $\theta = 9$ m, then the reduction becomes smaller and smaller as the increase of stress; on the contrary, the variance of the range increases with stress. The correlation length of void ratio has a small variance ($\sigma_\theta^2 = 0.0834$) for low stress($\sigma = 0$ MPa) levels compare to higher stress levels ($\sigma = 0$ MPa). As the stress increase, we find that the correlation length for the void ratio decrease quickly from $\theta = 10$ m at $\sigma = 0$ MPa to about $\sigma_\theta^2 = 3.5$ m at $\sigma = 400$ MPa, while some correlation lengths change only a little bit, what is more, some correlation lengths even increase with stress in figure 4. At a load level of $\sigma = 400$ MPa, the resulting correlation length range from $\theta = 3.48$ m to 19.74 m with a variance of $\sigma_\theta^2 = 3.13$ m, which implies the correlation lengths after compression have a big fluctuation. From this we can conclude that the variance of correlation length increases with stress.

4 Summary and conclusions

In this contribution we study the effects of loading on the spatial soil variability. We demonstrate in a simplified case study that the correlation length of void ratio decreases

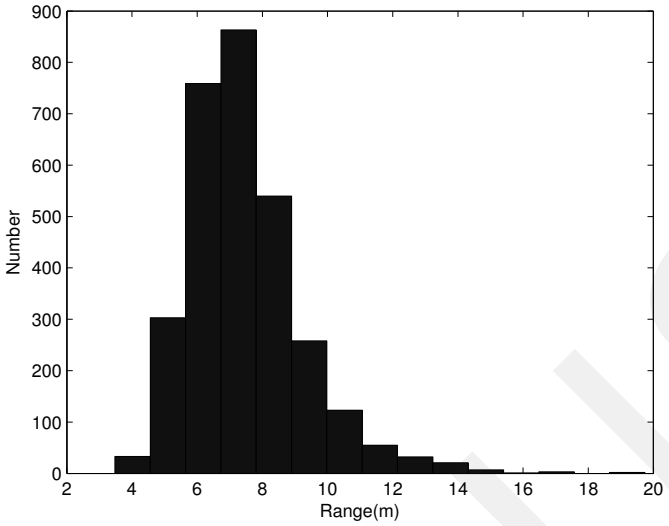

Figure 4: Histogram of the correlation length of the void ratio at the stress levels $\sigma = 400$ MPa.

with the increase of stress during loading, while the variance of the correlation length increases with increasing stress.

As far as the geotechnical properties of natural layers are concerned, we can derive from this that the vertical correlation length of the void ratio decreases with the level of stress, i. e. with the depth under the surface.

Of course, the stress level changes not only the void ratio, but also the other soil properties like density, permeability, stiffness and strength. We believe that the correlation lengths of these parameters should be changed by loading too, which needs to be investigated in further studies.

Due to the rather small changes of the correlation length due to loading, the effects in static geotechnical problems in the ultimate and serviceability state are expected to be rather small. Therefore, the main focus of future research efforts will investigate dynamical problems like e.g. a dynamically loaded footing. The power of the changing spatial patterns of soil properties will have a significant contribution to describing soil behaviour more accurate.

References

[1] H. Akaike. Information theory and an extension of the maximum likelihood principle. In *Selected Papers of Hirotugu Akaike*, pages 199–213. Springer, 1998.

[2] M. Armstrong. *Basic linear geostatistics.* Springer, 1998.

[3] E. Bauer. Calibration of a comprehensive hypoplastic model for granular materials. *Soils and Foundations*, 36(1):13–26, 1996.

[4] J.-P. Chiles and P. Delfiner. *Geostatistics: modeling spatial uncertainty*, volume 497. John Wiley & Sons, 2009.

[5] N. Cressie. Fitting variogram models by weighted least squares. *Journal of the International Association for Mathematical Geology*, 17(5):563–586, 1985.

[6] D. J. DeGroot and G. B. Baecher. Estimating autocovariance of in-situ soil properties. *Journal of Geotechnical Engineering*, 119(1):147–166, 1993.

[7] G. Fenton and D. Griffiths. *Risk assessment in geotechnical engineering*. John Wiley & Sons, 2008.

[8] G. Gudehus. A comprehensive constitutive equation for granular materials. *Soils and Foundations*, 36(1):1–12, 1996.

[9] M. A. Hicks and K. Samy. Influence of heterogeneity on undrained clay slope stability. *Quarterly Journal of Engineering Geology and Hydrogeology*, 35(1):41–49, 2002.

[10] Y. Honjo. Challenges in geotechnical reliability based design. In *Proceedings from the 3rd International Symposium on Geotechnical Safety and Risk*, pages 11–27, 2011.

[11] M. Huber. *Soil variability and its consequences in geotechnical engineering*. PhD thesis, Institute of Geotechnical Engineering, University of Stuttgart, 2013.

[12] F. Kulhawy, K. Phoon, and W. Prakoso. Uncertainty in the basic properties of natural geomaterials. In *Proc. 1st Intl. Conf. Geotech. Engrg. Education and Training*, pages 297–302, 2000.

[13] E. J. Pebesma. Gstat user manual. *Dept. of Physical Geography, Utrecht University, Utrecht, The Netherlands*, 2001.

[14] K.-K. Phoon. *Reliability-based design of foundations for transmission line structures*. PhD thesis, Cornell University, 1995.

[15] K.-K. Phoon and F. H. Kulhawy. Characterization of geotechnical variability. *Canadian Geotechnical Journal*, 36(4):612–624, 1999.

[16] K. J. Witt. *Grundbau-Taschenbuch: Teil 1: Geotechnische Grundlagen*. John Wiley & Sons, 2009.

Publications in the Series of the Research Training Group 1462

Speakers
Univ.-Prof. Dr. Ing. habil. T. Schanz (2007-2008)
Univ.-Prof. Dr. Ing. habil. F. Werner (2008-till know)

Disclosures of the Research Training Group 1462 "Evaluation of Coupled Numerical Partial Models in Civil Engineering" (2007 – 2012)

Issue 1: M.M. Zimmerer (2010)

Identifikation konstitutiver Parameter von weichen feinkörnigen Böden - Beitrag zum Konsolidationsverhalten von Ton

Issue 2: H. Keitel (2011)

Evaluation Methods for Prediction Quality of Concrete Creep Models

Issue 3: M. C. Reuter (2012)

Multicriterial evaluation method for the prognosis quality of complex engineering models

Issue 4: G. Karaki (2011)

Assessment of coupled models of bridges considering time-dependent vehicular loading

Issue 5: S. Nikulla (2012)

Quality assessment of kinematical models by means of global and goal-oriented error estimation techniques

Issue 6: T. Fröbel (2012)

Data coupled civil engineering applications: Modeling and quality assessment methods

Issue 7: P. Stein (2012)

Procedurally generated models for Isogeometric Analysis

Issue 8: M. Nasser (2012)

Quality Assessment of Dynamic Soil-Structure Interaction Models Using Energy Measures

Disclosures of the Research Training Group "Evaluation of Coupled Numerical and Experimental Partial Models in Civil Engineering" (2013 - 2017)

Issue 9: Dr. Ing. T. Most (2013)

Effiziente Methoden zur Analyse des Einflüsses von Unsicherheiten in komplexen Ingenieurmodellen

Issue 10: Dr. Ing. F. Wuttke: (2014)

Mehrphasensysteme in der Geotechnik - Experiment und Simulation

Issue 11: T. Lahmer, M. Huber, D. Proske, T. Most und F. Werner (Editors) (2014)

Proceedigs of the 12th International Probabilistic Workshop, November 4.-5., 2014.